SEE Proceedings

18-20 November 2020
Kyoto, Japan

Edited by
Zakaria Hossain

ISBN: 978-4-909106056 C3051

SEE 2020, KYOTO, JAPAN
STRUCTURE, ENGINEERING AND ENVIRONMENT

PROCEEDINGS OF SIXTH INTERNAONAL CONFERENCE – SEE 2020
STRUCTURE, ENGINEERING & ENVIRONMENT KYOTO, JAPAN 18-20 NOVEMBER, 2020

Structure, Engineering and Environment

Edited by

Prof. Zakaria Hossain
Graduate School of Bioresources
Mie University, Japan

THE GEOMATE INTERNATIONAL SOCIETY

Published by:
The GEOMATE International Society
Tsu city, Mie, Japan
E-mail: society@geomate.org
http://www.geomate.org/

ISBN Number: 978-4-909106056 C3051

Table of Contents

Preface

On behalf of the SEE 2020 Organizing Committee, it is our great pleasure to welcome you to the Sixth International Conference on Structure, Engineering & Environment, held at Kyoto Research Park, Kyoto, Japan organized in conjunction with Mie University Research Center for Environmental Load Reduction, The GEOMATE International Society, Useful Plant Spread Society, Glorious International, AOI Engineering, HOJUN, JCK, CosmoWinds and Beppu Construction, Japan.

The conference covers three major themes with many specific themes including:

Advances in Building Structure
Advances in Infrastructures
Advances in Civil Engineering
Advances in Structural Engineering
Advances in Geological Engineering
Advances in Geometics Engineering
Advances in Chemical Engineering
Advances in Environmental Engineering
Advances in Geotechnical Engineering
Advances in Architectural Engineering
Advances in Industrial Engineering
Advances in Manufacturing Engineering
Advances in Materials Engineering
Advances in Mechanical Engineering
Advances in Petroleum Engineering
Advances in Process Engineering
Advances in Environmental Technology
Advances in Geophysics
Advances in Hydrology
Advances in Recycle Solid Wastes
Advances in Use of reclaimed Waters
Advances in Water Distribution
Advances in Water Treatment
Advances in Irrigation and Drainage
Advances in Farm Structures

Due to COVID-19, this year we have received less submissions from different countries all over the world. The technical papers were selected from the vast number of contributions submitted after a review of the abstracts. The final papers in the proceedings have been peer reviewed rigorously and revised as necessary by the authors. It relies on the solid cooperation of numerous people to organize a conference of this size. Hence, we appreciate everyone who support as well as participate in the joint conferences.

Last but not least, we would like to express our gratitude to all the authors, session chairs, reviewers, participants, institutions and companies for their contribution to SEE 2020. We hope you enjoy the conference onsite and ZOOM online and find this experience inspiring and helpful in your professional field. We look forward to seeing you at our upcoming conference next year.

Best regards,

Prof. Dr. Zakaria Hossain, Chairman

Organization

Scientific Committees:

Honorary Chairman: Dr. Sohji Inoue, E/Prof. Mie University, Japan
Conference Chairman: Dr. Zakaria Hossain, Prof. Mie University, Japan

Conference Organizing Committee:

Dr. Zakaria Hossain, Prof. Mie University, Japan (Chair)
Dr. Satoshi Kaneco, Prof., Mie University, Japan (Co-Chair)
Dr. Sohji Inoue, E/Prof. Mie University, Japan (Co-Chair) Dr.
Toshinori Sakai, Prof. Mie University, Japan (Co-Chair) Dr.
Takamitsu Kajisa, Prof. Mie University, Japan (Co-Chair)
Dr. Masaaki Kondo, A/Prof. Mie University, Japan (Co-Chair)

National & International Advisory Committee:

Dr. Fumio Tatsuoka, Prof., Tokyo University of Science, Japan
Dr. Junichiro Takeuchi, Prof., Kyoto University, Japan
Dr. Kingshuk Roy, Prof., Nihon University, Japan
Dr. Nakib Dan Khan, A/Prof. Mie University, Japan
Dr. Sai Vanapalli, Prof., University of Ottawa, Canada
Dr. Musharraf Zaman, Prof. Univ. of Oklahama, USA
Dr. Rafiqul Tarefder, Prof. University of New Mexico, USA
Dr. M. Bouassida, Prof., National Sch. of Engg. of Tunis Dr.
L.R. Austriaco, Prof., Angles Univ. Found., Philippines Dr.
A.S.M. Abdul Awal, Prof., Univ. Technology Malaysia
Dr. M. Ibn Ibrahimy, Prof., Int. Islamic Univ., Malaysia
Dr. Mohammad Shariful Islam, Prof., BUET, Bangladesh.
Dr. Bujang B.K. Huat, Prof., Univ. Putra Malaysia
Dr. Nemy Banthia, Prof., UBC, Canada
Dr. Ian Jefferson, Prof., Univ. of Birmingham, UK
Dr. John Bolander, Prof., Univ. of California, USA
Dr. Shamsul Chowdhury, Prof., Roosevelt Univ., USA
Dr. Isabel Pinto, Prof., University of Coimbra, Portugal
Dr. Mark Jaksa, Prof., University of Adelaide, Australia
Dr. Jim Shiau, A/Prof., USQ, Australia
Dr. Hj. Ramli Bin Hj. Nazir, A/Prof., UTM, Malaysia
Dr. H.M. Shahin, Prof., Islamic University of Technology, Bangladesh
Dr. Md. Ariful Islam, A/Prof. Dhaka University, Bangladesh
Dr. Md. Nurul Amin, Prof. Dhaka University, Bangladesh
Dr. D.K. Chauhan, Prof. Noida International Univ., India
Dr. Chan Chee-Ming, A/Prof. Universiti Tun Hussein Onn Malaysia
Dr. Ahmed H. A. Dabwan, A/Prof. TATI Univ. College, Malaysia

International Technical Program Committee:

Prof. Adolf Heinrich Horn, Geological Institute - Federa University of Minas Gerais, Brazil
Prof. Bang-Fuh Chen, National Sun Yat-sen University, Taiwan
Prof. Bindeshwar Singh, Kamla Nehru Institute of Technology, India
Prof. Catherine Mulligan, Concordia Institute of Water, Energy and Sustainable Systems, Canada
Prof. Chi-Min Liu Chienkuo Technology University, Taiwan
Prof. Daffalla Rabih, Kenana Sugar Company, Sudan
Prof. Essaid Bilal, Ecole Nationale Superieure Des Mines De Saint Etienne, France
Prof. Hakan Caliskan, Usak University, Faculty of Engineering, Turkey
Prof. Ibrahim Maiyza, National Institute of Oceanography & Fisheries, Egypt
Prof. Loc Nguyen, Sunflower Soft Company, Vietnam
Prof. Marilia Hagen, Indiana University, United States
Prof. Md Najib bin Ibrahim, Universiti Teknologi MARA, Malaysia
Prof. Md. Abdul Baset Mia, BSMR Agri. Univ., Bangladesh
Prof. Mihaela Popescu, University of Craiova, Romania
Prof. Mohamed Abdou, Faculty of Education Department of Mathematics, Egypt
Prof. Mohamed Tahiri, Présidnce de l'Université Hassan II de Casablanca, Morocco
Prof. Nazar Oukaili, University of Baghdad, Iraq
Prof. Radim Cajka, Technical University Ostrava, Faculty of Civil Engineering, Czech Republic
Prof. Rajaraman Jambunathan, AMET University, India
Prof. Saad Farhan Ibrahim Alabdullah, University of Almustansiriyah, Iraq
Prof. Salem Alsanusi, Benghazi, Libya
Prof. Sudhir Kumar Das, Retired Senior Project Manager of Indian Railways, India
Prof. Zachary Senwo, Alabama A&M University, United States
Prof. Imed Jabri, University of Tunis, Tunisia
A/Prof. Bindeshwar Singh Kamla Nehru Institute of Technology, India
A/Prof. Hasi Rani Barai, Yeungnam University, South Korea
A/Prof. Jamaluddin Mahmud, Universiti Teknologi MARA, Malaysia
A/Prof. Mohamed Ramadan, University of Hail, Saudi Arabia
A/Prof. Najam Hasan, Dhofar University, Oman
A/Prof. Nosina Krishna Chaitanya, Jawaharlal Nehru Technological University, India
A/Prof. Nurbek Saparkhojayev, Almaty Management University, Kazakhstan
A/Prof. Pandian Vasant, Universiti Teknologi Petronas, Malaysia
A/Prof. Teodor Lucian Grigorie, University of Craiova, Romania
A/Prof. Zawawi Daud, Universiti Tun Hussein Onn Malaysia
A/Prof. Abdull Halim Abdul, OIl and Gas department, Malaysia
A/Prof. Baoping Cai, China University of Petroleum, China
A/Prof. Dariusz Jakóbczak, Koszalin University of Technology, Poland
A/Prof. Edgar Allan Mendoza, University of the Philippines
A/Prof. Lakhveer Singh, Universiti Malaysia Pahang (UMP) Malaysia, Malaysia
A/Prof. Lidia Sas Paszt, Research Institute of Pomology, Poland
A/Prof. Mahmood Barbooti, University of Yechnology, Iraq
A/Prof. Majid Mirzaei, Universiti Tunku Abdul Rahman, Malaysia
A/Prof. Najeh Lakhoua, University of Carthage, Tunisia
A/Prof. Ryan Joseph Calinao, Lyceum of the Philippines University-Laguna
A/Prof. Sarawut Thepanondh, Mahidol University, Thailand
A/Prof. Yasir Al Hussein, Jerash University, Faculty of Engineering, Jordan
A/Prof. Grigorie Teodor Lucian, University of Craiova, Romania
A/Prof. Hêriş Golpîra, Islamic Azad University, Sanandaj, Iran
A/Prof. Muhammad Aslam, King Abdulaziz University, Saudi Arabia
A/Prof. Tomasz Plech, Medical University of Lublin, Poland
A/Prof. Fellah Mamoun, Abbes laghrour University, Algeria
A/Prof. R. S. Ajin, GeoVin Solutions Pvt. Ltd., India
A/Prof. Roman Szewczyk, Industrial Research Institute for Automation and Measurements, Poland

Dr. Abolghasem Akbari, University Malaysia Pahang, Malaysia
Dr. Ahmad Safuan A Rashid, Universiti Teknologi Malaysia, Malaysia
Dr. Akinola Johnson Olarewaju, Federal Polytechnic Ilaro, Ogun State, Nigeria
Dr. Alexandre Costa, Federal University of the valleys of Jequitinhonha and Mucuri, Brazil
Dr. Angelo Gallone, Scotland's Rural College (SRUC), United Kingdom
Dr. Azizul Azhar Ramli, Universiti Tun Hussein Onn Malaysia
Dr. Bashir Dar, University of kashmir Delina Baramulla J&K India, India
Dr. Bassam Abdellatif, National Authority for Remote Sensing and Space Sciences, Egypt
Dr. Binh Phu Nguyen, National University of Singapore, Singapore
Dr. Cazacu Gabriela, S.C. Geotech Dobrogea, Romania
Dr. Chengen Yang, Intel Corporation, United States
Dr. Dayang Norulfairuz Abang Zaidel, Universiti Teknologi Malaysia
Dr. Evgeni Starikov, KIT, Karlsruhe, Germany; Chalmers, Gothenburg Sweden, Germany
Dr. Fatma Khanchel, University of Tunis El Manar, Tunisia
Dr. Hamidreza Khataee, Griffith University, Australia
Dr. Hêriș Golpîra, Islamic Azad University, Iran
Dr. Iskhaq Iskandar, Dept. Physics, University of Sriwijaya, Indonesia
Dr. Jingwei Zhao, University of Wollongong, Australia
Dr. Jitendra Agrawal, Rajiv Gandhi Proudyogiki Vishwavidyalaya, India
Dr. Liza Patacsil, Malayan Colleges Laguna, Philippines
Dr. Mohamed Amine, Ferrag Guelma University, Algeria
Dr. Mohd Afendi Rojan, Universiti Malaysia Perlis, Malaysia
Dr. Mohd Altaf, University of kashmir Delina Baramulla J&K India, India
Dr. Mohd Hairy Ibrahim, Sultan Idris Education University, Malaysia
Dr. Mostafa Khater, Egypt - El sharqia - Zagazig, Egypt
Dr. Najam Hasan, Dhofar University, Oman
Dr. Namir Alkawaaz, University of Almustansiriyah, Iraq
Dr. Nashrul Fazli Mohd Nasir, Universiti Malaysia Perlis, Malaysia
Dr. NaufaL Mansor Kampus Uniciti Alam, Universiti Malaysia Perlis (UniMAP), Malaysia
Dr. Obed Majeed Ali, Northern Technical University, Iraq
Dr. Piyapong Janmaimool, King Mongkhut' University of Technology, Thailand
Dr. Po-Sheng Chiu, National Cheng Kung University, Taiwan
Dr. Prabu Mohandas, Adhiyamaan College of Engineering, India
Dr. Raman Kumar, D A V Institute of Engineering and Technology, India
Dr. Riccardo Colella, University of Salento, Italy
Dr. Rolando Javellonar, Romblon State University, Philippines
Dr. Shikha Agrawal, Rajeev Gandhi Technical University, India
Dr. Stefania Tomasiello CORISA, University of Salerno, Italy
Dr. Sumiyyah Sabar, Universiti Sains Malaysia, Malaysia
Dr. Suphaphat Kwonpongsagoon, Mahidol University, Thailand
Dr. Wei Hong Tan, Universiti Malaysia Perlis, Malaysia
Dr. Yoshiro Fujii, Shin Kobe Dental Clinic, Japan
Dr. Yuk Feng Huang, Universiti Tunku Abdul Rahman (UTAR), Malaysia
Dr. Zongyan Zhou, Monsh University, Australia
Dr. Purnanand Savoikar, Goa Engineering College, India
Dr. Ahmed Toaha Mobashsher, University of Queensland, Australia
Dr. Chupong Pakpum, Maejo University
Dr. Emanuele Quaranta, Politecnico di Torino, Italy
Dr. Jiangling Yin, Apple Inc., Cupertino, CA, United States
Dr. Khor Shing Fhan, Universiti Malaysia Perlis, Malaysia
Dr. Mario Chauca, Ricardo Palma University, Peru
Dr. Santosh Gaikwad, Model College, Ghansawangi, India
Dr. Tse Guan Tan, Universiti Malaysia Kelantan
Dr. Vikas Panthi, National Institute of Technology, India
Dr. Watoo Phrompittayarat, Naresuan University, Thailand

Dr. Hamidreza Namazi, Nanyang Technological University, Singapore
Dr. Parichat Phumkhachorn, Ubon Ratchathani University, Thailand
Dr. Subhasis Roy, University of Calcutta, India

Conference Correspondence:

Prof. Dr. Zakaria Hossain (Director)
Dept. of Environmental Science and Technology, Mie University, Japan
Mr. Md. Aminul Islam (Secretary)
Dept. of Environmental Science and Technology, Mie University, Japan
E-mail: conference@geomate.org
Tel & Fax: +81-59-231-9578

Editorial and Executive Committee:

Prof. Dr. Zakaria Hossain
Engr. Alex Otieno Owino
Engr. Md. Aminul Islam
Ms. Najmun Nahar
Mr. Sayful Kabir Khan
Mr. Jamie Ovia

Technical Papers

Structure

6th Int. Conf. on Structure, Engineering & Environment (SEE), Kyoto, Japan, Nov.18-20, 2020, ISBN: 978-4-909106056 C3051

DEFECT DETECTION ON ASPHALT PAVEMENT BY DEEP LEARNING

Jonpaul Nnamdi Opara[1], Aunt Bo Bo Thein[2], Shota Izumi[3], Hideaki Yasuhara[4] and Pang-Jo Chun[5]
[1,2,3,4] Graduate School of Science and Engineering, Ehime University, Japan; [5] School of Engineering, The University of Tokyo, Japan

ABSTRACT

The importance of road infrastructure to the economy of any nation cannot be overemphasized, however, it is not easy to maintain it properly. Since the inspection of pavements is particularly difficult, an efficient inspection method is required. In this study, a method for detecting damage in asphalt pavements was developed using one of the deep learning techniques, YOLOv3. YOLOv3 is a method for detecting the position and type of an object from an input image, which fits the purpose of this study. The developed method can distinguish between longitudinal crack, transverse crack, alligator crack and pothole. In order to confirm the accuracy of the developed method, images of pavements acquired on National Route 4 in Japan are analyzed. From the analysis, it is found that the precision value is 0.7 and average IoU is 50.39%. From the visualization of the analysis results, it was found that this method based on YOLOv3 was able to detect the damage with good accuracy.

Keywords: Asphalt pavement, Deep learning, YOLOv3, Crack detection, Pothole

INTRODUCTION

The importance of road infrastructure to the economy of any nation cannot be overemphasized [1]. Roads are the arteries through which the economy pulses. By linking producers to markets, workers to jobs, students to school, and the sick to hospitals, roads are vital to any development agenda. Countries all over the world are currently finding the path towards attaining the Sustainable Development Goal 9 (SDG9), efficient transportation services are key drivers of economic development [2]. The importance of roads is infinite, but most importantly is how safe the road is and the ease of maintenance. No matter the amount of road constructed, proper maintenance is essential in order for the road to continue to serve its design purpose. In order to achieve this, a robust road management system has become a necessity. Road inspection is one of key processes of a pavement management system, whose function is to examine and describe the road infrastructure condition [3]. If done right, will provide adequate information required to implement a robust and all-encompassing road policy and maintenance schedule.

In Japan for instance, amid the aging of infrastructures, the increase in maintenance and repair expenditures are topics of concern. In a 2016 survey, the total length of road in Japan is about 1,210,000 kilometers and the number of roads that needs maintenance is constantly on the increase [4]. Among those, 77.3% of the total road length is in asphalt concrete structure. It means the inspection and maintenance processes must be cost effective and efficient. In this study, we focus on inspection.

Traditional evaluation method is usually done by a human expert and it is a process that always involves a certain degree of subjective judgment. In order to minimize the subjectivity, save time and labour cost, a computerized system for analysis that automatically evaluates the condition of pavement is desired. Many such studies have been conducted to automatically detect cracks in asphalt pavements (e.g. [5-11]). If we include the detection of damages in concrete or steel structure, there are many papers on this subject including author's researches (e.g. [12-20]). However, considering that almost all of the methods have not yet been put to practical use, we still need to accumulate more research developments. Therefore, in this study, we developed a method for detecting cracks using YOLOv3 [21], which is a deep learning technique to detect the position and type of an object from an input image. Then, images of pavements acquired on National Route 4 in Japan are analyzed to confirm the accuracy of the developed method. We will discuss these in the following chapters.

LITERATURE REVIEW

With a lot of research in developing defect detection and inspection system from the survey database images. Deep learning and AI applications has become vital for maintenance infrastructure management. And lots of advancement is been made in this area especially with the application of computer vision techniques. [22] Identified Faster R-CNN as a better algorithm in terms of speed and proposed a solution to detect road potholes, deep ridges and speed breakers with an R-CNN based model. The proposed approach used the custom-built Bumpy Dataset which was created, both trained model and the dataset used to develop the model

could easily be integrated into an assistive driving technology.[23] made comparative study on automatic asphalt pavement cracks recognition based on image processing and machine learning approaches. Six machine learning approaches, Na¨ıve Bayesian Classifer (NBC), Classifcation Tree (CT), Backpropagation Artifcial Neural Network (BPANN), Radial Basis Function Neural Network (RBFNN), Support Vector Machine (SVM), and Least Squares Support Vector Machine (LSSVM), have been employed. Additionally, Median Filter (MF), Steerable Filter (SF), and Projective Integral (PI) have been used to extract useful features from pavement image.

The findings showed that input pattern including the diagonal PIs enhances the classifcation performance significantly by creating more informative features. LSSVM had the highest classification accuracy, which indicates that machine leaning can in understanding pavement condition properly. Although in this research we dived in deeper, works like this set the bases for more research.

In [24] the authors narrowed down to crack defects on pavement and propose the CrackSeg—an end-to-end trainable deep C-NN for pavement crack detection, that has proven to be effective in achieving pixel-level, and automated detection via high-level features. Novel multiscale dilated convolutional module that can learn rich deep convolutional features was introduced, making the crack features acquired under a complex background more discriminant. Using their own custom CrackDataset to train and evaluate the CrackSeg net the experimental results showed that the CrackSeg can achieve high performance with a precision of 98.00%, recall of 97.85%, F-score of 97.92%, and a mIoU of 73.53%. Comparing this with other state-of-the-art methods, the CrackSeg performs more efficiently, and robustly for automated pavement crack detection and could be deployed for other forms of pavement defects detection.

CRACK DETECTION METHOD

In recent years, many deep learning techniques have been developed. Among them, YOLOv3 is positioned as extremely fast and accurate object detection algorithm. YOLOv3 makes use only features learned by a deep convolutional neural network to detect an object, making it a fully convolutional network (FCN), the algorithm can not only classify objects into a category, but it can also detect multiple objects within an image outputting the 4-coordinate of the bounding boxes for each object.

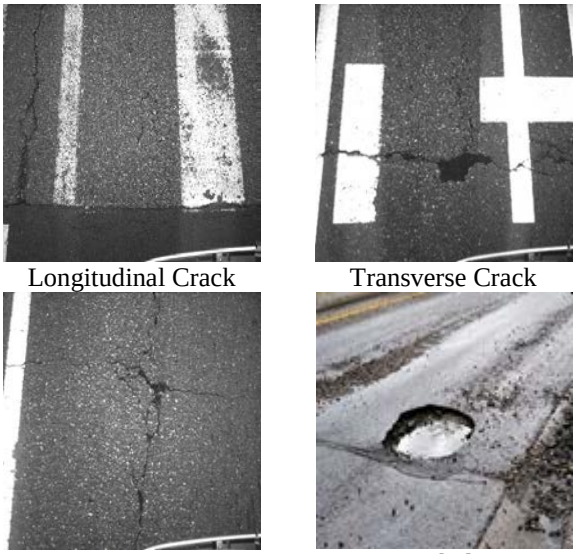

Fig.1 Classes of asphalt pavement defects

Fig.2 Example of annotation with LabelImg

The structure of YOLOv3 is complicated. YOLOv3 uses Residual Blocks which consists of several convolutional layers and shortcut paths for feature learning. It is difficult to train in very deep neural networks because of the vanishing and exploding gradients types of problems. Residual networks known as ResNet which is famous for its short cut connection which is basically the feeding (by summation) of the features from the preceding layers to the next level layers are built by residual blocks. The accuracy of YOLOv3 making use of the residual blocks and ResNet is known to be high. See [21] for a detailed structure and explanation.

In this study, we aimed to detect four types of defects: longitudinal crack, transverse crack, alligator crack and pothole. Examples of each are shown in Fig. 1. YOLOv3 is classified as supervised machine learning, which is a procedure for predicting an output corresponding to a new input based on prior training that uses manually prepared inputs and outputs. In other words, to train the YOLOv3, the

training dataset is required. In this study, the training dataset were made using the annotation tools LabelImg [25]. An example of annotation is shown in Fig.2.

Hyperparameters

Hyperparameters are the variable which control the network architecture and training process of YOLOv3. Hyperparameter can be changed according to the own network architecture. In our defects detection model the hyperparameters are set as below.

In this research, we use the network size of 448 x 448 with 3 channels. The momentum and decay rate are set to 0.9 and 0.005 respectively. Saturation and Exposure are set to 1.5. Learning rate of the YOLOv3 network is set to 0.001 burning in at 1000 training steps. Policy is set up to do in step by step. As our crack detection network has 4 classes, we use the YOLOv3 layers with 27 filters using linear activation function. Ignore threshold is set to 0.7. We use 9 anchors cluster for the network which is calculated by using computing function presented in latest YOLOv3 repository. We adjust the anchors value and test the training. Maximum iteration is set to 20000 iteration. Usually sufficient 2000 iterations for each class (object), but not less than number of training images and not less than 6000 iterations in total. As our network has 4 classes, we only need about 8000 iteration. However, for the better performance and for the research, we train up to 20000 iteration.

DATA COLLECTION

In this research, survey data were taken by survey vehicle called RIM (Road space Information Management system), owned by Obayashi Road Cooperation (Fig. 3). It is a vehicle mounted with the GPS instruments with mobile mapping system MMS with surface recording cameras which collect the road surface information up to mm units in three-dimensional perspective. The RIM vehicles enables highly detailed mapping of roads and high accuracy and excellent positioning, within a short period of time while minimizing nuisance to traffic and risks of accidents. The image data taken by RIM vehicle are 2400 x 2000 pixels images and the light content measurement is in RGB. In this study, the survey data is taken along the Nation Highway Road No.4 inside Tochigi Prefecture.

Fig.3 RIM vehicle owned by Obayashi Road Cooperation

Table 1 The number of images obtained for each class

Defect class	The number of pictures
Transverse crack	1,035
Longitudinal crack	1,676
Alligator crack	672
Pothole	11
No crack	1,968

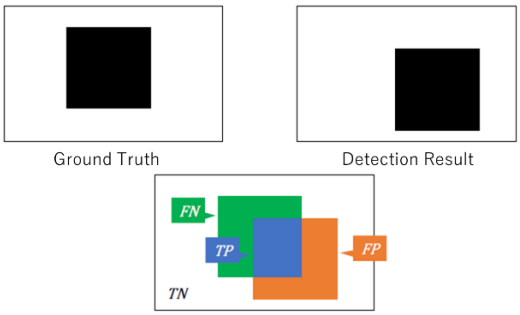

Fig.4 Definition of TP, TN, FP, FN.

Table 1 shows the number of images obtained for each class. Although the number of pot holes is small, it is inevitable because pot holes are quickly repaired in Japan. In the future, more pothole images are required to improve the detection performance of pothole, but the methodology is still under consideration.

CRACK DETECTION BY YOLOV3

Training YOLOv3

In this chapter, we train YOLOv3 using the data collected in the previous chapter. In this study, the ratio of training, validation and test was 7:2:1. In order to prevent overfitting, the training was conducted to the extent that the accuracy of the training dataset and the accuracy of the validation dataset did not deviate.

During the training process, precision, recall, and F1 value of validation dataset are obtained. These indices are defined by the following equations.

$$\text{Precision} = \frac{TP}{TP + FP} \tag{1}$$

$$\text{Recall} = \frac{TP}{TP + FN} \tag{2}$$

$$\text{F1 value} = \frac{2\text{Recall} \times \text{Precision}}{\text{Recall} + \text{Precision}} \tag{3}$$

where TP, TN, FP, FN are defined as like in Fig.4. Fig. 5 shows the changes in these indices with the

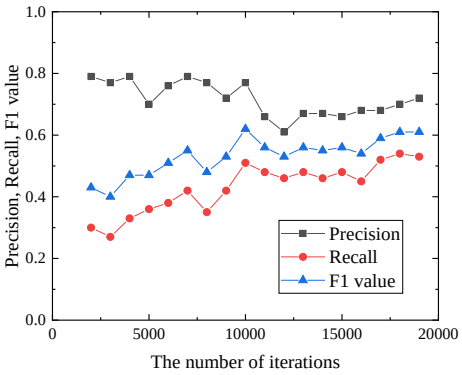

Fig.5 Changes in precision, recall, F1 value.

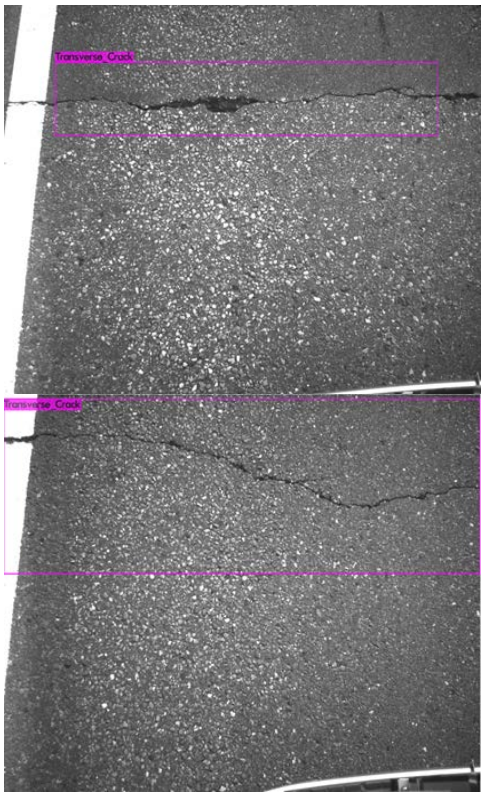

Fig.6 Detection results of transverse crack

number of iteration increases.

According to the results, the maximum value of precision is at iteration 2000 and 7000, that of recall is at iteration 18000, and that of F1 value is almost at iteration 10000, 18000, and 19000. Considering the above, we decided to adopt the model using the results of iteration 18000 as the analysis model.

Analyzing test images

Fig. 6 illustrates some examples of the detection results of transverse crack obtained by applying the proposed method. As in the figures, the transverse cracks are accurately detected. Similarly, longitudinal cracks and alligator cracks are also accurately

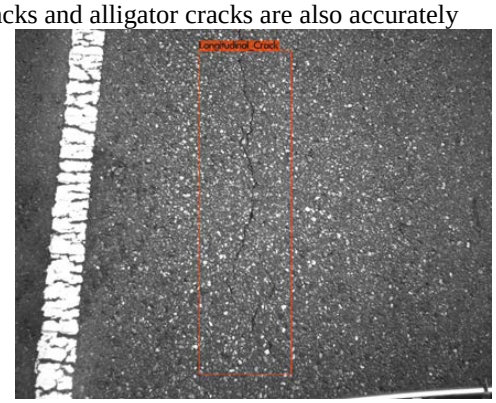

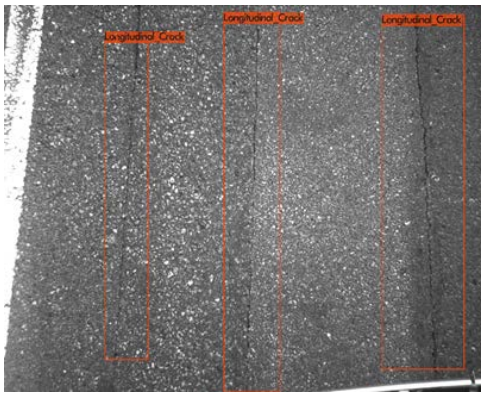

Fig.7 Detection results of longitudinal crack.

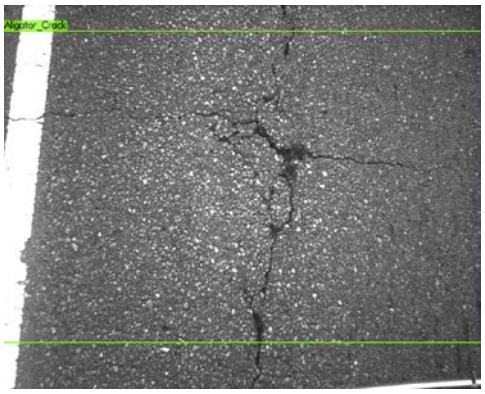

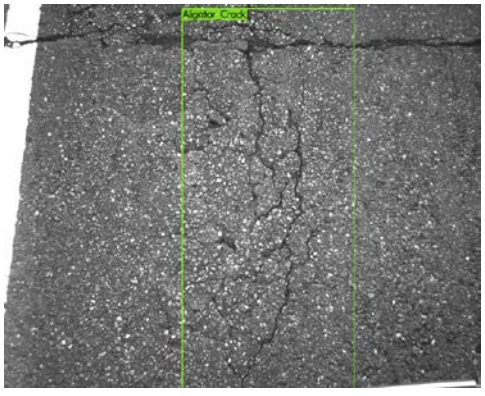

Fig.8 Detection results of alligator crack.

detected as in Fig. 7 and Fig.8, respectively. As for

the pothole, because there was only one test image, it is difficult to say that the accuracy is confirmed. However, the pothole was properly detected on one image as in Fig.9. However, it is needed to examine again after the number of images including pothole increases in future study. Fig. 10 shows an example of the detection results when several types of cracks are present in the same image. The top and middle pictures were properly detected, but the bottom picture was confused between alligator crack and transverse crack. We would like to solve this problem by increasing the amount of data. Nevertheless, this is not a bad result in terms of the detection of cracks. Considering the results from Fig.6 to Fig.9, it can be said that the effectiveness of this method has been proved.

Fig.9 Detection results of pothole.

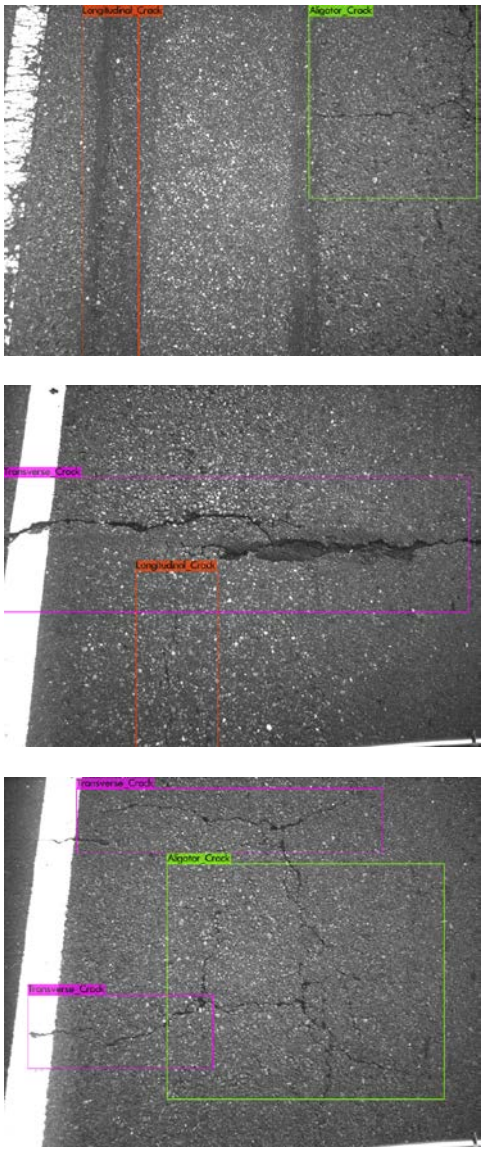

Fig.10 Detection results when multiple types of cracks are in one image.

CONCLUSIONS

This study uses YOLOv3, one of the deep learning techniques, to detect cracks in pavements automatically. In addition, the pavement of the National Road was photographed using RIM and analyzed by YOLOv3 to examine the crack detection performance. As a result, it became clear that the crack could be detected with very high accuracy as shown in Figs. 6 to 10.

Future problems are described below. When there are multiple types of cracks in one image, as shown in the bottom figure in Fig. 10, there is a case in which the exact answer cannot always be obtained. This can be solved by increasing the number of training data. It is also necessary to increase the number of images for the pothole. However, it is generally appropriate as a technique, and it is considered to be one step forward for the practical use.

ACKNOWLEDGMENTS

We would like to take this opportunity to thank Obayashi Road Corporation for taking the image with their RIM.

REFERENCES

[1] Ivanova E., and Masarova J., Importance of road infrastructure in the economic development and competitiveness. Economics and management, Vol. 18, Issue 2, pp.263-274, 2013.

[2] Claudia B., Uwe D., and Harris S., How roads support development, World bank blogs, https://blogs.worldbank.org/developmenttalk/how-roads-support-development (accessed Jun. 29, 2020).

[3] Staniek M., Detection of cracks in asphalt pavement during road inspection processes, Scientific Journal of Silesian University of Technology. Series Transport., Vol. 96, pp.175-184, 2017.

[4] Ministry of Land, Infrastructure, Transport and Tourism, The maintenance of national road network in Japan, https://www.mlit.go.jp/road/road_e/03key_challenges/1-2-2.pdf (accessed Jun.

29, 2020).

[5] Hoang N. D. and Nguyen Q. L., A novel method for asphalt pavement crack classification based on image processing and machine learning. Engineering with Computers, Vol.35, Issue 2, pp.487-498, 2019.

[6] Zhang A., Wang K.C., Fei Y., Liu Y., Chen C., Yang G., Li J., Yang E., and Qiu S., Automated pixel‐level pavement crack detection on 3D asphalt surfaces with a recurrent neural network. Computer‐Aided Civil and Infrastructure Engineering, Vol. 34, Issue 3, pp.213-229, 2019.

[7] Nhat-Duc H., Nguyen Q.L., and Tran V.D., Automatic recognition of asphalt pavement cracks using metaheuristic optimized edge detection algorithms and convolution neural network. Automation in Construction, Vol. 94, pp.203-213, 2018.

[8] Zhang D., Li Q., Chen Y., Cao M., He L., and Zhang B., An efficient and reliable coarse-to-fine approach for asphalt pavement crack detection. Image and Vision Computing, Vol. 57, pp.130-146, 2017.

[9] Zhang L., Yang F., Zhang Y.D., and Zhu Y.J., Road crack detection using deep convolutional neural network. In 2016 IEEE international conference on image processing (ICIP), pp.3708-3712, 2016.

[10] Chun P., Hashimoto K., Kataoka N., Kuramoto N., and Ohga M., Asphalt pavement crack detection using image processing and naive bayes based machine learning approach. Journal of Japan Society of Civil Engineers, Ser. E1 (Pavement Engineering), Vol. 70, No. 3, pp.I_1-I_8, 2015.

[11] Saar T., and Talvik O., Automatic asphalt pavement crack detection and classification using neural networks. In 2010 12th Biennial Baltic Electronics Conference, pp.345-348, 2010.

[12] Zou Q., Zhang Z., Li Q., Qi X., Wang Q., and Wang S., Deepcrack: Learning hierarchical convolutional features for crack detection. IEEE Transactions on Image Processing, Vol.28, Issue 3, pp.1498-1512, 2018.

[13] Chun P., Izumi S., and Yamane T., Automatic detection method of cracks from concrete surface imagery using two-step light gradient boosting machine. Computer-Aided Civil and Infrastructure Engineering, pp.1-12, 2020.

[14] Park S., Ahmad, S., Yun, C. B., and Roh, Y. , Multiple crack detection of concrete structures using impedance-based structural health monitoring techniques. Experimental Mechanics, Vol. 46, Issue 5, pp.609-618, 2006.

[15] Sohn, H. G., Lim, Y. M., Yun, K. H., and Kim, G. H., Monitoring crack changes in concrete structures. Computer-Aided Civil and Infrastructure Engineering, Vol. 20, Issue 1, pp.52-61, 2005.

[16] Chun, P., Ujike, I., Mishima, K., Kusumoto, M., and Okazaki, S., Random Forest-based evaluation technique for internal damage in reinforced concrete featuring multiple nondestructive testing results. Construction and Building Materials, Vol.253, 119238, 2020.

[17] Okazaki, Y., Okazaki, S., Asamoto, S., and Chun, P., Applicability of machine learning to a crack model in concrete bridges. Computer‐Aided Civil and Infrastructure Engineering, 2020.

[18] Chun, P., Yamane, T., Izumi, S., and Kameda, T. , Evaluation of tensile performance of steel members by analysis of corroded steel surface using deep learning. Metals, Vol. 9, Issue 12, pp.1259, 2019.

[19] Chun, P., Tsukada, K., Kusumoto, M., and Okubo, K., Investigation and repair plan for abraded steel bridge piers: case study from Japan. Proceedings of the Institution of Civil Engineers-Forensic Engineering, Vol. 172, Issue 1, pp.11-18, 2019.

[20] Chun, P., Yamane, T., Izumi, S., and Kuramoto, N., Development of a Machine Learning-Based Damage Identification Method Using Multi-Point Simultaneous Acceleration Measurement Results. Sensors, Vol. 20, Issue 10, pp.2780, 2020.

[21] Redmon, J., and Farhadi, A., Yolov3: An incremental improvement. arXiv preprint arXiv:1804.02767, 2018.

[22] Zahid H., Samsoon N., Tasmia R. and Shahnewaz S., Pothole and Speed Breaker Detection Using Smartphone Cameras and Convolutional Neural Networks 2020 IEEE Region 10 Symposium (TENSYMP), 5-7 June 2020, Dhaka, Bangladesh

[23] Nhat-Duc H. and Quoc-Lam N., Automatic Recognition of Asphalt Pavement Cracks Based on Image Processing and Machine Learning Approaches: A Comparative Study on Classifier Performance. Mathematical Problems in Engineering, Vol.2018, Article ID 6290498, 2018.

[24] Weidong S., Guohui J., Hong Zhu , Di J., and Lin G., Automated Pavement Crack Damage Detection Using Deep Multiscale Convolutional Features. Mathematical Problems in Engineering Vol. 2020, Article ID 6412562, 2020.

[25] LabelImg, https://github.com/tzutalin/labelImg (accessed Jun. 29, 2020).

6th Int. Conf. on Structure, Engineering & Environment (SEE), Kyoto, Japan, Nov.18-20, 2020, ISBN: 978-4-909106056 C3051

NONLINEAR SECTIONAL ANALYSIS OF STRUCTURAL CONCRETE MEMBERS OF ARBITRARY SHAPE UNDER CYCLIC LOADING

Ahmed Alkhairo[1], Nazar Oukaili[2], and Riadh Al-Mahaidi[3]
[1]University of Baghdad, Iraq; [2]University of Baghdad, Iraq;[3]Swinburne University of Technology, Australia.

ABSTRACT

This paper presents a new numerical methodology for the analysis of the sectional behaviour of structural concrete members with arbitrary cross-sectional configurations under repeated loading. The proposed methodology is accompanied by computer software written in the Python language to perform the sectional analysis at different loading stages from serviceability to ultimate limit conditions. The software uses a mesh generator to discretise sections of arbitrary shapes, a combination of polygons and circles, into infinitesimal triangles. The contribution of each mesh element is then determined based on the stiffness and the concrete secant modulus of elasticity of that element. The stress-strain concrete model under repeated loading proposed by Karpenko et al. [1] is adopted to calculate the concrete secant modulus of elasticity of each mesh element independently based on the level of stress attained at the start of the unloading and reloading stages. The change in the concrete secant modulus of elasticity is reduced for each cycle until stabilisation is achieved. After each cycle, the deformation (strain and curvature) is calculated. The software is also capable of analysing the beam-column section under biaxial bending moment combined with normal force. It outputs the results in a video format containing all steps of the loading behaviour and plots the moment-curvature relation and the bending-axial force interaction diagram.

Keywords: Stiffness matrix, Constitutive relationship, Strain vector, Secant modulus, Residual strain

INTRODUCTION

Concrete sections are designed to withstand static external loads. Although structural elements, such as bridge girders, most often undergo subsequent loading and unloading stages, most design standards exaggerate the estimated external static loads to account for the repeated load effect. As a result, the cyclic effect may be under-estimated, which in turn causes excessive deformation during service life, or over-estimated, which increases the cost of construction. Therefore, the cyclic effect of structural elements has recently attracted the attention of researchers.

Traditional design methods were developed for manual calculations. However, with current technologies and computer power, more accurate results can be obtained using sophisticated analytical models and repetitive calculation procedures. Although discretised section analysis was developed in the late nineteenth century, it has only been used in recent years due to its long and tedious calculations.

A nonlinear stress-strain relationship developed by Karpenko et al.[2], [3] is adopted in this research. Karpenko et al.'s model can be used to simulate any nonlinear material behaviour by changing specific parameters. Consequently, the stress-strain behaviours of both concrete and steel have been produced using just one pattern with input data specific to each material. The model was further developed by Karpenko et al. [1] to involve the cyclic behaviour of concrete material using linear unloading and reloading relationships. The research reported in this paper investigates the implementation of the repeated loading effect in the sectional analysis of different structural concrete members, including reinforced and prestressed concrete members.

THEORETICAL BACKGROUND

The concept of sectional analysis is mainly dependent on Bernoulli-Navier's assumption that a plane section before deformation remains plane after deformation [4]. Hence, the strain (ε) at any point over the beam section can be expressed by a linear relationship:

$$\varepsilon = \varepsilon_o + \psi_x \times y + \psi_y \times x \qquad (1)$$

where
ε_o: the axial strain magnitude at the reference point,
ψ_x, ψ_y: biaxial bending curvatures, and
x, y: the coordinates of the corresponding point relative to the global coordinates.

For any material, the constitutive relationship can be presented by the modulus of elasticity (E), where:

$$E = \frac{\sigma}{\varepsilon} \quad \Rightarrow \quad \sigma = E \times \varepsilon \qquad (2)$$

The three equations of classical beam theory can be rewritten in a matrix form as follows [5]:

$$\begin{Bmatrix} N \\ M_x \\ M_y \end{Bmatrix} = \begin{bmatrix} \int \sigma \, dA \\ \int \sigma \times y \, dA \\ \int \sigma \times x \, dA \end{bmatrix} \quad (3)$$

Substituting Eq. (1) and Eq. (2) into Eq. (3) and solving the integration by numerical summation results in:

$$\{F\} = [\boldsymbol{C}] \times \{\varepsilon\} \quad (4)$$

$$\begin{Bmatrix} N \\ M_x \\ M_y \end{Bmatrix} = \sum \left(E \times \begin{bmatrix} 1 & y & x \\ y & y^2 & xy \\ x & xy & x^2 \end{bmatrix} \times A \right) \begin{Bmatrix} \varepsilon_o \\ \psi_x \\ \psi_y \end{Bmatrix} \quad (5)$$

where A corresponds to the cross-sectional area of an elementary unit in the section which has a specific material type and (E) is the secant modulus of that material at the given strain vector.

Several models and algorithms have been developed to perform sectional analysis of arbitrary shapes utilising Eq. (5). However, two main approaches have been investigated in the literature, either solving for the load vector or solving for the strain vector. The first approach [6]-[8] involves a given strain magnitude at the reference point and an iterative procedure to calculate the biaxial curvature caused by a given biaxial moment ratio. Therefore, the load vector can be easily obtained from Eq. (5). On the other hand, the second approach [5], [9] adopts an iterative procedure using the Newton-Raphson technique to calculate the strain vector at a given load vector such that:

$$\{\varepsilon\}_i = [\boldsymbol{C}(\{\varepsilon\}_{i-1})]^{-1} \times \{F\} \quad (6)$$

For a given load vector, Eq. (6) can be solved to determine the corresponding strain vector. This calculation requires a repetitive process to find the stiffness matrix of each mesh element based on a strain vector from the previous iteration and numerically summed over all elements. Hence, accurate results depend mainly on the number of mesh elements used to discretise the section. The iterative process continues until an acceptable tolerance of the strain vector between two successive iterations is achieved, as shown in Eq. (7). After convergence is reached, the stress and strain at any point can be calculated using Eqs. (1) and (2).

$$|\varepsilon_i - \varepsilon_{i-1}| \leq given\ tolerance \quad (7)$$

The first approach is recommended when calculating the failure load vector by predicting a vertex in the cross-section of the beam which will fail first, depending on the orientation of the externally-applied moment and the location of the plastic centroid. Solving for the failure load vector is then achieved based on the knowledge that the strain in that vertex is the maximum strain defined by the material stress-strain diagram. Furthermore, the descending part of the moment-curvature diagram can be obtained by increasing the strain vector beyond the maximum strain specified by the material properties. On the other hand, the second approach is more convenient for the analysis of beams under a given load vector, and it satisfies the requirement of Karpenko et al.'s [1] concrete cyclic behaviour model. Furthermore, the computational algorithm is less complicated and leads to fewer errors. The failure load vector can still be determined using the bisection method by increasing the external load vector until an acceptable tolerance is reached while checking if the strain has exceeded the ultimate strain in any vertex in the cross-section for each increment.

MATERIAL MODELS

Equation (2) requires a function to determine the secant modulus at a specific strain magnitude. It can be calculated for any material model such that stress is a function of strain. The nonlinear stress-strain model for both concrete and steel proposed by Karpenko et al.[2], [3] is adopted for this research. The model was developed based on the coefficient of change of the secant modulus (ν), Thus:

$$E = E_i \times \nu \quad (8)$$

$$\nu = \hat{\nu} + (\nu_o - \hat{\nu})\sqrt{1 - \omega \times \eta - (1 - \omega) \times \eta^2} \quad (9)$$

$$\eta = \frac{\sigma - \sigma_{el}}{\hat{\sigma} - \sigma_{el}} \quad (10)$$

where,
E_i: the initial modulus of elasticity,
ν_o: the coefficient of change of the secant modulus at the start of the $(\sigma - \varepsilon)$ diagram,
$\hat{\nu}$: the coefficient of change of the secant modulus at the peak of the $(\sigma - \varepsilon)$ diagram,
ω: the $(\sigma - \varepsilon)$ diagram curvature parameter,
η: relative stress level, ($0 \leq \eta \leq 1$),
σ_{el}: the elastic stress limit, and
$\hat{\sigma}$: the stress at the peak of the $(\sigma - \varepsilon)$ diagram.

Any parameter designated with a hat (^) corresponds to the point of peak stress in the stress-strain diagram. Now, substitution Eq. (2) and Eq. (10) into Eq. (9) and re-arrangement into a quadratic form leads to Eq. (11):

$$a \times \nu^2 + b \times \nu + c = 0 \quad (11)$$

where,

$a = (1-\omega) \times (\nu_o - \hat{\nu})^2 \times \varepsilon^2 + (\hat{\nu} \times \varepsilon - \varepsilon_{el})^2$,
$b = (\nu_o - \hat{\nu})^2 \times \varepsilon \times [\omega \times (\hat{\nu} \times \hat{\varepsilon} - \varepsilon_{el}) - 2 \times \varepsilon_{el} \times (1-\omega)] - 2 \times \hat{\nu} * (\hat{\nu} \times \hat{\varepsilon} - \varepsilon_{el})^2$, and
$c = (\nu_o - \hat{\nu})^2 \times \varepsilon_{el} \times [(1-\omega) \times \varepsilon_{el} - \omega \times (\hat{\nu} \times \hat{\varepsilon} - \varepsilon_{el})] + (\hat{\nu} \times \hat{\varepsilon} - \varepsilon_{el})^2 \times (2 \times \hat{\nu} - \nu_o) \times \nu_o$

The roots of Eq. (11) involve two solutions. However, the value of ν should be selected such that $(0 < \nu \leq 1)$. Equation (11) can be solved for any material for which the constant input data are the coordinates of the start and peak points and the elastic properties. The only variable is the strain of the point under consideration. Figures (1) and (2) demonstrate the stress-strain relationship of concrete material and mild steel, respectively, generated by solving Eq. (11) for all values of strain (ε) for each material. The input data were extracted from [10].

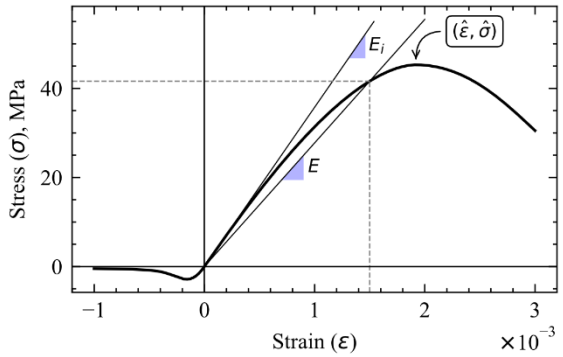

Fig.1 Stress-strain diagram for concrete

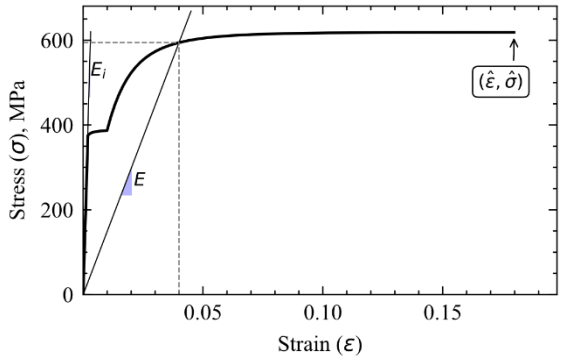

Fig.2 Stress-strain diagram for mild steel

CYCLIC ANALYSIS MODEL

The nonlinear stress-strain relationship is further investigated in [1] to involve the behaviour of concrete material under repeated load. The concept of the proposed Karpenko et al.'s model involves linear unloading and reloading paths with strength degradation in each cycle until stabilisation is reached, in which subsequent unloading and reloading stages follow one linear path. The model is developed in the material level and verified by experimental data with an acceptable error level. Therefore, the present research implements the cyclic model at the section level.

The model is developed for a constant stress amplitude for all cycles and full unloading in each cycle. The parameters corresponding to the points of unloading in the stress-strain diagram are designated with the tilde (~) (i.e. $\tilde{\sigma}, \tilde{\varepsilon}, \tilde{\eta}$). The stabilised concrete stress-strain relationship proposed by Karpenko et al. [1] depends on reducing the peak stress ($\hat{\sigma}$) and the initial modulus of elasticity (E_i) of the initial diagram by 17% and 10%, respectively. Therefore:

$$\hat{\sigma}_{stab} = 0.83 \times \hat{\sigma}$$
$$E_{i,stab} = 0.90 \times E_i \quad (12)$$

The number of cycles required to achieve stabilisation, N_c, at any stress level ($\tilde{\eta} \leq 0.83$) can be calculated using Eq. (13), where (η_{stab}) is a constant value assumed to be 0.83 as shown in Eq. (12). Based on the experimental data reported by Karpenko et al. [1], the number of cycles required to achieve stabilisation, ($\hat{N}$), at a stress level corresponding to η_{stab} equals 50 cycles. Accordingly, the predicted number of cycles (N_f) required to reach the failure stress at any stress level ($\tilde{\eta} > 0.83$) can be calculated using Eq. (14) [1].

$$N_c = \hat{N} \times \left(\frac{1-\eta_{stab}}{1-\tilde{\eta}}\right)^2, \quad 0 < \eta_c \leq \eta_{c,stab} \quad (13)$$

$$N_f = \hat{N} \times \sqrt{1-\tilde{\eta}}, \quad \eta_c > \eta_{c,stab} \quad (14)$$

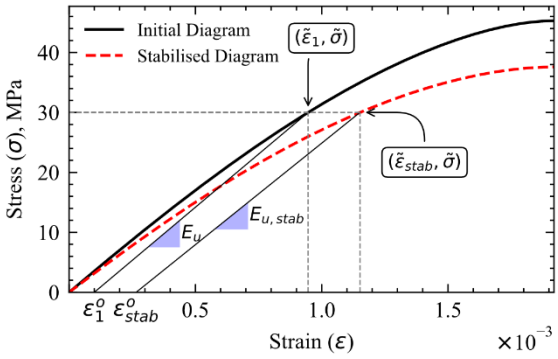

Fig. 3 Initial vs stabilised concrete stress-strain diagrams

The strain of the stabilised diagram ($\tilde{\varepsilon}_{stab}$) corresponding to unloading stress ($\tilde{\sigma}$) can be easily calculated using Eq. (9) with ($\hat{\nu}$) being replaced by ($\hat{\nu}_{stab}$). The residual strain (ε^o) in the first cycle (ε_1^o) and the last cycle (ε_{stab}^o) can be calculated using Eq. (15), in which ($\tilde{\varepsilon}, \tilde{\sigma}$) are the coordinates of the unloading point of the cycle under consideration, and (E_u) is the unloading modulus, which represents the slope of the unloading line in the diagram. Figure (3) illustrates the difference between the stress-strain

relationship before the start of the cyclic load and after stabilisation.

$$\varepsilon^o = \tilde{\varepsilon} - \frac{\tilde{\sigma}}{E_u} \quad (15)$$

$$E_u = \frac{\sqrt{\tilde{\nu}}}{0.95} \times E_i \quad (16)$$

The residual strain (ε_k^o) and the strain at the unloading point ($\tilde{\varepsilon}_k$) for the subsequent cycles between first unloading and stabilisation are determined using Eqs. (17) and (18) in which (β_k) represents the ratio of the change in strain between the current cycle (k) and the stabilisation cycle (N_c), where ($k = 2,3,\dots,N_c$).

$$\tilde{\varepsilon}_k = \tilde{\varepsilon}_1 + \beta_k \times (\tilde{\varepsilon}_{stab} - \tilde{\varepsilon}_1) \quad (17)$$

$$\varepsilon_k^o = \varepsilon_1^o + \beta_k \times (\varepsilon_{stab}^o - \varepsilon_1^o) \quad (18)$$

$$\beta_k = 1 - \frac{0.2}{\tilde{\eta}^2} \times \ln\left(\frac{N_c}{k}\right), (0 \le \beta_k \le 1) \quad (19)$$

Now, the stress-strain relationship in cyclic mode can be obtained for any element with known first unload strain ($\tilde{\varepsilon}_1$) and cycle number (k) under consideration. However, the stress-strain relationship after the linear, cyclic path when stabilisation is not reached yet is not investigated in [1].

The present study suggests the application of the (β_k) factor in Eq. (12) as shown in Eq. (20). Solving Eq. (9) for ($E_{i,k}$) of the k^{th} cycle to obtain the full stress-strain relationship by substituting the coordinates of the two known points ($\tilde{\varepsilon}_k, \tilde{\sigma}$) and ($\hat{\varepsilon}, \hat{\sigma}_k$). The diagram curvature parameter of concrete, ω, is assumed to be a linear relationship, as shown in Eq. (21) where ζ and λ are the linear coefficients. Therefore, Eq. (9) is rearranged into cubic form, as shown in Eq. (22).

$$\hat{\sigma}_k = (1 - 0.17 \times \beta_k) \times \hat{\sigma}_1 \quad (20)$$

$$\omega = \zeta + \lambda \times \hat{\nu} \quad (21)$$

$$a \times E_{i,k}^3 + b \times \hat{E}_k \times E_{i,k}^2 + c \times \hat{E}_k^2 \times E_{i,k} + d \times \hat{E}_k^3 = 0 \quad (22)$$

where,

$a = (1 - \zeta) \times \eta^2 + \zeta \times \eta - 1,$

$b = (2 \times \zeta - 2 + \lambda) \times \eta^2 + (\lambda - 2 \times \zeta) \times \eta + 2,$

$c = (1 - \zeta + 2 \times \lambda) \times \eta^2 - (\zeta + 2 \times \lambda) \times \eta - 1 + \left(1 - \frac{\hat{E}_k}{\tilde{E}_k}\right)^2$, and

$d = \lambda \times (\eta - \eta^2)$

Although Eq. (22) involves three mathematical solutions, the only correct solution should be verified such that ($E_{i,k} \ge E_k$). The plots of the stress-strain diagram for the initial, intermediate and stabilisation cycles are presented in Fig. (4). This model is developed for compression only and with ($\tilde{\varepsilon} < \hat{\varepsilon}$). However, it can be extended by using the unloading modulus technique for ($\tilde{\varepsilon} \ge \hat{\varepsilon}$) while keeping the stress-strain relationship after the cyclic path unchanged. In the present study, for simplicity, the tension phase under cyclic loading would have similar treatment following the same procedure adopted for cyclic loading in compression.

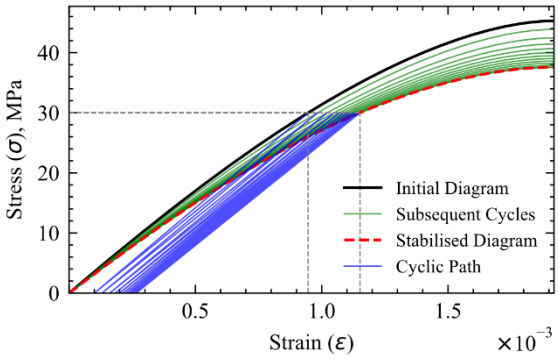

Fig.4 Concrete cyclic stress-strain diagram

Implementing the cyclic model into Eq. (5) requires the calculation of secant modulus (E) being performed independently for each elementary area in the section because each element is undergoing cyclic loading at different stress amplitudes, due to the location of the element relative to the adopted global axes and the load vector being applied. Hence, it is necessary to achieve this programmatically by assigning a different material object for each element in the section.

PROGRAMMING INTERFACE

Previous studies conducted by Oukaili [5] involved the development of a program using Fortran. The program was built to perform sectional analysis of structural concrete members with a general cross-section of rectangular-shaped components undergoing static loads and detect the failure load vector and the flexural crack depth across the section at different loading stages [11], [12]. The present research involves rebuilding a new software package written in Python [13] and named SectionPy. It was developed using an object-oriented programming concept by distributing the code into reusable modules and classes. The software consists of eight modules named as following: material, mesh, element, section, load, solver, postprocessor, and miscellaneous functions. The material module generates the stress-strain diagram from the nonlinear relationship by computing the corresponding stress of a massive number of strain ordinates (i.e. more than 1000 points), which is then used to calculate the secant modulus of elasticity at given strain values by linear interpolation. This method adds flexibility for the implementation of any material model. However,

the software currently adopts Karpenko models for both steel and concrete when generating stress-strain coordinates. The mesh module is used to discretise the section being analysed using the Gmsh software [14], which enables the software to analyse sections of arbitrary shapes including polygons, circles, and a combination of both. Moreover, sections with voids can also be discretised using Boolean operations such as the hollow-core slab section shown in Fig. (5). The section can be discretised as structured rectangles, right triangles, and non-structured triangles.

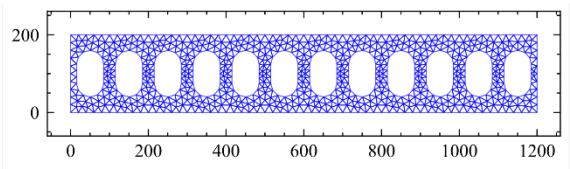

Fig.5 Hollow-core slab section mesh

The element module includes Subsection and Wire classes. Subsection represents a 2-D solid element with specific material properties. It takes a mesh object and material object as an input and calculates areas and centroids for all mesh elements. It is worth mentioning that the calculation is performed at an array level using the NumPy library [15], which enhances the performance of calculation compared to Python for-loop. Cells areas are computed using the shoelace technique based on cell vertices regardless of the shape of the mesh element. The wire element represents a reinforcing bar or a prestressing strand in which area, location, and prestressing value are provided as an input.

Both elements accept initial strain either in vector form or as a number. Initial strain represents the initial condition corresponding to a zero externally applied load vector (i.e. dead or live load) such as initial strain in concrete and non-prestress steel due to elastic shortening, creep and shrinkage, and pre-strain in prestressing strands. The primary function of the element module is to calculate the stiffness matrix at the strain vector provided.

The section module represents a collection of elements where solving the matrix is conducted by summing up all elements: subsections and wires. Although the software is used to analyse composite sections with different materials, such an analysis assumes a full bond between all elements and implements fictitious strain for nonhomogeneous materials. The load module is a small module used to calculate the load vector for any load type. Currently, it consists of force, moment, and a combination of forces and moments.

The solver module consists of special analysis procedures used to calculate the required data by implementing the above modules. One of the solvers is the static analysis solver which calculates the failure load vector using the bisection method and the behaviour of the section between two load vectors. The determination of the failure load vector requires an incremental load vector that represents the orientation of the applied load. Therefore, the static analysis is carried out by multiplying the specified incremental load vector by a factor until the failure load vector is determined and convergence is achieved. The failure load vector represents the load vector that results in an unsolvable singular stiffness matrix or produces a strain at any vertex of the beam section that exceeds the maximum strain defined in the material instance of that element. Finally, the postprocessor is used to visualise the output steps from solvers into the desired form, such as the stress-strain curve at a specific point, or a biaxial moment-curvature diagram. The stress-strain curve along a specific line and the stress-strain map can be generated in a video format that shows the behaviour of the beam between two load vectors.

COMPUTATIONAL EXAMPLE

A beam with a tee-shaped section is adopted to demonstrate the output of the developed program. The general section is defined as two rectangles (200 mm * 300 mm) for the web and (100 mm * 500 mm) for the flange using the input data in Table 1. A reference point located in the middle of the soffit of the beam is adopted as the origin of the global coordinate system. A structured mesh 10 mm in size is nominated. The concrete material stress-strain profile shown in Fig. (1) is assigned for the subsection instance. The rebars used are three ($\phi 20$ mm) placed at the bottom and four ($\phi 10$ mm) distributed at the top of the beam. The bars are placed such that a 30 mm cover to the rebar edge is achieved. The input data on the reinforcement bars, including the area and location relative to the reference point, are listed in Table 2. The steel material stress-strain relationship used for all rebars is shown in Fig. (2). Figure (6) shows the final section plot generated by the software.

Table 1 Concrete subsection input data

Items	Type	X	Y	Width	Height
web	Rect.	-100	0	200	300
flange	Rect.	-250	300	500	100

Table 2 Reinforcement detailing input data

Items	X, mm	Y, mm	Area, mm^2
B1	-57.5	42.5	314
B2	0	42.5	314
B3	57.5	42.5	314
T1	-215	365	78.5
T2	-65	365	78.5
T3	65	365	78.5
T4	215	365	78.5

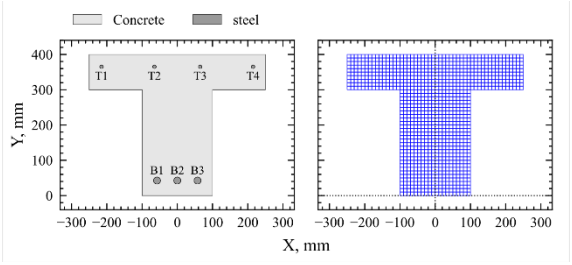

Fig.6 T-beam section and discretisation used in the analysis

The applied load vector is then defined as a moment instance in the software. A 10 kN.m moment about the x-axis is used as an incremental load vector. The maximum bending moment about the x-axis before tensile steel starts to yield is expected to exceed 130 kN.m, while, the load vector which causes complete failure can reach up to 190 kN.m. After determining the failure load vector, the moment-curvature diagram can be plotted from the successful steps between the initial and failure load vectors. Figure (7) illustrates the moment-curvature diagram about the x-axis generated by the software.

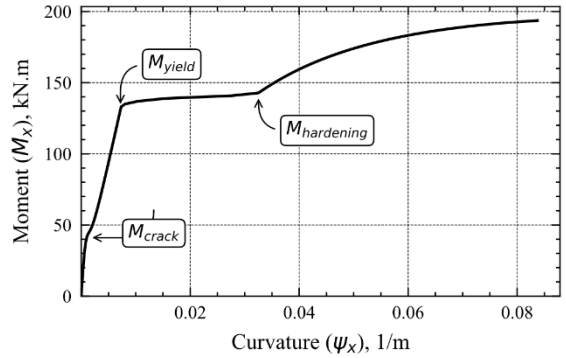

Fig.7 Moment-curvature about x-axis

After finishing the static analysis, it is necessary to select a load vector to be used for the cyclic analysis. The selected load vector represents the load amplitude of the cyclic analysis. 25, 75 and 125 kN.m are adopted for this example to demonstrate the results at different loading stages. After initiating the cyclic solver, the material stress-strain diagram is modified for each element in the mesh according to their stress level and the cycle number provided. After modification, the section analysis is repeated for the same load vector but with modified material properties. The calculation of secant modulus (E) in Eq. (5) requires a strain vector from the previous iteration. However, starting with a zero strain vector results in an infinite solution because the modified material stress-strain diagram no longer passes through (0,0). Therefore, overcoming this issue can be accomplished by using the strain vector before modification as a starting point.

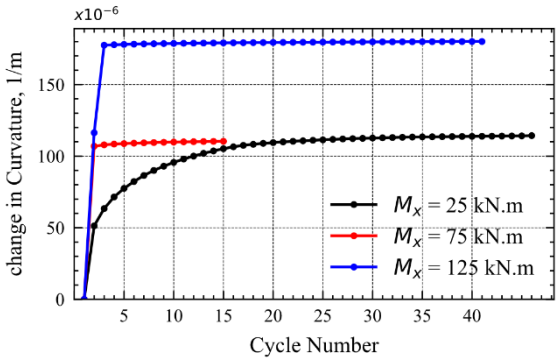

Fig.8 Curvature in x-axis during the cyclic analysis

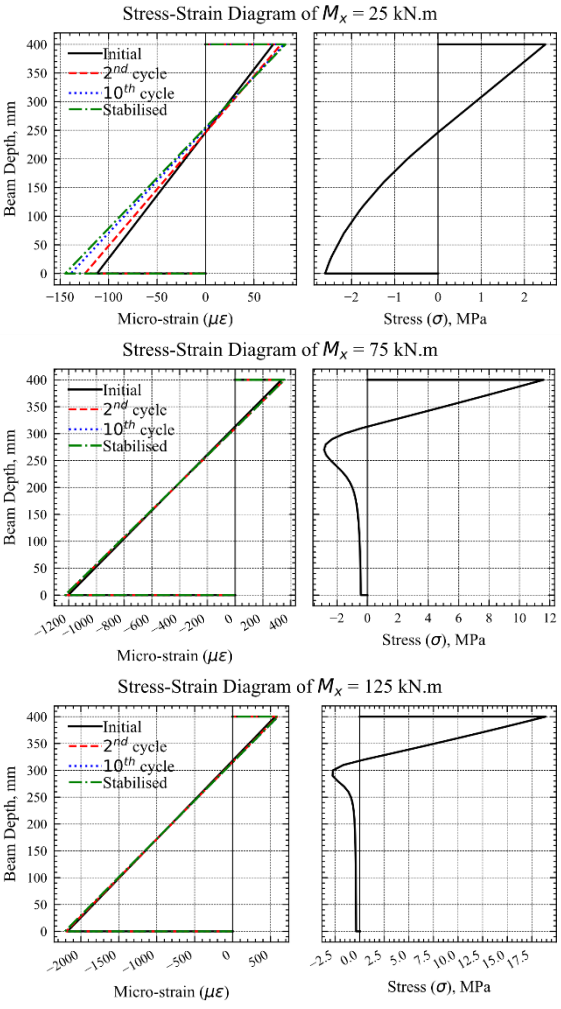

Fig.9 Stress-strain diagrams across the depth of the beam

Stabilisation is achieved after 46, 15 and 41 cycles, respectively. The strain vector is calculated in each cycle, and curvature about the x-axis is noted. Figure (8) shows the change in curvature over each cycle up to stabilisation. The strain diagram of the

initial, second cycle, tenth cycle, and stabilised cycle accompanied by the stress diagram of the initial cycle across the depth of the concrete beam are plotted in Fig. (9). The sign convention used assumes that compression is positive, and tension is negative. The strain diagram in Fig. (9) is shifted upward in each cycle since the stress level in the tension zone is higher than that in the compression zone. Hence, the β_k of cells in tension is higher.

DISCUSSION

The present study demonstrates a promising methodology for calculating the effect of repeated loading on structural concrete sections. Sectional analysis is a versatile technique for simulating beam deformation under different types of loading. Therefore, the development of this technique for cyclic loading will improve its accuracy. Although the proposed method does not consider the frequency of cyclic loading, a wide range of applications can employ this technique. The proposed method can be effectively used for simulating structural concrete sections with prestressing strands [16]. For instance, during the release of pre-tensioned steel, concrete elements near strands are compressed due to the transfer of loading from strands. Therefore, the application of external load will eventually cause unloading of the concrete elements in that zone. As a result, traditional static sectional analysis over-estimates beam capacity when using the stress-strain relationship of static elements. This technique requires an improvement when the stress level exceeds 0.83 of peak stress ($\eta > 0.83$). However, current results at a low-stress level are quite encouraging.

CONCLUSIONS

This paper presents an analytical methodology for the analysis of structural concrete sections under cyclic loading. Karpenko et al.'s cyclic model [1] is employed to simulate the stress-strain relationship of concrete elements under repeated loads. Furthermore, the Bernoulli–Navier assumption is utilised to perform sectional analysis of finite discretised concrete sections of arbitrary shape. A software package developed to perform the proposed analysis is also presented. Finally, a tee-shaped beam section is implemented to illustrate the output. The moment-curvature diagram is generated and the strain vector observed at different cycles. The analysis results show an increase in the curvature during each cycle. After cracking, the change in curvature follows a bilinear relationship because the increase in curvature in the subsequent cycles is vanished rapidly due to the low-stress amplitude of the cells in compression. Further research could be conducted to upgrade the present methodology to consider the residual strain in the section after full unloading and verify the results with experimental data. Finally, the presented cyclic model can be developed to simulate cyclic loading accompanied by a sustained dead load which conflicts with the full unload assumption currently used in this study.

REFERENCES

[1] Karpenko N. I., Eryshev V. A., and Latysheva E. V., Stress-Strain Diagrams of Concrete Under Repeated Loads with Compressive Stresses. Procedia Eng., 111, 2015, pp. 371-377.

[2] Karpenko N. I., Mukhamediev T. A., and Petrov A. N., The Initial and Transformed Stress-Strain Diagrams of Steel and Concrete, Special Publication, Stress-Strain Condition for Reinforced Concrete Construction, Reinforced Concrete Research Center, Moscow, 1986, pp. 7-25.

[3] Karpenko N. I., Mukhamediev T. A., and Petrov A. N., The Use of Transformed Concrete Stress-Strain Diagrams in Construction Design, Special Publication, The Limit State of Concrete and Reinforced Concrete Construction, Energyatomizdat, Leningrad, 1986, pp. 170-180.

[4] Alameh A. S. and Harajli M. H., Deflection of Progressively Cracking Partially Prestressed Concrete Flexural Members, PCI Journal, Vol. 34, Issue 3, 1989, pp. 94-128.

[5] Oukaili N. K., Moment Capacity and Strength of Reinforced Concrete Members Using Stress-Strain Diagrams of Concrete and Steel, Journal of King Saud University, Engineering Sciences (2), Vol. 10, 1998, pp. 23-44.

[6] Rodriguez J. A. and Aristizabal-Ochoa J. D., Biaxial Interaction Diagrams for Short RC Columns of Any Cross Section, Journal of Structural Engineering, Vol. 125, No. 6, 1999, pp. 672-683.

[7] Charalampakis A. E. and Koumousis V. K., Ultimate Strength Analysis of Composite Sections Under Biaxial Bending and Axial Load, Advances in Engineering Software, Vol. 39, Issue 11, 2008, pp. 923-936.

[8] Chiorean C. G., A Computer Method for Moment-Curvature Analysis of Composite Steel-Concrete Cross-Sections of Arbitrary Shape, Engineering Structures and Technologies, Vol. 9, Issue 1, 2017, pp. 25-40.

[9] Kwak H. G. and Kim S. P., Nonlinear Analysis of RC Beams Based On Moment-Curvature Relation, Computers and Structures, Vol. 80, 2002, pp. 615-628.

[10] Oukaili N.K., Strength of Partially Prestressed Concrete Elements with Mixed Reinforcement by Highly Strength Strands and Steel Bars, PhD Thesis, Moscow Civil Engineering University, Russia, 1991.

[11] Oukaili N. K., Model for Predicting the Cracking Moment in Structural Concrete Members, Abhath Al-Yarmouk Basic Science & Engineering – AYBSE, Vol. 8, Issue 2, 1999, pp. 9-39.

[12] Oukaili N. K. and Al-Shawi I. N., Strengthening and Closing Cracks for Existing Reinforced Concrete Girders Using Externally Post-Tensioned Tendons, Journal of Engineering, University of Baghdad, Vol. 19, 2013, pp. 1354-1374.

[13] Python Language Documentation, V. 3.8.2, https://docs.python.org/3/.

[14] Gmsh documentation, V. 4.5.6, http://gmsh.info/doc/texinfo/gmsh.html.

[15] NumPy Package Documentation, V. 1.18.1, https://numpy.org/doc/.

[16] Peera I. and Oukaili N., Methodology for Monitoring the Flexural Behavior of Structural Concrete Members with Unbonded Internal Steel, International Journal of GEOMATE, Vol.18, Issue 69, 2020, pp. 9-17.

6th Int. Conf. on Geotechnique, Construction Materials and Environment, Kyoto, Japan, 18-20 November 2020, ISBN: 978-4-909106049 C3051

QUANTITATIVE EVALIATION OF BUCKLING STRENGTH OF DAMAGED PLATES

Hani Doummar and Yoshitaka Suetake
Civil engineering, Ashikaga University, Japan.

ABSTRACT

The main aim of this paper is to investigate an approach to evaluate buckling strength of plates that have a change in their thickness. In general, all structural members can have a change in cross section for several reasons. For example, architectural esthetic reasons, necessity to serve the design, and changes either by slow damage factors due to severe service environment or sudden damage like accident or explosion in case of war. In case of damaged members, it is required that the plate members maintain their original performance as much as possible. This goal can be achieved by estimate the level of damage that happens to the cross section of members after the incident. In this research, we deal with damaged plates which are subjected to a partial loss in cross sections. The damage is represented by step-formed change in cross section due to reduction of plate thickness at the area of the damage. A criterion is needed to evaluate this state of change. In the present investigation Damage Index is introduced by using critical loads of the plate buckling. Many numerical examples are demonstrated, in which thickness and area of the damaged parts are changed in wide range. The damage level, in which plate members are usable, can be evaluated from the results of the damage index.

Keywords: Plate, Buckling load, Damage index, Variation in thickness.

INTRODUCTION

In the recent decades, after the worldwide expansion in the sector of infrastructures and structural construction. The managers of these structures face a major problem represented by specify the criteria to evaluate the amount of depreciation, that was exposed to during its period of service and affect directly the decision tacked by renovation or replacement and reflect directly on the final cost. This challenge encourage the researcher to study in deep several kinds of deterioration factors under its related service circumstances that cause the lost in cross section.

The damage can be classified by the duration of exposure, as sudden damages in structures provoked by sudden short-term incidents for example earthquakes [1] and fire, or long term effects that the structure is undergoing during its life service-circle like chemical deterioration, loading history [2] static steady or repeating cycles accompanied with over-loading.

Recently, the studies distinguish between the assessment the amount of damage that structures as whole and specific structural elements in precise to evaluate the usefulness of the remain section by develop several kinds of indices depending on parameters that contribute in the sustain of the subjected element.

In this paper, in-plane buckling strength of damaged plates is dealt with, in which all sides of a plate are simply supported. The factor chosen to evaluate the damage called the damage index DI that is based on the change of stiffness before and after the occur of damage as a status quo.

METHODOLOGY

It is substantial to clarify the methodology adopted in this paper. By using the energy method, it is possible to obtain the magnitude of the buckling load, K, for the plate of both the original and the damaged state under the uniaxial buckling load. Subsequently, the levels of damage to the plate are evaluated by applying the damage index.

Energy method

To specify the critical load of plates. This paper employ the principle of energy method [3] that is denoted by the following equation

$$\Delta \mathbf{U} = \Delta \mathbf{T} \tag{1}$$

where $\Delta \mathbf{U}$ is defined as the strain energy and $\Delta \mathbf{T}$ is the potential energy of load.

In case of a rectangular plate with constant thickness, all edges are simply supported, the deflection surface can be represented by the double trigonometric series, so called double Fourier series, determined by the Eq. (2) [3]

$$\boldsymbol{\omega} = \sum_{\mathbf{m=1}}^{\infty} \sum_{\mathbf{n=1}}^{\infty} \mathbf{a_{mn}} \sin \frac{\mathbf{m\pi x}}{\mathbf{a}} \sin \frac{\mathbf{n\pi y}}{\mathbf{b}} \tag{2}$$

where $\mathbf{a_{mn}}$ is the maximum deflection which remains indefinite provided we consider it small and neglect stretching the middle plane of the plate during buckling. This series expression satisfies the boundary conditions of the simply supported plates.

For simplification, we set the width of plate b is constant as a result n=1. In this case, the relation becomes the following:

$$\boldsymbol{\omega = a_{m1} \sin \frac{m\pi x}{a} \sin \frac{\pi y}{b}} \quad (3)$$

This means that the plate buckles in such a way that there can be several half-wave in length direction and one half-wave in width direction.

The strain energy $\Delta \mathbf{U}$ is given by:

$$\Delta U = \frac{1}{2} D \int_0^a \int_0^b \left\{ \left(\frac{\partial^2 \omega}{\partial^2 x} + \frac{\partial^2 \omega}{\partial^2 y} \right)^2 - 2(1-\nu) \left[\frac{\partial^2 \omega}{\partial^2 x} \frac{\partial^2 \omega}{\partial^2 y} - \left(\frac{\partial^2 \omega}{\partial x \partial y} \right)^2 \right] dx dy \right\} \quad (4)$$

After substituting of Eq. (2) into Eq. (4), we have

$$\Delta U = \frac{D}{8} \frac{\pi^4 m^2 {a_{m1}}^2}{a^3 b^3} \left(b^2 + \frac{a^2}{m} \right)^2 \quad (5)$$

The potential energy $\Delta \mathbf{T}$ is given by:

$$\Delta T = \frac{1}{2} \int_0^a \int_0^b \left\{ N_x \left(\frac{\partial^2 \omega}{\partial^2 x} \right)^2 + N_y \left(\frac{\partial^2 \omega}{\partial^2 x} \right)^2 + 2 N_{xy} \left(\frac{\partial \omega}{\partial x} \frac{\partial \omega}{\partial y} \right) \right\} dx dy \quad (6)$$

In this study, the loading is apply in the x direction only, therefore $\mathbf{N_x \neq 0}$ but both $\mathbf{N_y = N_{xy} = 0}$.

$$\Delta T = \frac{1}{2} \int_0^a \int_0^b \left\{ N_x \left(\frac{\partial^2 \omega}{\partial^2 x} \right)^2 \right\} dx dy \quad (7)$$

Therefore, we have

$$\Delta T = \frac{\pi^2}{8} \frac{b}{a} m^2 {a_{m1}}^2 \bar{N}_X \quad (8)$$

Substituting the results into Eq. (1), we obtain the critical load $\bar{\mathbf{N}}_\mathbf{X}$ as shown the following equation:

$$\bar{N}_X = \frac{\pi^2 D}{b^2} \left(\frac{mb}{a} + \frac{a}{mb} \right)^2 \quad (9)$$

This equation also can be represented:

$$\bar{N}_X = K \frac{\pi^2 D}{b^2} \; ; \; K = \left(m\gamma + \frac{1}{m\gamma} \right)^2 \; , \gamma = \frac{a}{b} \quad (10)$$

The factor K represents the magnitude of the buckling load. Curves of the factor K are drawn in Fig. 1, in which the number of the half-wave of the buckling mode is changed from m=1 to m=5.

Figure 1 obtained by [3] represents the relation between a/b and K. It can be seen from Fig. 1 that all curves for different values of the half-wave number m have the minimum value K=4. In later sections, this value of K=4 is employed as $\mathbf{K_{Standard}}$.

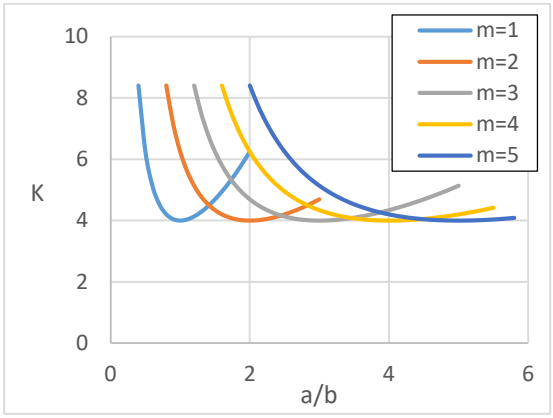

Fig.1 Curves of factor K.

When the buckling load was determined, the value of Poisson's ratio set as ν =0.3. And the flexural rigidity D is defined by the Eq. (11) [4].

$$D = \frac{Eh^3}{12(1-\nu)} \quad (11)$$

The damage index:

The index that will be used in this study is the response-based damage index so-called Damage Index or shortly DI. DI can be distinguished into three sorts according to the factors that it considers: (a) maximum deformation. (b) cumulative damage. (c) maximum deformation and cumulative damage.

The damage index [1] that fit with the requires of this study, it defined by:

$$DI = 1 - \frac{K_{final}}{K_{initial}} \quad (12)$$

where $\mathbf{K_{final}}$ represents the stiffness of the damaged element, the $\mathbf{K_{initial}}$ is the original stiffness (initial slope of behavior) of the element before incident.

The previous shape of DI in Eq. (12) can be obtained easily using the $\bar{\mathbf{N}}_\mathbf{X}$ obtained from the energy method [3] and $\bar{\mathbf{N}}_{\mathbf{X\,Damage}}$ derived later for one change and two changes in cross-section.

$$DI = 1 - \frac{\bar{N}_{X\,Damage}}{\bar{N}_{X\,Standard}} \quad (13)$$

where $\bar{\mathbf{N}}_{\mathbf{X\,Damage}}$ represents the critical load of the damaged plate and $\bar{\mathbf{N}}_{\mathbf{X\,Standard}}$ is the critical load of the plate in the original state before the incident.

The physical interpretation of this index presented by [5] is clarified in Table 1.

Table 1 The physical interpretation of DI.

Degree of Damage	Damage Index, DI	State
Collapse	$\mathbf{DI > 1}$	Loss of building
Severe	$\mathbf{1 > DI > 0.4}$	Beyond repair
Moderate	$\mathbf{DI < 0.4}$	Reparable
Slight	$\mathbf{DI < 0.2}$	

THE STUDIED CASES:

This paper studies two cases of change in cross-section due to happening damage, for one or two changes in thickness, by applying the same boundary and loading conditions for simply supported rectangular plate, subjected in the middle plane by forces uniformly distributed along the sides x=0 and x=a [3]. As numerical models, two types of damaged plates were adopted. The first is a two-steps model as shown in Fig. 2 (Model A); the second is a three-steps model as shown in Fig. 3 (Model B).

One change in thickness

This applied change in the internal part wherein the plate is symmetric about a plane at its half-length. Fig. 2 shows the dimensions of parts of a damaged plate in case of one change in thickness.

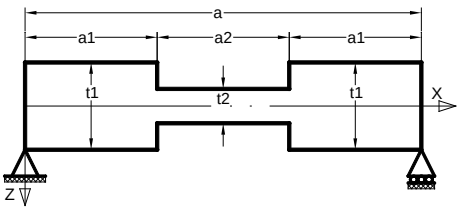

Fig. 2 Plate with one change in thickness.

Figure 2 shows a longitudinal section in simply supported plate symmetric about a plane normal on the mid-plane of the plate. The original thickness of the plate is t_1 and t_2 is the thickness of the plate after the damage happens. The calculated proportions t_2/t_1 were 20%, 40%, 60%, 80% of the original thickness.

In this case, a_1 defined as the non-damaged length on both opposite sides near the supports of the plate. a_2 is the length of the middle damaged part. The length ratios of Model A are as follows: (A1) a1/a=0.1, (A2) a1/a=0.2, (A3) a1/a=0.3, and (A4) a1/a=0.4.

By using the energy method, the internal energy can be represented in the following equation.

$$\Delta\mathbf{U} = \frac{\mathbf{D_1}}{\mathbf{8}}\mathbf{a_{m1}}^2\frac{\mathbf{m^2\pi^4}}{\mathbf{a^2b^2}}\left[\left(\frac{\mathbf{mb}}{\mathbf{a}}+\frac{\mathbf{a}}{\mathbf{mb}}\right)^2 \left\{\left(\frac{\mathbf{2a_1}}{\mathbf{a}}-\frac{\mathbf{1}}{\mathbf{m\pi}}\mathbf{sin}\left(\mathbf{2m\pi}\frac{\mathbf{a_1}}{\mathbf{a}}\right)\right)+\left(\frac{t_2}{t_1}\right)^3\left(\frac{a-2a_1}{a}+\frac{1}{m\pi}\left(\sin\left(2m\pi\frac{a_1}{a}\right)\right)\right)\right\}+\frac{4(1-\vartheta)}{m\pi}\left(1-\left(\frac{t_2}{t_1}\right)^3\right)\sin\left(2m\pi\frac{a_1}{a}\right)\right] \quad (14)$$

By substituting $\Delta\mathbf{U}$ the in Eq. (1) the critical load $\bar{\mathbf{N}}_{\mathbf{X\,Damage}}$ is denoted as $\bar{\mathbf{N}}_{\mathbf{X\,D}}$ in the following relation

$$\bar{\mathbf{N}}_{\mathbf{X\,D}} = \frac{\mathbf{\pi^2 D_1}}{\mathbf{b^2}}\left[\left(\mathbf{m\gamma}+\frac{\mathbf{1}}{\mathbf{\gamma m}}\right)^2\left\{\left(\frac{\mathbf{t_2}}{\mathbf{t_1}}\right)^3+\left(\mathbf{1}-\left(\frac{\mathbf{t_2}}{\mathbf{t_1}}\right)^3\right)\left(\frac{\mathbf{2a_1}}{\mathbf{a}}-\frac{\mathbf{1}}{\mathbf{m\pi}}\mathbf{sin}\left(\mathbf{2m\pi}\frac{\mathbf{a_1}}{\mathbf{a}}\right)\right)\right\}+\frac{\mathbf{4(1-\nu)}}{\mathbf{m\pi}}\left(\mathbf{1}-\left(\frac{\mathbf{t_2}}{\mathbf{t_1}}\right)^3\right)\mathbf{sin}\left(\mathbf{2m\pi}\frac{\mathbf{a_1}}{\mathbf{a}}\right)\right] \quad (15)$$

By comparing the $\bar{\mathbf{N}}_{\mathbf{X}}$ in Eq. 15 with the relation of the $\bar{\mathbf{N}}_{\mathbf{X}}$ in Eq. 10, the value of K in case of one change in thickness is shown in the Eq. 16.

$$\mathbf{K_D} = \left[\left(\mathbf{m\gamma}+\frac{\mathbf{1}}{\mathbf{\gamma m}}\right)^2\left\{\left(\frac{\mathbf{t_2}}{\mathbf{t_1}}\right)^3+\left(\mathbf{1}-\left(\frac{\mathbf{t_2}}{\mathbf{t_1}}\right)^3\right)\left(\frac{\mathbf{2a_1}}{\mathbf{a}}-\frac{\mathbf{1}}{\mathbf{m\pi}}\mathbf{sin}\left(\mathbf{2m\pi}\frac{\mathbf{a_1}}{\mathbf{a}}\right)\right)\right\}+\frac{\mathbf{4(1-\nu)}}{\mathbf{m\pi}}\left(\mathbf{1}-\left(\frac{\mathbf{t_2}}{\mathbf{t_1}}\right)^3\right)\mathbf{sin}\left(\mathbf{2m\pi}\frac{\mathbf{a_1}}{\mathbf{a}}\right)\right] \quad (16)$$

After the substitution of $\mathbf{K_{Damage}}$ and $\mathbf{K_{Standard}}$ in the relation of DI can be represented in Eq. 17.

$$\mathbf{DI} = \mathbf{1} - \left[\left\{\left(\frac{\mathbf{t_2}}{\mathbf{t_1}}\right)^3+\left(\mathbf{1}-\left(\frac{\mathbf{t_2}}{\mathbf{t_1}}\right)^3\right)\left(\frac{\mathbf{2a_1}}{\mathbf{a}}-\frac{\mathbf{1}}{\mathbf{m\pi}}\mathbf{sin}\left(\mathbf{2m\pi}\frac{\mathbf{a_1}}{\mathbf{a}}\right)\right)\right\}+\frac{\mathbf{4(1-\nu)}}{\mathbf{m\pi}\left(\mathbf{m\gamma}+\frac{\mathbf{1}}{\mathbf{\gamma m}}\right)^2}\left(\mathbf{1}-\left(\frac{\mathbf{t_2}}{\mathbf{t_1}}\right)^3\right)\mathbf{sin}\left(\mathbf{2m\pi}\frac{\mathbf{a_1}}{\mathbf{a}}\right)\right] \quad (17)$$

Two changes in thickness

In this case, the applied change in thickness in the internal zone where the plate is symmetric about a plane at the half-length of the plate. The first change of the plate thickness is t_2, applied on length a_2, will be calculated for each of the following cases t_2/t_1 are 20%, 40%, 60%, 80% separately and the middle part percentage of change in thickness t_3/t_1= 0.5 t_2/t_1 is the half of each of the previous percentage respectively, applied on length a_3.

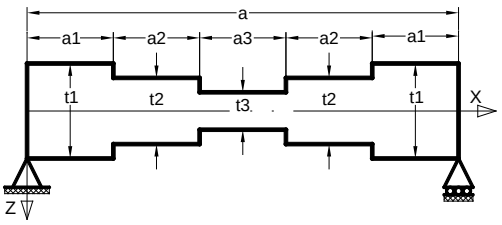

Fig. 3 Plate with two changes in thickness.

This figure shows the change in thickness and the lengths of these changes that is symmetrical about a plane normal on the middle plane of plate. And the length ratios of Model B: (B1) (a1/a, a2/a) = (0.1,0.1), (B2)(a1/a, a2/a)=(0.1,0.2), (B3) (a1/a, a2/a)=(0.1,0.3), (B4) (a1/a,a2/a)=(0.2,0.1), (B5) (a1/a, a2/a)=(0.2,0.2), and (B6) (a1/a, a2/a)=(0.3,0.1).

Using the energy method, the internal energy can be represented in the following equation

$$\begin{aligned}\Delta U = \frac{D_1}{8} a_{m1}{}^2 \frac{m^2\pi^4}{ab}\Bigg[\left(\frac{mb}{a}+\frac{a}{mb}\right)^2\left\{2\frac{a_1}{a}+2\frac{a_2}{a}\left(\frac{t_2}{t_1}\right)^3\right.\\ +\left(1-2\frac{a_2+a_1}{a}\right)\left(\frac{t_3}{t_1}\right)^3\\ -\frac{1}{m\pi}\left(\left(1-\left(\frac{t_2}{t_1}\right)^3\right)\sin\left(2m\pi\frac{a_1}{a}\right)\right.\\ \left.+\left(\left(\frac{t_2}{t_1}\right)^3-\left(\frac{t_3}{t_1}\right)^3\right)\sin\left(2m\pi\frac{a_2+a_1}{a}\right)\right)\Big\}\\ +\frac{4(1-\nu)}{m\pi}\left\{\left(\sin\left(2m\pi\frac{a_1}{a}\right)\left(1-\left(\frac{t_2}{t_1}\right)^3\right)\right)\right.\\ \left.+\sin\left(2m\pi\frac{a_2+a_1}{a}\right)\left(\left(\frac{t_2}{t_1}\right)^3-\left(\frac{t_3}{t_1}\right)^3\right)\right\}\Bigg] \qquad (18)\end{aligned}$$

By substituting ΔU the in Eq. (1) the critical load is $\bar{N}_{X\,Damage}$ .Where $\bar{N}_{X\,D} = \bar{N}_{X\,Damage}$

$$\begin{aligned}\bar{N}_{X\,D} = \frac{\pi^2 D_1}{b^2}\Bigg[\left(\frac{mb}{a}+\frac{a}{mb}\right)^2\left\{2\frac{a_1}{a}+2\frac{a_2}{a}\left(\frac{t_2}{t_1}\right)^3\right.\\ +\left(1-2\frac{a_2+a_1}{a}\right)\left(\frac{t_3}{t_1}\right)^3\\ -\frac{1}{m\pi}\left(\left(1-\left(\frac{t_2}{t_1}\right)^3\right)\sin\left(2m\pi\frac{a_1}{a}\right)\right.\\ \left.+\left(\left(\frac{t_2}{t_1}\right)^3-\left(\frac{t_3}{t_1}\right)^3\right)\sin\left(2m\pi\frac{a_2+a_1}{a}\right)\right)\Big\}\\ +\frac{4(1-\nu)}{m\pi}\left\{\left(\sin\left(2m\pi\frac{a_1}{a}\right)\left(1-\left(\frac{t_2}{t_1}\right)^3\right)\right)\right.\\ \left.+\sin\left(2m\pi\frac{a_2+a_1}{a}\right)\left(\left(\frac{t_2}{t_1}\right)^3-\left(\frac{t_3}{t_1}\right)^3\right)\right\}\Bigg] \qquad (19)\end{aligned}$$

Comparing with relation of the shape the $\bar{N}_X$ in Eq. 10, the value of K in case of two change in thickness is shown in the Eq. (20).

$$\begin{aligned}K_D = \Bigg[\left(\frac{mb}{a}+\frac{a}{mb}\right)^2\left\{2\frac{a_1}{a}+2\frac{a_2}{a}\left(\frac{t_2}{t_1}\right)^3+\left(1-2\frac{a_2+a_1}{a}\right)\left(\frac{t_3}{t_1}\right)^3\right.\\ -\frac{1}{m\pi}\left(\left(1-\left(\frac{t_2}{t_1}\right)^3\right)\sin\left(2m\pi\frac{a_1}{a}\right)\right.\\ \left.+\left(\left(\frac{t_2}{t_1}\right)^3-\left(\frac{t_3}{t_1}\right)^3\right)\sin\left(2m\pi\frac{a_2+a_1}{a}\right)\right)\Big\}\\ +\frac{4(1-\nu)}{m\pi}\left\{\left(\sin\left(2m\pi\frac{a_1}{a}\right)\left(1-\left(\frac{t_2}{t_1}\right)^3\right)\right)\right.\\ \left.+\sin\left(2m\pi\frac{a_2+a_1}{a}\right)\left(\left(\frac{t_2}{t_1}\right)^3-\left(\frac{t_3}{t_1}\right)^3\right)\right\}\Bigg] \qquad (20)\end{aligned}$$

NUMERICAL RESULTS

In this section, the numerical values of K and DI are calculated for both cases of change in thickness.

One change in thickness

The curves of factor K are classified into 4 cases corresponding to m values. Figure 4 is an example of those curves obtained from the present numerical calculations in the group (A2) when t1/t=0.2.

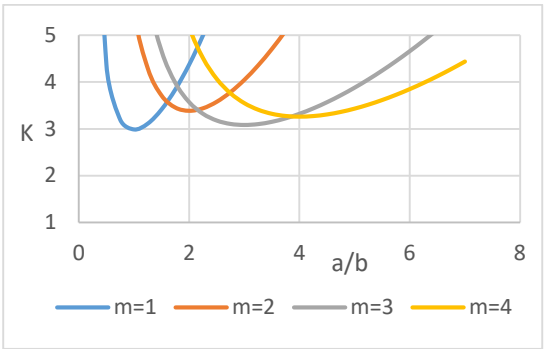

Fig. 4 Curves of factor K for (A4), t_2/t_1=0.2.

Notably, that the minimum values of curves differ following the diverse of m. This tendency is different from the result in Fig. 1, which is the case of undamaged plate obtained in [3]. This behavior is similar in all studied cases.

The next figures of DI, Fig. 5 to 8, for one change in thickness are classified using the proportion of non-damaged length a_1/a into four groups.

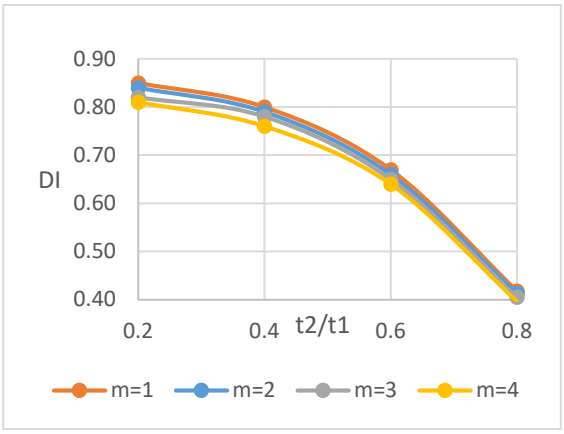

Fig. 5 DI of group (A1) with one step.

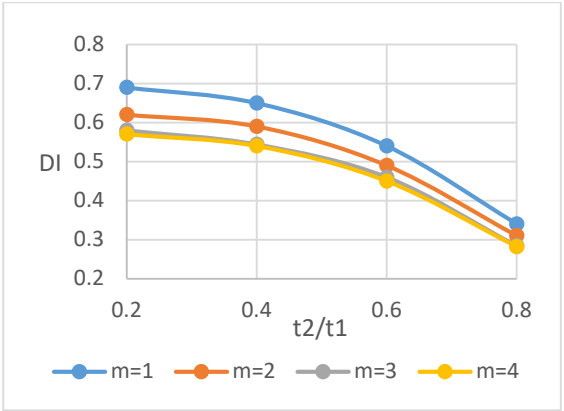

Fig. 6 DI of group (A2) with one step

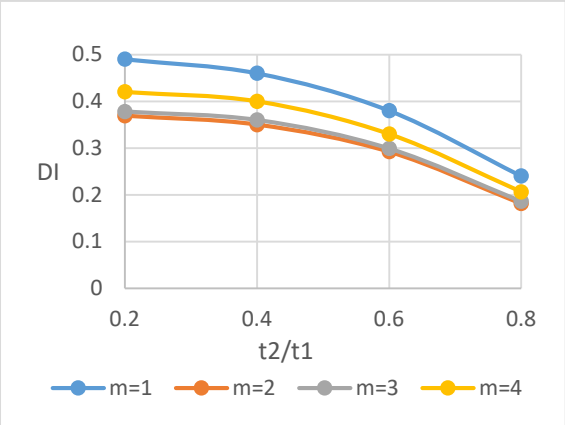

Fig. 7 DI of group (A3) with one step.

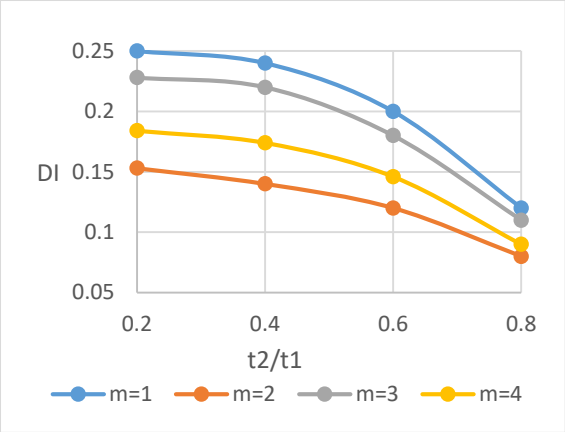

Fig. 8 DI of group (A4) with one step.

Referring to Table 1, we can find the physical interpretation of DI in each group. In Fig. 5 to Fig. 8, no case is classified into "Collapse." The damage indices, DI, decrease with the increase of t_2/t_1. In all groups, the most dangerous cases are when m=1.
Most cases of the group (A1) and 75% of the group (A2) are classified into "Sever." In groups of (A2) and (A3), "Moderate" cases are observed. While only two "Slight" cases appear in the group (A3), 11 "Slight" cases can be found in the group (A4).

Two changes in thickness

The curves of the factor K and DI classified into six groups defined previously by the proportion of non-damaged length a_1/a and a_2/a.

As an example of K curves for two changes in thickness, the result of the case (B2), (a1/a, a2/a) = (0.1,0.2), is shown in Fig. 9.

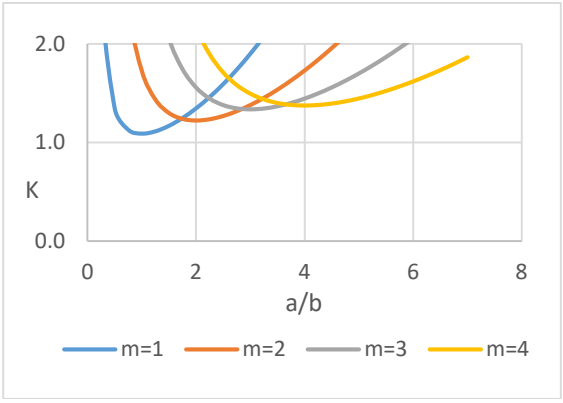

Fig .9 Curves of K for (B1), t2/t1=0.8.

Figure 9 shows that in two changes in thickness the minimum value of each curve differs in case with the change of m, while in case of the non-damaged minimum K=4 for all m curves [3].

The next figures of DI, Fig. 10 to 15, for two changes in thickness classified into six groups using the proportion combination of lengths (a_1/a, a_2/a).

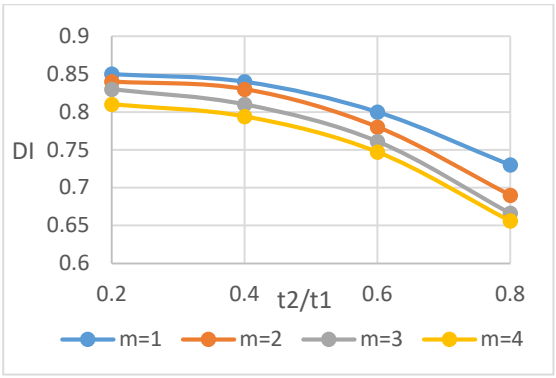

Fig. 10 DI of group (B1) Plate with Two steps.

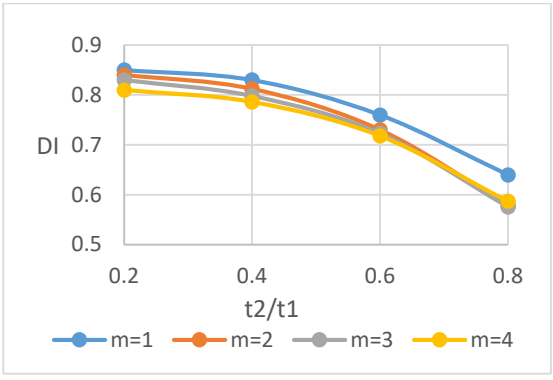

Fig. 11 DI of group (B2) Plate with Two steps.

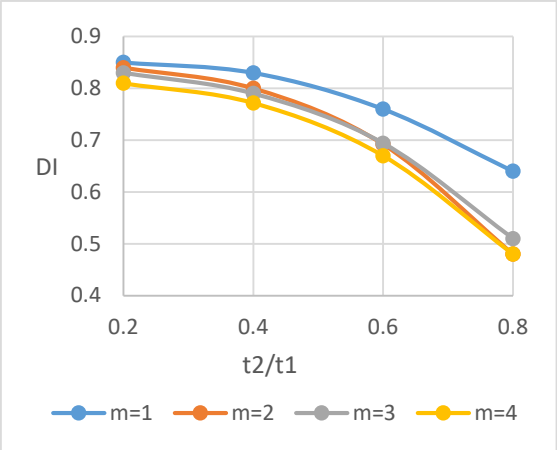

Fig. 12 DI of group (B3) Plate with Two steps.

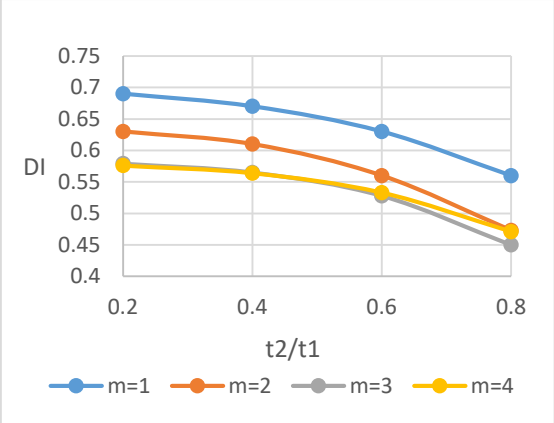

Fig. 13 DI of group (B4) Plate with Two steps.

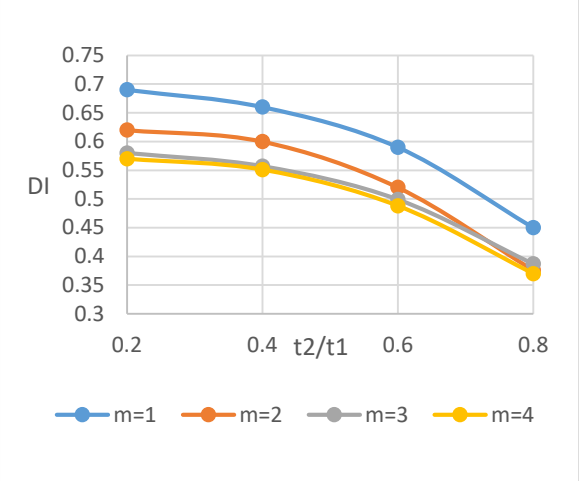

Fig. 14 DI of group (B5) Plate with Two steps.

In Fig. 10 to Fig. 14, most cases are classified into "severe" damage the highest when m=1. It is notifiable that three "Moderate" damage cases in Group (B5). There is no case classified under "Slight" damage.

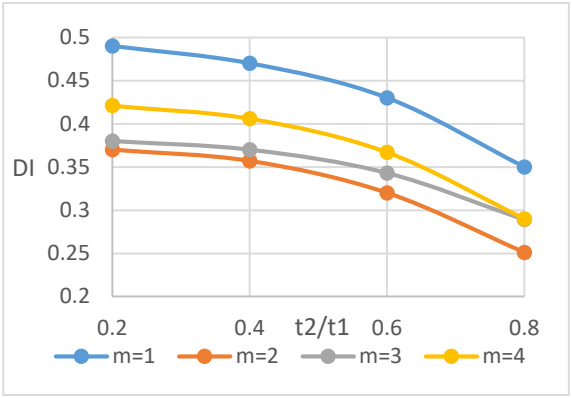

Fig. 15 DI of group (B6) Plate with Two steps.

In Fig. 15, half of cases are classified under a "severe damage" case. The most dangerous cases occur when m=1. And half of the Group (B6) is "Moderate."

CONCLUSIONS

1) The introduced index DI for the damaged plates under critical buckling loads is a useful numerical evaluation to repair the damage. The highest level of damage is "Severe" which means all cases are repairable by different levels
2) The minimum curves values of the magnitude of the buckling load K for specific number half-wave in damaged plate decreases with the increase of the damage in both model.
3) In case of one change in thickness, the occurred level of damage varied from "Severe" till "slight" damage with the decrease of damage.
4) The dominant level of damage in the case of two changes in thickness is "Severe" in all groups. But cases of "Moderate" appear in (B5) and (B6) in which the length of the damaged part is relatively shorter and the reside section bigger.

REFERENCES

[1] Ghobarah A., Abou-Elfath, and Biddah A. (1999). " Response-based damage assessment of structures", *Earthquake Engineering and Structural Dynamics* 28,79-104.
[2] Chung Y.,Meyer C. and Shinozuka M.(1987)."Seismic damage assessment of reinforced concrete members". *Technical Report* NCEER-87-0022.Columbia University, USA.
[3] Timoshenko S. and Gere J. (1989)." Theory of elastic stability". Dover Publications, Inc. New York, USA
[4] Yu, Chen. (2003). "Buckling of rectangular plates under intermediate and end loads". Master thesis, National university of Singapore, Singapore.
[5] Park YJ, Ang AH, Wen YK, Damage-limiting a seismic design of buildings. Earthquake Spectra 3(1);1-26.

6th Int. Conf. on Structure, Engineering & Environment (SEE), Kyoto, Japan, Nov.18-20, 2020, ISBN: 978-4-909106056 C3051

PERFORMANCE LEVEL PREDICTION OF STRUCTURE BUILDING USING LOG-SIGMOID METHODS

Muhammad Gala Garcya[1], *Reni Suryanita[2], Zulfikar Djauhari[3] and Harnedi Maizir[4]
[1,2,3]Civil Engineering Department, University of Riau, Indonesia;
[4] Civil Engineering Department, Sekolah Tinggi Teknologi Pekanbaru

*Corresponding Author

ABSTRACT

Earthquake is one of the biggest threats towards the building, so it needs to be designed with calculating the earthquake loads that happened. The finite elements can obtain the structure response such as displacement, velocity, and acceleration that happened because of an earthquake. The study aims to predict structural damage using structure response data with short relative analysis time than analyzing by each. The research used 5 (five) earthquake data with different high-intensity magnitude. The finite element generated ANN data is 14534 data. In this research, the composition used for training, validating, and testing is 60%,15%, and 25% by each. The input data consist of time, acceleration in x and y directions, velocity in x and y directions, and also displacement in x and y directions. Meanwhile, the target data are structure performance determined by FEMA 356 and story drift for x and y directions. The result indicated the regression value by ANN analysis reached 97,379%. Evaluation results by ANN show that Log-sigmoid transfer functions are small enough and show the smallest error value (MSE) approximately 3,9774 E-07. Therefore, ANN analysis with the Log-Sigmoid transfer function can be used to predict the performance level of the structure appropriately and accurately. The method can be recommended tools for structural engineers and building designers in designing earthquake-resistant buildings.

Keywords: Structure Response, Structure damage, Log-Sigmoid Transfer Function, Mean Square Error (MSE)

INTRODUCTION

The development of human life was increased rapidly and made the use of technology that aims to facilitate human life from how to communicate until to fulfil any daily needs. It can solve all kinds of problems and can be solved better and faster. Now, the era of humans has entered the era of the Industrial Revolution 4.0, where humans have solved the problems of life only by utilizing technology, which is to fulfil all kinds of problems by not needing to waste a lot of time but only in a very short time.

In the development of technology, there is a term known as AI (Artificial Intelligence). AI has entered into human life in various forms and functions. One product of AI is very useful in human life in terms of disaster mitigation, namely as Artificial Neural Network (ANN). ANN is one of the AI products that can be used to predict building damage that occurs due to natural disasters, which is one of them is an earthquake. Earthquakes are one of the biggest threats that occur in human life because earthquakes cannot be predicted how long the intensity and duration up to how much impact damage they cause. By using ANN in predicting building damage index towards an earthquake, the condition of the building can be known more quickly, and disaster evacuation will be faster to minimize the number of lives that are not saved.

ANN works by studying previous patterns to predict data later. ANN works like the human brain, and the more practice makes the ability will increase as well too. So, the more data are used, the level of accuracy generated by the ANN in predicting will also be higher as well. Otherwise, getting a bit of data will make the accuracy of the ANN will be lower. ANN can predict many models, such as towers, bridges, roads, and even road damage. And the main target ANN utilization is to simplify and save time in designing the structure for the future of mankind.

LITERATURE STUDIES

Modal Analysis

Variance analysis or commonly known as the modal analysis is an analysis that determines the motion of the structure under the free vibration conditions, where the motion is only influenced by the initial conditions. This analysis is very important because this analysis provides the dynamic nature response of the most important in the structural design is a natural period and mode shapes.

Free vibrations are vibrations that occur due to the operation of forces on the structure itself without the forces occurring. The force acting on free vibration is the weight of the structure itself. From this vibration

can be seen in the large frequency of a structure. The natural frequency is very important to be taken into account in the planning of the structure because the natural frequency of the structure which is the same as the external force (resonance) will be dangerous for the structure that causes a collapse in the structure.

In SNI 1726-2019, a value of participating mass ratio requirement has been set, which is a value that explains the amount of participation of structural components to hold external forces. The value of the mass participation ratio must be greater than 90%.

Time History Analysis

Earthquake analysis is divided into 2 (two) methods, which is a static analysis and dynamic analysis (Chopra, 1995). In a structural analysis needs to be done more thoroughly to obtain an economical design. Generally, analysis of the structure of the earthquake is divided into 2 (two) types, namely:

In general, structural analysis of earthquakes is divided into two types, namely:

1. Static analysis is an analysis where the effect of an earthquake on a structure is considered as a horizontal static load was obtained by only calculating the natural frequency and period in the first shape mode.
2. Dynamic analysis is an analysis of the structure in which the division of earthquake shear forces at all levels is obtained by taking into account the dynamic influence of ground motion on the structure. Dynamic analysis is divided into 2 (two) types, which are spectrum response analysis and time history analysis.

In the time history analysis, the earthquake load included in the loading of the structure is in the form of recorded ground motion data from the earthquake that occurred. Dynamic analysis is used to obtain a more accurate evaluation of earthquake and structural behaviour. Dynamic time history analysis is divided into 2 (two) types, namely:

1. Dynamic analysis of linear time history

   Dynamic analysis of linear time history is an analysis of the dynamic response history of a 3-dimensional building structure that behaves fully elastic to the planned earthquake load.
2. Dynamic analysis of non-linear time history

   Dynamic analysis of non-linear time history is an analysis in which the dynamic response of 3-dimensional building structures behaves in full elastic (linear) and elastoplastic (non-linear) behavior against ground motion due to designed earthquake loads.

Dynamic loads give responses that change with time, therefore the structure will also vibrating or moving when it occurred. Apart from that time, history analysis can also cause deformation in the structure as well as other burdens. The one thing that can happen is the deviation between floors (story drift). In SNI 1726-2019 article 7.12.1 concerning inter-floor level intersections have been regulated and can be seen in the following Table 1.

Table 1 Allowed Story Drift, Δa

Structure	Risk Category		
	I or II	III	IV
Structure, apart from the shear wall structure brick, 4 level, or less with the interior walls, partitions, ceilings, and exterior wall systems that have been designed to facilitate floor-level drift.	0,025 h_{sx}	0,020 h_{sx}	0,015 h_{sx}
Brick cantilevered shear wall structure.	0,010 h_{sx}	0,010 h_{sx}	0,010 h_{sx}
Other cantilevered shear wall structure.	0,007 h_{sx}	0,007 h_{sx}	0,007 h_{sx}
All other structures.	0,020 h_{sx}	0,015 h_{sx}	0,010 h_{sx}

Artificial Neural Networks

An artificial neural network or known as ANN is a system that has a way of working as the human brain, this system can be modelled to predict complex things between inputs and outputs to determine a specific pattern. The use of ANN produces a good approach in spectrum response analysis. So ANN is a tool that can recognize patterns and produce output based on network weights in the training process.

In terms of function, ANN was created to design a computer, which can be used to carry out the process of learning from an example of an event. ANN has many methods for predicting values, one of them is the Backpropagation method. Backpropagation methods can estimate errors with gradient values for each network in the ANN architecture. MATLAB Backpropagation is known as a feed-forward backpropagation because this method learning data from the past to predict the value for the future. This method has been widely used in predicting such as flood discharge, water level, up to the performance of a structure. So that the predicted results that will affect the pattern that will occur.

The output generated by the function is activated and calculated the number of errors generated. If the error value has not reached the specified target, then it needs to estimating by error square function or known as Mean Square Error (MSE). MSE is a cost function that forms quadratic parabolic shapes. Activation characteristics function of backpropagation ANN must be continuous,

distinguishable, and monotonous does not go down. In the backpropagation, the ANN calculation process, there are three counting processes, namely forward calculation, backpropagation, and weight and bias changes.

RESEARCH METHODOLOGY

Loads

Based on SNI 1727-2019, loads that used for this building divide into 2 (two) types, that are dead and live loads. In this research using 1,92 kN/m2 distributed loads for dead and live loads on the first floor until the top of this building.

Modal Analysis Steps

Modal analysis is needed to design the structure of the building. With modal analysis, the building response towards external forces that happened can be seen and characteristic of the building based on its frequency and natural periods.

Time History Analysis Steps

In this analysis steps, it needs to design the structure formerly with the standard that defined start from materials data, beam and column profiles, until slab that strong against modal loads. After getting an optimal dimension of the structure, earthquake data were inputted into programs, and time history analysis begins to start, but before these steps begin to run, it needs to defined hinges value first. The value needs to be inputted are IO = 0,003, Ls=0,012, and CP=0,015. Time history analysis generated performance level from the structure of the building after earthquake loads from PEER were inputted. The performance level of structure building and story drift that happened needs to collect to be target data in neural network tools (nntool) from licensed MATLAB.

Meanwhile, story drift that being an objective gets from calculating 2 (two) on the top of the building that can be seen in Figures 1 and 2 below.

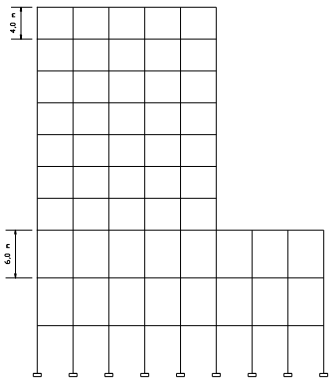

Fig. 1 Building Side View

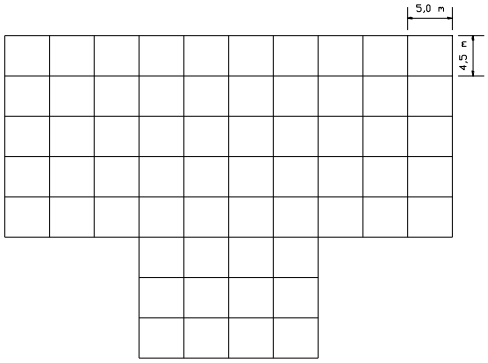

Fig. 2 Floor Plan Top View

Artificial Neural Network Steps

ANN is a tool that used to calculating as biology process like human brains. Human brains have many neural networks and connect to each other. This algorithm architecture has 3 (three) layers consisting of input, hidden, and output.

Other research illustrating networks give input patterns as training patterns; the patterns lead to hidden layer units and be forwarded to output layers. After this process, output layers will give a response named as output networks when output did not generate expected output, it will spread back to the hidden layer and forwarding to input layers. That's why this mechanism named as backpropagation training.

Structure Response such as displacement, velocity, and acceleration are collected will be used as input data. Meanwhile, target data that will be used is performance level data generated by finite element software that used performance level based on FEMA 356. Nntool from licensed MATLAB is helping in predicting the performance level of the building without running all earthquake data one by one from the beginning. Output data generated from ANN processed data will be plotted in the graph and shows how much MSE data and R^2 generated by the networks. Furthermore, the result can be compared with the result from finite element software.

RESULT AND DISCUSSIONS

Modal Analysis

Modal analysis means analyzing the structure from itself weight before external forces such as live loads, dead loads, up to dynamics loads were inputted. In this analysis can be seen how the structure reacts when it holding of its own weight. This analysis of the frequency and the natural periods generated by the structure can be used in designing the building. And furthermore, this analysis can provide a capability percentage of the structural elements that participating withstand external forces

known as Mass Participation Ratio.

In this modal analysis can be seen how the structure deformed starting from rotation, translation, up to torsion. In first mode shapes that generated by the software can be seen in Figure 3 below.

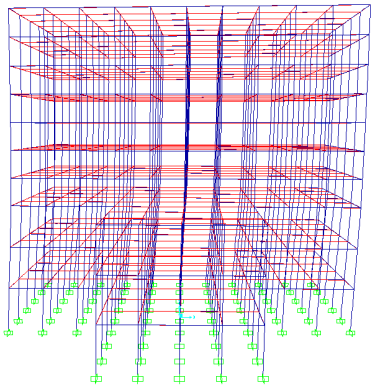

Fig. 3 First Mode Shapes generated by Modal Analysis

With 12 mode shapes is done at first mode with 3,882 cycle/sec frequency and 0,257 seconds natural periods were obtained. So the conclusion that can be taken is the structure need 0,257 second to do translation. For other frequency and periods values, can be seen in Table 2 below.

Table 2 Result of Natural Periods and Frequency

Mode Shapes	Frequency (cyc/sec)	Periods (sec)
1	0.25754	3.882835
2	0.26965	3.708535
3	0.302	3.311207
4	0.89595	1.11614
5	0.89827	1.113253
6	0.96005	1.041608
7	1.4785	0.67637
8	1.4875	0.672252
9	1.5847	0.63103
10	2.0213	0.494734
11	2.0362	0.491121
12	2.1629	0.462342

In SNI 1726-2019 mass participation ratio is not allowed below 90%, and this analysis has reached more that requirement value, which means more than 90% of the structure element has participating withstand external forces. The value generated by this analysis can be seen in Table 3 below.

Table 3 Result of Mass Participation Ratio Modal Analysis

Direction	Static Percent	Dynamic Percent
UX	99.9917	99.2717
UY	99.9917	99.2903
UZ	0.0014	0.00007043

Time History Analysis

Time history analysis in this research is analyzing the structure in linear and non-linear using earthquake record data. From time history analysis results it generated structure response value such as acceleration, velocity, and displacement that happened because earthquake data that were inputted.

Meanwhile, non-linear analysis can generate a performance level of the structure that has been regulated by FEMA 356 as a condition level value of the building. It is just from finite element software only shows the joint that sustains damage against load based on the criteria points that have been set.

Time history analysis can show performance level from the that modeled structures. In this research, level observed every 0,01 seconds, it means the performance of the structure being observed every 0,01 seconds is it has been damaged or yet because of an earthquake. Time history analysis utilizing a hinges to determine damage index that tolerated by FEMA 356 based on used materials. Acceptance criteria used in this research can be seen in the research methodology in the time history analysis steps above. The output from time history analysis can be seen in Figure 4 below.

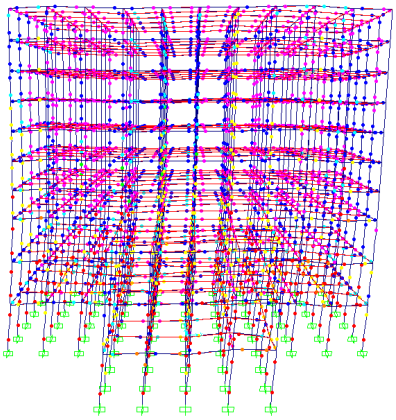

Fig. 4 Performance level result using time history analysis

FEMA 356 has assigned a damage index value that is tolerated in some categories, that is IO, LS, CP. This analysis shows the joint that was damaged by the earthquake loads. This analysis shows the performance levels such as the damage index by FEMA 356 and the story drift that happened.

The data shows that the building suffered different damage each earthquake that occurred, but from the various earthquake data entered no story drift exceeded the specified limit that is less than 0,100 m (0,025 h_{sx}).

ANN with Log-Sigmoid

Log-sigmoid running with calculating an output layer from its input itself. This function carrying input

value to output by log-sigmoid calculation. This analysis generates MSE value of 3,9774 E-07 so the analysis being stopped because the analysis result has reached defined parameters.

In figure 5 below can be seen that training data generated by 97,681%, testing data of 95,153%, validating data of 97,591% and for all is 97,379%. This analysis can be concluded that data have reliable value and fairly accuracy that is 90%, and regression line data approached the desirable line so prediction value by using the log-sigmoid function is credible. The result generated by this analysis can be seen in the graph in Figure 5 below.

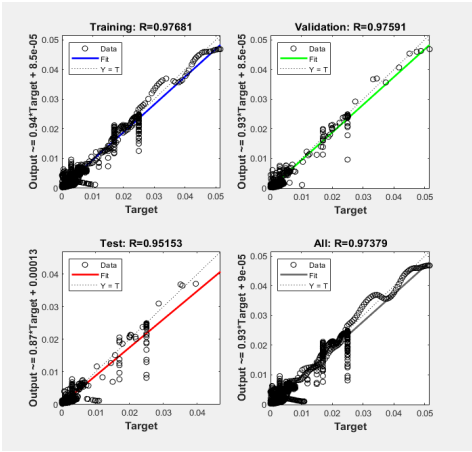

Fig. 5 Result of Log-Sigmoid Analysis Regression Graph Plots

From the analysis can be seen comparison of story drift value predicted by the ANN and the original data as can be seen in Figure 6 and 7 below.

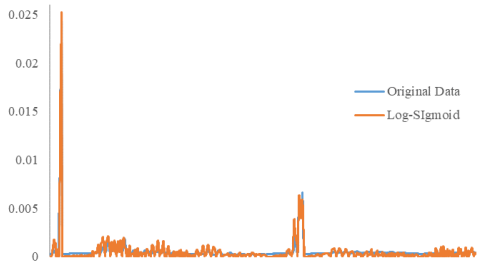

Fig. 6 Story drift Originals vs Log-Sigmoid Predict X direction

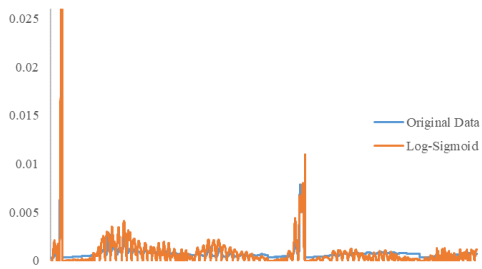

Fig. 7 Story drift Originals vs Log-Sigmoid Predict Y direction

The original and predicted value of the structure performance level used in ANN analysis didn't show much difference.

CONCLUSION

Based on the analysis that has been done, here the following conclusions below.

1. Modal analysis, from this analysis frequency generated by the software, is 0,257 cycle/seconds and periods of 3,882 seconds. Meanwhile, the mass participation ratio has reached a defined standard by that is SNI 1726-2019 is more than 90%.
2. Time history analysis that has been done, some earthquake data shows damage structure up to more than collapse prevention (CP) index levels.
3. Story drift that occurred by the analysis, nothing is exceeded defined value by the SNI 1726-2019 that is 0,100 m (0,025 h_{sx}).
4. ANN analysis using Log-sigmoid analysis shows 97,379% regression value (R_2) and 3,9774 E-07 MSE, it means analyze using Log-Sigmoid function generated reliable data.

REFERENCES

[1] Adnan, A., Suryanita, R. (2012). Intelligent Monitoring System on Prediction of Building Damage Index using Neural-Network. TELKOMNIKA, 10(1). 155-164

[2] American Society of Civil Engineers (ASCE); *Federal Emergency Management Agency* (FEMA). (2000). FEMA 356 Prestandard.

[3] Chopra, A.K. (2012). Dynamics of Structures. University of California at Berkeley.

[4] Indonesian National Standard 03-1727-2013. (2013). Minimum for the Design of Buildings and others structure.

[5] Indonesian National Standard 03-2847-2013. (2013). Structural Concrete Requirements for Buildings.

[6] Indonesian National Standard 03-1726-2019. (2019). Earthquake resistant design procedures for building and nonbuilding structures.

[7] Inel, M. (2007). Modeling ultimate deformation capacity of RC columns using artificial neural networks. 29, 329–335.

[8] Richard, O., Lautour, D., & Omenzetter, P. (2009). Prediction of seismic-induced structural damage using artificial neural networks. *Engineering Structures*, 31(2), 600–606.

[9] Vazirizade, S. M., Nozhati, S., & Zadeh, M. A. (2017). Seismic reliability assessment of structures using artificial neural network. *Journal of Building Engineering*, 11(November 2016), 230–235.

6th Int. Conf. on Structure, Engineering & Environment (SEE), Kyoto, Japan, Nov.18-20, 2020, ISBN: 978-4-909106056 C3051

PERFORMANCE ANALYSIS OF LIGHTWEIGHT CONCRETE BRICKS DUE TO EXPOSURE HIGH TEMPERATURE USING EXPERIMENTAL STUDY

Reni Suryanita[1], Yohannes Firzal[2], Harnedi Maizir[3], Imam Mustafa[4], Mohd Fadzil Bin Arshad[5]
[1]Civil Engineering Department, University of Riau, Kampus Binawidya Jl. HR Soebrantas KM 12,5, Pekanbaru, 28000, Indonesia
[2]Architecture Department, University of Riau, Kampus Binawidya Jl. HR Soebrantas KM 12,5, Pekanbaru, 28000, Indonesia
[3]Civil Engineering Department, Sekolah Tinggi Teknologi Pekanbaru, Jl. Dirgantara No.4, Pekanbaru, 28000, Indonesia
[4]Civil Engineering Department, University of Riau, Kampus Binawidya Jl. HR Soebrantas KM 12,5, Pekanbaru, 28000, Indonesia
[5]Faculty of Civil Engineering, Universiti Teknologi MARA, Shah Alam, Selangor, Malaysia

ABSTRACT

Generally, the effort to make the building load lighter is to use Cellular Lightweight Concrete bricks (CLC) on wall components. CLC bricks contain pores, so the weight is less than red-bricks. Changes in temperature due to building fires have an impact on the characteristics and performance of CLC bricks, especially in density, compressive strength and visual shape of the brick. The research aims to analyse the performance of CLC bricks; compressive strength and appearance of brick surfaces after exposure to high temperatures. The CLC brick model size was 60 cm length, 10 cm width, and 20 cm height. Variation of temperature exposure time is 10 minutes, 20 minutes, 30 minutes and 40 minutes. CLC bricks are placed close to conventional brick kilns with an average surface temperature of 370 degrees Celsius along 40 minutes of combustion. The value of the CLC brick compressive strength test due to exposure to high temperatures for 40 minutes is 0.39 MPa. The compressive strength value decreases 38% from the value at room temperature without temperature exposure. Whereas, the visual form on the surface of the CLC brick gives rise to a blackish grey colour resulting from exposure to high temperatures. The results of this study indicate that the dry and cracked surface texture on CLC brick has caused a decrease in the performance includes density and compressive strength of CLC bricks. Therefore, CLC bricks need to be repaired after being exposed to high temperatures.

Keywords: CLC brick, conventional brick, compressive strength, high temperature

INTRODUCTION

Red-brick is one of the most widely used construction materials in Indonesia. This brick is made by using clay as a primary material in its manufacture conventionally. An excellent red brick has the characteristics of a rough surface, not cracked, not easily broken, a deep red uniform colour, both on the inside or outside of the brick which indicates that the brick is ripe [1]. Nowadays, the development of construction technology is increasing. The impact of technological developments in the field of construction is the discovery of new construction materials such as Cellular Lightweight Concrete (CLC) and Autoclaved Aerated Concrete (AAC). AAC brick is a cellular concrete with air bubbles produced from the chemical reaction of aluminium powder or aluminium paste as a mixture developer [2]. In comparison, CLC bricks are cellular bricks that undergo natural treatment processes. The CLC brickwork process uses organic foam which is very stable, and no chemical reactions occur during the material mixing process [3]-[6].

CLC brick has low strength and density index that can be used as partition walls, acoustic and thermal insulation materials [7]-[8]. CLC brick contains fine air cavity due to the addition of foam to the mass of the mortar, which aims to reduce the value of volume weight [9]. The advantages of CLC bricks make it a viable alternative to wall partitioning compared to red clay bricks.

Increased temperature due to heat exposure from a burning building or direct sunlight can affect the properties of CLC bricks, such as mechanical properties. In the previous study [10], the authors have studied the mechanical properties of CLC bricks such as deformation, tensile strength, compressive strength, and shear strength in various sand and cement ratio. In addition to influencing the mechanical properties of lightweight bricks, the effect of heat transfer also affects the physical properties of CLC bricks [11]. The CLC brick physical properties are measured without changing their original identity

[4],[12]-[13]. One example of material properties is a colour change.

Testing mechanical properties, especially compressive strength testing can be done with several methods including tests that are non-destructive (Non-Destructive Test), and tests that are destructive to all parts of the CLC brick (Destructive Test). In that study, the compressive strength of CLC bricks was produced through destructive testing using a load cell mounted on a steel frame.

The fundamental problem of CLC bricks exposed to high temperatures is how to estimate the compressive strength and what happens to the surface of the CLC bricks after the temperature rise. Therefore, the study aims to identify changes visually and analyse the compressive strength of CLC bricks after exposure to high temperatures. Therefore, the walls of buildings were made of CLC bricks exposed to high temperatures can be anticipated with improvements so that the walls are still suitable for use.

THEORETICAL BACKGROUND

Red-brick, natural stone, brick, wood, plywood, asbestos are materials commonly used in wall construction. Today, the development of these materials is replaced by renewable materials such as Cellular Lightweight Concrete (CLC) brick, as shown in Fig. 1.

(a) (b)

Fig. 1 (a) The Cellular Lightweight Concrete (CLC) brick, (b) and the texture of CLC brick [10].

CLC brick is considered more economical compared to conventional red-brick. Also, the relatively larger form of CLC bricks can shorten the wall working time. CLC bricks are made from a mixture of cement, water, sand and foam to produce a mix of mortar that is ready to be poured on a CLC brick mould [5]. The most critical aspect in planning CLC bricks is how to create lightweight and economic bricks, without ignoring the strength of these lightweight bricks [13]-[15].

The advantages of CLC bricks compared to conventional bricks and concrete bricks are low cost, time-saving, comfortable to work, soundproof, and lightweight so that it does not overload the underlying structure [5]. Therefore, CLC bricks are very suitable for use in tall buildings. In addition, CLC bricks are also suitable for use in building walls of soft soil areas, because they can reduce the load on the foundation.

Another advantage of CLC bricks is in terms of dimensions. CLC bricks have larger dimensions than conventional bricks. Fig. 2 shows the difference in dimensions of conventional brick (red-brick) and CLC bricks. In-wall installation, every 1 m^2 requires 8.3 CLC bricks, whereas for conventional bricks 125 bricks are needed

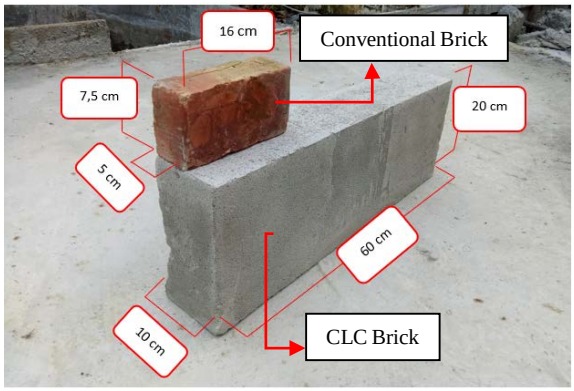

Fig. 2 Dimension of conventional and Cellular Lightweight Concrete (CLC)

According to [6] foam stability is very critical for achieving the optimal density of the CLC mix and for having a closed pore structure. Hydrolysed protein foaming agents impart the desired properties to the produced foam. Commercially available foaming agent called Sunlite Foam SF-30 SPL was used for this analysis. The foaming agent and water were combined in a ratio of 1:40 and fed into the foam generator to achieve a preformed foam density of 70 g/litre. The volume fraction of the mixture of foam is 16 per cent of the overall volume.

The material used in making CLC brick is cement, water, fine aggregate and foaming agent [5], [16]. The composition of the mixture greatly influences the quality of CLC. Cement water factor is essential in making lightweight bricks. Based on research conducted by [6]-[7], [17]-[18], by varying the cement water factor in making concrete, the compressive strength value of the concrete decreases due to an increase in the cement water factor. The selection of aggregates is essential in making CLC bricks. The use of coarse aggregate tends to be difficult during the lightweight brick mixing process because the aggregate will settle to the bottom so that the lightweight brick is not mixed evenly.

The necessary ingredients of foam agents consist of synthetic materials and protein components. Synthetic based foam has a density of around 40 kg/ m^3 and can expand about 25 times the initial volume.

This type of foaming agent is very stable for CLC bricks with masses above 1000 kg / m3. The ratio of foam and water used is 1:19. The solution of 20 litres of foam can expand into about 500 litres of foam with a weight of about 40 kg / m3.

In comparison, protein-based foam obtained from natural materials weighs around 80 kg /m^3 and can expand about 12.5 times the original volume. This foam is relatively more stable and has a higher strength compared to synthetic foam. But this foam can only last up to 12 months in an open state. The ratio of foam and water is 1:33 to 1:39. For a solution of 40 litres of foam can expand into about 500 litres of stable foam weighing around 80 kg /m^3 [10].

High temperature is very influential on CLC bricks. Light bricks exposed to high temperatures can experience colour changes such as in concrete. According to [8] and [19], the colour change of the physical properties of post-burnt concrete is very influential on the temperature during combustion. Discolouration of the concrete begins to appear at a temperature of 500 ^oC, which is greyish brown. The condition occurred because of the presence of iron salt compounds in the aggregate or concrete sand that causes the concrete to change colour. For temperatures reaching 750 ^oC, brick can create a carbonation process that is formed of Calcium Carbonate (CaCO3), which is whitish in colour. So the brick becomes brighter. Based on research conducted by [9], [20], the higher the combustion temperature of the concrete, the higher the damage to the concrete.

RESEARCH METHODOLOGY

This work used two different mass-ratio cement and sand compositions. The first composition is called Variation 1, with the cement-sand ratio being 1:2, and the second composition is called Variation 2, with the cement-sand ratio being 2:3. Table 1 describes the variable composition of the CLC bricks. The research has tested 24 specimens to get lightweight brick strength and density: the foaming agent and water-mass ratio of 1:30 and Sikamen addictive. The CLC paste was made with cement to water ratio (W/C) of 0.5.

The material consists of cement, sand, water and foam agent. At the same time, the leading equipment used in this research included foam generator with a capacity of 200 litres per minute and a capacity of 100 kN compression test machine.

Table 1. Plan for mortar mixture

Specimen Code	Material			
	Cement (kg)	Sand (kg)	W/C ratio	Sikamen (ml)
Variation (1)	100	200	0.5	200
Variation (2)	100	150	0.5	200

Compressive strength testing is carried out in the structure laboratory to obtain the strength of the CLC brick using a loading frame. Compressive strength testing is carried out after 28 days since CLC bricks are made and heated in a brick kiln on the temperature 465 ^oC as shown in Fig 3.

Fig. 3 The process of heating CLC bricks in a furnace.

The test equipment is worked until the full load when the experiment was a collapse is collected. The value of the compressive strength of lightweight brick has been reported using a data logger. Fig. 4 displays the full image of the instrumentation.

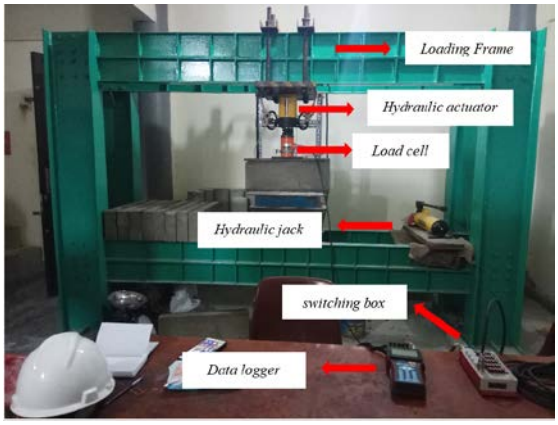

Fig. 4 Instrumentation setting out

RESULT AND DISCUSSION

Table 2 shows the results of the fine-aggregate test suggested the amount of mud on the fine aggregates used in this study met condition according to ASTM C-33 [21], and the fine aggregates provided a medium sand group with a fineness modulus of 2.04. The fine-aggregates mud average is 4.87 per cent. The fine sum has an apparent absolute gravity of 2.65. The findings of the sieve review on fine aggregates showed that fine aggregates were based on Indonesian Standard SNI 03-2828-2011 [22] in Specification No. 4, which notes fine aggregates are fine grading. The value of the fine modulus is an indication that the amount of the fine aggregate is in the mortar.

Table 2. Fine Aggregate Characteristic

No	Testing item	Result	Standard Range
1	Mud rate (%)	4.87	< 5
2	Specific Gravity		
	a. Apparent Specific Gravity	2.65	2.58-2.83
	b. Bulk Specific Gravity on Dry	2.28	2.58-2.83
	c. Bulk Specific Gravity on SSD	2.40	2.58-2.83
	d. Absorption (%)	5.49	2.0 – 7.0
3	Water content (%)	3.73	3 – 5
4	Volume weight (gr/cm^3)		
	a. Solid condition	1787.77	1400-1900
	b. Dry condition	1297.74	1400-1900
5	Rate of Organic	No. 2	Max No. 3
6	Fine-Modulus	2.04	1.5-3.8

Fig. 5 and Table 3 display the effect of the contents of variation composition on the compressive intensity of the CLC brick. Variation 2 with higher cement content demonstrates higher compressive strength at 3, 7, 14, and 28 days of age than Variation 1.

The research resulted in the various compositional effects, including density and compressive strength, of the physical and mechanical properties of CLC brick. In Variation 1 and Variation 2, the use of sand consumption in 1 m^3 of mixing concrete was 200 kg and 150 kg, respectively, when the cement consumption was 100 kg for both variations. Therefore, the use of sand consumption in a fixed quantity for 1 m^3 of concrete mixture in Variation 1 and Variation 2 resulted in decreased cement use in Variation 2 instead of Variation 1. The research affects the mean foam concrete density at the age of 28 days, as shown in Table 3. Variation 2 indicates a higher value for density than Variation 1. The condition shows that increased use of cement in Variation 2 has caused the mixing foam concrete to increase mixed density.

Experimental research shows specimens failure at the bottom at the age of 28 days. The broken texture shows itself around the surface of the CLC brick. Test colours for 28 days, Variation 1 showed the specimen is brighter than Variation 2, as shown in Fig 6 and Fig 7.

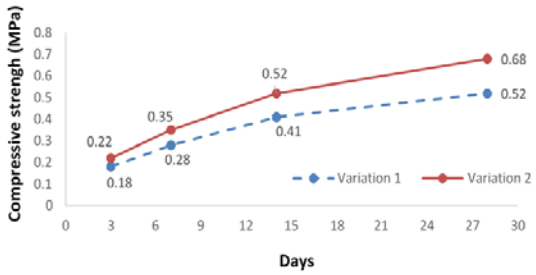

Fig. 5. Compressive strength of The CLC brick

Table 3. The Compressive strength with the variation of composition cement and sand

Variation No.	Cement : Sand	Compressive Strength (MPa)			
		3 days	7 days	14 days	28 days
1	1 : 2	0.18	0.28	0.41	0.52
2	2 : 3	0.22	0.35	0.52	0.68

Fig 6. The compressive test on specimen Variation 1 age 28 days.

The increased density allowed the addition of cement to the lightweight mixture of concrete. Hence Variation 2 power is higher than Variation 1. Nevertheless, due to small additions (low strength) the increase in force generated is not large. While the findings of this study are similar to studies published in the literature, such as [4] and [5], so reducing the size of sand particles will lead to increased foam concrete resistance. Replacing sand with materials

such as fly ash might lead to greater strength, and fine aggregate fillers could also produce higher strength and density ratios.

Fig 7. The compressive test on specimen Variation 2 age 28 days

Based on visual observations of brick CLC due to exposure to high temperatures, several changes such as CLC brick colour changes and changes in pore size have occurred. Colour-changes in the CLC brick began to be seen since the CLC brick was exposed for 30 minutes. The exposed brick surface has turned brownish. Table 4. shows the exposure temperature of CLC bricks in parts directly exposed to high temperatures.

Table 4. The temperature of CLC brick exposure

Minute	Variation 1 (°C)	Variation II (°C)
10	313	289
20	340	358
30	345	366
40	370	370

In addition to changes in colour, due to exposure to high temperatures also cause changes in pore size of the lightweight brick. Pores that have initially been small in size, as shown in Fig 8, due to exposure to high temperatures caused the size of the brick pores to become enlarged, as shown in Fig 9.

Fig. 8 The CLC brick pores before exposure high temperature

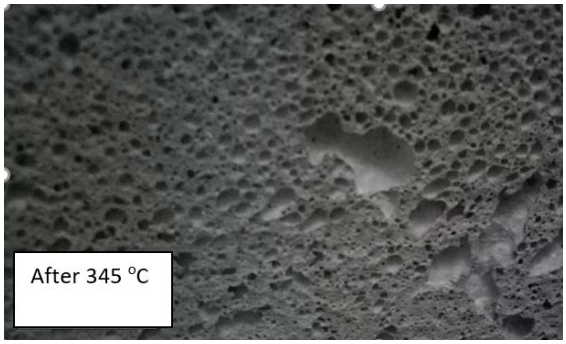

Fig. 9 The CLC brick pores after exposed high temperature.

Based on the results of the compressive strength test on 28 days CLC bricks before exposure to high temperatures has a density value 0.850 grams/cm^3. Exposure to high temperatures for 10, 20, and 30 minutes, has led to a decrease in the weight of the volume of CLC bricks respectively to 0.833 grams/cm^3, 0.811 grams/cm^3 and 0.808 gram/cm^3. Finally, at 40 minutes exposed to high temperature, there was a decrease to 0.803 gram/cm^3. Figure 10 shows the relationship between density and compressive strength during high temperature exposure.

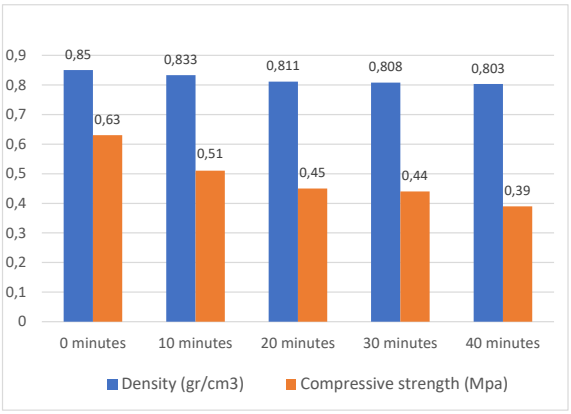

Fig. 10 The performance of CLC brick before and after exposed high temperature

CONCLUSION

Based on the research that has been done, the following conclusions can be drawn:

1. Exposure to high temperatures in CLC bricks can cause discolouration, change in pore size, change in volume weight, and change in compressive strength of the bricks.
2. CLC bricks exposed to high temperatures for 40 minutes have caused a decrease in volume weight from the original 0.85 gram/cm3 to 0.803 gram /cm3. In addition to the reduction in density, the compressive strength test results of the CLC brick

show the compressive strength of the CLC bricks changed from 0.63 MPa to 0.39 MPa.

ACKNOWLEDGMENTS

The author would like to thank the financial support from the University of Riau for funding this research under the AKSI project through the PNBP Grant for the International Research Collaboration 2020 scheme.

REFERENCES

[1] T. V. Vakalova and I. B. Revva, "Use of zeolite rocks for ceramic bricks based on brick clays and clay loams with high drying sensitivity," *Constr. Build. Mater.*, vol. 255, p. 119324, 2020.

[2] A. Artino, G. Evola, G. Margani, and E. M. Marino, "Seismic and energy retrofit of apartment buildings through autoclaved aerated concrete (AAC) blocks infill walls," *Sustain.*, vol. 11, no. 14, 2019.

[3] F. Koksal, Y. Sahin, and O. Gencel, "Influence of expanded vermiculite powder and silica fume on properties of foam concretes," *Constr. Build. Mater.*, vol. 257, p. 119547, 2020.

[4] S. Zhang, K. Cao, C. Wang, X. Wang, J. Wang, and B. Sun, "Effect of silica fume and waste marble powder on the mechanical and durability properties of cellular concrete," *Constr. Build. Mater.*, vol. 241, p. 117980, 2020.

[5] D. Jain, A. K. Hindoriya, and S. S. Bhadauria, "Evaluation of properties of cellular light weight concrete," *AIP Conf. Proc.*, vol. 2158, no. September, 2019.

[6] A. Bhosale, N. P. Zade, P. Sarkar, and R. Davis, "Mechanical and physical properties of cellular lightweight concrete block masonry," *Constr. Build. Mater.*, vol. 248, p. 118621, 2020.

[7] M. A. Rasheed and S. S. Prakash, "Behavior of Hibrid-Synthetic Fiber Rereinforced Cellular Lightweight Concrete under Uniaxial Tension – Experimental and analytical studies," *Constr. Build. Mater.*, vol. 162, pp. 857–870, 2018.

[8] M. R. Ahmad, B. Chen, and S. Farasat Ali Shah, "Investigate the influence of expanded clay aggregate and silica fume on the properties of lightweight concrete," *Constr. Build. Mater.*, vol. 220, pp. 253–266, 2019.

[9] E. Papa *et al.*, "Porosity and insulating properties of silica-fume based foams," *Energy Build.*, vol. 131, pp. 223–232, 2016.

[10] H. Maizir, R. Suryanita, and R. Arditama, "Study on performance of lightweight concrete bricks with a ratio of sand and cement composition," *IOP Conf. Ser. Mater. Sci. Eng.*, vol. 615, no. 1, 2019.

[11] A. Thongtha, S. Ketchaona, J. Wattana, and T. Patanin, "Influence of portland cement on physical, mechanical and thermal properties of cellular lightweight concrete," *Key Eng. Mater.*, vol. 751 KEM, pp. 532–537, 2017.

[12] Z. Liu, K. Zhao, C. Hu, and Y. Tang, "Effect of Water-Cement Ratio on Pore Structure and Strength of Foam Concrete," *Adv. Mater. Sci. Eng.*, vol. 2016, 2016.

[13] F. K. Alqahtani and I. Zafar, "Characterization of processed lightweight aggregate and its effect on physical properties of concrete," *Constr. Build. Mater.*, vol. 230, p. 116992, 2020.

[14] T. J. Chandni and K. B. Anand, "Utilization of recycled waste as filler in foam concrete," *J. Build. Eng.*, vol. 19, pp. 154–160, 2018.

[15] Z. Zhang and H. Wang, "The pore characteristics of geopolymer foam concrete and their impact on the compressive strength and modulus," *Front. Mater.*, vol. 3, no. August, pp. 1–10, 2016.

[16] L. Chica and A. Alzate, "Cellular concrete review: New trends for application in construction," *Constr. Build. Mater.*, vol. 200, pp. 637–647, 2019.

[17] H. S. Gökçe, D. Hatungimana, and K. Ramyar, "Effect of fly ash and silica fume on hardened properties of foam concrete," *Constr. Build. Mater.*, vol. 194, pp. 1–11, 2019.

[18] E. Namsone, G. Šahmenko, and A. Korjakins, "Durability Properties of High Performance Foamed Concrete," *Procedia Eng.*, vol. 172, pp. 760–767, 2017.

[19] J. A. Bogas and D. Cunha, "Non-structural lightweight concrete with volcanic scoria aggregates for lightweight fill in building's floors," *Constr. Build. Mater.*, vol. 135, pp. 151–163, 2017.

[20] R. Suryanita, H. Maizir, Ismeddiyanto, R. Andriano, and R. Arditama, "Experimental study and numerical analysis of flexural behaviour of post-fire reinforced concrete beam," *IOP Conf. Ser. Mater. Sci. Eng.*, vol. 615, no. 1, 2019.

[21] ASTM Standard C33, "Standard Specification for Concrete Aggregates," *ASTM Int.*, vol. i, no. C, p. 11, 2003.

[22] BSN, *SNI-2828-2011 Soil Density Test Method in Place (Field) with a Sand Cone*. 2011.

Engineering

6th Int. Conf. on Structure, Engineering & Environment (SEE)
Kyoto, Japan, Nov.18-20, 2020, ISBN: 978-4-909106032 C3051

EVALUATION OF RECOVERY OF DEBRIS FLOW CONTROL BY CHECK DAMS AFTER REMOVING DEBRIS BASED ON NUMERICAL SIMULATION

Naomasa Honda[1]

[1] Faculty of Regional Environment Science, Tokyo University of Agriculture, Japan

ABSTRACT

The present paper evaluated the recovery of a debris flow control by check dams after removing debris from check storage areas based on the numerical results of both a model and an actual torrent. A one-dimensional numerical simulation is conducted to investigate the variations in the debris flow characteristics along a river reach with check dams. In the calculation, the check storage area was either filled with sediment or emptied by removing debris. The analytical results show that check dams effectively reduced the sediment transport when the initial bed slope of the deposition area at the dam's upstream region is gentler than the equilibrium slope of the debris flow, even if the area is filled with sediment. Removing debris from the check storage area is much more effective for controlling the debris flow, but a priority ranking for removing the works of a number of check dams must be carefully determined when considering the sediment runoff process and its characteristics throughout a torrent.

Keywords: Check dam, Check storage area, Removing debris, Debris flow control, Numerical simulation

INTRODUCTION

A check dam basically controls sediment runoff based on its storage volume [1], [2]. It can control the debris flow with a change of the deposition gradient at the check storage area even if it is filled with sediment. Since check dams, which were constructed a long time ago, have check storage areas that are filled with sediment, their ability must be restored to control the debris flow by removing debris from them. But no debris has been removed, and as alternative facilities, new check dams have been constructed, because removing debris faces the following difficulties:

- Securing such sites as approach paths to dams and the stock yards of removed debris:
- Disposal and recycling methods of the removed debris:
- Influence on neighboring environments

Since appropriate places at which to build new check dams are limited, they must be restored the check storage ability to control debris flow by removing debris. In addition, in an actual torrent, the recovery of debris flow control by check dams that removed the debris should be evaluated as a group of dams, not as individual structures, because the actual bed slope and the width irregularly changes in the river, and strongly influences the debris flow characteristics and the storage's ability to check the flow.

The present paper evaluates the recovery of the debris flow control by check dams after removing debris from the check storage area based on the numerical analysis results of virtual and actual torrents.

A one-dimensional numerical simulation, which is comprised of mass and momentum conservation equations for debris flow and erosion velocity formula on debris from riverbeds, is conducted to investigate the variations in the debris flow characteristics along a river that reaches the check dams. In the calculation, the check storage area was either filled with sediment or emptied by removing the debris. Such debris flow characteristics as sediment discharge and sediment flux concentration can be predicted to estimate the recovery of the debris flow control by check dams after removing the debris.

METHOD AND PROCEDURE FOR STUDY

Characteristics of check storage area

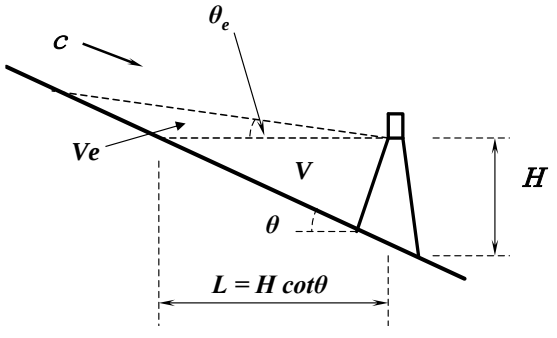

Fig. 1 Check storage area

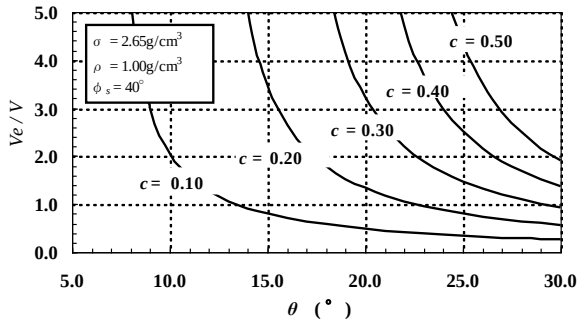

Fig. 2 Relationship among θ, c, and V_e/V: Flow width is constant in all section.

Figure 1 shows a schematic diagram of the check storage area of a check dam, where θ is the bed slope, c is the sediment concentration by volume, θ_e is the equilibrium bed slope that correspond to the sediment concentration, H is the check dam's height, V is the deposited amount of sediment to H (θ_e.= 0), and V_e is the additional deposition amount of sediment with θ_e, defined by Eq. (1) [3]:

$$\theta_e = \tan^{-1}\left\{\frac{(\sigma/\rho-1)c}{(\sigma/\rho-1)c+1}\tan\phi_s\right\} \tag{1}$$

where σ is the mass density of the gravel, ρ is the mass density of the water, and ϕ_s is the internal friction angle of the sediment.

The following is the relationship among θ, c, and V_e:

- When θ is constant, V_e is large and c is large (therefore, θ_e is large, as shown in Eq. (1)).
- When c is constant (therefore, θ_e is a constant shown in Eq. (1)), V_e is large, and θ is small.

When the flow width is constant in all the sections, the following is the relationship between V_e and V:

$$V_e/V = \frac{\cos\theta\sin\theta_e}{\sin(\theta-\theta_e)} \tag{2}$$

Figure 2 shows Eq. (2) as a horizontal axis in θ. Generally, in actual torrents, their flow width and the storage area's width irregularly change, but Fig. 2 directly shows the relationship among θ, c, and V_e.

Governing equations for debris flow

To analyze the sediment transport in a river reach [4], [5], the one-dimensional equations developed by Egashira et al. [4] is used. The following are the mass conservation equations for the flow mixture and the sediment alone:

$$\frac{\partial h}{\partial t}+\frac{1}{B}\frac{\partial Bvh}{\partial x}=\frac{E}{c_*} \tag{3}$$

$$\frac{\partial \varepsilon ch}{\partial t}+\frac{1}{B}\frac{\partial \varepsilon cBvh}{\partial x}=E \tag{4}$$

where t is the time, x is the coordinate axis along the flow, h is the flow depth, B is the flow width, v is the flow velocity, E is the erosion velocity (its negative value designates the deposition), ε is the correction factor (Egashira et al. [6], $\varepsilon c = c_t$, c_t is the sediment flux concentration), and c_* is the sediment concentration of the bed layer. The following is the momentum conservation equation:

$$\frac{\partial v}{\partial t}+v\frac{\partial v}{\partial x}=g\sin\theta-\frac{1}{\rho_m h}\frac{\partial P}{\partial x}-\frac{vE}{c_* h}-\frac{\tau_b}{\rho_m h} \tag{5}$$

$$\rho_m=(\sigma-\rho)c+\rho \tag{6}$$

The second term on the right-hand side of Eq. (5) is the pressure gradient, and the third term is the resistance due to the sediment erosion. g is the gravity acceleration, P is the pressure, τ_b is the bed shear stress, and ρ_m is the mass density of the flow mixture defined in Eq. (6). The mass conservation equation of the bed sediment takes the following form:

$$\frac{\partial Z_b}{\partial t}=-\frac{E}{c_*\cos\theta} \tag{7}$$

$$\theta=\sin^{-1}\left(-\frac{\partial Z_b}{\partial x}\right) \tag{8}$$

where Z_b is the bed elevation, and θ is expressed by Eq. (6). As mentioned above, even though E and τ_b play an important role in the governing equations, no general formulas have been developed for them. In this study, the formulas for E [4] and τ_b [7] developed by Egashira et al. are used

Erosion velocity E is the as following:

$$\frac{E}{v}=c_*\tan(\theta-\theta_e) \tag{9}$$

The following is bed shear stress τ_b:

$$\tau_b=\tau_y+\rho f v^2 \tag{10}$$

$$\tau_y=\left(\frac{c}{c_*}\right)^{1/5}\rho(\sigma/\rho-1)cgh\cos\theta\tan\phi_s \tag{11}$$

$$f=\frac{25}{4}\left\{k_f\frac{(1-c)^{5/3}}{c^{2/3}}+k_g\frac{\sigma}{\rho}(1-e^2)c^{2/3}\right\}\left(\frac{h}{d}\right)^{-2} \tag{12}$$

In Eq. (10), τ_y is the yield stress caused by the particle to particle contacts defined in Eq. (11), and f is the friction factor defined as Eq. (12), where e is the restitution coefficient, d is the reference grain size, and k_f and k_g are coefficients: k_f=0.16, k_g =0.0828.

Examination cases and calculation conditions

In actual torrents, the flow width and the bed slope change irregularly, and the sediment that becomes the constitution materials of the debris flow is partly distributed on the bed. These geographical conditions greatly influence the calculation results of such debris flow characteristics as h, c, and v. They also influence both the sediment and the flow discharges, which closely affect the debris flow characteristics of check dam's storage.

In this study, the following two torrents are set: the virtual torrent with a constant width, the actual torrent whose width irregularly changes.

Virtual torrent's case

Figure 3 shows a river-bed profile of the virtual torrent. The following is its conditions:

- Total river length; L=900m (horizontal distance =985m, relative height=187m);
- Flow width; B =constant=20m (in all sections);
- Bed inclines are 18degrees, 12degrees, and 6 degrees every 300m from the upper reaches.
- Three dams exist from Nos.1 to 3 at the change points of the bed incline. No.1 dam's height is H_1=3.0m, No.2 dam's height is H_2=4.0m, and No.3 dam's height is H_3=5.0m. But the storage areas of all three dams are filled with sediment.
- The sediment has eroded and exists fat a thickness of 2.0m (the critical erosion depth of the bed material) on the bed.
- If just a little water is supplied, and the bed sediment begins to move in a saturated soil state, it is adequate in a numerical simulation. Therefore, an inflow water discharge is constantly supplied 0.10m^3/sec at the upstream boundary, and for convenience assumed sediment concentration c_{in} by volume.

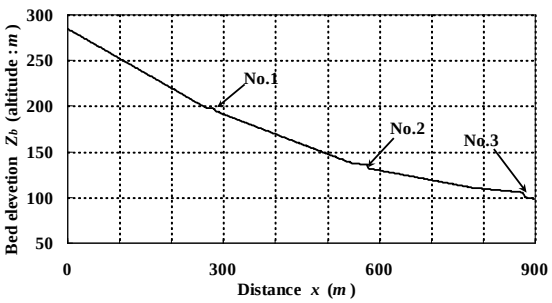

Fig. 3 Bed profile of virtual torrent

Actual torrent's case

Ohzedani River, a tributary of the Sendai River in Tottori Prefecture, flows into the Japan Sea (Figs. 4(a) and (b)). It has drainage of 3.2km^2 and a river reach of 4.1km. Its mean bed slope is 10.8degrees, and its width changes irregularly (Figs. 4(c) and (d)). During drainage, the mountain slope is steep, and weathering granite rock, which is very susceptible to erosion, is widely distributed on the mountainside. Unstable sediment is often produced during drainage. This torrent is defined as a river's stream that poses the risk of a debris flow.

In this basin, a very active sediment runoff was caused in September 1961 by the Second Muroto typhoon. Debris flow arrived at the lowest stream reach near Kofune Village (Fig. 4(b)). However, the torrent did not overflow its banks because a check dam (No. 3 dam in Fig. 4(c)) and channel works, constructed at a village located downstream of the river's reach (Fig. 4(b)), effectively reduced the sediment transport and controlled the debris flow [8]. After the disaster, two check dams were constructed as countermeasures against sediment-related disaster's hazards: No. 2 and No. 3 dams in Fig. 4(c).

In this paper, the following are the actual torrent's conditions:

- This study analyzed a 3,200m long river reach 380 to 990m above sea level from the point where the bed slope changes suddenly to a confluence of the Ochiori River.
- The bed and width profiles are shown in Figs. 4(c) and (d).
- Three dams are shown in Fig. 4(c). No. 1 dam's height is H_1=5.2m, and its width is B_1=25.0m; No. 2 dam's height is H_2=8.8m, and its width is B_2=42.0m; No. 3 dam's height is H_3=5.5m, and its width is B_3=53.0m. The storage areas of all three dams are filled with sediment.
- This study assumed that the sediment was mainly supplied by bed erosion and estimate that the critical erosion depth of the bed material equaled 2.5m based on previous study's results [8].
- The maximum hourly precipitation was 58.0mm in the September 1961 debris flow hazard. The rainfall intensity of this value is chosen, which yields 0.50m^3/sec at the reach's upstream end, using a rational formula with a drainage area of 0.05km^2 and a runoff coefficient of 0.60. Such an inflow water discharge is supplied constantly, and for convenience sediment concentration c_{in} is assumed to be 5% by volume.

Conditions shared by two cases

The storage area's state before and after removing the debris and the conditions of the check dam's storage area are set in the numerical simulation (Fig.5, Table 1).

(a) Location of Tottori Prefecture in Japan

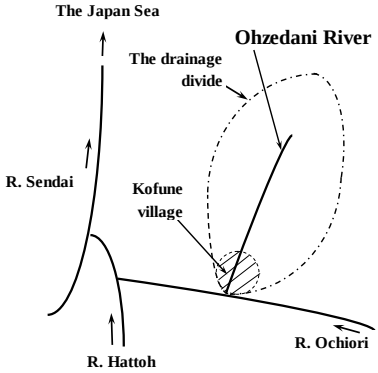

(b) Schematic diagram of Ohzedani River basin

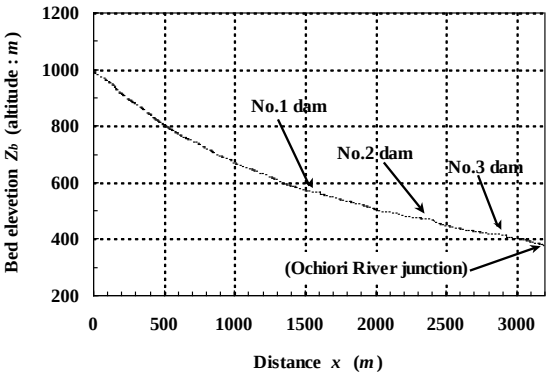

(c) Bed profile of Ohzedani River

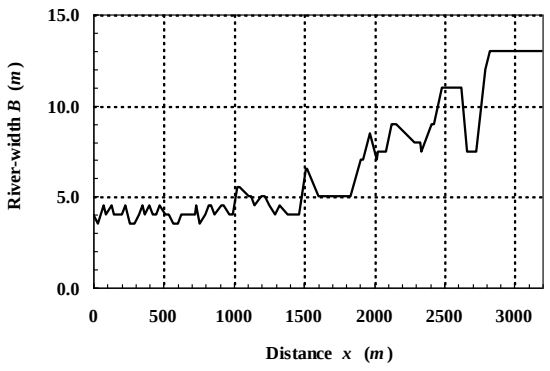

(d) Width of Ohzedani River

Fig. 4 Outline of actual torrent: Ohzedani River

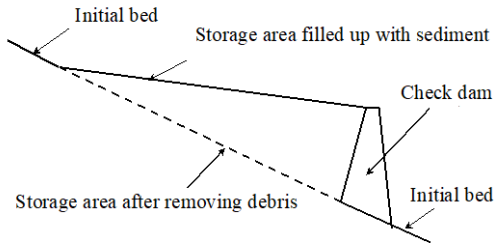

Fig.5 Schematic diagram of dam's storage area in numerical simulation

Table 1 Conditions of check dam's storage area in numerical simulation

Case.	Sediment storage conditions of dams ●: Being filled up ○: after removing		
	No.1	No.2	No.3
1	●	●	●
2	●	●	○
3	●	○	●
4	●	○	○
5	○	●	●
6	○	●	○
7	○	○	●
8	○	○	○

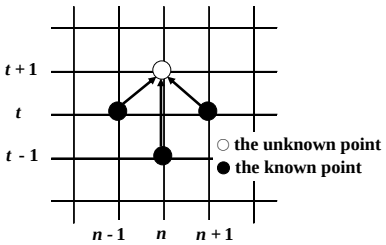

Fig.6 Schematic diagram of leap-frog scheme

The following parameters are required for computation: σ= 2.70g/cm^3, ϕ_s = 39.0degrees, d= 5.0cm, and c_*= 0.50, respectively.

Fine sand concentration in water c_s, is the closely related to a rise in the water's density (muddy water). Because such a rise increases buoyancy, the analysis cannot ignore its influence [9], [10]. When it is assumed that c_s equals 10%, ρ is calculated by Eq. (8) as follows: ρ =1.17g/cm^3 (c_s = 10%)

In this study, the finite difference method is used (leap-frog scheme in Fig. 6). The time and distance are discriminated as Δt=0.025 seconds and Δx=5.0 m, respectively.

RESULTS AND DISCUSSIONS

Virtual torrent's case

Figures 7(a), (b), and (c) show the temporal changes of the bed elevation near three check dams after 300 seconds with their water supply as an

example (all three check dam's storage areas are filled with sediment, i.e., Case 1 in Table 1). All the check dams deposited sediment at their storage areas and controlled the debris flow's power by changing of the check storage gradient. The bed erosion immediately downstream of the check dams was caused by overflow from the dam.

Figures 8(a) and (b) show the temporal changes of sediment flux concentration c and sediment discharge Q_s at the cross-sections: x=200m and 300m (upstream and downstream of No. 1 dam), x=500 and 600m (upstream and downstream of No. 2 dam), x=800m and 900m (upstream and downstream of No. 3 dam) as an example (Case 1 in Table 1). In these figures, the debris flow control with every check dam can be evaluated by the peak cut value, i.e., comparing two values between check dam's upstream and downstream. Similarly, the debris flow control as a check dam group can be estimated by the maximum values of c and Q_s and total sediment volume ΣQ_s at the downstream end (x=900m).

Table 2 shows the numerical results based on the conditions of the check dam's storage area in Table 1. Removing the debris from the check storage of No.1 dam (from Cases 5 to 8) is generally affective for the comprehensive evaluation shown as ΣQ_s. But after removing debris from the check storage of No. 1, its sediment discharge downstream is larger than the upstream value, because the bed erosion immediately downstream of the check dams occurred due to the dam's overflow.

After carefully removing the debris from the check storage of No. 2 dam, the ΣQ_s of Case 3, which only removed the debris from No. 2, is larger than Case 1, where all three check storages are filled with sediment (▲ in Table 2). This is because the check storage slope of No. 2 (after removing debris) became steeper than before removing it and bed erosion was accelerated.

In Table 2, note that the ΣQ_s of Case 6 (No. 1 and No. 3 dams are removed the debris, and No. 2 dam isn't removed). Case 6 is smaller and more effective for the debris flow control than Case 8, which removed debris from all three check storages and is the smallest and most effective case.

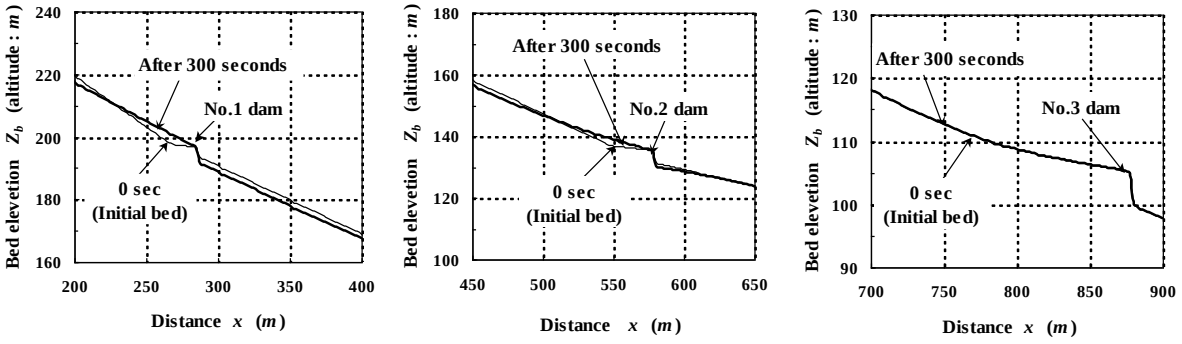

(a) Near No. 1 dam (b) Near No. 2 dam (c) Near No. 3 dam

Fig. 7 Temporal changes of bed elevations near check dams in virtual torrent
(Case 1 in Table 1: all three check dam's storage areas are filled up with sediment.)

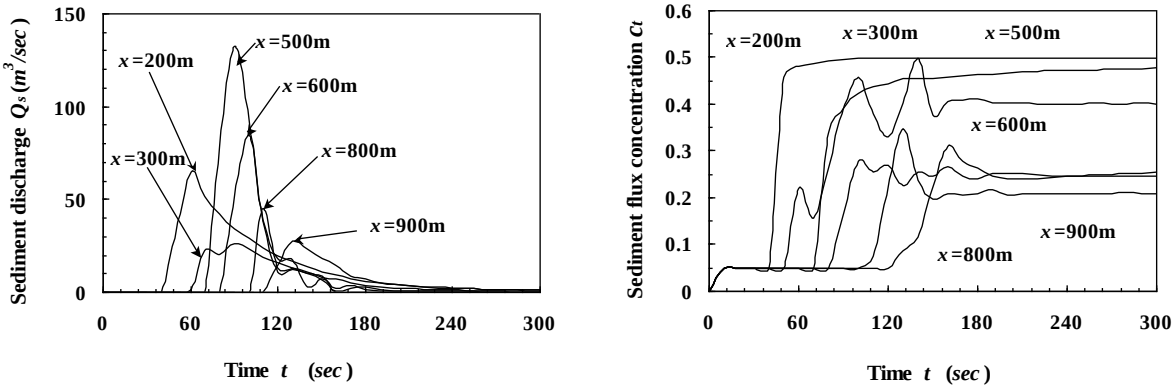

(a) Sediment discharge (b) Sediment flux concentration

Fig.8 Temporal changes of debris flow characteristics as an example in virtual torrent
(Case 1 in Table 1: all three check dam's storage areas are filled up with sediment.)

Table 2 Debris flow runoff control by check dams evaluated by peak cut quantity of sediment discharge Q_s in the virtual torrent

Case	Sediment storage conditions of dams ●: Being filled up ○: after removing			Peak cut quantity of sediment discharge *Qs* using several dams									*Qs* max (m^3/sec) (x=500m)	Debris flow runoff control using three check dams evaluated by peak cut quantity of sediment dischaerge *Qs*			
				No.1 dam (x=285m)			No.2 dam (x=578m)			No.3 dam (x=878m)				Downstream end (x=900m)			
	No.1	No.2	No.3	Upstream (x=200m)	Downstream (x=300m)	Peak cut (m^3/sec)	Upstream (x=500m)	Downstream (x=600m)	Peak cut (m^3/sec)	Upstream (x=800m)	Downstream (x=900m)	Peak cut (m^3/sec)		*Qs* max (m^3/sec)	Σ*Qs* (m^3)	Rate with Case.1	Comprehensive Evaluation
1	●	●	●	65.08	26.52	38.56	132.60	84.18	48.43	45.41	27.85	17.56	132.60 (x=500m)	27.85	1430.23	1.00	
2	●	●	○							96.72	20.05	76.67		20.05	965.97	0.68	**3**
3	●	○	●				128.51	82.08	46.43	48.44	27.76	20.68	128.51 (x=500m)	27.76	1496.26	1.05	▲
4	●	○	○							88.15	26.74	61.40		26.74	1174.12	0.82	
5	○	●	●		107.31	-42.23	131.44	72.77	58.67	59.35	20.95	38.40	131.44 (x=500m)	20.95	1040.40	0.73	
6	○	●	○							101.97	13.14	88.82		13.14	594.55	0.42	**1**
7	○	○	●				124.95	69.76	55.19	41.39	22.98	18.41	124.95 (x=500m)	22.98	1025.73	0.72	
8	○	○	○							85.50	11.51	73.99		11.51	662.89	0.46	**2**

With Based on economic and feasibility reason, intensively removing debris from the check storage of No. 3, which is the most downstream (debris flow deposition area) location, is the most effective for the debris flow control shown Case 2 in Table 2.

Actual torrent's case

Figures 9(a), (b), and (c) show the temporal changes of the bed elevation near the check dams after 600 seconds with their water supply as an example (all three check dam's storage areas are filled with sediment, i.e. Case 1 in Table 1). All the check dams deposited sediment in their storage areas and controlled the debris flow's power by the check storage width and the changes of the check storage gradient. Bed erosion immediately downstream of the check dams was caused by overflow from the dam.

Figures 10(a) and (b) show the temporal changes of sediment flux concentration c_t and sediment discharge Q_s at the cross-sections: x=400m (debris flow occurrence area), x=1,500m and 1,700m (upstream and downstream of No. 1 dam), x=2,300m and 2,500m (upstream and downstream of No. 2 dam), x=2,800m and 3,000m (upstream and downstream of No. 3 dam) as an example (Case 1 in Table 1).

Tables 3(a) and (b) show the numerical results based on the conditions of the check dam's storage area in Table 1. By scrutinizing the No. 1 and No. 2 dams in Table 3(a), it can be confirmed the peak cut of c_t from Cases 1 to 6. The reason is because the check dams changed the sediment transport modes based on their check storage width even if the check storage areas were filled with sediment. On the other hand, focusing on No. 3 dam, there are cases when c_t increases downstream of No.3 (Cases 1, 2, 5, 6, and 7 in Table 3(a)) because the sediment was deposited in the channel works downstream of No. 3.

Focusing on Cases 2, 3, and 5 in Table 3(b), which show debris that was separately removed, Case 2 removes the debris from the check storage of the No. 2 dam, which is the most effective decision for debris flow control of all the three cases as shown Q_{smax} and ΣQ_s at the downstream end. The reason is because the check storage volume of No. 2 is the largest of all three dams and Q_{smax} occurs near No. 2 shown in Case 1 in Table 3(b).

Focusing on Cases 4, 6, and 7 in Table 3(b), which removed debris from two check storages, Cases 4 and 7,

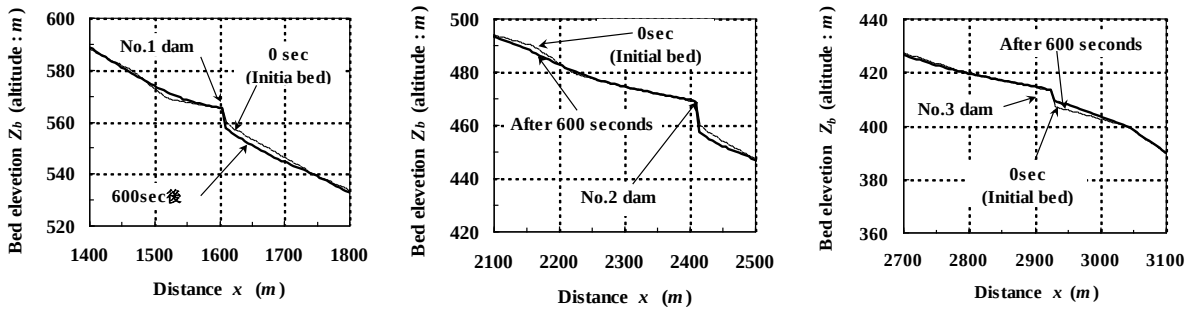

(a) Near No. 1 dam (b) Near No. 2 dam (c) Near No. 3 dam

Fig. 9 Temporal changes of bed elevations near check dams in actual torrent
(Case 1: all three check dam's storage areas are filled up with sediment.)

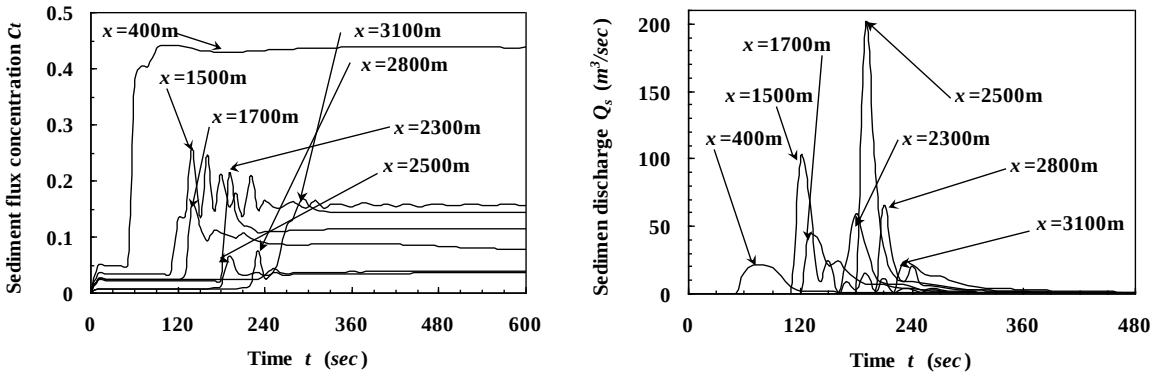

(a) Sediment flux concentration (b) Sediment discharge

Fig. 10 Temporal changes of debris flow characteristics as an example in actual torrent (Case 1: all three check dam's storage areas are filled up with sediment.)

Table 3 Debris flow runoff control by check dams evaluated by peak cut quantity in actual torrent

(a) Sediment flux concentration

Case	Sediment storage conditions of dams ●: Being filled up ○: after removing			Peak cut quantity of sediment flux concentration c_t using several dams									Debris flow runoff control using three check dams evaluated by peak cut quantity of sediment flux concentration c_t		
				No.1 dam (x=1,605m)			No.2 dam (x=2,410m)			No.3 dam (x=2,925m)			$c_{t\,max}$		
	No.1	No.2	No.3	Upstream (x=1,500m)	Downstream (x=1,700m)	Peak cut	Upstream (x=2,300m)	Downstream (x=2,500m)	Peak cut	Upstream (x=2,800m)	Downstream (x=3,100m)	Peak cut	Debris flow occurrence (x=400m)	Downstream end (x=3,200m)	Comprehensive Evaluation
1	●	●	●	0.27	0.16	0.11	0.21	0.07	0.14	0.08	0.17	-0.09	0.44	0.13	
2	●	●	○							0.09	0.16	-0.07		0.13	
3	●	○	●				0.29	0.23	0.06	0.17	0.15	0.02		0.13	
4	●	○	○							0.22	0.12	0.10		0.09	**2**
5	○	●	●		0.21	0.06	0.17	0.04	0.13	0.05	0.14	-0.09		0.13	
6	○	●	○							0.08	0.15	-0.07		0.13	
7	○	○	●				0.18	0.12	0.06	0.09	0.14	-0.05		0.12	**3**
8	○	○	○							0.19	0.08	0.11		0.05	**1**

(b) Sediment discharge

Case	Sediment storage conditions of dams ●: Being filled up ○: after removing			Peak cut quantity of sediment discharge Qs using several dams									Debris flow runoff control using three check dams evaluated by peak cut quantity of sediment discharge Qs			
				No.1 dam (x=1,605m)			No.2 dam (x=2,410m)			No.3 dam (x=2,925m)			Qs max (m^3/sec)	Downstream end (x=3,200m)			
	No.1	No.2	No.3	Upstream (x=1,500m)	Downstream (x=1,700m)	Peak cut (m^3/sec)	Upstream (x=2,300m)	Downstream (x=2,500m)	Peak cut (m^3/sec)	Upstream (x=2,800m)	Downstream (x=3,100m)	Peak cut (m^3/sec)		Qs max (m^3/sec)	ΣQs		Comprehensive Evaluation
															ΣQs (m^3)	Rate with Case.1	
1	●	●	●	101.87	44.34	57.53	58.91	200.74	-141.83	65.20	23.20	42.00	200.74 (x=2,500m)	20.68	1742.46	1.00	
2	●	●	○							109.14	14.42	94.72		10.82	891.16	0.51	
3	●	○	●				77.94	81.85	-3.91	24.83	5.23	19.60	101.87 (x=1,500m)	5.13	675.38	0.39	
4	●	○	○							38.76	2.54	36.22		1.99	226.59	0.13	**2**
5	○	●	●		64.92	36.95	32.49	49.05	-16.56	48.91	12.82	36.09	101.87 (x=1,500m)	11.64	1060.16	0.61	
6	○	●	○							81.45	6.30	75.15		5.47	460.87	0.26	
7	○	○	●				64.13	57.48	6.65	10.95	2.15	8.80		2.06	238.76	0.14	**3**
8	○	○	○							15.73	0.91	14.82		0.77	78.81	0.05	**1**

which always removed debris from the check storage of No. 2, are equally effective for the debris flow control shown by Q_{smax} and $\Sigma\, Q_s$ at the downstream end. Removing debris from the check storage of No. 2 is the most effective strategy.

Focusing on Cases 4, 7, and 8 in Tables 3(a) and (b), where debris flow is always removed from the check storage of No. 2, Case 8 removed the debris from all three check storages and is the most effective choice for debris flow control for the comprehensive evaluation shown by c_{tmas} , Q_{smax} and $\Sigma\, Q_s$ at the downstream end

But No. 1 dam changes the sediment transport modes even if its check storage areas are filled with sediment (Cases 1, 2, 3, and 4 in Tables 3(a) and (b)). Therefore, based on economic and feasibility

concerns, the check storage of the No. 1 dam located upstream should not remove any debris. Thoroughly. removing debris from the check storage dams No. 2 and No. 3 located midstream and downstream is the most effective option for debris flow control (Case 4 in Table 3(b)).

CONCLUSIONS

The present paper evaluated the recovery of debris flow control by check dams after removing debris from check storage areas based on the results a numerical analysis of a virtual and an actual torrent. Then this study obtained the following results.

1) A check dam effectively reduced sediment transport when the initial bed slope of the deposition area upstream of the dam is milder than the equilibrium slope of the debris flow, even if the area is filled with sediment.
2) With economy and possibility of works, a check dam, which is located upstream whose check storage area is filled with sediment, should not aggressively remove debris or expect a function that changes sediment transport modes.
3) On the other hand, a check dam, located midstream and downstream, should aggressively remove debris and maintain its storage volume for debris flow control.
4) Removing debris from check storage areas is much more effective for controlling the debris flow, but the priority ranking for removing works for a number of check dams must be carefully determined when considering the sediment runoff process and its characteristics throughout a torrent.

ACKNOWLEDGEMENTS

Part of the present study was supported by the Strategic Research Project from Tokyo University of Agriculture.

REFERENCES

[1] Honda N. and Egashira S., Prediction of Debris Flow Characteristics in Mountain Torrents. The 1st International Conference on DFHM, American Society of Civil Engineering, 1997, pp. 707-716.

[2] Egashira S. and Honda N., Debris Flow Control with Sabo Dams. The 10th APD-IAHR Congress, Vol. 2, 1998, pp.180-187.

[3] Takahashi T., A Mechanism of Occurrence of Mud-Debris Flow and Their Characteristics in Motion. Annuals of Disaster Prevention Research Institute, Kyoto University, Vol. 20, Issue B-2, 1977, pp.405-435 (in Japanese).

[4] Egashira S., Ashida K., Yajima H., and Takahama J., Constitutive Equations of Debris Flow. Annuals of Disaster Prevention Research Institute, Kyoto University, Vol. 32, Issue B-2, 1989, pp.487-501 (in Japanese with English abstract).

[5] Suzuki T. and Hotta N., Coupling of particle and grid-based methods for debris flow simulation. Journal of the Japan Society of Erosion Control Engineering, Vol. 71(2), 2018, pp. 13-21 (in Japanese with English abstract).

[6] Egashira S., Itoh T., Miyamato K., and Honda N., Importance of Correction Factor Associated with Sediment Concentration Profile in Debris Flow Simulation. 2th International Symposium on Flood Defence 2002, Vol.2, 2002, pp.1658-1666.

[7] Egashira, S., Miyamoto K., and Itoh T., Constitutive Equations of Debris Flow and Their Applicability. 1st International Conference on DFHM, American Society of Civil Engineering, 1997, pp. 340-349.

[8] Honda N., Evaluation Debris Flow Using Sabo Facilities Based on Numerical Simulations. 9th International Conference on GEOMATE, 2019, pp.75-81.

[9] Egashira, S., N. Honda and K. Miyamoto, Numerical simulation of debris flow at the Gamaharazawa in the Hime River basin. Annuals of Hydraulic Engineers, Japan Society of Civil Engineering, Vol.42, 1998, pp. 919-924(in Japanese with English abstract).

[10] Nakatani K., Furuya T., Hasegawa Y., Kosugi K., and Satofuka Y., Study on fine sediment phase change factors and on influence on debris flow behavior. Journal of the Japan Society of Erosion Control Engineering, Vol. 70(6), 2018, pp. 3-11 (in Japanese with English abstract).

6th Int. Conf. on Structure, Engineering & Environment (SEE), Kyoto, Japan, Nov.18-20, 2020, ISBN: 978-4-909106056 C3051

EFFECT OF TEMPERATURES MALTODEXTRIN ON PHYSICAL PROPERTIES OF DATE PALM POWDER BY SPRAY DRYING

Wattana Wirivutthikorn[1]
[1]Faculty of Agricultural Technology, Rajamangala University of Technology Thanyaburi (RMUTT)
2 Phaholyothin 87 Soi 2 Phaholyothin Road Thanyaburi Pathumthani 12130 Thailand

ABSTRACT

Fruit juices have tendency to loose nutrients during processing when subjected for heating. Fruit juices could be preserved by several drying methods. Spray drying has been one of the most a well-known method of particle production which comprises the transformation of a liquid material into dried particles. The advantages of this method is a rapid, continuous, cost-effective and reproducible. The objective of this research was to determine the suitable spray drying conditions and the date palm powder qualities. The maltodextrin at concentrations of 20, 25, and 30 percent were added in finished palm date juice. Three of the inlet and fixed the outlet temperatures as 130, 140, 150 and 90ºc, respectively were performed. The physico chemical properties as water activity (a_w), moisture, brightness (L*), redness (+a*), yellowness (+b*) and solubility values were analyzed. As a result, the maltodextrin concentrations at 30 percent provided good characteristics of date palm powder with high powder recovery and low water activity and moisture content. It appeared that the inlet temperature of 150°c was more appropriate than 130°c and 140°c because it concerned higher powder recovery, low water activity of 0.15, and low moisture of 2.15 percent, but gave the low solubility of 13.85 percent. From the information obtained, describes the most outstanding advantages of the spray drying method for the production of food particles and the potential of this technique and the more advanced equipment to develop processes and industrial scale processes that are essential to the bench-to-bedside translation of innovative instant powdered fruit beverage products.

Keywords: Date palm, Powder, Temperature, Spray drying, Maltodextrin

INTRODUCTION

Date palm is a kind of fruit as sweet taste and abundant in many essential and essential nutrients including vitamins, minerals and dietary fiber, which have antioxidant effects. It has a long shelf life, and many varieties, including the common Deglet - Noor, are often sold dried and processed. Although this fruit is small. In which one weight is about 7.5 grams and 100 grams of body gives 314 kilocalories of energy and provides up to 10 minerals such as copper, potassium, magnesium, selenium and etc. in amounts greater than 15 percent of the amount recommended for each day. Polyphenol compound that helps prevent health problems caused by the degeneration of the body, such as protecting cells and tissues from being destroyed by free radicals. It is also rich in vitamin C, vitamin B, vitamin K, iron and fiber. As a results, the date palm is a fruit that tastes good, quenches thirst, and has an easy form of consumption. However, it can be processed into fruit juice, which, when exposed to heat, causes physical and chemical changes, such as the loss of smell, taste, easily during storage. There are also limitations in storage area, temperature, humidity, storage space and transportation costs. In order to enhance the nutritional quality of processed date palm juice, the processing techniques must be carefully selected [1]. Various drying processing methods including drum drying, freeze drying hot air oven, tray drying, spray drying is one of the most technique applied to efficiently dehydrate sugar and acid-rich fruit juice by using different drying agents under optimal processing conditions to obtain powdered foods with advantages of heat short-contact time, microbial growth inhibition, and storage stability [2]. The spray drying parameters such as drying air temperature and feed rate are influential to the attributes of spray-dried food such as particle size, bulk density, moisture content, average time of wettability and insoluble solids. The carrier substances normally used in the spray drying of fruit juice is maltodextin due to its high solubility and low viscosity which is important conditions for the spray drying method [3]. Date palm powder is an interesting product because of its long shelf life at ambient temperature, convenience to consume and low transportation expenditure. Date palm powder can be consumed as an instant juice powder or a flavoring agent. Some researchers reviewed that drying of fruit juice could produce the fruit powder that reconstituted rapidly to a fine product resembling the original juice. It is because the product temperature is rarely raised above 100°c during drying process. However, there are some difficulties in drying techniques the date palm juice with high sugar content, the sticky behavior of sugar and acid rich materials such as fructose, glucose,

sucrose and organic acid such as citric acid, malic acid and tartaric acid due to their thermoplasticity and hygroscopicity at high temperatures and humidities causing their packaging and utilization in trouble. Jittanit et al 2010 has investigated that fresh pineapple juices were added with maltodextrin at 15, 20 and 25 percent by spray drying before exposing to the drying temperatures at 130, 150 and 170°c with the feed rate 0.020, 0.022 and 0.035 litre per minute respectively. Then, the qualities of pineapple powders and reconstituted pineapple powders were investigated in the aspects of moisture content, solubility, color, pH and the consumer acceptance. The results indicated that the pineapple juice should be added with maltodextrin at 15 percent and dried at 150°c. Furthermore, the moisture content and solubility of the pineapple powder produced under this condition were 5.1 percent and 6.2 minutes respectively while its solution had the lightness 58.8, redness 5.2, yellowness 25.1 and pH 3.5 [4]. The next research concluded that to determine the suitable spray-drying conditions and the inulin powder qualities. The inulin extracts at concentrations of 10, 20, and 30 ºBrix were spray-dried using the inlet/outlet drying temperatures at 150/90ºc. As a result, the feed material at 30 ºBrix provided good characteristics of inulin powder with high powder recovery and low moisture content. Then the drying experiments were conducted at inlet air temperatures of 150, 170, and 190ºc whereas the outlet air temperature and the JA extract concentration were fixed at 90ºc and 30 ºBrix. It appeared that the drying temperature of 190°c was more appropriate than 150°c and 170°c because it provided higher powder recovery, lower moisture content, better solubility and absorptivity, and more stability of powder. The SEM micrographs showed that the inulin powders produced by the spray-drying temperatures at 150°c and 170°c had more sphere shaped and had attached particles than those at 190°c [5]. The last research concerned about to develop lime powder products with 20 percent of combined maltodextrin and gum arabic at a ratio of 4:1. A high shear homogenization was applied to encapsulate phytochemical compounds before spray drying with the purpose of protecting bioactive compounds from thermal degradation. The particle size, morphology, moisture content, color, solubility, hygroscopicity, ascorbic acid, total polyphenol and flavonoid contents, antioxidant activity of the spray-dried powder undergoing the homogenization were compared with those of the non-homogenized powder. The higher yield (30 percent) was obtained in the homogenized powder compared with the control (28 percent) with no significant difference. The average particle diameter of the homogenized powder was 0.1-4.0 micrometers, smaller than 18-26 micrometers of the untreated powder. Morphological study revealed that the powder without homogenization was densely packed compared with the homogenized powder. Moisture content of homogenized powder and that of the particles without homogenization were 3.91 percent and 5.42 percent, respectively. Higher solubility and less hygroscopicity values and color after spray drying were observed in reconstituted lime powder with high shear homogenization [4]. However, due to the knowledge and technique about the production of date palm powder is still limited knowledge. This study from finished date palm juice and it was then spray dried into a powder form. The main factor aims of this study were to determine the suitable spray drying conditions and the date palm powder characteristic as physico chemical qualities in terms of water activity, water solubility capability percentage, brightness and color (L, a* and b* values) moisture content and powder recovery percentage of date palm powder.

METHODOLOGY

The research was carried out at the Division of Food Science and Technology, Faculty of Agricultural Technology, Rajamangala University of Technology Thanyaburi (RMUTT) Pathum Thani Province Thailand.

Raw Material Preparation

The finished date palm juice was purchased by the factory (In one date palm Brand) in Kanchanaburi Province, Thailand. The prepared mixtures were diluted and filtered to remove insoluble solids before spray drying [6].

The maltodextrin DE 10-12 was supplied from Chemical Bangkok Co., Ltd in Bangkok, Thailand [6].

Determination of Suitable Spray Drying Temperature for Date Palm Powder Production

The samples prepared by the procedure described in the previous section (2.1) were dried in a Lab Plant Spray Dryer Model SD-Basic (Fig. 1). The amounts of maltodextrin filled into the hot water in order to provide maltodextrin content 20, 25 and 30 percent of the combination of hot water. The maltodextrin content 20, 25 and 30 percent of the feed mixture can be approximately converted to be the ratios of date palm juice (based on total soluble solids) until dissolved homogenous aliquot. The drying experiments were carried out using three maltodextrin content levels (20, 25 and 30 percent) and three inlet temperatures (130, 140 and 150°c) in order to keep the temperature of the outlet drying air at approximately 90°c. At the end of drying, the date palm powders were collected, weighed, and kept in the sealed container for the physico chemical quality determination. The total weight value of powder

collected from each drying run was used for the calculation of powder recovery percentage [6].

Physico Chemical Quality of Date Palm Powder

Spray-dried date palm powder was analyzed for moisture content following by infrared method [7]. Brightness and color of the samples determined using a Hunter Laboratory Mini Scan XE colorimeter (Hunter Associates, Reston, VA) in the L*, a*, b* scale. L* represents lightness ($0 \leq L \leq 100$), while a*(+), a*(-), b*(+) and b*(-) represent redness, greenness, yellowness, and blueness, respectively [7]. Water activity (a_w) was measured and recorded as values according to [7]. The solubility of the powder (water solubility capability) was evaluated according to the method described by adaptation [8]. The solubility was calculated using the equation below:

$$\% \text{ solubility} = \frac{\text{weight of supernatant after drying}}{\text{weight of sample}} \times 100 \quad (1)$$

The powder recovery percentage of each spray drying experiment was calculated applying the equation (2) [5].

$$\% \text{ powder recovery} = \frac{\text{solid weight of powder after spray drying}}{\text{total solid weight in raw material before spray drying}} \times 100 \quad (2)$$

Recording of Data

Data from experiments (three replications) were collected and recorded numerical and statistical analysis. The Experimental design for physico chemical quality analysis were evaluated by using a Factorial Completely Randomized Design (CRD). Analysis of variance and the mean differences of experiments was performed using Duncan's new multiple range test [9].

RESULTS AND DISCUSSION

The physical appearance of the date palm powder spray drying experiments using various concentrations of maltodextrin were illustrated in (Fig 2). Table 1 showed that as the inlet temperature of the hot air increased, resulting in the value of water activity decreasing by the inlet temperature 150°c at 30 percent maltodextrin was as low as 0.15 and inlet temperature at 130°c at 20 percent maltodextrin was the highest values which obtained value of 0.32. Because the addition of maltodextrin has an effect on increasing solid content and maltodextrin binds with the water part, which corresponded in decreasing of water activity. Water activity is the partial vapor pressure of in a substance divided by the standard state partial vapor pressure of water. In the field of food science, the standard state is most often defined as the partial vapor pressure of pure water at the same temperature. Most foods have a water activity above 0.95 and that will provide sufficient moisture to support the growth of bacteria, yeast, mold [6], [10]–[11]. The analysis of the Water solubility capability of date palm powdered showed in Table 2. In regard to the water solubility capability, it showed that the amount of solubility of instantized powdered date palm. When comparing the solubility of powder palm water at the inlet air temperature of 130, 140 and 150°c, the value at the inlet air temperature at 150°c and maltodextrin at 20, 25 and 30 percent, respectively, had the capability to dissolve of 18.75, 16.51 and 13.85 percent, respectively, and the inlet temperature of hot air 140°c at 20 percent. Maltodextrin had the water capability to dissolve of 19.24 percent and the inlet temperature of 130°c at 20 percent maltodextrin had a solubility of 23.45 percent. Therefore, when the inlet temperature was higher, resulted in a worse solubility and absorptivity of the powder. This was because the higher drying temperature caused a higher drying rate leading to a less porous structure of the date powder [6], [10]–[12]. It was found that the amount of maltodextrin and the outlet hot air temperature had no effect on solubility [6], [10]–[12]. Furthermore, the moisture content of the powder sample produced from maltodextrin concentration 30 percent was significantly lower than those of 25 percent and 20 percent, respectively. This may be due to the fact that the increase in solid contents of feed material led to the reduction of water proportion in the feed. As a consequence, when applying the same drying temperature, the moisture content of date palm powder was less than those of 25 and 20 percent counterparts. The condition in which the product has the most moisture is the condition with the temperature of hot air inlet temperature 130°c and the amount of maltodextrin 20 percent with moisture content 4.03 percent and the condition with the least moisture was the condition that has. The temperature of hot air inlet temperature 150°c and the amount of maltodextrin 30 percent had a moisture of 2.15 percent. Because the increase in the temperature of the hot air (inlet temperature) causes the moisture content of reduced product. As higher temperatures cause the water in the product to evaporate more quickly and more than the lower inlet temperature. By considering the influence of inlet temperature found that the temperature rises, humidity percentage will decrease. This is because when the temperature rises, the water in the product evaporates more quickly and more than the temperature of the hot air inlet is lower. At the same time, it was found that when the amount of maltodextrin was increased, the moisture content of

the product will tend to decrease. This is because maltodextrin has main properties as a drying aid. It will reduce the moisture absorption characteristics towards date palm powder products by using 30 percent maltodextrin have a lower moisture content than 20 percent and 25 percent of maltodextrin, respectively [6], [10]–[13]. Regarding the brightness (L*) and color (a* and b*) values, they revealed that the brightness of the solutions of date palm powders were significantly different (P≤0.05) but except for redness and yellowness. In general, the solutions had the more brightness than the redness and yellowness were higher. The cause of the lower brightness was that a small proportion of powder could not dissolve completely in the solution. As the temperature rises, it results in a brown reaction causing the powder palm water at the inlet temperature of 150°c to produce less brightness than using the inlet temperature at 130 and 140°c [6], [10]–[14]. The another reason for the brightness decrease could be the non enzymatic browning reactions occurring during the spray drying [6], [10]–[15]. For the higher redness and yellowness of the solutions, it may be also as a result of some non-enzymatic browning reactions such as caramelization and Maillard reactions happening during the drying process. These reactions could take place because of the high sugar content in the finished date palm juice and heat supplied to the juice in the drying chamber [6], [10]–[16]. Maltodextrin has a white powder, when using higher maltodextrin concentration, the date palm increased the brightness. Furthermore, the maltodextrin concentration is another cause of the color difference between the fresh, finished and the reconstituted date palm juices. However, the color difference among reconstituted samples did not have obvious trend because for these samples the spray-dried powders were diluted in distilled water before analysis. Moreover, the effect of drying temperature on the product color was not apparent because the feed rates were also increased at higher drying temperature [6], [10]–[17]. The powder recovery as percent values showed in Table 7. It indicated that all drying conditions provided high powder recovery in the range 15.87-25.02 percent. Although, these values were very low, they were revealed that the concentration of maltodextrin at 30 percent provided a significantly higher powder recovery percentage than those of 10 and 20 percent. Low powder recovery values were due to the addition of malodextrin contents greater than 20 percent that resulted in the non-sticky products and subsequently low amount of product sized in the drying chamber and cyclone [6], [17]–[19]. Besides, there was a trend of better powder recovery along the increasing maltodextrin concentrations. This occurrence might be explained by the method applied for the powder collection. In this study, all the powder (each treatment) was collected at the cyclone; nonetheless, the drying chamber was periodically knocked by the hard-rubber hammer during the experiment in order to keep the remaining powder on the drying chamber surface and its accessories as minimum as possible. As a result, although the powder recovery percentage was very low for every drying run, there were higher amount of powder stuck in the drying system for the drying conditions that had more total soluble solids in the inlet feed (added higher maltodextrin concentration) because of the limitation using of the hammer force applied in this powder collection method [6], [17]–[20]. On the other hand, if at the end of drying run, all the powder on the drying chamber surface was manually swept and combined with those collected at the cyclone, the trend of powder recovery percentage might change from the original characteristic [6], [17]–[21].

Table 1 Water activity of instantized date palm powder by variation of 3 inlet temperature.

Maltodextrin (%)	Water activity Inlet temperature (°c)*		
	130°c	140°c	150°c
20	0.32[a]	0.31[a]	0.26[a]
25	0.27[b]	0.24[b]	0.24[b]
30	0.25[b]	0.18[c]	0.15[c]

Note: *a-d The different letters in the same column mean significant difference (P ≤ 0.05)

Table 2 Water solubility capability of instantized date palm powder by variation of 3 inlet temperature.

Maltodextrin (%)	Water solubility capability (%) Inlet temperature (°c)[ns]		
	130°c	140°c	150°c
20	23.45	19.24	18.75
25	21.89	26.21	16.51
30	22.84	18.70	15.33

Note: ns = non-significant difference

Table 3 Moisture content of instantized date palm powder by variation of 3 inlet temperature.

Maltodextrin (%)	Moisture content (%) Inlet temperature (°c)*		
	130°c	140°c	150°c
20	4.03[a]	3.84[a]	2.88[a]
25	3.52[b]	3.29[b]	2.39[b]
30	3.21[c]	2.39[c]	2.15[c]

Note: *a-d The different letters in the same column mean significant difference (P ≤ 0.05)

Table 4 Brightness of instantized date palm powder by variation of 3 inlet temperature.

Maltodextrin (%)	Brightness Inlet temperature (°c)*		
	130°c	140°c	150°c
20	55.99[b]	52.86[c]	52.01[c]
25	56.39[b]	56.26[b]	55.97[b]
30	59.21[a]	58.38[ab]	58.63[ab]

Note: *a-d The different letters in the same column mean significant difference ($P \leq 0.05$)

Table 5 Redness of instantized date palm powder by variation of 3 inlet temperature.

Maltodextrin (%)	Redness Inlet temperature (°c)[ns]		
	130°c	140°c	150°c
20	0.52	0.81	1.26
25	1.23	0.56	1.12
30	1.26	0.81	1.16

Note: ns = non-significant difference

Table 6 Yellowness of instantized date palm powder by variation of 3 inlet temperature.

Maltodextrin (%)	Yellowness Inlet temperature (°c)[ns]		
	130°c	140°c	150°c
20	33.48	32.23	32.44
25	34.25	33.31	33.14
30	32.50	32.18	32.92

Note: ns = non-significant difference

Table 7 Powder recovery of instantized date palm powder by variation of 3 inlet temperature.

Maltodextrin (%)	Powder recovery (%) Inlet temperature (°c)*		
	130°c	140°c	150°c
20	15.87[a]	18.23[a]	19.76[a]
25	16.78[ab]	20.42[b]	23.87[b]
30	22.12[b]	23.12[c]	25.02[c]

Note: *a-d The different letters in the same column mean significant difference ($P \leq 0.05$)

Fig. 1 Lab Plant Spray Dryer Model SD-Basic.

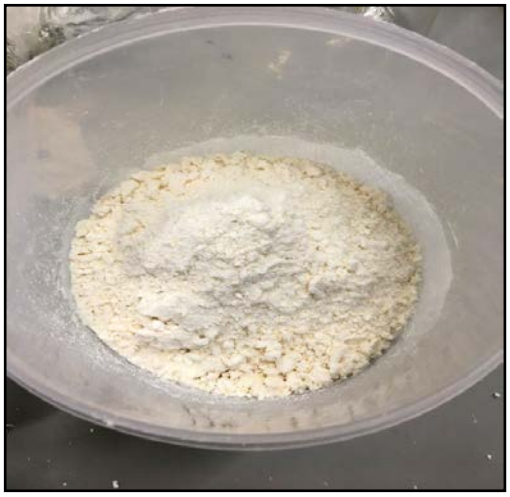

Fig. 2 Physical appearance of date palm powder after spray drying.

CONCLUSION

1. The results showed that the practicability of producing the date palm powders from finished date palm juice and the aliquots of maltodextrin by applying the spray drying method. After reconstituting the date palm powder in the distilled water, the most appropriate maltodextrin concentration for spray drying was 30 percent, while the inlet temperature of 150°c was more appropriate for date palm production than 130°c and 140°c. Because, it provided a higher powder recovery, lower moisture content, better solubility and absorptivity, and more stability of powder.

2. There are useful for the fruit powder producers and researchers., the researchers will be able to launch new products in the future by selecting the appropriate other Thai local fruits and vegetables that develop processes and industrial scale processes that are essential to the bench-to-bedside translation of innovative instant powdered fruit and vegetable beverage products.

ACKNOWLEDGMENTS

The researchers would like to thank the 4 th grade students and officials of the Division of Food Science and Technology, the Faculty of Agricultural Technology Rajamangala University of Technology Thanyaburi (RMUTT), Pathum Thani Thailand that contributed some parts in the research. The Faculty of Agricultural Technology provided support facilities and budgets on our research and travel expense for this conference.

REFERENCES

[1] Chao C.C.T., and Krueger R.R., The date palm (Phoenix dactylifera L.): Overview of biology,

uses, and cultivation, HORTSCIENCE, Vol. 42, No. 5, 2007, pp.1077-1082.

[2] Phisut N., Mini Review: Spray drying technique of fruit juice powder: some factors influencing the properties of product, International Food Research Journal, Vol. 19, No. 4, 2012, pp.1297-1306.

[3] Chuacharoen T., Development of spray-dried lime juice powder with improved bioactive compound retention, Suan Sunandha Science and Technology Journal, Vol. 4, No. 2, 2017, pp.7-12.

[4] Jittanit W., Niti-Att S., and Techanuntachaikul O., Study of spray drying of pineapple juice using maltodextrin as an adjunct, Chiang Mai J. Sci, Vol. 37, No. 3, 2010, pp.498-506.

[5] Jirayucharoensak1 R., Jittanit W., and Sirisansaneeyakul S., Spray drying for Inulin powder production from Jerusalem Artichoke tuber extract and product qualities, Ubon Ratchatani Science and Technology Journal, Vol 17, No. 3, 2015, pp.13-18.

[6] Tiyakulpanich K., and Kongratch A., Development of ready to drink date palm powdered juice by spray drier, Bachelor of Science and Food Technology, Faculty of Agricultural Technology, Rajamangala University of Technology Thanyaburi, Pathum Thani, 2019, pp.1-50.

[7] AOAC, Official method of analysis, Verginia: The Association of Official Analytical Chemists, 2000, pp. 103-1100.

[8] Cano-chauca M., Stringheta P.C., Sardagna, L.D. and Cal-Vidal, J., Mango juice dehydration spray drying using different carriers and function characterization, In: Proc. of the 14th International Drying Symposium (IDS 2004) São Paulo, Brazil, 22-25 August 2004, Vol. C, 2004, pp.2005-2012.

[9] Damnum A., Statistical analysis and data analysis, Kasetsat University Press. Bangkok, 2006, pp.10-150.

[10] Kha T.C., Nguyen M.H., and Roach P.D., Effects of spray drying conditions on the physicochemical and antioxidant properties of the Gac (*Momordica cochinchinensis*) fruit aril powder. Journal of Food Engineering, Vol. 98, No. 3, 2010, pp.385-392.

[11] Sawaya W., Miski A., Khalil J., Khatchadourian H. and Mashadi A., Physical and chemical characterization of the major date varieties grown in Saudi Arabia: I Morphological measurements, proximate and mineral analyses, Date Palm J, Vol. 2, No.1, 1983, pp.1-25.

[12] Peighambardoust S.H., Golshan Tafti A., and Hesari J., Application of spray drying for preservation of lactic acid starter cultures: A review, Trends in Food Scienceand Technology, Vol. 22, No. 5, 2011, pp.214-224.

[13] Adhikari B., Howes T., Bhandari B.R., and Troung V., Characterization of the surface stickiness of fructose-maltodextrin solutions during drying, Dry. Technol, Vol. 21, No. 1, 2003, pp.17-34.

[14] Adhikari B., Howes T., Bhandari B.R., and Troung V., Effect of addition of maltodextrin on drying kinetics and stickiness of sugar and acid-rich foods during convective drying experiments and modeling, J. Food Eng, Vol. 62, No. 1, 2004, pp.53-68.

[15] Sinija V.R., Mishra H.N., and Bal S., Process technology for production of soluble tea powder, J. Food Eng, Vol. 82, No. 1, 2007, pp.276-283.

[16] Grabowski J.A., Truong V.D., and Daubert C. R., Spray drying of amylase hydrolyzed sweetpotato puree and physicochemical properties of powder, Journal of Food Science, Vol. 71, No. 1, 2006, pp.E209-E217.

[17] Finney J., Buffo R., and Reineccius G.A., Effects of type of atomization and processing temperatures on the physical properties and stability of spray-dried flavors, Journal of Food Science, Vol. 67, No. 3, 2002, pp.1108-1114.

[18] Jaya S., and Das H., Effect of maltodextrin, glycerol mono stearate and tricalcium phosphate on vacuum dried powder properties, Journal of Food Engineering, Vol. 63, No. 1, 2004, pp.125-134.

[19] Bhandari B.R., Snoussi A., Dumoulin E.D., and Lebert A., Spray drying of concentrated fruit juices, Dry Technol, Vol. 11, No. 5, 1993, pp.1081-1092.

[20] Fazaeli M., Djomeh Z.E., Ashtari A.K., and Omid M., Effect of spray drying conditions and feed composition on the physical properties of black mulberry juice powder, J. of Food and Bioproducts Processing, Vol. 90, No. 1, 2012, pp.667-675.

[21] Sarabandi K., Peighambardoust S.H., and Shirmohammadi M., Physical properties of spray dried grape syrup as affected by drying temperature and drying aids, International Journal of Agriculture and Crop Sciences, Vol. 7, No. 12, 2014, pp.928-934.

6th Int. Conf. on Structure, Engineering & Environment (SEE), Kyoto, Japan, Nov.18-20, 2020, ISBN: 978-4-909106056 C3051

PARTIAL REPLACEMENNT OF CEMENT WITH FLY ASH AND FGD GYPSUM TO DEVELOP STRENGTH OF SUBBASE

Pisut Rodvinij[1] and Chotikan Ratchakrom[2]
[1]Faculty of Engineering, Rajamangala University of Technology Lanna, Thailand; [2]Faculty of Industrial Technology, Valaya Alongkorn Rajabhat University under the Royal Patronage, Thailand

ABSTRACT

Portland cement is used as an admixture to improve the strength of poor subbase. However, this induced a high cost for the road construction. The replacement of cement with by-product materials from Mae Moh power plant in the admixture is a good alternative to reduce the amount of cement and reduce the cost for subbase improvement. Therefore, this study focused on fly ash, and FGD gypsum replaced cement in the admixture. The soil samples mixed with the admixture at 3% were conducted on unconfined compressive strength test to determine the strength of soil improvement. The results demonstrated that soil mixed with cement at 1%, fly ash 1.5%, and FGD gypsum 0.5% can develop the compressive strength more than the requirements recommended by the Thailand Department of Highways. The compressive strength of soil improvement was 702 kPa. This admixture can develop the strength of soil 384 kPa from the non-improvement soil. Moreover, the strength of soil mixed with cement at 1.5%, fly ash 1%, and FGD gypsum 0.5% can reach 90% of the soil mixed with cement at 3%. The results showed that the strength of soil improvement tended to increase with an incremental amount of fly ash. However, the strength of soil improvement decreased with the increased FGD gypsum in the admixture. In conclusion, the partial replacement of cement by fly ash and FGD gypsum can develop the strength of soils and reduce the amount of cement in the admixture.

Keywords: Fly ash, FGD gypsum, Soil improvement, Compressive strength, Subbase

INTRODUCTION

The lateritic soil has been used in the road construction of Thailand and widespread in the rural area. Subbase of the road in Thailand was constructed by lateritic soil. However, it becomes the realize problem because of the low compressive strength of the poor lateritic soil and poor durability. The bearing capacity of poor subbase was lower than the minimum requirement for the road construction. Moreover, the rain infiltration or the water inundates of the subbase can be causing road damage [1].

The most commonly used additive for soil stabilization is ordinary Portland cement. To build a subbase with cement stabilized ash alone is not yet common, but this is one of the high volume ash applications being promoted by ash producers [2]. The use of ash or the pozzolanic materials combined with cement to improve the strength of soil can reduce the cost of soil stabilization. Therefore, this study investigated the replacement of cement with fly ash and FGD gypsum to improve the strength of poor subbase.

Mae Moh power plant produces three types of lignite by-products from the lignite-fired power generation include fly ash, bottom ash, and FGD gypsum. Fly ash is the most widely used pozzolanic material all over the world. In recent times, the importance and use of fly ash in concrete have grown so much that it has almost become a common ingredient in concrete, particularly for making high strength and high-performance concrete. ASTM broadly classifies fly ash two classes, Class F and Class C. Class F fly ash is normally produced by burning anthracite or bituminous coal and has pozzolanic properties only. While Class C fly ash is normally produced by burning lignite or sub-bituminous coal and can possess pozzolanic as well as cementitious properties [3]. Mae Moh lignite fly ash is a Class C type. The chemical composition of fly ash includes 30.1% CaO, 20.6% SiO_2, 16.1% Al_2O_3, 6.1% SO_3, 12.0% Fe_2O_3, 1.9% MgO, 1.7% Na_2O, 2.2% k_2O, 1.0% TiO_2, 8.3% etc. Fly ash has all the quality of being a pozzolan material [4]. In the cement hydration development, the calcium silicate hydrate (C-S-H) and calcium hydroxide ($Ca(OH)_2$, or CH) are released within the hydration of two main components of cement namely tricalcium silicate (C_3S) and dicalcium silicate (C_2S) where C, S represent CaO and SiO_2. The C-S-H gel is generated by the hydration of C_3S and C_2S. This is the main strengthening constituent [5]. It is known that by adding pozzolanic material to the mortar of concrete mix, the pozzolanic reaction will only start when CH is released/CH interaction exit. In the pozzolan-lime reaction, OH^- and Ca^{2+} react with the SiO_2 or Al_2O_3-SiO_2 framework to form calcium silicate hydrate (C-S-H), calcium aluminate hydrate (C-A-H) and calcium aluminate ferrite hydrate [6]. Normally, fly ash is used as a pozzolanic material in the concrete industry. The partial replacement of Portland cement with fly ash reduces the heat of hydration and

improves the strength and durability of concrete [7], [8].

SO_2 is one of the major environmental contaminations generated from coal-burning power stations and heating plants. It is very important to develop flue gas desulphurization (FGD) technologies to remove SO_2 for FGD clean coal combustion. Although FGD technology is successful in reducing SO_2 discharge, it generates a large quantity of FGD gypsum at the same time. FGD gypsum from Mae Moh power plant is shown in Figure 1. The chemical composition of FGD gypsum includes 3**7.7**% CaO, 4.0% SiO_2, 2.0% Al_2O_3, 54.1% SO_3, 0.5% FeO_3, 1.6% MgO, 0% Na_2O, 0.1 k_2O, 0% TiO_2 [9]. Normally, FGD gypsum contains in the mixture of mortar can increase the durability and compressive strength [10], [11]. FGD gypsum is effective in providing the additional calcium and sulfate required to activate the clinker to form ettringite. The compressive strength produces high early strength than ordinary Portland cement. Additional long-term strength is possible provided by hydration of dicalcium silicate (C_2S) within the clinker [12]. However, the excessive amount of FGD gypsum can decrease the workability and the strength of mortar [13].

Fig. 1 FGD gypsum obtained from Mae Moh power plant.

Therefore, the objective of this study is to investigate the utilization of fly ash and FGD gypsum to improve the strength of lateritic soil and reduce the cost of soil improvement. The target strength of the soil improvement is 689 kPa. This target strength is recommended by the Thailand Department of Highways.

MATERIALS PREPARATION AND MIXTURE OF SOIL IMPROVEMENT

The poor quality of lateritic soil was used in this experiment. The strength of the soil samples was less than the requirement of the Thailand Department of Highways. The soil samples were conducted on Atterberg limits test and sieve analysis test to determine the properties and classification of the samples. Portland cement type 1, fly ash, and FGD gypsum were used as an admixture to improve the strength of soil. Fly ash and FGD gypsum were obtained from Mae Moh power plant. All admixtures stored in plastic bags to maintain their dry condition. The soil samples were mixed with cement, fly ash, and FGD gypsum in the ratio according to Table 1. The amount of admixture mixed with the soil samples was 3% by weight. Table 1 shows the mixture code of C, D, and E was fly ash, and FGD gypsum replace cement in the mixture.

Table 1 The mixture ratio of the admixture for stabilized the soil samples

Mixture code	Cement (%)	Fly Ash (%)	FGD Gypsum (%)
A	-	-	-
B1	1.5	-	-
B2	3.0	-	-
C1	0.5	-	2.5
C2	0.5	0.5	2.0
C3	0.5	1.0	1.5
C4	0.5	1.5	1.0
C5	0.5	2.0	0.5
D1	1.0	-	2.0
D3	1.0	1.0	1.0
D4	1.0	1.5	0.5
E1	1.5	-	1.5
E2	1.5	0.5	1.0
E3	1.5	1.0	0.5

This study investigated on the partial replacement of cement with fly ash and FGD gypsum to develop the strength of poor subbase. The mixture code in group A presented the non-improvement soil samples. The mixture code in group B presented soil mixed with cement at 1.5-3.0%. Whereas, the mixture in group C represented the soil samples mixed with cement at 0.5%, fly ash 0-2.0%, and FGD gypsum 0.5-2.5%. The mixture code in group D presented the soil samples mixed with cement at 1.0%, fly ash 0-1.5%, and FGD gypsum 0.5-2.0%. The mixture code in group E presented the soil samples mixed with cement at 1.5%, fly ash 0-1.0%, and FGD gypsum 0.5-1.5%. The combination of cement, fly ash, and FGD gypsum of the admixture in groups C, D, and E was 3%.

The soil samples mixed with the admixture in the ratio according to Table 1 were compacted by the modified compaction test method. The moisture used in the compaction method was the optimum moisture content (OMC) of soil. The samples were manually compacted in five equal layers using the modified compaction effort. After completing the compaction process, each sample was extruded from the compaction mold and then cured in the plastic bag for 3, 5, and 7 days. Following the curing process, the samples were soaked in water for 2 hours, and then

compressed the samples by the compression machine, as shown in Fig.2. The compressive strength values for each mixture are the average of three specimens.

Fig. 2 The samples conducted on unconfined compressive strength tests.

The results can represent the possibility to use by-product materials replace cement in the admixture. However, the Thailand Department of highways suggested that the unconfined compressive strength of subbase improvement should be more than 689 kPa at the curing time of 7 days. Therefore, the optimum content of fly ash and FGD gypsum replaced cement in the admixture to improve the strength of soil can be determined.

RESULTS AND DISCUSSIONS

Engineering Properties of Lateritic Soil

The soil samples were conducted on Atterberg limits test, sieve analysis test, and modified compaction test to determine the engineering properties of the soil samples. The results demonstrated that the liquid limit, plastic limit, and plasticity index of the soil samples was 27%, 17%, and 10%, respectively. Fig. 3 shows the particle size distribution of the soil samples in this study. According to the AASHTO classification system, the soil samples were A-2-4. The gradation of the soil sample is excellent or good for subgrade materials when considered on the general subgrade rating of AASHTO. Moreover, the results of modified compaction tests are shown in Fig.4. The results demonstrated the maximum dry density of the soil samples was approximately 1,978 kg/m^3, and optimum moisture content was 10.9%.

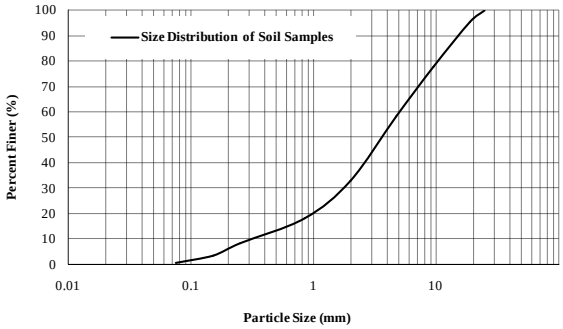

Fig. 3 Particle size distribution of the soil samples.

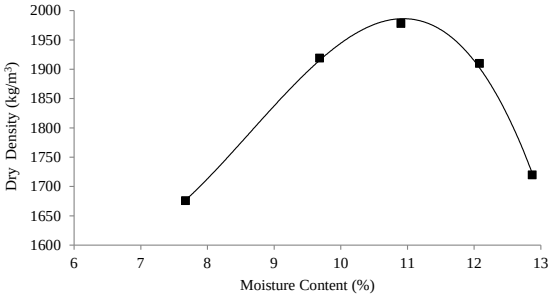

Fig. 4 The relation between dry density and moisture content of the soil samples.

Unconfined Compressive Strength of Soil Improvement

The unconfined compressive strength of the non-improvement soil (A) was 318 kPa. The results illustrated that the strength of the soil samples increased when the soil mixed with an admixture. The unconfined compressive strength of the soil mixed with the admixture in group C is shown in Fig 5. The results demonstrated that the strength of C5 was higher than the soil mixed with cement at 1.5% and gave the highest strength in group C. The compressive strength of C5 was 471 kPa, while the compressive strength of B1 was 456 kPa at the curing time of 7 days. The compressive strength of C5 increased by 3% from B1. However, by-product materials can develop the compressive strength of C5 by approximately 10% from B1 at the curing time of 3 days. Moreover, the compressive strength of C4 was near the samples B1 at the curing time of 5 days and 7 days. Nevertheless, the compressive strength of C4 increased by 5% from B1 at the curing time of 3 days. Therefore, this result represented that the replacement of cement with fly ash and FGD gypsum efficient to develop the strength of soil, especially at 3 days. Nevertheless, the compressive strength of soil improvement with the admixture in group C was lower than the suggestion of the Thailand Department of highways.

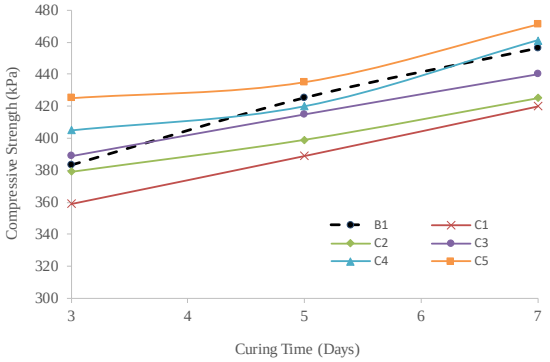

Fig. 5 Unconfined compressive strength of the soil mixed with an admixture in group C.

The results of the soil samples mixed with admixture in group D are shown in Fig. 6. Cement content of the admixture in group D was 1%. Fig.6 shows the strength of the soil samples mixed with the admixture in group D can reach 70-92% and 66-78% of the samples B2 at 5 days and 7 days, respectively. The compressive strength of D1, D2, D3, and D4 at the curing time of 7 days was 589 kPa, 599 kPa, 625 kPa, and 702 kPa, respectively. D4 has the highest compressive strength of the mixture in this group. Moreover, the results demonstrated the compressive strength of soil mixed with admixture D4 was higher than B1, approximately 51-54%. While the samples D4 used cement less than B1 at 0.5%. Therefore, this result can verify the replacement of by-product materials in the admixture to develop the compressive strength of soils. Moreover, the strength of D4 was near B2 at 3 days. The compressive strength of D4 at 3 days was 579 kPa. However, the compressive strength of D4 less than B2 at 5 days and 7 days.

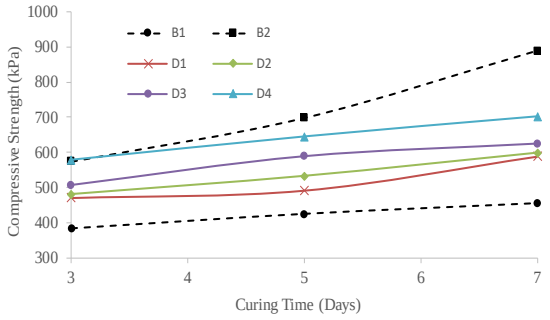

Fig. 6 Unconfined compressive strength of the soil mixed with an admixture in group D.

Fig. 7 shows the compressive strength of the samples mixed with the admixture in group E. The results demonstrated that the strength of soil mixed with the admixture in group E was higher than B2, approximately 5-17% at the curing time of 3 days. Moreover, the samples mixed with the admixture in this group can develop the strength of 2-6% from B2 at the curing time of 5 days. However, the compressive strength of the soil mixed with the admixture in group E was less than B2, approximately 10-15% at the curing time of 7 days. Therefore, the results demonstrated that the replacement of cement with fly ash and FGD gypsum can develop early strength. FGD gypsum consists of SO_3 approximately 54.1%. SO_3 seems to be responsible for the higher early compressive strength. However, the later strength is controlled mainly by calcium silicate hydrate [14]. Fly ash affects the early strength gain probably due to the free lime that is still reacting during the curing process [3].

Moreover, the samples in group E can develop compressive strength higher than the samples B1. While the mixture in group E and B1 used a similar amount of cement at 1.5%. However, the admixture in group E added fly ash at 0-1.0% and FGD gypsum at 0.5-1.5%. The results illustrated the strength of the samples in group E was higher than the samples in group B1 approximately, 58-77%, 67-74%, and 64-76% at the curing time of 3 days, 5 days, and 7 days, respectively. Therefore, the results verified the addition of fly ash and FGD gypsum in the admixture can develop the strength of soil.

Consideration of the compressive strength of soil improvement at the curing time of 7 days, the results demonstrated that the strength in this group was higher than the requirement at 689 kPa. The compressive strength of E1, E2, and E3 at the curing time of 7 days was 748 kPa, 768 kPa, and 804 kPa, respectively.

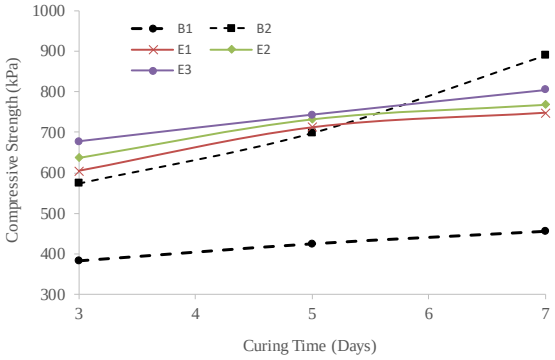

Fig. 7 Unconfined compressive strength of the soil mixed with an admixture in group E.

Effect of Fly Ash and FGD Gypsum on Strength of Soil Improvement

The effect of fly ash and FGD gypsum on the compressive strength of soil improvement is shown in Fig. 8, Fig. 9, and Fig. 10. The results demonstrated that the strength of soil improvement tended to increase with fly ash increment. However, the compressive strength of soil improvement was decreased by the increase of FGD gypsum in the admixture.

Fig. 8 shows the relation between the compressive strength, amount of fly ash, and FGD gypsum in the

admixture group C. The results demonstrated the strength increased by approximately 12-18% when fly ash increased from 0% to 2.0% and FGD gypsum reduced from 2.5% remaining to 0.5%.

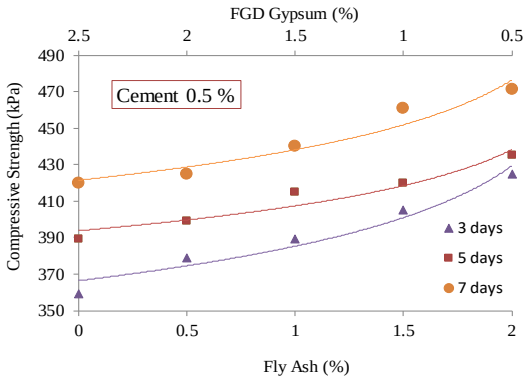

Fig. 8 Relation between the compressive strength, fly ash, and FGD gypsum in the admixture group C.

Fig. 9 shows the relation between the compressive strength, amount of fly ash, and FGD gypsum in the admixture group D. The results demonstrated that the compressive strength increased 20-31% when fly ash increased from 0% to 1.5%, and FGD gypsum reduced from 2.0% remaining to 0.5%. The strength rapidly increased when fly ash increased from 1.0% to 1.5%, and FGD gypsum decreased from 1.0% remaining to 0.5%.

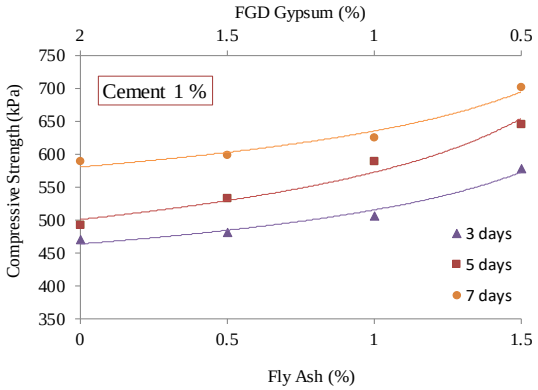

Fig. 9 Relation between the compressive strength, fly ash, and FGD gypsum in the admixture group D.

Fig. 10 shows the relation between the compressive strength, amount of fly ash, and FGD gypsum in the admixture group E. The results demonstrated that the compressive strength increased 5-12% when fly ash increased from 0% to 1.0%, and FGD gypsum decreased from 1.5% remaining to 0.5%. The results presented the strength of soil samples mixed with admixture groups C, D, and E tended to increase with fly ash increment and the reduction in FGD gypsum.

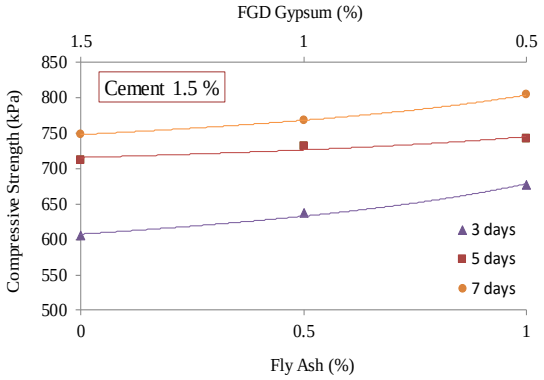

Fig. 10 Relation between the compressive strength, fly ash, and FGD gypsum in the admixture group E.

Strength Requirement for Subbase Improvement

The unconfined compressive strength of subbase improvement suggested by the Thailand Department of Highways was 689 kPa. Fig. 11 shows the strength of soil mixed with an admixture at the curing time of 7 days. The results demonstrated that the samples passed the requirement include B2, D4, E1, E2, and E3. The unconfined compressive strength of B2, D4, E1, E2, and E3 was 889 kPa, 702 kPa, 748 kPa, 768 kPa, and 804 kPa, respectively.

Fig. 11 Unconfined compressive strength of the soil improvement at the curing time of 7 days.

Fig. 12 shows the relation between the compressive strength and cement content in the admixture. The results demonstrated that the strength of soil tended to increase with cement increment. The mixture D4 can develop the strength higher than the requirement. Whereas the cement content of D4 less than B2 and the admixture group E at 2% and 0.5%, respectively. Moreover, the strength of D4 can reach 79% of B2, while D4 used cement only 33% of B2. The results presented that E3 used cement content, only 50% of B2. However, the compressive strength of E3 can reach 90% of B2. Therefore, the use of admixture D4 and E3 to improve the strength of soil can reduce the cost for construction approximately

67% and 50%, respectively.

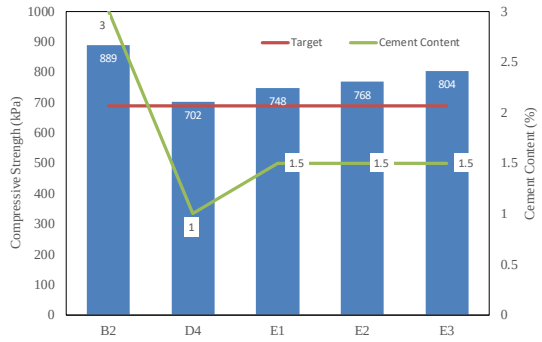

Fig. 12 Relation between compressive strength and cement content.

CONCLUSIONS

Based on the results obtained from this study, the following conclusion was made:

1. The replacement of cement with fly ash and FGD gypsum can increase the strength of poor subbase and reduce cement content in the admixture.

2. The strength of subbase improvement by cement at 1.5%, fly ash 1.0%, and FGD gypsum 0.5% can reach 90% of the soil mixed with cement at 3%. This result shows the replacement of cement with fly ash and FGD gypsum can develop the strength of subbase.

3. The compressive strength of soil improvement tended to increase with incremental fly ash in the admixture. However, the compressive strength of soil improvement decreased with the incremental FGD gypsum.

4. The replacement of cement with fly ash at 1.5% and FGD gypsum at 0.5% was the optimum content to replace cement in the admixture. This mixture can develop the strength of soil more than the requirement of the Thailand Department of Highways, and it can reduce costs by approximately 67%.

REFERENCES

[1] Ratchakrom C., The Effect of Bottom Ash and Kaolin on The Strength of Poor Subbase, International Journal of GEOMATE, Vol. 16, Issue 57, 2019, pp. 76-81.

[2] Hausmann M. R., Modification by admixture, Engineering Principles of Ground Modification, International Edition, McGraw-Hill Publishing Company, 1990, pp. 302-324.

[3] Bendapudi S. C. K., and Saha, P., Contribution of Fly Ash to The Properties of Mortar and Concrete, International Journal of Earth Science and Engineering, Vol 04, 2011, pp. 1017-1023.

[4] Rodvinij P., Slope Stability Improvement of Claystone Backfill by Rock Bund and Shotcrete Mixed with By-Product Materials from Mae Moh Power Plant, Department of Civil Engineering, Chiang Mai University, Doctoral Thesis, 2019.

[5] Omotosoa O. E., Ivey D.G., and Milulab R., Characterization of Chromium Doped Tricalcium Silicate Using SEM/EDS, XRD and FTIR, Journal of Hazardous Materials, 1995, pp.87-102.

[6] Villar C. E., Valencia M. E., Gonzalez R. R., and Harnandez R. J., Kinetics of the Pozzolanic Reaction between Lime and Sugar Cane Straw Ash by Electrical Conductivity Measurement: A Kinetic-Diffusive Model, Cement Concrete Research, 2003, pp.517-524.

[7] Chindaprasirt P., Jaturapitakkul C., Chalee W., and Rattanasak U., Comparative Study on The Characteristics of Fly Ash and Bottom Ash Geopolymers, Waste Management, Vol. 29, 2008, pp. 539-543.

[8] Englehardt J. D., and Peng C., Pozzolanic Filtration/Solidification of Radionuclides in Nuclear Reactor Cooling Water, Waste Management, 1995, pp. 585-592.

[9] Boonserm k., Sata V., Pimraksa k., and Chindaprasirt P., Improved Geopolymerization of Bottom Ash by Incorporating Fly Ash and Using Waste Gypsum as Additive, Cement Concrete Composites, Vol. 34, 2012, pp. 819-824.

[10] Guo X. L., and Shi H. S., Thermal Treatment and Utilization of Flue Gas Desulphurization Gypsum as An Admixture in Cement and Concrete, Construction and Building Materials, Vol. 22, 2008, pp. 1471-1476.

[11] Guo X. L., Shi H. S., and Liu H. Y., Effects of Combined Admixture of Slag Powder and Thermally Treated Flue Gas Desulphurization (FGD) Gypsum on The Compressive Strength and Durability of Concrete, Materials and Structures, Vol. 42, 2009, pp. 263-270.

[12] Jewell R. B., Rath R. F., Duvallet T.Y., Robl T. l., and Mahboub K. C., Fabrication and Testing of Low-Energy Calcium Sulfoaluminate-Bilite Cements that Utilize Circulating Fluidized Bed Combustion By-Products, Coal Combustion and Gasification Products, 2015, pp. 9-18.

[13] Rodvinij P., Wattanachai P., and Chaiwithee S., The Effect of FGD Gypsum Addition in The Mixture of Shotcrete Used Bottom Ash as Fine Aggregate, International Journal of GEOMATE, Vol. 16, Issue 57, 2019, pp. 1-8.

[14] Agabaglou A. M., Boyaci O. C., Hosseinnezhad H., Felekoglu B., and Ramyar K., Effect of Gypsum Type on Properties of Cementitious Materials Containing High Range Water Reducing Admixture, Cement and Concrete Composites, Vol. 68, 2016, pp. 15-26.

6th Int. Conf. on Structure, Engineering & Environment (SEE), Kyoto, Japan, Nov.18-20, 2020, ISBN: 978-4-909106056 C3051

THE VARIATIONAL ITERATION METHOD FOR SOLVING VOLTERRA INTEGRAL EQUATION OF THE SECOND KIND USING MAPLE

Dalal Adnan Maturi [1]

[1]Departement of Mathematics, Faculty of Science, King Abdulaziz University, P.O.Box 42664,Jeddah 21551, Saudi Arabia

ABSTRACT

In this paper, the Variational Iteration Method (VIM) is applied to obtain an approximate solution to linear and non-linear Volterra equations. The Volterra integral equation in mathematics is a special case of integral equations. Volterra integral equations have applications in demographics as well as the study of viscous elastic materials as well as in risk mathematics through the theory of regeneration in probability theory. By means of this method an algorithm Maple is successfully established for solving Volterra integral equation of the second kind. Finally, several examples are presented to illustrate the application of the algorithm. The study revealed that the Variational iteration method are effective methods for solving the Volterra integral equation of the second type. And, the results demonstrate great potential and potential for methods as algorithms in order to obtain the exact solution of Volterra integral equation of the second kind and the results demonstrate great potential and potential for methods as algorithms using Maple18 in order to obtain the exact solution of Volterra integral equation of the second kind.

Keywords: Volterra Integral Equation Of The Second Kind, Variational Iteration Method, Maple18 .

INTRODUCTION

In this paper, we consider the Volterra integral equation of the second kind [1,2,3,17,18,21,28,31]

$$\boldsymbol{u(x) = f(x) + \lambda \int_0^x K(x,t)u(t)dt} \quad (1)$$

The unknown function $\boldsymbol{u(x)}$,The kernel $\boldsymbol{K(x,t)}$ and the function $\boldsymbol{f(x)}$ are given real-valued functions, and $\boldsymbol{\lambda}$ is a parameter.

Volterra integral equation has many scientific applications, and many numerical and analytical methods can also be applied to Volterra integral equation from [4-32]. Also, The variational iteration method; a reliable tool for solving linear and nonlinear wave equations [1] , and the variational iteration method for solving the Volterra integro-differential forms of the lane-Emden and the Emden-Fowler problems with initial and boundary value conditions [3], the modified decomposition method for solving Volterra integral equation of the second kind using Maple [28], the modified decomposition method for solving Volterra Fredholm integro-dfferential equation using Maple [31].

In this paper, we present paper is to study the solution of Volterra integral equation of the second kind using algorithm Maple18.

THE VARIATIONAL ITERATION METHOD (VIM)

Consider the differential equation [3]

$$\boldsymbol{Lu + Nu = g(x),} \quad (2)$$

where *L* and *N* are linear and nonlinear operators respectively, and *g*(*x*) is the inhomogeneous source term. The variational iteration method admits the use of a correction functional for Equation (2) in the form

$$\boldsymbol{u_{n+1}(x) = u_n(x) + \int_0^x \lambda(t)\left(Lu_n(t) + N\widetilde{u_n}(t) - g(t)\right)dt,} \quad (3)$$

where $\boldsymbol{\lambda}$ is a general Lagrange's multiplier, which can be identified optimally via the variational theory, and ˜u*n* is a restricted variation which means $\boldsymbol{\delta\widetilde{u_n} = 0}$. The Lagrange multiplier $\boldsymbol{\lambda}$ is crucial and critical in the method, and it can be a constant or a function. Having $\boldsymbol{\lambda}$ determined, an iteration formula should be used for the determination of the successive approximations $\boldsymbol{u_{n+1}(x), n \geq 0}$ of the solution *u*(*x*). The initial approximation *u*0 can be any selective function. However, the initial values $\boldsymbol{u(0), u'(0)}$ and $\boldsymbol{u''(0)}$ are preferably used for the selective zeroth approximation *u*0 as will be seen later. Consequently, the solution is given by

$$\boldsymbol{u(x) = \lim_{n\to\infty} u_n(x)} \quad (4)$$

It is interesting to point out that the distinct forms of the Lagrange multipliers $\boldsymbol{\lambda}$ were formally derived in

[2], hence we skip the details. It suffices to present a brief summary of such results: For firrst order ODE of the form

$$\boldsymbol{u' + p(x)u = q(x), \quad u(0) = \alpha} \tag{5}$$

it was found that $\boldsymbol{\lambda = -1}$, and the correction functional gives the iteration formula

$$\boldsymbol{u_{n+1}(x) = u_n(x) - \int_0^x (u'_n(t) + p(t)u_n(t) - q(t))dt}. \tag{6}$$

Generally, for the *n*th-order ODE

$$\boldsymbol{u^{(n)} + f\left(u, u', u'', \cdots u^{(n-1)}\right) = g(x), u(0) = \alpha_0, u'(0) = \alpha_1, \cdots, u^{(n-1)}(0) = \alpha_{n-1}} \tag{7}$$

we found that $\boldsymbol{\lambda = \frac{(-1)^n}{(n-1)!}(t-x)^{n-1}}$, and the iteration formula takes the form

$$\boldsymbol{u_{n+1}(x) = u_n(x) + \frac{(-1)^n}{(n-1)!}\int_0^x (t-x)^{n-1}\left(u^{(n)} + f\left(u, u', u'', \cdots, u^{(n-1)}\right) - g(t)\right)dt}. \tag{8}$$

The successive approximations $\boldsymbol{u_{n+1}, n \geq 0}$ of the solution *u*(*x*) will be readily obtained upon using any selective function *u*0(*x*).

SEVERAL EXAMPLE

Example1. Consider the Volterra integral equation of the second kind

$$\boldsymbol{u(x) = 1 + \int_0^x u(t)dt, \quad u(0) = 1}$$

Applying the Variational Iteration Method using Maple, we find

Table 1 Numerical results and exact solution of Volterra integral equation of the second kind for example 1

$\boldsymbol{x}$	$\boldsymbol{u(x)}$	$\boldsymbol{Exact = e^x}$	$\boldsymbol{Error}$
0.10000	1.1051709	1.1051709	0.0000000
0.20000	1.2214028	1.2214028	0.0000000
0.30000	1.3498588	1.3498588	0.0000000
0.40000	1.4918247	1.4918244	0.0000003
0.50000	1.6487213	1.6487196	0.0000017
0.60000	1.8221188	1.8221128	0.0000060
0.70000	2.0137527	2.0137348	0.0000179
0.80000	2.2255409	2.2254948	0.0000462
0.90000	2.4596031	2.4594964	0.0001067
1.00000	2.7182818	2.7180556	0.0002263

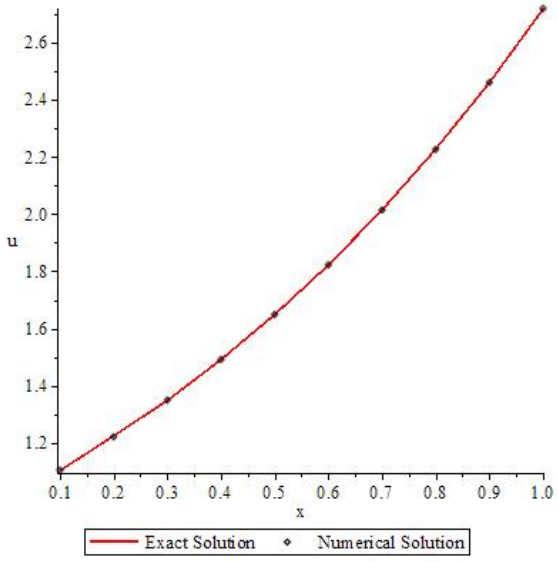

Fig.1 Plot 2D of the exact solutions result Of Volterra integral equation of the second kind for example 1.

Example2. Consider the Volterra integral equation of second kind

$$\boldsymbol{u(x) = x + \int_0^x (x-t)\,u(t)dt, u(0) = 0, \quad u'(0) = 1}$$

Applying the Variational Iteration Method using Maple, we find

Table 2 Numerical results and exact solution of Volterra integral equation of the second kind for example 2.

$\boldsymbol{x}$	$\boldsymbol{u(x)}$	$\boldsymbol{Exact = sinh(x)}$	$\boldsymbol{Error}$
0.10000	0.1001668	0.1001668	0.0000000
0.20000	0.2013360	0.2013360	0.0000000
0.30000	0.3045203	0.3045203	0.0000000
0.40000	0.4107523	0.4107523	0.0000000
0.50000	0.5210953	0.5210953	0.0000000
0.60000	0.6366536	0.6366536	0.0000000
0.70000	0.7585837	0.7585837	0.0000000
0.80000	0.8881060	0.8881060	0.0000000
0.90000	1.0265167	1.0265167	0.0000000
1.00000	1.1752012	1.1752012	0.0000000

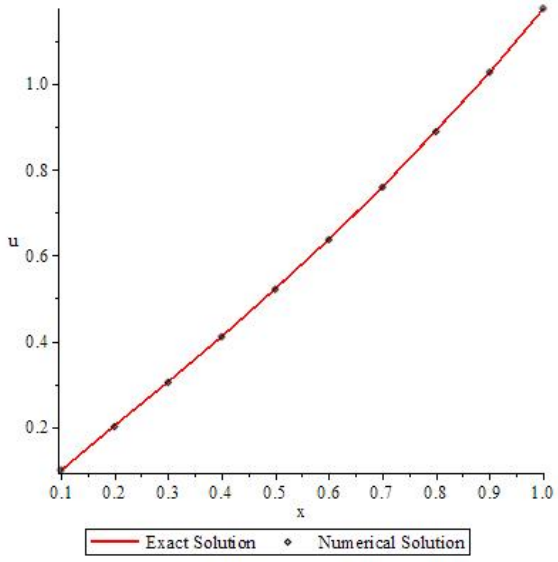

Fig.2 Plot 2D of the exact solutions result Of Volterra integral equation of the second kind for example 2.

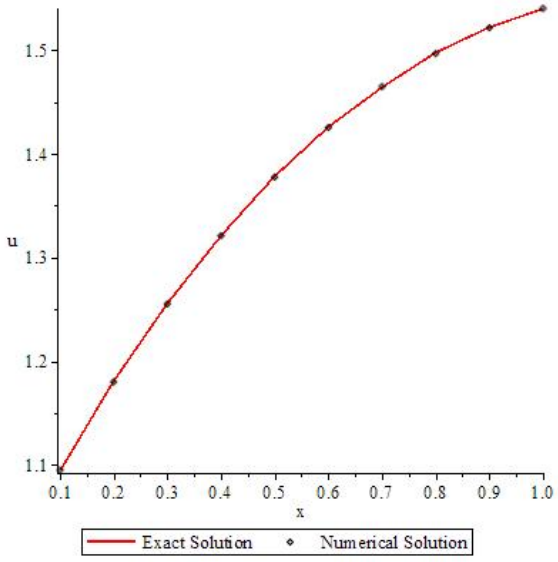

Fig.3 Plot 2D of the exact solutions result Of Volterra integral equation of the second kind for example 3.

Example3. Consider the Volterra integral equation of second kind

$$\boldsymbol{u(x) = 1 + x + \frac{1}{3!}x^3 - \int_0^x (x-t)\,u(t)dt,}$$
$$\boldsymbol{u(0) = 1, u'(0) = 1}$$

Applying the Variational Iteration Method using Maple, we find

Table 3 Numerical results and exact solution of Volterra integral equation of the second kind for example 3.

x	$u(x)$	$Exact = x + cos(x)$	$Error$
0.10000	1.0950042	1.0950042	0.0000000
0.20000	1.1800666	1.1800666	0.0000000
0.30000	1.2553365	1.2553365	0.0000000
0.40000	1.3210610	1.3210610	0.0000000
0.50000	1.3775826	1.3775826	0.0000000
0.60000	1.4253356	1.4253356	0.0000000
0.70000	1.4648422	1.4648422	0.0000000
0.80000	1.4967067	1.4967067	0.0000000
0.90000	1.5216100	1.5216100	0.0000000
1.00000	1.5403023	1.5403023	0.0000000

CONCLUSION

In this paper, the Variational iteration method is used to solve the Volterra integral equation of the second type using Maple 18. By presenting and interpreting the method on a number of examples, the results are shown through examples and it is shown that this method is very effective and the process of finding results from the tables and drawings very easily and clearly The approximate solution is very close to the exact solution.

ACKNOWLEDGMENTS

This paper was supported by the Deanship of Scientific Research (DSR), King Abdulaziz University, Jeddah.

REFERENCES

[1] A.M. Wazwaz, The variational iteration method; a reliable tool for solving linear and nonlinear wave equations, Comput. Math. Appl., 54 (2007) 926–932.

[2] A.M. Wazwaz, A First Course in Integral Equations, World Scientific, Singapore, (1997).

[3] A.M. Wazwaz, Suheil A. Khuri, The variational iteration method for solving the Volterra integro-differential forms of the lane-Emden and the Emden-Fowler propblems with initial and boundary value conditions, DE GRUYTER Open Eng.(2015) ;5:31-41.

[4] J. H. He, “Homotopy perturbation technique", Computer Methods in Applied Mechanics and engineering. 178, 1999, pp. 257-262.

[5] J. H. He, “A coupling method of a homotopy technique and a perturbation technique for non-linear problems”, International Journal of Non-Linear Mechanics, Vol. 35, 2000, pp. 37-43.

[6] J. H. He, “Homotopy perturbation method: anew non-linear analytical technique”, Applied Mathematics and Computation, Vol. 135, 2003, pp.73-79.

[7] J. H. He, “Asymptotology by homotopy perturbation method”, Applied Mathematics and Computation. 156, 2004, pp. 591-596.

[8] J. H. He, “Application of homotopy perturbation method to nonlinear wave equations", Chaos, Solitons and Fractals, Vol. 26, 2005, pp. 695-700.

[9] J. H. He, “Homotopy perturbation method for solving boundary value problems”, Physics Letters A, Vol. 350, 2006, pp. 87-88.

[10] J. H. He, “New interpretation of homotopy perturbation method”, International Journal of Modern Physics B, Vol. 18, 2006, pp. 2561-2568.

[11] V. Balakumar, K. Murugesan, Numerical Solution of Systems of Linear Volterra Integral Equations Using Block-Pulse Functions, Malaya Journal of Matematik, S(1)(2013)77-84.

[12] L.C. Becker and M. Wheeler, Numerical and Graphical Solutions of Volterra Equations of the Second Kind, Maple Application Center, 2005.

[13] R.L. Burden and J. Douglas Faires, Numerical Analysis, 8th ed., Thomson Brooks/Cole, Belmont, CA, 2005.

[14] T. A. Burton, Volterra Integral and Differential Equations, 2nd ed., Mathematics in Science & Engineering, 202, Elsevier, 2005.

[15] M.I. Berenguer, D. Gamez, A. I. Garralda-Guillem, M. Ruiz Galan, and M.C. Serrano Perez, Biorthogonal Systems for Solving Volterra Integral equation Systems of the Second Kind, Journal of Computional and Applied Mathematics,235(7)(2011),1875-1883.

[16] J. Biazar and M. Eslami, Modified HPM for Solving Systems of Volterra Integral Equation of the Second Kind, Journal of King Saud University-Science, 23(1) (2011),35-39.

[17] P. Linz, Analytical and Numerical Methods for Volterra Equations, Studies in Applied Mathematics 7, SIAM, Philadelphia, 1985.

[18] P. Linz, A simple approximation method for solving Volterra integro-differential equations of the first kind, J. Inst. Math. Appl., 14 (1974) 211–215.

[19] F. Mirzaee, Numerical Computional Solution of the Linear Volterra Integral Equations System Via Rationalized Haar Functions, Journal of King Saud University- Science, 22(4) (2010),265-268.

[20] A.M. Wazwaz, Linear and Nonlinear Integral Equation: Methods and Applications, Springer, 2011.

[21] S. Effati and M.H. NooriSkandari, Optimal Control Approach for Solving Linear Volterra Integral Equations, I.J. Intelligent Systems and Applications, 2012,4,40-46.

[22] D.A. Maturi, Numerical Solution of System of Two Nonlinear Volterra Integral Equations, International Journal of Computers & Technology,Vol12,No.10,pp.3967-3975,2014.

[23] D.A.Maturi, A.Z.Bajamal, B.M.AlGethami, Numerical Solution of Volterra Integral Equation of Second Kind Using Implicit Trapezoidal , Journal of Advances In Mathematics, Vol8,No.2,pp.1540-1553,2014.

[24] Dalal A. Maturi, Adomian Decomposition Method of Fredholm Integral Equation of the Second Kind Using Maple, Journal of Advances In Mathematics, Vol9, No.1, pp.1868-1875,2014.

[25] Dalal A. Maturi, Application of Adomian Decomposition Method for Solving of Fredholm Integral Equation of the Second Kind, European Journal of Science and Engineering, Vol9, No.2, pp.1-9,2014.

[26] H.H. Sorkun, S. Yalcinbas, Approximate solutions of linear Volterra integral equation systems with variable coefficients, Applied Mathematical Modeling, 34(2010) 3451-3464.

[27] Dalal A. Maturi, Honaida M. Malaikah, Numerical Solution of System of Three Nonlinear Volterra Integral Equation Using Implicit Trapezoial, Journal of Mathematics Research; Vol. 10, No. 1; February 2018,ISSN 1916-9795 E-ISSN 1916-9809, doi:10.5539/jmr.v10n1p44URL: https://doi.org/10.5539/jmr.v10n1p44.

[28] Dalal Adnan Maturi, The Modified Decomposition Method For Solving Volterra Integral Equation Of The Second Kind Using Maple, International Journal of GEOMATE, Oct., 2019 Vol.17, Issue 62, pp. 23-28.

[29] Dalal Adnan Maturi, Amal Ibrahim Aljedani, Eman Salem Alaidarous, Finite Difference Method For Solving Heat Conduction Equation Of The Granite, International Journal of GEOMATE, Sept., 2019 Vol.17, Issue 61, pp. 135 -140 . ISSN: 2186-2982 (P), 2186-2990 (O), Japan.

[30] Dalal Adnan Maturi, Finite Difference Method For Solving Heat Conduction Equation Of The Brick, International Journal of GEOMATE, April, 2020 Vol.18, Issue 68, pp. 114-119.

[31] Dalal Adnan Maturi, Eman Ahmed M. Simbawa, The Modified Decomposition Method For Solving Volterra Fredholm Integro-Differential Equation Using Maple, International Journal of GEOMATE, March 2020 Vol.18, Issue 67, pp. 84-89.

[6th] Int. Conf. on Structure, Engineering & Environment (SEE), Kyoto, Japan, Nov.18-20, 2020, ISBN: 978-4-909106056 C3051

EFFECT OF DEGREE OF SATURATION ON PARTICLE BREAKAGE OF RECYCLED CONCRETE AGGREGATE UNDER CYCLIC LOADING

Syed Kamran Hussain Shah[1], Junaid Qayyum Kayani[1,2], Taro Uchimura[1] and Ken Kawamoto[1]
[1]Department of Civil and Environmental Engineering, Saitama University, Saitama, Japan
[2]Neelum Jhelum Hydropower Company, Muzaffarabad, Azad Jammu Kashmir, Pakistan

ABSTRACT

The recycled concrete aggregates (RCA) are extracted from construction and demolition waste. If it meets all the engineering aspects of the material, then its use not only decreases the exhaustion of natural resources but also effectively help to utilize the waste. The use of recycled concrete aggregate (RCA) as a granular material highly depends upon its performance under actual field loading conditions and environmental factors it may undergo. The particle breakage is one of the important factors that affect the performance of recycled concrete aggregate, especially in the long-term pavement performance under different environmental conditions. The present study focuses on the particle breakage of recycled concrete aggregate with the variation in the degree of saturation during cyclic loading through triaxial testing. The test results indicated that breakage of particles decreases with an increase in saturation under cyclic loading. The particles more prone to breakage can be identified through coloring technique.

Keywords: Saturation, Breakage, Recycled Concrete Aggregate, Cyclic Triaxial

INTRODUCTION

After the demolition of existing infrastructure or the occurrence of natural disasters in recent times, a large amount of construction waste is being produced. This construction waste material mostly containing demolished concrete from roads and buildings, is often dumped as waste causing a disposal problem. It is difficult to handle a large quantity of construction waste materials in designated landfill sites due to the shortage of land with an increasing population and an increase in public confrontation. Solving the problem of utilization of construction waste materials mixed with industrial by-products such as wastewater sludge and incineration ash in the construction industry is also gaining attention [1].

History of utilizing recycled materials in construction leads back to the end of World War II when the extensive demolition of infrastructure occurred and high demand to both get rid of the waste material and rebuild ruined countries. In the 70s, the United States introduced the use of RCA in non-structural uses, such as fill material, foundations, and base course material [2]. Since then, researchers became interested in how to utilize RCA is as an option to replace natural aggregate (NA) in construction activities to protect the natural resources [3].

The increase in demand and use of NA is causing depletion of natural resources, as for large construction projects a big amount of material is required. Therefore, more use of construction and demolition waste, especially recycled concrete aggregates (RCA) in geotechnical applications, is increasing [4].

Alongside the long-term durability of the material, particle breakage is a critical aspect exposed to dynamic loading. That is why it has drawn the attention of past researches focused on the long-term durability of aggregates and breakage behavior. To understand the impact of particle breakage on strength and deformation behavior several studies have been done using different laboratory tests including triaxial test and numerical methods [5]. Studies found out that particle breakage influences the shear strength of granular materials and induce more irrecoverable deformation [6]. Other than mechanical factors influencing the breakage behavior, physical characteristics of the granular materials were also reported in the literature that affects the breakage extent, for example increasing coefficient of uniformity decreases particle breakage with similar relative density [7]. Comprehensive laboratory assessment of physical and strength characteristics has been established for the utilization of recycled aggregates [8]. However, the effect of variation in the degree of saturation on the breakage behavior of RCA was not conclusive. Therefore, it is important to study the influence of the degree of saturation on breakage behavior of RCA to assess the long-term durability as pavement base material.

MATERIAL PROPERTIES

Recycled concrete aggregate (RCA) collected from a recycling plant in Japan is used in these experiments as shown in Fig. 1.

Fig. 1 Recycled Concrete Aggregate (RCA) graded in accordance with RM-30 (2010).

The specific gravity of RCA use is 2.59. Absorption of particles > 2.36 mm is 5.9% and particles < 2.36 mm is 15.7%. Maximum dry density of RCA is 1.89 g/cm^3 with optimum moisture content (OMC) of approximately 10% with corresponding degree of saturation 67.2 %.

This material was sieved and adjusted from 19.0 mm to 0.075 mm in accordance with RM – 30 gradation [9] suggested by Japan Road Association (2010), refer Fig. 2.

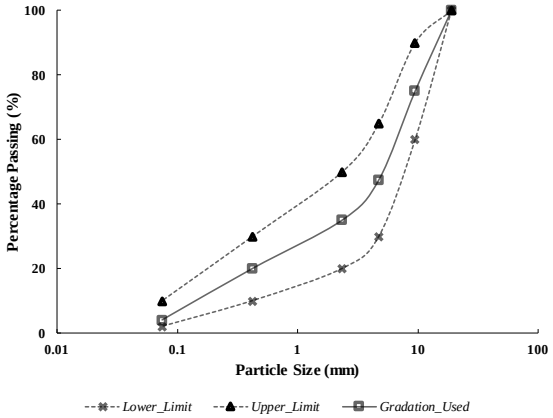

Fig. 2 Gradation curves of the RCA samples with upper and lower limit curves of RM-30 suggested by Japan Road Association (2010)

EXPERIMENTAL SETUP AND TESTING CONDITIONS

The performance of recycled concrete aggregate (RCA) was determined by conducting a series of static and cyclic triaxial tests on the compacted specimens at different degrees of saturation and selected stress conditions. The schematic of triaxial system used in these experiments is shown in Fig. 3. Cylindrical RCA specimen of 75 mm diameter and 150 mm height was used in the study. The confining pressure was applied by pressurizing the air in the cell and distributed through water and it was continuously monitored by a transducer connected to the cell.

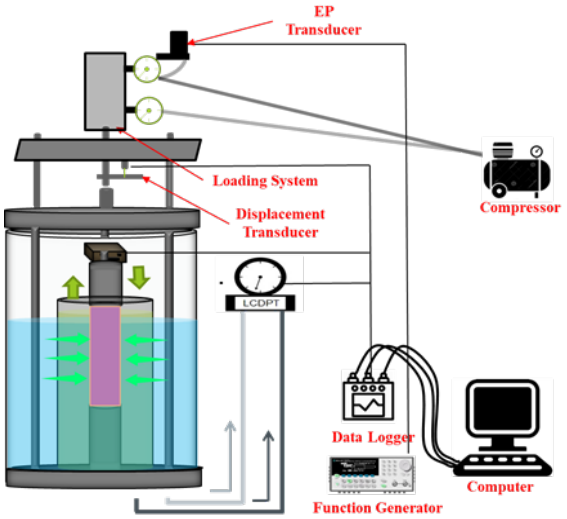

Fig. 3 Schematic diagram of cyclic triaxial system.

The cyclic loading was applied using double action pressure cylinder mounted on top of the system. EP transducer was used to convert signal into pressure given from function generator. The vertical deformation of the specimen was calculated by the measurements provided by linear variable differential transformer (LVDT) attached to the vertical shaft on top of triaxial cell. Whereas volumetric deformation was measured by low capacity displacement transducer (LCDPT) by measuring the difference of water level in double cell. Cell pressure transducers and the load cell were connected to a data logging system which collected the responses of the transducers at specified time intervals.

The test conditions used in cyclic triaxial tests are shown in Table 1.

Table 1 Test conditions

Test Conditions	
Compaction Energy [kJ/m^3]	2700
Degree of Saturation [%]	30, 40, 60, 80
Frequency [Hz]	0.2
Number of Cycles [Nos.]	2000, 4000
Confining Pressure [kPa]	70
Max. Cyclic Deviatoric Stress [kPa]	590
Min. Cyclic Deviatoric Stress [kPa]	59

Sample Preparation and Placing

For evaluating the strength and deformation characteristics of RCA, samples were compacted at optimum moisture content with energy equivalent to modified proctor energy (2700 kJ/m^3).

To assess the particle breakage of RCA under cyclic loading, coarse content of the material ranging from 19.0 mm to 4.75 mm was painted. The color codes used for these particle ranges is illustrated in Fig. 4. Whereas the fine content is kept in its original color due to difficulty in coloring. Sample was then mixed with pre-determined water content for target degree of saturation. The sample is then compacted in the mold in three layers with specified compaction energy of 2700 kJ/m^3.

Compacted specimen is then enclosed in rubber membrane and placed on the pedestal of triaxial cell. The specimen is sealed by O-rings at the top and the bottom. Inner and outer cells were installed. After filling the water in both cells to the required level, predetermined cell pressure (σ_3) was applied and the sample was allowed to consolidate.

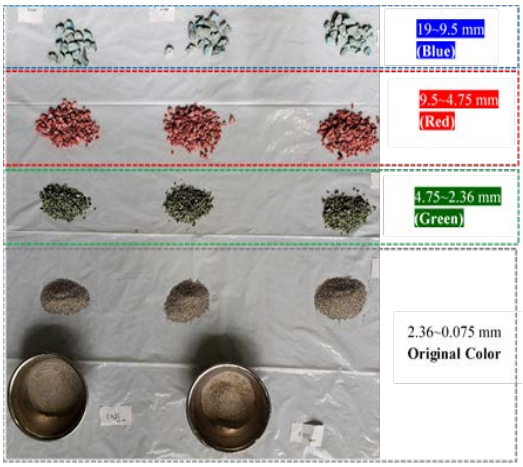

Fig. 4 Color scheme of each particle size range.

Loading and Data Acquisition

Static triaxial test

Strain controlled static triaxial tests were performed in drained condition, to get the strength and deformation characteristics of RCA samples.

Cyclic triaxial test

Stress controlled cyclic triaxial tests were performed to study performance of RCA. Vertical axial load (σ_1) corresponding to selected maximum and minimum deviatoric stress (q) was applied as a waveform by generating the signal through function generator and EP transducer.

Tests were conducted under drained conditions. Constant contact stress (10% of maximum deviatoric stress) was applied to ensure the constant contact between load assembly and specimen. Under constant confining pressure, 2000 and 4000 repeated load cycles were applied. After completing the desired cycles, sample was retrieved carefully, oven dried and sieved to evaluate the breakage.

The results were analyzed to study the particle breakage behavior by using the data acquired through data acquisition system, sieving analysis and particle segregation based on color schemes used.

RESULTS AND DISCUSSION

Static Triaxial Test

Prior to evaluating the performance of RCA during cyclic loading, static triaxial tests were performed. The test results are shown in Fig. 5. At the confining pressure (σ_3) of 70 kPa, the peak strength achieved by sample compacted at optimum moisture content is approximately 900 kPa. The sample failed after gaining slightly over 3% axial strain value. The peak strength achieved is used to fix the maximum and minimum cyclic deviatoric stress values to assess the long-term performance of RCA during cyclic triaxial tests.

The most distinctive feature of RCA is mortar layer surrounding the thick core particles, which might affect initial stiffness and volumetric strain characteristic.

The results show that when recycled concrete is well compacted it showed good strength, other researchers also concluded that when well compacted, recycled concrete aggregates can exhibit strength and stiffness even higher than those of selected well graded gravelly soil [10]. When subjected to triaxial compression loading, some crushing of mortar takes place at inter-particle contact points, resulting in a low initial stiffness. Then a better inter-particle contact condition between adjacent stiff cores of the aggregate develops resulting in increase of tangent stiffness and ultimately a high compressive strength. The negative effects of mortar layer on the compressive strength of RCA can be eliminated by better compaction [11].

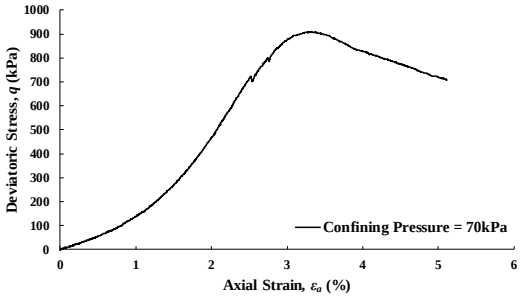

Fig. 5 Strength of RCA during static triaxial test.

Cyclic Triaxial Test

Two series of cyclic triaxial tests were conducted to evaluate the long-term performance and breakage behavior of RCA with variation in degree of saturation.

Figure 6 shows the maximum and minimum value of cyclic deviatoric stress used in cyclic triaxial test. The maximum deviatoric stress is taken approximately 65% of the maximum stress achieved in the static triaxial test 10% of the maximum deviatoric stress was taken as the contact stress in order to ensure constant contact between loading rod, top cap and sample [12].

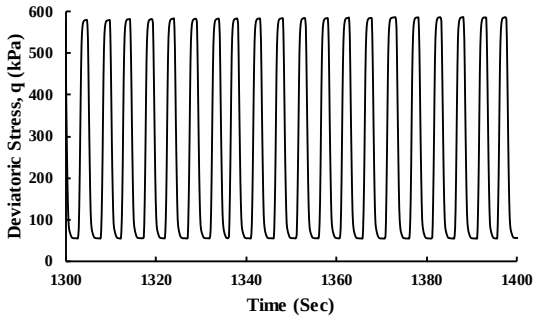

Fig. 6 Maximum and minimum cyclic deviatoric stress.

Accumulation of axial permanent strain of the RCA specimens with number of load cycles is shown in Fig. 7 for 2000 and 4000 cycles. This figure illustrates the effect of degree of saturation on the accumulated axial strain at a constant σ_3 of 70 kPa. The figure illustrates the increase of plastic strain with number of load cycles at various values of degree of saturation.

The higher the saturation value, the higher the permanent axial strain.

The rate of increase of permanent axial strain slows down as the number of load cycles increased at constant maximum value of deviatoric stress (σ_d) and confining stress (σ_3). The curves show a tendency towards attaining a steady state of plastic response at the end of the test, especially, at the low values of degree of saturation i.e., 30 and 40 % in comparison to higher degrees of saturation. This behavior indicates the state of energy absorption by RCA on each stress-strain loop and its ability to resist after gaining minor permanent deformations. Decrease in the permanent axial strain over the number of loading cycles in RCA sample indicates a state of plastic shakedown limit [13]. This behavior of accumulated permanent axial strain of RCA sample at lower degrees of saturation suggests illustrates its approach to plastic limit. However, enough volume of water on lower side of optimum value of the RCA positively affected the strength and stiffness of the RCA sample compacted at modified proctor energy and reduced the rate of permanent deformation.

Moreover, results in Fig. 7 show the rise of permanent axial strain with increasing degree of saturation, but RCA sample did not collapse under cyclic loading albeit the strain values were high at saturation over the optimum value of RCA samples. It seems to be a significant performance characteristic of RCA which demonstrates resistance against plastic deformation at high water contents without collapse which establishes its capacity for load bearing and its suitability as a high-quality granular pavement material. This is in accordance to the natural behavior to many conventional pavement materials which exhibit increase in plastic strain with increase in the water content [14].

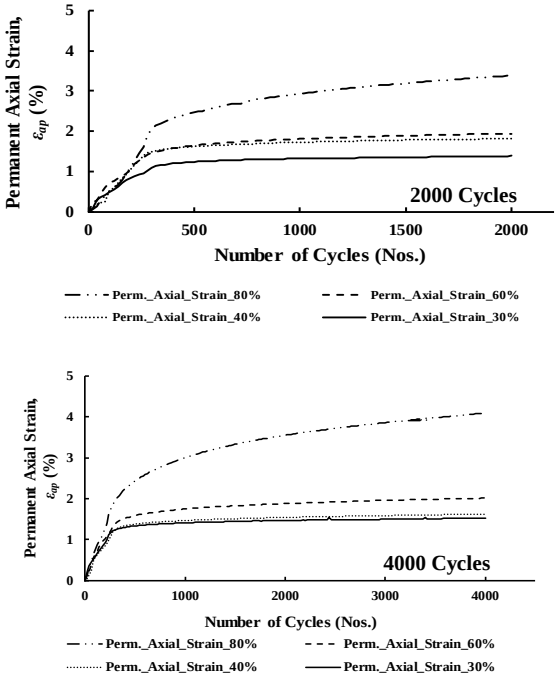

Fig. 7 Permanent axial strain with loading cycles.

Particle Breakage Analysis

To assess the effect of degree of saturation on particle breakage of RCA under cyclic loading, following methods were adopted for analysis in this study.

Marsal's breakage ratio (B_g)

To quantify the extent of particle breakage, most common method, the Marsal's breakage ratio (B_g) was used [15]. It is a quantitative breakage index and is defined as the percentage by weight of the solid phase that has broken. It measures the percentage increase in mass of particles that pass through each sieve size as expressed in Eq. (1) and (2).

$$B_g = \Sigma\,(\Delta W_k > 0) \quad (1)$$

$$\Delta W_k = W_{ki} - W_{kf} \quad (2)$$

Wherein, W_{ki} is the percentage of sample weight retained before test in each sieve size and W_{kf} is the percentage of sample weight retained after test in each sieve size respectively.

Marsal's breakage ratio is shown in Fig. 8 as function of degree of saturation. Solid line represents the data obtained in tests where RCA sample was subjected to 2000 loading cycles and dotted line for 4000 load cycles. Results depict that there is a minor shift in the curve upwards with increase in number of cycles from 2000 to 4000.

An almost linear decreasing trend can be observed in Marsal's breakage ratio with increasing degree of saturation until 60% degree of saturation value which is in close range to corresponding optimum moisture value. However, a slight increase was observed at higher degree of saturation in both the cases. Overall trend suggests that with increase in moisture particle breakage in the sample reduces.

It is presumed that with the increase in degree of saturation, water provides a cushion and/or slippage surface around the particles which result in less breakage of particles.

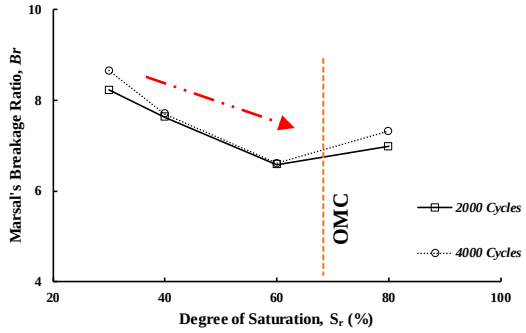

Fig. 8 Marsal's breakage ratio as function of degree of saturation.

Coloring technique

To assess that which fraction of the material is more prone to breakage or more influenced by the testing conditions assumed, coloring technique is adopted in this study.

Material after the test was sieved. Then coarse fraction which was colored is segregated and particles which shifted from one color scheme to another color scheme were picked up by color identification and weighed as shown in Fig. 9. With this methodology, it can be observed that the fraction size which has moved to the next size range and actual breakage or mass reduction/accumulation can be calculated.

The results shown in Fig. 10 indicated coarser fraction such as 19.0 mm, 9.5 mm and 4.75 mm broke and this breakage decrease with increase in moisture content.

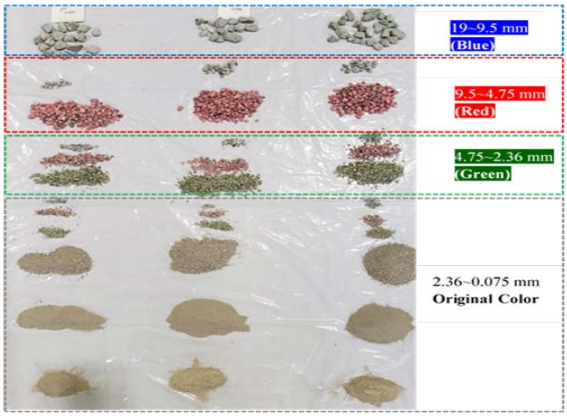

Fig. 9 Each particle size fraction after test.

The mass reduction percentage is described as;

Mass Reduction/Accumulation (%) =
[*(Initial Mass – Final Mass)/Initial Mass x 100****)]***

The finer particles (2.36 ~ 0.075 mm) didn't show considerable breakage but their final mass increased due to the accumulation from top sizes of coarse fraction (19.0, 9.5 and 4.75 mm). Particularly particle size range 9.5~4.75 mm of the coarse fraction shows higher mass reduction as compared to 19.0~9.5 and 4.75~2.36 mm size ranges at both 2000 and 4000 cycles.

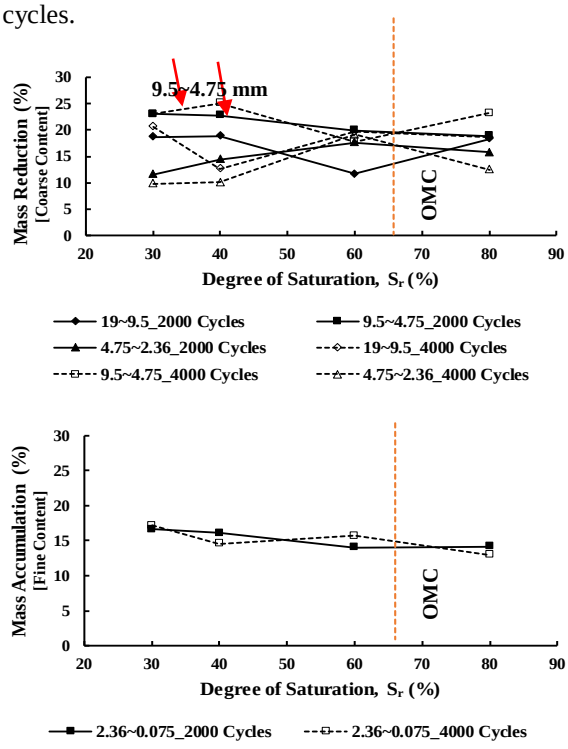

Fig. 10 Mass reduction and accumulation.

CONCLUSIONS

This study contributes to advancement in geotechnical engineering in terms of utilization of recycled materials. The performance characteristics of RCA were investigated by conducting a series of cyclic triaxial tests under different degree of saturation and number of load cycles. The following conclusions were drawn from this study

- Permanent axial strain was notably affected by high value of degree of saturation of the compacted RCA which revealed sensitivity RCA to moisture.
- Accumulation of permanent axial deformation of RCA move towards plastic state with the increase of the load cycles, especially at low degrees of saturation. This behavior corresponds to the natural good quality pavement materials.
- Breakage of particles decreases with increase in saturation as evident from the results. Therefore, it is important to consider the particle breakage of RCA as an important factor to influence the long-term durability as a pavement material.
- Marsal's breakage ratio, B_g, showed a decreasing relationship between overall breakage and degree of saturation. However there is a slight increase in breakage ratio at higher saturation.
- The coloring technique introduced in this study is capable to indicate the particle size more prone to breakage and particle tracing is possible to track the particle movement after testing from one size range to the other especially in coarse fractions.
- 9.5~4.75 mm range of coarse fraction shows more breakage as compared to other coarse fractions. Mass accumulation happens in finer content due to breakage of large particles.
- Along with the traditional breakage indices, the coloring technique can be used to study the breakage of particles in long term durability tests.

ACKNOWLEDGEMENTS

This research was partially supported by JST-JICA, Science and Technology Research Partnership for Sustainable Development (SATREPS) project (No. JPMJSA1701).

REFERENCES

[1] Iqbal M.R., Hashimoto K., Tachibana S., and Kawamoto K.., Geotechnical Properties of Sludge Blended with Crushed Concrete and Incineration Ash. International Journal of GEOMATE, Vol. 16, Issue 57, 2019, pp. 116–123.

[2] Buck A. D., Recycled Concrete as a Source of Aggregate. ACI Journal. 74, 1977, pp. 212–219.

[3] McNeil K., Kang T.H.K., Recycled Concrete Aggregates: A Review. International Journal of Concrete Structures and Materials. Vol. 7, No. 1, 2013, pp. 61-69.

[4] Abukhettala M., Use of Recycled Materials in Road Construction. Proceedings of the 2nd International Conference on Civil, Structural and Transportation Engineering, ICCSTE'16, 2016, Paper No. 138.

[5] Coop M., Sorensen K., Freitas TB., and Georgoutsos G., Particle Breakage during Shearing of a Carbonate Sand. Geotechnique, 54(3), 2004, pp. 157-163.

[6] Yu F., Characteristics of Particle Breakage of Sand in Triaxial Shear. Powder Technology, 320, 2017a, pp. 656-667.

[7] Sun Y., Zheng C., Breakage and Shape Analysis of Ballast Aggregates with Different Size Distributions. Particuology, 35, 2017, pp. 84-92.

[8] Arulrajah A., Disfani M.M., Horpibulsuk S., Suksiripattanapong C., and Prongmanee N., Physical Properties and Shear Strength Responses of Recycled Construction and Demolition Materials in Unbound Pavement Base/Subbase Applications. Constr. Build. Mater, 58, 2014b, pp. 245-257.

[9] RM-30, Gradation Standard for Recycled Materials. Japan Road Association (JRA), 2010 (in Japanese).

[10] Aqil U., Tatsuoka F., Uchimura T., Lohani T.N., Tomita Y., and Matsushima K., Strength and Deformation Characteristics of Recycled Concrete Aggregate as a Backfill Material. Soils and Foundations, 45(4), 2005, pp. 53-72.

[11] Tatsuoka F., Tomita Y., Iguchi Y., and Harikawa D., Strength and Stiffness of Compacted Crushed Concrete Aggregate. Soils and Foundations, 53(6), 2013, pp. 835-852.

[12] Frost M.W., Fleming P.R., and Rogers C.D.F., Threshold Stress and Asymptotic Stiffness of UK Clays in the Repeated Load Triaxial Test. Proceedings of the 6th International Conference

[13] Cerni G., Cardone F., Virgili A., and Camilli S., Characterization of Permanent Deformation Behavior of Unbound Granular Materials under Repeated Triaxial Loading. Constr. Build. Mater., 28, 2012, pp. 79–87.

[14] Thom N.H., Brown S.F., Effect of Moisture on the Structural Performance of a Crushed-limestone Road Base. Transportation Research Record, 1 12 1, (1987).

[15] Marsal R.J., Large Scale Testing of Rockfill Materials. Journal of the Soil Mechanics and Foundation Division ASCE, 93(2), 1967, pp. 27-43.

6th Int. Conf. on Strucrture, Engineering & Environment (SEE),
Kyoto, Nov.18-20, 2020, ISBN: 978-4-909106032 C3051

INVESTIGATION ON RUPTURE OF GROUND ANCHORS DUE TO LANDSLIDE FLUCTUATIONS

Yoshihiro TSUNEKAWA[1], Toshinori SAKAI[2],
[1]Soai, Japan; [2]Mie University, Japan

ABSTRACT

Ground anchors are widely used as landslide prevention measures. In recent years, record heavy rains and huge earthquakes have occurred frequently, and there is a high likelihood that damage will be caused by external forces exceeding design conditions. It has been reported that some anchors have experienced tensions exceeding 100 kN and will be ejected from their installation sites if the anchor breaks. Because some anchors are installed on slopes facing roads and houses, ensuring safety in the event of damage is important. In this study, a survey was conducted over a period of five years at a site where anchors have broken due to landslides exceeding the design load of the anchors. It was found that the fracture of the anchors progressed stepwise, and although 42 out of 86 anchors fractured, the slope in which they were installed did not collapse. It was confirmed that 14 of the fractured anchors were ejected, and their flight distance reached approximately 100 m.

Keywords: Ground anchor, Landslide, Anchor fracture, Flight distance

INTRODUCTION

Ground anchors (hereafter referred to simply as anchors) are widely used for landslide prevention. In recent years, record heavy rains and huge earthquakes have frequently occurred, and the possibility that damage will occur as a result of external forces exceeding the anchor design conditions is increasing. Tensile forces of over 100 kN have been introduced to anchors, and, as shown in Photo 1, anchors have been reported to break out of structures when they rupture [1]. Anchors may be installed on slopes facing roads and houses, so it is important to ensure safety in case of breakage.

SURVEY SITE OVERVIEW

Figure 1 shows the landslide block considered in this study and the survey site. This survey site is located in the A-1 block at the end of the landslide block, and there is a large-scale landslide block that fluctuates in the upper part. Figure 2 shows the positions of the anchors in block A-1. The landslide scale of the A-1 block is approximately 100 m wide, 120 m long, and 15 m deep, and part of the A block passes through the A-1 block. In 2009, 86 anchors

Photo 1. Damage due to anchor rupture

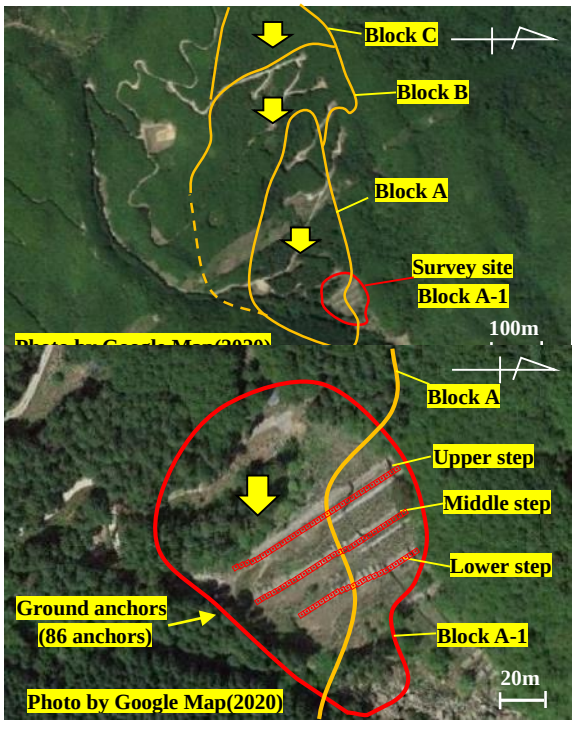

Fig 2. Ground anchors in the A-1 block

were constructed to prevent landslides in the A-1 block. The anchor installation angle is 25°, the designed load T_d is 414.5 kN, and the lock-off load P_t is 207 kN, which is approximately 50% of the designed load.

Figure 3 shows a typical anchor countermeasure cross section of block A-1. The anchor fixed length l_a is 4.5 m, and the anchor free length l_f ranges from 5.5 to 29 m. For the free anchor length part, three ∅15 mm prestressed concrete (PC) steel stranded wires were used. These wires have a tendon yield strength T_{ys} of 666 kN, and a tendon ultimate strength of T_{us} of 783 kN. Photo 2 shows the configuration of the anchor head. The PC steel stranded wire is fixed with a wedge at the anchor head, and the anchor head is protected by an aluminum cap containing rust preventive oil.

Anchor fracture was confirmed in 2014, five years after construction. Figure 4 shows the distribution of the anchor load obtained one year before the anchor rupture occurred. The loads are categorized according to the soundness categories given in Table 1. Regarding the change in the anchor load, Figure 4 demonstrates that the landslide displacement of the A block increases the anchor load only on the A block side. It has been confirmed in previous studies that if continuous rainfall exceeds 400 mm, anchors loaded with at least 90% of the yield tensile force will break [2].

Photo 3 shows the condition of a typical fractured anchor observed in the field. As shown in Photo 3(a), the anchor head and the PC steel stranded wire were left protruding by the fracture. In addition, as shown in Photo 3(b), it was confirmed that the broken portion of the PC steel stranded wire traveled over 30 m when it was ejected from its place of installation. This photograph shows evidence of the collision of the broken PC steel stranded wire with a tree and where it was left hanging on the tree.

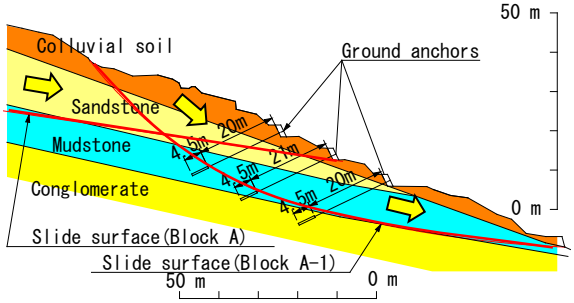

Fig. 3. Typical anchor countermeasure cross section in block A-1

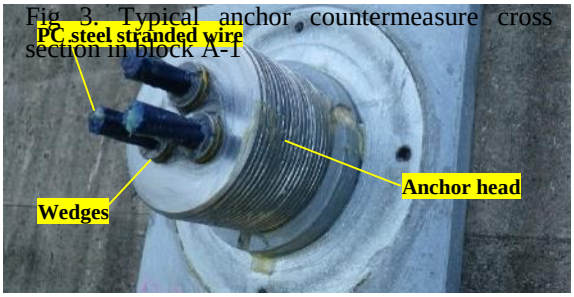

(a) Installation of PC steel stranded wires

(b) Filled with corrosion inhibitor

Photo 2. Configuration of the anchor head

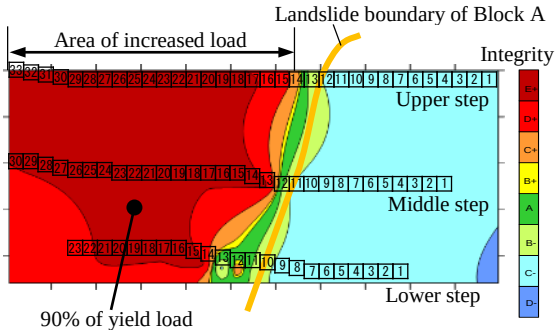

Fig. 4. Soundness classification diagram

FIELD SURVEY

Table 1. Guidelines for residual tensile load and anchor integrity [3] (Additional writing)

Range of residual tensile load	Integrity	Situation	Countermeasure
	E +	Possibility of failure	Emergency countermeasure is necessary
0.9 Tys	D +	Possibility of dangerous situation	Countermeasure is necessary
1.1 Ta	C +	Beyond toletance	
Allowable load (Ta)	B +		Need for countermeasure is examined after inspection
Design load (Td)	A +	Sound	
Lock-off Load (Pt)	A −	Sound	
0.8 Pt	B −		Need for countermeasure is examined after inspection
0.5 Pt	C −	Drastic deterioration of function	
0.1 Pt	D −	Non-functional	Countermeasure is necessary

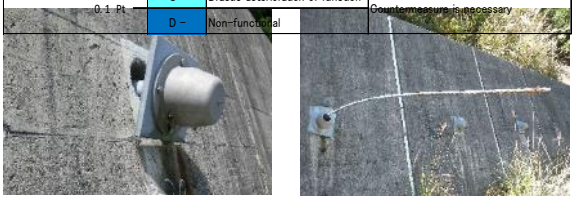

(a) Protruding anchor head and PC steel stranded wire

(b) Flight of PC steel stranded wire and traces of collision

Photo 3. Condition of the ruptured anchor

A field survey was conducted over the course of five years from 2014 to 2019, and the progress of anchor rupture and the condition of anchor pop-out were confirmed. After heavy rainfalls with a daily rainfall of 300 mm or more, visual inspection was conducted, and the progress of the fracture of the anchor was recorded. In addition, regarding the flight of anchors due to fracture, anchors no longer in their installation locations were found by searching the site, and the length and flight distance of these anchors were measured. The survey results are presented below.

Figure 5 shows the daily precipitation [4] and the number of newly fractured anchors each year. The numbers of yearly anchor ruptures from 2014 to 2019 were 6, 22, 13, 1, and 1, respectively. It was confirmed that the fracture of the anchor proceeded in stages. Figure 6 shows the anchor fracture locations and the flight distances in the case of anchor flight. It was confirmed that 42 anchors broke, which was approximately 80% of the anchors in the area associated with load increase due to landslide. Of these, 14 fractured anchors were ejected from their sites, and it was confirmed that all of the ejected anchors fractured inside the ground. Furthermore, for the anchors that broke behind the anchor head, no anchor flight was observed. Ejected anchors were found in four areas. PC steel stranded wires were ejected from the anchors that were broken, and a flight distance of up to 120 m was confirmed.

Photo 4 shows the slope condition of the upper anchor after the anchor fracture. Although slight displacement was observed in the supporting structure and water channel, it was confirmed that there was no collapse at present (five years after the start of rupture) and that the shape of the slope was maintained.

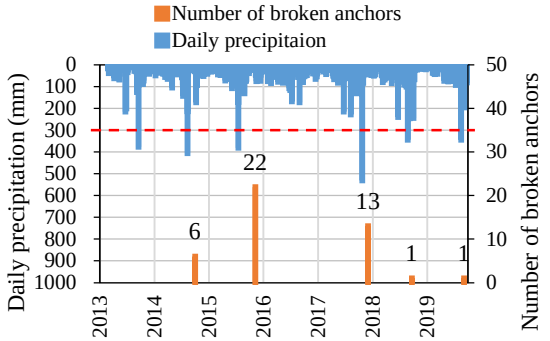

Fig 5. Precipitation and number of broken anchors

ANCHOR FLIGHT ANALYSIS

Photo 4. Condition of the slope after anchor rupture

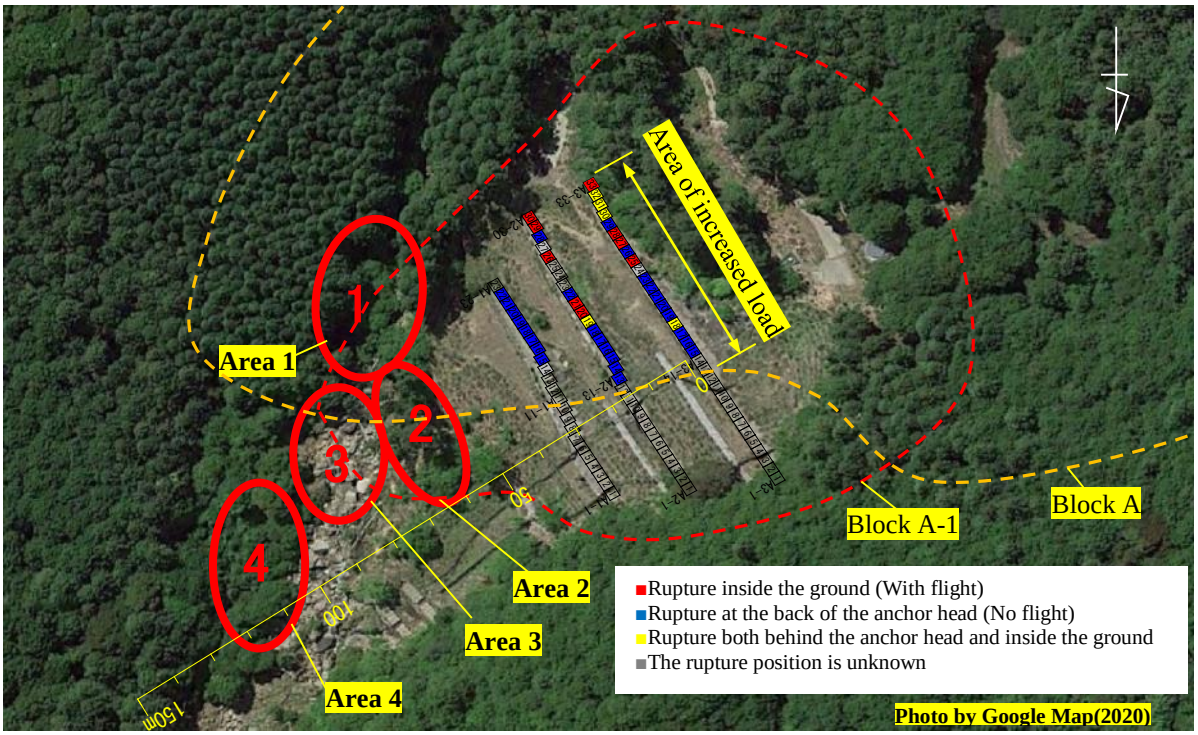

Fig. 6. Locations of anchor rupture and flight distance

To evaluate anchor flight due to fracture, the energy at the time of ejection was calculated from the flight distance, and a basic study was carried out regarding measures to prevent this ejection.

The elastic energy U at the fracture of a PC steel strand is given by the following equation:

$$\boldsymbol{U = \frac{1}{2} k x^2 \frac{1}{1000}} , \quad (1)$$

where $\boldsymbol{U}$ [kJ] is the elastic energy of the PC steel stranded wire, $\boldsymbol{k}$ [N/mm] is the spring coefficient of the wire, and $\boldsymbol{x}$ [mm] is the displacement of the wire. The displacement x of the PC steel stranded wire is then given by

$$\boldsymbol{x = \frac{1000 P l_f}{E_s A_s}} , \quad (2)$$

where $\boldsymbol{P}$ [kN] is the load of the PC steel stranded wire, $\boldsymbol{l_f}$ [m] is the wire fracture length, $\boldsymbol{E_s}$ [kN/mm^2] is the modulus of elasticity of the wire, and $\boldsymbol{A_s}$ [mm^2] is the cross-sectional area of the wire.

The relationship between the load and displacement of the PC steel stranded wire is

$$\boldsymbol{k = \frac{P}{x}} . \quad (3)$$

Substituting Equations (2) and (3) into Equation (1) yields the following equation:

$$\boldsymbol{U = \frac{P^2 l_f}{2 E_s A_s}} . \quad (4)$$

The elastic energy U when a PC strand breaks is determined by the load and length at the breaking point.

Furthermore, the kinetic energy K when the PC steel stranded wire breaks is expressed by

$$\boldsymbol{K = \frac{1}{2} m v^2 \frac{1}{1000}} , \quad (5)$$

where $\boldsymbol{m}$ [kg] is the mass of broken PC steel stranded wire and $\boldsymbol{v}$ [m/s] is the speed of the wire as it is ejected from the site.

The mass m of the fractured PC steel stranded wire is given by the following equation:

$$\boldsymbol{m = u l_f} , \quad (6)$$

where $\boldsymbol{u}$ [kg/m] is the mass per unit length of PC steel stranded wire and $\boldsymbol{l_f}$ [m] is the wire fracture length.

From the law of conservation of energy, Equations (4) and (5) must be equal, i.e., $U = K$. Substituting Equation (6) into this gives the initial velocity v_0 of the PC steel stranded wire at the break point, as

$$\boldsymbol{v_0 = \sqrt{\frac{1000 P^2}{u E_s A_s}}} . \quad (7)$$

The PC steel stranded wire at this survey site has u = 1.1 kg/m, E_s = 194 kN/mm^2, and A_s = 138.7 mm^2. From the fact that the minimum load to break an anchor is 90% of the yield tension, corresponding to P = 199.8 kN, the initial velocity of the PC steel wire would be approximately 37.6 m/s. From this initial velocity v_0, the trajectory and flight distance of the PC steel wire were calculated. Figure 7 shows the estimated flight trajectory and flight distance of the wires in area 4, where the maximum flight distance was confirmed. The flight distance calculated at a fracture load of 199.8 kN was approximately 170 m, and the actual observed distance was 120 m. Because of this discrepancy, the velocity at the time of ejection that matches the actual flight distance was calculated. As shown in Fig. 8, the calculation conditions were obtained for a trajectory that intersects with the tip of a tree near the edge of each region. The tree height was set to 12 m, which is the average tree height in the surrounding area. From this computation, the

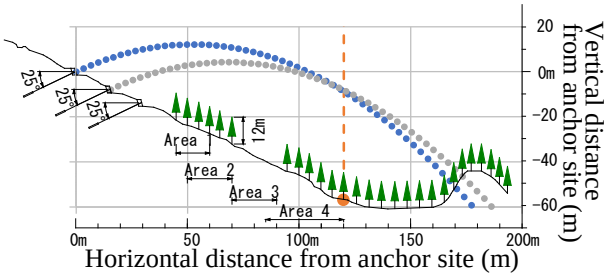

Fig. 7. Anchor flight trajectory
(Area 4, l_f = 20.1 m, P = 199.8 kN, v_0 = 36.7 m/s)

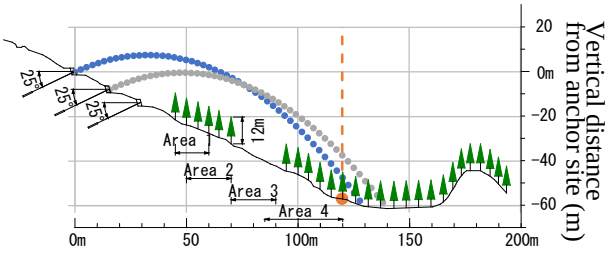

Fig. 8. Anchor flight trajectory
(Area 4, l_f = 20.1 m, v_0 = 29 m/s)

initial velocity at a flight distance of 120 m was determined to be approximately 29 m/s.

Table 2 lists the calculation results. Area 0 is the place where there was no flight and the protrusion of the anchor was 2.5 m. It was confirmed that the initial velocities of the PC steel strands at ejection were lower than the initial velocities at the time of fracture. Figure 9 shows the relationship between the fracture length of the PC steel wire, the elastic energy *U* at rupture with a load of 199.8 kN, and the kinetic energy *K* at ejection with the initial velocity obtained from the actual flight distance.

The energy at fracture increased in proportion to the fracture length. The energy at the time of ejection was approximately 3 kJ lower than the energy at time of breakage, to a fracture length of approximately 20 m. The energy at the time of ejection reached a maximum of 9 kJ near a fracture length of 20 m, after which it was confirmed that the energy dropped.

Photo 7 shows the damage to the head cap caused by the anchor rupture. It can be seen that the head cap is severely cracked, and the anchor head is rotated and slipping downward. From this, it was considered that the cause of the overall energy decrease at the time of ejection was the decrease in energy due to the frictional resistance of the PC steel wire prior to complete ejection. In addition, other factors, such as

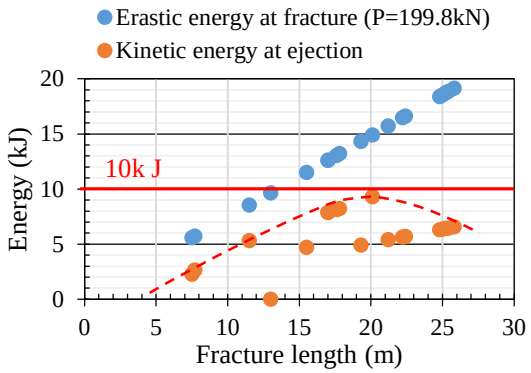

Fig. 9. Anchor energy and fracture length for ejected anchors

Photo 7. Breakage of anchor head by anchor rupture

Table 2. Measurement results of ejected PC steel strands and calculation results of energy at ejection

Area	Measured value				Analysis result					
	PC steel stranded wire				At anchor breakage			At ejection		
	No.	Flight distance(m)		Fracture length (m)	Breaking load	Initial velocity	Energy	Velocity	Wire mass	Energy
		Min	Max		*P* (kN)	v_0 (m/s)	*U* (kJ)	v_0 (m/s)	*m* (kg)	*K* (kJ)
0	1	2.5	2.5	12.7			10	-	-	-
1	1	30	60	22.2			16	21.5	24.4	6
	2			21.2			16	21.5	23.3	5
	3			25.4			19	21.5	27.9	6
	4			25.2			19	21.5	27.7	6
	5			25			19	21.5	27.5	6
	6			19.3			14	21.5	21.2	5
	7			24.8			18	21.5	27.3	6
	8			22.4			17	21.5	24.6	6
	9			25.8	199.8	37.6	19	21.5	28.4	7
2	1	50	70	15.5			11	23.5	17.1	5
	2			7.5			6	23.5	8.3	2
3	1	70	90	7.7			6	25.0	8.5	3
4	1	85	120	20.1			15	29.0	22.1	9
	2			17.6			13	29.0	19.4	8
	3			17			13	29.0	18.7	8
	4			17			13	29.0	18.7	8
	5			11.5			9	29.0	12.7	5
	6			17.8			13	29.0	19.6	8
Min		2.5	2.5	7.5	199.8	37.6	6	21.5	8.3	2
Max		85	120	25.8	199.8	37.6	19	29	28.4	9

the energy reduction due to the collision of the wire with the head cap, were considered to also contribute to the lower velocity. It was considered that the reason the energy decreased for fracture lengths of 20 m or more was that a greater fracture length yields a greater influence on the internal friction resistance. In addition, as shown in Photo 7, it was confirmed that there were many places where the spirals were broken one by one rather than the PC steel stranded wire. These results indicate that it necessary to take measures to prevent the ejection of a single PC steel stranded wire multiple times, even for anchors with three PC steel stranded wires.

From the above, although a tensile load of several hundred kilonewtons has been introduced to the anchor, the energy required for countermeasures per PC stranded wire is approximately 10 kJ or less, which is relatively small in comparison with other natural events such as rockfall. Furthermore, the mass of the PC steel stranded wire is as small as several tens of kilograms. If the ejection speed can be effectively reduced, the energy can be greatly attenuated, and it is possible that effective ejection protection measures can be implemented.

CONCLUSIONS

At a site where anchors ruptured as a result of a landslide producing a load that exceeded the design load, the rupture conditions of the anchors were investigated over the course of five years following the initial anchor fracture. The following observations were confirmed, although these were obtained under limited conditions.

It was confirmed that the rupture of the anchor progressed in stages, and although 42 anchors, which accounted for approximately 80% of the anchors within the deformation range, broke, the slope did not collapse. Of the fractured anchors, 14 were ejected from their installation sites, and a maximum flight distance of approximately 105 m was confirmed.

The load and kinetic energy when the anchors were ejected were estimated from the flight distance of the anchors, and it was confirmed that the maximum ejection energy of a PC steel strand of wire was approximately 10 kJ or less, which was relatively small. It was confirmed that the energy at ejection may not increase above a certain level depending on the fracture length of the anchor and the internal friction conditions.

In the future, we will continue to conduct field surveys on the fracture of anchors, accumulate data, and work toward developing slope stabilization measures that are safe and effective even when unexpected external forces occur.

ACKNOWLEDGMENTS

In carrying out this survey, the cooperation of the manager of the landslide countermeasure, Public Works Research Institute, and Anchor Asset Management Study Group was kindly provided. This research was supported in part by the Grant-in-Aid for Scientific Research Project (Project No. 19K04595). We would like to express our deep gratitude to all those involved for their cooperation.

REFERENCES

[1] Yoshihiro Tsunekawa,Toshinori Sakai,Hiroaki Miyatake,Masuo Kondoh,and Tomohiro Fujita Survey on fractures of ground anchors caused by inland earthquakes, Journal of Geotechnical Society, Vol.15 No. 2,2020, pp.339-354.

[2] Toshinori Sakaie, EVALUATION OF SLOPE STABILITY BASED ON MONITORING OF RESIDUAL LOADS ON GROUND ANCHORS USING THE SAAM SYSTEM, Seventh International Conference on Geotechnique, Construction Materials and Environment, Mie, Japan, 2017,pp.10-18

[3] Public Works Research Institute,JAPAN ANCHOR ASSOCIATION, Inspection and Maintenance Manual for Ground Anchors,2015,pp.58 .

[4] Japan Meteorological Agency: Various data and materials, https://www.data.jma.go.jp/gmd/risk/obsdl/index.php(Confirmed on September 17, 2019)

6th Int. Conf. on Structure, Engineering & Environment (SEE), Kyoto, Japan, Nov.18-20, 2020, ISBN: 978-4-909106056 C3051

EXAMINATION OF APPLICABILITY OF DYNAMIC LOAD TEST AND HILEY FORMULA TO SMALL DIAMETER STEEL PILE

Takaaki Ariki[1]
[1] Ex- General Incorporated Association of Advanced Geotechnical Technology, Japan

ABSTRACT

The purpose of this study was to assess the adequacy of using Hiley formula and the dynamic load test to estimate the bearing capacity of the steel pile with small diameter and length. The same specification piles were used and the static and dynamic load tests were performed at the same site, and compared these results. In the examination, the penetration and the rebound reflected the characteristics of the ground strength both the bearing pile and the friction pile, and the amount of work obtained by the dynamic load test. Furthermore, it was revealed that the work calculated from the rebound was directly proportional to the ultimate bearing capacity and the work calculated from the penetration was inversely proportional to the ultimate bearing capacity in the examination. These results suggested that Hiley formula was appropriate for the evaluation of the bearing capacity of the small diameter steel pile. In addition, by back calculating with the known values, the range of the hammer efficiency was obtained and the hammer efficiency could be used to correct the bearing value estimated by the formula.

Keywords: Small diameter steel pile, Dynamic load test, Hiley formula, Applicability, Hammer efficiency

INTRODUCTION

Hiley pile driving formula [1] is generally used for the assessment of bearing capacity of driving piles. This dynamic pile driving formula is still widely used. In general, the accuracy of the Hiley formula decreases with increasing pile length. In addition, it is also said that the accurate prediction of pile capacity using this formula is not possible in case of saturated silts, clays, muds, etc. The other hand, local buckling stress is enough to for the bearing capacity of the pile. But for the large diameter steel pile, the impact load/energy applied during dynamic load test might be larger whereas it might be smaller in case of small diameter steel piles.

Some studies have claimed that the estimated bearing capacity by Hiley formula is not accurate toward the bearing capacity on the static load test. The Hiley formula was induced assuming that equilibrium state of the energy. By the way, in this formula, the hammer efficiency is unknown. Chelis [2] mentions that the hammer efficiency varies from 0.6 to 1.0. And, Cornfield [3] points out that the Hiley formula is not valid for long pile. Furthermore, Ryan et al. [4] roused attention in using the average value of the hammer efficiency and showed the hammer efficiency of the actual survey. This problem might have aroused from the fact that there is wide variation in the size (e.g., diameter and length) and the material property (e.g., steel or concrete) of the pile. Thus, if the variation in the size and the material property of the pile is limited, the variation in the bearing capacity can be estimated in relation with the variation in the hammer efficiency.

The present study puts its focus on the applicability of the Hiley formula and the dynamic load test by the comparison of the test results of the static load test and the dynamic load test which were examined on the same test site using the piles of same specifications; limiting the size to small diameter and length and material to steel.

THE STATIC LOAD TEST

For the comparison with the results of the dynamic load test, the static load test was also conducted for the pile with same specification as that used for dynamic load test.

The Specifications of Pile, Installation and Curing of the Pile and Method of the Test

Table 1 shows the specification of the pile, such as the diameter, thickness and length for each test site. Figure 1 shows the lid with the digging claw and the open hole. This lid which has the same diameter as that of steel pipe, was joined to the tip of steel pipe by welding.

The pile was constructed by rotary penetration so as to satisfy the designed length. In the test site V, the intermediate hard layer, which has SPT value, N>20, was seen from 2 m to 7 m depths. This layer was drilled by the same diameter pile before installing the test pile. At this V test site, one pile showed shorter length than the design length in that the bearing layer appeared to be shallow during the

ground survey. Such cases are noted on Table 1 with * and ** symbols.

The static load test was examined by the step loading method until the tip displacement reached to the 10 % of the pile diameter after about one month curing from the construction. During the test, the applied load for the pile, the displacement of the pile head and the axial strain of the pile tip were measured. The ultimate resistance shall be defined as the load where the displacement of pile tip was reached to 10 % of pile diameter. And, the yielding resistance shall be defined as the load at the inflection point that appears clearly in the log *P* - log *s* curve or *P* - *s* curve.

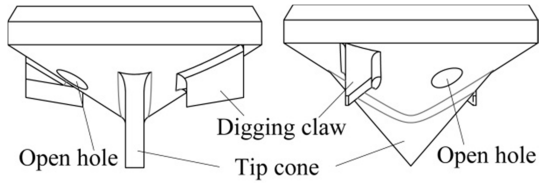

Fig. 1 Lid on tip of the pile

Table 1 Test site and specification of pile

Test site	Diameter of pile (mm)	Thickness of pile (mm)	Length of pile (m)
I	114.3	4.5	12.5
	114.3	4.5	10.5
II	114.3	4.5	8.25
	89.1	4.2	6.0
III	165.2	6.0	8.0
	114.3	4.5	6.0
	114.3	3.5	3.0
	89.1	3.2	1.0
IV	165.2	6.0	17.0
	89.1	4.2	8.0
	89.1	4.2	8.0
	89.1	3.2	3.0
	89.1	3.2	1.5
	89.1	4.2	18.0
V	165.2	6.0	15.635*, **
	165.2	6.0	16.0**
	114.3	6.0	13.5**
	89.1	4.2	4.5
	165.2	6.0	21.5**
VI	165.2	6.0	21.5
	114.3	4.5	15.0
	89.1	3.2	3.0
VII	89.1	4.2	13.25

Note: * Remaining high toward the design length, **: Pre-drilling of intermediate hard layer

The Results of the Test

Figure 2 (a) shows the relationship obtained between the yielding displacement and the yielding or ultimate bearing capacity for three types (diameters) of piles tested. Figure 2 (b) shows the relationship between the elastic rebound and the ultimate bearing capacity on the ultimate condition for same three types (diameters) of piles tested.

As Figure 2 (a) indicates, the yielding displacement and the yielding or ultimate bearing capacity are nearly in linear relationship. Also, Figure 2 (b) indicates, the elastic rebound on ultimate and the ultimate bearing capacity are nearly in linear relationship. From these relationships, the relationship between the yielding displacement and the elastic rebound at ultimate condition is plotted as shown in Figure 3. Here also, linear relationship is observed.

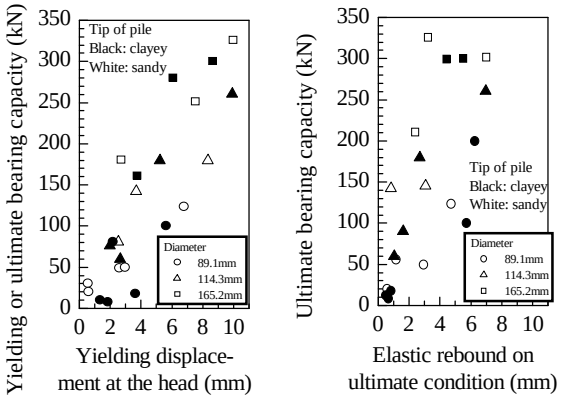

(a) Yielding displacement (b) Elastic rebound

Fig. 2 Yielding displacement and elastic rebound

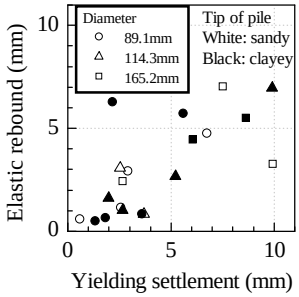

Fig. 3 Relations of yielding settlement and elastic rebound

THE DYNAMIC LOAD TEST

In order to compare the results of the static load test and examine the applicability of Hiley formula in the dynamic load test, piles of similar specification as those used in the static load test were used. Also, the same test sites were used.

The Specifications of Pile, Installation and Curing of the Pile and Method of the Test

The test sites, specification and installation of the pile for the dynamic load test are same as that used for the static load test (Table 1). Also, the curing period after installation of pile is same as for the static load test. As explained earlier, Figure 1 shows the lid to be connected at the pile tip. Two open holes are provided in that lid to reduce the effect of excess pore water pressure which is generated during dynamic loading [5].

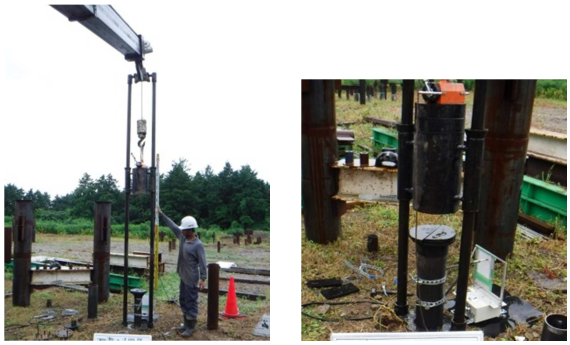

(a) Set of the height (b) Record

Fig. 4 A situation sample of dynamic load test

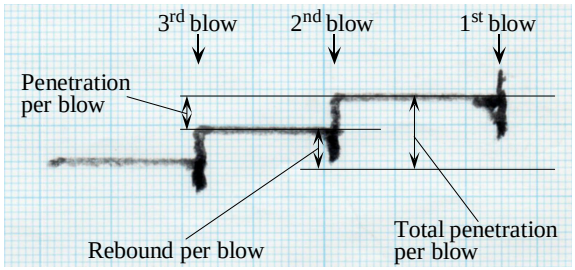

Fig. 5 A sample record of dynamic load test

In Figures 4 (a) and 4 (b), test set up height and recording process are shown. The hammer is allowed to free fall from the height of the set to the cap with of the pile. A rubber plate of 2 cm thick is kept on the pile cap and displacement of the pile per blow after each free fall of the hammer on the pile cap was recorded. One of the test records of hammer impact and penetration amount is shown in Figure 5. The penetration per blow, rebound per blow and total penetration are shown in Figure 5. During the dynamic load test, the pile is impacted (hammered) 3 times by the same hammer (weight) by allowing it to free fall from the same hammer height. Finally the penetration per blow and rebound per blow were added. Then the average penetration and rebound were calculated for each case.

In addition, the tests were also done by varying the impact energy to check the hammer efficiency. The test sites and test pile specifications were same as those used earlier. In total, 53 tests were conducted.

The weight and height of the hammer were determined by checking the local buckling of the steel pipe by using Equation (1). From the test results, it is observed that the hammer weight is 1.92 kN or 1.47 kN and the maximum height of the hammer (weight) kept is 2 m.

$$\sigma_2 = \left(\frac{E}{C} \sqrt{2gH} \cdot 10^{-3} \right) \cdot e^{-788A/W} \quad (1)$$

Where,

σ_2 : the impact stress in N/mm^2.
E : the young's modulus of the steel pile in N/mm^2.
C : the velocity of elastic wave of the steel pile in m/sec.
g : the acceleration of gravity in m/sec^2.
H : the height of the free fall of hammer in m.
A : the cross-sectional area of the steel pipe in m^2.
W : the weight of the hammer in kN.

The Results of the Test

Figure 6 shows the relationship between the penetration and the rebound. It shows that with the increase in penetration, there is decrease in the rebound amount.

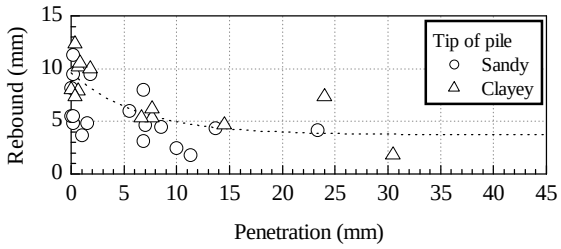

Fig. 6 Relations of the penetration and the rebound

Figure 7 shows the relationship between the ground strength (in terms of *N*' value), the penetration, and the rebound/length or the elastic strain of the pile in regard with the pile tip. Figure 8 shows the relationship of the ground strength (in terms of *N*' value), the penetration, and the rebound/length or the elastic strain in regard with the pile side. Here, the ground strength is shown in terms of *N*' value. The Swedish weight sounding can conduct a consecutive investigation in the ground. The *N*' value is the converted value of Swedish weight sounding method in terms of *N* value of the Standard Penetration Test (SPT). It is observed that the averaged *N*' value on the pile tip is calculated in the range of 3 times of the pile diameter from the pile tip, and the averaged *N*' value on the pile side is

calculated in the range of pile length. Where, the rebound was shown in the elastic strain by dividing by the pile length for comparing to the elastic strain of the ground. And, the elastic strain of the steel pipe caused the impact stress of Equation (1) is obtained by subtracting the elastic strain of the rebound and elastic deformation of cap from the total elastic strain of the ground. Here, elastic deformation of the cap is not considered.

As shown in Figure 7, when the averaged *N*' value on the pile tip is smaller than 10, the penetration, the rebound and the elastic strain of ground decreases. When the averaged *N*' value is more than 10, the penetration, the rebound and the elastic strain of the ground remains nearly constant. Therefore, these values are dependent on the ground strength on tip of pile, and these values are reflecting the ground properties on tip of the pile.

In Figure 8, a trend of decrease in the value of the penetration, the rebound and the elastic strain of ground when the averaged *N*' value on the pile side is smaller than 5. Also, the figure shows that when the averaged *N*' value is more than 5, the penetration, the rebound and the elastic strain of the ground is nearly constant. Therefore, these values are depending on the ground strength on side of pile, and these values are reflecting the ground properties on side of the pile.

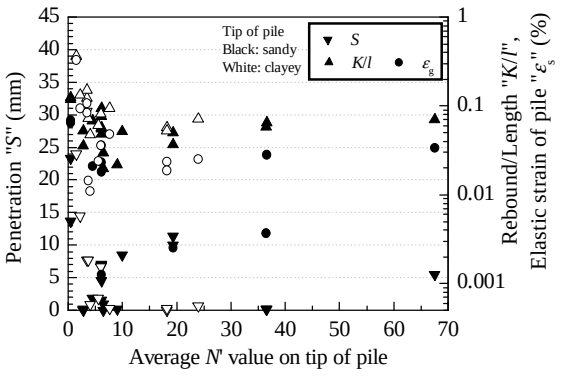

Fig. 7 Penetration, rebound and elastic strain of ground toward the *N*' value on tip of pile

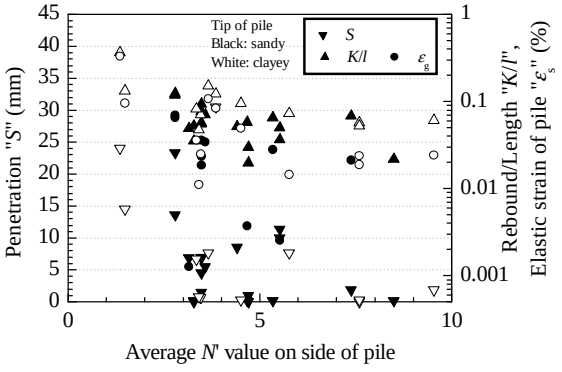

Fig. 8 Penetration, rebound and elastic strain of ground toward the *N*' value on side of pile

Figure 9 shows the relationship between the pile length and the penetration, the rebound, the elastic strain of the ground and the elastic strain of the steel pipe. As shown in Figure 9, the penetration amount is dependent on the pile length clearly. And, when the pile length is more than 15 m, the penetration amount is almost 0. This relationship agrees with indication given by Cornfield [3] that the Hiley formula is not valid for the longer pile. However, this relation is not influenced by the Hiley formula in that the impact energy is limited by the local buckling stress. Thus, it is considered that this relation is attributed to the relations of the impact energy and the local buckling stress.

Therefore, the penetration and the rebound are reflecting the ground properties, but the upper limit by this test device which the ground strength can be reflecting exists, because of the upper limit of the impact energy.

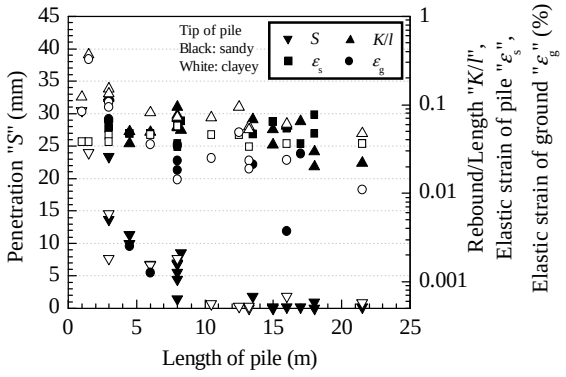

Fig. 9 Penetration, rebound, elastic strain of ground and elastic strain of pile toward the length of pile

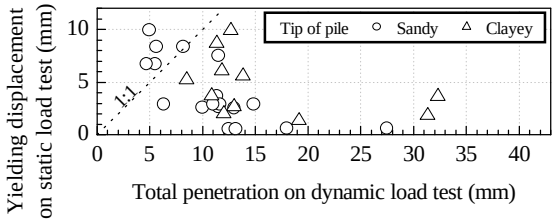

Fig. 10 Comparison total penetration and yielding displacement

The Comparison the Results of the Dynamic Load Test and the Results of the Static Load Test

Figure 10 shows the relationship of the total penetration of the dynamic load test and the yielding displacement of the static load test. The total penetration included all deformation by the dynamic load test. As shown in Figure 10, the total penetration was nearly larger than the yielding displacement. Therefore, it is considered that the ground has reached to the yielding condition by this

dynamic load test. But, when the total penetration was nearly less than 10 mm, the total penetration was smaller than the yielding displacement.

Figure 11 shows the relations of the rebound of the dynamic load test and the elastic rebound of the static load test. As Figure 11 indicates, when the elastic rebound increased, the rebound also increased, and the rebound was bigger than the elastic rebound. By the way, the impact stress on the dynamic load test which is calculated by the Equation (1) is nearly larger than the ultimate stress on the static load test of which the ultimate bearing capacity is divided by the cross section of the steel pipe, such as shown in Figure 14, and as Figure 2 indicated, the yielding displacement and the elastic rebound increased linearly when the loading weight increased on the static load test.

Because of the foregoing reasons, as the total penetration and the rebound were nearly bigger than the yielding displacement and the elastic rebound. It shows that the ground was reached to the yielding condition by this dynamic load test.

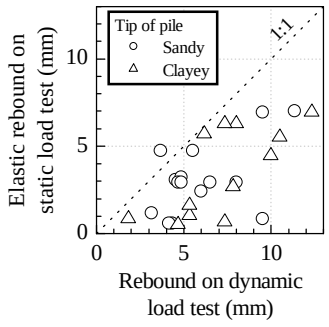

Fig. 11 Comparison rebound and elastic rebound

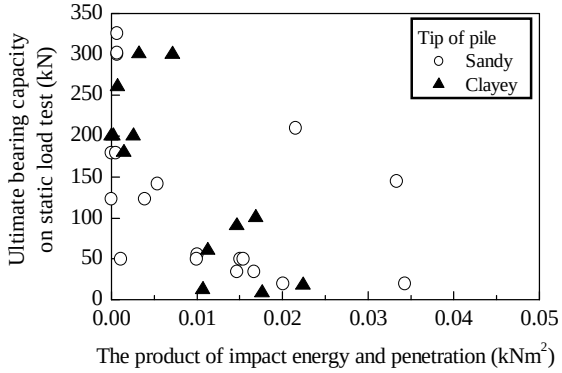

Fig. 12 Relations of the product of the impact energy and the penetration and the ultimate bearing capacity

Next, Figure 12 shows the relations of the product of the impact energy and penetration and the ultimate bearing capacity. Figure 13 shows the relations of the product of the impact energy and rebound and the ultimate bearing capacity relationship. The product of the impact energy and the penetration, the product of the impact energy and the rebound are showing the work done by the impact energy on the dynamic load test.

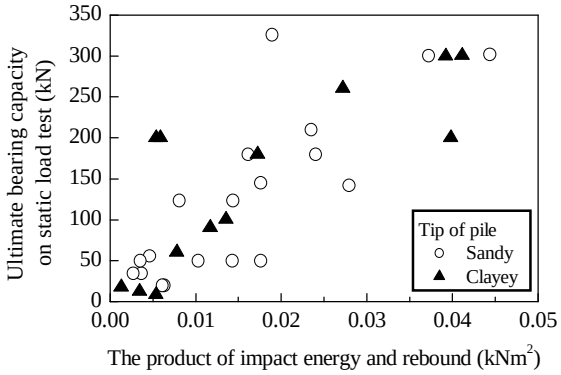

Fig. 13 Relations of the product of the impact energy and the rebound and the ultimate bearing capacity

In Figure 12, the ultimate bearing capacity is large when the penetration is small on the same impact energy where the work done by the penetration is inversely proportional to the ultimate bearing capacity. And, in Figure 13, the ultimate bearing capacity is larger when the rebound is large on the same impact energy in that the work done by the rebound is proportional to the ultimate bearing capacity. Therefore, the penetration and the rebound were depending on the ground strength, these results enable the penetration and the rebound to assume the ground strength on the same impact energy, but as Figures 7 and 8 indicated, this assumption has an upper limit.

EXAMINATION IN THE APPLICABLITY AND RANGE OF THE DYNAMIC LOAD TEST

Because the equilibrium condition of the work done by both the penetration and the rebound which reflected the ground strength from the bearing pile to the friction pile on the dynamic load test was confirmed in the foregoing chapter and sections, the applicability of the dynamic load test and the Hiley formula is high. What is the noted is the range of the application will have the upper limit, like a situation that the total penetration was equal to the rebound. Thus, it can be presumed that the foregoing situation is the upper limit of the range of the application of using this test device. As the situation indicated in Figure 9, when the pile length is 15 m, the rebound and the elastic strain of the steel pipe are same as 0.07 %., then the calculated bearing capacity is about 400 kN. In this dynamic load test, the upper limit of the application range is enough is that the designed ultimate bearing capacity is almost same for the small diameter pile.

HAMMER EFFICIENCY ON HILEY FORMULA

Equation (2) shows the Hiley formula. The penetration, the rebound, the weight of the hammer and the height of the free fall of hammer are known in this dynamic load test. Generally, the ultimate bearing resistance is estimated from the Equation (2). Where, it is same as the ultimate bearing capacity in the static load test. Then, the hammer efficiency was back calculated using these known values.

$$R_{du} = \frac{e_h WH}{S + K/2} \quad (2)$$

Where,

R_{du} : the ultimate driving resistance in kN.
e_h : the hammer efficiency.
W : the weight of the hammer in kN.
H : the height of the free fall of the hammer in m.
S : the penetration by the dynamic load test in m.
K : the rebound by the dynamic load test in m.

Figure 14 shows the relationship of the impact stress per the ultimate stress and the hammer efficiency relationship. The value that the ultimate bearing capacity is divided by the cross section of the steel pipe was defined as the ultimate stress. As shown in Figure 14, the hammer efficiency varies from 0.2 to 0.5, when the impact stress per the ultimate stress is larger than 1. When the impact stress per the ultimate stress is less than 1, the impact stress per the ultimate stress decreased. At the same point, the hammer efficiency was increased.

Therefore, when the impact weight is enough to the ultimate bearing capacity, the hammer efficiency is almost same. In contrary, when the impact weight is less than the ultimate bearing capacity, the hammer efficiency was increased.

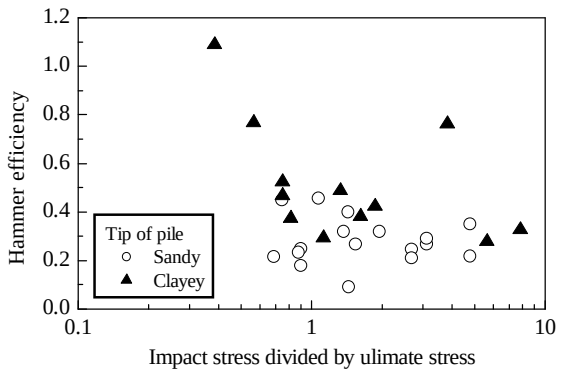

Fig. 14 Relations of the impact stress divided by ultimate stress and the hammer efficiency

It is considered that this result can be applied to the calibration of the estimated bearing capacity by the Hiley formula. And, when the designed ultimate bearing capacity is known, the impact energy should not be larger than the ultimate resistance necessarily if the range of the application is shown clearly.

CONCLUTION

The present study puts its focus on the applicability of the Hiley formula and the dynamic load test by the comparison of the test results of the static load test and the dynamic load test which were examined on the same test site used by the same specification of pile, when the applied range of the steel pipe pile is limited to the small diameter and length.

The fact that the equilibrium condition of the work done by both the penetration and the rebound which reflected the ground strength from the bearing pile to the friction pile on the dynamic load test was confirmed by the following relations reveals that the applicability of the dynamic load test and the Hiley formula is high. The confirmed relations are the relations with the ground strength and the penetration or the rebound, and the relations with the ultimate bearing capacity and the work done by the penetration or the rebound. In addition, the upper limit of the application range of this dynamic load test is enough in that the maximum designed ultimate bearing capacity is almost same for the small diameter pile.

Furthermore, an existing range of the hammer efficiency calculated back using known values in the Hiley formula was shown. It is considered that this result can be applied to the calibration of the estimated bearing capacity by the Hiley formula. And, when the designed ultimate bearing capacity is known, the impact energy should not be bigger than the ultimate resistance necessarily if the range of the application is shown clearly.

REFERENCES

[1] Hiley, A., A rational pile-driving formula and its application in piling practice explained, Engineering, 119, pp.657 and 721, 1925.
[2] Chelis, R.D., Pile foundations, McGraw Hill, pp.29-31, 1961.
[3] Cornfield, G.M., Discussion on “Pile-driving analysis by the wave equation”, J. Soil Mech. Found. Div., ASCE 87, No.SM1, pp.63-75, 1961.
[4] Ryan Allin, Garland Likins, Jon Honeycutt, Pile Driving Formulas Revised, Proceedings of the international foundations congress and equipment expo, ASCE, 2015.
[5] Randolph, M. F., Carter, J. P. and Worth, P. C. : Driven piles in clay – the effects of installation and subsequent consolidation, Geotechnique, Vol.29, No.4, pp.361-393, 1979.

6th Int. Conf. on Structure, Engineering & Environment (SEE), Kyoto, Japan, Nov.18-20, 2020, ISBN: 978-4-909106056 C3051

ASSESSING FACTORS INFLUENCING ROUTE CHOICE A CASE STUDY OF TERPEKA TOLL ROAD, INDONESIA

Aleksander Purba[1], Darmawan Adi Susanto[2], Rosalia Dwi Werena[3] and Tiara[4]
[1,3,4]Engineering Faculty, the University of Lampung, Indonesia
[2]Post Graduate Program, Civil Engineering, the University of Lampung, Indonesia

ABSTRACT

TERPEKA is part of the Trans Sumatera toll road network that is planned to connect the northern part of Sumatera to the southern part and will link the province of Nanggroe Aceh Darussalam with Lampung. The TERPEKA section is located in the Lampung and South Sumatera provinces with a total length of 189 km and expected to increase accessibility to and from regions located in close proximity to the toll road and to stimulate economic growth, particularly in palm oil and rubber sectors. A total of 190 respondents were collected in the rest area of KM 234A and KM 215B on end year vacation of 2019. Respondents in the age range of 26 to 55 years who were in the productive age category had a percentage of 84%, and age range of 36 to 45 years was recorded as 32% which included the most productive age category. These figures indicate that Indonesia is enjoying a demographic bonus. The most significant factor influencing route choice when deciding to determine to travel using toll road is income followed by spending for transport attribute. The equation of $Y = -1.711 – 0.00000921X_1 + 0.186X_2 + 0.446X_4$ is differences in the utility related to the attributes or characteristics of TERPEKA route which was analyzed. With the correlation coefficient, the income level and time saving variables are those variables that most influence the TERPEKA's toll road users. Instead, increase in toll fares reduces vehicle use.

Keywords: TERPEKA, Fare, Income, Spending for transport, Indonesia

INTRODUCTION

A Terbanggi Besar–Pematang Panggang–Kayu Agung (TERPEKA) along 189 km is part of the planned development of 2,974 km of Trans Sumatra toll road. The construction of this toll road is one of the packages of a national strategic project initiated by the central government. At the beginning of development, the TERPEKA toll road segment was declared economically feasible but financially unfeasible, so the central government assigned a state owned company to build it. According to the feasibility study document, the total volume of traffic of TERPEKA is 14,000 vehicles per day and segments that are considered financially viable are usually with total volume more than 20,000 vehicles per day. Such conditions are not only phenomena in developing country such as Indonesia but also in the developed country, since costs derived from through traffic would also not be covered by the fees, but this issue may be moot, as most through traffic uses arterials that are funded by higher levels of government [1].

Hence, through Presidential Regulation No. 117/2015 jo. No.100/2014 the central government assigned PT Hutama Karya (Persero) to implement the acceleration of development of Trans Sumatera toll road [2]. After constructed around two years, in mid-November 2019 the TERPEKA segment began operating with toll fares of Rp170,500 from the starting point of Terbanggi Besar to the end point of the segment in Kayu Agung or Rp902/km. Generally, the determination of toll fares is decided by considering the financial condition of the government, investors and road users and fares must meet user benefits and meet environmental requirements [3]. Toll road financing is allocated for construction, operation and maintenance. Toll fare and the number of users are the two main factors affecting revenue, investment and development of toll roads. Travel demand depend on the number and type of trips to be selected by individuals under certain conditions. Factors that influence travel demand in general are demographic, geographic and economic factors, which the available space can exceed capacity faster than the predicted as found by Selmoune et. al in many cities such as Singapore, Stockholm, and London [4]. Demographic factors are the individual preference of road users and economic factors usually related to travel expenses. Travel expenses include fares, additional travel time, inconvenience and risks. Modeling the relationship factors will be useful in estimating the trip behavior and future transport policy strategies. Changes in fares can affect the frequency, route, mode, and destination of the trip and their impact can be known through measuring price impacts [5] and change of utility function [6]. Study area in China has found the travel cost and travel time have a significantly negative impact on the utilities [7]. The purpose of

the study is to model user preference on the selection of routes between toll roads or non-toll road.

MATERIAL AND METHOD

Study Area

TERPEKA is part of the Trans Sumatra toll road which is planned to link from the north of the island of Sumatra to the south and connects the province of Nangroe Aceh Darussalam to Lampung province. This section is located in Lampung and South Sumatra provinces and is divided into three sections namely section 1 Terbanggi Besar - Menggala, section 2 Menggala - Simpang Pematang and section 3 Simpang Pematang - Kayu Agung. So that this section is a combination of the Terbanggi Besar – Pematang Panggang (100 km) section which was built and operated first and Pematang Panggang - Kayu Agung (89 km) section which was operated later as shown in Fig. 1.

As part of the main network of the island of Sumatra, this section is important to support the transportation of goods and people from the Bakauheni port and is expected to be able to open access to the surrounding areas and support economic growth, especially natural resources of oil palm and rubber plantations. In addition, one of the vital roles expected is to reduce travel time and reduce logistics costs from the Bakauheni port to South Sumatera and surrounding areas [8].

Fig. 1 A section of TERPEKA toll road

Stated Preference Techniques

The stated preference (SP) technique is widely used in research and practice in travel behavior. Generally, this method is applied to identify behavioral responses to selected situations that are not or have not yet been fully revealed in the market. In practice the SP method is modified in such a way as to the importance of the attributes in the choices provided as conducted by Saeed & Majid [9]. An example of a choice not revealed on the market is the case of choosing a route between using a toll road or non-toll road. In this case study condition, there is no specific information or data that can be processed with statistics to get the desired route choice. With the stated preference technique, researchers can fully control the factors that exist in a hypothetical situation. In the case of choosing a route between a

toll road and a non-toll road, alternative options are designed that show variations in toll fares and time saving (compared to non-toll routes). Individuals will state their response to these alternatives. Then the data is processed using statistical software to determine the choice of the route by considering the factors of toll fare and time saving variations.

RESULT AND DISCUSSION

Field Survey

A total of 190 respondents were collected in the rest area of KM 234A and KM 215B of TERPEKA on December 26 and 27, 2019 between 9am and 6pm. It is important to note that the number of respondent is not large enough compared to about 18,000 vehicles per day of TERPEKA at the time the survey was conducted, as is also stated by Xiao et. al [10], biases may occur in the process of characterizing the population by using samples [11], each person has a characteristic daily motif [12], and the underestimation of the relatively high mobility at the city scale [13]. The socioeconomic characteristics of respondent are described below: they are age group, education level, job, monthly income range, spending for transport, annual travel frequency, trip purpose, and reason for using toll road, respectively.

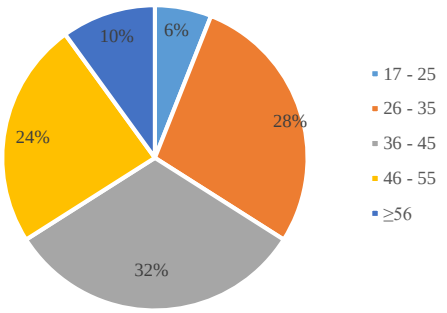

Fig. 2 Age group

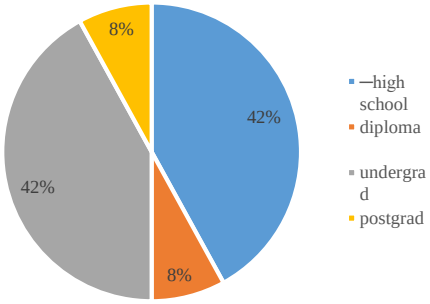

Fig. 3 Education level

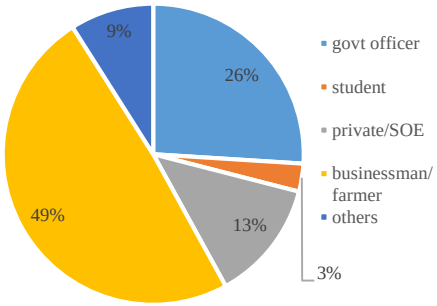

Fig. 4 Job

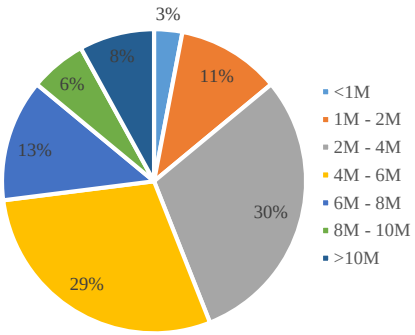

Fig. 5 Income range

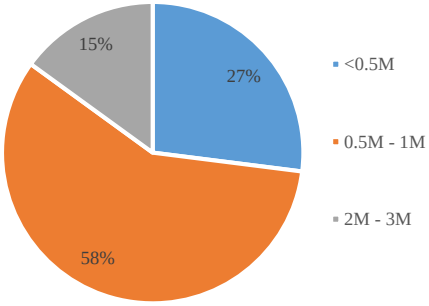

Fig. 6 Spending for transport

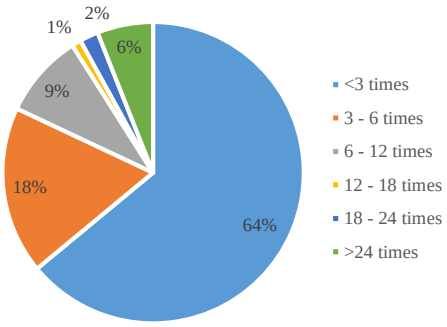

Fig. 7 Annual travel frequency

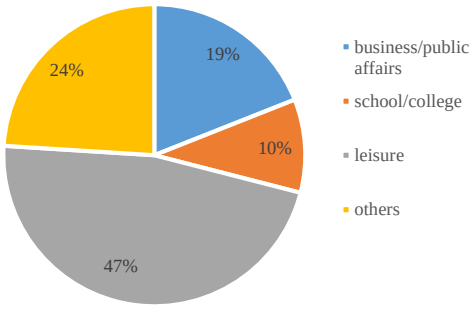

Fig. 8 Trip purpose

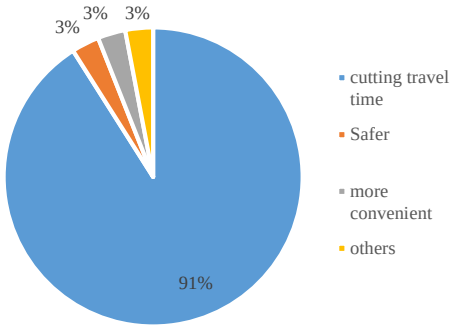

Fig. 9 Reason for using toll road

Correlation Analysis

Correlation analysis of respondent characteristics was conducted to determine the influence of a number of socioeconomic factors in determining route choice. The correlation coefficient of variables expressing the respondents' characteristics is shown in Figure 10 below. The figures of correlation coefficient were obtained from the correlation analysis by using statistical software. The significance test of the correlation coefficient is conducted based on probability with a confidence level of 95%.

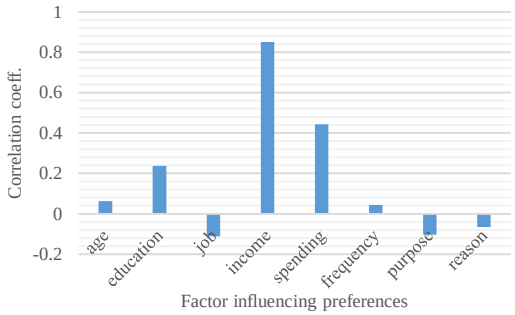

Fig. 10 Correlation coefficient of toll user characteristics

Here are the four most important factors influencing preferences (Fig. 10). First, respondent characteristics that influence the route choice are education, income and spending for transport, respectively. Second, the correlation coefficient related to education factor for route choice using toll road is 0.237 (low correlation). The sign (+) indicates a positive correlation, meaning that the higher education, the higher tendency of respondents to choose toll road. Third, the correlation coefficient in terms of income related to route choice of TERPEKA is 0.851 (very strong). This figure indicates that the income factor is the most influential factor comparing to other characteristic factors while determining the option of using toll roads. The sign (+) indicates a positive correlation, meaning that the higher income the higher tendency to determine to travel using toll road. Fourth, the correlation coefficient associated with spending for transport over route choice of toll road is 0443 (moderate). The sign (+) indicates a positive correlation, which means the higher spending for transport the more people use toll road.

Route Choice Probability

Based on the toll fare variables, the respondent's largest preference for "may be not use toll" if the fare increase amounted to Rp50,200 was 20.50% for income group of 2M to 4M. These income groups have the potential to switch for choosing non-toll road if toll fares increased more than Rp50,200. The respondent preference on the route choice can be seen in the following Table 1.

Table 1. Income group, fare, and route choice

Income	Preference	Δ-Fare	%
2M-4M	May be not use toll	50,200	20.50
4M-6M	May use toll	25,200	17.89
1M-2M	Definitely not use toll	80,200	10.53
6M-8M	Definitely use toll	9,200	6.32

In terms of time saving variable, the respondent's largest preference for "may be not use toll" if the time saving range is only two hours with a percentage of 11.58% for income group of 2M to 4M.

These income groups have the potential to switch for choosing non-toll roads if time saving is less than two hours. Route choice preferences for various income group categories and time saving ranges is shown in Table 2.

Furthermore, based on the results of the respondent's preference, an equation approach can be made to predict the binary logit model of route choice between toll roads and non-toll roads.

Table 2 Income group, time-saving, and route choice

Income	Preference	Δ-t-save	%
2M-4M	May not use toll	2	11.58
4M-6M	May use toll	3	8.95
2M-4M	May not use toll	1	7.89
1M-2M	Definitely not use toll	1	7.37

The model is to specify differences in the utility associated with both available routes. Hence, equation (U_{toll} - $U_{non\text{-}toll}$) is the difference in the utility of toll road route and non-toll road route. The general form of a multiple linear regression analysis formed is as follows:

$$Y = a + b_1(X_{1toll} - X_{1non\text{-}toll}) + b_2(X_{2toll} - X_{2non\text{-}toll}) + \ldots + b_n(X_{ntoll} - X_{nnon\text{-}toll}) \quad (1)$$

Furthermore, the model with the best performance on the backward elimination validation set is selected as below:

$$Y = -1.711 - 0.00000921X_1 + 0.186X_2 + 0.446X_4$$

with,

X_1: toll fares

X_2: time saving

X_4: income level

With the correlation coefficient, the variables X_4 and X_2 are those variables that most influence the TERPEKA's toll road users. Instead, increase in toll fares reduces vehicle use.

CONCLUSION

Respondents in the age range of 26 to 55 years who were in the productive age category had a percentage of 84%, and age range of 36 to 45 years was recorded as 32% which included the most productive age category. This figure is almost three times higher compared to the HOT and HOV – HOT markets of the USA which is only 12% [14]. These findings indicate that Indonesia is enjoying a demographic bonus, which are shown through a high percentage of the age range of productive categories and also the most productive age range, which is much higher compared to developed countries such as the USA. Respondents with education level of high school and diploma have the largest percentage of 42%. In terms of job, respondents with self-employed/farmers had the highest percentage of 49%. According to monthly income, respondents with 2M to 4M income range had the highest percentage of 30%. Respondents with a spending for transport of 0.5 M to 1M were recorded at 58% and respondents with the annual travel frequency less than three times had the highest percentage of 64%. Respondents with trip purpose for leisure have the highest percentage of 47% and the respondents determined a toll road with a percentage of 91% due to the reason would cutting travel time. The most significant factor influencing route choice when deciding to determine to travel using toll road is income with a correlation coefficient of (+) 0.851. This figure indicates that the higher income the higher tendency to determine to travel using toll road. Findings on this research are not much different compared to respondent behavior of other cities as expressed by Atlanta [15, 16] and Abu Dhabi [17]. Attribute related to spending for transport is quite influential on the route choice for determining toll roads with a correlation coefficient of (+) 0,443. It means the higher spending for transport of respondents, they have tendency to determine for using toll road compared to non-toll road. The equation of $Y = -1.711 - 0.00000921X_1 + 0.186X_2 + 0.446X_4$ is differences in the utility related to the attributes or characteristics of TERPEKA route which was analyzed. Route choice probability between the toll roads and non-toll roads is represented by attributes of toll fares, time saving and income level and its differences in utility would maximized by respondents according to his/her characteristics individually in deciding of available options. With the correlation coefficient, the income level and time saving variables are those variables that most influence the TERPEKA's toll road users. Instead, increase in toll fares reduces vehicle use.

ACKNOWLEDGEMENT

Authors thank DIPA Engineering Faculty the University of Lampung to support research project and the people who have helped field survey and also the reviewers for all useful and helpful comments on our manuscript.

REFERENCES

[1] Junge, J. R., and Levinson, D., Prospects for transportation utility fees, J. of Transport and Land Use, Vol. 5, No. 1, 2012, pp. 33-47.

[2] Retrieved from http://www.jdih.kemenkeu.go.id/fullText/2015/117TAHUN2015PERPRES.pdf, (*In Indonesian*)

[3] Yusuf, J. E. (Wie)., O'Connell, L., and Anuar, K. A., For Whom the Tunnel Be Tolled: A Four-Factor Model for Explaining Willingness-to-Pay Tolls, School of Public Service Faculty Publications, Vol. 1, 2014, pp.1-28.

[4] Aya, S., Qixiu, C., Lumeng, W., and Zhiyuan, L., Influencing Factors in Congestion Pricing Acceptability: A Literature Review, J. of Advanced Transportation, Vol. 2020, 2020, pp. 1-11.

[5] Litman, T., Understanding Transport Demands and Elasticities How Prices and Other Factors Affect Travel Behavior, Victoria Transport Policy Institute, 2019, pp. 1-79.

[6] Saeed, A. B., Mitra, H., Madjid, T., and Debora C., A logit-based model for measuring the effects of transportation infrastructure on land value, J. of Transportation Planning and Technology, Vol. 40, No. 2, 2017, pp. 143–166.

[7] Xiaomei, L., Yusak, O. S., Chunfu, S., and Chengxi, L., The Implication of Road Toll Discount for Mode Choice: Intercity Travel during the Chinese Spring Festival Holiday, J. of Sustainability, Vol. 10, No. 2700, 2018, pp. 1-16.

[8] Retrieved from https://kppip.go.id/en/priority-projects/road/15-sections-of-the-sumatera-toll-road/

[9] Saeed, A. B., and Majid S., A modern congestion pricing policy for urban traffic: subsidy plus toll, J. of Modern Transportation, Vol. 25, 2017, pp. 133–149.

[10] Xiao, Y. Y., Wen, X. W., Zi, Y. G., and Ying, C. L., Universal model of individual and population mobility on diverse spatial scales, J. of Nature Communications, Vol. 8, No. 1639, 2017, pp. 1-9.

[11] Zhengbing, H., Spatial-temporal fractal of urban agglomeration travel demand, J. of Physica A: Statistical Mechanics and its Applications, Vol. 549, 2020, pp. 1-11.

[12] Christian, M. S., Vitaly, B., Thomas C., Zbigniew, S., and Marta, C. G., Unravelling daily human mobility motifs, J. of Royal Society Interface, Vol. 10, No. 84, 2013, pp. 1-8.

[13] Xiao, Y. Y., Chen, Z., Ying, F., Zengru, D., and Wen, X. W., Universal predictability of mobility patterns in cities, J. of Royal Society Interface 11(100), 2014, pp. 1-7.

[14] Sara, K., and Randall, G., Socioeconomic Assessment: Conversion of I-85 High-Occupancy Vehicle to High-Occupancy Toll in Atlanta, Georgia, Transportation Research Record: Journal of the Transportation Research Board, No. 2450, 2014, pp. 52–61.

[15] Randall, G., Joonho, K., Daejin, K., Sara, K., Adnan, S., and Yanzhi, X., Factors affecting Atlanta commuters' high occupancy toll lane and carpool choices, International Journal of Sustainable Transportation, 2019, pp. 1-12.

[16] Adnan, S., Aditi, M., and Randall, G., High-Occupancy Toll Lane Decision Making: Income Effects on I-85 Express Lanes, Atlanta, Georgia, Transportation Research Record: Journal of the Transportation Research Board, No. 2531, 2015, pp. 45–53.

[17] Ammar, A., and Zaidan, Analysis of factors affecting willingness to pay for high-occupancy-toll lanes: Results from stated-preference survey of travelers, J. of Transport Geography, Vol. 66, 2018, pp. 91-105.

6th Int. Conf. on Structure, Engineering & Environment (SEE), Kyoto, Japan, Nov.18-20, 2020, ISBN: 978-4-909106056 C3051

DEVELOPING NUMERICAL MODEL FOR LIQUEFACTION-INDUCED LATERAL DEFORMATION USING SPH

Erly Bahsan[1], Budi Susilo Soepandji[1], Dwinanti Rika Marthanty[1] and Widjojo Adi Prakoso[1]
[1]Department of Civil Engineering, University of Indonesia

ABSTRACT

Numerical simulation on lateral displacement after liquefaction has been a focus for the latest studies in geomechanics. However, the use of finite element and finite different as the most popular numerical methods in geomechanics has some limitations in representing such large failure. As an alternative, the smoothed particle hydrodynamics (SPH) has been used for this purpose. This recent study tries to apply the SPH to simulate the very large lateral displacement following the liquefaction as part of bigger research in studying such phenomenon in some locations near Palu City, Central Sulawesi, Indonesia, after the big earthquake on 28 September 2018. The SPH model will be developed by assuming the liquefied sand as fluid particles that interacts with pore water particles. Some hypotheses regarding the main factors that possibly related to the large displacement will be simulated using the SPH model, which are the effect of the very gentle sloping ground and the effect of water film that might be developed during the liquefaction. The outcomes of this recent study were expected to complement the previous studies regarding the use of SPH for liquefaction and lateral spreading.

Keywords: Smoothed Particle Hydrodynamics, liquefaction, numerical method

INTRODUCTION

The big earthquake in Central Sulawesi, Indonesia, on 28 September 2018 showed some major impact such as tsunamis, rockslides and landslides, structural damages, and liquefactions. Yet, the most notable phenomenon was the large lateral soil deformation following the liquefactions. According to [1] at least there were 5 locations near Palu City that experienced the large lateral displacement after the earthquake: Petobo, Jono Oge, Lolu Village, Sibalaya, and Balaroa. Those were noted as the largest lateral displacement ever recorded [2].

To avoid more damage due to this phenomenon, it is necessary to study its behavior and the influencing factors using numerical models. However, the commonly used numerical methods in geotechnical studies such as Finite Element and Finite Difference have difficulties to represent the large deformation since both methods are grid based. In the other hand, Smoothed Particle Hydrodynamics (SPH) as a mesh-free numerical method can overcome this limitation. In SPH, the materials are represented by a set of particles that can freely move and interact with each other within a range controlled by a weighting function [3].

Smoothed particle hydrodynamics is a mesh-free particle method based on Lagrangian formulation, that was first applied to solve the astrophysical problems in open space (e.g., [4], [5]). Recently, this method is also applied for geomaterials and geodisaster models as mentioned by [6]. Examples of applications are for dam-break analysis [7], large deformation and slope failure [8], seepage [9], and liquefaction [10].

This article presents the progress of the on-going research on the use of SPH model to simulate the lateral deformation after liquefaction. This research is a part of the bigger research to study the mechanism of the phenomenon that occurred in Central Sulawesi. It is expected that this numerical model could help in understanding the factors that caused such thing, hence it will be easier to identify the risk in the future.

BASIC CONCEPT OF SPH

The concept of SPH as mentioned by [3] is that a state of system is represented by a set of particles, which possess the material properties and interact with each other within a range that controlled by a weight or smoothing function. SPH is built on interpolation theory with two essential aspects, which are the kernel approximation and particle approximation (e.g., [6]). Consider a particle α as shown in Fig. 1, the value of a function at computing particle α is approximated using the average of those values of the function at all particles in the influence domain of particle α, weighted by the smoothing

function, which is W in Fig. 1. The neighboring particle is shown as β, and the radius of influence from particle α is h.

The kernel approximation can be written as a function f(x) as the position of vector x:

$$\langle f(x)\rangle = \int_{\Omega} f(x')\ W(x-x',h)dx' \quad (1)$$

where f Ω is the volume of integral that contains x. The smoothing function W should satisfy a number of conditions:

1. the unity or normalization condition:
$$\int_{\Omega} W(x-x',h)\ dx' = 1 \quad (2)$$

2. delta function property:
$$\lim_{h\to 0} W(x-x',h) = \delta(x-x') \quad (3)$$

3. compact condition
$$W(x-x',h) = 0 \quad \text{when} \quad |x-x'| > \kappa h \quad (4)$$

where κ is a constant related to the smoothing function for a particle at x, and κh defines the effective (non-zero) area of the smoothing function.

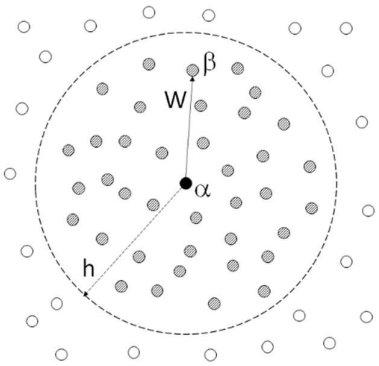

Fig. 1 Concept of SPH

The particle approximation can be written as

$$\langle f(x)\rangle = \sum_{j=1}^{N} \frac{m_j}{\rho_j} f(x_j)\ W(x-x_j,h) \quad (5)$$

where N is the total number of particles within the influence area of the particle at x, and m/ρ is the ratio off mass to density of particle j.

In hydrodynamics, the dynamic characteristic of fluid can be described as:

$$\tau = \eta_0 \dot{\gamma}^n + \tau_y \quad (6)$$

where τ is shear stress, $\dot{\gamma}$ is the rate of shear strain, and η_0, n, and τ_y are material parameters related to the type of fluid. The relationships between shear stress and shear strain are shown in Fig. 2, as taken from Huang et al. (2014).

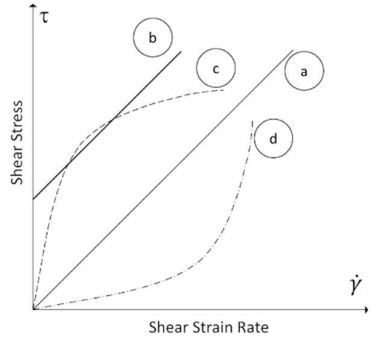

Fig. 2 Relationship between shear strain rate and shear stress (reproduced from [6])

Line (a) in Fig. 2 show the characteristic of Newtonian fluid, where n = 1 and $\tau_y = 0$. Thus η_0 as the gradient represent the viscosity of Newtonian fluid. For n = 1 and $\tau_y > 0$, this equation represents the characteristics of Bingham fluid as shown by line (b) where η_0 represents the viscosity after yield. Line (c) represents the pseudoplastic fluid, where $\tau_y = 0$ and n < 1, while line (d) represents the dilatant fluid with $\tau_y = 0$ and n > 1. The Bingham model is suggested by [6] to simulate the large deformation of soil.

The Bingham fluid constitutive should be interpreted using the equivalent Newtonian viscosity to be incorporated into an SPH model. The equivalent viscosity derived from Eq. (6) with n = 1 becomes:

$$\eta' = \eta_0 + \frac{\tau_y}{\dot{\gamma}} \quad (7)$$

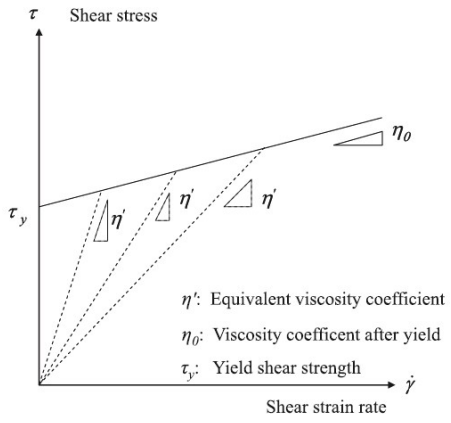

Fig. 3 Concept of equivalent viscosity [6]

The concept of equivalent viscosity (η') is shown in Fig. 3. The solid line is the viscosity after yield that represents the relationship between shear stress and shear strain rate for the Bingham model (η_0), whereas

the dashed lines are the equivalent Newtonian viscosity that represent motion characteristics expressed by the Bingham model.

METHODOLOGY

This study will be conducted in two parts: the first part will focus on modelling the process of liquefaction, while the second part will focus on the interaction of water and impermeable soil layer that is suspected as the important factor that affecting the large lateral soil displacement following the liquefaction.

All the simulation here are conducted in Fortran language.

Sand and Water at Liquefaction

Basic modeling of sand and pore water behaviour as a dummy fluid-like material with different density and viscousity (e.g., [10], [11]), continuing the results from previous study by [12]. Sand as granular material is assumed to have a fluid-like behavior, especially when liquefaction occurs, based on the study by Hamada and Wakamatsu as mentioned in [11]. It was stated that the physical and mechanical properties of liquified sand can be represented by function of viscosity.

In this study, the liquefaction phenomenon will be approached by modeling the behavior of two different type of particles that have different properties (unit weight and viscosity).

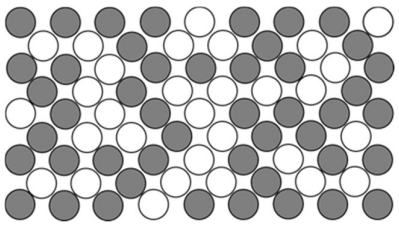

Fig. 4 Particles of sand (dark circles) and water (white circles) are placed randomly before liquefaction

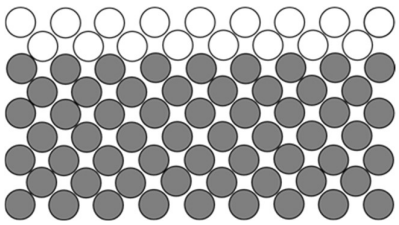

Fig. 5 Particles of sand will be compacted down while the particles of water pushed to the top

The condition of liquefaction will be modeled as saturated sand, where the particles of sand and particles of water mixed randomly as shown in Fig. 4. When the liquefaction happen, the sand usually settle down due to the dynamic load (from earthquake) and the pore water will rise to the top, and sometimes burst up above the surface as shown in Fig. 5.

Interaction of Water and Impermeable Layer

The second part of this study tries to represent the behavior of trapped water below the relatively impermeable soil layer after liquefaction, as mention in [13] as the water film effect. The model is built by placing the particles of water below the sets of particles of soil that cannot be penetrated by the particles of water, as shown in Fig. 6.

The impermeability of the particles will be represented by the coefficient of damping (noted as Kd) and coefficient of stiffness (noted as Ks). The sensitivity analysis will be conducted to check the effect of those coefficient to the impermeability behavior.

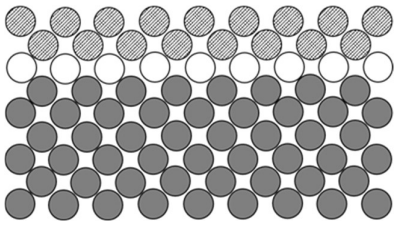

Fig. 6 The model for water trapped below the impermeable soil layer (top grey circles are the impermeable soil particles)

The algorithm of the SPH numerical model is drawn in a flowchart as shown in Fig. 1Fig. 7, where the particle i is the main particle and particle j is the neighboring particle. The steps are started with defining the initial conditions for the particles' parameters and positions, and followed by calculating the particles' distances, forces, accelerations, and positions. The particles' positions and velocity will be updated through the simulation time.

CURRENT PROGRESS

For the first part of this study, the sensitivity analysis on the effect of assigned viscosity to change of unit wight of the particles of sand was conducted. Some of the results are shown in Fig. 8. It can be seen that the increase of viscosity value above 1 Pa.s will result to zero changes on density after certain simulation time.

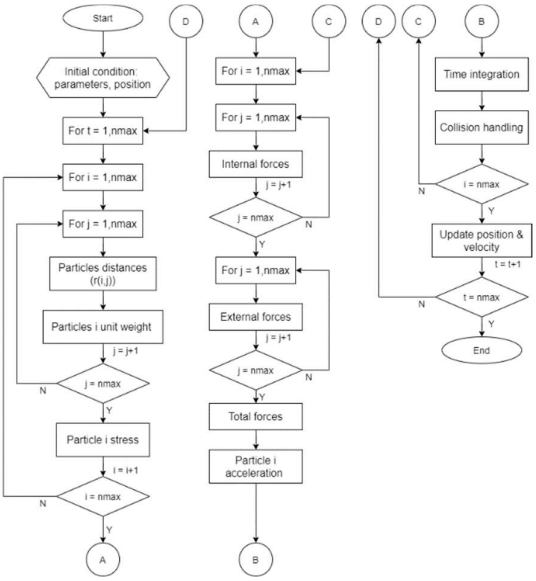

Fig. 7 Flowchart of the SPH simulation

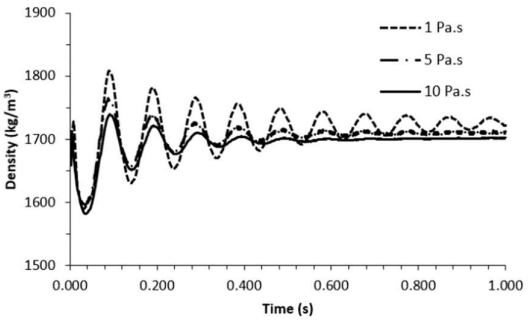

Fig. 8 The effect of different viscosity to density

Table 1 show the current results of visualization of the simulation results to model the simple liquefaction process. The initial condition is to represent the condition as shown in Fig. 4 where the sand and water particles are placed randomly, and during the liquefaction the sand particles will move and settled down. The liquefaction is considered stopped when the particles are positioned unmoved at the end of simulation time (1 second).

Table 1 Visualization of the simulation results

Initial Condition	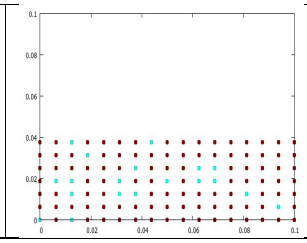
0.002 s	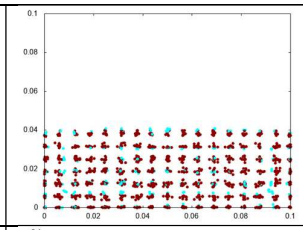
0.2 s	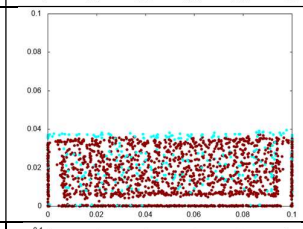
1 s	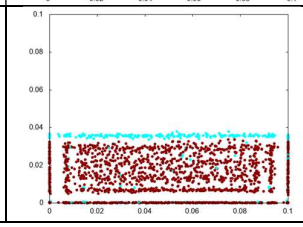

CONCLUSIONS

This paper presents the current proress of an on-going study about the development of numerical method using the Smoothed Praticle Hydrodynamics. The final target is to model the behavior of large soil displacement after liquefaction. This initial phase is aimed to find the suitable parameters to the SPH particles to behave as the actual materials in the field.

ACKNOWLEDGMENTS

The authors would like to thank to Hana Saffanah, Hutami Mahardima, and Yudha Wicaksana, the students of the Department of Civil Engineering University of Indonesia who helped the authors in doing this study.

REFERENCES

[1] H. B. Mason *et al.*, "Geotechnical Reconnaissance: The 28 September 2018 M7.5 Palu-Donggala, Indonesia Earthquake," GEER-061, 2019.

[2] I. M. Watkinson and R. Hall, "Impact of communal irrigation on the 2018 Palu earthquake-triggered landslides," *Nat. Geosci.*, vol. 12, pp. 940–945, 2019, doi: https://doi.org/10.1038/s41561-019-0448-x.

[3] M. B. Liu and G. R. Liu, "Smoothed Particle Hydrodynamics (SPH): an Overview and Recent

Developments," *Arch. Comput. Methods Eng.*, vol. 17, no. 1, pp. 25–76, 2010.

[4] L. B. Lucy, "A numerical approach to the testing of the fission hypothesis," *Astron. J.*, vol. 82, no. 12, p. 1013, 1977.

[5] R. A. Gingold and J. J. Monaghan, "Smoothed particle hydrodynamics: theory and application to non-spherical stars," *Mon. Not. R. Astron. Soc.*, vol. 181, no. 3, pp. 375–389, 1977.

[6] Y. Huang, Z. Dai, and W. Zhang, *Geo-disaster Modeling and Analysis: An SPH-based Approach*. Springer, 2014.

[7] Z. Wang and H. T. Shen, "Lagrangian simulation of one-dimensional dam-break flow," *J. Hydraul. Eng.*, vol. 125, no. 11, pp. 1217–1220, 1999.

[8] H. H. Bui, R. Fukagawa, and K. Sako, "Smoothed particle hydrodynamics for soil mechanics," in *Numerical Methods in Geotechnical Engineering*, London: Taylor & Francis Group, 2006.

[9] K. Maeda and M. Sakai, "Development of seepage failure analysis procedure of granular ground with Smoothed Particle Hydrodynamics (SPH) method," *J. Appl. Mech.*, vol. 7, 2004.

[10] M. Naili, T. Matsushima, and Y. Yamada, "A 2D Smoothed Particle Hydrodynamics method for liquefaction induced lateral spreading analysis," *J. Appl. Mech.*, vol. 8, pp. 591–599, 2005.

[11] J.-I. Hwang, C.-Y. Kim, C.-K. Chung, and M.-M. Kim, "Viscous fluid characteristics of liquefied soils and behavior of piles subjected to flow of liquefied soils," *Soil Dyn. Earthq. Eng.*, vol. 26, pp. 313–323, 2006.

[12] S. Rachman, J. Sjah, R. R. D. R. Marthanty, and H. Soeryantono, "Fluid-fluid Interaction Study of Different Density and Viscosity Using Smoothed Particle Hydrodynamics Method," in *IOP Conference Series: Materials Science and Engineering*, Jakarta, 2018, vol. 453, doi: 10.1088/1757-899X/453/1/012048.

[13] T. Kokusho, "Mechanism for water film generation and lateral flow in liquefied sand layer," *Soils Found.*, vol. 40, no. 5, pp. 99–111, 2000.

6th Int. Conf. on Structure, Engineering & Environment (SEE), Kyoto, Japan, Nov.18-20, 2020, ISBN: 978-4-909106056 C3051

STUDY ON ADSORPTION OF HEAVY METALS BY RICE HUSK AND EXTRACTION OF HEAVY METALS ADSORBED IN RICE HUSK

Ayane Yanaka[1], Keiichiro Shibata[2], Naomichi Matsumoto[3] and Hidenori Yoshida[4] [1]
Graduate School of Engineering, Kagawa University, Japan; [2] Kajima Corporation, Japan, [3] Technical staff, Kagawa University, Japan; [4] Faculty of Engineering and Design, Kagawa University, Japan

ABSTRACT

Heavy metals with strong toxicity are contained in the mine drainage generated from the suspended or abandoned mines that once had mining activities. The mine drainage continues to flow semi-permanently. Thus the treatment of mine drainage must be continued. As the current treatment method for the mine drainage treatment, the neutralization treatment process utilizing alkali chemicals is mainly conducted. However, few alkali chemicals satisfy both low cost and high neutralizing ability. In addition, regarding the neutralized deposits generated during the treatment of mine drainage, it is difficult to secure the disposal sites. Moreover, in recent years, the metal demand increases by the development of IC chip and electric automobile. In this study, in order to achieve both low cost and high adsorption performance, focusing on the rice husk which is an industrial waste, the purposes of this study are to verify the adsorption performance of rice husks for heavy metals and to verify whether the extraction of heavy metals from rice husks to which heavy metals are adsorbed is possible or not. From the test results, it is turned out that the rice husks have a sufficient adsorption performance for zinc, copper and cadmium. Furthermore, it is proved to be possible to extract them from the rice husks which adsorbs such heavy metals. It is clarified that the utilization of rice husk can be an effective method for removing heavy metals in mine drainage.

Keywords: Mine drainage, Rice husk, Adsorbent, Heavy metals, Extraction

INTRODUCTION

In recent years, the soil and groundwater pollution by heavy metals have been frequently confirmed in former factory sites. The purification methods for those pollutions are complicated, and many of them are costly as in [1]. The treatment of mine drainage in the suspended or abandoned mines has a similar problem. The mining activities are suspended or closed the suspended or abandoned mines which are scattered all over Japan. Heavy metals with strong toxicity are contained in the mine drainage generated from the suspended or abandoned mines. Once the mine is operated, the mine drainage continues to flow semi-permanently. Even if the mine is suspended or closed, the mine drainage does not stop. If the mine drainage containing harmful substances such as heavy metals is discharged without any treatment, it causes pollution to river water and groundwater in the vicinity. Thus the treatment of mine drainage must be continued. The current treatment method for the mine drainage treatment is mainly the neutralization treatment method utilizing alkali chemicals such as slaked lime as in [2]. However, few alkali chemicals satisfy both low cost and high neutralizing ability. In addition, the treatment process to purify the mine drainage to the level where it can be released into rivers is complicated, and it seems that the current treatment method will be costly. Additionally, there are agendas such as the disposal of neutralized deposits generated during the neutralization treatment and the security of the disposal site for the deposits. Furthermore, heavy metals contained in the neutralized sludge may be eluted from the sludge to clarified water when the neutralization treatment by calcium hydroxide are conducted as in [3]. On the other hand, metals with high resource value such as zinc (Zn) and copper (Cu) are included in the mine drainage. In recent years, the resource recycling by the urban mine development is promoted, because the metal demand increases by the development of IC chip and electric automobile. Therefore, adsorption treatment is suitable for a simple treatment method instead of the current neutralization treatment in order to solve these problems. An adsorbent utilized as the mine drainage treatment method is desirable to consider the following three issues; one is that adsorbents are inexpensive, another is that heavy metals adsorbed after adsorption can be recovered, and the other is that the adsorbents after recovering heavy metals should be recycled. Then, in this study, in order to achieve both of low cost and high performance, focusing on the rice husk which is an industrial waste, the purposes are to verify the adsorption of heavy metals by rice husks and to verify whether the extraction of heavy metals from rice husks to which heavy metals are adsorbed is possible or not.

ADSORBENT

Photo. 1 shows the rice husk utilized as an adsorbent in this study. In Japan, about 2 million tons of rice husks are discharged annually. Rice husks containing much silica have high hardness, and it is difficult to process rice husks. Therefore, rice husks have no use other than simple agricultural materials, and many of them are discarded. At present, there are few effective utilization methods for rice husks, and various research institutes are actively conducting the research on utilization methods for rice husks. As one example, Kobayashi et al. states that the rice husk charcoal has an adsorption performance for cesium (Cs) and strontium (Sr) in aqueous solution as in [4]. In addition, it is reported that the rice husk ash has an adsorption ability for heavy metals such as lead (Pb), mercury (Hg), zinc (Zn), nickel (Ni) and cadmium (Cd) as in [5], [6]. However, it takes labor and cost to process into coal and ash. Additionally, it is difficult to collect rice husk charcoal and ash after utilized as an adsorbent. Moreover, there are few studies in which the adsorption performance and adsorption mechanism of raw rice husks for heavy and the reuse method considering the tight disposal site are investigated. In this study, various tests are conducted using the raw rice husks dried at 100 ° C for 24 hours.

Photo. 1 Raw Rice Husks

TEST METHOD

Since zinc (Zn), copper (Cu), and cadmium (Cd) have been detected in mine drainage water leaked from many suspended mines, three kinds of heavy metals are examined in this study.

Heavy Metals Adsorption Test (Shaking Test)

Based on the adsorption isotherms obtained from shaking tests for zinc, copper and cadmium, the adsorption performance of raw rice husks (RRH) for them is evaluated. In the test, three solutions are prepared. One contains zinc nitrate solution, another contains copper nitrate solution and the other contains cadmium nitrate solution. First, seven initial concentrations (3 ppm, 4 ppm, 5 ppm, 6 ppm, 7 ppm, 30 ppm, 60 ppm) of each solution are prepared and the initial pH of these solutions is adjusted to 6. Next, 10 mL of the prepared solution is poured into a centrifuge tube to which 20 mg of raw rice husk is added. Then, 10 mL of solution with 20 mg of raw rice husk is shaken for 24 hours at 200 revolutions at a temperature of 20 ° C. After that, the solutions are centrifuged at 2000 rpm for 3 minutes, and the residual concentration of heavy metals: Zn, Cu and Cd, in the solutions are analyzed by an ICP-AES. In the study, the adsorption amount per unit mass of the raw rice husks is employed as the evaluation of the test result. The adsorption amount per unit mass of the raw rice husks is defined by the following equation (1).

$$W_i(\mathrm{mg/g}) = \frac{V(C_o - C_i)}{M_i} \qquad (1)$$

In the equation (1), "*V*" is the amount of the solution, "C_o" is the initial concentration of the solution, "C_i" is the residual concentration (equilibrium concentration) and "M_i" is the mass of the raw rice husks.

In order to ensure reproducibility, the average results obtained from the tests conducted three times are adopted as test results. In addition, the test results are applied to Langmuir and Freundlich models so as to clarify the adsorption mechanism of the adsorbent for the heavy metals. Langmuir and Freundlich models are typical adsorption equilibrium equations in liquid-phase adsorption. Langmuir and Freundlich models are defined by the following equation (2) and (3), respectively.

$$\text{Langmuir: } \frac{C_i}{W_i} = \frac{1}{aW_s} + \frac{1}{W_s} C_i \qquad (2)$$

$$\text{Freundlich: } \log W_i = \log K_F + \frac{1}{n} \log C_i \qquad (3)$$

In the equation (2), "*a*" is the adsorption equilibrium constant, "W_s" is the amount of saturation adsorption. In the equation (3), "1/*n*" is the affinity between adsorbent and adsorbate, "K_F" is the adsorption capacity.

Extraction Test Of Heavy Metals From The Rice Husks To Which Heavy Metals Are Adsorbed

In order to confirm whether it is possible to recover heavy metals which are valuable resources from the used rice husks (uRRH) adsorbing heavy metals, the extraction of heavy metals adsorbed from uRRH is tried with nitric acid solution.

Preparation of the raw rice husks adsorbing heavy metals

First, a solution similar to the shaking test is

prepared, and the initial concentration and pH are adjusted to 5 ppm and 6, respectively. Next, 50mL of the solution is poured into a centrifuge tube, and 1.0g of the raw rice husks is added. Then, the prepared solutions are shaken and centrifuged under the same conditions as has already mentioned in shaking test. After that, the raw rice husks which adsorb heavy metals are separated from the solutions by a filtration apparatus, and the residual concentration of heavy metals in the solutions is analyzed by an ICP-AES. The difference between the initial concentration and the analyzed one is defined as the concentration of heavy metals contained in the raw rice husks which adsorb heavy metals.

Extraction of heavy metals by nitric acid solution

First, 50 mL of a solution of nitric acid (Concentration: 0.1 mol/L) is poured into a centrifuge tube, and then the raw rice husks to which heavy metals have been adsorbed are added. Then, the solutions are shaken at 200 rpm for 6 hours by a shaking apparatus. After that, the solutions are centrifuged at 2000 rpm for 3 minutes, and the residual concentration of heavy metals in the solutions is analyzed in an ICP-AES. In order to ensure reproducibility, the average results obtained from the tests conducted three times are adopted as test results as mentioned in shaking test.

RESULT

Result Of Adsorption Test For Heavy Metals

The adsorption isotherms obtained in the tests with the Langmuir model are shown in Fig. 1, and those with the Freundlich model are shown in Fig. 2. The horizontal and vertical axes in Fig. 1 are the equilibrium concentration of heavy metals (Zn, Cu and Cd), and the value obtained by dividing the equilibrium concentration by the adsorption amount of heavy metals (C/W), respectively. The horizontal and vertical axes in Fig. 2 are the logarithm of the equilibrium concentration of heavy metals (logC) and the logarithm of the adsorption amount of heavy metals (logW), respectively. The Langmuir model suggests whether the adsorption mode is monolayer adsorption or not. The applicability of the Langmuir model depends on whether the linear relationship between the equilibrium concentration of heavy metals and the value of equilibrium concentration divided by the adsorption amount of heavy metals holds or not. When Langmuir model is not applied, it is possible that the adsorption mode is multi-molecular layer adsorption. In addition, Freundlich model shows that a large amount of heavy metals are adsorbed in the case of logarithm shape, and the amount of heavy metals are adsorbed is not so large in the case of exponential shape. Since the value of the coefficient of determination (R^2) is close to 1 in Fig. 1, it is indicated that the adsorption mode of the raw rice husks to Cd is likely to be monolayer adsorption. Fig. 2 shows that the amount of Cd adsorbed in the low concentration region is not so large. It is also confirmed that a large amount of Cd can be adsorbed as the concentration increases. It is confirmed that the amount of Zn or Cu adsorbed in the low and high concentration regions is not so large, and that a large amount of Zn or Cu can be adsorbed in the medium concentration region. Water molecules are more abundant than heavy metal ions in the low concentration region. As described in the reference, liquid phase adsorption is a competitive adsorption of solvent and adsorbate on the adsorbent surface. In the low concentration region, it is considered that it does not become the adsorption of the logarithmic function type for either heavy metal, that is, a large amount of heavy metals are not adsorbed to an adsorbent. The adsorption mode of the raw rice husks for Cd is monolayer adsorption, and it seems to be able to adsorb more Cd because of the strong attractive force between adsorbent surface and adsorbate. On the other hand, with respect to Zn and Cu, it is considered that Zn and Cu are further attached on the first layer on which Zn and Cu have already been adsorbed, that is, the adsorption mode is likely to be multi-molecular layer adsorption. It is considered that the adsorption

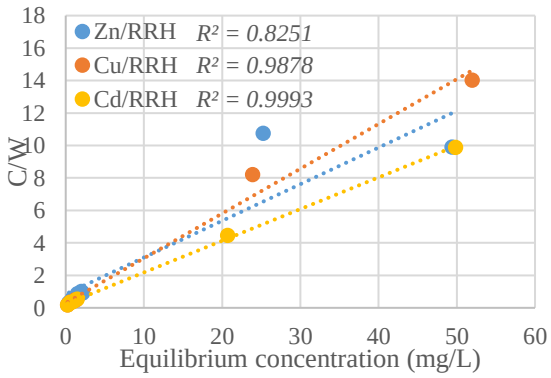

Fig. 1 The adsorption isotherm (Langmuir model)

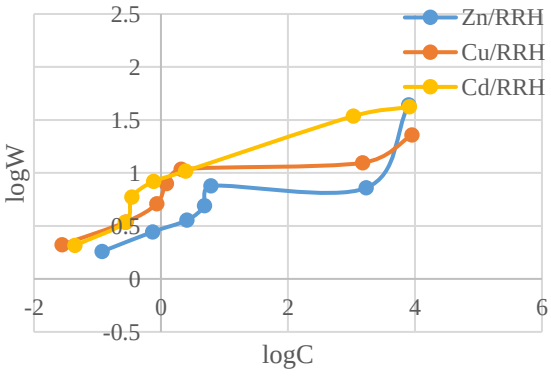

Fig. 2 The adsorption isotherm (Freundlich model)

amount of Zn and Cu in the second and subsequent layers is less than the one of Cd in the first layer, since the attractive force does not work between adsorbent.in the adsorption of Zn and Cu.

Result Of The Extraction Test Of Heavy Metals From The Raw Rice Husks To Which Heavy Metals Are Adsorbed

Fig. 3 shows the concentrations of heavy metals contained in raw rice husks before and after the extraction tests with nitric acid solution. “before” and “after” indicate that the concentration of heavy metals contained in the raw rice husks before and after the extraction tests. The difference concentration between “before” and “after” means the extracted concentration of heavy metals, respectively. From Fig. 3, more than 90% of Zn, about 60% of Cu, and about 90% of Cd are extracted, which indicates that heavy metals adsorbed on the raw rice husks can be extracted by nitric acid. This is considered to be because heavy metals adhering to the surface of unprocessed rice husks were washed away by bleaching action of acid. The reason why there is the difference in the extraction concentration by the heavy metal is mainly dependent on whether the adsorption mode is monolayer adsorption or not. However, there is the difference in the extraction concentration between Zn and Cu both of which have similar adsorption mode. This is considered to be due to the elution of trace element Zn as well as Zn adsorbed on the raw rice husks.

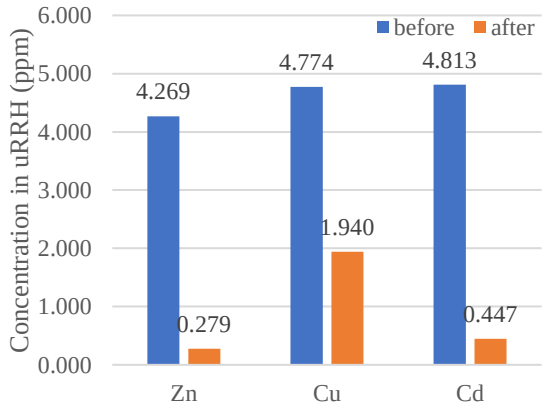

Fig. 3 The result of extraction test (by HNO_3 aq)

CONCLUSIONS

As a current treatment method of mine drainage, the neutralization treatment process is frequently conducted utilizing alkali chemicals. However, few alkali chemicals satisfy both low cost and neutralizing ability. In addition, there are agendas such as the complication of the neutralization treatment process, the disposal of neutralized deposits generated during the neutralization treatment and the security of the disposal site for the deposits. Moreover, in recent years, the metal demand increases by the development of IC chip and electric automobile. As the simple treatment method to solve these problems, the adsorption treatment is conducted utilizing the raw rice husks as an adsorbent with focusing on the rice husk which is industrial waste. In this study, it is turned out the raw rice husks has the adsorption performance of heavy metals (Zn, Cu and Cd) contained in mine drainage. Additionally, it is found that it is possible to recover heavy metals from the raw rice husks adsorbed heavy metals by a nitric acid. As the reuse method of the raw rice husks after the adsorption of heavy metals, in the future, the following are examined: the reuse of raw rice husk after heavy metal extraction as an adsorbent again or as a concrete admixture by processing it into rice husk ash as in [8].

ACNOWLEDGMENTS

This work was supported by Seeds Development Research Fund (Emergence type) of Kagawa University Research Promotion Program 2019 (KURPP) and Japan Society for Promotion of Science (JSPS), the Grants-in-Aid for Scientific Research (KAKENHI) (Grant number: 20K04684, 18J12343).

REFERENCES

[1] Daigobo H., Nishikawa K., Mihara K., Inoue Y. and Fujimoto H., Countermeasures for the Soil Environmental Problems, Sumitomi Chemical, Technical report 2003-1, 2003, pp. 13-23

[2] Japan Oil Gas and Metals National Corporation (JOGMEC), The Principle of an acid mine drainage treatment, 2006, pp. 13-24

[3] Sato D. and Tazaki K., Mineralization and Heavy Metal Interaction after Lime Treatment of Mine Drainage, Journal of the Clay Science Society of Japan, Vol. 40, No. 4, 2001, pp. 218-228

[4] Kobayashi S., Noda K., Shibata H., Matsubara S., Kawamura N., Nonami T., Adsorption Properties of Rice Hull Charcoal for Cesium and Strontium in Aqueous Solution, Journal of the Society of Materials Science, Japan, Vol. 67, No. 10, 2018, pp. 898-903

[5] Feng Q., Lin Q, Gong F., Sugita S. and Shoya M., Adsorption of lead and mercury by rice husk ash, Journal of Colloid and Interface Science, Vol. 278, No. 1, 2004, pp. 1-8

[6] Srivastava C. V., Mall D. I. and Mishra M. I., Characterization of mesoporous rice husk ash (RHA) and adsorption kinetics of metal ions aqueous solution onto RHA, Journal of Hazardous Materials, Vol. 134, No. 1-3, 2006,

pp. 257-267
[7] Chikazawa M. and Tajima K., Interface Chemistry, Maruzen Publication, 2001, pp. 108-117
[8] Kajiwara N., Uehara T. and Saito K., Fundamental Study of Fresh and Hardening Property of Concrete with Non-crushed Rice Husk Ash, Concrete Research and Technology, Vol. 28, 2017, pp. 1-13

6th Int. Conf. on Structure, Engineering & Environment (SEE), Kyoto, Japan, Nov.18-20, 2020, ISBN: 978-4-909106056 C3051

STUDY ON REMOVAL OF CESIUM FROM CONTAMINATED SOIL BY ELECTROPHORESIS USING POTASSIUM ACETATE AS ELECTROLYTE

Ayane Yanaka[1], Keiichiro Shibata[2], Naomichi Matsumoto[3] and Hidenori Yoshida[4]

[1] Graduate School of Engineering, Kagawa University, Japan; [2] Kajima Corporation, Japan, [3] Technical staff, Kagawa University, Japan; [4] Faculty of Engineering and Design, Kagawa University, Japan

ABSTRACT

9 years have passed since a large amount of radioactive materials were diffused by the nuclear accident at the Fukushima Daiichi Nuclear Power Station of Tokyo Electric Power Company. The decontamination works have almost been completed, and some of the contaminated soil whose topsoil was stripped and collected was transported to the intermediate storage and incineration facilities. However, the contaminated soil containing the radioactive cesium stored in the temporary storage place has not decreased significantly. Additionally, the transportation of the intermediate storage and incineration facilities have an agenda from the viewpoint of cost. Therefore, it is needed to investigate the method of decontamination by which the radiation dose of contaminated soil can be reduced below 8000 Bq/kg at the temporary storage place. Considering the decontamination in the actual temporary storage place, electrophoresis is the simple method as a decontamination method, and it is desirable to utilize zeolite with ion-exchange property as an inexpensive adsorbent. Ammonium acetate has been considered to be effective as an electrolyte because it has ammonium ion that has high ion-exchange reaction with cesium ion. However, an efficient decontamination cannot be achieved since the adsorption of cesium ions to zeolite is inhibited by ammonium ions. The purpose of this study is to discuss the efficient removal of cesium by using zeolite as an adsorbent and potassium acetate as an electrolyte through the electrophoresis test. From the test results, it is turned out that potassium acetate is suitable to extract cesium efficiently in electrophoresis.

Keywords: Radioactive materials, Cesium, Zeolite, Electrophoresis, Extraction

INTRODUCTION

The nuclear accident at the Fukushima Daiichi Nuclear Power Station of Tokyo Electric Power Company occurred due to the effect of the huge tsunami by the Great East Japan Earthquake, and a large amount of radioactive materials were diffused extensively widely around Fukushima Prefecture. Most of the released radioactive materials were radioactive cesium. Radioactive cesium has a long half-life and affects over a long period of time as in [1]. Vermiculite is widely distributed in soils in Fukushima Prefecture and has interlayers called frayed edge. Since radioactive cesium is selectively fixed to the interlayers of mineral particles such as vermiculite, it is difficult to extract cesium which is once fixed. Since most of the accumulated radioactive cesium exists in the surface soil of the contaminated soil as in [2], the surface decontamination work has been carried out by stripping the surface soil. The contaminated soil collected by the stripping of the topsoil is enclosed in a flexible container bag and temporarily stored in the temporary storage place. At present, 9 years have passed since the occurrence of the accident, the decontamination works have almost been completed. Additionally, some of the contaminated soil enclosed in flexible container bags have been transported to the intermediate storage facilities in Fukushima Prefecture successively since 2015. However, the contaminated soil containing the radioactive cesium of about 6.67 million m^3 remains to be stored in the temporary storage place. Furthermore, the contaminated soil transported to an intermediate storage facility is sorted through sieves, and incinerated at a high temperature above 800 ° C or higher as in [3]. Therefore, it is expected that not only the transportation cost of a large amount of contaminated soil but also the incineration cost will be enormous. According to the basic policy by the Ministry of the Environment, since it is shown that the contaminated soil with radiation dose below 8000 Bq/kg is reused as construction materials as in [4], the reuse of low dose of soil as construction materials can reduce the volume of contaminated soil. To achieve the volume reduction of the contaminated soil, it is desired to reduce the dose to 8000 Bq/kg or less by the partial removal of the radiation cesium for t the contaminated soil exceeding 8000 Bq/kg at present. It is necessary to remove only radioactive cesium efficiently in order to reduce the dose of soil in the flexible container bag stored in the temporary storage place. As one of the means for efficiently realizing the removal of only the radioactive cesium, the technique using the electrophoresis is mentioned as a candidate.

By using this method, cesium ions, which are cations, can be extracted from the soil using a solution which also serves as an electrolyte and an extract, and transferred to the cathode by electric force. Ammonium or potassium salts are necessary for the extraction of cesium ions in soil, and ammonium acetate is known to have relatively higher extraction performance than potassium acetate as in [5]. Therefore, ammonium acetate with ammonium ion which has high ion exchange reactivity with cesium ion seems to be effective as an electrolyte for the electrophoresis. However, it is reported that the adsorption of cesium ions on zeolite is inhibited by the presence of ammonium ions when zeolite is used as an adsorbent as in [6]. Potassium acetate is slightly inferior in the extraction performance, but from the viewpoint of the cesium adsorption ability of zeolite and the volume reduction of contaminated soil containing radioactive cesium, it is expected that the cesium adsorption capacity of zeolite can be increased by using potassium acetate as an electrolyte and extraction solution. The purpose of this study is to discuss the efficient extraction and adsorption of cesium by using zeolite as an adsorbent and potassium acetate as an electrolyte through the electrophoresis test.

THE BEHAVIOR OF CESIUM IN SOIL

Cesium exists as monovalent cation in soil and is adsorbed to the soil particles which carry a negative charge in soil. Cesium selectively adheres to soil composed of clay minerals mainly of 2: 1 type layered silicate among the minerals constituting clay minerals. The 2: 1 type layered silicate is a generic name of minerals having a 2: 1 relationship between the lamination of silicon tetrahedral sheets and the lamination of aluminum octahedral sheets. A silicon tetrahedron sheet is a tetrahedron formed by surrounding silicon atoms with four oxygen atoms, and an aluminum octahedron sheet is a tetrahedron formed by surrounding aluminum atoms with six oxygen atoms in two dimensions. In a silicon tetrahedral sheet or an aluminum octahedral sheet, when some silicon or aluminum elements are replaced by other elements having a small amount of positive charge, the amount of positive charge is not sufficient in either sheet or both sheets as in [7]. After that, negative charge appears due to lack of positive charge, and the interlayers are neutralized by the adsorption of cations. The interlayer charge shows high adsorption selectivity for cesium ions. This is because the size of the cavity called six-membered ring formed by oxygen atom on the basal surface of a silicon tetrahedral sheet is approximately equal to the ionic radius of cesium ions. As the hydration energy decreases, the binding force to the six-membered ring increases, and in particular, the cesium ion has the highest binding force. However, potassium ions occupy the six-membered ring because an abundance of potassium ion in the soil is overwhelmingly large (see Fig. 1). Potassium ions are released by the fray at the end of the layer in clay minerals accompanied by soil weathering (see Fig. 2). As a result, a region in which other cations can penetrate is formed. This is called frayed edges. It is difficult that cesium ion fixed in the frayed edge is displaced by other cations as in [8].

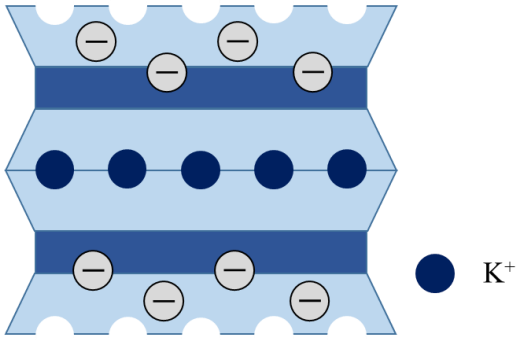

Fig. 1 The 2: 1 layered silicate

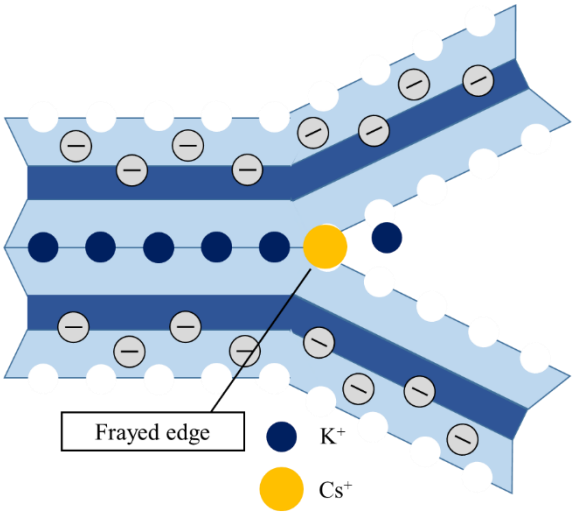

Fig. 2 Frayed edge

TEST METHOD

Electrophoresis

In the electrolyte used in electrophoresis, charged particles in the solvent move under the electric field generated by the application. In the electric field, cations and anions transfer to the cathode side and the anode side, respectively. Cesium ions, which are cations, are transferred to the cathode side by utilizing the electrophoretic phenomenon, and the transferred cesium ions are adsorbed on zeolite which is placed between the soil and the cathode.

Electrophoresis test

Electrophoresis test is conducted using potassium acetate aqueous as an electrolyte and extraction solution. Electrolyte and extract solutions are prepared at three different concentrations (1.0%, 1.5%, 3.0%). Electrophoretic tests are carried out at each concentration, and the amount of Cesium remaining in the soil is measured. According to the obtained results, the extraction and adsorption at each concentration are discussed. As a test equipment, a simulated flexible container bag is prepared (see Photo. 1). First, a simulated contaminated soil is prepared. 114g of standard sand and 6g of vermiculite are mixed, and 36mL of pure water is poured into the mixed sand in order to adjust the 30% of moisture content. 1 mL of cesium chloride solution is added to the soil, and the test sample is cured for 168 hours. Next, the simulated soil is put into an acrylic container bag, a carbon rod to (15mm of diameter, 40mm of length) as an anode is placed perpendicularly to the center of the soil. In this stage, a 35 μm opening bolting cloth is laid on the inside of the acrylic container bag, and then a simulated contaminated soil is put there so as to prevent mixing with zeolite and the test sample. In addition, 60 - 70 mL of potassium acetate solution, which is an electrolyte solution, is put into the acrylic container bag, and the simulated contaminated soil is immersed in the electrolyte. An aluminum plate as a cathode is placed so as to surround the simulated contaminated soil, and 10g of zeolite is installed between the bolting cloth and the aluminum plate. In the electrophoresis test, a constant current of 50 mA is applied for 48 hours with a voltage value of 40 V as an upper limit. In conducting electrophoretic tests, potassium acetate solution is sequentially put into the acrylic container bag to maintain the lowest possible voltage during the test. After energization, using potassium acetate solution as an extraction cleaning solution, the soil is stirred and washed by using a stirring device. Moreover, the concentration of cesium contained in the filtered and separated solution is analyzed by an atomic absorption spectrometer. The extraction ratio is defined by the following equation (1).

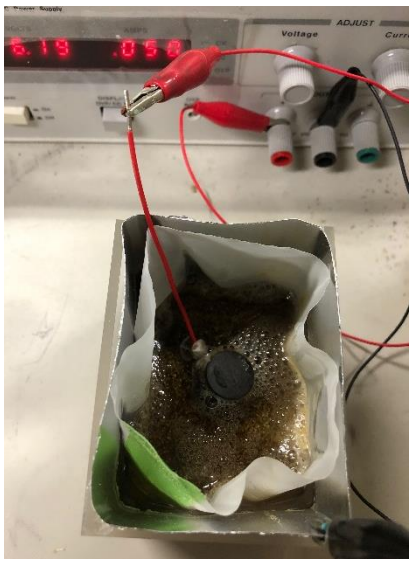

Photo. 1 A simulated flexible container bag (test equipment)

$$\text{Extraction ratio (\%)} = \frac{\text{Extracted amount (mg)}}{\text{Added amount (mg)}} \times 100 \quad (1)$$

In order to ensure reproducibility, the average results obtained from the tests conducted three times are adopted as test results.

RESULT OF ELECTROPHORESIS TEST

Fig. 3 shows the extraction rate of cesium under various concentrations of potassium acetate solution. The horizontal and vertical axes are the concentration of potassium acetate solution and the extraction ratio of cesium, respectively. The difference between the extraction rate of cesium with zeolite and that without zeolite is interpreted as the adsorption rate of cesium adsorbed on zeolite. Fig. 3 suggests that the extraction ratio of cesium from the soil increases as the concentration of potassium acetate solution decreases. It is also found that the highest concentration of 3.0% potassium acetate solution results in the lowest rate of cesium extraction from the soil. In the electrophoresis, due to the electrolysis reaction of water with the application of voltage, hydrogen ions and hydroxide ions are generated at an anode and a cathode, respectively as in [9]. Therefore, the solution near an anode and a cathode indicates acidity and basicity, respectively. In the case of the highest concentration of potassium acetate solution (3.0%), the pH of the solution near an aluminum plate as a cathode indicates a high value (pH over 10). For aluminum, corrosion occurs at pH outside the range of 4 to 8. In the case of the high concentration of potassium acetate solution, it is considered that the electrophoresis is inhibited by the corrosion of an aluminum plate, and as a result, the extraction ratio of cesium decreases. Judging comprehensively from the extraction and adsorption ratios of cesium, it is found that potassium acetate has the highest performance for extraction and ion transport at the lowest concentration of 1.0% of potassium acetate solution. The concentration of potassium acetate solution as the electrolyte becomes lower, as the voltage is increased. Then, the potassium acetate solution is sequentially put into the acrylic container bag from the viewpoint

of ensuring the safety. A lot of potassium ions are required to extract cesium ions. It is considered that the potassium ions necessary for the extraction of cesium can be supplied more efficiently by sequentially adding a low concentration of potassium acetate solution as an extraction and electrolyte for the electrophoresis than by using a high concentration of potassium acetate solution.

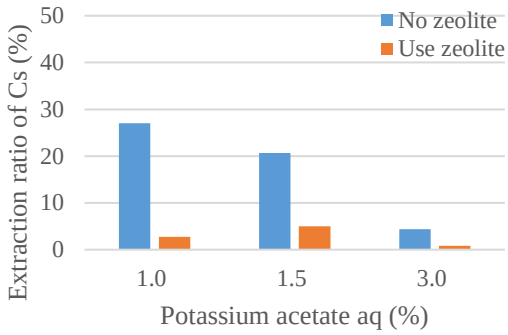

Fig. 3 The extraction ratio of cesium by potassium acetate solution

Incidentally, it is generally known ammonium acetate has a higher extraction capacity than potassium acetate in order to extract cesium fixed to clay minerals. For the reason, in regard to the extraction from the soil and the adsorption on zeolite, the result of the electrophoresis test utilizing ammonium acetate as extraction solutions and electrolytes is compared to that utilized potassium acetate as extraction solutions and electrolytes. Fig. 4 shows the extraction ratio cesium under various concentrations of ammonium acetate solution. Fig. 4 shows The horizontal and vertical axes are the concentration of ammonium acetate solution, and the extraction ratio of cesium. As with Fig. 3, the difference between the extraction rate of cesium with zeolite and that without zeolite is interpreted as the adsorption rate of cesium adsorbed on zeolite. In the electrophoretic test using ammonium acetate solution as an extraction and electrolyte solution, not only a bolting cloth but also a filter paper is laid on the inside of an acrylic container bag to prevent mixing of zeolite and the specimen. Then, the simulated contaminated soil is put into the acrylic container bag. Except this condition, all the conditions for the electrophoretic test using ammonium acetate solution as an extraction and electrolyte solution are the same as those for the electrophoretic test using potassium acetate solution as an extraction and electrolyte solution. As compared to Fig. 3 with Fig. 4, whether or not filter paper is used, it is indicated that the adsorption ratio of cesium by a potassium acetate solution is more than that by an ammonium acetate solution in the lowest concentration of the electrolyte and extraction solution (1.0%). Ammonium and potassium acetate solution show neutrality and weakly basicity, respectively. When the pH falls below the zero charge point, it is possible that the electroosmotic flow reverses due to the changes of the surface electric charge of the soil from a negative charge to a positive one as in [10]. It is considered that the flow of cesium ions to a cathode is inhibited by the back run of the electroosmotic flow because the pH of the ammonium acetate solution is less than that of the potassium acetate solution. It seems that the pH of an electrolyte and extraction solutions affects the extraction ratio of cesium.

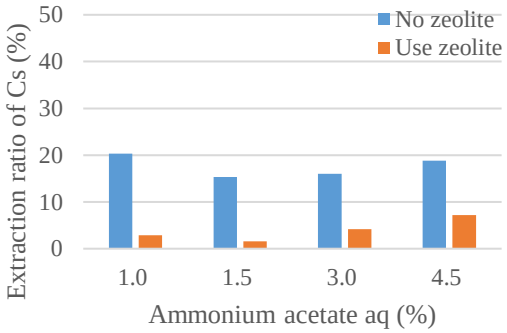

Fig. 4 The extraction ratio of cesium by ammonium acetate solution

CONCLUSION

9 years have passed since a large amount of radioactive materials were diffused due to the accident at the Fukushima Daiichi Nuclear Power Station of Tokyo Electric Power Company. At present, the decontamination work by stripping of the topsoil soil has almost been completed. However, a large amount of the contaminated soil containing the radioactive cesium remains to be stored in the temporary storage place. Considering the agendas of transportation to an intermediate storage facility and disposal in an incineration facility, it is desirable to reuse materials that can be used as construction materials instead of bringing all contaminated soil in an intermediate storage facility into an incineration facility. It is desirable to remove only radioactive cesium efficiently in the flexible container bag in order to reduce the dose of contaminated soil in a flexible container bag stored in a temporary storage place by decontamination below 8000 Bq/kg. As one of the methods which efficiently realize the removal of only the radioactive cesium, the technique using the electrophoresis is employed. Adsorption to zeolite is inhibited by the presence of ammonium ion when an electrophoretic test is conducted using ammonium acetate as an electrolyte and extract solution and zeolite as an adsorbent. Therefore, the electrophoretic tests are conducted by changing the electrolyte and extract solution from ammonium acetate to potassium

acetate. In this study, it is demonstrated that cesium can be removed efficiently by the low concentration of the potassium acetate solution in electrophoresis. It is necessary to clarify the relationship between the pH of the contaminated soil and the extraction ratio of cesium in the future.

ACNOWLEDGMENT

This work was supported by Seeds Development Research Fund (Emergence type) of Kagawa University Research Promotion Program 2019 (KURPP) and Japan Society for Promotion of Science (JSPS), the Grants-in-Aid for Scientific Research (KAKENHI) (Grant number: 20K04684, 18J12343).

REFERENCES

[1] Ministry of the Environment: Unified basic data on health effects from radiation, 2019, p. 11

[2] Kato H., Onda Y. and Teramage M.: Depth distribution of 137Cs, 134Cs, and 131I in soil profile after Fukushima Dai-ichi Nuclear Power Plant Accident, Journal of Environmental Radioactivity, Vol. 111, 2012, pp. 59-64

[3] National Institute for Environmental Studies, Proper treatment of wastes contaminated by radioactive materials, 2014, pp. 1-20

[4] Ministry of the Environment: Policy for disposal of disaster waste in Fukushima Prefecture, 2011, pp. 1-13

[5] Yamaguchi N., Eguchi S., Ikeba M., Fujiwara E., Makino T. and Taniyama I.: Radiocesium extraction from arable soils at the initial stage after deposition of radionuclides, Agricultural Environmental Technology Research Institute Report, No. 34, 2015, pp. 29-32

[6] Igawa M., Doi R., Ikai Y. and Matsuno C., Volume reduction of decontaminated waste using electrophoresis and cesium ion adsorbent, The 8th Workshop of Remediation of Radioactive Contamination in Environment, S8-1, 2019, p. 40

[7] Nakano A.: Cesium Adsorption and Fixation on Soils, Trends in the Sciences, Vol. 17, No. 10, 2012, pp. 40-45

[8] Yamaguchi N.: Adsorption mechanism of radiocesium on soil, Journal of the Japanese Society of Soil Physics, No. 126, 2014, pp. 11-21

[9] Tanaka S. and Akemoto Y.: Soil and related interfacial electric phenomena. 6. Remediation of contaminated soil by electrokinetic process, Japanese Journal of Soil Science and Plant Nutrition, Vol. 86, No. 1, 2015, pp. 48-53

[10] Miura T., Kabir M., Suzuki M., Nakajima S. and Mori S.: Effect of Organic Acids on Cesium Removal from Contaminated Soil by Electrokinetic Remediation, Journal of the Institute of Electrostatics Japan, Vol. 40, No. 1, 2016, pp. 14-19

6th Int. Conf. on Structure, Engineering & Environment (SEE), Kyoto, Japan, Nov.18-20, 2020, ISBN: 978-4-909106056 C3051

EFFECT OF WATER HYACINTH FIBER ON STRENGTH AND DURABILITY OF ADOBE BRICKS

Chotikan Ratchakrom[1], Pisut Rodvinij[2]
[1] Faculty of Industrial Technology, Valaya Alongkorn Rajabhat University under the Royal Patronage, Thailand; [2]Faculty of Engineering, Rajamangala University of Technology Lanna, Thailand

ABSTRACT

This study focused on the development of the strength and durability of adobe bricks by used water hyacinth as fiber reinforcement. The mixture of adobe bricks was a combination of clay and sand in the ratio of 1:1. Cement at 5% added in the mixture of adobe bricks. Water hyacinth at the length of 3 cm, 5 cm, and 7 cm was mixed with soil samples at 0.5% by weight. The results demonstrated that the adobe bricks reinforced with water hyacinth reduced the shrinkage approximately 31-34%. Moreover, the flexural strength of adobe bricks reinforced with water hyacinth can reach 61-74% of the compressive strength. While the flexural strength of non-reinforced adobe bricks can reach only 17% of the compressive strength. The results presented that the alteration in the length of water hyacinth slightly affected the strength of adobe bricks. Moreover, the addition of water hyacinth in the adobe bricks can decrease the unit weight by approximately 20%. However, the compressive strength of adobe bricks reinforced with water hyacinth decreased by approximately 35-42%. The compressive strength tended to decrease with the reduction in the unit weight of adobe bricks. The results of the capillary rise test demonstrated that non-reinforced samples broke down after soaked in the water for 24 hours. However, water hyacinth fiber can maintain the characteristic of adobe bricks. Therefore, water hyacinth fiber can use as reinforcement materials to increase the flexural strength, durability, and reduce the shrinkage of adobe bricks.

Keywords: Water Hyacinth, Fiber Reinforcement, Flexural Strength, Durability

INTRODUCTION

Adobe, Earth building is the oldest building material. It is most commonly used in the current. Nearly 30% of the total population of the world still resides in a mud house [1], [2]. Brick is the most commonly used building. Adobe (sun-dried) bricks were used in ancient times during the Sumerian and Harappan civilizations. The utilization of the adobe as a building material in the construction industry is an alternative [3]. Sun-dried adobe bricks are simply made with low energy consumption and locally available materials such as cohesive soil and straw [4]. The properties of bricks depend upon soil selection and the process of brick making to obtain the desired strength. The suitable soil required for making adobe brick should contain adequate clay, silt, and sand. The soil is mixed with the water until plastic consistency is obtained. Mainly the adobe construction is vulnerable to water absorption [5]. Some of the problems of the adobe construction are erosion of earth walls, shrinkage, cracking, and frequent maintenance of the structure [3].

Therefore, this study focused on the improvement of the mixture of adobe bricks by ordinary Portland cement and water hyacinth fiber. Literature reviews demonstrated that brick reinforced with natural fibers are feasible to be used as a building material. The presence of fibers in brick reduces brick density and shrinkage, prevents deformation and crack [6], [7], [8], [9]. Thus, this paper investigated the effect of water hyacinth fiber on the volume change, strength, and durability of adobe bricks.

Water hyacinth is a free-floating perennial plant. The water hyacinth plant is easily spread over the water. It grows over a variety of wetland types from lakes, ponds, streams, ditches, waterways, and black water areas. The plant height may vary from few inches. It may rise above the water surface as much as 1 meter in height. The leaves are 10-20 cm in diameter which float above the water surface. The plant can produce thousands of seeds each year and these seeds can remain viable for more than 28 years. The common water hyacinth is double its population in two weeks [10]. Thailand is facing serious water pollution problems, especially in natural water sources such as rivers and canals. One of the main reasons is the widespread water hyacinth plant. Since it can grow and reproduce very fast, it covers the water surface in natural water sources. This prevents oxygen from penetrating and dissolving into the water. A water source can be considered polluted when the dissolved oxygen in the water is lower than a standard limit [11]. Therefore, the utilization of water hyacinth as construction materials can be an alternative to reduce the environmental problem in Thailand. Moreover, the improvement of adobe brick can increase durability, and reduce unit weight. The use of water hyacinth may reduce the unit weight of adobe bricks more than the other type of natural

fibers. This is because of the high pores in water hyacinths. Therefore, this can result in increased use of adobe brick in house construction.

MATERIALS PREPARATION

Normally, a combination of clay and sand was used as adobe bricks materials. Clay soils from Pathum Thani Province, Thailand were used in this study. The consistency limit of clay samples includes a liquid limit, plastic limit, and shrinkage limit was investigated. The liquid limit was 45.0%, the plastic limit was 27.7%, the shrinkage limit was 12.6%, and the plastic index was 17.3%. The soil was classified as low plasticity clay, according to the Unified Soil Classification System (USCS). Fine sand collected from the river. Dried sand passed sieve #10 was used in this test. The soil samples for build up the adobe bricks were a combination of clay and fine sand in a ratio of 1:1. Atterberg's limit value of the soil samples reduced from clay. Liquid limit, plastic limit, plastic index, and shrinkage limit of the soil samples was 21.1%, 10.8%, 10.3%, and 8.8%, respectively. Moreover, Portland cement type 1 used as a cementitious material. Portland cement was mixed with the soil samples at 5% by weight.

This study focused on the use of water hyacinth as fiber reinforcement in the adobe bricks. The water hyacinth fiber was dried in the air for 2 weeks before mixed with the soil samples, as shown in Fig. 1. The effect of water hyacinth on the volume change, the compressive strength, the flexural strength, and the durability of adobe bricks have been investigated. Water hyacinth at the length of 3 cm, 5 cm, and 7 cm was mixed with the soil samples at 0.5% by weight. Table 1 shows the mixture of adobe bricks reinforced with water hyacinth in this study.

Fig. 1 Water hyacinth fiber dried in the air.

Table 1 Mixture of adobe bricks

Mixture Code	Clay: Sand	Cement (%)	Length of Fiber
S1	1:1	0	-
S1C	1:1	5	-
S1CW3	1:1	5	3
S1CW5	1:1	5	5
S1CW7	1:1	5	7

Note: Water at liquid limit of the soil samples was used in the mixing procedure.

MECHANICAL PROPERTIES OF ADOBE BRICKS

The compressive strength, flexural strength, and durability of adobe bricks reinforced with water hyacinth have investigated by the unconfined compressive strength tests, flexural strength tests, and capillary rise tests, respectively.

Compressive Strength Tests

The soil samples mixed with water, cement, and water hyacinth, according to Table 1 were used in the test. The samples were compacted in the mold at 10×10×10 cm, as shown in Fig. 2. After the samples dried in the air for 1 day, the samples were extruded from the mold and curing in the dried air for 14 days. Then the samples were conducted on an unconfined compressive strength test. The compressive strength values for each mixture are the average of five specimens.

Fig. 2 The samples prepared for unconfined compressive strength tests.

Flexural Strength Tests

The soil samples mixed with water, cement, and water hyacinth according to Table 1 were used in this test. The samples were compacted in the mold at 4×4×16 cm. After the samples dried in the air for 1 day, the samples were extruded from the mold and curing in the dried air for 14 days. The simple beam

with center-point loading was used in the test, as shown in Fig. 3. Turn the test specimen on its side concerning its position as molded and center it on the support blocks. Center the loading system to the applied force. Bring the load-applying block in contact with the surface of the specimen at the center. The load shall be applied at the constant rate to the breaking point (ASTM, C293). The flexural strength values for each mixture are the average of three specimens.

Fig. 3 Flexural strength test of the specimen.

CAPILLARY RISE AND DURABILITY TESTS

The soil samples mixed with water, cement, and water hyacinth according to Table 1 were used in this test. Capillary rise and durability cube specimens, 10×10×10 cm was compacted in the mold and cured in the dried air for 14 days in the same condition as unconfined compressive strength specimens. Three specimens were prepared for each mixture. After the curing process, the specimens were placed in a tray with water level maintained at 10 mm and room temperature of 25±2 °C [12], as shown in Fig. 4. The average level of rising water measured from the base of the specimens.

Fig. 4 The specimens conducted on capillary rise tests.

In order to investigate the durability of adobe bricks reinforced by water hyacinth, the specimens through the capillary rise tests at 7 days were conducted on unconfined compressive strength tests. The results can demonstrate the reduction in the compressive strength of adobe bricks due to the increased moisture.

RESULTS AND DISCUSSION

Volume Change and Density

The volume change was investigated by measuring the width, length, and height of specimens by Vernier Caliper at the curing time of 1, 3, 7, 14, and 21 days, as shown in Fig. 5. The volume change of adobe bricks for each mixture is shown in Fig. 6. The initial volume of the specimens was 1,000 cm^3. The results demonstrated that the volume of specimens tends to decrease with rising time. The results showed the volume of the sample S1 rapidly decreased in 3 days followed by slightly decreased. The remaining volume of S1 was 721 cm^3 at 21 days. The reduction in the volume of S1 was approximately 28%. However, the addition cement at 5% in the mixture can reduce the shrinkage of the specimens, as shown in the results of S1C. The volume of S1C decreased by only 13% by the remaining volume of S1C was 872 cm^3. Moreover, the volume of the samples mixed with cement and reinforced by water hyacinth decreased by approximately 5-7%. The volume of S1CW3, S1CW5, and S1CW7 was 934 cm^3, 951 cm^3, and 926 cm^3, respectively at the curing time of 21 days. Therefore, the results demonstrated that the water hyacinth reinforced in the bricks can reduce the shrinkage of adobe bricks. Moreover, the results illustrated that the length of water hyacinth slightly affected the shrinkage of adobe bricks.

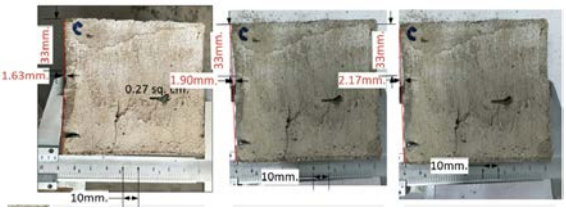

Fig. 5 The specimen volume measurement.

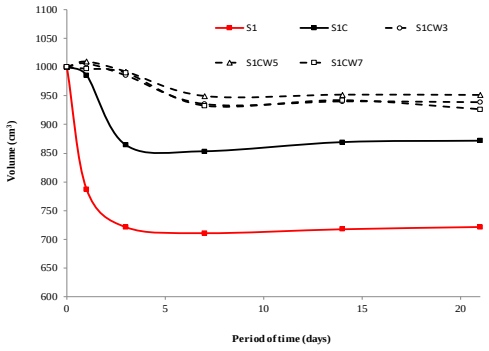

Fig. 6 Relation between volume change and period of time.

Consideration of the density of the specimens for each mixture, the density of the specimens tended to decrease with the rising time, as shown in Fig. 7. The results demonstrated that the density of S1 was higher

than S1C approximately 13-17%. Moreover, the specimens reinforced with water hyacinth can reduce the density of approximately 5-11% from S1C. The density of the specimens reinforced with water hyacinth was between 1,422-1,452 kg/m^3 at the curing time of 21 days. The results illustrated that the changing length of water hyacinth was not affecting the density of adobe bricks, as shown in Fig. 7. The density of the reinforcement samples reduced 19-23% from S1.

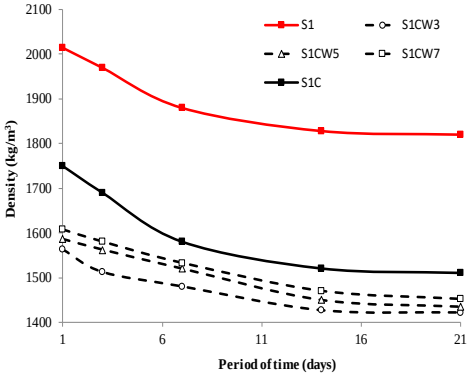

Fig. 7 The relation between density of adobe bricks and period of time.

The low density of the reinforcement samples can be described by the relation between the alteration in volume and weight of the sample for each mixture, as shown in Fig. 8. It shows the results of the samples at the curing time of 21 days. The results illustrated that the weight of the sample for each mixture slightly different, as shown the weight was between 1.31-1.38 kg. However, the volume of S1and S1C less than S1Cw3, S1CW5, and S1CW7 due to the high shrinkage of the samples. Therefore, this result shows the water hyacinth fiber can assist to maintain the volume of adobe bricks. This induced the density of the reinforcement specimens less than the specimens without reinforcement.

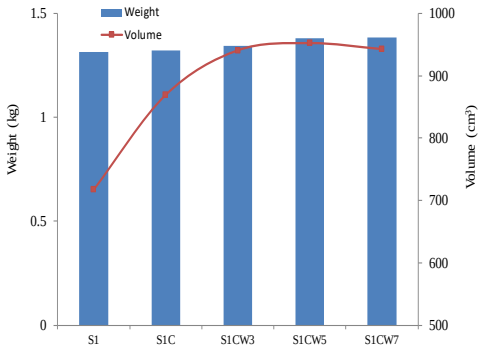

Fig. 8 Relation between the alteration in weight and volume of the specimens for each mixture.

Compressive Strength

The compressive strength of the specimens for each mixture is shown in Fig. 9. The results demonstrated that S1 gave the highest strength. The compressive strength of S1 was 13.68 ksc. However, the addition of cement at 5% in the soil samples decreased the compressive strength by approximately 64% from S1. The compressive strength of S1C was 4.97 ksc. Moreover, the specimens reinforced by water hyacinth have the lowest compressive strength. The compressive strength of S1CW3, S1CW5, and S1CW7 was 2.91 ksc, 3.05 ksc, and 3.25 ksc, respectively. The results illustrated that the compressive strength of the samples reinforced by water hyacinth tended to increase with the additional length of the fiber.

The reduction in the compressive strength can describe by the density of the samples for each mixture. The results illustrated that the compressive strength tended to decrease with the reduction in density. This phenomenon causes the shrinkage of the samples. The high shrinkage of S1 induced the high density and low porosity of the specimen. However, the samples S1C, S1CW3, S1CW5, and S1CW7 shrink less than S1. This induced low density and high porosity. Therefore, the high porosity is the causes of the compressive strength of S1CW3, S1CW5, and S1CW7 decreased 35-42% from S1C.

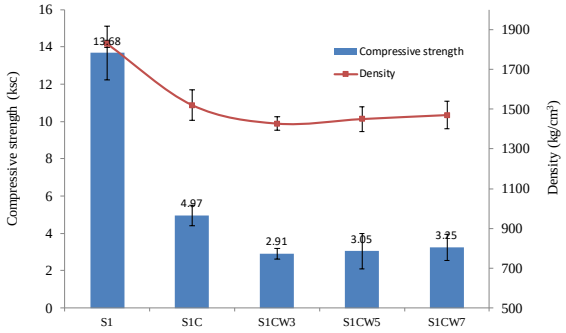

Fig. 9 Relation between compressive strength and density of the samples for each mixture.

Flexural Strength

The flexural strength of the samples for each mixture is shown in Fig. 10. The results demonstrated that the flexural strength of the samples for each mixture slightly different. The flexural strength of S1, S1C, S1CW3, S1CW5, and S1CW7 was 2.3 ksc, 2.3 ksc, 2.2 ksc, 2.0 ksc, and 2.0 ksc, respectively. The results illustrated that the flexural strength of S1 extremely decreased from the compressive strength. The flexural strength can reach only 17% of the compressive strength. However, the addition of cement at 5% can enhance the flexural strength of the samples. The flexural strength of S1C can reach 46% of compressive strength. Moreover, the flexural

strength of the samples reinforced with water hyacinth can reach 61-74% of the compressive strength. Therefore, the results illustrated the reinforcement of water hyacinth can enhance the flexural of adobe bricks approximately 15-28% from the non-reinforced adobe bricks.

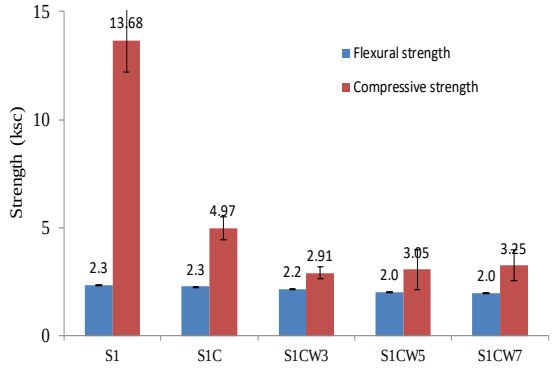

Fig. 10 Flexural strength of the samples for each mixture.

Capillary Rise and Durability

The results of capillary rise tests demonstrated that the samples S1 heavily of capillary rise after 24 hours. S1 samples broke down, as shown in Fig. 11. This is due to the high amount of clay in the soil samples. Therefore, it induced high water pressure in the samples and broke down the samples. However, the samples mixed with cement at 5% and reinforced by water hyacinth can maintain the characteristics of the specimens during soaked in the water for 7 days.

Fig. 11 The samples without reinforcement after soaked in the water for 24 hours.

Moreover, the results illustrated that the density of S1CW3, S1CW5, and S1CW7 tended to increase after soaked in the water for 7 days, as shown in Fig. 12. The density of S1CW3, S1CW5, S1CW7 after soaked in the water for 7 days increased approximately 20-25%.

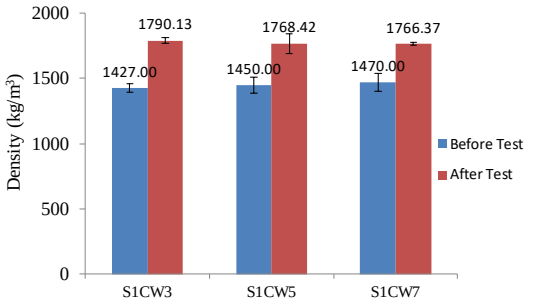

Fig. 12 Density of the reinforced samples after 7 days of capillary rise tests.

The samples S1C3, S1CW5, and S1CW7 after through the capillary rise tests were conducted on the unconfined compressive tests to investigate the durability of adobe bricks. The results of the durability test are shown in Fig. 13. The compressive strength of S1CW3, S1CW5, and S1CW7 after soaked in the water for 7 days was 1.03 ksc, 1.08 ksc, and 1.09 ksc, respectively. The compressive strength decreased approximately 65% from the dry samples. However, the samples S1 cannot conduct on the unconfined compressive strength tests due to the samples broke down after soaking in the water for 24 hours. Therefore, the results of capillary rise tests and unconfined compressive strength tests demonstrated the water hyacinth fiber can increase the durability of adobe bricks.

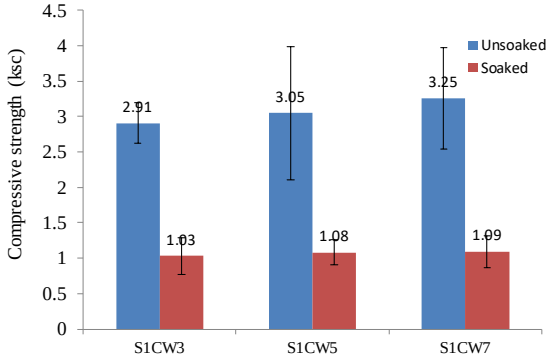

Fig. 13 Compressive strength of the reinforced specimens after soaked in the water.

CONCLUSIONS

Based on the results obtained from this study, the following conclusion was made:

1. Water hyacinth can reduce the drying shrinkage of adobe bricks approximately 31-34%, and decrease the density of adobe bricks approximately 20%.

2. The compressive strength of adobe bricks reinforced with water hyacinth decreased by approximately 35-42% from the non-reinforced bricks.

3. The flexural strength of adobe bricks reinforced with water hyacinth can reach 61-74% of the compressive strength. However, the flexural strength of non-reinforced adobe bricks can reach only 17% of the compressive strength.

4. The non-reinforced adobe bricks broke down after soaking in the water for 24 hours. However, water hyacinth fiber can maintain the characteristic of adobe bricks.

5. Water hyacinth fiber can increase the flexural strength, durability, and reduce the shrinkage of adobe bricks.

REFERENCES

[1] Detheir, J., Des Architectures De Terre, Edition De Centre Pompidou, 1986, Paris.

[2] Coffman, R., Agnew, N., Auiston, G., Doehne, E., Adobe Mineralogy: Characterization of The Conservation of Adobes from Around The World, 6th International Conference on The Conservation of Earthen Architectures, Las Cruces, NM, 1990, 14-19.

[3] Prakash, V., Raj, A., Aravind, S., Mathew, B., and Sumith, V. R., Studies on Stabilized Mud Block as A Construction Material, International Journal of Innovative Research in Advanced Engineering, Vol. 3, No. 1, 2016, 19-24.

[4] Banjonkliang, E., Capability of Rain Washing Resistance Improvement of External Rubber-Clay Plaster for Adobe Walls, Doctor Thesis, Chiang Mai University, 2015.

[5] Monika, H., and Unnikrishnan, S., Characterisation of Jute Fibre Reinforced Adobe Brick and Brick Masonry, International Journal of Advanced Research Trends in Engineering and Technology, Vol. 4, Issue 22, 2017, 16-21.

[6] Binichi, H., Aksogan, O., and Shah, T., Investigation of Fibre Reinforced Mud Brick as A Building Material., Construction and Building Materials, Vol. 19, 2005, 313-318.

[7] Ananth, C., A Brief Outline on Microwave Semiconductor Devices, RF & Microwave Engineering Book 4, Kindle Edition, Vol. 11, 2017, 129-192.

[8] Ghavami, K., Filho, R, D, T., and Barbosac, N, P., Behavior of Composite Soil, Reinforced with Natural Fibres, Cement and Concrete Composites, Vol. 21, 1999, 39-48.

[9] Ngowi, A, B., Improving the international Earth Construction: A Case of Botswana, Construction and Building Materials, Vol. 11, 1997, 1-7.

[10] Punitha, S., Sangeetha, K., and Bhuvaneshwari, M., Processing of Water Hyacinth Fiber to Improve Its Absorbency, International Journal of Advanced Research, Vol. 3, Issue 8, 2015, 290-294.

[11] Potiyaraj, P., Panchaipech., and Chuayjuljt, S., Using Water-Hyacinth Fiber as Filler in Natural Rubber, Journal of Scientific Research Chulalongkorn University, Vol. 26, No.1, 2001, 12-19.

[12] Ferdrigo, W., Nunez, W, P., Kleinert, T, R., Matuella, M, F., and Ceratti, J, A, P., Strength, Shrinkage, Erodibility, and Capillary Flow Characteristics of Cement-Treated Recycled Pavement Materials, International Journal of Pavement Research and Technology, 10, 2017, 393-402.

6th Int. Conf. on Structure, Engineering & Environment (SEE), Kyoto, Japan, Nov.18-20, 2020, ISBN: 978-4-909106056 C3051

A NEW TYPE OF ACTUATOR FOR APPEARANCE INSPECTION OF IRON STRUCTURE

Hiroyuki Yaguchi[1]
[1] Faculty of Engineering, Tohoku Gakuin University, Japan

ABSTRACT

Due to economic development, many types of social infrastructure, such as various large structures, are being constructed around the world. Inspection and maintenance of social infrastructure, such as large bridges and tanks, are extremely important. In the present study, a new vibration actuator that extends the principle of operation proposed by the authors was proposed and tested. The experimental results indicate that reciprocating motion can be realized by controlling the phase of the vibration displacement of two vibration components. Experimental results reveal that this vibration actuator was able to pull a load mass of 190 g and that the maximum efficiency of the actuator was approximately 12.5% for the own-weight case. The actuator was confirmed to be able to easily control the direction of movement with a two-channel function generator and a power amplifier.

Keywords: vibration, actuator, phase difference, electromagnetic force, inertial force.

INTRODUCTION

Due to economic development, many types of social infrastructure, such as various large structures, are being constructed around the world. The safety of large structures constructed in recent years is ensured by design standards. On the other hand, older social infrastructure can collapse because of low design standards. In addition, the number of endangered structures has increased due to damage and deterioration as a result of aging. For this reason, inspection and maintenance of social infrastructure, such as large bridges and tanks, is extremely important. However, inspection of such structures is very difficult due to site conditions. For this reason, inspection robots have been developed in order to ensure worker safety and reduce costs.

Robots with various movement principles have been proposed for the inspection of structures. Previously proposed operating principles are as follows: a permanent magnetic adhesion system coupled with a tracked locomotion mechanism [1], the adhesive force of a suction cup manufactured from a sponge [2] or flexible rubber [3-5], control of the attractive force of an electromagnet inserted therein [6], a permanent magnet and an iron wheel [7, 8], negative pressure generated by a pump [9], the wind force produced by a propeller [10], vibration of the many caps of a sucker to obtain mobile power [11], a claw gripper [12,13], and adhesive materials [14].

In such mobile robots, the moving speed is low as a result of the problem of controllability and the increase in the weight of the actuator due to its complex structure. The authors previously proposed a lightweight actuator with excellent operability [15]. However, movement of this actuator was limited to one direction.

In the present study, a new vibration actuator that extends the principle of operation is proposed. The vibration actuator, in which two vibration components with the same specifications are arranged orthogonally, was prototyped. The experimental results indicate that reciprocating motion can be realized by controlling the phase of the vibration displacement of the two vibration components. It was confirmed through actual machine tests that the maximum propulsion force for this actuator was 1.9 N and the maximum efficiency was approximately 12.5%. In addition, the vibration actuator was found to be able to easily control the direction of movement with a two-channel function generator and a power amplifier.

STEUCTURE OF THE VIBRATION ACTUATOR OPERATING INERTIA FORCE

Fig.1 shows a vibration actuator capable of movement on a magnetic substance proposed by the authors. This vibration actuator is composed of a

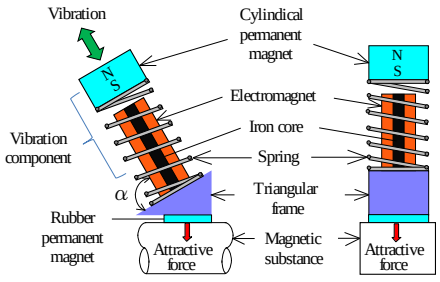

(a) Front view (b) Side view

Fig. 1. Structure of the vibration actuator.

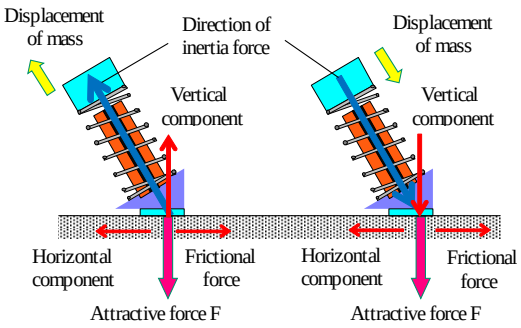

(a) Sliding (b) No sliding

Fig. 2. Principle of locomotion.

permanent magnet, a coil spring, an electromagnet, a triangular acrylic frame, and a rubber permanent magnet. When the diagonally mounted vibration component is excited by the electromagnet, an inertial force is generated in the diagonal direction. The angle α of the vibration component was set to 60 degrees based on the results obtained in a previous study [15]. The attractive force generated by the rubber magnet attached at the support part acts on the vibration actuator when it is placed on a magnetic substance, as shown in Fig. 2. The frictional force between the rubber magnet and the magnetic substance alternates periodically during one cycle of vibration. Since the horizontal component of the inertial force exceeds the frictional force, the vibration actuator is propelled by the difference between the frictional forces in the forward and backward directions acting on the rubber magnet in the support, as shown in a previous study [15]. This vibration actuator has a very simple structure and can generate propulsion equivalent to approximately 10 times its own weight. However, the movement direction is limited to only one-directional movement from the principle of operation.

STRUCTURE OF THE NEW VIBRATION ACTUATOR

Fig. 3 shows the new vibration actuator capable of reciprocating movement. It is composed of two vibration components, A and B, having the same specifications, an acrylic frame and plate, and two rubber permanent magnets. Vibration components A and B are orthogonally arranged on the acrylic frame. The vibration components are composed of a coil spring, a ring-type permanent magnet, and an electromagnet having a bobbin-type iron core proposed in the previous paper [16]. The magnetic field generated by an electromagnet can be converted to an electromagnetic force with high efficiency. Details of the vibration component and the bobbin-type iron core are shown in Fig. 4. The coil spring is a compression coil spring with a free length of 25 mm, an outer diameter of 12 mm, and a spring constant k = 2,689 N/m. The ring-type permanent magnet is an NdFeB magnet with an outer diameter of 12 mm, an inner diameter of 9 mm, a thickness of 8 mm, and is magnetized in the height direction. For the electromagnet, the experimental results for the optimization of the bobbin-type iron core shape and the number of turns obtained in the previous study [16] were applied. As shown in Fig. 3, for the iron disk, the diameter is D = 8 mm and the thickness is h = 1 mm. In addition, the shaft diameter is d = 3 mm, and the length is H = 26 mm. The electromagnet was produced by winding a copper wire having an outer diameter of 0.14 mm around a bobbin-type iron core of 1,200 turns.

Two vibration components are glued to the acrylic frame, and two rubber permanent magnets are attached to the bottom of the acrylic frame in order to hold the actuator against the magnetic substance. One is the main rubber permanent magnet for holding the actuator against a magnetic substance. Another secondary rubber permanent magnet was attached in order to achieve stable straight movement. This main rubber magnet has a length of 13 mm, a width of 15 mm, and a thickness of 3 mm. The average surface magnetic flux density measured using a tesla meter was 128 mT. The secondary rubber magnet has a length of 6 mm, a width of 15 mm, and a thickness of 3 mm. The average surface magnetic flux density was 121 mT. When the vibration actuator is set on an iron structure, the attractive forces of the main and secondary permanent magnets are F_s = 5.2 N and F_m

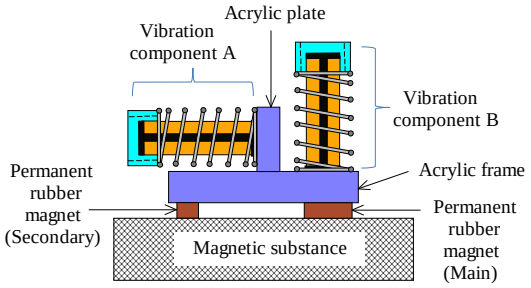

Fig. 3. Structure of the new vibration actuator capable of reversible motion.

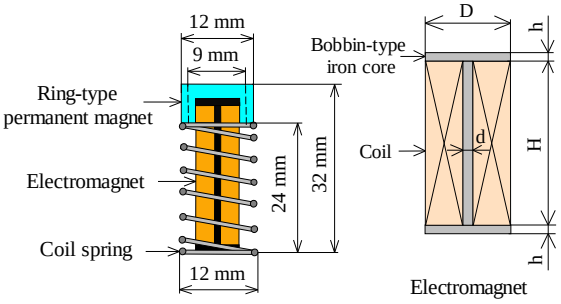

Fig. 4. Vibration components and electromagnet.

= 0.5 N, respectively. The vibration actuator has a height of 43 mm, a length of 58 mm, a width of 20 mm, and a total mass M_a of 39 g.

PRINCIPLE OF OPERATION FOR THE NEW VIBRATION ACTUATOR

As shown in Fig. 3, when two vibration components, A and B, are arranged orthogonally, the movement direction of the actuator can be changed by controlling the phase of the vibration displacement in each component. The cases of displacement in the horizontal and vertical directions are referred to as vibration components A and B, respectively. The displacement coordinates x and y for vibration components A and B are determined, as shown in Fig. 5.

When the vibration actuator is set on a magnetic substance, the frame of this actuator is held by the main and secondary rubber permanent magnets with attractive forces of F_m and F_s. Due to this reaction, the vibration component can be displaced. The vibration components A and B were assumed to vibrate at an angular frequency ω. First, as shown in Fig. 5(a), consider the case in which the phase difference for displacement between vibration components A and B is 0 degrees (in-phase). Focusing on one cycle of the displacement (ω/2π) in the vibration component B, the holding force F and the frictional force F_f of the support part for the actuator change periodically, as shown in Equation(1), due to the inertial force I_B by the permanent magnet of the vibration component B:

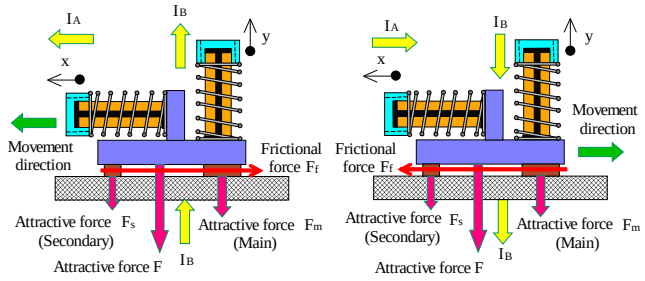

(a) Sliding (b) No sliding

Fig. 5. Principle of reversible motion (in-phase).

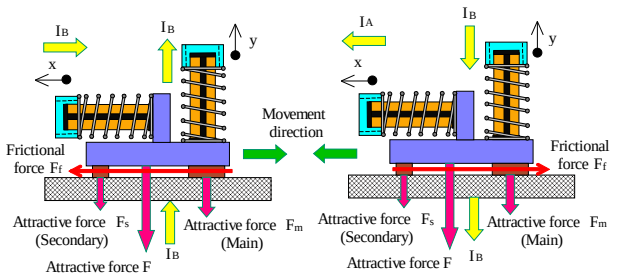

(a) Sliding (b) No sliding

Fig. 6. Principle of reversible motion (out-of-phase).

$$F = F_m + F_s - I_B \sin \omega t \ (0 < t < \pi/\omega) , \ F_f = \mu F \quad (1)$$

where t is time, and μ is the friction coefficient. When component A is displaced in the +x direction in the same phase while vibration component B is displaced in the +y direction, the vibration actuator easily slides in the +x direction. As shown in the following equation, when the inertial force I_A of the permanent magnet in vibration component A exceeds the friction force F_f, the actuator can move in the +x direction:

$$I_A > F_f \quad (2)$$

On the other hand, as shown in Fig. 5(b), when vibration component B is displaced in the -y direction, the holding force F and the frictional force F_f increase as shown in the following equation, due to the inertial force I_B by the permanent magnet:

$$F = F_m + F_s + I_B \sin \omega t \ (\pi/\omega < t < 2\pi/\omega) , \ F_f = \mu F \quad (3)$$

Even if the component A is displaced in the -y direction in opposite phase, the inertial force I_A cannot exceed the friction force F_f. Therefore, the actuator cannot move, as shown in the following equation:

$$I_A < F_f \quad (4)$$

The actuator can move in one direction by changing the frictional force of the rubber permanent magnet attached to the frame.

Fig. 6 shows a case in which the phase difference of the displacement between vibration components A and B is 180 degrees (opposite phase). The actuator can move in the -x direction according to the principle of movement by the frictional force and the inertial force described above. Accordingly, the actuator can change between forward and backward motion by controlling the phase of displacement of the two vibration components.

BASIC CHARACTERISTICS OF THE NEW VIBRATION ACTUATOR

Fig. 7 shows an outline of the experimental apparatus used to determine the basic characteristics. In the experiment, two vibration components were driven resonantly by a two-channel signal transmitter and amplifier. The resonance frequency was 128 Hz. The voltage, current, and power input to the electromagnet for the vibration component were measured by a power analyzer. As the magnetic substance, an iron rail having a width of 50 mm, a thickness of 50 mm, and a length of 500 mm was used. In the measurement, the vibration actuator was set on a horizontal plane. As described above,

the attractive forces produced by the main and sub rubber permanent magnets are F_s = 5.2 N and F_m = 0.5 N, respectively. The coefficient of friction between the rubber permanent magnet and the iron rail is 0.84. The directions of movement of the actuator are defined as shown in Fig. 7. Fig. 8 shows a photograph of the vibration actuator.

Fig. 9 shows the relationship between the input current to each electromagnet and the displacement amplitude in vibration components A and B. Using an acrylic stopper, the state in which the vibration actuator is freely held was set. For the measurement of the displacement amplitude, a laser displacement meter and an FFT analyzer were used as shown in Fig. 7. For both vibration components, the displacement amplitude increases approximately linearly with an increase in the input current. Therefore, the displacement amplitude in each vibration component can be estimated by measuring the input current.

The input current to the electromagnet for vibration component B is set to 50 mA, and Fig. 10 shows the relationship between the amplitude of vibration component A and the speed of movement for the vibration actuator. In this case, the two acrylic stoppers were removed. As shown in Fig. 7, Direction A (Forward) is a case in which the phase difference of displacement between the vibration components is 0 degrees, and Direction B (Backward) is a case in which the phase difference is 180 degrees. The movement speed varies greatly depending on the movement direction. This is due to the attractive force of the secondary rubber permanent magnet attached to the support part of the actuator. However, as described above, the movement speed of the actuator depends approximately on the displacement amplitude. By controlling the input current to the electromagnet, the movement speed in both directions can be adjusted to be the same.

The input current to the electromagnet for vibration component A at 50 mA was set, and Fig. 11 shows the relationship between the vibration amplitude of vibration component B and the movement speed of the vibration actuator in two directions. As the input current to vibration component B increases, the holding force of the actuator increases. Due to the increase in the holding force, the amplitude of the two vibration components increases, so that the movement speed increases. For the reasons described above, a difference in speed occurs depending on the movement direction.

Fig. 12 shows the relationship between the displacement phase difference for vibration components A and B and the movement speed. The input current to the electromagnet for both vibration components was varied as 50, 60, and 70 mA. In this case, the frequency of vibration components A and B was 128 Hz, and the phase of component A was changed from -180 degrees to 180 degrees using the

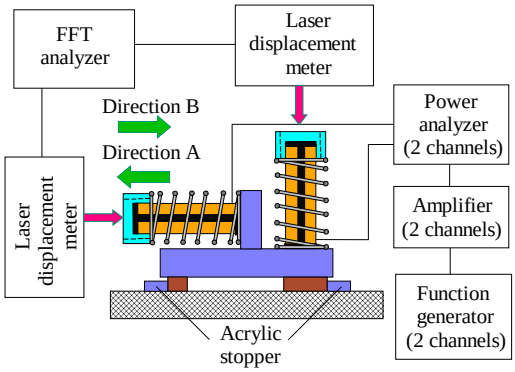

Fig. 7. Experimental apparatus.

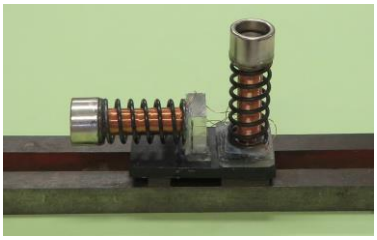

Fig. 8. Photograph of vibration actuator.

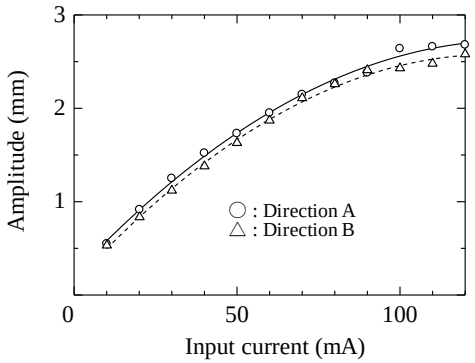

Fig. 9. Relationship between input current and amplitude.

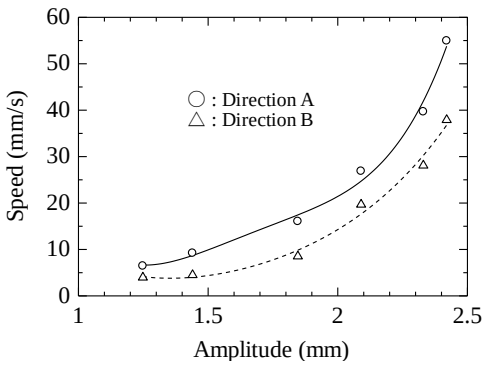

Fig. 10. Relationship between amplitude and speed.

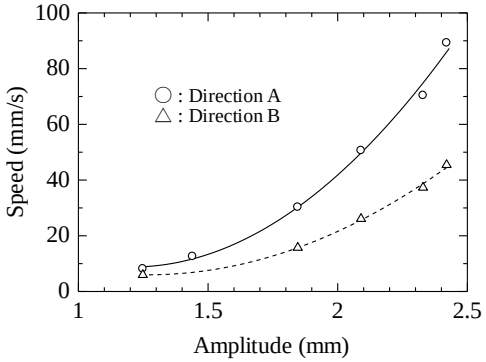

Fig. 11. Relationship between amplitude and speed.

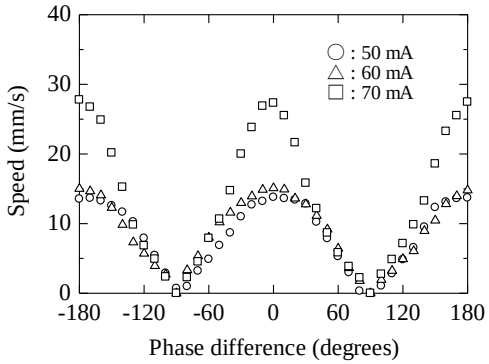

Fig. 12. Relationship between phase difference and speed.

phase adjustment of the two-channel signal generator. The movement speed shows a maximum value when the phase difference of the displacement is 0 degrees and 180 degrees. In these cases, the movement speed of the actuator is approximately 30 mm/s. When the phase difference is -90 degrees or 90 degrees, the vibration actuator cannot move due to the movement principle.

MOVEMENT CHARACTERISTICS OF THE VIBRATION ACTUATOR

As shown in Fig. 13, the tilt angle of the iron rail was set to β_1 and β_2, and the movement characteristics of the vibration actuator were measured. In the experiment, the phase difference of displacement in each vibration component was set to 0 degrees and 180 degrees.

Figs 14 and 15 show the relationship between the tilt angles β_1 and β_2 of the iron rail and the speed for Direction A (forward) and Direction B (backward) of the vibration actuator by changing the input current to the electromagnet for each vibration component. In the figure, -90 degrees indicates vertical downward movement, 0 degrees indicates horizontal movement, and 90 degrees indicates vertical upward movement. As the tilt angle of the iron rail increases, the movement speed of the actuator decreases. This is due to the weight of the

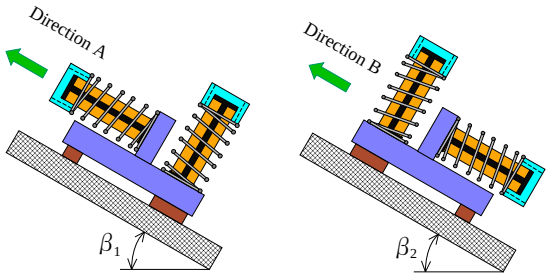

Fig. 13. Vibration actuator moving on iron rail with tilt angle.

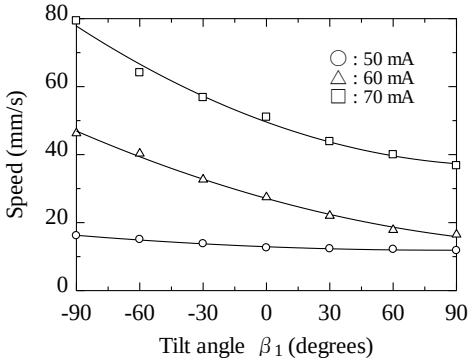

Fig. 14. Relationship between tilt angle and speed.

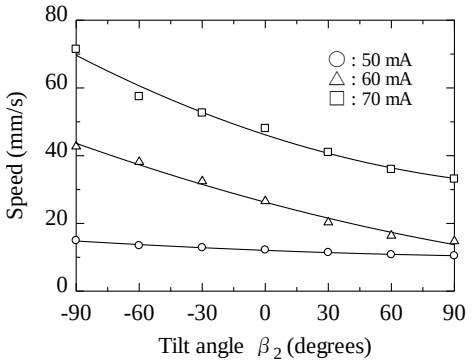

Fig. 15. Relationship between tilt angle and speed.

actuator itself. The actuator can move with approximately the same amount in the forward and backward directions.

A load mass was attached to the frame of the actuator using a string. The tilt angle of the iron rail was set to 90 degrees.

Figs 16 and 17 show the relationship between the load mass mounted on the actuator and the vertical upward speed when the actuator moves in the forward and backward directions. The input current to the electromagnet for each vibration component was changed from 50 mA to 110 mA. As shown in the figure, the maximum pulling force of the actuator in the case of forward movement is 1.9 N, while that in the case of backward movement is only

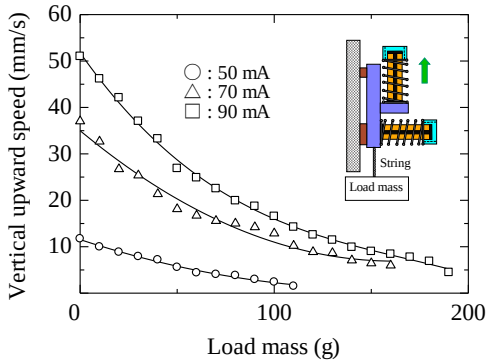

Fig. 16. Relationship between load mass and vertical speed.

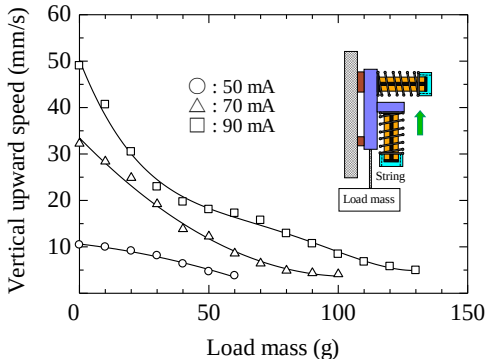

Fig. 17. Relationship between load mass and vertical speed.

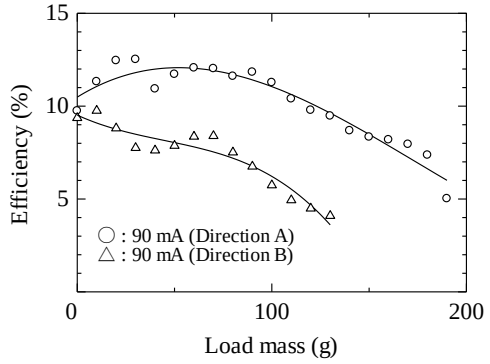

Fig. 18. Relationship between load mass and efficiency.

1.3 N. As described above, this is because the attractive force of the secondary rubber permanent magnet has an effect. The presence of the attractive force asymmetric with respect to vibration component B degrades the movement characteristics of the actuator. However, the secondary rubber permanent magnet is needed to drive the actuator straight.

Fig. 18 shows the relationship between the load mass and the efficiency of the vibration actuator. The efficiency η is expressed as follows:

$$\eta\,[\%] = (M_a + M_m)\, v_{up}\, g \times 100 / P_I \qquad (5)$$

where M_a is the total mass of the actuator, M_m is the load mass, v_{up} is the vertical speed, g is the acceleration due to gravity, and P_I is the input power. The solid line indicates the results for Direction A (forward) for the actuator pulling its own weight, and the dashed line indicates the results for Direction B (backward). The maximum efficiency of the actuator was approximately 12.5 % for the case of direction A.

CONCLUSION

A new type of a vibration actuator that is capable of reciprocating movement by means of a displacement phase difference between two vibration components has been proposed and tested. The experimental results reveal that this vibration actuator is able to pull a load mass of 190 g. The maximum efficiency of the vibration actuator was approximately 12.5 % for the own-weight case. By setting the phase difference of the displacement between the vibration components to 0 and 180 degrees, the vibration actuator can perform reciprocating movement at maximum speed. This vibration actuator was confirmed through actual tests to be able to easily control the direction of movement with a two-channel function generator and a power amplifier. In the future, by mounting a CCD camera on the frame of the actuator, it becomes possible to inspect the appearance of the iron structure.

ACKNOWLEDGEMENTS

I would like to thank the students of Yaguchi Laboratory and the staff of the machine factory of Tohoku Gakuin University for their involvement in this research.

REFERENCES

［1］ G. Lee, J. Park, H. Kim and T. W. Seo, “Wall Climbing Robots with Track-wheel Mechanism”, in Proc., IEEE International Conference on Machine Learning and Computing, pp.334-337 (2011).

［2］ T. Fukuda, H. Matsuura, F. Arai, K. Nishibori, H. Sakauchi and N. Yoshi, “A Study on Wall Surface Mobile Robots”, Trans. Japan Soc. Mec. Eng., vol. 58, no. 550, pp. 286-293 (1992).

［3］ S. Kawasaki and K. Kikuchi, “Development of a Small Legged Wall Climbing Robot with Passive Suction Cups”, in Proc., International Conference on Design engineering and science, pp.112-116 (2014).

［4］Y. Yoshida and S. Ma, “A Wall-Climbing Robot without any Active Suction Mechanisms”, in Proc., IEEE International Conference on Robotics and Biomimetics, pp.2014-2019 (2011).

［5］M. Akhtaruzzaman, N. Samsuddin, N. Umar and M. Rahman, “Design and Development of a Wall Climbing Robot and its Control System”, in Proc., International Conference on Computer and Information Technology, pp.309-313 (2009).

［6］M. Suzuki and S. Hirose, “Proposal of Swarm Type Wall Climbing Robot System Anchor Climber and Development of Adhering Mobile Units”, The Robotics Society of japan, Vol. 28, No. 5, pp. 614-623 (2010).

［7］N. Khirade, R. Sanghi and D. Tidke, “Magnetic Wall Climbing Devices - A Review”, in Proc., International Conference on Advances in Engineering & Technology, pp.55-59 (2014).

［8］J. H. Kim, S. M. Park, J. H. Kim and J. Y. Lee, “Design and Experimental Implementation of Easily Detachable Permanent Magnet Reluctance Wheel for Wall-Climbing Mobile Robot”, Journal of Magnetics Vol. 15, No. 3, pp. 128-131 (2010).

［9］A. Subramanyam, Y. Mallikarjuna, S. Suneel and L. Bhargava Kumar, “Design and Development of a Climbing Robot for Several Applications”, International Journal of Advanced Computer Technology, Vol. 3, No. 3, pp. 15-23 (2011).

［10］S. Jae-Uk, K. Donghoon, J. ong-Heon and M. Hyun, “Micro aerial vehicle type wall-climbing robot mechanism”, in Proc., IEEE RO-MAN International Symposium on Robot and Human Interactive Communication, pp. 722-725 (2013).

［11］W. Wang, K. Wang, H. Zhang and J. Zhang, “Internal Force Compensating Method for Wall-Climbing Caterpillar Robot”, in Proc., IEEE International Conference on Robotics and Automation, pp. 2816-2820 (2010).

［12］F. Xu, X. Wang and G. Jiang, “Design and Analysis of a Wall-Climbing Robot Based on a Mechanism Utilizing Hook-Like Claws”, International Journal of Advanced Robotic Systems, Vol. 9, No. 261, pp.1-12 (2012).

［13］M. Funatsu, Y. Kawasaki, S. Kawasaki and K. Kikuchi,
“Development of cm-scale Wall Climbing Hexapod Robot with Claws”, in Proc., International Conference on Design Engineering and Science, pp. 101-106 (2014).

［14］C. Kute, M. Murphy, Y. Menguc and M. Sitti, “Adhesion Recovery and Passive Peeling in a Wall Climbing Robot using Adhesives”, in Proc., IEEE International Conference on Robotics and Automation, pp. 2797-2802 (2010).

［15］H. Yaguchi and S. Sakuma : Vibration Actuator Capable of Movement on Magnetic Substance Based on New Motion Principle, Journal of Vibroengineering, Vol. 19, Issue 3, pp. 1494 - 1508 (2017).

［16］H. Yaguchi and T. Izumikawa : Wireless In-Piping Actuator Capable of High-Speed Locomotion by a New Motion Principle, IEEE/ASME Transactions on Mechatronics, Vol. 18, No. 4, pp. 1367 - 1376 (2013).

6th Int. Conf. on Structure, Engineering & Environment (SEE), Kyoto, Japan, Nov.18-20, 2020, ISBN: 978-4-909106032 C3051

VIBRATION ANALYSIS OF A GASOLINE-ENGINE CAR DRIVING UPON THREE TYPES OF ROADS

Suphattharachai Chomphan
Faculty of Engineering at Sriracha, Kasetsart University, Thailand

ABSTRACT

This paper presents a problematic analysis of vibration signals inside a personal gasoline-engine car while driving upon three types of roads including paved road, concrete road, and gravel road. The vibration sensors are allocated over three positions inside the passenger room; the right-front (driver's) seat surface, the left-front seat surface, and the rear seat surface. A couple of purposes of this study are to compare the vibration affecting from driving upon three types of roads, and to compare the vibration at three different areas of sensor allocations. The proposed signal analysis technique is Fast Fourier Transform (FFT), the output spectrum are used to extract the dominant peaks. The averaged values for six engine speeds ranging from 0-30 km/h are conducted. The averaging calculations are based on 50 five-second-length samples of vibration signals. As for the first purpose, the experimental results confirm that the highest peak values are mostly of the gravel road, meanwhile the lowest peak values are of the paved road. As for the second purpose, the evident results can be strongly concluded as follows. In case of paved road, the highest peak values are at the rear seat surface, moreover in case of concrete road, the highest peak values are at the left-front seat surface. Last but not least, in case of gravel road, the highest peak values are at the rear seat surface. All in all, this study confirmed that the proposed approach can be used to differentiate the signal features of all scenarios.

Keywords: Fast Fourier transform, Vibration analysis of gasoline engine, Paved road, Concrete road, Gravel road

INTRODUCTION

Nowadays, land transportation are playing many important roles in our daily lives. Especially in the newly-developed or developing countries, trailers, trucks, pick-up trucks, or cars, have been used to transport products, raw materials, tools, and equipment. Not only the non-living things but also the living things are carried upon automobile on land. Therefore the effects of the road surface type and condition are very dominant factors on the vibration and sound within the transportation vehicles.

A study of the effects of the road surface type and condition on the traffic flows management mode in case of directive management has been explored by Novikov et al., [1]. Its focus is the method of assessment of effect of the road surface type and condition on the capacity rate of the signalized area and therefore its effects on the traffic flow management mode. It has been concluded that there is a correlation between the friction coefficient and the capacity of the managed area resulting in the change of the traffic lights cycle, which is also corroborated by the conducted field experiment on a signalized intersection.

In the vehicle durability aspect, Hu and Zhong applied a conventional finite element model for linear and nonlinear analysis for multibody full-vehicle-durability simulation. Six different kinds of test road surfaces are conducted in the simulation, it has been concluded that the explicit–implicit co-simulation techniques are efficient and accurate enough for engineering purposes [2].

The interaction between the type and technical condition of road surfaces, dynamic vehicle loads, and the level of vibration propagated to the environment has been introduced by Czech [3]. It has been insisted that the type of road surface and the technical condition and varied dynamic vehicle loads are affecting the level of vibration propagated to the environment explicitly.

Since the vibration is one of the main environmental stress in vehicles. A study of the discomfort caused by vibration for three models of micro commercial vehicles running in four types of road conditions has been performed by Huang and Li [4]. Noise is also investigated in the study. Moreover, Litak et al., investigated the chaotic vibration which was the effect of critical Melnikov amplitude of the road surface profile to a quarter car model [5]. Blekhman and Kremer also conducted a study of the effect of road unevenness on the dynamics of the averaged longitudinal motion of a vehicle [6]. In the aspects of detection and diagnosis of the faults in rotating machinery, a number of the mechanical

vibration–based studies have been tremendously pursued [7]-[9].

Investigating the associated signal processing for machine diagnosis, several research of signal processing adaptation have been investigated for fault diagnosis [8]. The discrete wavelet transform in temporal and spatial domain was successfully applied with the vibration signal for the engine fault diagnosis of the diesel engine and the gearbox [8], [9]. The power spectrum analysis with high order, cepstrum analysis, and neural network approach were utilized for fault diagnosis and indication of some of the specific induction motors [10]. The power of signal analysis with less time consumption and low computational cost was conducted in a comparative study of LPG-modified engine and normal oil-usage engine [11], and also in a fault diagnosis of rolling element bearings [12]. The problems of gasoline-substitution with LPG boiling system installation cause some significant variation in vibration and sound signals of the modified engines [13]-[16]. Thereafter some analysis techniques of the vibration and sound signals were developed to differentiate between the LPG–modified engine and the conventional gasoline engine, subsequently some significant attributes were used to indicate the irregularities of the corresponding engines [17], [18]. Another study of vibration and sound signal analysis for a gasoline engine with LPG-installation and some specified fault simulations was investigated, LPG–installation and the specified faults concretely affected the engine efficiency degradations [19]-[21].

This study proposed an approach of vibration signal analysis for a personal gasoline-engine automobile while driving upon three types of road surfaces including paved road, concrete road, and gravel road as mentioned in the previous related studies [4]-[6]. Two core purposes are to compare the vibration affecting from driving upon three types of roads, and then to compare the vibration at three different areas of sensor positions. The Fast Fourier Transform is adopted to extract the signal spectrum and the corresponding features [11], [20]-[22].

MATERIAL AND METHODS

In this section, the road surface types selected in the experiment has been explained. The experimental procedure has been illustrated step by step. Finally the experimental setups have been therefore presented.

Road Surface Types

Almost all road surfaces in Thailand include three main types of paved road, concrete road, and gravel road. Their attributes are concluded as follows.

1. Gravel Road, this type of road surface is abundant in rural areas of the Thailand. It does not require frequent maintenance as long as its surface is still smooth. However, its major disadvantage is the existing dust that occurs during its usage.

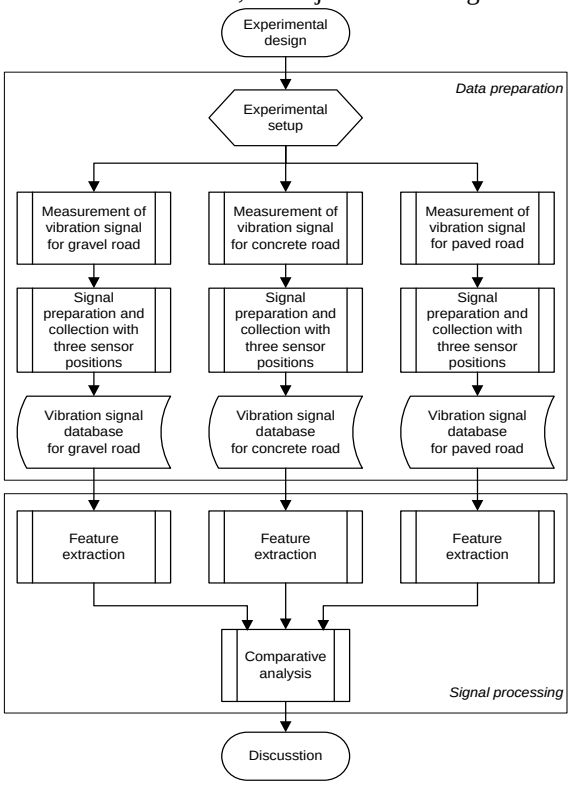

Fig. 1 Experimental Procedure.

2. Concrete Road, this type of road takes a long time to build and has high construction costs with high durability.

3. Paved road, this type of road is considered a road that has both advantages and disadvantages. Asphalt is commonly used in this road type construction. Its advantage is its inexpensive quick-time construction, however some disadvantages are still existing. For example, spray water asphalt to coat the road surface is needed while broken surface is detected.

Experimental Procedure

In this study, the experiment procedure comprises of data preparation and signal processing sub-procedures as illustrated in Fig. 1. At the data preparation stage, the experimental setup has been conducted at the beginning. Thereafter, the measurement of vibration signal of the experiment automobile for all three types of road surfaces has

been performed. Subsequently, the signal preparation and collection has been conducted to construct the signal database for three positions of sensors inside the passenger room; the right-front seat surface, the left-front seat surface, and the rear seat surface. The signal database consists of all scenarios of car speeds including 0, 10, 15, 20, 25, and 20 km/h, respectively.

At the data preparation stage, signal feature extraction has been inaugurated. Fast Fourier transform of the initially-provided signal has been applied to obtain its corresponding frequency spectrum. Monitoring the frequency spectrum brings about some frequencies at the dominant peak points and their corresponding amplitudes. These highest peaks are assumed to represent the important components of the vibration signal inherited from movement of the automobile. These features are averaged among all collected samples and therefore analyzed comparatively. At the end of this stage, the discussion of this study has been done and summarized.

Experimental Setups

In the experiments, the specimen automobile is a personal gasoline engine car of Mazda-2 model with 1,499-cc cylinder volume, Skyactiv-D, 4 cylinders, and 16 valves. The vibration sensors and their complementary parts, NI9234 card for interfacing with computer, and a computer for signal processing are provided. The interface of NI9234 card, and installation locations of vibration sensors are illustrated in Fig. 2.

EXPERIMENTAL RESULTS

In the signal analysis, FFT the efficient tool of frequency spectrum extraction has been selected to determine frequency components of the collected vibration signals in the databases. The most dominant frequencies emerging peak along the frequency spectrum at six different engine speeds are extracted.

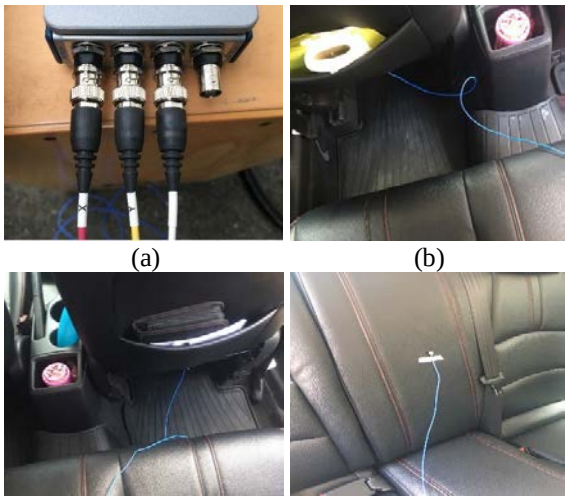

(a) (b)

(c) (d)

Fig. 2 Experimental setups: (a) interface of NI9234 card, and installation locations of vibration sensors; (b) the left-front seat surface, (c) the right-front seat surface, and (d) the rear seat surface.

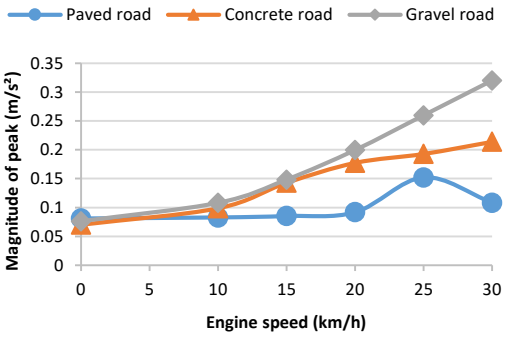

Fig. 3 The averaged magnitude of emerging peak of frequency spectrum of the vibration signal measured at the left-front seat surface at different engine speeds.

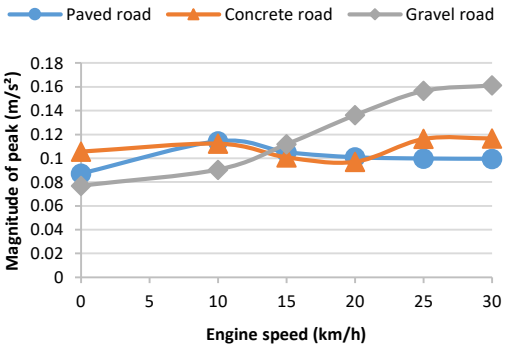

Fig. 4 The averaged magnitude of emerging peak of frequency spectrum of the vibration signal measured at the left-front seat surface at different engine speeds.

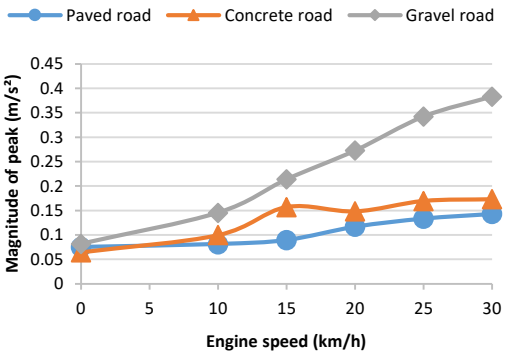

Fig. 5 The averaged magnitude of emerging peak of frequency spectrum of the vibration signal

measured at the rear seat surface at different engine speeds.

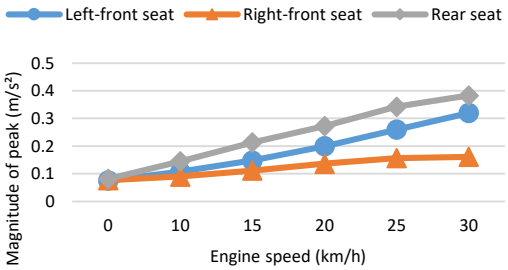

Fig. 6 The averaged magnitude of emerging peak of frequency spectrum of the gravel road at different engine speeds.

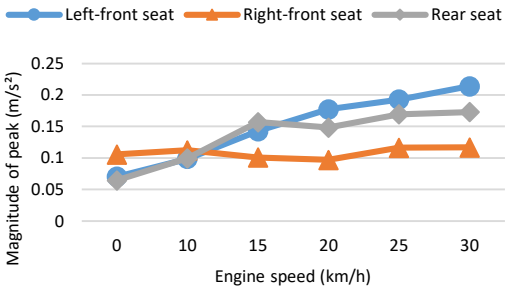

Fig. 7 The averaged magnitude of emerging peak of frequency spectrum of the concrete road at different engine speeds.

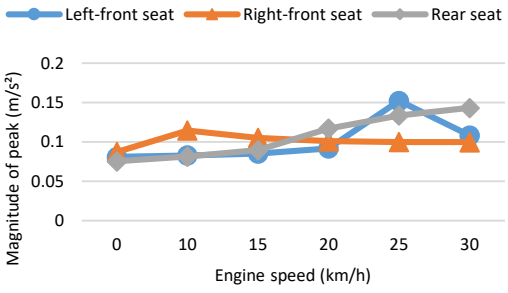

Fig. 8 The averaged magnitude of emerging peak of frequency spectrum of the paved road at different engine speeds.

The plotting of the averaged magnitude of emerging peak of frequency spectrum has been performed along the different engine speeds. Three lines in each figure represent the characteristics of three types of roads including paved road, concrete road, and gravel road, respectively. These plots have been conducted for all three installation locations of vibration sensors.

From Fig. 3 with focusing at the left-front seat, the averaged magnitude of emerging peak of frequency spectrum of the vibration signal increases while the engine speed is being raised. The gravel road reflects the highest impact to the averaged magnitude when comparing with the others, meanwhile the paved road shows the least vibration magnitude. Furthermore, it can be observed that the magnitudes of the FFT for all road surface scenarios at the low engine speeds of 0 and 10 km/h are quite not different.

From Fig. 4 with focusing at the right-front seat, the averaged magnitude of emerging peak of frequency spectrum of the vibration signal increases while the engine speed is being raised as same as that of the left-front seat depicted in Fig. 3. The paved road and the concrete road are quite similar to each other especially at the engine speed under 15 km/h.

From Fig. 5 with focusing at the rear seat, the averaged magnitude of emerging peak of frequency spectrum of the vibration signal has the same movement along the engine speed axis as those of the left-front seat surface and the right-front seat surface illustrated in Figs. 3 and 4, respectively.

From Fig. 6 with focusing the gravel road, the averaged magnitude of emerging peak of frequency spectrum of the vibration signal increases while the engine speed is being raised for all of the vibration at all sensor locations. The rear seat gives the highest impact to the averaged magnitude when comparing with the others, meanwhile the right-front seat gives the least vibration magnitude.

From Fig. 7 with focusing the concrete road, the trends of all averaged are as same as those of the gravel road in Fig. 6. However it has been noticed that the left-front seat rises from the second highest to the top highest impact for the engine speeds over 20 km/h.

From Fig. 8 with focusing the paved road, the trends of all averaged are as same as those of the gravel road in Fig. 6.

CONCLUSIONS

An analysis of vibration signals measured inside a gasoline-engine automobile of Mazda-2 model driving upon three types of roads has been presented. The installation of vibration sensors are at the driver's seat surface, the left-front seat surface, and the rear seat surface. The frequency spectrum of FFT is used to extract a number of peaks where the dominant frequencies is located. The averaged magnitude of emerging peak for six engine speeds ranging from 0-30 km/h are calculated. Comparing among three types of roads, the experimental results confirm that the highest peak values are mostly of the gravel road, meanwhile the lowest peak values are of the paved road. Comparing among three locations of vibration sensors, the explicit results can be strongly concluded as follows. In cases of paved road and gravel road, the highest peak values are of the rear seat surface,

moreover in case of concrete road, the highest peak values are of the left-front seat surface. Summarily, this study concludes that the proposed analysis technique of vibration signals can be used to differentiate the signal features of all scenarios of a personal gasoline-engine car while driving upon three types of roads. In the future study, the other associated signal processing techniques should be developed to approach more efficient identification of all scenarios or automobile condition diagnosis.

ACKNOWLEDGMENTS

The research was sponsored by Kasetsart University, Faculty of Engineering at Sriracha. The instruments were supported by the Mechanical Syetem and Signal Processing research group.

REFERENCES

[1] Novikov A., Novikov I., Shevtsova A., Study of the impact of type and condition of the road surface on parameters of signalized intersection, Transportation Research Procedia, Vol. 36, 2018, pp. 548-555.

[2] Hu H., Zhong Z., Explicit–Implicit Co-Simulation Techniques for Dynamic Responses of a Passenger Car on Arbitrary Road Surfaces, Engineering, Vol. 5, Issue 6, 2019, pp. 1171-1178.

[3] Czech K. R., The Impact of the Type and Technical Condition of Road Surface on the Level of Traffic-Generated Vibrations Propagated to the Environment, Procedia Engineering, Vol. 143, 2016, pp. 1358-1367.

[4] Huang Y. and Li D., Subjective discomfort model of the micro commercial vehicle vibration over different road conditions, Applied Acoustics, Vol. 145, 2019, pp. 385-392.

[5] Litak G., Borowiec M., Friswell M. I., Szabelski K., Chaotic vibration of a quarter-car model excited by the road surface profile, Communications in Nonlinear Science and Numerical Simulation, Vol. 13, Issue 7, 2008, pp. 1373-1383.

[6] Blekhman I., Kremer E., Vibrational resistance to vehicle motion due to road unevenness, Journal of Sound and Vibration, Vol. 405, 2017, pp. 306-313.

[7] Yujun L., Peter W. T., Xin Y., Jianguo Y., EMD-based fault diagnosis for abnormal clearance between contacting components in a diesel engine, Mechanical Systems and Signal Processing, Vol. 24, Issue 1, 2010, pp.193–210.

[8] Xia W., Changwen L., Fengrong B., Xiaoyang B., Kang S., Fault diagnosis of diesel engine based on adaptive wavelet packets and EEMD-fractal dimension. Mechanical Systems and Signal Processing, Vol. 41, Issue 1-2, 2013, pp. 581–597.

[9] Binqiang C., Zhousuo Z., Chuang S., Bing L., Yanyang Z., Zhengjia H., Fault feature extraction of gearbox by using over complete rational dilation discrete wavelet transform on signals measured from vibration sensors. Mechanical Systems and Signal Processing, Vol. 33, Issue 11, 2012, pp. 275–298.

[10] Liang B., Iwnicki S. D., Zhao Y., Application of power spectrum, cepstrum, higher order spectrum and neural network analyses for induction motor fault diagnosis. Mechanical Systems and Signal Processing, Vol. 39, Issue 1-2, 2013, pp. 342–360.

[11] Chomphan S., Chaimanatsakun A., Sakornsin R., Khumneungratavongsa S., Rattanarat K., A Comparative Study of LPG-modified Engine and Normal Oil-usage Engine. in Proc. Int. Conf. On Engineering and Applied Sciences, 2016, pp. 219-225.

[12] Akhand R., Upadhyay S. H., A review on signal processing techniques utilized in the fault diagnosis of rolling element bearings, Tribology International, Vol. 96, Issue 4, 2016, pp. 289-306.

[13] Ahmad T. A., Barat G., Teymour T. H., Seyed S.M., Vibration analysis of a diesel engine using biodiesel and petro diesel fuel blends, Fuel, Vol. 102, Issue 12, 2012, pp. 414–422.

[14] Zunmin G, Jin C., Barry H., Analysis of engine vibration and design of an applicable diagnosing approach. International Journal of Mechanical Sciences, Vol. 45, Issue 8, 2003, pp. 1391–1410.

[15] Xianhua L., Randall R. B., Jerome A., Blind separation of internal combustion engine vibration signals by a deflation method. Mechanical Systems and Signal Processing, Vol. 22, Issue 5, 2008, pp.1082–1091.

[16] Xianhua L., Randall R. B., Blind source separation of internal combustion engine piston slap from other measured vibration signals. Mechanical Systems and Signal Processing, Vol. 19, Issue 6, 2005, pp. 1196–1208.

[17] Zbigniew S., Jan W., Application of vibration signals in the diagnosis of combustion engines – exploitation practices. Journal of KONES Powertrain and Transport, Vol. 18, Issue 3, 2011, pp. 405-412.

[18] Carlucci A. P., Chiara F. F., Laforgia D., Analysis of the relation between injection parameter variation and block vibration of an internal combustion diesel engine. Journal of Sound and Vibration, Vol. 295, Issues 1–2, 2006, pp. 141–164

[19] Boonsit S., Chomphan S., Vibration Signal Analysis for LPG-modified Engine and Normal Oil-usage Engine with Different Engine Speeds and Faults. in Proc. International Congress on Engineering and Information, 2017, pp. 102-107.

[20] Chomphan S., Vibration Signal Analysis of A

Motorcycle, International Journal of GEOMATE, Vol.16, Issue 56, 2019, pp. 27-32.

[21] Chomphan S., Kingrattanaset T., Boonsit S., Signal Analysis for LPG-modified Gasoline Engine with Engine Faults, International Journal of GEOMATE, Vol.16, Issue 56, 2019, pp. 65-72.

[22] Chomphan S. and Wongchai B., Correlation Analysis Of Vibration And Sound Signals Of A Gasoline-Engine Car, International Journal of GEOMATE, Vol.18, Issue 67, 2020, pp. 195-201.

6th Int. Conf. on Structure, Engineering & Environment (SEE), Kyoto, Japan, Nov.18-20, 2020, ISBN: 978-4-909106056 C3051

STUDY ON RIVER PATROL USING IMAGES CAPTURED BY DRONES AND MACHINE LEARNING

Ryo Yahara[1], Koki Sakita[2], Satoshi Nishiyama[3], Tomohiro Shimono[4], Michinari Fujiki[5] and Tatsuya Chigira[6]
[1,2,3]Environmental and Life Science, Okayama University, Japan; [4,5,6] Kokusai Kogyo Co., Ltd., Japan

ABSTRACT

Owing to the frequent occurrence of heavy rainfall in recent years, river patrols are increasingly crucial for evaluating local situations to prevent large-scale disasters, such as bank breaks. Qualitative anomalies are grasped visually by personnel, and a large amount of effort is spent on patrolling long dikes. In this study, we used aerial images captured by drones. We aim to quantify abnormalities in rivers during river patrols and reduce the burden on staff. We also investigated a method that can automatically extract abnormal points from captured images by object detection using local binary pattern features. The features described in the river patrol could be identified from the images captured by the drone, enhancing the practicality of river patrols. Regarding automatic extraction, we were able to sort out the differences in results based on shooting conditions and machine learning process and obtain results for the future for automatic extraction.

Keywords: Machine learning, Object detection, Local binary pattern (LBP), River patrol

INTRODUCTION

In recent years, occurrence of heavy rainfall and strong typhoons has become frequent in Japan, resulting sequential flooding of rivers. Therefore, river patrol to grasp the local situation is becoming more important for preventing large-scale disasters such as bank breaks. However, the inspection method for river patrols has been carried out as before, and the qualitative abnormality can be grasped visually by the patrol staff. In addition, much effort is spent on patrols of long dikes. Therefore, in this study, we focused on drones as a measure to reduce the burden on staff in river patrol operations and to prevent oversight. Drones are used as an efficiency method in various fields, such as bridge inspection and collection of agricultural crop growth information [1]-[5]. However, there is no example that it is applied to river patrol, and this study verified whether the efficiency improvement of the work by drone can be applied to river patrol. First, we verified how high the height of an image taken by a drone equipped with a camera could be to visually confirm the features. In addition, we also verified the method of automatically extracting abnormal points by using object detection by machine learning. A study on the efficiency of quality inspection and facility inspection using machine learning has also been reported [6]-[8]. However, there is no example applied to river patrol work. LBP features are used as features. The method proposed by Ojala et. al. [9] has the advantage that it is robust against changes in brightness and requires a small amount of calculation, and is still widely used as a feature amount. [10]-[12]

In this paper, we analyze the accuracy of the captured images depending on the shooting conditions and the relationship between this feature amount and the output of machine learning, and consider the practicality of river patrol using the drone captured images.

RIVER PATROL

In river maintenance, it is very important to detect abnormal points at an early stage, and it is essential to grasp river conditions on a daily basis. In Japan, “river inspection” and “river patrol” are performed as a means to understand the situation of a river and its peripheral equipment. River inspections are conducted approximately twice a year to have detailed understanding on the conditions of rivers. Conversely, river patrol, which is the aim of this research to improve the efficiency of this technique, is performed approximately twice a week to understand the river situation generally and detect abnormalities.

According to Standards established by the Ministry of Land, Infrastructure, Transport and Tourism (Ministry of Land, Infrastructure, Transport and Tourism River Bureau, May 2011), the river patrol covers the following four topics:

(1) Discovery of illegal acts in river areas
(2) Grasping the status of river management facilities and maintenance of permitted works
(3) Collecting information on the use of river space

(4) Collecting information regarding the natural environment of rivers.

Currently, river patrols are mainly performed visually using patrol vehicles, and workers monitor and record the data on field and peruse the acquired data at offices. Additionally, areas that are difficult for vehicles to enter, such as river banks, are assessed by walking. Evidently, observing a vast river space visually is laborious and time consuming.

MACHINE LEARNING

Machine learning is a technology that allows a computer to have a learning mechanism similar to humans; unknown data can be predicted by learning features, regularity, and patterns from previous data. With machine learning image recognition, voice analysis, class classification, regression, clustering, etc., can be realized. In this method, a human must specify a feature amount, and the machine must learn the feature amount.

Deep learning is one of the machine learning methods (Fig. 1), and it is used in many studies because of its high performance [13],[14]. Deep learning technique is based on neural networks, which are systems that can imitate the mechanism of human nerve cells. By using neural networks in multiple layers, the step-by-step features contained in the data can be learned. When a large amount of images, text, and audio data is input into a multi-layered neural network, the computer automatically learns the features contained in the data in each layer. One of the merits of deep learning is that the accuracy is improved by the machine automatically selecting the feature amount that should be originally performed by humans. However, since humans cannot adjust small parts such as parameter adjustment, the contents become a black box, and it is difficult to understand the process leading to the result. Therefore, in this study, we conducted a study on machine learning, which is a basic study for deep learning, and examined how factors such as shooting conditions and feature quantities affect.

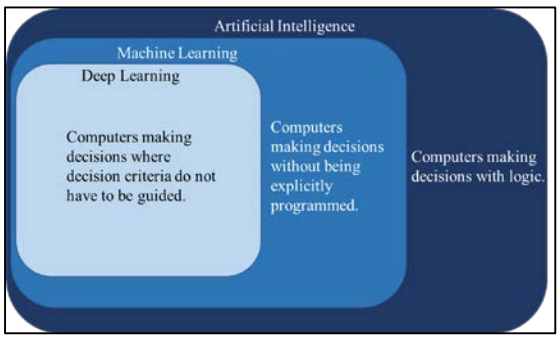

Fig. 1 Machine learning conceptual diagram

Object Detection

We used object detection, which is a part of machine learning, as a method for automatic extraction of abnormal points during a river patrol. Object detection is a method of automatically distinguishing a target object comprised in an image from a background and categorizing this object. Further, by using the rectangular search window, even if the image comprises a plurality of target objects, their positions can be located and their classification can be identified. In this study, “Traincascade,” which is one of the functions in OpenCV, is used as a method to develop a detector for object detection. The procedure can be divided into two phases, learning and recognition phases. In the learning phase, training data are fed to the machine, and the features are repeatedly learned. Meanwhile, in the recognition phase, the computer determines whether the learned object is included in the input image.

Learning Phase

In the learning phase, the properties and characteristics of the target object are learned from the pixel data of the image, which is the training data. Hence, providing assessments based on rules is possible even for data. In this study, the target object was manually extracted from the images captured by the drone at altitudes of 37, 74, and 110 m as training data, and the machine was made to learn the number of correct images (i.e., images containing the target object)(Fig.2). We also verified the difference in accuracy depending on the number of training data. The maximum number of learning images is 2000 for correct images and 2000 for incorrect images (i.e., images that do not include the target object).

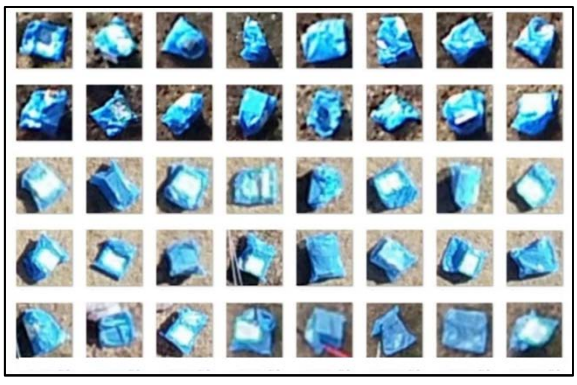

Fig. 2 Garbage bag training data

Detection Phase

In the recognition phase, a new input image that is not used in learning is converted into feature quantity data by using the same procedure used in the

learning phase. The target area is identified based on characteristics that have been input and learned, and the judgment criteria on whether the target area is the detection target or the non-detection target (Fig.3).

Fig. 3 Search in object detection

Learning Algorithm

The learning algorithm is a type of ensemble learning called “AdaBoost.” In summary, ensemble learning is a method of taking a majority vote. And It is a method for improving the prediction ability for unlearned data by merging those learned as separate learners. is there. In AdaBoost, multiple weak classifiers are sequentially applied to the training data, and it is determined whether or not each is correct.(Fig.4) At this time, it is a mechanism for making adjustment by increasing the weight for the incorrectly classified sample or, conversely, reducing the weight for the correct sample.

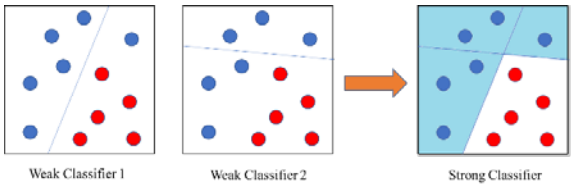

Fig. 4 Theory of Adaboost

LOCAL BINARY PATTERN FEATURES

In the learning phase, it is necessary for the machine to learn a large number of images. However, as the images are fed to the machine as a sequence of meaningless numbers, they should be converted into meaningful data representing the features of the image and then extracted. Therefore, in this study, local binary pattern (LBP) features are adopted as the ones to be converted. LBP features are the local representation of the image, and each pixel is compared with the surrounding neighboring pixels. They are composed of relative values and has the characteristics of low calculation cost and robustness against changes in terms of image brightness.

LBP Feature Process

The specific method for extracting LBP features is as follows. First, the image given as training data is converted into gray scale and the image is segmented. One part of the image is taken, paying attention to 3 × 3 pixels (Fig.5).

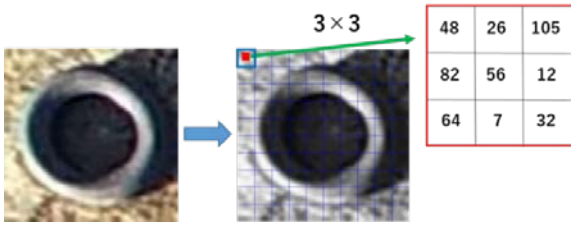

Fig. 5 Extraction of local pixels

The central pixel of this local area is converted into binary form. The difference between that pixel value and the surrounding eight pixels is considered. If the brightness value of the surrounding pixels is higher (if the difference in the brightness values is positive), then the value of the surrounding pixels is set to 1, and if it is low (if the difference is negative), then the value of the surrounding pixels is set to 0. In this manner, when 8 pixels surrounding the central pixel are selected as peripheral pixels, the LBP value of the central pixel is represented by 8 bits. A weight of 2^i (i = 0,...,7) is assigned in a clockwise direction from the upper left side of the center pixel(Fig.6).

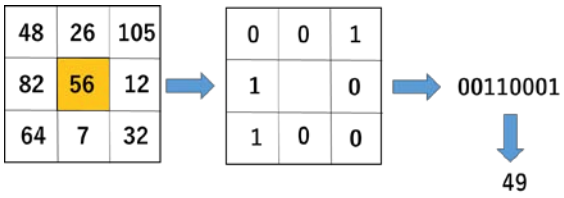

Fig. 6 Convert to binary

If this calculation is performed for the complete mesh, a collection of one block of binary data is obtained. This collection of binary data is a histogram of one part.

When this operation is performed for all pixels, a collection of histograms is obtained, which is the LBP feature quantity (Fig.7).

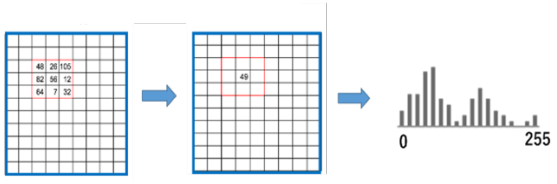

Fig. 7 LBP feature extraction

EVALUATION METHOD

The detection accuracy is evaluated using three indices: recall rate, precision rate and F value. Each evaluation method will be described using the following four types of detection patterns.
(1) TP: The number of objects that actually exist and correctly judged by the detector
(2) FP: The number of objects mistakenly determined to be an object other than the object
(3) FN: The number of objects that the detector mistakenly determined not to be the object although it is actually the object
(4) TN: The number of objects other than the object that are judged not to be the object

Recall refers to the ratio of the number of correctly determined objects to the number of actually existing objects. That is, if the recall is low, the rate at which objects are actually detected but not detected (missing rate) is high. It can be calculated using the following formula:

$$\textbf{recall rate} = \frac{TP}{TP + FN} \quad (1)$$

Precision is an index that evaluates the accuracy of the detector and indicates the ratio of the number of detection frames that have been judged to be correct by the detector and are actually judged correctly to the output detection frames. That is, if the matching rate is low, the rate at which the detector determines that the target object is included (erroneous detection rate) is high even though it is not actually the target object. It can be calculated using the following formula:

$$\textbf{precision rate} = \frac{TP}{TP + FP} \quad (2)$$

The F value is an index showing the balance between recall and precision and is a value calculated by the harmonic mean of recall and precision. It is calculated using the following formula:

$$\textbf{F Value} = \frac{2 \times \textbf{recall rate} \times \textbf{precision rate}}{\textbf{ecall rate} + \textbf{precision rate}} \quad (3)$$

EXPERIMENTAL OUTLINE AND RESULT

The drone uses a DJI Phantom 4 in terms of versatility and was installed with a digital camera with 20 million pixels and an aperture value of 5.6 from altitudes of about 40, 70, and 110 m. Additionally, to perform verification based on the difference in illuminance, we changed the shooting time and shot under an illuminance of approximately 25,000 Lux and 3000 Lux. This study aims to detect illegally dumped materials in rivers by using drones. Hence, garbage bags, bicycles, tires, PET bottles and bat were placed in the river as objects to be photographed. Figure 8 is an example of an image of a garbage bag. As shown in the figure, the feature amount of the subject in the image changes depending on the altitude and illuminance.

In this study, we examined the practicality of river patrolling via drone photography by organizing the differences in feature quantities depending on the shooting conditions of these images and the relationship between this feature quantity and the output of machine learning.

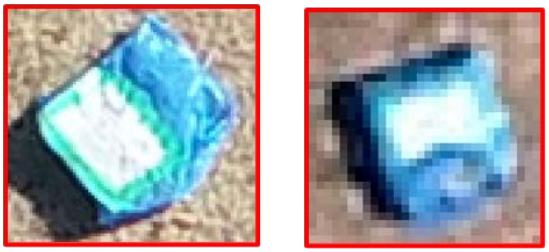

Fig.8 Left: Altitude about 40 m, illuminance 25000 Lux. Right: Altitude about 100 m, illuminance 25000 Lux

Practicality of Drone Photography for River Patrol

Figure 9 shows a shooting example of this verification. Each image shows the condition of the revetment, crotovine, and vegetation described in the river patrol item for each altitude (37m, 74m, 110m).

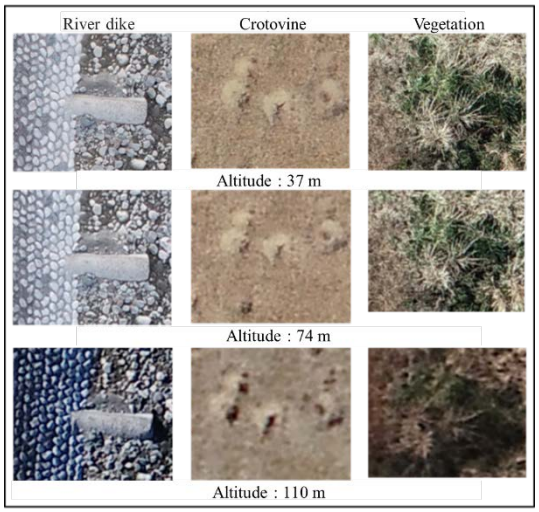

Fig. 9 Shooting case

Difference in F Value Owing to the Difference in the Number of Training data

Figure 10 shows the relationship between the number of pieces of training data and the F value.In this verification, the detection results were compared between a case where object detection was performed

using only the learning images that could be collected in 2 days of image shooting and a case where the number of learning images was increased by rotating or reversing the images. The initial number is the number that can be collected in 2 days of image shooting, and the initial number of each feature is shown in Table 1. The shooting altitude of the verification image is 37 m, and the number of incorrect images is 2000.

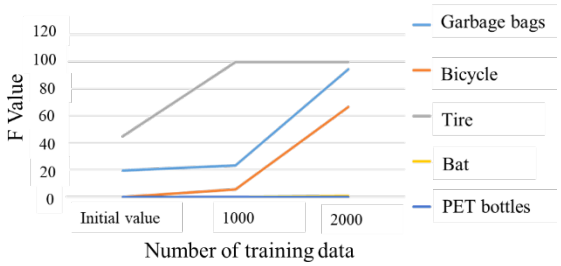

Fig. 10 Difference in F value owing to the difference in the number of training data

Table 1 Initial value of training data

Garbage bag	Bicycle	Tire	Bat	PET bottle
800	150	50	200	50

Difference in F Value Depending on the Shooting Altitude

Figure 11 shows the F value for each photographing altitude. The Value when shooting the dust bag was 19.42% at an altitude of about 40 m and 6.70% at an altitude of about 70 m.

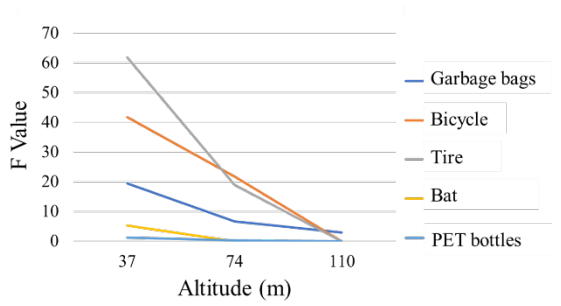

Fig. 11 Difference in F value depending on the shooting altitude

Difference in F value depending on shooting illuminance

Figure 12 shows the relationship between the shooting illuminance and the F value. The illuminance when shooting from 8:46 to 8:52 is about 25000 Lux, and the illuminance when shooting from 15:39 to 15:46 is about 3000 Lux. Verification was performed at a shooting altitude of 37 m. Regarding the garbage bags, the F value is 32.77 % at an illuminance of 25000 Lux and 22.91 % at 3000 Lux.

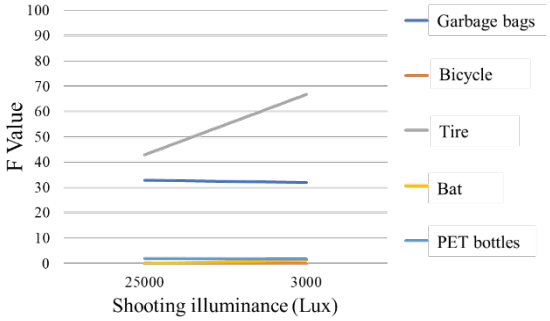

Fig. 12 Relationship between illuminance and F value

CONSIDERATION

In visual confirmation of features from images taken by drones, if the image is taken at an altitude of 74 m or less, it is possible to check the condition of the river dike, vegetation, and crotovine described in the patrol item. It is considered possible to improve the efficiency of the patrol of the river by appropriately using it according to the management level of the river. As the altitude increases, the shooting range becomes wider (Table 2), which leads to more efficiency. In the future, it will be necessary to examine the machine parameters in detail to obtain results at high altitudes.

Table 2 Relationship between altitude and shooting range

Altitude (m)	37	74	110
Shooting range (m^2)	37×56	74×111	110×165

We verified each factor regarding automatic extraction, and confirmed that the detection accuracy was improved by increasing the number of training data for garbage bags, bicycles, and tires. Since the task of creating training data is also labor-intensive, it will be necessary to verify the optimum number of training data for each objects and improve efficiency in the future.

Regarding the difference in F-value depending on the shooting altitude, it is considered that the F-value decreased due to the decrease in ground resolution accompanying the increase in altitude. As mentioned above, the higher the altitude, the more efficient it is. Therefore, it is necessary to proceed with the verification of the internal factors so that the object can be detected with high accuracy even with a small amount of features in the future.

Furthermore, the illuminance at the time of

shooting had less effect on the F value than the resolution. As shown in Fig. 13, in the LBP feature amount, the difference in the brightness is used by comparison with the surrounding pixels, and therefore the change in the brightness of the entire image is unlikely to affect. That is, the obtained feature amount data is hardly affected by the shooting time. Therefore, it is possible to perform river patrol operations without being bound by the time of day, which is expected to contribute to efficiency improvement.

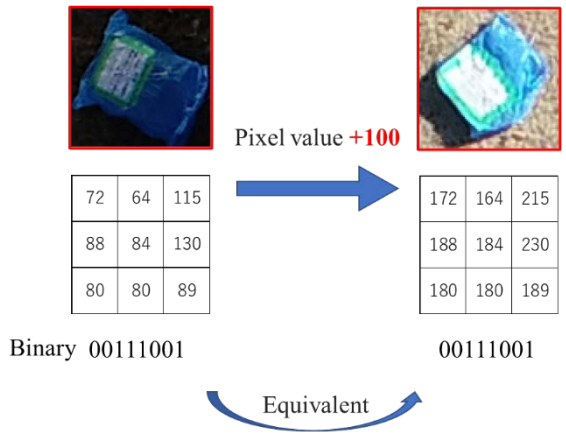

Fig. 13 Robustness of LBP features against illuminance changes

CONCLUSION

In this study, we aimed to establish a river patrol method using drone measurement for efficient river patrol, and attempted automatic detection of abnormal points using drone image and machine learning. The results obtained are summarized below.

・If it is 74m or less, We can visually check the features of the river patrol items from the aerial image.

・F-value improves as the number of training data increases

・F value decreases as altitude increases

・There is little effect of shooting illuminance

In the future, among the influential factors that are considered to affect the detection accuracy, not only external factors such as the shooting environment but also internal factors such as the creation method and number of training data, learning method, and results will be considered. We will examine in more detail how the parameters on the machine learning side, such as the threshold, affect detection accuracy, and proceed with research toward practical application.

REFERENCES

[1] Karim M. M., Dagli C. H., and Qin R., Modeling and Simulation of a Robotic Bridge Inspection System, Procedia Computer Science, Vol. 168, 2020, pp.177-185.

[2] Metni N. Hamel T. and Derkx F., A UAV for bridge's inspection: visual servoing control law with orientation limits, IFAC Proceedings Volumes, Vol. 37, Issue 8, 2004, pp. 454-459.

[3] Seo J. Duque L. Wacker J., Drone-enabled bridge inspection methodology and application, Automation in Construction, Vol. 94, 2018, pp. 112-126.

[4] Nakshmi J.V.N., Hemanth K.S., and Bharath J., Optimizing Quality and Outputs by Improving Variable Rate Prescriptions in Agriculture using UAVs Procedia Computer Science, Vol. 167, 2020, pp. 1981-1990.

[5] Wang X. Sun H. Long Y. Zheng L. Liu H. and Li M., Development of Visualization System for Agricultural UAV Crop Growth Information Collection, IFAC-PapersOnLine, Vol. 51, Issue 17,2018, pp. 631-636.

[6] Kuchi A. Hoque M.T., Abdelguerfi M. and Flanagin M.C., Machine learning applications in detecting sand boils from images, Array, Vol. 3–4, 2019, Article 100012.

[7] Li Y. Wang X. Zhao Z. Han S. and Liu Z., Lagoon water quality monitoring based on digital image analysis and machine learning estimators, Water Research, Vol. 172, 2020, Article 115471.

[8] Schmitt J. Bönig J. Borggräfe T. Beitinger G. and Deuse J., Predictive model-based quality inspection using Machine Learning and Edge Cloud Computing, Advanced Engineering Informatics, Vol. 45, 2020, Article 101101.

[9] Ojala T. Pietikäinen M. and Harwood D., A comparative study of texture measures with classification based on featured distributions Pattern Recognition, Vol. 29, Issue 1, 1996, pp 51-59.

[10] Lahiani H. and Neji M., Hand gesture recognition method based on HOG-LBP features for mobile devices, Procedia Computer Science, Vol. 126, 2018, pp 254-263.

[11] Mahale V. H., Ali M. M. H., Yannawar P. L., and Gaikwad A. T., Image Inconsistency Detection Using Local Binary Pattern (LBP), Procedia Computer Science, Vol. 115, 2017, pp 501-508.

[12] Smolka B. and Nurzynska K., Power LBP: A Novel Texture Operator for Smiling and Neutral Facial Display Classification, Procedia Computer Science, Vol. 51, 2015, pp 1555-1564.

[13] Fujiyoshi H. Hirakawa T. and Yamashita T., Deep learning-based image recognition for autonomous driving, IATSS Research, Vol. 43, Issue 4, 2019, pp 244-252

[14] Lundervold A. S., and Lundervold A., An overview of deep learning in medical imaging focusing on MRI, Zeitschrift für Medizinische Physik, Vol. 29, Issue 2, 2019, pp 102-127

6th Int. Conf. on Structure, Engineering & Environment (SEE), Kyoto, Japan, Nov.18-20, 2020, ISBN: 978-4-909106056 C3051

VERIFY THE PREDICTION OF SLOPE FAILURE BY SOIL CREEP WITH LABORATORY EXPERIMENTS

Makoto Fukuhara[1], Taro Uchimura[2] and Shanging Tao[3]
[1,2] Saitama University, Japan; [1,3] Chuokaihatsu Corporation, Japan

ABSTRACT

More than a thousand cases of rainfall-induced slope failure occur in Japan every year. Predict the slope failure is social needs. In this paper, we propose and verify a method to predict the instability of the slope surface layer by soil creep combined with the creep theory of metallic materials. To investigate the creep theory affected by soil moisture and deformation and to verify the relationship between creep and soil moisture, deformation, two kinds of laboratory experiment was conducted to simulate the process of rainfall induce slope failure, the first one was multi-layer shear model and the second one was the direct shear test. The soil moisture was controlled by artificial rainfall in the multi-layer shear model whereas water infiltrates in the direct shear test. The inverse number of velocity calculated by Fukuzono's equation and the surface displacement have been compared, the results show that the tendency of the change of the inverse number of velocity is similar in both model tests. The effect of volumetric water content on the displacement also has been confirmed, when the volumetric water content increased, the displacement trended to start increasing with an accelerated rate. From these results, the prediction of slope failure time can be improved with higher accuracy.

Keywords: Slope failure, Early warning, Soil creep, Shear deformation

INTRODUCTION

Rainfall-induced slope failure occurs commonly in Japan. Before the slope failure, the continuous slow movement of soil mass has been traditionally considered as soil creep[1]-[2], the time to slope failure can be predicted from the process of soil creep. So the prediction of the time to slope failure is very important for the countermeasures designed to avoid human losses and reduce the property damages from slope failure. Nowadays with the development of the technology, the mass movement can be easily monitored by means of simple wire extensometers[3], inclinometers[4], or tilt sensors[5]. Uchimura [6] has proposed a simple monitoring method for the early warning of rainfall-induced slope failure, the distinct behaviors of mass movement expressed by tilting angles at several sites can be detected in the pre-failure stages. The methods to predict the time of slope failure had been developed by many researchers [7],[8],[9],[10], they showed that the behavior of the soil creep is similar to the metal creep. In this paper, we focus on one of the methods, the Fukuzono's equation[8], to predict the instability of the slope surface layer.

To verify the accuracy of the prediction of the time to slope failure, two kinds of laboratory experiments were conducted to simulate the process of rainfall-induced slope failure. The inverse number of velocity calculated by Fukuzono's equation and the surface displacement have been compared and the effect of volumetric water content on the displacement also has been confirmed.

BEHAVIOR DURING SLOPE FAILURE

Deformation until failure

The creep can be explained by the time-dependent deformation of solids under constant stress. In general, three creep stages of movement are included in creep behavior before failure:

-Primary: strain rate decreases over time.
-Secondary: strain rate is constant.
-Tertiary: strain rate is rapidly increasing until failure.

In the case of soil failure (Fig.1), displacement rate increases at a constant at the secondary creep, and then increases rapidly at the tertiary creep, finally failure. The behavior of soil creep varies depending on conditions such as particle size, soil moisture, and slope angle, etc., the duration of tertiary creep may be different from sites. Metal creep is shown in Fig.2. It shows that the behavior of the soil creep (Fig.1) and metal creep is similar.

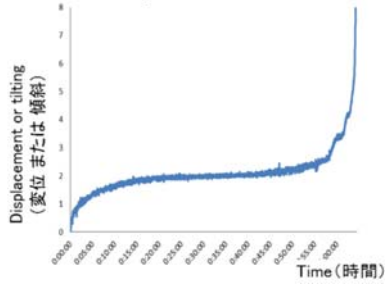

Fig. 1 Example of soil creep in slope failure

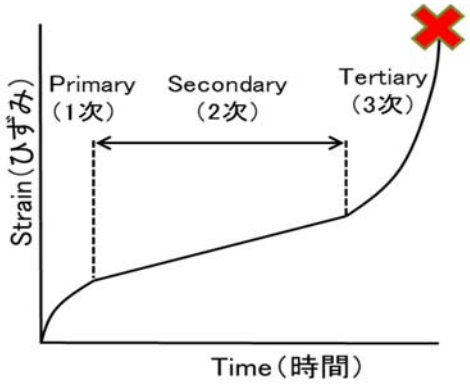

Fig. 2 Metal creep development model

The method of failure prediction

Fukuzono[8] found that rapid failure in the tertiary creep base on an experimental study of small scale slope model tests under monotonically increasing load, and proposed the following general expression:

【Fukuzono method】

$$\frac{1}{v} = \{a(\alpha-1)\}^{\frac{1}{\alpha-1}} \cdot (t_r - t)^{\frac{1}{\alpha-1}} \qquad (1)$$

Where v is **the velocity of the slope surface displacement,** t is current time, t_r is the estimating time to failure, a,α:constant.

In the case of $\alpha = 2$, Eq.1 can be expressed in terms of deformation, proposed by Saito[7]:

【Saito method】

$$\varepsilon = C \cdot \log\frac{(t_r - t_0)}{(t_r - t)} \qquad (2)$$

Where ε is strain, t_r is the estimating time to failure, t_0 is hte time at strain = 0, t is current time, C is constant.

Fig. 3 shows the typical figures of Fukuzono's method. The changes of the inverse number of velocity of surface displacement (1/v) are represented by y-axis and the elapsed time is represented by the x-axis. The failure time is defined by an intersection point which is extension of the dotted line to the x-axis .

This prediction method is verified by laboratory experiments that were conducted to simulate the process of rainfall-induced slope failure. Even if the results show complicate behavior of soil creep, but it is possible to predict the time to failure from the linear part corresponding to the tertiary creep.

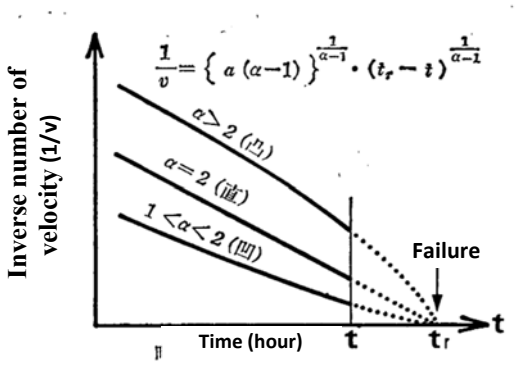

Fig. 3 Typical figures of the changes of the inverse number of velocity of surface displacement just before the failure. (after Fukuzono[8])

LABORATORY TEST METHOD

Properties of the test soils

In this study, two types of material were used in laboratory tests. The first one is mixed sand which is comprised of Silica sand No4, No5, No7, and No8 mixed with a ratio of 1:1:3:1. The other one is Silica No.7. The soil property is shown in Table 1 and the grain size distribution curve is shown in Fig. 4.

Table 1 Soil property of material

Soil property		Mixed Silica	Silica No.7
Relative density(Dr)	%	50	50
Dry density(ρd)	g/cm^3	1.481	1.340
Initial volumetric water content(θ)	%	7	7
Strength parameters(Φ)	Φ°	43.9	37.1
Strength parameters(C)	kN/m^2	7.4	28.6

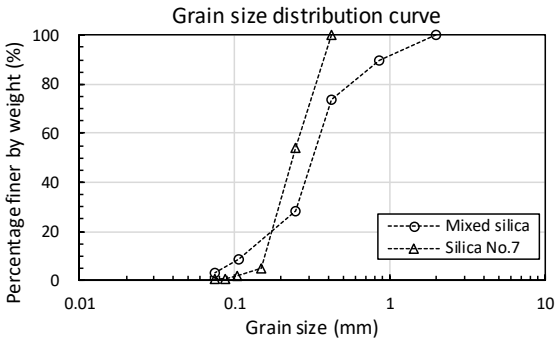

Fig. 4 Grain size distribution curve of test soil

Multi-layer shear model

Laboratory experiments were performed using a multi-shear model to simulate the process of rainfall-induced slope failure. The concept and the detail of the multi-shear model were summarized at [11]. It is a model including 20 frames with a total height of 1m. Every frame has a height of 0.05m, length of 0.6m, and width of 0.54m, the soil is filled in the frame. Wheels are setup at every frame to reduce friction. A constant horizontal force is applied on every interface between the layers by air cylinders to simulate the shear force corresponding to the slope angle. Load cells and displacement meters are also set at every layer. The artificial rainfall intensity is 60mm/h. Rainwater infiltrates into the top layer and drains out from the bottom. The volumetric water content is measured by the Soil moisture sensor EC-5. (Fig.5)

Direct shear test

Direct shear tests also are conducted to **simulate** the **slip surface** failure**.** Two layers are included. Every layer has a height of 0.035 m, length of 0.31m, and width of 0.21m. Vertical stress is applied by the upper layer; Constant horizontal force is applied by air cylinders. Water is infiltrated to the soil via ceramic disks which set up at the bottom (Fig.6).

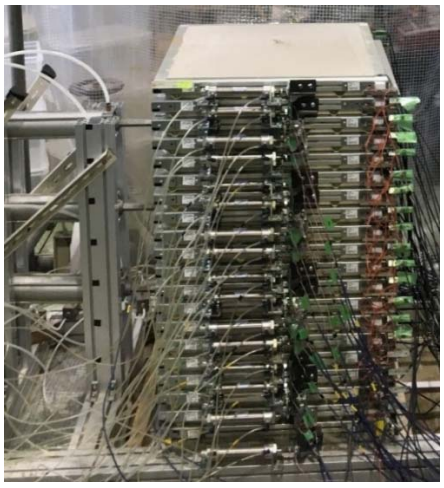

Fig. 5 Multi-layer shear model test apparatus

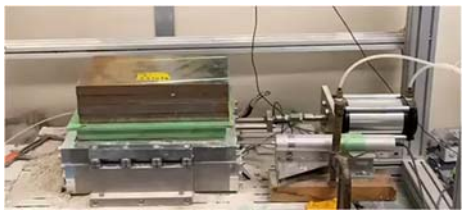

Fig. 6 Direct shear test apparatus

EFFECT OF DISPLACEMENT RATE ON PREDICTING THE TIME TO FAILURE

Results of multi-layer shear model test

The method of prediction the time to failure by the displacement rate has been studied at many slop surface using extensometers. However, the progress of ground deformation is not constant in the depth direction. In this study, laboratory experiments using multi-layer shear model can confirm the detailed displacements of a part of soil subdivided into many layers at the depth direction (Fig.7).

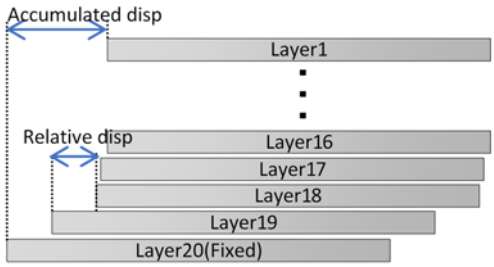

Fig. 7 Concept of displacement in multi-layer shear model test

The effect of the displacement rate on the time to failure was verified by multi-layer shear model tests. Fig. 8 shows the time history of the displacement in the test using silica No. 7. Fig. 8 a) shows the relative displacement of layer 19 and layer 18 are large, especially the displacement of layer 18 progresses rapidly after 0.1 hours, whereas the displacements of the other upper layers are small. Fig. 8 b) shows the accumulated displacement at to top layer, layer 19, and layer 18.

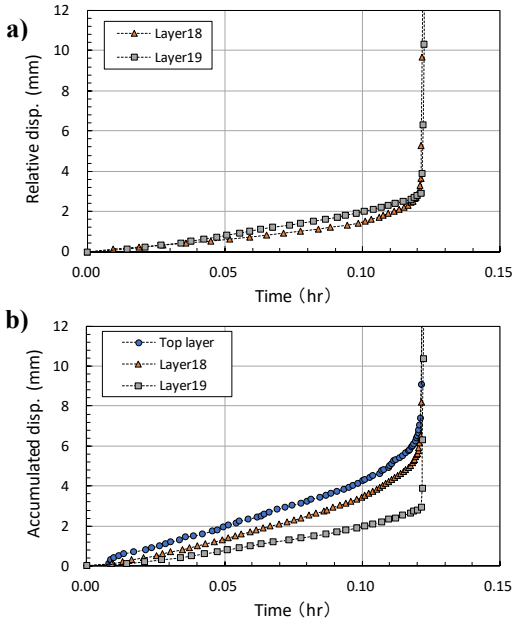

Fig. 8 Time history of displacement (Silica No. 7)

Application of failure prediction method

To obtain the time to failure, the following data were calculated by the prediction method (Eq.1).

- Accumulative displacement at the top layer (corresponding to the bottom layer).
- Relative displacement near the bottom (layer18 and 19) which shows particularly remarkable changes.

Fig. 9 shows the results of the time history of displacement and the inverse number of velocity at the multi-layer shear model. The time to failure obtained from the accumulative displacement of the top layer is 0.126 hour. The time calculated from the relative displacement is different, 0.122 hour at layer 18 and 0.144 hour at layer 19. The inverse number of velocity at layer 18 gradually increased from 0.1 hours, whereas at layer 19 did not change so much but increased rapidly before failure. It is observed that the inverse number of velocity at the top layer is the sum of the layer 18 and layer 19, so it is considered that the time to failure is the following relationship of the prediction method.

[Early] [Late]
Layer 18 → Surface layer → Layer 19

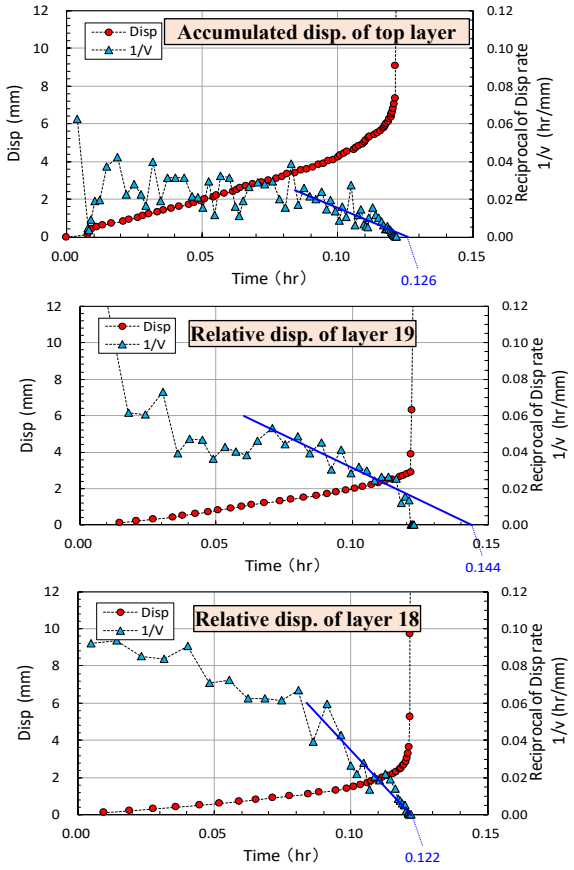

Fig. 9 Time history of displacement and the inverse number of velocity(Silica No. 7)

Fig. 10 shows the time history of displacement and the inverse number of velocity at direct shear test. In this case, the surface layer progresses slowly displacement, the time to failure which calculated by the prediction method was later than the actual time. Therefore, it is safe to predict the failure time using the layer which observed fast displacement to prevent damage due to failure.

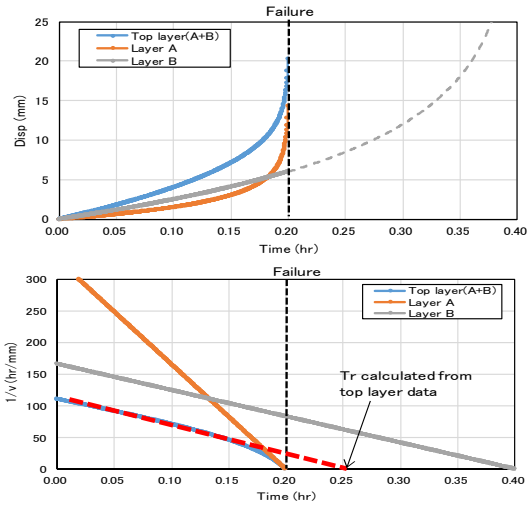

Fig. 10 Displacement and the inverse number of velocity at direct shear test

CHANGE IN DISPLACEMENT RATE DURING THE TERTIARY CREEP STAGE

Test results for each method

The method of prediction the time to failure is performed by the tertiary creep. The time to failure is obtained by plotting the time and the inverse number of velocity. In the secondary creep stage, the inverse number of velocity shows a large value because the displacement proceeds at a constant small speed. During the tertiary creep stage, the displacement increases at an accelerating rate, so the inverse number of velocity gradually decreases. In particular, when $\alpha = 2$, the inverse number of velocity becomes linear as shown in fig.3.

In this study, the effect of the displacement rate change in the tertiary creep stage was verified by direct shear test and multi-layer shear model test.

Results of direct shear test

Direct shear test was performed using the mixed Silica sand under the conditions shown in Table 2. Fig. 11 shows the time history of the displacement and the corresponding inverse number of velocity. According to the test results of case 1, the tertiary creep stage starts from 0.4 hour, the inverse number of velocity decreases from 0.4 hour and then accelerates from 0.6 hour, finally failure at 0.82 hour.

In case 2, the tertiary creep stage starts from 0.3

hour, the inverse number of velocity decreases from 0.3 hour and then accelerate from 0.4 hour, finally failure at 0.55 hour.

Results of multi-layer shear model test

Multi-layer shear model test (10 layers) was conducted using the mixed Silica sand, Fig. 12 shows the relationship of displacement and the inverse number of velocity in time series. the inverse number of velocity decreases from 2.4 hours, and accelerate decreases from 3 hours, showing the same tendency as the result of the direct shear test.

The effect of volumetric water content on displacement

The changes of inverse number of velocity(1/v) in the tertiary creep stage have been confirmed by both of direct shear test and multi-layer shear model test. The effect of volumetric water content on soil creep also has been investigated by both tests. In the multi-layer shear model test, artificial rainfall (60mm/h) was applied, and the rainwater infiltrated into the top layer. In the direct shear test, water was injected into soil from mode bottom. The following results show how volumetric water content affects the soil creep.

direct shear test

Fig.13 shows the relationship of the volumetric water content and the inverse number of velocity(1/v) in time series in the direct shear test. starts to increase at a constant rate after the supply of water from the time history. At the same timing that the volumetric water content starts to increase at an accelerated rate, the inverse number of velocity(1/v) also starts to decrease quickly.

multi-layer shear model test (10 layers)

Fig. 14 summarizes the results of multi-layer shear test. In this test, the volumetric water content at each layer was different depending on the time for water infiltration from the upper layer. The volumetric water content began to increase with the infiltration of rainwater from the upper layer, and changed at a constant rate from 1.4 hours, increased again from 2.6 hours. The slope of the inverse number of velocity(1/v) changed from 3 hours. The change timing is different from the result of the direct shear test. However, the timing of the accelerate of the inverse number of velocity(1/v) is the same when the volumetric water content increases to over 0.25.

discussion

Because the speed of water infiltration was different between the two kinds of laboratory experiments, the failure time also showed differently.

From these results, it is confirmed that in the tertiary creep stage, the slope of the inverse number of velocity(1/v) tended to increase rapidly when the water content rose high. This phenomenon may be considered that the increase of soil moisture leads to a decrease in soil matric suction, resulting in the weakening of soil strength.

In the direct shear test, the changes of inverse number of velocity(1/v) in the tertiary creep stage have been confirmed that it is the same results with the previous research [6]. Considering the uniform of the soil and the various physical properties of strata, it is possible to predict the time to failure more accurately by understanding not only the ground surface but also the deformation in ground.

Table 2 Test conditions of direct shear test

Case	Vertical pressure (kPa)	Horizontal pressure (kPa)	Water injection pressure (kPa)	Water injection speed (%/min)
1	7	6.7	0.3	0.41
2	7	7.5	0.15	0.59

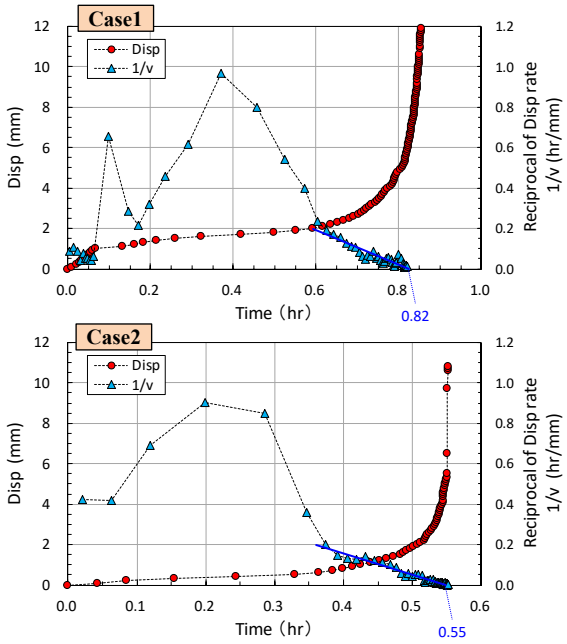

Fig. 11 Time history of displacement and the inverse number of velocity (Direct shear test)

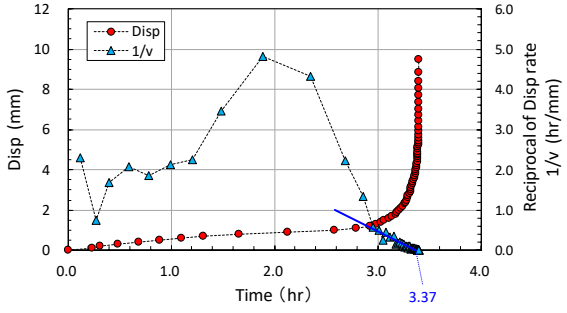

Fig. 12 Time history of displacement and the inverse number of velocity (Multi-layer shear model test(10 layers))

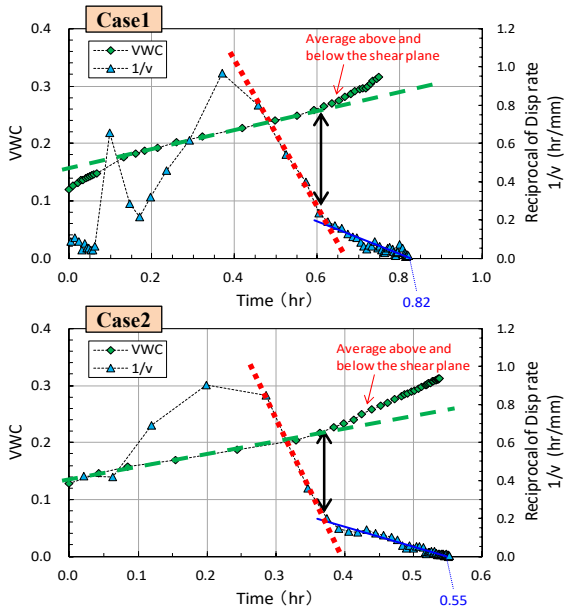

Fig. 13 Time history of VWC and displacement rate(1/v) (Direct shear test)

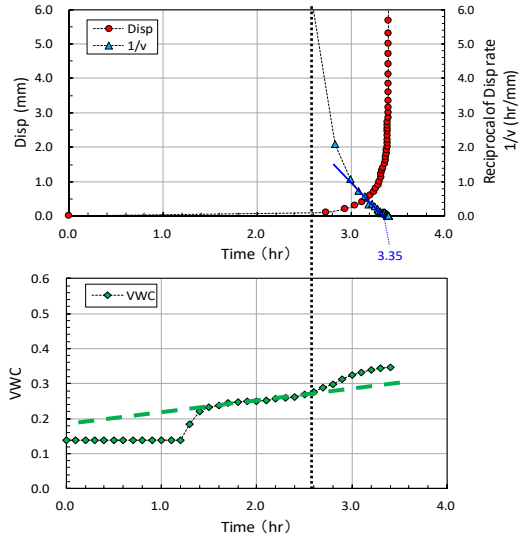

Fig. 14 Time history of VWC and displacement rate(1/v)(Multi-layer shear model(10 layers))

CONCLUSIONS

Two kinds of laboratory experiments were conducted to simulate the process of rainfall-induced slope failure. Predicting the time to failure using the inverse number of velocity calculated by Fukuzono's equation has been verified. The conclusion is summated as following:

- The method of prediction the time to failure time by the inverse number of velocity(1/v) in the tertiary creep stage has been confirmed that it was the same results as the previous research.
- The deformation tended to increase rapidly when the soil moisture increased to a high level.

Prediction of the time to failure can be possible to improve more accurately by understanding not only the ground surface but also the deformation in ground.

ACKNOWLEDGMENTS

This research was supported by Grant-in-Aid for JSPS Scientific Research (B).

REFERENCES

[1] Terzaghi, K. Mechanism of Landslides. In *Application of Geology to Engineering Practice*; Geological Society of America: New York, N. Y., 1950; pp. 83–123 ISBN 9780813759418.

[2] Varnes, D.J. Landslide Types and Processes. *Highw. Res. Board Spec. Rep.* 1978, 1–4, doi:Fact Sheet 2004-3072.

[3] Angeli, M.G.; Pasuto, A.; Silvano, S. A critical review of landslide monitoring experiences. *Eng. Geol.* 2000, *55*, 133–147, doi:10.1016/S0013-7952(99)00122-2.

[4] Lollino, G.; Arattano, M.; Cuccureddu, M. The use of the automatic inclinometric system for landslide early warning: The case of Cabella Ligure (North-Western Italy). *Phys. Chem. Earth* 2002, *27*, 1545–1550, doi:10.1016/S1474-7065(02)00175-4.

[5] Uchimura, T.; Towhata, I.; Anh, T.T.L.; Fukuda, J.; Bautista, C.J.B.; Wang, L.; Seko, I.; Uchida, T.; Matsuoka, A.; Ito, Y.; et al. Simple monitoring method for precaution of landslides watching tilting and water contents on slopes surface. *Landslides* 2010, *7*, 351–357, doi:10.1007/s10346-009-0178-z.

[6] Uchimura, T.; Towhata, I.; Wang, L.; Nishie, S.; Yamaguchi, H.; Seko, I.; Qiao, J. Precaution and early warning of surface failure of slopes using tilt sensors. *Soils Found.* 2015, *55*, 1086–1099, doi:10.1016/j.sandf.2015.09.010.

[7] Saito, M. Forecasting time of slope failure by tertiary creep. *Proc. 7th Int. Conf. soil Mech. Found. Eng.* 1969, *Mexico*, 677–683.

[8] Fukuzono, T. A Method to Predict the Time of Slope Failure Caused by Rainfall Using the Inverse Number of Velocity of Surface Displacement. *Landslides* 1985, *22*, 8-13_1, doi:10.3313/jls1964.22.2_8.

[9] Voight, B. A Relation to Describe Rate-Dependent Material Failure. *Science (80-.).* 1989, *243*, 200–203, doi:10.1126/science.243.4888.200.

[10] Federico, A.; Popescu, M.; Elia, G.; Fidelibus, C.; Internò, G.; Murianni, A. Prediction of time to slope failure: a general framework. *Environ. Earth Sci.* 2012, *66*, 245–256, doi:10.1007/s12665-011-1231-5.

[11] Tao, S.; Uchimura, T.; Fukuhara, M.; Tang, J.; Chen, Y.; Huang, D. Evaluation of Soil Moisture and Shear Deformation Based on Compression Wave Velocities in a Shallow Slope Surface Layer. *Sensors* 2019, *19*, 3406, doi:10.3390/s19153406.

6th Int. Conf. on Structure, Engineering & Environment (SEE), Kyoto, Japan, Nov.18-20, 2020, ISBN: 978-4-909106056 C3051

ARCHITECTURAL PHOTOGRAMMETRY: A LOW-COST IMAGE ACQUISITION METHOD IN DOCUMENTING BUILT ENVIRONMENT

Yohannes FIRZAL
Faculty of Engineering, Universitas Riau, Indonesia

ABSTRACT

Architectural photogrammetry, as a digital survey method requires photographic images that have produced by using a precision camera. This method in the particular the close-range photogrammetry has found more effectively used compare to other techniques such as laser scanning. This paper has aimed to show that the close-range photogrammetry is as a practical way and low-cost image acquisition in architectural projects. By applying a sequential two-step process method, capturing images in the field and using photogrammetry software has conducted to generate from the point cloud to the architectural model. This model shows at a high level of accuracy detail from a part of the *Sewu* temple Indonesia where this research has conducted. Thus, this research concludes that using architectural photogrammetry is not only to obtain accuracy detail of architecture object in complex nature but also as a low cost and effective methods.

Keywords: Architectural Photogrammetry, Photographic Image, Acquisition, Software

INTRODUCTION

Photogrammetry is known as a digital image processing method in orthoimages and image mosaics. Photogrammetry has mostly used in the field of archaeology [1]. However, today's photogrammetry has widely recognized as an alternative low-cost solution in the image processing [2] compare to laser scanning method [3]. Photogrammetry has applied in various disciplines [4] such as geoscience [5], structural engineering [6], zooarchaeology [7], heritage documentation [8] [9], archaeology [10], buildings inspection [11] and architectural representation [12].

There are groups of kinds in photogrammetry. One of them is known as close-range photogrammetry (CRP). The CRP has adopted from the aerial photogrammetry. This adaptation has aimed to fit with a specific field such as architecture [13]. The adoption of this CRP gives a new possibility in the digital image processing by using less equipment. At least, CRP requires a camera, personal computer and scale bar to obtain a 3D image [14]. The application of CRP in architecture is a non-intrusive technique in documenting and producing a 3D model. Conventionally, the documenting and 3D image have collected from 2D technics such as sketch, mechanical drawing that is following up to vector and massing software.

In contrast, the photogrammetry sequentially generates serial images to points cloud that can conduct in fast and accurate detail of the 3D object. As digitally formed, a virtual model of CRP represents not only existing built forms but also possible used in the process of designing and reconstructing of the built form. Therefore, photogrammetry becomes an effective tool and a low-cost method [15]. Photogrammetry is not to change the role of an architect, but a means in helping to present the architecture [16].

METHODS

The method in photogrammetry has organized in sequential steps. In this paper, close-range photogrammetry has conducted in a two-step process. The first step is capturing photographic images from various angles by using a DSLR camera and Drone. This step is called the fieldwork phase that has applied to collect quality and geometric information of the images such as position, size, contrast, filtering and shape. This first step has much more relied on the skill of the person who has operated the devices [17]. The second step is to arranged the images by applying photogrammetry software to generate dense cloud and texture data. The software is automatically interpreting the semantic information of the image [18]. This computational phase is sequentially run in the workflow of the software to obtain 3D images at the end of the process.

RESULT AND DISCUSSION

The field operator must understand several technical parameters. The most basic setting is multi-image restitution of a block of overlapping images and collinearity equations [19]. The block images must be arranged in between 60% to 80% overlaid on each image. This block means that the degree of overlapping is correlating to effects on detail

obtained.

Another fundamental parameter is image distortion that is caused by reasons such as operator position, lenses-used, amount of light, the angel of the device, and assistive devices. Therefore, in practical ways, the number of technical images captured are significant not only to reduce the distortion [20][21] but also to contribute in generating the density of the points cloud [22].

As using a metric device, DSLR camera with metric attributes is an ideal tool to produce technical images. However, it is necessary to set lenses-used to ensure consistency of the focal length. Therefore, the metric camera calibration [23] [24] needs to control continuously during the process of collecting images. In practical ways, using the prime lenses or the fixed lenses can avoid this control (fig. 1 left).

Slightly different on a drone, as having a non-metrical camera, it is necessary to use a drone with a high-quality camera to ensure the image quality produced [25]. A drone is a useful device to acquire fast and accurate images that cannot be captured on certain positions by DSLR camera such as at a high-level place, large area, delicate angels [26] [27]. In practical ways, besides numbers and overlapping images, it is also necessary for a drone operator to have a correct flight plan in avoiding an images overabundance (fig. 2 right).

Fig.1 Using DSLR Camera (left) and Drone (right) in Acquiring Image Mosaics

All images that have been acquired by cameras then are generated by photogrammetry software. There are several alternatives software which can process the image. The selection of suitable software which is available both commercial and open-source options based on computer skills and requirements [28].

This generating process is following the workflow. The workflow starts with aligning images. In this first phase, the interface software shows a position and orientation of images and builds a sparse of a point cloud model. From here, this earliest model displays two groups of arranged images on the main windows, and sources images on the bottom pane (fig. 2 left). The next phases are sequentially building dense point cloud and building mesh (3D polygonal model) (fig. 2 right).

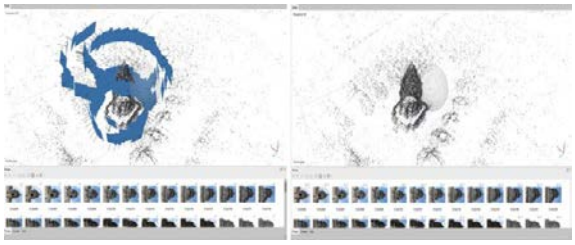

Fig. 2 Aligning Images (left) and Point Cloud Model (right) in Photogrammetry Software

The process has continued to build generating texture, building tiled model, building digital elevation model (DEM), and building ortho-mosaic (fig. 3 left). In every phase, the photogrammetry software shows the preferences dialogue command before continuing the processing that is giving a chance to correct or adjusting during the process (fig. 3 right). The last phase in the photogrammetry software is exporting the result and making the 3D model available to other software such as BIM platform [29] [30] [31].

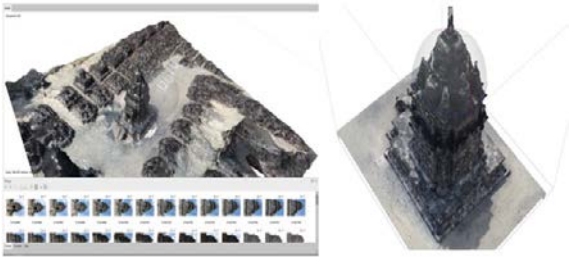

Fig. 3 Ortho-mosaic Images (left) and Point Cloud 3D Model (right)

From the whole process, this close-range photogrammetry (CRP) shows more advantageous than conventional methods. CRP can be conducted in limited time to obtain a 3D model [32][33]. The process in photogrammetry also can be accurately recovered regardless of the size of the object [34].

As a comparison of the result, this research has also used a laser scanner device on the same research object (fig. 4 left). The laser scanner can produce a significant volume of points cloud (fig. 4 right) and generates very great detail in fast and precision both on an object and large area [35]. For this reason, the laser scanner still the best device in documenting field data until today. However, a part of its advantage, the price of this device is still high, and for maintaining and routines calibration make laser scanner less practical and economical in reason. Therefore, it is necessary to provide a low-cost alternative method and also practice in used such as close-range photogrammetry.

Fig. 4 Using Laser Scanner Device (left) and Point Cloud Model (right)

CONCLUSION

The close-range photogrammetry (CRP) overs architecture not only efficiency in time process, but also giving alternative and valuable method in obtaining a 3D model. From this paper, a combination of DSLR camera, Drone and the photogrammetry software shows the 3D architectural model produced can be generated from a natural setting into a high technical accuracy detail.

However, due to less familiar with the workflow of the software, the photogrammetry becomes less used in the practice of obtaining information in architectural objects. The software also requires mastery of more advanced software to further process on architectural models that have produced to be compatible with other fields.

REFERENCES

[1] M. Hemmleb and A. Wiedemann, "Digital Rectification And Generation Of Orthoimages In Architectural Photogrammetry," in *IAPRS*, 1997, vol. XXXII, pp. 261–267, [Online]. Available: https://www.researchgate.net/publication/2354891.

[2] P. Grussenmeyer and O. Al Khalil, "From metric image archives to point cloud reconstruction: Case study of the great mosque of aleppo in Syria," in *International Archives of the Photogrammetry, Remote Sensing and Spatial Information Sciences - ISPRS Archives*, Aug. 2017, vol. 42, no. 2W5, pp. 295–301, doi: 10.5194/isprs-archives-XLII-2-W5-295-2017.

[3] S. G. Barsanti, F. Remondino, and D. Visintini, "3D SURVEYING AND MODELING OF ARCHAEOLOGICAL SITES," in *ISPRS Annals of the Photogrammetry, Remote Sensing and Spatial Information Sciences, Volume II-5/W1, 2013 XXIV International CIPA Symposium, 2 – 6 September 2013, Strasbourg, France*, 2013, pp. 145–150.

[4] M. Yakar, H. M. Yilmaz, Saadet Armagan Gülec, and Mustafa Korumaz, "Advantage of digital close range photogrammetry in drawing of muqarnas in architecture," *Inf. Technol. J.*, vol. 8, no. 2, pp. 202–207, 2009, doi: 10.3923/itj.2009.202.207.

[5] M. J. Westoby, J. Brasington, N. F. Glasser, M. J. Hambrey, and J. M. Reynolds, "'Structure-from-Motion' photogrammetry: A low-cost, effective tool for geoscience applications," *Geomorphology*, vol. 179, pp. 300–314, Dec. 2012, doi: 10.1016/j.geomorph.2012.08.021.

[6] J. Han, K. Hong, and S. Kim, "Application of a Photogrammetric System for Monitoring Civil Engineering Structures," 2012.

[7] A. Evin *et al.*, "The use of close-range photogrammetry in zooarchaeology: Creating accurate 3D models of wolf crania to study dog domestication," *J. Archaeol. Sci. Reports*, vol. 9, pp. 87–93, Oct. 2016, doi: 10.1016/j.jasrep.2016.06.028.

[8] F. Remondino, "Heritage recording and 3D modeling with photogrammetry and 3D scanning," *Remote Sens.*, vol. 3, no. 6, pp. 1104–1138, Jun. 2011, doi: 10.3390/rs3061104.

[9] M. Morita and G. Bilmes, "Applications of low-cost 3D imaging techniques for the documentation of heritage objects," *Opt. Pura y Apl.*, vol. 51, no. 2, pp. 1–11, 2018, doi: 10.7149/OPA.51.2.50026.

[10] K. Nakano and H. Chikatsu, "Camera-variant calibration and sensor modeling for practical photogrammetry in archeological sites," *Remote Sens.*, vol. 3, no. 3, pp. 554–569, Mar. 2011, doi: 10.3390/rs3030554.

[11] A. Murtiyoso, F. Remondino, E. Rupnik, F. Nex, and P. Grussenmeyer, "Oblique aerial photography tool for building inspection and damage assessment," in *International Archives of the Photogrammetry, Remote Sensing and Spatial Information Sciences - ISPRS Archives*, 2014, vol. 40, no. 1, pp. 309–313, doi: 10.5194/isprsarchives-XL-1-309-2014.

[12] M. A. Núñez Andrés and F. Buill Pozuelo, "Evolution of the architectural and heritage representation," *Landsc. Urban Plan.*, vol. 91, no. 2, pp. 105–112, Jun. 2009, doi: 10.1016/j.landurbplan.2008.12.006.

[13] K. Hanke, M. A-B Ebrahim, and A. Professor, "Monument Presentation Using Digital Architectural Photogrammetry," 1997. [Online]. Available: https://www.researchgate.net/publication/236155255.

[14] A. Murtiyoso and D. Suwardhi, "Teknik Pencocokan Citra dalam Fotogrametri untuk Dokumentasi Cagar Budaya Indonesia Banana Biodiversity and Biogeography Big Data View project DBAT-The Damped Bundle Adjustment Toolbox in Matlab View project," in *Bunga Rampai Forum Peneliti Muda Indonesia 2017*, 2017.

[15] E. Alby, P. Grussenmeyer, J.-P. Perrin, E. Alby, P. Grussenmeyer, and J.-P. Perrin, "INTEGRATION OF CLOSE RANGE PHOTOGRAMMETRIC SURVEYS IN THE DESIGN PROCESS OF ARCHITECTURAL PROJECTS 'New perspectives to save Cultural Heritage,'" in *XIXth CIPA International Symposium, Oct 2003, Antalya, Turkey*, 2003, pp. 46–51, [Online]. Available: https://halshs.archives-ouvertes.fr/halshs-00263999.

[16] A. Murtiyoso and P. Grussenmeyer, "Virtual disassembling of historical edifices: Experiments and assessments of an automatic approach for classifying multi-scalar point clouds into architectural elements," *Sensors (Switzerland)*, vol. 20, no. 8, Apr. 2020, doi: 10.3390/s20082161.

[17] P. Grussenmeyer, K. Hanke, and A. Streilein, "Architectural photogrammetry," in *Digital Photogrammetry*, 2002, pp. 300–339.

[18] A. Wiedemann, "From Analogue To Digital Close-Range Photogrammetry," 1998. [Online]. Available: https://www.researchgate.net/publication/2332200.

[19] A. Alexandru and G. POPESCU, "INTRODUCTION IN ARCHITECTURAL PHOTOGRAMMETRY,"

2016.

[20] G. Karras, E. Petsa, G. E. Karras, G. Mountrakis, P. Patias, and E. Petsa, "Modeling Distortion Of Super-Wide-Angle Lenses For Architectural And Archaeological Applications SAVEMEDCOASTS (Sea level rise scenarios along the Mediterranean coasts) View project GEOEssential View project MODELING DISTORTION OF SUPER-WIDE-ANGLE LENSES ," 2001. [Online]. Available: https://www.researchgate.net/publication/2357325.

[21] J. Sužiedelytė-Visockienė, R. Bagdžiūnaitė, N. Malys, and V. Maliene, "Close-range photogrammetry enables documentation of environment-induced deformation of architectural heritage," *Environ. Eng. Manag. J.*, vol. 14, no. 6, pp. 1371–1381, 2015, doi: 10.30638/eemj.2015.149.

[22] K. Kwiatek and R. Tokarczyk, "Immersive photogrammetry in 3D modelling," *Geomatics Environ. Eng.*, vol. 9, no. 2, p. 51, 2015, doi: 10.7494/geom.2015.9.2.51.

[23] T. Luhmann, C. Fraser, and H. G. Maas, "Sensor modelling and camera calibration for close-range photogrammetry," *ISPRS J. Photogramm. Remote Sens.*, vol. 115, pp. 37–46, May 2016, doi: 10.1016/j.isprsjprs.2015.10.006.

[24] C. Balletti, F. Guerra, V. Tsioukas, and P. Vernier, "Calibration of action cameras for photogrammetric purposes," *Sensors (Switzerland)*, vol. 14, no. 9, pp. 17471–17490, Sep. 2014, doi: 10.3390/s140917471.

[25] Z. Sun and Y. Zhang, "Using drones and 3D modeling to survey Tibetan architectural heritage: A case study with the multi-door stupa," *Sustain.*, vol. 10, no. 7, Jun. 2018, doi: 10.3390/su10072259.

[26] C. Achille *et al.*, "UAV-based photogrammetry and integrated technologies for architectural applications—methodological strategies for the after-quake survey of vertical structures in Mantua (Italy)," *Sensors (Switzerland)*, vol. 15, no. 7, pp. 15520–15539, Jun. 2015, doi: 10.3390/s150715520.

[27] A. Murtiyoso, P. Grussenmeyer, M. Koehl, and T. Freville, "Acquisition and processing experiences of close range UAV images for the 3D modeling of heritage buildings," in *Lecture Notes in Computer Science (including subseries Lecture Notes in Artificial Intelligence and Lecture Notes in Bioinformatics)*, vol. 10058 LNCS, Springer Verlag, 2016, pp. 420–431.

[28] S. P. Bemis *et al.*, "Ground-based and UAV-Based photogrammetry: A multi-scale, high-resolution mapping tool for structural geology and paleoseismology," *J. Struct. Geol.*, vol. 69, no. PA, pp. 163–178, 2014, doi: 10.1016/j.jsg.2014.10.007.

[29] H. Macher, T. Landes, and P. Grussenmeyer, "Point clouds segmentation as base for as-built BIM creation," in *ISPRS Annals of the Photogrammetry, Remote Sensing and Spatial Information Sciences*, Aug. 2015, vol. 2, no. 5W3, pp. 191–197, doi: 10.5194/isprsannals-II-5-W3-191-2015.

[30] D. Stober, R. Žarnić, D. Penava, M. Turkalj Podmanicki, and R. Virgej-Đurašević, "Application of HBIM as a Research Tool for Historical Building Assessment," *Civ. Eng. J.*, vol. 4, no. 7, p. 1565, Jul. 2018, doi: 10.28991/cej-0309195.

[31] H. A. Abd ElWahab, A. F. Bakr, and R. A. Raslan, "Towards a parametric plug-in for the conservation of built heritage," *Alexandria Eng. J.*, vol. 58, no. 1, pp. 325–331, Mar. 2019, doi: 10.1016/j.aej.2018.12.001.

[32] H. Karabörk, E. Yaldiz, and L. Karasaka, "3D documentation of portal muqarnases in Anatolian Madrasahs with digital close range photogrammetric method," *Mediterr. Archaeol. Archaeom.*, vol. 17, no. 3, pp. 137–148, 2017, doi: 10.5281/zenodo.1005534.

[33] A. H. İncekara *et al.*, "EXAMINING THE POTENTIAL AND LIMITATIONS OF CLOSE-RANGE PHOTOGRAMMETRY WITHIN SCOPE OF FAÇADE IMPROVEMENT AUTOMATIC 3D SHORELINE EXTRACTION AND ANALYSIS FROM UAV AND UAV-LIDAR DATA FOR SUSTAINABLE SHORELINE MONITORING: CASE STUDY OF TERKOS (ISTANBUL) View," 2018. [Online]. Available: https://www.researchgate.net/publication/339030918.

[34] F. Remondino and S. El-hakim, "Image-based 3D modelling: A review," *Photogramm. Rec.*, vol. 21, no. 115, pp. 269–291, 2006, doi: 10.1111/j.1477-9730.2006.00383.x.

[35] Y. J. Hoon and S. Hong, "Three-dimensional digital documentation of cultural heritage site based on the convergence of terrestrial laser scanning and unmanned aerial vehicle photogrammetry," *ISPRS Int. J. Geo-Information*, vol. 8, no. 2, Jan. 2019, doi: 10.3390/ijgi8020053.

6th Int. Conf. on Structure, Engineering & Environment (SEE), Kyoto, Japan, Nov.18-20, 2020, ISBN: 978-4-909106056 C3051

EVALUATION LIQUEFACTION AND LATERAL FLOW ON THE PALU MW 7.5 EARTHQUAKE 2018 USING STANDARD PENETRATION TEST AT LOLU VILLAGE SITE

Dandung Sri Harninto[1] and Widjoyo A. Prakoso[2]
[1,2] Civil Engineering and Environmental, Indonesia University, Indonesia

ABSTRACT

Palu Mw 7.5 earthquake on 28 September 2018 caused extra ordinary geotechnical event in the world. Not only building damage, tsunami caused by submarine landslide, but also the most devastating event was extreme scale of flow liquefaction. In the area studied (Lolu Village), down slope flow movements were more than 150 meters, and in other location events were more than 1,000 meters. This must be extra ordinary phenomena of liquefaction, which have never happened at other places.

Geological formation of Palu city has been formed from young alluvial fan sourced from mountain at east-west of the city. The formation was dominated by non-cohesive material and fully saturated due to very shallow ground water table. Several standard penetration tests (SPT) were conducted after the earthquake both inside and outside area of flow liquefaction. These data can be used to estimate thickness of liquefiable layer, movable soil layer, and site characterization based on factor of safety against liquefaction used ratio cyclic resistance ratio (CRR) to cyclic stress ratio (CSR).

This report will also discuss comparison data between inside flow and outside-flow area studied, with appreciation for non-commercial map application which can help to make superimpose before-after earthquake map with quite good approximate. The report also will discuss site characterization by standard test of SPT completed by soil gradation test at every layer of soil stratum which prone to highly potential flow liquefaction.

Keywords: Palu earthquake 2018, Liquefaction, Standard penetration test, CRR/CSR

BACKGROUND

Mw 7.5 earthquake struck Palu and Donggala City, Central Sulawesi, Indonesia on 28 September 2018, as consequence of releasing energy of Palu-Kore fault where aligned west side of Palu City. This event created several catastrophic disasters, and caused large number of casualties, destroyed housings, buildings, and many infrastructures such roads, power lines, bridges, and water channels, etc. Tsunami, ground shaking, landslide arrived almost at the same time and the most extreme liquefaction disaster ever on earth caused by earthquake.

Indonesia Meteorology, Climatology and Geophysical Agency [4] reported that epicenter of the mainshock was about 72 km north of the city with depth 10 km. Series of significant foreshocks (Mw > 4.4) occurred four hours before and main shock arrived with magnitude Mw 7.5, and it was followed also by series of aftershocks (Mw >5.7) for the period of 48 minutes since main shock. Epicenters of significant foreshocks-mainshock-aftershocks were documented sweep over area Palu City (fig. 1).

BMKG and JICA (Japan International Corporation Agency) [1] have released time history data of ground acceleration of mainshock from one survival seismograph station near Palu City (Balaroa Station) as fig. 2. Unfortunately, for other shocks writer have no access to get them. If we studied series of earthquake magnitude data in table fig. 3 from BMKG, other ground accelerations record should be significantly contributed for generating extreme disaster, especially liquefaction. BMKG web site (link : http://shakemap.bmkg.go.id) shown spread out earthquake magnitude data (as table at fig. 3). Recognize level of catastrophic occurred [2], USGS reported a much larger peak ground motion acceleration and reached magnitude of 0.7g and this value might be possible (fig. 2).

Before the Palu 2018 earthquake -such as devastating liquefaction in Niigata, Japan (1964) and Alaska, USA (1964)-, lateral spreading had magnitude of teen meters or even less and prompted some differential settlement which generated tilting of buildings or houses. However, Palu earthquake generated not only common liquefaction occurred, but also hundred meters either lateral spreading or soil mass flow which brought all objects moving downslope. Liquefaction itself so far has never made fatalities, but the liquefaction spawned thousand fatalities, buried, and revolved them under deposit of sand which changed from solid transformed to mud (liquid) for some period.

Palu City, Indonesia is located at complex tectonic formation where collision of three plates comprising Eurasian, Indo-Australia, and Philippines Sea. Besides. There were at least three features of Palu city associated to liquefaction disaster:

1. Palu city is just located across Palu-Kora fault, aligned from north to south of the city. This fault has slip rate around 58 mm/year [13]. This tectonic landscape will make Palu city become very susceptible to high earthquake event (fig.4).

2. Palu low land mostly consist of young alluvium formed by sediment transport from east and west side of mountains [2]. In general, deposit mostly originate from boulder, gravel, and sand with loose consistency. Natural water stream called Palu river divide the city at centre with slope of valley around 1-6 % (fig. 1).

3. The valley area is located at middle of mountains; annual rain intensity is extremely low at most 500-mili meter annually. Conversely, ground water table was very shallow and there were some water springs blown up ground surface and possibility artesian spring. There was unlined water irrigation canal system at eastern part of the city which has been operating since 80' (fig. 4), many experts alleged that this canal had contributed significantly saturated sand deposit at east side of Palu.

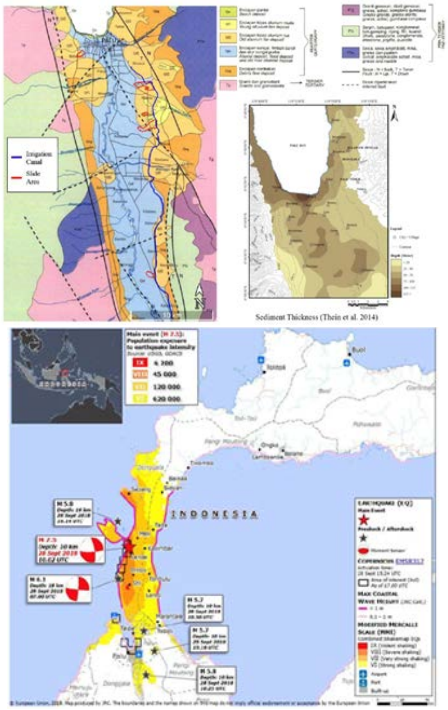

Fig.1 Geological landscape and epicenter of the earthquake [2].

LIQUEFACTION

Liquefaction is a phenomenon where saturated soil deposit reduces stiffness and strength due to the generation of high excess pore pressures during earthquake shaking. In certain condition the excess could be the same with total overburden pressure (r_u=1), and then effective pressure practiced zero, it means solid soil deposit for the time being behaves as liquid. Evidence of liquefaction in the event had been onsite, we found number of sand boils footprint (figure 5). Sand boil structure is formed by sand ejecta from sand deposit of underlayer as releasing excess pore water pressure which brought some fraction of sand.

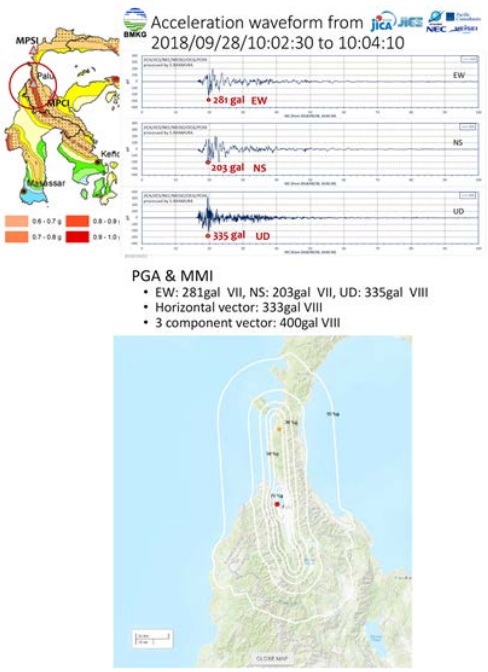

Fig.2 Time history of ground acceleration from BMKG&JICA (2018) [1], [2]

28-09-2018 18:42:49 WIB	-1.20	119.84	4.8	10 Km	Minahasa Peninsula, Sulawesi	ShakeMap	StationList
28-09-2018 18:39:13 WIB	-0.51	119.75	4.7	10 Km	Minahasa Peninsula, Sulawesi	ShakeMap	StationList
28-09-2018 18:36:28 WIB	-0.42	119.76	4.4	10 Km	Minahasa Peninsula,Sulawesi	ShakeMap	StationList
28-09-2018 17:50:28 WIB	-0.76	120.04	5.9	10 Km	Minahassa Peninsula, Sulawesi	ShakeMap	StationList
28-09-2018 17:47:45 WIB	-0.46	119.91	5.0	10 Km	Minahassa Peninsula, Sulawesi	ShakeMap	StationList
28-09-2018 17:34:53 WIB	0.04	119.76	4.7	10 Km	Minahassa Peninsula,Sulawesi	ShakeMap	StationList
28-09-2018 17:25:05 WIB	-0.98	119.99	5.7	14 Km	Minahassa Peninsula, Sulawesi	ShakeMap	StationList
28-09-2018 17:16:51 WIB	-0.8	120.01	5.8	10 Km	Minahassa Peninsula, Sulawesi	ShakeMap	StationList
28-09-2018 17:14:25 WIB	0.09	119.94	6.1	10 Km	Minahassa Peninsula, Sulawesi	ShakeMap	StationList
28-09-2018 17:14:21 WIB	0.1	119.83	6.3	17 Km	Sulawesi, Indonesia	ShakeMap	StationList
28-09-2018 17:02:45 WIB	-0.2	119.89	7.4	11 Km	Sulawesi, Indonesia	ShakeMap	StationList
28-09-2018 17:02:44 WIB	-0.18	119.85	7.7	10 Km	Minahassa Peninsula, Sulawesi	ShakeMap	StationList
28-09-2018 17:02:43 WIB	-0.22	119.85	7.4	10 Km	Minahassa Peninsula, Sulawesi	ShakeMap	StationList
28-09-2018 15:25:01 WIB	-0.38	119.96	5.1	10 Km	Minahassa Peninsula, Sulawesi	ShakeMap	StationList
28-09-2018 14:28:37 WIB	-0.35	119.87	4.9	10 Km	Minahassa Peninsula, Sulawesi	ShakeMap	StationList
28-09-2018 14:17:14 WIB	-0.09	119.86	4.6	10 Km	Minahassa Peninsula,Sulawesi	ShakeMap	StationList
28-09-2018 14:11:17 WIB	-0.35	119.96	4.4	10 Km	Minahassa Peninsula,Sulawesi	ShakeMap	StationList
28-09-2018 14:00:00 WIB	-0.35	119.82	5.9	10 Km	Minahassa Peninsula, Sulawesi	ShakeMap	StationList

Fig.3 Magnitude of foreshock, mainshock and aftershock of Palu earthquake 2018 (BKMG, 2018)

As Bradley [12] reported that mostly downhill area of unlined canal occurred lateral spreading (figure 4) with variation of magnitude. The crown of slide was generally along irrigation canal, however, at uphill of canals were still good, no evidence either liquefaction or lateral spreading at all. However, in several areas such as at Petobo, Lolu Village and Jono Oge (Sidera) where occurred in hundred-meter of spreading and it engendered huge number of casualties especially at Petobo area (figure 4).

Basic mechanism could be the same for all locations -even though the thesis is being still debatable-. It started with fluidization of certain area of sand deposit which initiated by liquefaction, with gentle slope of land commenced a long-distance lateral spreading caused by gravitational force. At the upper part of the area started to retrogressive collapse which caused by lost their counterweight at toe,

underwent high excess pore water pressure created water sprang out (seepage) huge volume of water on surface and perhaps followed by land subsidence as consequently of sand deposit contraction process. Water mixed with fine sand-silt formed mud flow and sparked more destructive process. Finally, all eroded and debris material with very high-water content glided to downstream or stacked create deposition fill. The hypothetic mechanism has not firmed yet, many researchers are still working to discover accurate one.

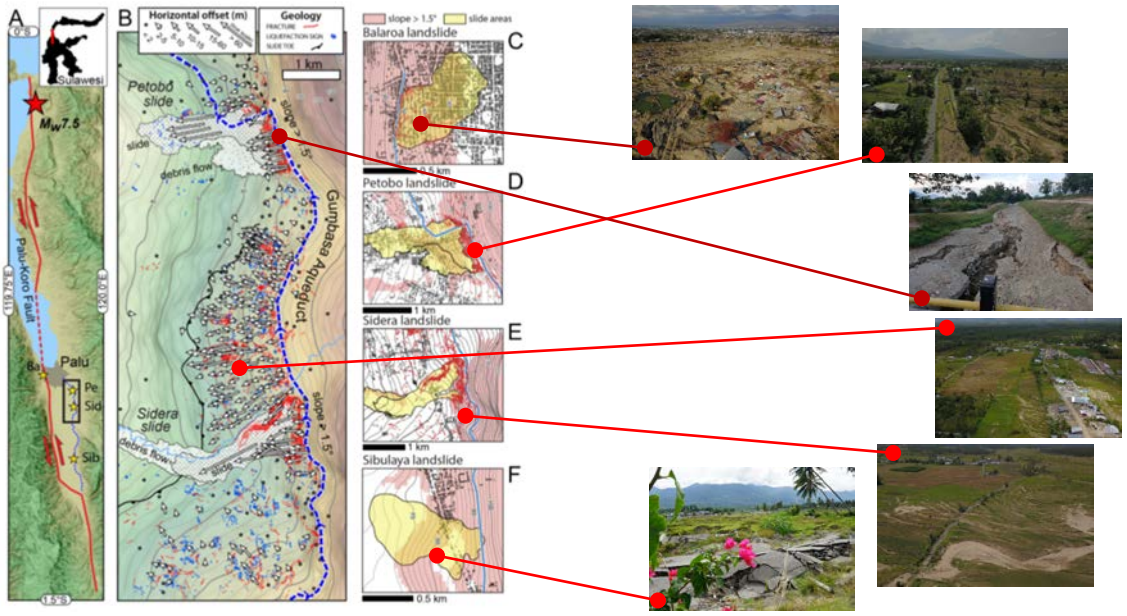

Fig.4 Lateral spreading magnitude generated by liquefaction [12] and Disaster footprint

The above mechanism proposed by writer was similar with Manson [2]. This suggestion is without any contribution of breakage of confined aquifer. Since JICA [9] suggested that there was contributed of confined aquifer breakage which maintenance excess pore water pressure kept high, this was argued by Ishihara [11] as well. This hypothesis must be quite difficult to be proven, even though that will be possibility happened. However, all the above mention researchers have agreed including Watkinson and Hall [5] and Bradley [12] that construction and operation an unlined agriculture canal (fig. 4) had played a large role in the slope failure. Yearly water seepage from the canal increased height of water table accordingly saturated the underlaying loose soil layer and caused of it making them liquefaction prone.

To know magnitude of lateral displacement, we also have measured magnitude of lateral spreading use Google Earth Pro. At time being, we have been only focusing at Lolu Village site with some reason which will discuss later. We use figure published by Bradley [12], to help describe magnitude of lateral spreading. The longest distance was 155-meters (yellow arrow line), and relative long distance occurred at northern part of area. At southern part, displacement distance was average 70-meters. At eastern part or upper hill, lateral displacement was average 25-meters. Outside landslide area, many objects were measured as well where lateral movement with magnitude less than 10-meters.

Fig.5 One of sand boil at Lolu Village site

SOIL INVESTIGATIONS

There must be distinct onsite sand deposit characteristic to make as discussed above could happen. Understanding of this mechanism is important since the flow liquefaction areas were most deadly compare to outside area. It should be valuable for mitigation hazards purposes for next communal

settlement planning. Lolu Village was exceptional site and thought as main mechanism of purely liquefaction without any involvement from other force such as water inundating from breakage of main water canal. Except Balaroa, other big lateral spreading including Petobo, Jono Oge and South Sibalaya, all of them involved huge volume of water from breakage canal since top-crown of landslides were also started at breakage of canal. Understanding at Lalo Village will be useful to recognize mechanism for other areas, because magnitude moving objects at ground surface were triggered purely by liquefaction.

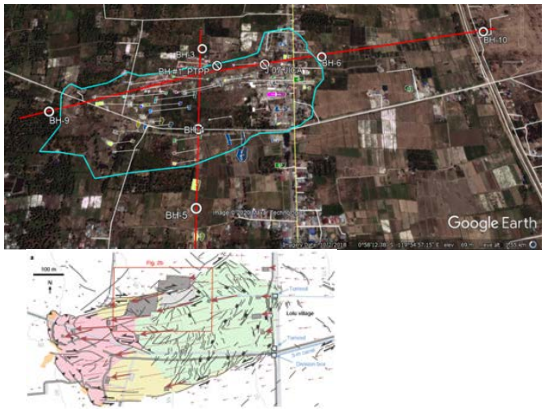

Fig. 6 Distance of lateral spreading at Lolu Village and Standard penetration test bore location Point

We have divided Lolu Village liquefaction area into two area; called “flow area” and “affected area”. Flow area is inside blue line (fig. 6) where lateral spreading generated more than 10-meters till maximum 153 meter and affected area is outside where less than 10-meter. As discussed above about basic mechanism argued by writer at long direction (east to west), the area has been alienated into several zones (fig. 7): tension, retrogressive, raft-initiation, stacking and stopper zone. For each zone, we have conducted bore hole and taken SPT data to know underlayer properties of sand deposit. Section BH10-BH9 is movement direction (long section) and section BH3-BH5 is perpendicular movement direction (cross section). For every hole, each 1.0-meter, we have taken series of disturb sample to know grain size gradation. This data will be used to recognized kind of soil and to determine fines content to calculate N-SPT corrected caused of fine content or N1(60) value for CRR7.5 calculation.

LIQUEFACTION ANALYSIS

Other researchers have reported that liquefaction could be re-occurred at the same location which activated by different earthquake events Towhata [7]. We conclude that engineering properties of sand deposit should be unchanged significantly and still susceptible to liquefaction if other parameter also preserved either magnitude of earthquake or saturation of sand deposit.

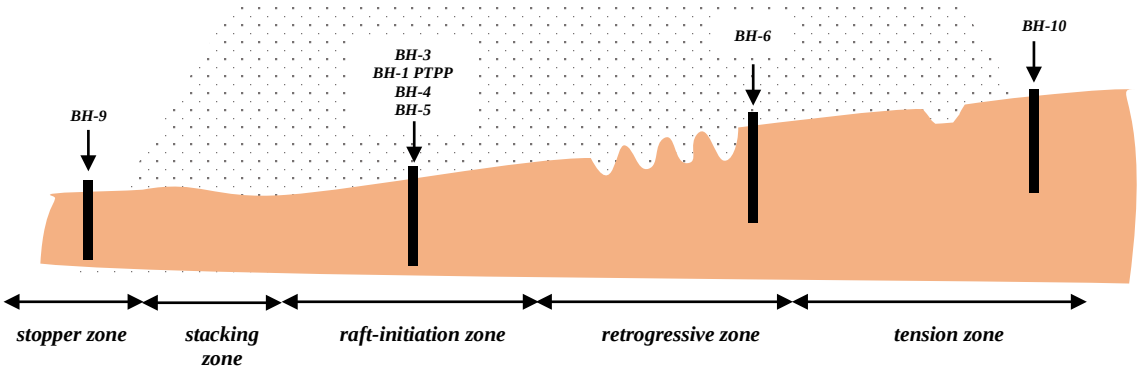

Fig. 7 Alienation of flow and affected area

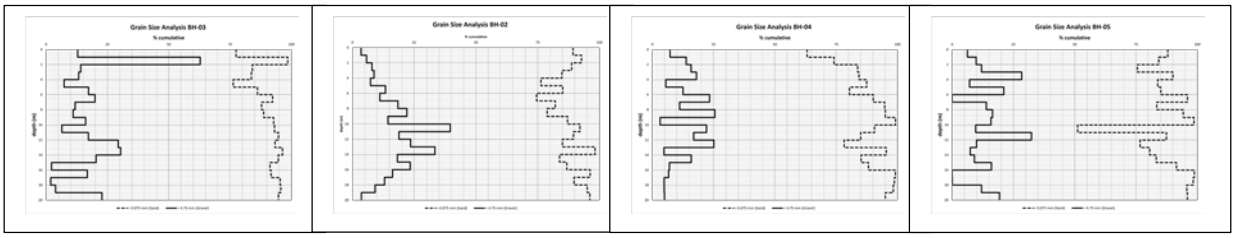

Fig. 8 Grain size distribution at cross section area

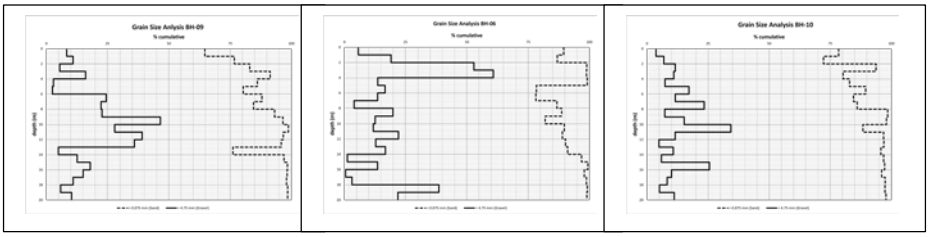

Fig. 9 Grain Size Distribution at Long Section Area

We will use post-event data to proceed a back analysis of the event and supposed this method should be still reliable. We use commercial software to calculate susceptibility of liquefaction soil deposit using SPT data called NovoSPT released by Novotechsoftware, Canada. The software will calculate safety factor of liquefaction by calculation ratio cyclic resistance ratio (CRR) to cyclic stress ratio (CSR).

This method was originally developed by Seed and Idriss [8] and are used to calculate a soil resistance to liquefaction during earthquake loading. The CSR can be defined as the seismic demand placed on a soil layer by a given earthquake, and the CRR can be defined as the capacity of the soil to resist liquefaction. The factor of safety, therefore, is equal to the CRR/CSR ratio. The CRR can be tested either using laboratory testing, preferably in quality, undisturbed samples. However as this can sometimes be difficult and expensive to obtain, it has become popular to use the SPT, or more recently the CPT.

These are seismic parameter for calculation:

1. Earthquake Magnitude Mw: 7.5
2. Distance from fault (km): 80
3. Peak Ground Acceleration (PGA): 0.4 g
4. Cyclic Stress Ration (CSR): Simplified Seed & Idriss

For SPT correction, we use as follow method:

1. Depth correction Cn: Liao & Whitman, 1986
2. Hammer energy level (%) Ce: 60
3. Borehole diameter (mm) Cb: 150
4. Sampling method Sc: Standard sampler
5. Rod length method Cr: Cetin et al.

For liquefaction analysis, we adopt ground water level approximately 1-meter below surface, CRR7.5: NCEER Workshop (1997) & Boulanger & Idriss (2014), Magnitude scaling factor (MSF): Idriss, 1997 (NCEER), Stress Reduction Factor (Rd): NCEER, 1997, Fines content correction for NCEER: Idriss & Seed, 1996 (NCEER Workshop).

We will not discuss regarding method used to calculate and focus on result and trend of result to generate some hypothetic mechanism, just select proposal method which available in the software. The results of calculation have presented at fig.10 dan fig. 11, for cross section and long section, respectively. Locations of each bore hole please refer to fig. 6.

DISCUSSION

We have made a hypothetic liquefied/non-liquefied soil layering which interpreted based on SF (safety factor) liquefaction calculation result. Soil deposit have been differed into two layers namely: liquefied layer and non-liquefied layer. Fig. 12 is cross section profile align north to south at raft-initiation zone, at northern side of flow liquefaction must the deepest liquefied layer, and this was correspondent with the longest distance of lateral movement (150-meter). Figure 13 is long section at approximately in centre of longest path of lateral deformation. Liquefied depth starts to be deeper between BH#6 and J#07 JICA. This area is started area for raft zone.

Generally, we found that soil deposits are not homogeneous, there are some interbedded layers. The interlayers are denser than other layers (N-SPT higher) and calculate as not liquefied layer. On affected area, liquefied layer is only at upper layer with thickness approximately 10-meter at most (refer to BH#10, BH#6, BH#9, BH#3 and BH#5). Inside flow area, liquefied layers are much thicker than affected area, please refer to BH#4, BH#1PTPP and J#7 JICA. BH#4 shows that liquefied layer around 17-meter, and two other data show even deeper layer. At BH#4 location, objects had been moved 80-meter (raft-initiation zone). At BH#1@PTPP: 120-meters (raft-initiation zone), at J#7JICA: 90-meters (retrogressive zone), and BH#4: 10-meters. These distances were traced from overlay of two google earth pro data: before (08/18/2018) dan after earthquake (10/02/2018). Thicker liquefaction layer has been initiated longer distance of lateral movement.

If at raft-initiation zone resides many objects such as housing, infrastructure and so on with different either size or weight, it will produce different movement magnitude. Raft movement could make an undulance movement, rolling, rotating and generate catastrophic disaster. From fig. 13 long section of the area study, we have found something interest that raft-initiation zone was just located over abandoned lake-look or deeper valley. Many liquefaction areas occurred at abandon ancient either lake or river [7].

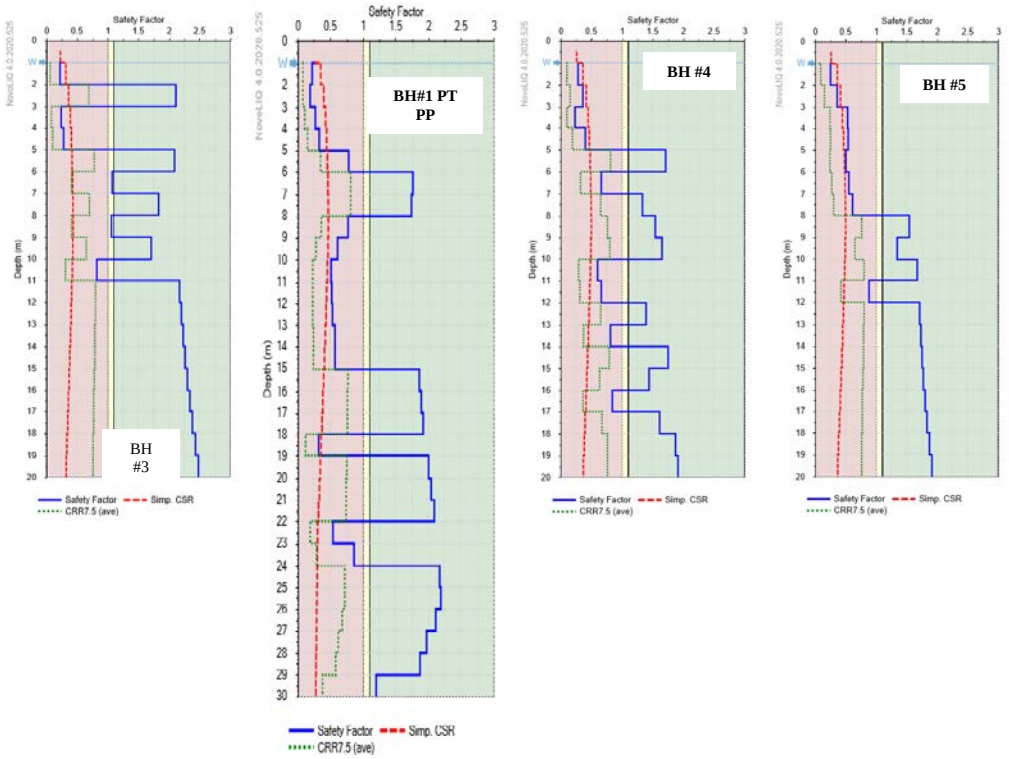

Fig. 10 Safety Factor Against Liquefaction at Cross Section of Area

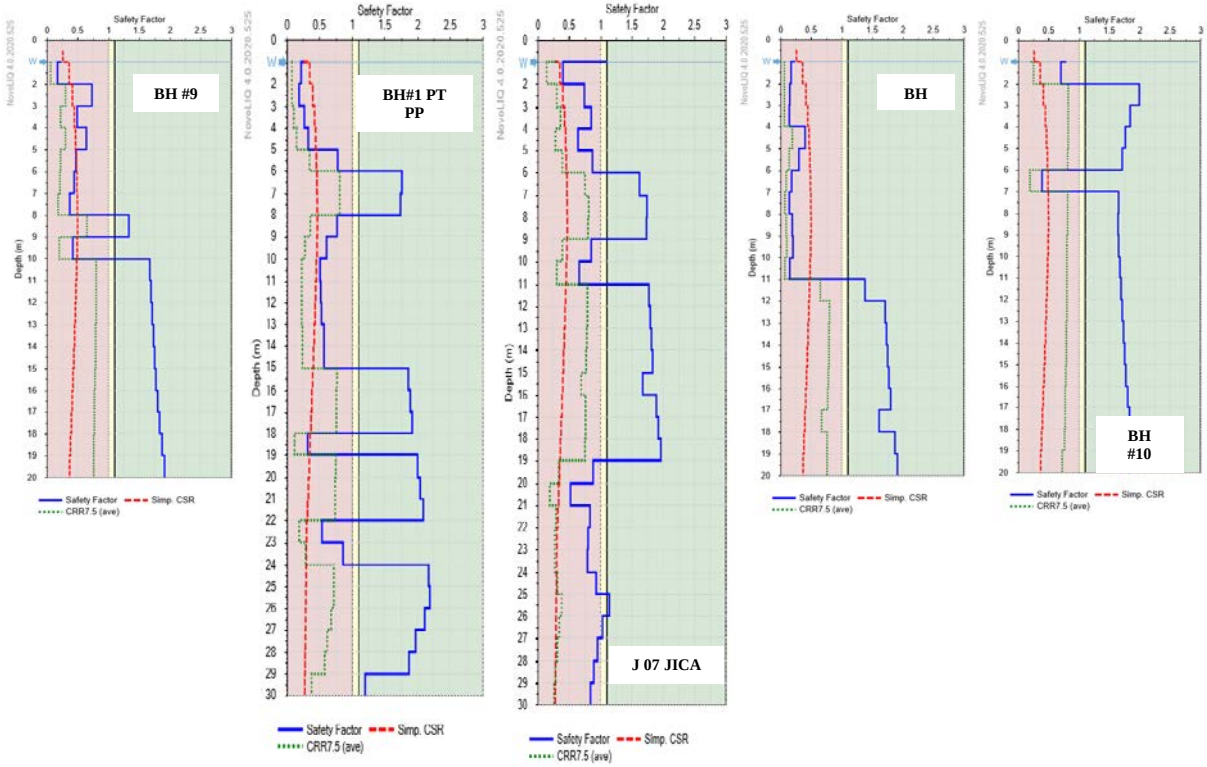

Fig. 11 Safety Factor Against Liquefaction at Long Section of Area

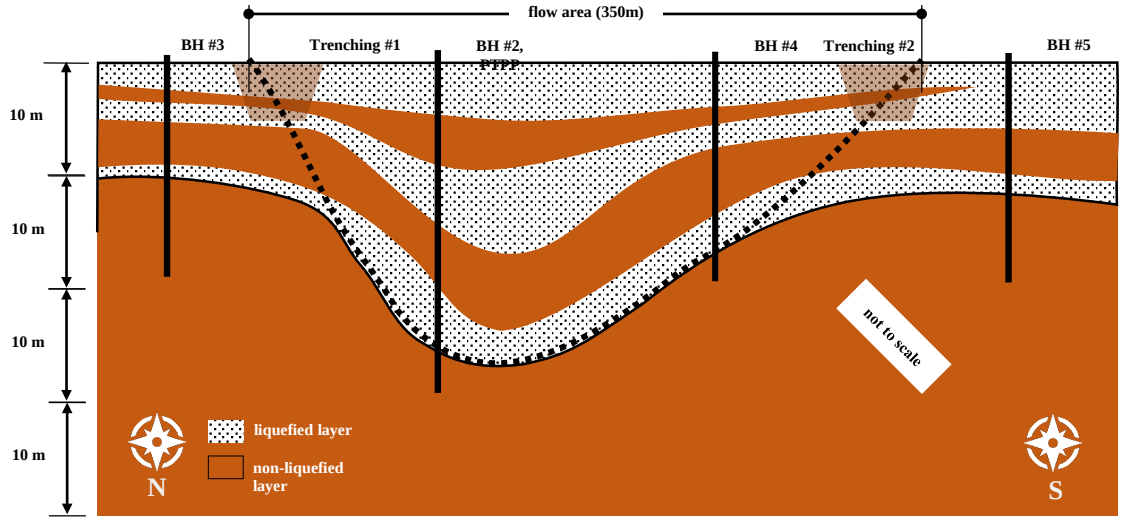

Fig. 12 Hypothetic Liquefaction Layers at Cross Section of Area

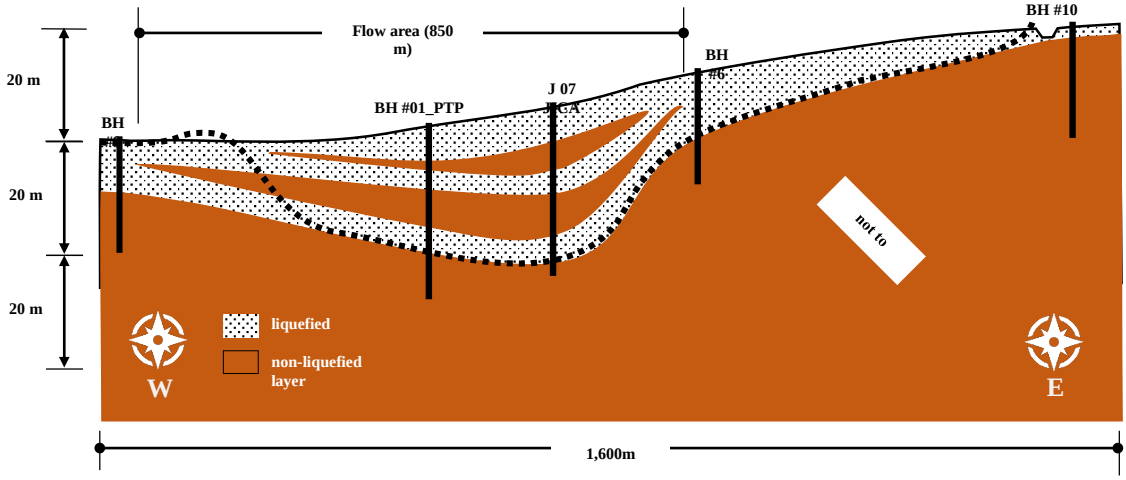

Fig. 13 Hypothetic Liquefaction Layers at Long Section of Area

CONCLUSIONS

We performed soil investigation including SPT-grain size analysis and conducted analysis by using commercial software available to determine susceptibility sand deposit at Lolu Village against liquefaction. As history recorded that liquefaction could re-occur at the same location, in that case we entitlement that post-event data still can be used for back calculation.

1. Based on standard penetration test (SPT) post event data, both flow area and affected area were liquefaction susceptible with variation of depth, by reference safety factor against liquefaction calculated is less than one.

2. Fine grain contents were significant according to grain gradation test, possibility that soil deposits were interbedded between sand and silt-clay. Existence of such kind of deposit will generate void redistribution or water film as proposed by Kokusho (2003) which cause soil deposit at certain layers lost their shear strength during liquefied and generate huge magnitude of lateral spreading.

3. Even tough area had relatively the same grade of slope and geological landscape, but in fact generated different magnitude of lateral deformation between flow area and affected area. This was caused by variation formation of underlaying deposit which correspond with thickness of liquefied layer.

4. Either figure 12 cross section or figure 13 long section of the area have studied, we have found something interest related to base elevation of liquefied layer that flow area was located on top of look-like an abandoned former lake or water stream or deep valley. As recorded by Towhata (2014) that re-liquefaction area could be occurred at abandon ancient lake or river, and from geological landscape this hypothetic should be understood since alluvial fan has formed this area.

With limited data taken would be too early to have precise relation between depth of liquefied layer and distance of lateral movement. Nevertheless, from initial data collected and the analysis discussed, we have suggested basic mechanism and site characteristic which make such a big liquefaction flow occurred.

For further research, it will need denser bore hole and SPT data, especially inside flow area to have more accurate of liquefied layer and preferably we are able to produce three-dimensional layering. Moreover, if we can conduct SPT tests at moved object track that must be much better, to know underlayer sand deposit underneath. By this data, we should be able to purposes a relation between thickness of liquefied zone against magnitude of lateral spreading.

ACKNOWLEDGMENTS

We have many parties to thank for giving encouragement of this report: our team in University Indonesia especially Prof. Widjoyo A. Prakoso, Past immediate Chairman of Indonesia Society for Geotechnical Engineering (HATTI) Prof Masyhur Irsyam and team, and GEER (Geotechnical Extreme Events Reconnaissance), USA team including H. Ben Banson, Aron P. Gallant, Jack Montgomery, Joe Wartman, and Daniel Hutabarat for worth moment along with all them for site reconnaissance joint survey in Palu. We would like also to thank for many valuable discussion and lecture from Kenji Ishihara, Susumu Yasuda, Takeji Kokusho, Ikou Towhata and Hisashi Furuichi (JICA) during they visited on site in Palu and series of lecture in Jakarta, Indonesia.

REFERENCES

[1] Andhika Sahadewa, Masyhur Irsyam, Rahma Hanifa, Andi Kartawiria, Agus Himawan, Requel Mikhail, Dandung Sri Harninto, Agus Muntohar, Didiek Djarwadi, Widjoyo Prakoso, D.H. Natawijaya, Hamzah Latief, M. Asrurifak, L. Faizal, A. Sabarudin, Sigit Pramono, M. Daryono, Ramli Nazir (2019), "Geotechnical Overview of the 2018 Indonesia Palu Earthquake", Handout of VII International Conference on Earthquake Geotechnical Engineering, Rome, Italy, 17-20 June 2019.

[2] Aaron P. Gallant, Jack Montgomery, H. Benjamin Mason, Daniel Hutabarat, A. Nicole Reed, Joseph Wartman, Masyhur Irsyam, Pintor T. Simatupang, Idrus M. Alatas, Widjojo A. Prakoso, Didiek Djarwadi, Rahma Hanifa, Paulus Rahardjo, Lutfi Faizal, Dandung S. Harninto, Aksan Kawanda, Agus Himawan, Widodo Yasin (2019), "The Sibalaya flowslide initiated by the 28 September 2018 MW 7.5 Palu-Donggala, Indonesia earthquake", Landslides DOI 10.1007/s10346-020-01254-1.

[3] H. Benjamin Mason, Aaron P. Gallant, Daniel Hutabarat, Jack Montgomery, A. Nicole Reed, Joseph Wartman, Masyhur Irsyam, Widjojo Prakoso, Didiek Djarwadi, Dandung S. Harninto, Idrus Alatas, Paulus Rahardjo, Pintor Simatupang, Aksan Kawanda, Rahma Hanifa (2019), "Geotechnical Reconnaissance: The 28 September 2018 M7.5 Palu-Donggala, Indonesia Earthquake Version 1.0", Geotechnical Extreme Events Reconnaissance Report.

[4] Indonesia Meteorology, Climatology and Geophysical Agency, 2018 http://shakemap.bmkg.go.id

[5] Ian M. Watkinson and Robert Hall (2019), "Impact of Communal Irrigation of the 2018 Palu Earthquake-triggered Landslide", Nature Geoscience, Article 10.1038/s41561-019-0448-x.

[6] Ikuo Towhata (2008), "Geotechnical Earthquake Engineering", Springer.

[7] Ikuo Towhata et. al (2014),"Liquefaction in the Kanto region during the 2011 off the pacific coast of Tohoku earthquake", Soil and Foundations 2014, 54(4):859-873.

[8] I.M. Idriss, R.W. Boulanger (2006), "Semi-empirical procedures for evaluating liquefactionpotential during earthquakes", Soil Dynamics and Earthquake Engineering, 26 : 115-130.

[9] JICA Study Team (2019), "Brief Explanation of "Nalodo" Assessment & Mitigation", Handout National Workshop on Joint Research, Assesment Mitigation of Liquefaction Hazards on 9th October 2019, Indonesia University.

[10] Kenji Ishihara (1993), "Liquefaction and Flow Failure During Earthquake", Geotechnique 43, No.3, 351-415.

[11] Kenji Ishihara (2019), "Site Characterization of Behavior of Sandy Soils", Handout National Workshop on Joint Research, Assesment Mitigation of Liquefaction Hazards, Indonesia University.

[12] Kyle Bradley, Rishav Mallick, Harisma Andikagumi, Judith Hubbard, Ella Meilinda, Adam Switzer, Nairong Du, Gilles Brocard, Dedy Alfian, Benazir Benazir, Guangcai Feng, San-Ho Yun, Jedrzej Majewski, Shengji Wei and Emma M. Hill (2019), "Earthquake-triggered 2018 Palu

Valley Landsliders Enabled by Wet Rice Cultivation", Nature Geoscience, Article 10.1038/s41561-019-0444-1.

[13] Mudrik Rahmawan Daryono (2016), "Paleoseismologi Tropis Indonesia (Dengan Studi Kasus Di Sesar Sumatra, Sesar Palukoro-Matano, dan Sesar Lembang)", Disertasi Doktor Program Studi Sain Kebumian, Institut Teknologi Bandung.

[14] Mitsu Okmura, Kohei Ono, Utari S. Minaka, Tadahiro Inoue, Ryuji Inaba, Rytaro Tanaka, Adi Maulana, Ardy, Arsyad, Sabri, Purwanto, Sukirman Nurdin (2019), "Liquefaction-induced Large Scale Flowslide in Sibalaya –Investigation to Underlying Mechanism-", Handout of International Seminar on Developing Mitigation Technique for Liquefaction Disasters : Case Study from Palu Earhquake 7.4Mw Sulawesi Tengah, Hasanuddin University.

[15] Pepen Supendi, Andri Dian Nugraha, Sri Widiyantoro, Chalid Idham Abdullah, Nanang T. Puspito, Kadek Hendrawan Palgunadi, D. Daryono and Samsul Hadi Wiyono, "Hypocenter Relocation Of The Aftershocks Of The Mw 7.5 Palu Earthquake (September 28, 2018) And Swarm Earthquakes Of Mamasa, Sulawesi, Indonesia, Using The BMKG Network Data", Geoscience Letter 6:18, Article 10.1186/s40562-0148-9.

[16] P.K. Robertson, and C.E. (Fear) Wride (1998), "Evaluation Cyclic Liquefaction Potential Using The Cone Penetration Test", Canadian Geotechnical Journal, Vol. 35, 442-459.

[17] Ross W. Boulanger and Stephen P. Truman (1996), "Void Redistribution in Sand Under Post-Earthquake Loading", Canadian Geotechnical Journal, Vol. 33, 829-834.

[18] R.W. Boulanger, D.M. Moug, S.K. Munter, A.B. Price and J.T. DeJong (2016), "Evaluating Liquefaction and Lateral Spreading in Interbedded Sand, Silt and Slay Deposit Using the Cone Penetrometer", Geotechnical and Geophysical Characterisation, Australian Geomechanics Society, Sydney, Australia, 81-97.

[19] Susumu Yasuda (2019), "Prediction of Liquefaction and Countermeasure Against Liquefaction", Handout National Workshop on Joint Research, Assesment Mitigation of Liquefaction Hazards on 9th October 2019, Indonesia University.

[20] Takaji Kokusho (2017), "Innovative Earthquake Soil Dynamics", Taylor & Francis Gorup.

[21] Takaji Kokusho, M.ASCE, Fumiko Ito, Yohta Nagao, and A. Russel Green, M. ASCE (2012), "Influence of Non/Low-Plastic Fines and Associated Aging Effect on Liquefaction Resistance", Journal of Geotechnical and Geoenvironmental Engineering ASCE, 138 (6), 747-756.

[22] Takeji Kokusho (1999), "Water Film in Liquefied Sand and Its Effect on Lateral Spread", Journal of Geotechnical and Geoenvironmental Engineering, 125 (10), 817-826.

[23] Takeji Kokusho and Tetsuro Kojima (2002), "Mechanism for Postliquefaction Water Film Generation in Layered Sand", Journal of Geotechnical and Geoenvironmental Engineering, 128 (2), 129-137.

[24] Takaji Kokusho (2003), "Current State of Research on Flow Failure Considering Void Redistribution in Liquefied Deposits", Soil Dynamic and Earthquake Engineering 23 (2003), 585-603.

[25] Takeji Kokusho (2000), "Mechanism for Water Film Generation and Lateral Flow in Liquefied Sand Layer", Soil and Foundations Vol. 40, No. 5, 99-111.

[26] Takeji Kokusho and Katsuhisa Fuji (2001), "Water Films Involved in Post-Liquefaction Flow Failure in Niigata City During the 1964 Niigata Earthquake" Pro. International Conferences on Recent Advances in Geotechnical Earthquake Engineering and Soil Dynamics. 25.

[27] Yamaguchi, T. Mori, M. Kazama, N. Yoshida, "Liquefaction in Tohoku district during the 2011 off the Pacific Coast of Tohoku Earthquake", Soils and Foundations 2012, 52 (5) : 811-8129.

6th Int. Conf. on Structure, Engineering & Environment (SEE), Kyoto, Japan, Nov.18-20, 2020, ISBN: 978-4-909106056 C3051

STRESS ANALYSIS IN AUXETIC TWO-DIMENSION MATERIAL WITH MODIFIED PEANUT PATTERN

Boonthum Wongchai
Faculty of Engineering at Sriracha, Kasetsart University, Thailand

ABSTRACT

Auxetic materials with negative Poisson's ratio are alternatively used in structure engineering. For negative Poisson's ratio material, the transverse deformation is different from the conventional materials with positive Poisson's ratio. When the tensile force is applied on the axial direction, the transverse deformation of auxetic material is expand, meanwhile the transverse deformation of conventional material is shrinking. In this research, the auxetic two-dimension material with modified peanut pattern is used to study the effect of the pattern geometric shape and the equivalent density on the stress. A four-circle punched pattern has been designed with the original peanut pattern. The equivalent density will be changed by varying their radius lengths. The results show that, the stress can be reduced by increasing the radius length. In the other word, by decreasing the equivalent density, the stress is decreased. The parabolic relationship between the radius length and the stress is found with high R-square value.

Keywords: Auxetic material, Modified peanut pattern, Negative Poisson's ratio, Stress analysis

INTRODUCTION

Auxetic materials with negative Poisson's ratio have recently received more attention in engineering materials. The dominant properties of auxetic materials differ from conventional materials. For convention materials, the Poisson's ratio is positive and its transverse deformation is decreased by applying the tensile force in the axial direction, meanwhile the transverse deformation of auxetic materials is increased [1]. For engineering advantage, auxetic materials can be applied with various engineering properties, such as, increasing of shear resistance, energy absorption, crashworthiness, indentation resistance, and energy dissipation ability [2]-[6].

In 1987, the first auxetic foam with negative Poisson's ratio was constructed [7]-[9]. Auxetic materials have been developed by various manufacturing. Nowadays, 3D printer is powerful device to create the test specimen and the real work piece. Two-dimensional and three-dimensional auxetic materials can be manufactured using 3D printer [10].

Auxetic materials are usually designed with re-entrant shape and chiral shape as shown in Fig. 1 [11]-[15]. Beam members with bending dominated topologies are commonly used to analyze the auxetic microstructures with these shapes [16]-[17]. High stress concentration at the sharp corners in the re-entrant and chiral auxetic microstructures is the main problem in the axetic microstructure design. The orthogonal elliptical hole pattern in solid material as shown in Fig. 2 was developed to reduce the stress concentration at the sharp corner [1], [18].

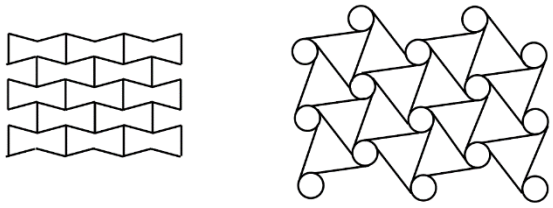

(a) (b)

Fig. 1 Popular shapes of auxetic materials (a) re-entrant shape (b) chiral shape.

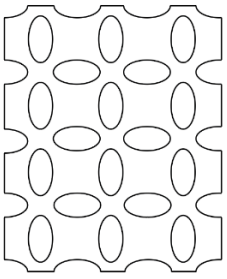

Fig. 2 The orthogonal elliptical hole pattern in solid material.

However, the elliptical pattern also induces high stress too. Hui *et al*., designed the peanut pattern as shown in Fig. 3 with smoothed boundary. By using

finite element method, it has been found that the maximum von Mises stress in the peanut pattern is lower than the elliptical hole pattern.

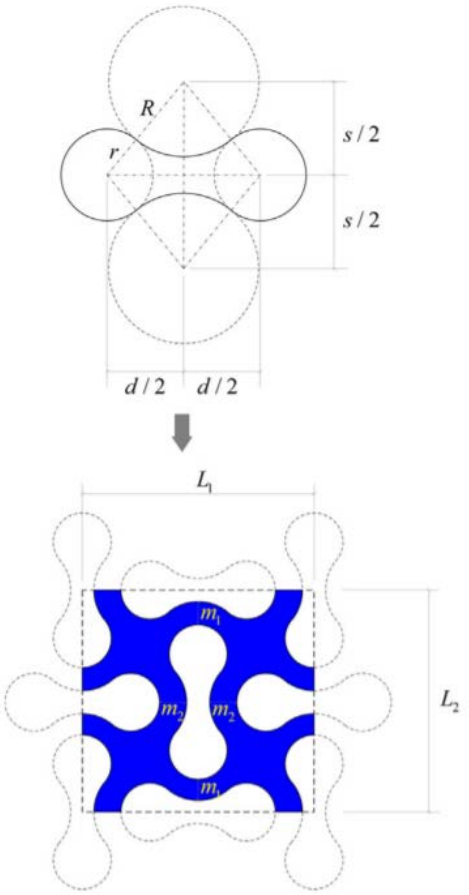

Fig. 3 The peanut pattern [1].

However, to reduce of the equivalent density, the unit cell of the peanut pattern lattice can be drilled with four circle holes. This research purposes to study the effect of the circle hole radius length and the equivalent density of the lattice on the stress.

PATTERN DESIGN

The peanut pattern

For peanut pattern as shown in Fig. 3, the centroid distance *s* of the two large circles can be computed by

$$s = 2\sqrt{(r+R)^2 - \frac{d^2}{4}}, \quad (1)$$

where *d* is the centroid distance of the two small circles. It has been assume that the lengths of the ligaments separating neighboring holes are equal, $m_1 = m_2 = m$, and the side lengths, $L_1 = L_2 = L$, are also equal, The relation is defined as follows,

$$L = d + 2r + s - 2R + 2m \quad (2).$$

The area *A* of each peanut-shaped hole can written as

$$A = 2\pi r^2 + \frac{ds}{2} - 2R^2 \arcsin\left(\frac{d}{2(R+r)}\right) - 2r^2 \arccos\left(\frac{d}{2(R+r)}\right) \quad (3).$$

The equivalent density ρ^* can be evaluated by

$$\frac{\rho^*}{\rho_s} = \frac{L^2 - 4A}{L^2} \quad (4)$$

where ρ is the density of the base material [1].

The modified peanut pattern

The modified peanut pattern is developed from the original peanut pattern with *r* = 2.7 mm, *R* = 7.2 mm, *d* = 10 mm, and *L* = 20 mm. The original peanut lattice is drilled by four-circle holes with radius *a* as shown in Fig. 4.

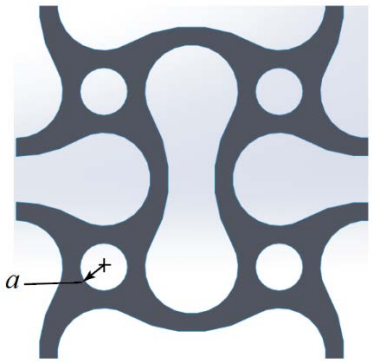

Fig. 4 The modified peanut pattern.

The equivalent density of the modified peanut pattern ρ_1^* can be written by

$$\varphi = \frac{\rho_1^*}{\rho_s} = \frac{L^2 - 4(A + \pi a^2)}{L^2} \quad (5)$$

where φ the equivalent density ratio. In this research, *a* is varied at seven values of *r*/4, *r*/3, *r*/2, 5*r*/8, 11*r*/16, 23*r*/32, and 3*r*/4.

STRESS ANALYSIS

Finite element method is used to analyze the stress

in the auxetic material. The PE high density is used for base materials with Young's modulus of 1.07 GPa, Poisson's ratio of 0.41, tensile strength of 22.10 MPa, and mass density of 952 kg/m^3. The model of the modified peanut pattern with 2×4 array is generated using SOLIDWORKS with thickness of 20 mm. The stress in the auxetic material is computed using SOLIDWORKS Simulation. The boundary conditions are setting with the displacement u_y in y direction at the top edge and fixed at the bottom edge as shown in Fig. 5. The model is meshed using triangular shell element with thickness of 20 mm.

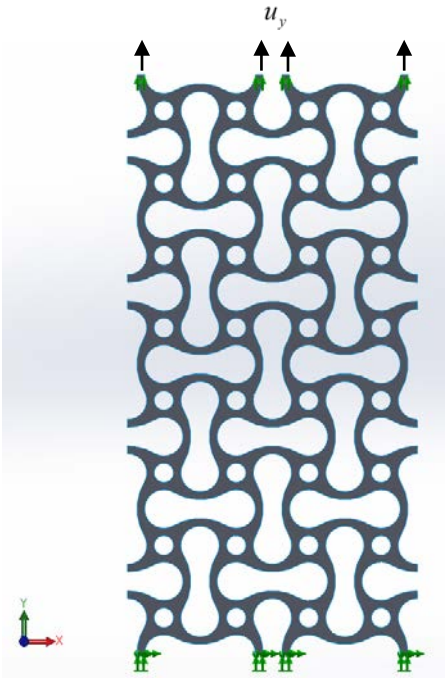

Fig. 5 Boundary conditions.

The maximum von Mises stress $\sigma_{von,\max}$ is computed from the simulation by varying the normal strain ε_y in y direction at 4%, 8%, 12%, 16% and 24%. For 2×4 unit-cells, the displacement u_y can be determined by

$$\varepsilon_y = \frac{u_y}{4L}. \tag{5}$$

RESULT AND DISCUSSION

Fig. 6 shows the von Mises stress in the auxetic material with modified peanut pattern for case of a = $r/4$ and $\varepsilon_y = 8\%$. For all cases, the maximum von Mises stress occurs at the top of the lattice as same as the case of a = $r/4$ and $\varepsilon_y = 8\%$. By varying the radius a and the normal strain ε_y, the maximum von Mises stress for all cases are shown in Table 1.

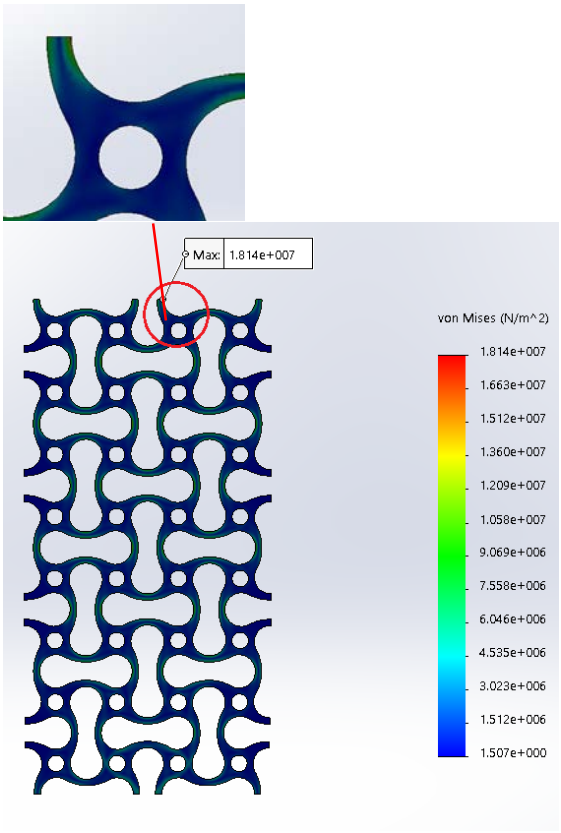

Fig. 6 The von Mises stress in case of a = $r/4$ and $\varepsilon_y = 8\%$.

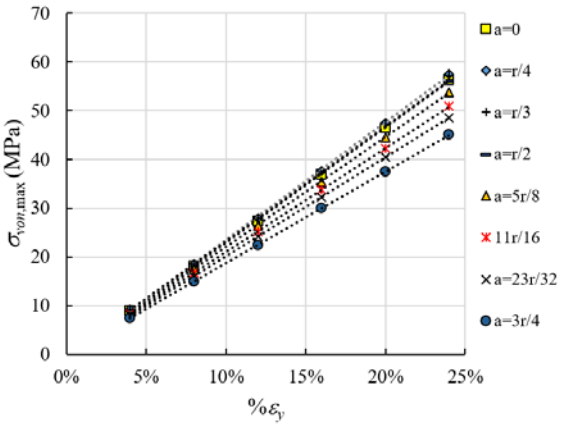

Fig. 7 The maximum von Mises stress-strain curve.

From Table 1, the $\sigma_{von,\max}$ and the ε_y can be plotted with linear trend line as shown in Fig. 7. For cases of a > $r/2$, the results show that the slope of the trend line less than the original peanut-shaped hole pattern (a = 0). In the other word, for a > $r/2$, the $\sigma_{von,\max}$ can be reduced by increasing the radius a.

Table 2 shows the percentage change of the

maximum von Mises stress compare with the original peanut-shaped hole pattern.

Table 1. The maximum von Mises stress

ε_y	$\sigma_{von,\max}$ (MPa)							
	$a = 0$	$a = r/4$	$a = r/3$	$a = r/2$	$a = 5r/8$	$a = 11r/16$	$a = 23r/32$	$a = 3r/4$
4%	8.91	9.146	9.12	8.991	8.687	8.298	7.964	7.43
8%	18.03	18.47	18.42	18.14	17.5	16.69	16	14.91
12%	27.33	27.97	27.88	27.43	26.42	25.15	24.09	22.41
16%	36.81	37.65	37.51	36.87	35.44	33.68	32.22	29.93
20%	46.49	47.49	47.31	46.65	44.56	42.27	40.39	37.47
24%	56.36	57.51	57.27	56.18	53.78	50.92	48.59	45.02

Note: The original peanut-shaped hole pattern has the radius $a = 0$.

Table 2. The percentage change of the maximum von Mises stress compare with the original peanut-shaped hole pattern

ε_y	The percentage change of the $\sigma_{von,\max}$ (%)						
	$a = r/4$	$a = r/3$	$a = r/2$	$a = 5r/8$	$a = 11r/16$	$a = 23r/32$	$a = 3r/4$
	$\varphi = 0.39$	$\varphi = 0.38$	$\varphi = 0.35$	$\varphi = 0.31$	$\varphi = 0.30$	$\varphi = 0.29$	$\varphi = 0.27$
4%	2.65	2.36	0.91	-2.50	-6.87	-10.62	-16.61
8%	2.44	2.16	0.61	-2.94	-7.43	-11.26	-17.30
12%	2.34	2.01	0.37	-3.33	-7.98	-11.86	-18.00
16%	2.28	1.90	0.16	-3.72	-8.50	-12.47	-18.69
20%	2.15	1.76	0.34	-4.15	-9.08	-13.12	-19.40
24%	2.04	1.61	-0.32	-4.58	-9.65	-13.79	-20.12
Average	2.32	1.97	0.35	-3.54	-8.25	-12.18	-18.36

The relationships between the percentage change of maximum von Mises stress $\%\sigma_{von,\max}$ and the normal strain in y direction ε_y are linear trend line with negative slope as shown in Fig. 8. By adding the normal strain in y direction, the percentage change of maximum von Mises stress is reduced. The negative values of the $\%\sigma_{von,\max}$ are occurred when the radius $a > r/2$.

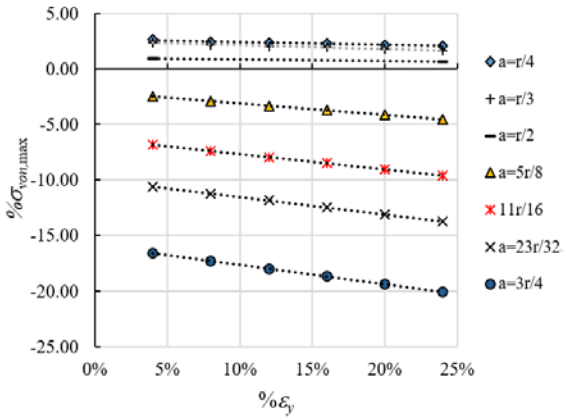

Fig. 8 The percentage change of the maximum von Mises stress versus the normal strain in y direction.

Fig. 8 shows the curve of the $\%\sigma_{von,\max}$ versus the radius a. All curves can be plotted with the parabolic curve. The parabolic curves are very closed to the adjacent curves. Thus, the average of the percentage change of the maximum von Mises stress $\%\sigma_{ave}$ from Table 2 is presented in Fig. 10.

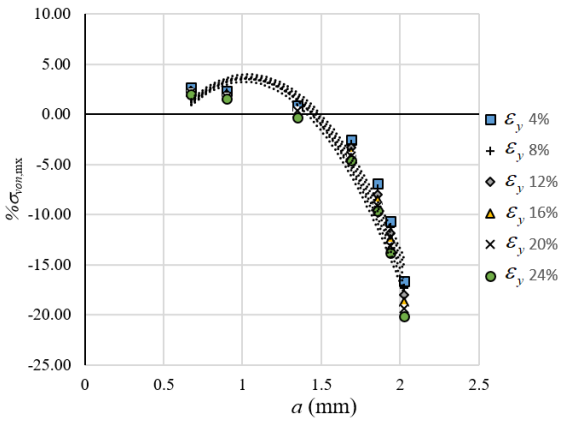

Fig. 9 The percentage change of the maximum von Mises stress versus the radius a.

The $\%\sigma_{ave}$ and the radius a can be plotted with the parabolic equation with high R-square as shown in Fig. 10. When $a > 1.46$ mm ($a > 0.54r$), the values

of the $\%\sigma_{ave}$ are negative. The $\%\sigma_{ave}$ is rapidly reduced by increasing a small value of the radius a when $a > 0.54r$. Thus, by comparing with the original peanut pattern lattice, the maximum von Mises stress will be reduced when $a > 0.54r$. By adding the radius a the maximum von Mises stress is decreased.

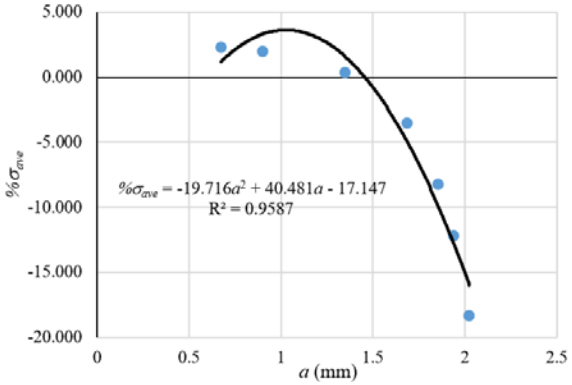

Fig. 10 The average of the percentage change of the maximum von Mises stress versus the radius a.

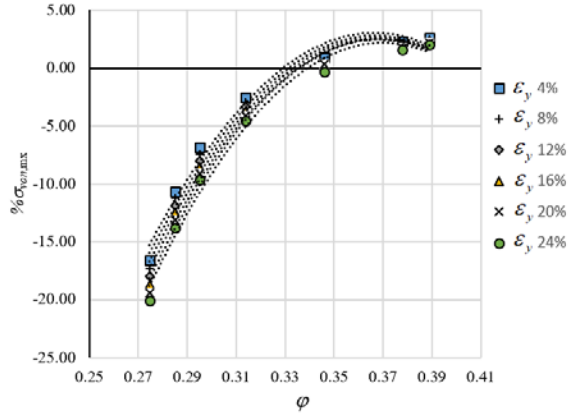

Fig. 11 The percentage change of the maximum von Mises stress versus the equivalent density ratio.

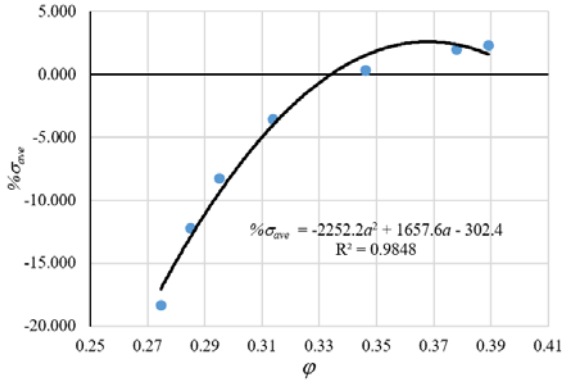

Fig. 12 The average of the percentage change of the maximum von Mises stress versus the equivalent density ratio.

Fig. 11 shows the parabolic curves of the percentage change of the maximum von Mises stress versus the equivalent density ratio φ. The parabolic curves are very closed to the adjacent curves. Similar to the curves of the $\%\sigma_{von,\max}$ versus the radius a, the parabolic curve of the $\%\sigma_{ave}$ and the equivalent density ratio φ is presented as shown in Fig. 12. The values of the $\%\sigma_{ave}$ are negative when $\varphi < 0.33$. By reducing of the equivalent density ratio, the average of the percentage change of the maximum von Mises stress is decreased. In the other words, by comparing with the original peanut pattern lattice, the maximum von Mises stress will be reduced when $\varphi < 0.33$. For the constant density of the base material, the maximum von Mises stress can be decreased by reducing the equivalent density of the modified peanut pattern lattice.

CONCLUSIONS

This study proposes the stress analysis in the auxetic two-dimension material with the modified peanut pattern. The original peanut pattern is drilled with four-circles holes. Finite element method is used to analyze the von Mises stress in the auxetic material by varying the circle radius and the normal strain in y direction.

The relationship between the normal strain in y direction and the maximum von Mises stress precisely linear. The maximum von Mises stress is added by increasing the normal strain in y direction meanwhile the percentage change of the maximum von Mises stress is decreased.

The average of the percentage change of the maximum von Mises stress and the circle hole radius can be plotted with parabolic trend line with high R-square. The average of the percentage change of the maximum von Mises stress is decreased by adding the circle hole radius. Thus, by increasing the circle hole radius, the maximum von Mises stress is reduced.

The curve of the average of the percentage change of the maximum von Mises stress versus the equivalent density ratio of the modified peanut pattern lattice can be plotted with parabolic trend line with high R-square. By adding of the equivalent density ratio, the average of the percentage change of the maximum von Mises stress is increased. For constant density of the base material, the maximum von Mises stress is increased by adding the equivalent density of the modified peanut pattern lattice.

REFERENCES

[1] Hui W., Yuxuan Z., Wanqing L., and Qing-Hua Q., A novel two-dimensional mechanical

metamaterial with negative Poisson's ratio. Computational Materials Science, Vol. 171, 2020, pp. 1-9.

[2] Yongguang G., Jian Z., Liming C., Bing D., Houchang L., Liliang C., Weiguo L., and Yizhi L., Deformation behaviors and energy absorption of auxetic lattice cylindrical structures under axial crushing load. Aerospace Science and Technology, Vol. 98, 2020, pp. 1-11.

[3] Chong L., Hui-Shen S., Hai Wa., and Zhefeng Y., Large amplitude vibration of sandwich plates with functionally graded auxetic 3D lattice core. International Journal of Mechanical Sciences, Vol. 174, 2020.

[4] Rohit R. M., and Rajib C., Anti-impact behavior of auxetic sandwich structure with braided face sheets and 3D re-entrant cores. Composite Structures, Vol. 236, 2020, pp. 1-16.

[5] Jonathan S., and Zafer K., Crushing investigation of crash boxes filled with honeycomb and re-entrant (auxetic) lattices. Thin-Walled Structures, Vol. 150, 2020, pp. 1-14.

[6] Qingsong W., Zhenyu Y., Zixing L., and Xiang L., Mechanical responses of 3D cross-chiral auxetic materials under uniaxial compression. Materials & Design, Vol. 186, 2020, pp. 1-12.

[7] Yunan P., Seeing auxetic materials from the mechanics point of view: A structural review on the negative Poisson's ratio. Computational Materials Science, Vol. 58, 2013, pp. 140-153.

[8] Mehrdad A., Sanaz S. H., and Akbar R., Auxetic materials materials with negative poisson's ratio. Material Science & Engineering International Journal, Vol. 1, Issue 2, 2017, pp. 62-64.

[9] Carneiro V. H. , Meireles J., and Puga H., Auxetic Materials – A Review. Materials Science-Poland, Vol. 31, Issue 4, 2013, pp. 561-571.

[10] Yuan C., and Qinghao H., 3D-printed short carbon fibre reinforced perforated structures with negative Poisson's ratios: Mechanisms and design. Composite Structures,Vol. 236, 2020, pp. 1-9.

[11] Zeyao C., Xian W., Yi M. X., Zhe W., and Shiwei Z., Re-entrant auxetic lattices with enhanced stiffness: A numerical study. International Journal of Mechanical Sciences, Vol. 178, 2020.

[12] Shengyu D., Li X., Weibin W., and Daining F., A novel design method for 3D positive and negative Poisson's ratio material based on tension-twist coupling effects. Composite Structures, Vol. 236, 2020, pp. 1-16.

[13] Carneiro V. H., Puga H., and Meireles J., Positive, zero and negative Poisson's ratio non-stochastic metallic cellular solids: Dependence between static and dynamic mechanical properties. Composite Structures, Vol. 226, 2020, pp. 1-9.

[14] Xiang-Long P., Celal S., and Swantje B., Phase contrast mediated switch of auxetic mechanism in composites of infilled re-entrant honeycomb microstructures. Extreme Mechanics Letters, Vol. 35, 2020, pp. 1-10.

[15] Zhengyang Z., Hanxing Z., Ru Y., Sanmin W., Tongxiang F., Yacine R., and Di Z., Auxetic interpenetrating composites: A new approach to non-porous materials with a negative or zero Poisson's ratio. Composite Structures, Vol. 243, 2020, pp. 1-8.

[16] Qiang G., Chin A. T., Greg H., and Liangmo W., Geometrically nonlinear mechanical properties of auxetic double-V microstructures with negative Poisson's ratio. European Journal of Mechanics / A Solids, Vol. 80, 2020, pp. 1-11.

[17] Bin L., Kai W., Zhonggang W., Xujing Y., Zhaoliang Q., and Daining F., Experimentally program large magnitude of Poisson's ratio in additively manufactured mechanical metamaterials. International Journal of Mechanical Sciences. Vol. 173, 2020.

[18] Yading X., Hongzhi Z., Erik S., Mladena L., and Branko S., Cementitious cellular composites with auxetic behavior. Cement and Concrete Composites, Vol. 111, 2020. Pp. 1-11.

6th Int. Conf. on Structure, Engineering & Environment (SEE), Kyoto, Japan, Nov.18-20, 2020, ISBN: 978-4-909106056 C3051

STUDY ON THE BEHAVIOR OF SANDBAR IN A RIVER CHANNEL AT THE BABAMEGAWA RIVER

Junya Taniguchi[1], Kazuya Watanabe[2], Noritoshi Saito[3] and Naoya Fujisawa[4]
[1,2,3,4] Graduate School of Engineering Science, Akita University, Japan

ABSTRACT

A flood disaster was frequently happened resulting from local heavy rainfall in Japan. Many farmlands and housing were damaged terribly in 2017 and 2018. High water level was observed in Babamegawa River which was the largest Class B river. Embankment on the left bank at Babamegawa River was collapsed owing to scouring was caused by sandbar at the downstream side. Like this, streamflow was greatly influenced by sandbar, so it was important to understand behavior of sandbar. However, only one percent rivers were conducted Periodic Vertical and Cross-sectional Survey while all Class A river were conducted measurement mainly because there were too many Class B river to measure. In this study, it was carried out that investigation using UAV to manage rivers easily. Sandbar was taken the photographs from 150 m above the ground from September in 2017 to November in 2018 and Sandbars' area, length and width were calculated with SfM (Structure from Motion technique). These data were investigated sharply when water level was decreased below ordinary. Moreover, it was important to remark width of sandbar as contraction of channel and loss of sandbar were needed to grasp for river management.

Keywords: Babamegawa River, sandbar, unmanned aerial vehicle, river management, water level

INTRODUCTION

Local heavy rain was caused flood damage in July and August 2017, May 2018 in Akita prefecture. High water level was observed in Babamegawa River. Babamegawa River is the largest Class B rivers in Alita prefecture. Such flood damage by local heavy rain was happened in Japan [1]. Left hand side had erosion due to this damage in Babamegawa River. Sandbar in Channel was caused meandered flow. And sandbar was caused transition in channel and destroyed. It was important to grasp sandbar shape and channel condition for channel management. According to research by Ministry of Land, Infrastructure, Transport and Tourism [2], all class A rivers were implemented longitudinal and transverse survey. On the other hand, class B rivers were implemented only 1 percent of the whole. Because class B rivers were many in Japan. River patrol conducted once or nothing per week in class B rivers.

In previous studies, river management method was proposed that numerical calculation using universal model [3]. And authors calculated recurrence calculation at the time of flood [4]. Data filling was lacking in class B rivers. This study proposed to maintain channel using UAV (Unmanned Aerial Vehicle) Babamegawa River to take aerial photographs. Many studies using UAV were implemented in Japan. For example, it had surveyed in inaccessible area using UAV [5]. In the coast, it conducted nearshore topography monitoring by using UAV [6]. UAV was also used in river. The method was maintenance management system [7].

This study proposed to evaluate quantitatively the relationship between the behavior of sandbar and water level using UAV at Babamegawa River. Generally, behavior of sandbar was surveyed three-dimensionally. In this study, surveying was carried out two-dimensionally for simple river management. The method will make it possible to examine easier and shorter than cross-sectioning. Firstly, aerial photographs were taken using UAV. Then, these photographs captured SfM (Structure from Motion) technique. Finally, the behavior of the sandbar grasped by measuring Sandbar area, length, and width.

RESEARCH SUBMIT

Babamegawa River is the largest class B rivers. Figure 1 shows that outline diagram of Babamegawa

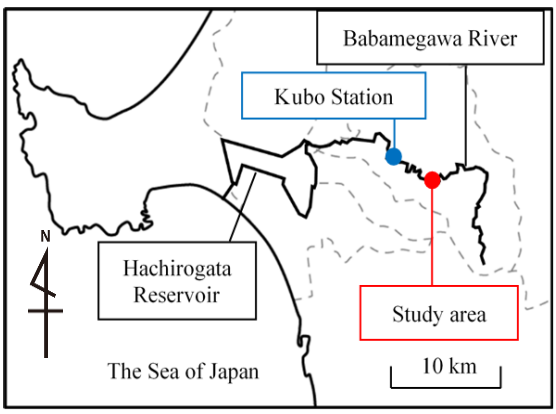

Fig. 1 The outline diagram of Babamegawa River.

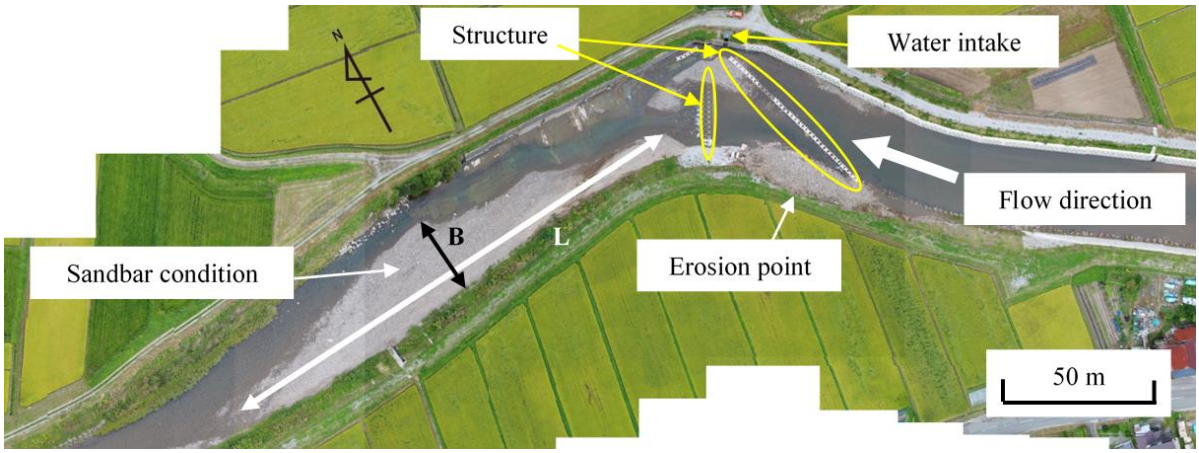

Fig. 2 State of the target area.

River. Akita It was originated from Babametake in Gojome Town, Minami-Akita-gun, Akita Prefecture, combines the surrounding tributaries into the Hachirogata Reservoir, pours into the Sea of Japan through the Funakoshi channel. Drainage area was 910.5 km^2 and Main line flow path extending was 47.5 km [8].

This target was Bababegawa River at Hiranoshita area. It was about 300 m length. Figure 2 shows that state of entire study area. This river width was about 30 m. The left-hand side was erosion due to heavy local rain damage July and August 2017. In Figure 2, there were intake for agricultural work in right hand side curved parts. The flow path was narrowed by the crossing structure so that water could be accumulated even at low water level. Therefore, sandbar was generated near the intake. Even if one year had passed since this damage, the situation of erosion damage still could be seen.

Figure 3 was taken at the time of flood. The revetment had collapsed like a landslide. In this study, sandbar condition was left-hand side in Figure 2. Figure 4 shows the situation of sandbar condition. The water level used data from Kubo station located several kilometers downstream from the study area shown in Figure 1.

Fig. 3 Babamegawa River at the flood. (August 28, 2017).

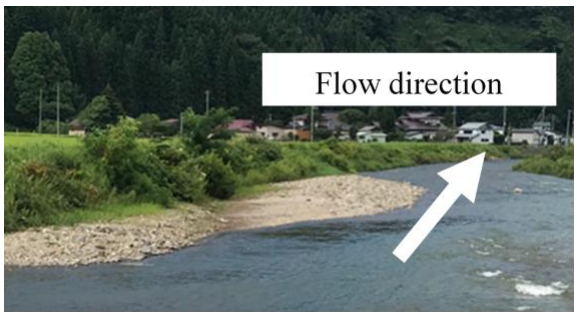

Fig. 4 Sandbar condition (August 22, 2018).

RESEARCH MERHOD

UAV Surveying

At the first, about 30 aerial photographs were taken along a river from ground to 150 m height. Then, aerial photographs were taken to overlap 80 % of the photographs horizontally and vertically. It was taken aerial photographs from September 2017 to November 2018. This study was chosen 5 times in case of low water level and high-water level.

SfM(Structure from Motion) Technique

At the first, it combined the aerial photographs Were taken. The behavior of the sandbar formation grasped from the aerial photographs. Sandbar area *A*, length *L*, and width *B* was measured in this area. *L* was maximum length of sandbar parallel to the flow path. *B* was maximum length of sandbar perpendicular to the flow path.

RESULT AND CONSIDERATIONS

Relationship between Water Level and Sandbar condition.

Sandbar was formed on the river channel. Then, river embankment erosion occurred immediately after water flow. Therefore, it was important grasping

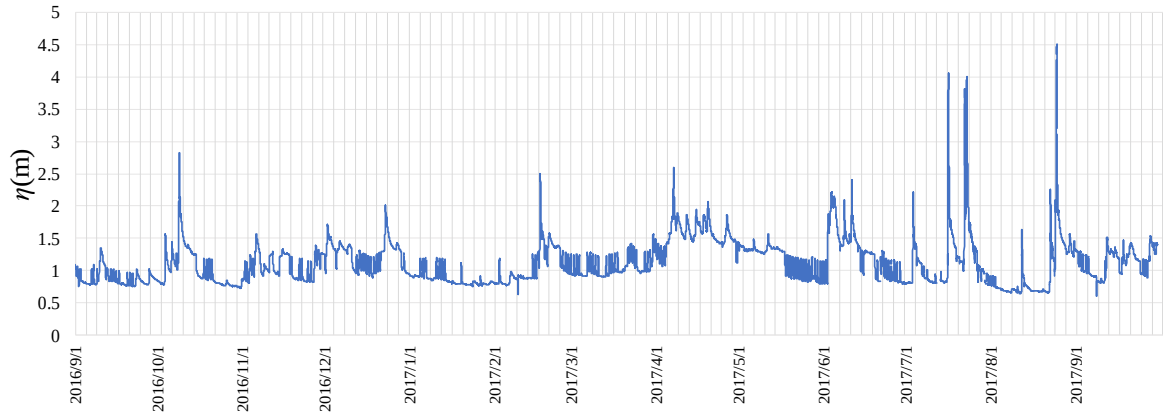

Figure. 5 Water level fluctuation from September, 2016 to September, 2017.

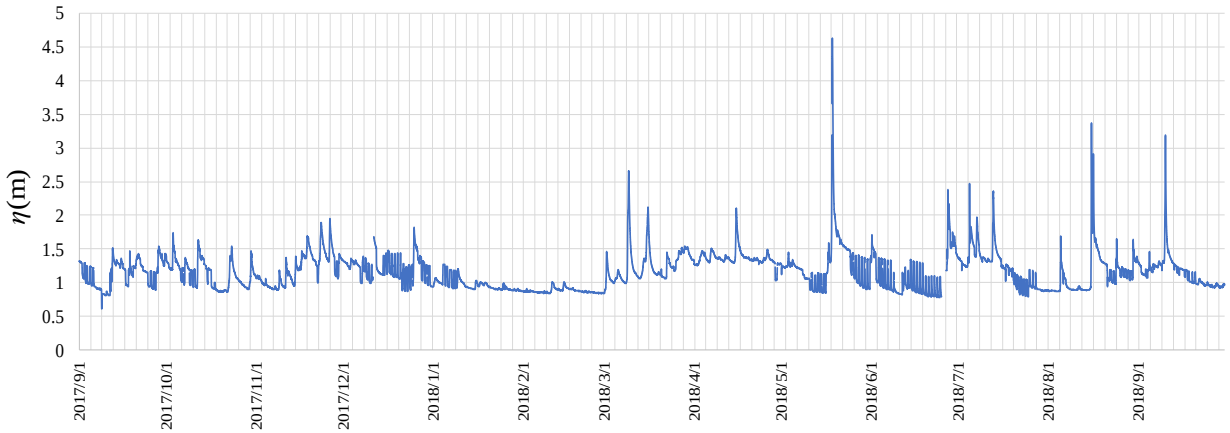

Figure. 6 Water level fluctuation from September, 2017 to September, 2018.

the form of Sandbar [10]. And, the hydrological conditions under which the form of sandbar changes was confirmed by the experiments. It needs to examine sandbar shape and flow near the flood peak. Therefore, it was necessary consideration before and after events such as precipitation. It was considered the relationship between water level and sandbar behavior. The water level was measured at Kubo station. In Figure 5, a maximum of 4.51 m was observed on August 25, 2017. In addition, water levels exceeding the flood risk water level are observed because of the effects of torrential rain. Looking at Figure 6, a maximum water level of 4.63 m was observed on May 18, 2018, far exceeding the flood danger level. In addition, water levels as high as the flood danger level were observed from August to September. Akita Prefecture has a feature that the water level rises from March to April because of the effect of snowmelt.

UAV Surveying

A, *L*, and *B* were derived for the area enclosed by the broken line shown in Figure 2. Figure 7 shows the condition of the sandbar on September 11, 2017. The river spreads so that *A* extends to 3124.4 m^2 and B extends to 26.3 m, and it occupied most of the flow path. η was 0.81 m, which was lower than the ordinary water level.

Figure 8 shows sandbar condition on August 3, 2018. *A* was 2947.0 m^2 and *B* was 19.4 m, and from September 11, 2017, *A* was 177.4 m^2 and *B* was 6.9 m. η was 0.88 m, which was close to the ordinary water level in the study area.

Figure 9 shows the condition of the sandbar on August 22, 2018. The *A* decreased from 2947.0 m^2 to 1159.7 m^2, and the flow path of the river was a minimum of 18.0 m, extending to about 60 % of the river width. In addition, η was 1.18 m higher than ordinary water level, and the sandbar became smaller because the water level rose due to rainfall.

Figure 10 shows the condition of the sandbar on September 7, 2018. *A* decreased to 1153.1 m^2, *L* decreased 2.0 m, and *B* decreased 1.5 m. In addition, since the water level was 1.24 m and the water level had risen from August 22, sandbar on the water surface was decreasing. Sandbar on the water surface decreased because the water level was rising due to the rainfall on August 15 on August 22 and September 7 when the field observation was

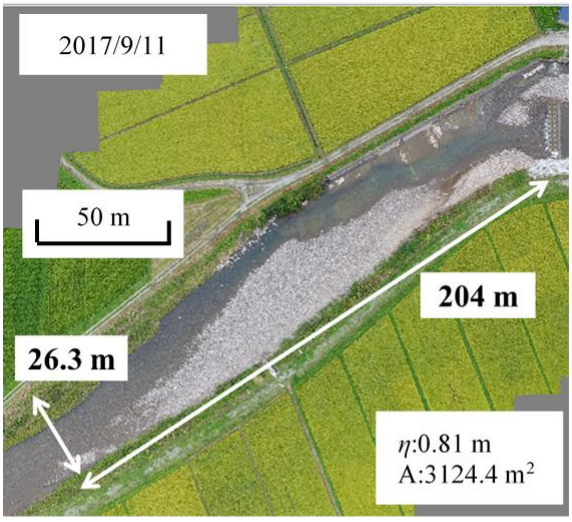

Fig.7 Sandbar condition (September 11, 2017).

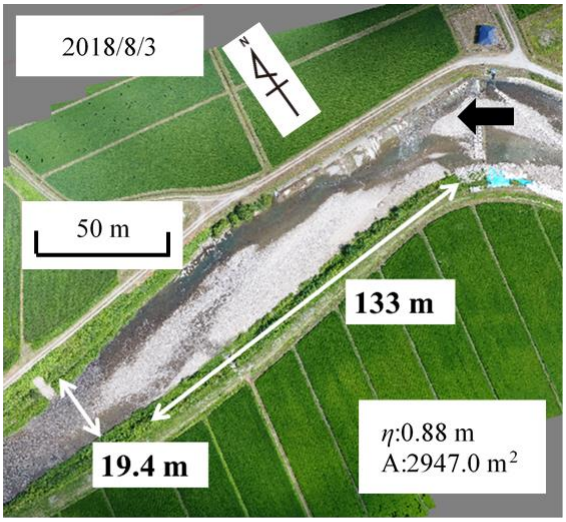

Fig.8 Sandbar condition (August 3, 2018).

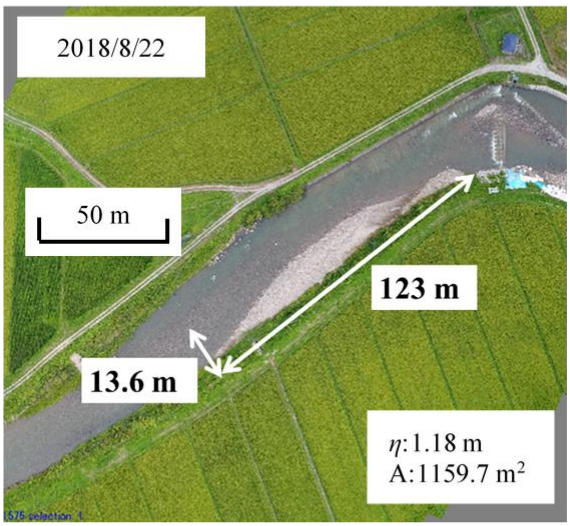

Fig.9 Sandbar condition (August 22, 2018).

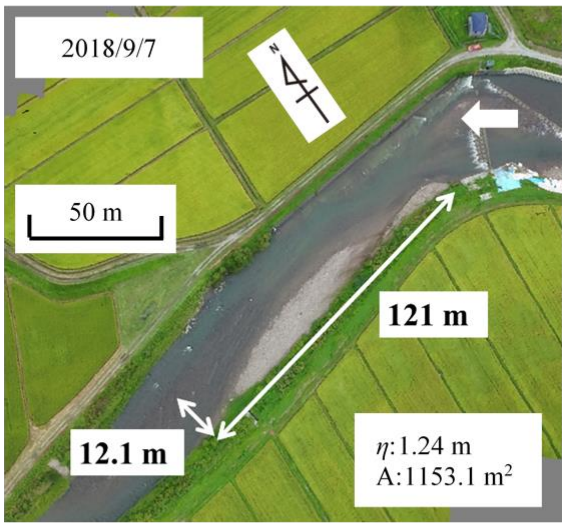

Fig.10 Sandbar condition (September 7, 2018).

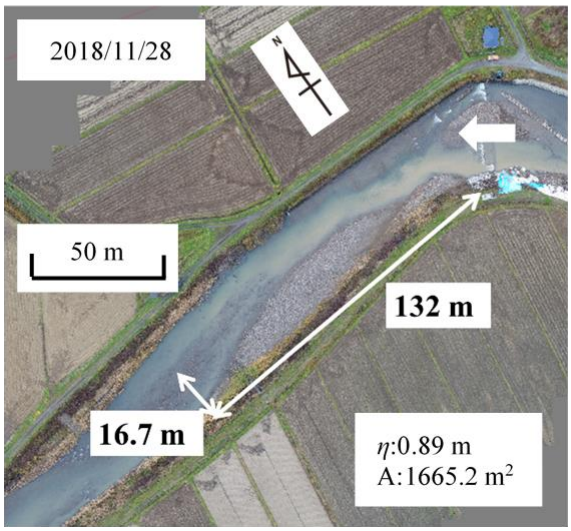

Fig.11 Sandbar condition (November 28, 2018).

Fig.12 Sandbar condition (December 13, 2018).

examined.

Figure 11 shows the condition of the sandbar on November 28, 2018. It again narrowed the channel of the river. However, A was 1665.2 m^2, L was 132 m, B was 16.7 m, and it was thought that the sandbar has flowed out, and η was 0.89 m, which was the ordinary water level.

Figure 12 shows the condition of the sandbar on December 13, 2018. A, L and B could not be derived because the sandbars to be observed were removed by dredging.

Relationship between Water Level and Sandbar Area

The relationship between sandbar area, length and width was examined. Figure 13 shows the relationship between water level and sandbar area. When the water level was lower than the ordinary water level (0.89 m), A increased rapidly, but decreased gradually when the water level rose.

Figure 14 shows the relationship between sandbar area and width. The B also increased as the A increased. Therefore, it was considered that the B greatly affected the A change.

In addition, Figure 15 shows the relationship among A, L and B. Compared data on August 3, 2018 with November 28, 2018, B was decreased due to decreasing A, while L was unchanged. A was reduced by 1281.8 m^2, so it was expected that sandbar was drained by flood when water level was observed more than 3.1 m such as August 15 and September 9, 2018.

CONCLUSIONS

It would be concluding as follows.

1) It was possible grasping the behavior of the sandbar on the water surface. It was possible to measure sandbar area, length, and width.
2) The sandbar was increased sharply when the water level falls below 0.89 m. The sandbar was decreased gently when the water level rises due to rainfall.
3) Evaluation of sandbar width was important to grasp constriction of the channel and erosion of sandbar in channel management.

UAV surveying has been able to quantitatively evaluate the area of the sandbar on the water surface. However, there are still issues such as not being able to derive the volume of the sandbar and evaluating the sandbar under the water. Therefore, in the future, it is necessary to understand the behavior of the sandbar under the water surface by combining the cross-section survey and the UAV survey. In addition, it is important to examine the relationship between the sandbar on the water surface and the sandbar under the water surface.

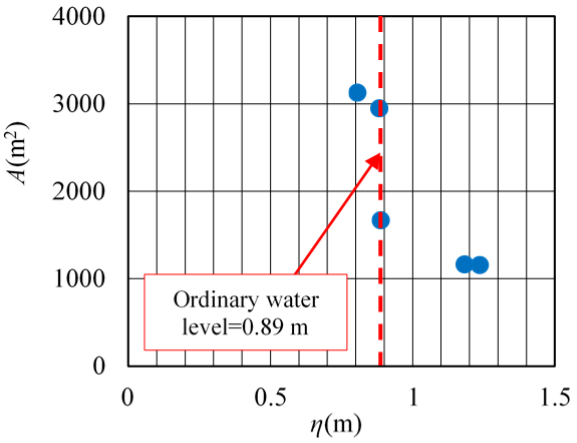

Fig. 13 Relationship between water level and sandbar area.

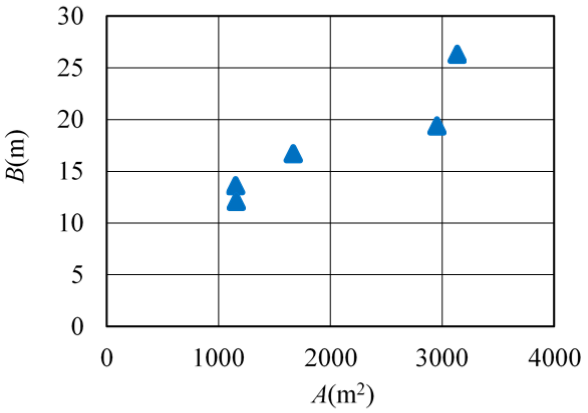

Fig. 14 Relationship between sandbar width and area.

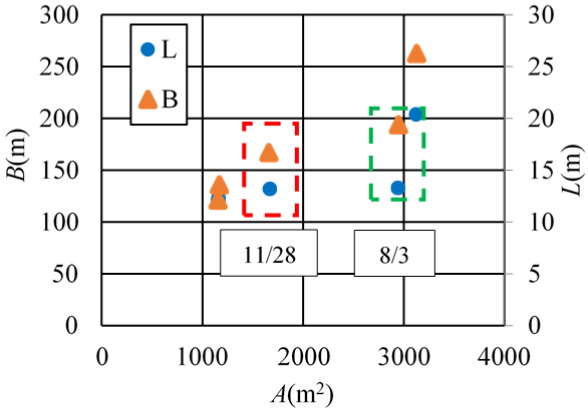

Fig.15 Relationship among sandbar width, length and area.

ACKNOWLEDGMENTS

The author would like to thank the Akita prefecture for their contributions to this study.

REFERENCES

[1] Meteorological Agency. Meteorological case that brought about disaster (from 1989 to this year), <http://www.datajma.go.jp/obd/stats/data/bosai/report/index_1989.html.> (accessed on May 23, 2020).

[2] Ministry of Land, Infrastructure, Transport and Tourism. River management status and issues, <https://www.mlit.go.jp/river/shinngikai_blog/shaseishin/kasenbunkakai/shouiinkai/anzenkakuho/dai01kai/dai01kai_siryou2.pdf> (accessed on May 23, 2020).

[3] Nomura K., and Watanabe K., Study on river management method using multipurpose numerical calculation at small and medium-sized river, Japan Society of Civil Engineers Papers G (Environment), Vol.70, No.5, 2014, pp.235-240.

[4] Ueki K., and Watanabe K., Study on levee damage using numerical calculation in Babame River, Conference of Tohoku Branch of Japan Society of Civil Engineerings, 2017, (CD-ROM).

[5] Obanawa H., Hayalkawa Y. and Gomez C., 3D modeling of inaccessible areas using UAV-based aerial photography and structure from motion, Transactions, Japanese Geomorphological Union, Vol.35, No.3, 2014, pp.283-294.

[6] Matsuba Y., Sato S. and Hadano K., Application of UAV based nearshore topography monitoring to a sand-bypassed beach on Fukude-asaba coast in Shizuoka prefecture, Japan Society of Civil Engineers Paper B2 (Coastal Engineering), Vol.72, No.2, 2016, pp.853-858.

[7] Kawai Y. and Kubota A., Proposal of maintenance management system for river using three- dimensional model, IPSJ SIG Technical Report, Vol.2015-IS-134, No.4, 2015.

[8] Akita Prefecture. Class B river Babame River water system River maintenance basic policy, <http://www.pref.akita.lg.jp/pages/arghive/10601> (accessed on May 23, 2020).

[9] Kawakami M. and Watanabe Y. Hydraulic experiments on influence of alternate bars to bank erosion, Japan Society of Civil Engineers Papers A2 (Applied mechanics), Vol72, No.2(Applied mechanics papers, Vol.19), 2016, pp.593-600.

[10] Kuwamura T. and Watanabe Y. Behavior of Bars under flow condition between single-row bars and double-row bars, Hokkaido Research Institute of Development Public Works Monthly Report, No.602, 2003, pp.3-14

6th Int. Conf. on Structure, Engineering & Environment (SEE), Kyoto, Japan, Nov.18-20, 2020, ISBN: 978-4-909106056 C3051

PASSIVE BASE ISOLATOR FOR VERTICAL DIRECTION USING A POST-BUCKLED SHAPE MEMORY ALLOY BEAM AND ITS DYNAMIC PROPERTY

Atsushi Urakawa [1], Takumi Sasaki [2] and Hiroki Cho [3]
[1] Graduate school of Environmental Engineering, The University of Kitakyushu, Japan;
[2,3] The University of Kitakyushu, Japan

ABSTRACT

Recent years, high-performance and compact vibration isolator has been demanded with the advancement of precise technology. Among various vibration isolators, a passive vibration isolator is the most commonly adopted form due to its simplicity, stability and low cost. In the previous studies, the authors have proposed a simple and compact passive vibration isolator for the vertical direction using a post-buckled shape memory alloy (SMA) beam. This isolator achieved a low natural frequency assuring high static stiffness by utilizing the negative tangent stiffness of a post-buckled SMA beam. It is expected that the appearance of the negative stiffness is related with the phase transformation of a post-buckled SMA beam, however, the fundamental principle of the appearance and the response for a reciprocating motion (vibration) have not been clarified. In this study, in order to clarify these characteristics, the restoring force of a SMA beam subjected to reciprocating motion in its post-buckled state was measured experimentally and predicted by the Finite Element Analysis in which the phase transformation of the post-buckled SMA was taken in account. As the result, it was found that the restoring force converged to a certain force when SMA was subjected to reciprocating motion; the negative tangent stiffness arose when the phase of SMA transforms from Austenite phase to Martensite phase in compression process; SMA with small hysteretic property in stress-strain curve is appropriate for an ideal isolation element. In future research, it is necessary to validate the performance of the isolator taking in account the phase transformation.

Keywords: Buckling, Shape memory alloy, Base isolation, Passive isolation, Nonlinear isolator

INTRODUCTION

For precise equipment, e.g. precision sensors, precision processing machinery, etc., base isolation is crucial technology for assuring their performance and reliability. In the base isolation technology, passive vibration isolators are the most commonly adopted form due to their simplicity, stability and low cost. Basically, their effectiveness, i.e., isolation performance and isolation frequency bandwidth, relies on being able to achieve a low natural frequency when supporting an isolated object, and a low natural frequency can be achieved by supporting an isolated object by a soft spring element. However, when they were applied to isolation in the vertical direction, low stiffness can result in impractically large static deflection due to the weight of the isolated object. Consequently, a key trade-off in the selection of a spring element for an isolator for vertical direction is their low dynamic stiffness, which govern the effectiveness of an isolator, versus their high static stiffness, which is needed for static load bearing capacity. In previous studies [1]-[3], in order to realize such stiffness, many nonlinear systems are proposed. One commonly used technique is making use of nonlinear restoring force of a post-buckled beam. Authors have detected the negative stiffness characteristic of a post-buckled tape-shaped Ti-Ni based shape memory alloy beam (hereafter, called SMA beam) in the previous study[4]. And also proposed a passive vibration isolator using a post-buckled SMA beam and investigated its isolation performance experimentally. In that study, the isolator achieved a low natural frequency of about 3 Hz and exhibited considerable isolation performance. However, few studies have examined the restoring force of a post-buckled SMA. Especially, the expression principle of the negative stiffness, the restoring force of a post-buckled SMA for reciprocating motion, dynamic characteristic of a post-buckled SMA, etc., have not been clarified although they are important for designing and predicting the performance of an isolator.

The motivation of the study is to clarify experimentally and numerically the fundamental characteristic of a post-buckled SMA beam which is needed for establishing the design guideline for an isolator using a post-buckled SMA beam. In this paper, we focused on following characteristics; (1)The response of a post-buckled SMA for reciprocating motion is experimentally and numerically investigated and their properties are compared qualitatively. (2)The expression principle of the negative stiffness is investigated numerically.

In section 2, the general overview of a passive isolator, the restoring force of a post-buckled SMA beam and the conceptual design of an isolator using a post-buckled SMA beam are described. In section 3, the restoring force of a post-buckled SMA beam for several reciprocating conditions is described. Section 4 concerned with the numerical investigation for the restoring force of a post-buckled SMA beam, which was obtained by FE analysis which considers the phase transformation of SMA material, and compared with the experimental results qualitatively.

OVERVIEW OF A POSSIVE VIBRATION ISOLATOR AND AN ISOLATOR USING A POST-BUCKLED SMA BEAM

Overview of a Passive Vibration Itolator

Figure 1 shows the most fundamental model of a passive vibration isolator for the vertical direction. An isolated mass is supported by a linear spring and a linear dashpot. Considering the frequency response of the vibration transmissibility between an isolated mass and base vibration for the vertical direction, the effectiveness of the isolator relies on being able to achieve a low natural frequency. However, low stiffness can result in impractically large static deflection due to the weight of the isolated object. This dilemma can in principle be solved by adopting a nonlinear isolator that exhibits high stiffness when loaded statically and low stiffness in relation to small oscillations about the static equilibrium position. One of tequnique to realize such nonlinearity is making use of nonlinear restoring force of a post-buckled beam.

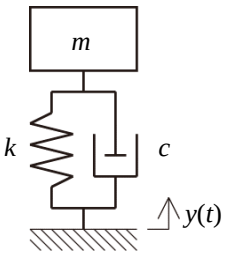

Fig. 1 The most fundamental model of a passive vibration isolator for the vertical direction

Static Restoring Force of a Post-Buckled SMA Beam and Vibration Isolator Using a Post-Buckled SMA Beam

Authors have reported that the static restoring force of a SMA beam, which is subjected to compressive external displacement at both ends of the beam for longitudinal direction , exhibits the negative tangent stiffness in its post-buckled state. Fig. 2 shows one of the measured static restoring force of a post-buckled SMA beam. As shown in the figure, the static restoring force decreases by increasing the imposed compressive displacement, that is , SMA exhibits the negative tangent stiffness characteristic. By utilising this characteristic, authors have proposed a vibration isolator using a post-buckled SMA beam. The conceptual diagram of an isolator is shown in Fig. 3. This isolator incorporated a post-buckled SMA beam, a coil spring and constraint elements that constrained the isolated object to vertical motion. The SMA beam was oriented vertically with one end fixed to a base and the weight of the isolated object acting at the other end. If the weight of the isolated object is larger than the buckling load of the SMA beam, the SMA beam will buckle. Then, if the spring constant of a coil spring, which is installed in parallel to the post-buckled beam, was chosen so as only just to cancels the negative tangent stiffness of the post-buckled SMA beam, in principle, quasi-zero-stiffness (QZS) will be achieved and ideal isolation would be realized.

For designing and predicting the performance of this isolator the static and dynamic property of a post-buckled SMA beam is the essential property. However, studies for these properties is insufficient so far. Then, in the following sections, the restoring force of SMA beam simulating the deflection when it is used for the isolator are examined experimentally and numerically.

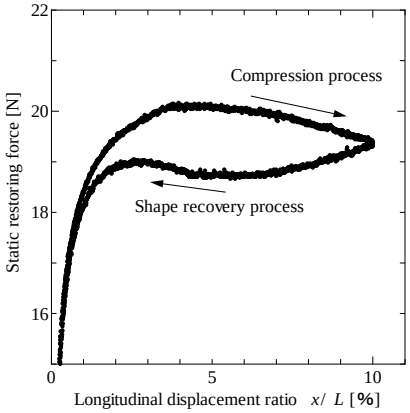

Fig. 2 Static restoring force of a post-buckled SMA beam

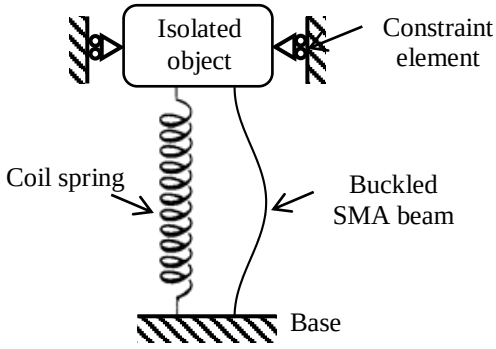

Fig. 3 Conceptual diagram of a vibration isolator using a post-buckled SMA beam

EXPERIMENTAL INVESTIGATION FOR THE RESTORING FORCE OF A POST-BUCKLED SMA BEAM

In order to apply a post-buckled SMA beam to a vibration isolator, it is necessary to examine the restoring force property of a post-buckled SMA beam when it is subjected reciprocal motion. In this section, the restoring force of a post-buckled SMA beam when it is subjected reciprocal motion is examined experimentally.

Figure 3 shows schematic view of the experimental setup. Titanium-Nickel based SMA beam, with specifications summarized in Table 1, was used for the experiment. Both ends of SMA beam was clamped by stainless steel plate. One end was fixed to the base rigidly. Another end was supported by a linear guide and a liear slider which correspond to a constraint element and a device for imposing longitudinal external displacement, respectively. The restoring force of the SMA beam for the original longitudinal direction was measured by a load cell. Since the moving speed of linear slider was controlled to 0.1mm/s, quasi-static restoring force was measured. Stainless plates at both ends had a electrode and the SMA beam could be heated by Joule heat that was generated by applying electric current directly to the SMA beam. The temperature of the SMA beas was monitored by a thermocouple set at the middle of the SMA beam (omitted in Fig. 3) and kept to 30°C by coutrolling the electric current with a PID control system.

In order to simulate the restoring force of the SMA beam when it was used to a base isolation system, following experiment was conducted.

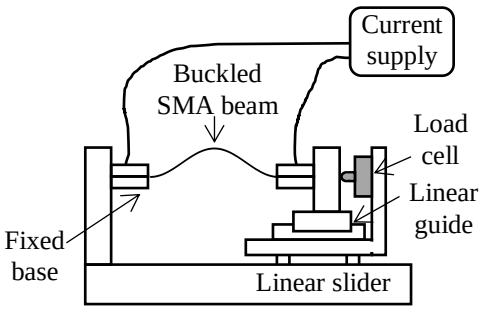

Fig.3 Schematic view of the experimental setup

Table 1 Specification of SMA used in the experiment

Material composition	Ti-50.2at%Ni	
Heat treatment condition	Temperature	753 [K]
	Time	40 [min]
	Cooling condition	Air cooling
Dimension	Width	5.5 [mm]
	Thickness	0.5 [mm]
	Length	110 [mm]

[Exp. 1] Impose 9mm longitudinal displacement firstly, and subsequently impose 10 times reciprocating displacement of which amplitude was increased by 0.2mm per one reciprocation. After the reciprocation, imposed displacement was recovered to the original position (0mm). By this experiment, the restoring force behaviour of the SMA beam when the amplitude of an isolated object was varied could be simulated.

[Exp. 2] Impose 10mm longitudinal displacement firstly, and subsequently let the displacement recover to (a)3mm, (b)4mm or (c)5mm, and finally impose 500 times reciprocating displacement of which peak-to-peak amplitude was 2mm. After the reciprocation, imposed displacement was recovered to the original position (0mm). By this experiment, the restoring force behaviour of the SMA beam after onece large displacement was imposed.

The solid line in Fig. 4(a) shows the measured restoring force for Exp. 1. The dashed line in the figure shows the restoring force for one time reciprocation for comparison. Fig. 4(b) is the magnification of Fig. 4(a). From the figure, it is confirmed that the magnitude of restoring force drops drawing a hysteretic loop while the reciprocating motion was imposed. Also, it is confirmed that the magnitude of hysteretic loop get larger when the amplitude of the reciprocation was large. The lower limit of the dropping restoring force will be considered in the following section.

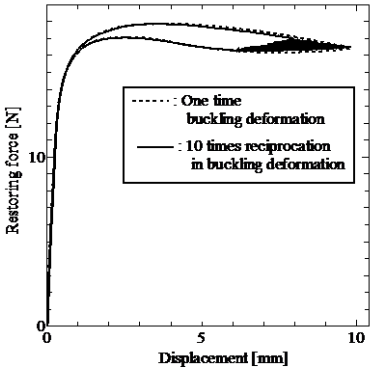

Fig.4(a) Measured restoring force of the SMA beam in reciprocating motion [Exp. 1]

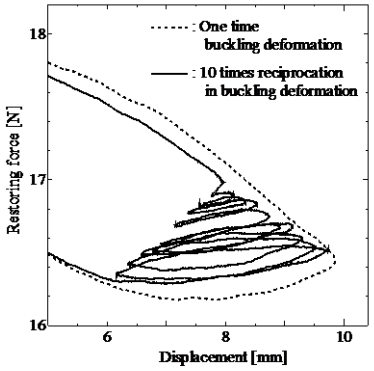

Fig.4(b) Magnification of Fig. 4(a)

Figure 5 shows the measured restoring force for Exp. 2. Marks of ○, □ and ◇ represent the restoring force of shape recover condition of (a)3mm, (b)4mm and (c)5mm, respectively. The dashed lines show the approximate line when the restoring force in reciprotating process were approximated by the linear function. From the figure, it is confirmed that the restoring force in reciprocating motion differed dipending on the start point of recprocating motion, while the restoring force on compression process and shape recover process of all conditions were the same except in reciprocal motion. The gradient of the dashed line corresponds to the approximative tangent stiffness in reciprocating mosion and that of shape recover doncition (a)3mm, (b)4mm and (c)5mm was 0.175 N/mm, 0.132 N/mm and 0.105 N/mm, respectively. From the figure it is confirmed that the approximative tangent stiffness also differed depending on the start point of recprocating motion and it didn't exhibit the negative tangent stiffness but the positive tangent stiffness. These properties, the restoring force and the tangent stiffness varies depending on reciprocational condition, are considered not to be appropriate for the use for an isolator, because the isolation performance varies depending on the vibration condition. However, in a later section, the appropriate material specification desired for the SMA for an isolator will be clarified.

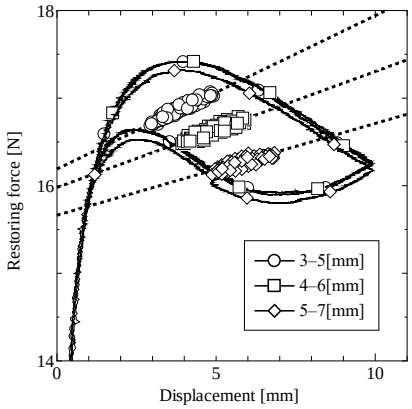

Fig. 5 Measured restoring force of the SMA beam in reciprocating motion [Exp. 2]

NUMERICAL INVESTIGATION FOR THE RESTORING FORCE OF A POST-BUCKLED SMA BEAM

In this section, the post-buckled properties of SMA beam is numerically investigated. On the numerical analysis, Finite Element Analysis was executed by using ANSYS 19.0.

Analytical Model

On the numerical analysis, the SMA beam of which dimension was 7.2mm in width, 50mm in length and 0.43mm in thickness was used. Both ends of the beam was rigidly fixed except the degree of freedom for longitudinal direction at one end was set free. The material property (stress-strain curve) of SMA was approximated by piecewise linear property composed of four linear lines as shown by solid line in Fig.6. The SMA beam was modelled by using three dimensional laminated solid-shell element in order to accurately figure out the stress and the phase transformation of inner part of SMA material.

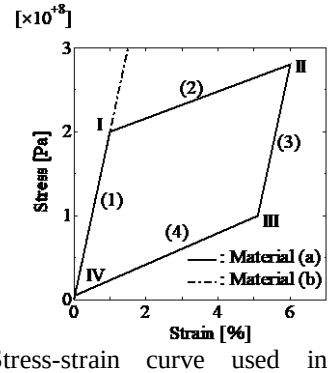

Fig.6 Stress-strain curve used in numerical analysis

Efect of Phase Transformation of SMA on Appearance of the Negative Tangent Stiffness

The effect of phase transformation of SMA beam on appearance of the negative tangent stiffness in its post-buckled state was investigated. In this anaysis two types of material, with specifications summarized in Table 2, was used, where σ_1, σ_2, σ_3 and σ_4 of material (a) represent the stress at the intersection point of I, II, III and IV, respectively. E, ε and ν represent the gradient of line (1), the difference of strain between intersection point of I and II, and also III and IV and Poisson's ratio, respectively. Deformation process on the line (1) can be regarded as deformation process of austenite phase, and that on the line (2) is deformation process of pahse transformation from austenite phase to martensite phase. Also, deformation process on the line (3) can be regarded as elastic deformation of martensite phase, and that on the line (4) is deformation process of pahse transformation from martensite phase to austenite phase. Material (a) approximates a

Table 2 Specification of SMA material used in the numerical analysis

Material (a)	Material (b)
$\sigma_1 = 200$ [MPa]	$\sigma_1 = 2000$ [MPa]
$\sigma_2 = 280$ [MPa]	$\sigma_2 = 2800$ [MPa]
$\sigma_3 = 100$ [MPa]	$\sigma_3 = 1000$ [MPa]
$\sigma_4 = 5$ [MPa]	$\sigma_4 = 50$ [MPa]
$E = 20$ [GPa], $\varepsilon = 0.05$, $\nu = 0.3$	

matereial property of Ti-Ni based SMA, while material (b) is the material of which pahse transformation is suppressed by setting large stress for σ_1.

Figure 7 shows force displacement curve of post-buckled beam when 5mm displacement was imposed for longitudinal direction. Imposed displacement (horizontal axis) and restoring force (primary vertical axis) are normalized by the length of the beam and the buckling load obtained from linear buckling theorem. The solid line and the dashed line show the restoring force of material (a) and (b). Marks ○ and △ show the volume fraction of martensite phase in compression process of material (a) and (b), respectively, by secondary vertical axis. From the figure, it is confirmed that the restoring force of material (a) exhibit negative tangent stiffness in the displacement range beyond 4% in compression process and within 4% in shape recover process. Also, in compression process of material (a), the negative tangent stiffness appears as phase transformation from austenite phase to martensite phase get advanced, while the restoring force of materical (b) exhibits positive stiffness in all displacement range in the figure and exhibit no phase transformation. From these results, it is considered that the appearance of the negative tangent stiffness deeply related to the phase transformatio of the SMA.

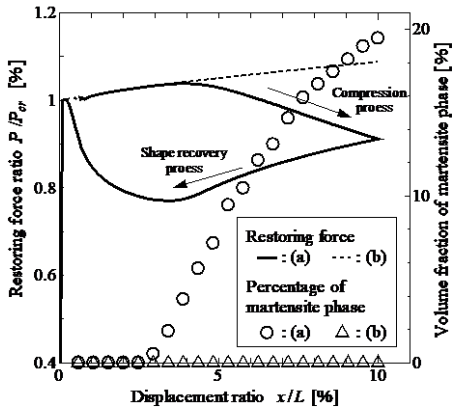

Fig. 7 Force displacement curve and volume fraction of martensite phase

Restoring Force in Reciprocating Motion

In order to investigate the restoring force in reciprocation motion, following analysis was executed.

[Analysis 1] Impose 4mm longitudinal displacement firstly, and subsequently impose reciprocating displacement of which amplitude was 0.25 mm for (a)10 times, (b)50 times, (c)100 times and (d)4999 times. After the reciprocation, imposed displacement was recovered to the original position (0mm).

[Analysis 2] Impose 4mm longitudinal displacement firstly, and subsequently let the displacement recover to 0.8mm, and subsequently impose reciprocating displacement of which amplitude was 0.5mm for 500 times. After the reciprocation, imposed displacement was recovered to the original position (0mm).

Material (a) in table 2 was used for the analysis.

Figure 8 shows the restoring force obtained in Analysis 1. Marks ◇, △, ○ and □ correspond to the restoring force of reciprocating dondition of (a), (b), (c) and (d). Figure 9 shows the magnisication of Fig.8 at reciprocating condition (d). From the figure, it is confirmed that the magnitude of restoring force drops while the reciprocating motion was imposed. Also, if the number of reciprocating time was increased more than 5000 times, it will not lowered than that of 4999 times.

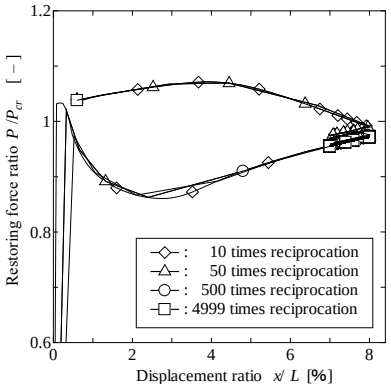

Fig. 8 Restoring force of the beam in reciprocating motion [Analysis 1]

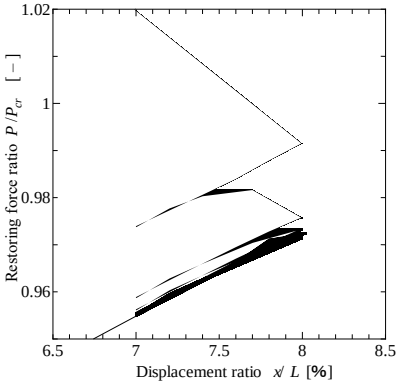

Fig. 9 Magnification of Fig. 8

Figure 10 shows the restoring force obtained in Analysis 2. From the figure, it is confirmed that the magnitude of restoring force rises while the reciprocating motion was imposed. Also, if the number of reciprocating time was increased more than 501 times, it will not lowered than that of 500 times.

From these results, it is confirmed that the magnitude of restoring force drops or rises while the reciprocating motion was imposed in compression process or shape recovery process, respectively, and converges to a certain force. This phenomenon qualitatively corresponds to the experimental result

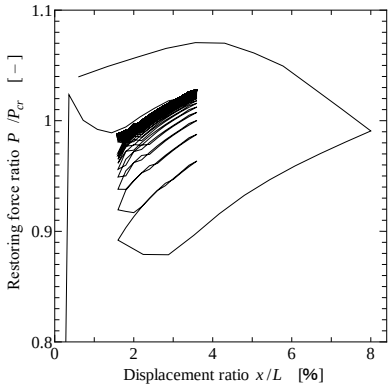

Fig. 10 Restoring force in reciprocating motion in shape recovery process [Analysis 2]

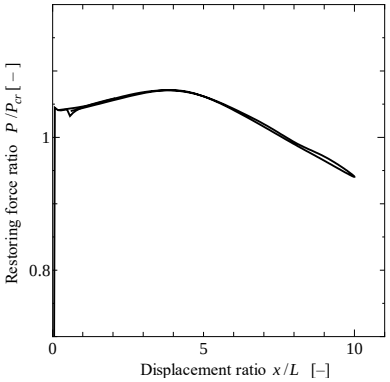

Fig. 11 Restoring force of the beam with small hysteretic material

refered in the last section. The restoring force in Fig.8 doesn't draw loop, which is different from experimental result, however this is because that the reciprocating amplitude of numerical analysis was smaller than the experiment and stress-strain curve was approximated by piesewise lines.

Desired specification of the SMA for an isolator

The restoring force characteristics refered in previous sections were not appropriate for a high performance isolator due to positive stiffness characteristic in reciprocating motion. The appearance of positive stiffness is thought to be the most likely cause of the difference of the gradient of restoring force among compression process and shape recovery process, that is, hysteretic property of SMA. Then, the restoring force of a beam with small systeresis material was calculated. The specification of the material is summarized in table 3.

Figure 11 shows the restoring force of the beam with material (c). The restoring force exhibits negative tangent stiffness in the displacement range beyond 4% and almost constant stiffness (gradient of the curve) could be obtaind in the displacement range beyond 5% even in compression process or in shape recovery process. This kind of property is appropriate for the system shown in Fig. 3, since desired isolation performance would be obtained regardless of vibration condition.

Table 3 Specification of a material of which hysteresis in stress-strain curve is small

Material (c)
$\sigma_1 = 200$ [MPa], $\sigma_2 = 280$ [MPa],
$\sigma_3 = 275$ [MPa], $\sigma_4 = 195$ [MPa]
$E = 20$ [GPa], $\varepsilon = 0.05$, $\nu = 0.3$

CONCLUSIONS

This paper has investigated the dynamic property of a post-buckled SMA beam experimentally and numerically. The restoring force of Ti-Ni based SMA beam exhibited negative tangent stiffness for one time buckling deformation, however, it exhibited positive stiffness when reciprocal motion was imposed in post-buckled state. The restoring force varied while in reciprocation and converged a certain force. The restoring force of a beam with small hysteretic material exhibit almost constant tangent stiffness in displacement range beyond 5%. For a high performance passive isolator, realizing SMA material which has such small hysteretic property needs to be addressed in future studies.

ACKNOWLEDGMENTS

This work was supported by JSPS Grant-in-Aid for Scientific Research (C) number 18K04025.

REFERENCES

[1] Ibrahim R. A., Recent advances in nonlinear passive vibration isolators, Journal of Sound and Vibration, 314, 2008, pp. 371-452.
[2] Sasaki T, Waters T. P., Analysis of a vibration isolation table comprising post-buckled Γ-shaped beam isolators, Journal of Physics: Conference series, Vol. 744, 2016, No. 1: 1-8.
[3] Chiyojima T. and Sasaki T., Development of a passive vibration isolator using a post-buckled Γ-shaped beam (Improvement of the isolation performance by considering mode shapes of a Γ-shaped beam), Proc. of Asia Pacific Vibration Conference 2017, 2017, pp. 11-16.
[4] Sasaki T. and Kimura Y., Experimental Study on a Passive Vibration Isolator Utilizing Dynamic Characteristics of a Post-Buckled Shape Memory Alloy, Proc. of Asia Pacific Vibration Conference 2019, 2019, pp. 1-6.

6th Int. Conf. on Structure, Engineering & Environment (SEE),

Kyoto, Japan, Nov.18-20, 2020, ISBN: 978-4-909106056 C3051

MRT JAKARTA: A SHORT EVALUATION AFTER 1 YEAR OF OPERATION

Aleksander Purba[1]
[1]Engineering Faculty, University of Lampung, Indonesia 35145

ABSTRACT

Jakarta has been planning the MRT project since the 1980s, but it has been canceled several times for a number of reasons, including the economic crisis in 1990s. The implementation of sustainable Jakarta MRT entails coordination among different sectors and levels of government. An increase in public transport would be more realistic if accompanied by disincentive mechanisms for users of private vehicles on the one side and incentives for public transport users on the other. Like it or not, the city's next job is to change people's behaviours through both educative and repressive measures. Within the framework of an integrated MRT development, the government should start thinking about reliable feeders connecting MRT routes to settlement centres. In addition, pedestrian paths linking shelters to central business districts and offices need also be improved. In the long term, the growth of settlements and new activity centres in the city's master plan needs to be integrated into the MRT. Building affordable apartments downtown to shorten residents' commuting journeys is unavoidable. As experienced by such cities, the built environment has significant impacts on the activity-travel behavior of private housing residents, partly because they could self-select into the types of residential environment matching their travel preference.

Keywords: MRT Jakarta, Evaluation, Integrated, Travel behavior

INTRODUCTION

The year 2019 has been marked by important milestones in the modernization of the country's railway transportation system with the inauguration of the first ever rail-based mass rapid transportation system and the development of the first high-speed train. On March 23, President Joko "Jokowi" Widodo inaugurated Jakarta's MRT system, marking a new era in Indonesia's railway transportation system. After almost a year since it began commercially operating, the Jakarta MRT has become an importation means of transportation for Jakarta residents. Phase 1 connects Lebak Bulus to Bundaran HI along 20.1 kilometres and consists of 13 stations (7 elevated stations and 6 underground stations). The Indonesian Ministry of Transport approved this plan in September 2010 and invited tenders. Construction began in October 2013. Phase 1 was opened for free service on 24 March 2019. Commercial service began on 1 April 2019. Phase 1 is expected to serve 212,000 passengers per day. This expected capacity may be maxed out to 960,000 per day. The 20.1 kilometres distance is covered in under 30 minutes. Within its first month of operations, 82,000 passengers used the line daily. The charged fare for a trip on the MRT starts at Rp3,000, increasing by Rp1,000 for every station passed. A trip spanning the entire existing line in 2019 would cost a passenger Rp14,000.

A refundable Rp15,000 deposit is required to purchase a single journey ticket, in addition to fares required for the journey. The Jakarta MRT employs a cashless fare payment system. A dedicated contactless smart card known as the 'Jelajah' can be purchased from the ticketing machines or ticket offices located at every station. The Jakarta MRT is expected to stretch across over 108 kilometres, including 26.9 kilometres for the red line (from Lebak Bulus to Kota) and 87 kilometres for the yellow line (from Cikarang to Balaraja).

Otherwise, during Covid-19 emergency period the number of MRT passengers jumped significantly. Referring to report on Tuesday, March 17, there were only 32,000 passengers from regularly 100,000 per day. It went further down to 28,000 on Wednesday and 24,000 on Thursday. The policy limits the number of MRT passengers on board of one car for only 60 people or 360 per train set of six cars or less than 30% of capacity. This paper focuses on the evaluation of projected and actual ridership of MRT Jakarta after one year of operation and after the heading, respectively.

A CASE STUDY: MRT JAKARTA

The Jakarta mass rapid transit (Indonesian: moda raya terpadu Jakarta or Jakarta MRT is a rapid transit system in Jakarta, the capital city of Indonesia. The system is operated by PT MRT Jakarta (Perseroda), a municipally owned of the city of Jakarta. Jakarta is the capital city of Indonesia, harbouring 10 million inhabitants, one-third of the population of Greater Jakarta. It is estimated that over four million residents of the surrounding Greater Jakarta area commute to and from the city each working day. Transport issues have increasingly begun to attract political attention and it has been foreseen that without a major

transportation breakthrough, the city will have complete traffic gridlock by 2020, as illustrated in Fig. 1.

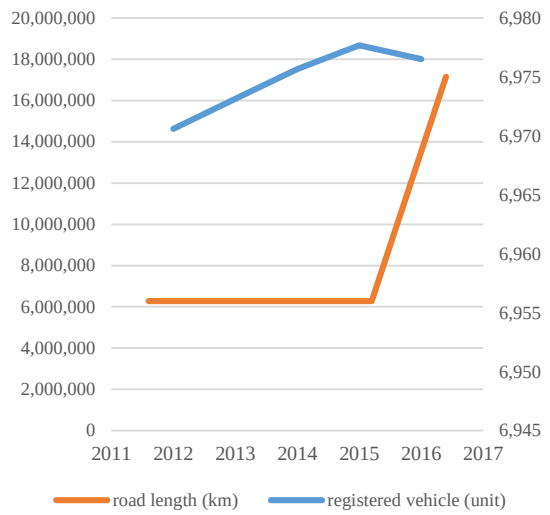

Fig. 1 Relationship between road length and registered vehicle

Previously, public transportation now mainly consists of the TransJakarta bus rapid transit system with a length of 230 kilometers and phase 1 of the MRT project was funded through a soft loan (Rp 16 trillion) from JICA with a 30 years tenure and 0.25% interest per annum. Trial run conducted since December 2018 until February 2019.

Besides serving as trial run and form of machinist familiarization prior to full operation, the parallel trial run is also part of the company's campaign to encourage the people of Jakarta to use public transportation modes in order to reduce congestion. Key performance and map of the line are shown in Table 1 and Fig. 2, respectively.

Table 1 Key performance of the line

Length network	20.1 km
Number of stations	13
Distance between stations	0.8~2.2 km
Track width	1,067 mm
Travel time	± 30 minutes
Headway	5 minutes
Operation hours	05:00~24:00
Targeted no of passenger	130,000 person/day
Number of train	16 (include 2 sets for reserve)
Electricity	60 MVA
Train operation system	Automatic train operation
Signaling system	Communication based train control
No of employees	520 (2018)

Fig.2 Line map of MRT Jakarta

URBAN REGENERATION

As perform by the MRT operating experience in other countries -though different in every city and country- MRT Jakarta is also designed to support the region's economy and improve the quality of life. Table 2 shows several of them, including the ongoing and will be implemented. Based on long experiences of such cities, it is undeniable that the development of MRT will lead to job losses since the city’s transportation sector is more capital-intensive by nature. Thus the government needs to explore every avenue dealing with the process of adaptation and the transfer of transportation sector employers in stages through capacity building, capital assistance and provision of new jobs

Table 2 The city's potential regeneration

Growth development
10.83 million m2 new mixed development area
Rp242.2 trillion growth of property value related to TOD
153,776 reduced parking lots
Contribution to regional income
Rp742 billion/year from land & building taxes in TOD area
Rp182 billion/year tax contribution from rental office & retail
Rp15.4 trillion contribution from buying property taxes (PJB/BPHTB)
Social & environmental contribution
34,047 units potential development of affordable housing in TOD area
639,380 employed workers
210,000 m2 area of public activities
739,000 m2 park and public open space
149.1 km development of sidewalk
56,854 m2 riverside area

As development of bicycle line is relatively a new project in Jakarta, its implementation may take a long time, such as the experience of other cities. Though as experienced by Beijing, public bicycle has be defined as a component of public transit by the authorities of Beijing. As a continuation of the public transit, public bicycle is helpful to implement a new trip mode of "Public Bicycle + Public Transit + Public Bicycle" to improve the accessibility of Public Transit. The new scheme of PBS is operated by professional public bicycle rental company, but funded by a state-owned enterprise under the supervision of the government.

The main profit point of private company does not rely on rental fees, but on the sale of maturement of bike rental technological system [1]. More advance, as performed by Brisbane, there is more scope for interventions based around the adoption of smart transport measures to shape attitudes and encourage changes in travel behaviour.

This work also indicates that both land use planning and complementary transport measures can impact on travel behavior [2]. Referring to Chava, Newman, and Tiwari [3], for increasing sustainable mode share especially among new build residents, measures need to be taken to encourage intensive mixed land use developments in new TODs like the traditional old residential area. To encourage walking, cycling and to provide safe access to PT, neighbourhood NMT infrastructure needs to be improved. In addition, to reap significant metro ridership benefits and to ensure transit equity, the TOD policy must include affordable housing policies, to accommodate people with low income and low vehicle ownership, as their willingness to use the metro is higher than the gentrifies.

At city level, for the metro to attract more TOD residents it is necessary to expand the metro influence area beyond walking distance destinations by integrating with other existing modes of travel such as bicycles, IPT and buses [3]. Based on the Regional Regulation of the DKI Jakarta Provincial Government No. 9/2018, the Company is granted the right to conduct property development and management at stations, station areas and depots as well as concession rights to manage and develop land, buildings both underground and above ground in all areas in stations and depots and in outside the stations and outside the depots in a certain area to be commercialized through ways of being leased or making cooperation to create potential income other than direct income from ticket sales. In accordance with Governor Regulation No. 140/2017, MRT Jakarta is assigned as the main operator included developing TOD along the line with the following functions: to coordinate land and or building owners in regional planning and development, to encourage efforts to accelerate the development of TOD infrastructure and facilities in accordance with the city design guidelines, to coordinate the land and or building owners, tenants and other stakeholders in the TOD area management, maintenance and supervision, and to monitor the TOD area development. Referring to Hong Kong experienced, the built environment has significant impacts on the activity-travel behavior of private housing residents, partly because they could self-select into the types of residential environment matching their travel preference. However, when it comes to public housing residents, density, accessibility, and self-containment have no significant impacts on their activity-travel behavior. Because they are not likely to self-select where to live and daily infrastructures and services are mandated in public housing development, the access to these facilities at the local level helps overcome transportation constraints of public housing residents in low-density (or suburban) areas. That is, neighborhood planning matters to activity-travel behavior of public housing residents in Hong Kong.

COMPANY ACHIEVEMENT

After about one year of operation, the financial performance of the company is shown as following figures. They are asset, equity, expenditure, income, and total asset and total equity, respectively. It is important to note that since its establishment until the end of 2018, the company has not yet operated commercially and has not yet distributed dividends to shareholders. The funding for MRT Jakarta project is sourced from the capital investment made by the company's shareholders comprising DKI Jakarta

Provincial Government, through the Regional Capital Investment (PMD) scheme. Project construction and development funders consist of grants (49%) and loans (51%). One of the company's best achievements is asset growth increased 37%, it was in line with the company physical progress at the end of 2018.

Fig. 3 Company's assets

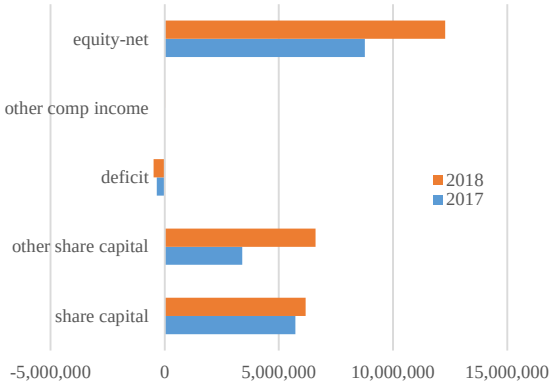

Fig. 4 Company's equity

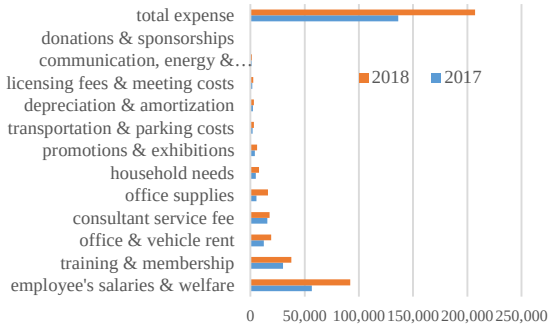

Fig. 5 Company's expenditure

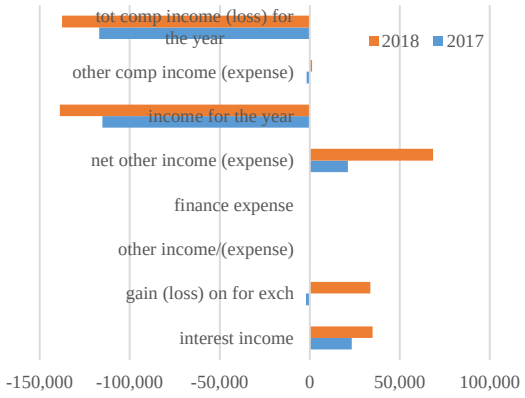

Fig. 6 Company's income

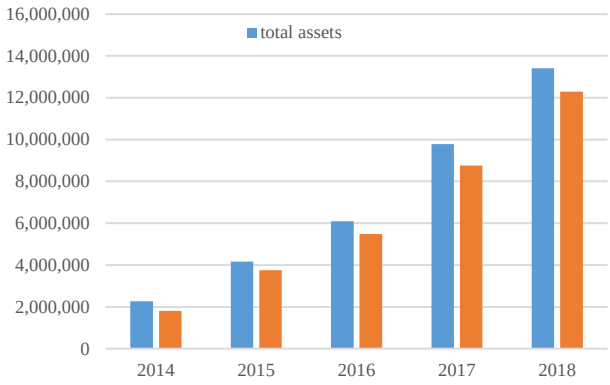

Fig. 7 Total assets and equity (2014-2018)

DISCUSSION

As experienced in other countries, challenges for the MRT and public transportation in the new line is to increase the passenger capacity. While the initial targeted daily ridership of 130,000 is a good target to aim for in the short term, it requires built environment characteristics measured in a neighbourhood-based unit, including residential density, distance to transit and bus stops within 500 m, significantly affect public transit behavior including travel distance, travel time and transit mode choice [4]. It is important to note that the number of passengers differs from station to station. The minimum volume is 964 passengers per day, while the maximum is more than 66,715 passengers per day refers to Metro Stations in Bangkok. The area around the metro station also ranges from the lowest population density (1995 population/km2) to the highest (19,814 population/km^2). The residential area comprises all metro stations. The station with the lowest density in the residential area has approximately 420,000 m^2 of residential floor area units. The highest portion of the

commercial, industrial, and mixed use relative to the residential area. Most stations are at a distance of less than 1 km from municipal public service facilities, landmarks, and retail services. The average distance from the metro stations to these locations is less than 300 m. Access to public transport facilities is found to vary from station to station [5]. Hong Kong experiences suggested the built environment has significant impacts on the activity-travel behavior of private housing residents, partly because they could self-select into the types of residential environment matching their travel preference. However, when it comes to public housing residents, density, accessibility, and self-containment have no significant impacts on their activity-travel behavior. Because they are not likely to self-select where to live and daily infrastructures and services are mandated in public housing development, the access to these facilities at the local level helps overcome transportation constraints of public housing residents in low-density (or suburban) areas. That is, neighborhood planning matters to activity-travel behavior of public housing residents in Hong Kong [6]. Moreover, the Washington metropolitan area as the study case: Household car ownership was found to be significantly associated with residential density, employment density, land use mix, average block size, and distance from CBD. The factors of residential density, average block size, and distance from CBD were found to have significant effects on commuter's transit, and walk and bicycling mode choice. Meanwhile, the mode of walk and bicycling was also influenced by employment density around residential location. People living in high density areas may travel less due to increased accessibility but they can also travel more due to reduced travel costs [7], [8]. Another cities of the USA are shown different findings: even classified by its transit connection, station Park (Salt Lake City region) is more of a TAD (transit adjacent development) than a TOD. Huge parking lots dominate the space between the commuter rail station and other components of the development [9]. In Los Angeles, Chakrabarti [10] concluded it is unrealistic to expect that transit can win over auto in a large number of circumstances. Transit agencies need to invest in better bike-transit and rideshare- (or car share-) transit integration for creating truly multi-modal cities, and improving door-to-door connections via active or shared travel modes. But most of literatures stated mixed land-use policies reduce transport energy consumption. When mixed-use land also has a good jobs-housing balance, transport efficiency is even greater. Mixed land-use policies should be encouraged to shape urban development in more sustainable ways during China's ongoing rapid urbanization [11]. Regarding the costs Zolnik [12] found at the household-level, private-vehicle commuting costs for the 55-to-64 age cohort are slightly less than for the 45-to-54 age cohort. Comparing Whites and Asians, costs are lower for Asians. In the $75,000-to-$99,999 and greater-than-or-equal to-$100,000 income categories each spent $0.21 more on the work trip than respondents in the $25,000-to-$49,999 income category. Private-vehicle commuting costs for respondents in the manufacturing, construction, and maintenance occupational category are higher than for respondents in the professional, managerial, and technical occupational category. Costs are also higher for males than females.

CONCLUSION

The Jakarta MRT has been just a dream the people of Jakarta have had for equalizing with the advanced transportation systems present in foreign developed countries. Referring to financial highlights, the MRT asset growth increased by 37% during 2017 to 2018 period. It was in line with the company physical progress while the company has not operated commercially due to trial run conducted since December 2018 until February 2019. MRT Jakarta announced it has surpassed the target of 65,000 passengers since its first day of commercial operation. Neighbouring countries such as Malaysia, Singapore, Thailand and the Philippines have long since developed MRT systems to cope with traffic congestion in their respective capital cities. Despite having smaller populations than Jakarta, Singapore and Kuala Lumpur have more extensive city rail networks. Singapore has 129.7 kilometres of MRT and 28.8 kilometres of feeder LRT (Light Rail Transit). Kuala Lumpur has 175 kilometres of city commuter trains, 56 kilometres of MRT, 57 kilometres of high-speed rail (ERL) and 8.6 kilometres of monorails. All in all, the benefits of MRT will be fruitless if the city does not draw up supporting policies as experienced of another city around the globe**.**

REFERENCES

[1] Liu, Z., Jia, X., and Cheng, W., Solving the Last Mile Problem: Ensure the Success of Public Bicycle System in Beijing, Procedia - Social and Behavioral Sciences, Vol. 43, 2012, pp. 73–78.

[2] Kamruzzaman, M., Shatu, F. M., Hine, J., and Turrell, G., Commuting mode choice in transit oriented development: Disentangling the effects of competitive neighbourhoods, travel attitudes, and self-selection, J. of Transport Policy, Vol. 42, 2015, pp. 187–196.

[3] Chava, J., Newman, P., and Tiwari, R., Gentrification of station areas and its impact on transit ridership, J. of Case Studies on Transport Policy, Vol. 6, No. 1, 2018, pp. 1–10.

[4] Yu, L., Xie, B., and Chan, E. H. W., Exploring impacts of the built environment on transit travel: Distance, time and mode choice, for urban villages in Shenzhen, China, J. of Transportation Research Part E: Logistics and Transportation Review, Vol. 132, 2019, pp. 57–71.

[5] Nyunt, K. T. K., and Wongchavalidkul, N., Evaluation of Relationships Between Ridership Demand and Transit-Oriented Development (TOD) Indicators Focused on Land Use Density, Diversity, and Accessibility: A Case Study of Existing Metro Stations in Bangkok, J. of Urban Rail Transit, Vol. 6, No. 1, 2020, pp. 56–70.

[6] Wang, D., and Cao, X., Impacts of the built environment on activity-travel behavior: Are there differences between public and private housing residents in Hong Kong? J. of Transportation Research Part A: Policy and Practice, Vol. 103, 2017, pp. 25–35.

[7] Ding, C., Wang, Y., Tang, T., Mishra, S., and Liu, C., Joint analysis of the spatial impacts of built environment on car ownership and travel mode choice, J. of Transportation Research Part D: Transport and Environment, Vol. 60, 2018, pp. 28–40.

[8] Hong, J., and Goodchild, A., Land use policies and transport emissions: Modeling the impact of trip speed, vehicle characteristics and residential location, J. of Transportation Research Part D: Transport and Environment, Vol. 26, 2014, pp. 47–51.

[9] Ewing, R., Tian, G., Park, K., Sabouri, S., Stinger, P., and Proffitt, D., Comparative case studies: trip and parking generation at Orenco Station TOD, Portland Region and Station Park TAD, Salt Lake City Region, J. of Cities, Vol. 87, 2019, pp. 48–59.

[10] Chakrabarti, S., How can public transit get people out of their cars? An analysis of transit mode choice for commute trips in Los Angeles, J. of Transport Policy, Vol. 54, 2017, pp. 80–89.

[11] Zhang, M., and Zhao, P., The impact of land-use mix on residents' travel energy consumption: New evidence from Beijing, J of Transportation Research Part D: Transport and Environment, Vol. 57, 2017, pp. 224–236.

[12] Zolnik, E. J., The costs of sprawl for private-vehicle commuters, J. of Transport Geography, Vol. 20, No. 1, 2012, pp. 23–30.

6th Int. Conf. on Structure, Engineering & Environment (SEE), Kyoto, Japan, Nov.18-20, 2020, ISBN: 978-4-909106056 C3051

LABORATORY OBSERVATION ON DESICCATION CRACKING OF THIN CLAY LAYER

Fauzilah Ismail[1], Ahmad Kamil Arshad[2], Nadiah Shaari[3], Nursafiah Khalid[1], Muhammad Haniff Asmuni[1], Muhammad Haziq Shuib[1] and Ekarizan Shaffie[2]
[1]Faculty of Civil Engineering, Universiti Teknologi MARA Shah Alam, Selangor, Malaysia; [2]Institute for Infrastructure Engineering and Sustainable Management (IIESM), Universiti Teknologi MARA Shah Alam, Selangor, Malaysia; [3]Faculty of Civil Engineering, Universiti Teknologi MARA Pasir Gudang, Johor, Malaysia

ABSTRACT

Desiccation is the state of extreme dryness, or the process of extreme drying. During drying process, clay soil shrank and developed a tiny crack from the surface. The crack propagation is able to progressed deep into the soil that can affect the stability and efficiency of the geotechnical structures such as dam failures. A series of laboratory work was conducted to investigate desiccation cracking of kaolin clay sample of different thickness placed on three different types of plate – ceramic, wood and steel. The crack propagation and pattern of these kaolin clay samples placed on ceramic base plates were examined and compared with the samples placed on wood and steel plates. From the test, it was revealed that 10 mm thick kaolin clay sample has the highest crack intensity factor (CIF) with rapid propagation of cracks, while samples that were placed on the steel plate experienced high rate of drying process as compared to samples put on ceramic and wood plates. It is also observed that the crack propagation and pattern are also influenced by the thickness of the samples and type of plates used.

Keywords: Desiccation, Kaolin clay, Crack propagation, Crack pattern, Thickness, Plates

INTRODUCTION

Clay soil usually can be found in many geotechnical structures such as embankment dam, slope and landfill. Clay soil potentially develops desiccation cracking during drying that can affect the stability and efficiency of the geotechnical structures such as dam failures [1] and slope failures [2]. Desiccation is the state of extreme dryness, or the process of extreme drying. During drying process, clay soil shrank and developed a tiny crack from the surface. As moisture content dissipates the crack opening becomes bigger and deeper.

Laboratory scale (small size) investigations on desiccation cracks of slurry, clay paste and starch-water mixed cakes have been carried out by several researchers [3], [4], [5] &[6]. This paper reports the results of a laboratory work that has been performed to investigate desiccation cracking of manufactured kaolin clay paste of different thickness and set on different base plates made of ceramic, wood and steel materials. Propagation of cracks and their patterns that appeared during the drying process are also presented herein.

LABORATORY EXPERIMENTS

A series of laboratory testing on desiccation cracking has been carried out to examine the effect of thickness and different base plate materials utilised for kaolin clay samples, as well as crack propagations and patterns.

Sample Preparation

The experimental work was carried out using manufactured kaolin clay. The basic properties and soil classification of kaolin clay was acquired using the Atterberg's Limit Test.

The samples were prepared in liquid state by mixing dry powder of kaolin with 70% of water content. The dry powder was mixed thoroughly with distilled water and left overnight to allow for the hydration process to take place. Prior to that, the moisture content (w%) of the sample paste was determined before storage. Three alternate layers of cling film and aluminium foil were used to preserve the moisture content of samples. These wrapped samples were then stored in air tight containers and kept away from direct sun light. The moisture content was checked again the next day for control purpose before desiccation test is conducted for the kaolin clay samples.

Test Methodology and Procedure

The Plastic Limit Test and Cone Penetration Test were done to obtain the plastic limit and liquid limit

of kaolin clay sample, following the procedure as stated in BS1337:1990 Part 2 – Classification Tests. The results are tabulated as shown in Table 1. The sample was classified as clay of high plasticity.

Table 1 Kaolin Clay Properties

Descriptions	Results
Type of soil used	Kaolin Clay
Liquid limit (%)	68
Plastic limit (%)	34
Plasticity index	34
Specific Gravity	2.68
Soil classified as clay of high plasticity	

Desiccation test was carried out in a room temperature of an average 30°C. Main equipment required for the test are desiccation plates made of steel, wood and ceramic, camera and weight balance.

A square kaolin paste sample of size 21 mm was placed on a desiccation plate. A camera was clamped at a fixed height of about 600 mm above the plate. The aerial photo and weight of the sample were monitored, measured and recorded for every 6 hours interval daily. However monitoring scheduled was lengthen to duration of 12 and 24 hours interval after the moisture content gradually reduced. This was experiential observed between 5 to 15 days after desiccation test was started dependent on the samples thickness.

A grid system of aperture size 1.5 cm × 1.5 cm was used for the purpose of monitoring the crack propagation. Figure 1 shows the aerial photo of the wet sample of kaolin paste placed on the ceramic plate and the grid system. The sample was labelled as C1-3010, of which C refers to ceramic plate followed by the number of sample (sample 1), room temperature (30°C) and thickness of the sample (10 mm). For other plates, S and W denote steel and wood, respectively. The monitoring program ended when the moisture content of sample remained constant and crack propagation ceased.

Fig. 1 Kaolin paste sample on ceramic plate and grid system.

DESICCATION TEST RESULTS

Desiccation test results are examined and discussed based on Crack Intensity Factor (CIF), loss of moisture content and evolution of crack pattern. The effects of different sample thickness and different plate material used in the test are also discussed in the conclusion.

Crack Intensity Factor

Crack Intensity Factor (CIF) is defined as the time-variable ratio of the surface crack area, A_c to the total dried surface area of the soil, A_t [8]. However only cracks formation with more than 2 mm depth are considered for the calculation of CIF [9]. Surface crack area, A_c is determined by an approximate method based on the manual grid system of size 1.5 cm × 1.5 cm by using tracing paper as shown in Figure 2. The tracing process was done upon completion of the drying process, i.e constant mass gained and when crack propagation ceased. Estimated area of crack (A_c) of related sample was then summarised manually based on the tracing drawing obtained using grid system.

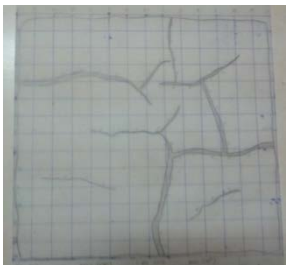

Fig. 2 The area of crack traced using grid system.

CIF result for all kaolin samples is tabulated in Table 2 and presented as a chart shown in Figure 3. Overall result indicates that the evolution of crack is high in the thinnest sample (10 mm) regardless of the types of base plate used. However, the highest CIF percentage of 5.02% is obtained from desiccation test of kaolin clay placed on steel plate. Almost similar CIF percentage results were attained for samples placed on wood and ceramic plates for both 10 mm and 15 mm thicknesses. For 30 mm thick kaolin clay the CIF percentage demonstrated a unique trend of no crack sign appearance on all samples.

Table 2 Crack Intensity Factor (CIF)

Base Plate	Sample No.	Crack area, A_c (cm^2)	Total area of dry soil, A_t (cm^2)	CIF (%)
S	S1-3010	21.08	420.27	5.02
	S2-3015	16.28	420.25	3.87
	S3-3030	nil	414.09	0
W	W1-3010	19.13	417.38	4.6
	W2-3015	3.94	368.55	1.1
	W3-3030	nil	401.85	0
C	C1-3010	17.43	412.09	4.2
	C2-3015	4.88	407.25	1.2
	C3-3030	nil	407.39	0

Note: S, W and C is refer to steel, wood and ceramic base plate respectively and whilst nil is denote no crack occurred.

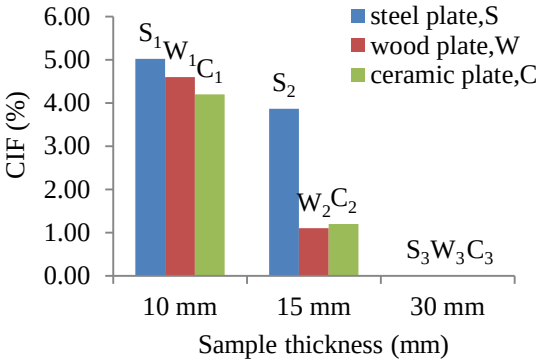

Fig. 3 CIF results for different thickness and plate used.

Moisture Content

Desiccation is the process of extreme drying therefore it is directly related with the loss of moisture content. Monitoring program for the measurement of moisture content is crucial. It must be done continuously and taken at appropriate interval until the constant mass achieved. The loss of moisture content for all kaolin paste samples are plotted on a graph as shown in Figure 4.

A drastic reduction of moisture content with rapid crack propagation in the first 5 days of testing period can be seen for kaolin clay of 10 mm thickness. Primary cracks were formed within this period followed by appearance of secondary cracks as moisture content gradually decreased till it remained constant. The monitoring program was stopped after a few constant readings of moisture content were recorded.

Overall results show the group of 10 mm thickness samples (S1, W1 and C1) has the highest CIF percentage as compared to the other groups of samples. As for kaolin clay of 15 mm thickness (S2, W2 and C2), the losses of moisture content are slightly slower than that of the first group of samples. However, the result of second group shows a significant dropped in moisture content for the first 9 days for kaolin clay placed on steel plate. Area of primary crack formation is also less than the primary crack formation area of the first group samples. The highest CIF calculated for this second group samples is 3.87% for kaolin clay placed on steel plate.

Different occurrence was observed for kaolin clay of 30 mm thickness whereby the result shows a gradual and steady reduction of moisture content throughout the drying process. Nearly 24 days passed by before the moisture content became constant. However, for kaolin clay placed on wood plate the drying process was prolonged up to 36 days. CIF percentage is zero and no crack formed for all samples in this third group (S3, W3 and C3). Nevertheless, the total surface area is reduced due to shrinkage.

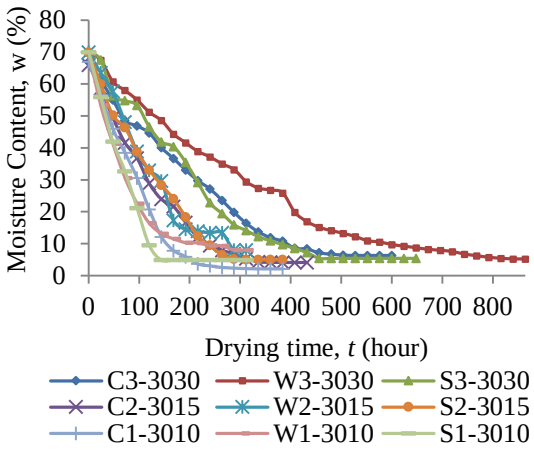

Fig. 4 The relationship between moisture content and drying time.

Evolution of Crack Pattern

The geometric features of cracks such as width, depth and surface area are important parameters because they influenced both the soil hydraulics and mechanics [8]. It also signifies the evolution of crack pattern on the surface area. The time-variable aerial photos were taken for all samples. These photos display the propagation of cracks and their formations at the end of the test.

It is evident that the primary cracks meet at a right angle and produce an orthogonal pattern for all samples of kaolin clay of 10 mm thickness, as shown in Figure 5. Secondary cracks appeared after the primary cracks ended and made a narrow opening. Yet, not much of secondary cracks can be viewed for all desiccation test categories (i.e. different plate used).

S1-3010 W1-3010 C1-3010

Fig. 5 Crack pattern for kaolin clay of 10 mm thickness at the end of the test.

Normally, the progression of crack starts from the edge of sample [7] but it is observed that for kaolin clay of 15 mm thickness the propagation of cracks start from the centre of the sample. It is suspected that a small defect exists on the surface during sample preparation where this defect can trigger crack formation due to stress concentration and shrinkage distortion of surrounding medium [7]. However, for an unknown reason the propagation of cracks for all kaolin samples of 15 mm thickness possess similar trait, in which it starts from the middle of the surface and develops outward to the edges. This is regardless of different types of plate used as shown in Figure 6.

S2-3015 W2-3015 C2-3015

Fig. 6 Crack propagation during drying process for samples of 15 mm thickness.

For kaolin clay of 30 mm thickness, there are no cracks forming on all samples as shown in Figure 7. Nevertheless, the total surface area is reduced during drying process due to shrinkage. A similar result was observed on Indian Head Till clay of 40 mm thickness as reported by Lau [10].

S3-3030 W3-3030 C3-3030

Fig. 7 No traced of crack occurred for all samples of 30 mm thickness.

CONCLUSIONS

Desiccation cracking process of kaolin clay samples of different thickness were thoroughly monitored and reported. Observation on the effect of different types of base plate used was also investigated. The results obtained from desiccation test can be concluded as following:

i) Cracks started at the edge of kaolin clay samples and developed inwards into the inner area.
ii) Secondary cracks appeared after the primary cracks ended and made a narrow opening.
iii) A clear crack propagation and orthogonal pattern dominated by primary cracks can be viewed on the thinnest sample.
iv) CIF decreased as the thickness of sample increased.
v) Rapid loss of moisture content was observed from the samples placed on steel plate.

ACKNOWLEDGMENTS

This work is supported by Universiti Teknologi MARA (UiTM), Shah Alam Campus, Selangor, Malaysia. The contributions of final year project (FYP) students in the collation of experimental data and related research are gratefully acknowledged and highly appreciated.

REFERENCES

[1] Y. Xu and L.M. Zhang, Breaching parameters of earth and rockfill dams, J.Geotech. Geoenviron. Eng., ASCE, Vol. 135, Issue 12, 2009, pp. 1957-1970.
[2] F.H. Lee, K.W. Lo and S.L. Lee, Tension crack development in soils, J. Geotech. Eng., 114 (8), 1988, pp. 915-929.
[3] K.A. Shorlin, J.R. de Bruyn, M. Graham and S.W. Morris, Development and geometry of isotropic and directional shrinkage-crack patterns, Phys. Rev., E 61 (6), 2000, pp. 6950-6957.
[4] J.K. Kodikara and X. Choi, A simplified analytical model for desiccation cracking of clay layers in laboratory tests, Geotechnical Special Publication, No. 147, ASCE, Reston, VA, 2006, pp. 2558-2569.
[5] H. Peron, L. Laloui, T. Hueckel and L. Hu, Experimental study of desiccation of soil, Geotechnical Special Publication, No. 147, ASCE, Reston, VA, 2006, pp. 1073-1084.
[6] J.H. Li, L.B. Guo and C.Z. Cai, Influence of water content and soil type on soil cracking, Advances in Civil, Env. And Material Research (ACEM' 12), Seoul, Korea, 2012, pp. 1543-1553.
[7] C.S. Tang, B. Shi, C. Liu, L. Goa and H.I. Inyang, Experimental investigation of the desiccation cracking behaviour of soil layers during drying, J. of Materials in Civil Eng., 2011, pp. 873-878.
[8] C.J. Miller, H. Mi and N. Yesiller, Experimental analysis of desiccation crack propagation in clay

liners, Journal of American Water Resources Association (AWRA), 34 (3), 1998, pp. 677-686.
[9] R.M. Al Wahab and M.A. El-Kedrah, Using fibers to reduce tension crack and shrink/swell in compacted clay, Geoenvironment, 2000, pp. 791-805.
[10] J.T.K. Lau, Desiccation cracking of clay soils, M.Sc. Thesis, Department of Civil Engineering, University of Saskatchewan, Saskatoon, Canada, 1987.

6th Int. Conf. on Structure, Engineering & Environment (SEE), Kyoto, Japan, Nov.18-20, 2020, ISBN: 978-4-909106056 C3051

STATIC PILE LOAD TESTS: CONTRIBUTION OF THE MEASUREMENT OF STRAINS BY OPTICAL FIBER

Fabien Szymkiewicz[1], Carlos Minatchy[2] and Philippe Reiffsteck[3]
[1, 2, 3]Université Paris-Est, France

ABSTRACT

The use of optical fiber for measuring strains and or temperature is increasing in civil engineering. Optical fiber is known to be relatively cheap, compared to the more traditional sensors commonly used, and can, depending on the chosen technology, give a complete distribution along the instrumented element, which can be very interesting in case of an element with variable dimensions along the length of said element. Therefore, for static pile loading tests, the use of optical fiber should present many advantages, compared to more conventional methods of measure of the strains. The aim of this publication is to shed new light on the advantages and disadvantages of using optical fiber for the measurement of deformations along a foundation element. After a state of the art of the methods commonly used, the contribution of the optical fiber for the instrumentation of the foundation elements is evaluated, by comparing the results obtained by the use of the fiber with those obtained thanks to more traditional methods, through some examples of full-scale load tests. Finally, some recommendations are given to maximize the interest of the use of optical fiber in future tests.

Keywords: Deep Foundations, Piles, Load Test, Optical Fiber

INTRODUCTION

Static pile load test are usually carried either for design purposes, whether it be for control of this design or design by trial, or for constitution of a database then used to elaborate design methods. Therefore, they are critical tests for geotechnical structures and shall be thoroughly prepared.

As such, they are covered by complete and well detailed test standards [1]. Depending on the purpose of the test, the pile may or may not be instrumented. When instrumentation is implemented inside the pile, the goal of this instrumentation is to measure whether forces or strains, which can be then derived in forces, knowing the geometry of the pile and the apparent modulus of the constitutive material of the pile. Then, from these forces, force-depth diagrams can be drawn (Fig. 1).

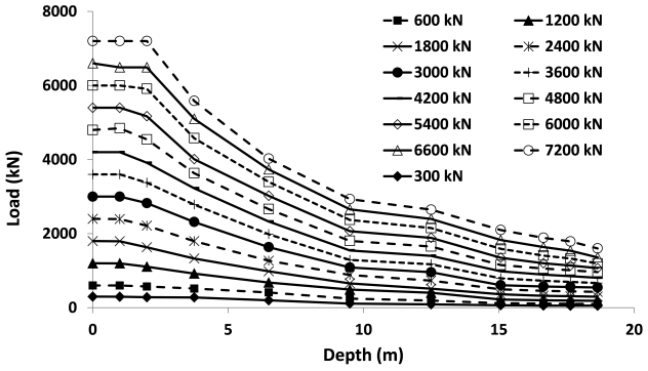

Fig. 1 Force distribution along a CFA pile instrumented with a retrievable extensometer

Shaft resistance and base resistance can then be dissociated, and unit shaft friction can be assessed for each soil layer encountered, depending on the number of measurement points available along the length of the pile. t-z curves, linking the development of the unit shaft friction of a segment of pile to the displacement of this segment, can then be drawn, as well as q_b-z curves

For lateral load tests, the principle is the same, except that it is p-y curves that are determined.

A number of different solutions exist for the measurement of these strains, each with its advantages and disadvantages.

Among these solutions is the optical fiber: since approximately a decade, a number of geotechnical projects have included these technologies for

monitoring, including piles [2]-[3]-[4].

This paper aims to first inventory the most common solutions for the measurement of strains along the shaft of a pile, listing in the process the pros and cons of these solutions. Then, a focus is made on the optical fiber and its use for the testing of geotechnical structures, and particularly piles. The encountered difficulties and the observed clear benefits of the use of the optical fiber for this purpose are then highlighted, through practical feedback. Conclusions are then drawn, and some innovative uses of the fiber for the monitoring of foundations are proposed.

TRADITIONNAL SOLUTIONS FOR THE MEASUREMENT OF STRAINS ALONG A PILE

In this section, the three main solutions for the measurement of strains along the shaft of a pile are described in details, and their technical, practical and economical strengths and weaknesses are listed.

Embedded Strain Gauges

This solution is one of the oldest: it consists in placing, at defined depth, strain gauges that will be bonded to the steel cage reinforcing bars (one or more per depth) or pipe.

The advantages of this solution are multiple:

- this is a proven technology, with which almost every actors is familiar,
- it is not very intrusive due to the small size of the gauges and the wires, which is a good point for small diameter piles,
- it is quite affordable,
- each sensor is independent from the others, which is important when encountering some damages,
- each sensor can be compensated in temperature.

However, there are a number of disadvantages when using this technology:

- It is time consuming to implement, as there are multiple steps to follow the whole process of preparation and bonding: first, flat rough surfaces should be grinded on the rebars, then should be smoothed using finer sandpaper. Surface has then to be cleaned of any impurity using chemical products. The strain gauge may then be bonded to the surface (Fig. 2), using another chemical product, and two layers of protection should then be added on top of the gauge. If the gauges are not pre-cabled, then an extra step will be the soldering of the cables to the gauge. Then, if necessary, soldering should be done for any extra cable length added,
- It necessitates multiple tools and chemical products, some of them having to be kept refrigerated, and a clean environment,
- Wires and gauges are very small, and may be damaged during the process of introducing the reinforcing cage inside the concrete (for CFA piles or equivalent), during the concreting phase (for bored piles), or during the driving phase (driven piles).

Fig. 2 Naked train gauge bonded to the rebar (a)

Vibrating Wire Strain Gauges

This solution is very close to the first one: vibrating wire sensors are attached to the reinforcing bars of the steel cage at different depths, with one or more per depth.

The advantages of this solution are as follow:

- the sensors are very robust (made of steel),
- the sensors are not very intrusive (usual length is around 150 mm for a diameter of 25 mm, but can go up to 400 mm in length for particular applications),
- the sensors need only to be attached to the rebars with ducktape or plastic zip ties (Fig. 3a),
- the sensors can be bought pre-cabled to the needed length,
- cables are strong enough to resist the tension during the different phases of manipulation and realization of the piles.
- The sensors are very quick to fix, even if the length of the cables (especially when working on long and / or heavily reinforced piles) can hinder the work and make the intervention longer,
- each sensor is independent from the others,
- each sensor can be compensated in temperature.

On the other hand, this solution presents some disadvantages:

- for piles heavily instrumented, the number and thickness of the cables can make this solution intrusive, especially for small diameter piles (Fig 3b),
- it can be expensive, when using a great number of sensor and instrumenting long piles, as the cost per sensor and per meter of cable is not negligible.

a b

Fig. 3 Vibrating wire strain gauge linked to a rebar (a) and cables exiting the top of the steel cages (b)

Retrievable extensometers

This solution is a totally different one. It consists in a chain of sensors that will have to be inserted inside the pile after it realization. Technologies used in retrievable extensometers are usually strain gauges, vibrating wires strain gauges, LVDT or potential sensor based.

The principle is as follow: one or more reservations made of PVC or steel (which can be sonic tube, for example) are cast in the pile. Just before the load test begins, the retrievable extensometer, made of multiple segments whose lengths can vary to adjust to the geology on site, is inserted inside the pipe [5]. When completely inserted and correctly positioned, it is locked into position, using either a pneumatic (with nitrogen being the gaz expanding the anchors) or a mechanical system (Fig. 4).

The advantages of this solution are as follow:

- it doesn't need the intervention of a team of external workers during the realization phase,
- the material is not expendable and can be re-used for another pile, which can be economically interesting in case of repeated tests on the same site,
- lengths of segments are adjustable, if needed,
- it is particularly well adapted for the instrumentation of driven piles, as the sensors are not present during the critical phases and therefore cannot suffer from it.

However, this solution presents some major disadvantages:

- extra pipes should be positioned inside the reinforcing cage, which implicate extra work for the contractor before the realization of the pile. These pipes shall also be chosen in relation to the model of extensometer that will be implemented. Particular attention should be paid to the connection/welding of the segments of the pipe, to ensure that nothing obstructs the passage of the extensometer,
- it is intrusive, especially for small diameter piles,
- these extensometers are often limited to 8 to 12 segments, which can sometimes not be enough for long piles in a multi-layers ground,
- nitrogen is needed for the use of most of these systems,
- duration of use is limited in time, as there may be leaks of nitrogen due to worn-out valves and connections,
- it is quite fragile and needs extra care when manipulated,
- spare parts are expensive and not always easily found,
- it needs constant maintenance and highly qualified technicians to maintain it, calibrate it and keep it ready to use,
- on site preparation takes time,
- during on site preparation phase, it necessitates a lot of space to be deployed safely.

All these aspects make the use of a retrievable extensometer expensive, compared to the embedded solutions.

EMBEDDED SENSORS VS RETRIEVABLE EXTENSOMETERS

While, for practical and economical reasons, the use retrievable extensometer are interesting when testing multiple piles of comparable size and/or driven piles, it becomes less competitive for projects with only a few piles, or with piles with different lengths, for the same reasons.

Furthermore, even if both solutions aim is to measure strains along the pile, the measurement may differs : indeed, while the technologies of the sensors used for one or the other are often the same, the principle of measures differs. The embedded sensors are measuring the strains over a length equal to their own length, while the retrievable extensometers measures strains between two anchors assumed to be fixed, and moving with the pile itself (Fig. 5) [6], making the strain measurement 'global' compared to the 'local' measurements achieved with embedded sensors.

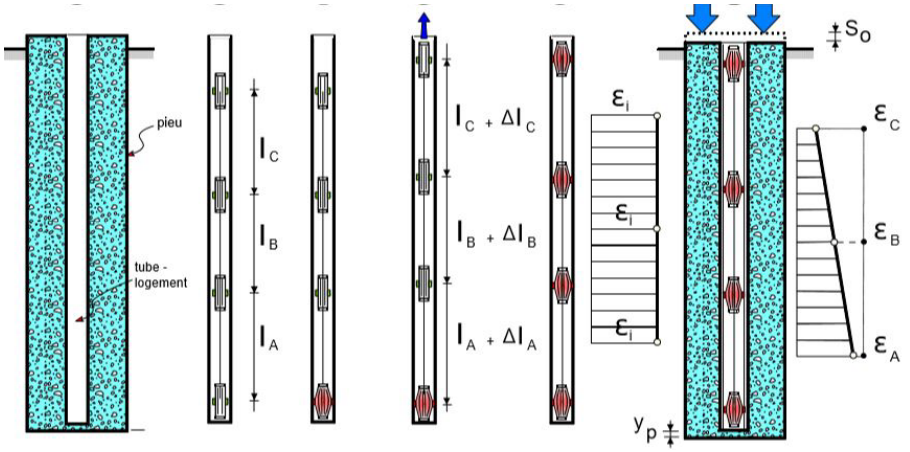

Fig. 4 operating principle of a retrievable extensometer

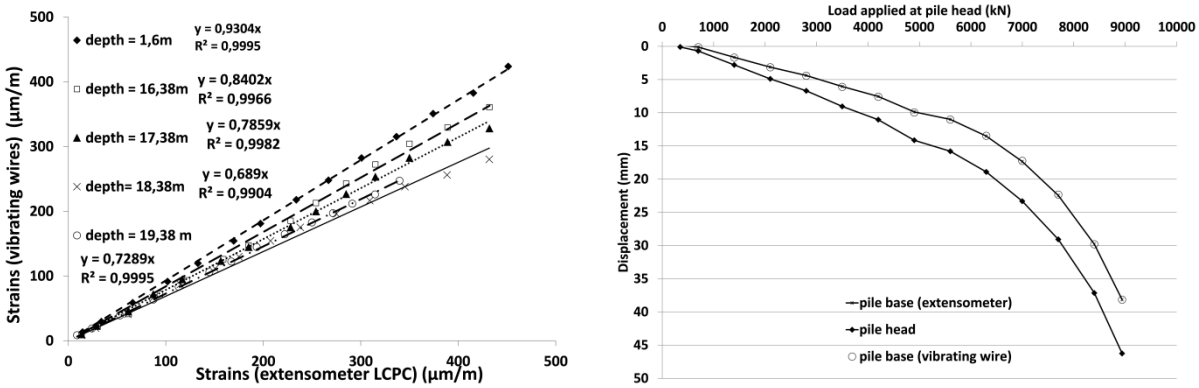

a b

Fig. 5 Comparison of measured strains at different depth (a) and calculated displacements of pile base (b) in a bored pile with a retrievable extensometer and vibrating wire strain gauges

Therefore, the retrievable extensometers integrate the strains over a longer sample. In consequence these measured strains are often larger than the ones achieved with embedded sensors, with a ratio dependent on the strain level (Fig. 5a). The resulting equivalent moduli derived from these measurements are in turn smaller.

In addition, the analysis of the results achieved are not as straight-forward as when using embedded sensors, as it is needed to interpolate results at the level of each anchor.

Nevertheless, results achieved with both measuring methods are quite comparable, as can be seen on Fig. 5b for the calculated displacement of the pile base, on Fig. 6a for the load distribution of a given load step and on Fig. 6b for the mobilization of shaft resistance during a static load test [6], and the utilization of one solution or the other should therefore be only linked to the context of the project, as it is not a question of accuracy.

CONTRIBUTION OF THE MEASUREMENT OF STRAINS BY OPTICAL FIBER

Implementing optical fiber for the measurement of strains in piles was first done when long term monitoring of strains and temperatures was needed : therefore, at first, piles instrumented with these technologies were thermo-active piles.

Nowadays, with positive practical feedbacks on the use of this solution available, it can be used for standard piles, for control or development purposes, as it allows measurements all along the fiber, with a resolution up to a few millimeters, depending on the technology used (Fig. 7), and measurements achieved are in excellent concordance with meaurements achieved with vibrating wire strain gauges (Fig. 8a).

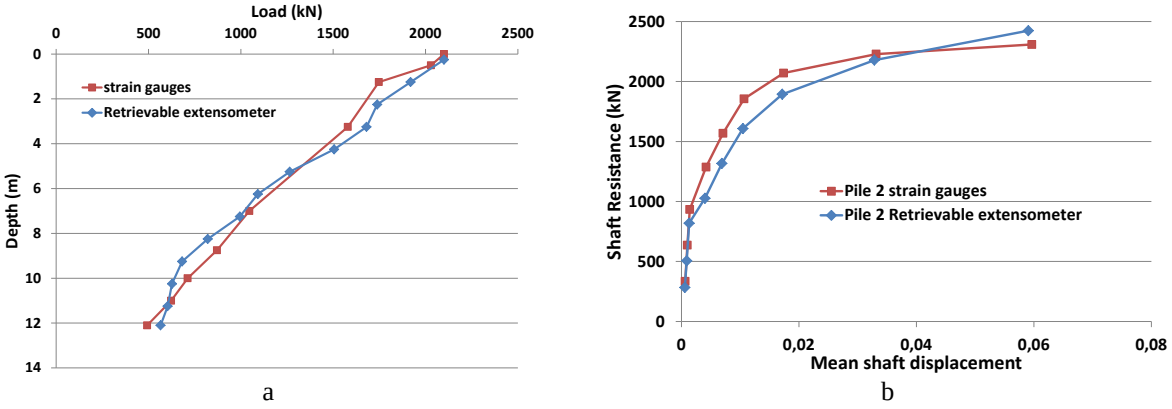

a b

Fig. 6 Comparison of load distribution for a given load step (a) and shaft resistance mobilization (b) for a CFA pile: results achieved with strain gauges and retrievable extensometer.

The use of optical fiber for the measurement of strains presents some advantages:

- implementation, when choosing to simply link the fiber with ducktape to the rebars, can be very quick,
- it is almost non intrusive, as the fiber is generally only a 3 or 4 mm in diameter (Fig. 3b),
- it is very interesting for determining moments and p-y curves, as it provides a very high number of measurements along the pile,
- it can be temperature conpensated,
- cost of the fiber in itself is very low and makes it possible to instrument most rebars.

Optical fiber can also be inserted inside a pipe if available, and then sealed with grout, allowing for a possibility to monitor a pile if something were to go wrong with the primary instrumentation. Results from such instrumentation can be seen on Fig. 8b, where they are compared to results achieved with a fiber linked to a rebar : measurements are quite comparable and therefore this solution can be used if needed. It is interesting to note that strains presented on Fig. 7b were also measured through this method, as the timing of the project did not allow for the pile to be instrumented before being realized.

Furthermore, it also allows to detect layers that where not detected during the geotechnical investigation, and to observe behaviour that would not be seen when using a discrete methods of measuring strains.

Figure 9 shows the strains measured with an optical fiber and vibrating wire strain gauges, on a bored pile tubed down to 16m: at the end of the tube, strains measured by the optical fiber increases, due to a decreased stifness of the pile, while the strain gauges, which are discretly distributed along the shaft, do not reflect this local behaviour.

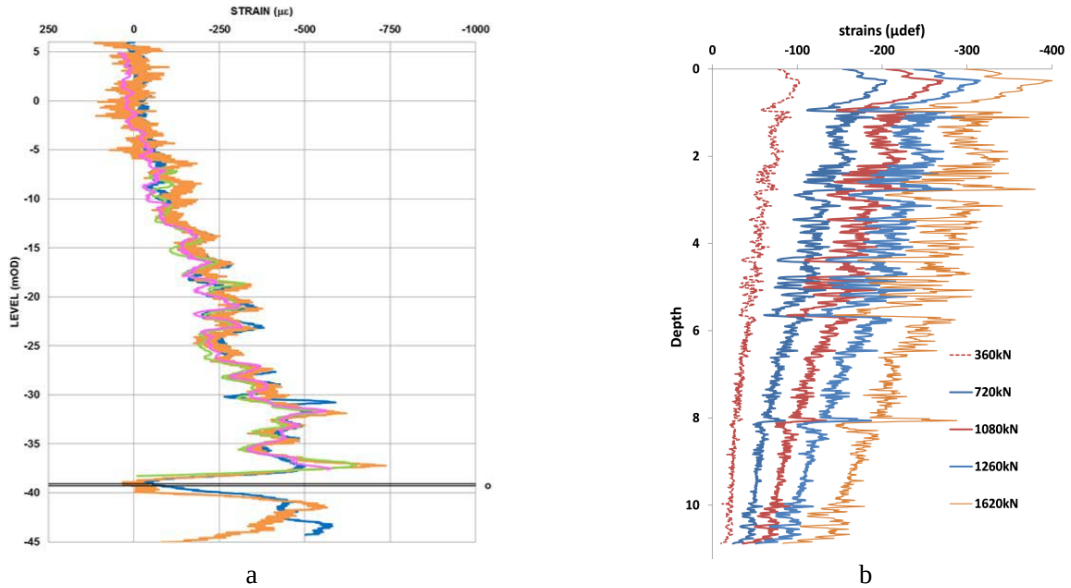

a b

Fig. 7 Strain distribution for a given load step (a) [2] and for different load steps (b)

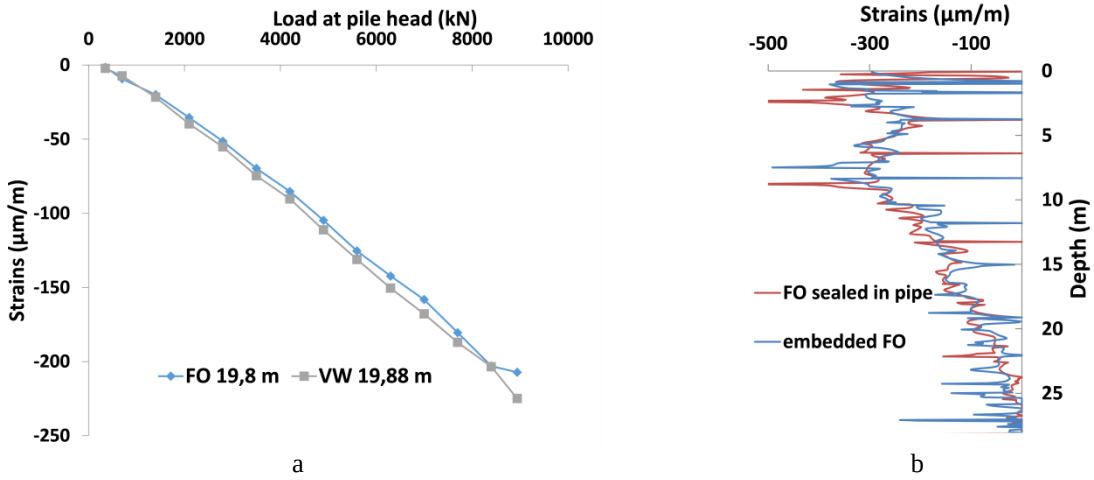

a b

Fig. 8 strain measurements comparison between optical fiber and vibrating wires (a) Strain distribution for a given load step with an embedded fiber and a fiber sealed in pipe (b)

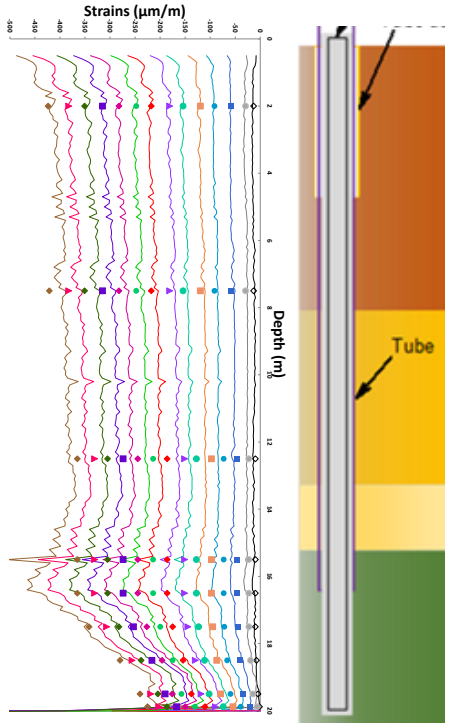

Fig. 9 Strains measurements along a bored pile: effect of tubing

However, it is important to be aware of the difficulties / disadvantages of the optical fiber :

- while the cost of the fiber in itself is very low, the interrogator price is usually very high,
- the interrogator are often not so rugged, and can be damaged during on site monitoring, due to dust presence mostly. Some interrogators are very vibration sensitive,
- the fiber is also very fragile, and must be treated with extra care during set up (Fig. 9), especially at the pile base, where the fiber is most exposed during concreting or insertion phases (Fig. 10a), and during construction phases such as lifting, when tensile stress due to the bending of the cage can exceed fiber tensile resistance (Fig. 10b), to avoid any break.
- the fiber acting as a chain of sensors, a broken fiber will result in the total loss of information under the break.

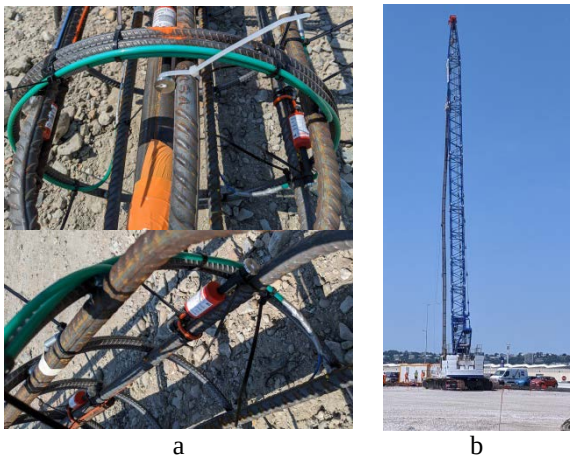

a b

Fig. 10 Fiber protection at the pile base (a) and cage lifting phase (b)

Furthermore, the steps of the realisation of a conection are numerous and tedious. The environment needs to be very clean, with close on site activities as low as possible. The apparatus needed are presented in Fig. 11.

Bad connections result in loss of signal that will in turn result in loss of precision, that will have to be added to the impact of the deployement method of the fiber and the pile, a seen on Fig. 12, which represent the variation of the frequenc.

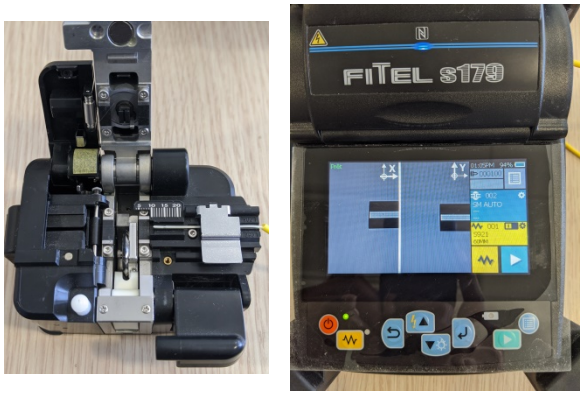

a b

Fig. 11 Presentation of the different welding stages

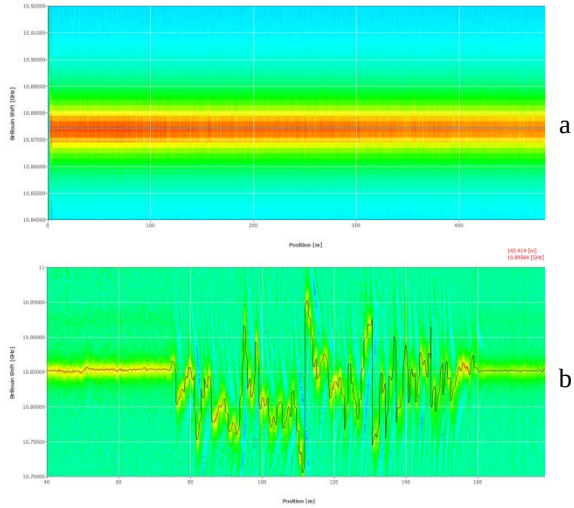

a

b

Fig. 12 Brillouin signal in a fiber used for calibration (a) and implemented in a pile (b) (frequencies vs length)

CONCLUSIONS

The use of optical fiber for the measurement of strains during pile load tests or other related projects is now a solution that is very reliable.

While measured values may differ from values achieved by more conventional technologies, this is only due to differences of measurement methods of the solutions. Interpretration of the data shall gives the same results as the other solutions, whether it be displacements of the pile segment or load distributions along the pile, albeit with a higher resolution.

Nonetheless, it is still very rare to see this technology used for pile monitoring, the two main reasons for this being that:

- the set up, implementation and manipulation of the fiber should be done in a very controlled environment and with extra care, as it is very fragile.
- while the cost of the fiber is relatively low, the price of the interrogator, coupled with its fragility, leads to a certain reluctance to deploy them in dusty environments prone to hazards endangering their integrity and their proper functioning.

However, further applications like the monitoring of piles at a young age for quality control purposes (by measuring of temperature inside the pile along the shaft to assess its possible change in diameter) may entice contractors to develop the use of this technology.

REFERENCES

[1] Szymkiewicz F, Sanagawa T and Nishioka H., 2020. Static Pile Load Test: International Practice Review And Discussion About The European And Japanese Standards, International Journal of GEOMATE, Vol.18, Issue 66, pp. 76-83.

[2] Soga, K., Kwan, V., Pelecanos, L., Rui, Y., Schwamb, T., Seo, H., and Wilcock, M., 2015. The role of distributed sensing in understanding the engineering performance of geotechnical structures. XVI European Conference on Soil Mechanics and Structures.

[3] Klar, A., Bennett, P.J., Soga, K., Mair, R.J., Tester, P., Fernie, R., St John, H.D., and Torp-Peterson, G., 2006. Distributed strain measurement for pile foundations. Proceedings of the Institution of Civil Engineers-Geotechnical Engineering, 159, pp. 135-144.

[4] Mohamad, H., Tee, B.P., Chong, M.F., and ANG, K.A., 2010. Investigation of shaft friction mechanisms of bored piles through distributed optical fibre strain sensing. 19th International Conference on Soil Mechanics and Geotechnical Engineering 2017, Seoul.

[5] Laboratoire Central des Ponts et Chaussées, 2001. La mesure des déformations à l'aide des extensomètres amovibles LPC : Méthodes d'essai LPC n°34, 17 pages (in French)

[6] Szymkiewicz, F., S. Burlon, F. Guirado, C. Minatchy and G. Vinceslas, 2015. Experimental study of heating-cooling cycles on the bearing capacity of CFA piles in sandy soils, XVI ECSMGE, Edinburgh.

Environment

6th Int. Conf. on Structure, Engineering & Environment (SEE), Kyoto, Japan, Nov.18-20, 2020, ISBN: 978-4-909106056 C3051

SPATIAL DISTRIBUTIONS IN GROUNDWATER DISCHARGE ON VARIOUS TIDAL FLATS IN A SMALL AND STEEP ISLAND, WESTERN JAPAN

Shingo Nozaki[1], *Shin-ichi Onodera[1], Yusuke Tomozawa[1], Mitsuyo Saito[2]

[1]Graduate School of Graduate School of Advanced Science and Engineering, Hiroshima University, Japan
[2] Graduate School of Environmental and Life Science, Okayama University, Japan

*Corresponding Author, Received: 00 Oct. 2018, Revised: 00 Nov. 2018, Accepted: 00 Dec. 2018

ABSTRACT: To manage and conserve the seagrass bed and ecosystem in tidal flats, this study examined to confirm spatial distribution in groundwater (SGD) on tidal flats with the area of around 100m square in a small and steep island. Various groundwater and nutrient discharges were observed at the W and E sites. 1) Based on the water budget, the groundwater flux was estimated to be 8.68 m/yr or 23.9 mm/day in E, and 17.75 m/yr or 48.6 mm/day in W, respectively. 2) Spatial distributions of groundwater contribution ratio (%) in pore water at W was around 60% in average, which was 8 times of that in E site. 3) The NO_3-N concentration in pore water at W site was about 30 times of that at E because of the low attenuation rate with high groundwater velocity. 4) The temporal variation in groundwater flux with tidal fluctuation indicated 2.5m/day in maximum and -4.0m/day in minimum. This huge difference between the average flux and maximum indicated also large seawater recirculation and heterogeneous distribution of SGD. This heterogeneous distribution at this tidal flat would contribute to the activity of seagrass and diversity of ecosystem.

Keywords: Submarine groundwater discharge, Spatial distribution, Tidal flat, Island

1. INTRODUCTION

The tidal flats and shallow coastal areas are naturally covered by seaweed and seagrass, these area contributes to biodiversity in the ecosystem [1]. One of the reasons for the rich seagrass bed from the tidal flat to the shallow bottom in a coastal zone is various physical and chemical environments. Submarine groundwater discharge (SGD) defined as any flow of water at land margins from the seabed to the coastal ocean [2,3] has spatial distribution in the km scale and includes fresh groundwater with the stable temperature [4,5]. SGD has significant impacts is an important source of not only freshwater [2,3] but nutrients [6,7,8].

Recently, the coastal ecosystem such as coral reef and seagrass bed has been degraded by the development and overuse of coastal zone [9]. Because the degradation of seagrass bed causes biodiversity loss in coastal zones, this is one of global environmental issues [10]. In urban regions, the huge nutrient supply from the sewage plant [11], the recycling of accumulated nutrient in sea bed [12] by the tidal pumping [13] caused the eutrophic condition and was degraded ecosystem. In addition, the groundwater depression by over pumping in the coastal city caused seawater intrusion and stop of SGD [14,15,16].

On the other hand, in the rural regions, the contribution of SGD and coastal current controls the nutrient and freshwater supply. The groundwater discharge into the sea bed near shore line has conceptually been understood [8,17]. However, spatial variation of SGD in a tidal flat scale has not been clarified enough [18,19].

The purpose of this study was to confirm spatial distribution in groundwater (SGD) and nutrient discharge on tidal flat with the area of around 100m square in a small and steep island.

2. METHOD

2.1 Study Area

The experimental sites were located on Ikuchi Island in Onomichi City, Hiroshima Prefecture, in the central Seto Inland Sea, western Japan. (Fig. 1). The regional climate is warm (average temperature of 15.6°C), with less precipitation in Japan (approx. 1100mm/y). Ikuchi Island is one of the most famous and important orange and citrus production areas. The orange groves cover 42% of the total catchment area, and are mostly located in the downstream area. Forests cover 43% of the upper area. Groundwater resources are important water supply resources for irrigation. However, due to the small annual precipitation with large inter-annual variation, and steep sloping topography, the island faces a risk of water shortage, especially in the drought season.

Ikuchi Island is characterized by a steep terrain and granite bedrock [20], and the total area is 32.7 km^2. The alluvial fan and plain in the coastal zone is narrow, but is generally deposited by the sediment composed of gravel and sand including clay with the thickness of around 15m [8,20,21].

The research catchments (E and W catchments) are located in the southern area of the island (Fig. 1), and are approximately 1700m and 900m in length, and 300m and 150m in width, with an area of 0.434 km^2 and 0.242km^2, respectively. These catchments have steep slopes, particularly in the upstream mountainous area, with a top elevation of 396m and 472m in E and W catchments, respectively. And experimental tidal flats (E and W) have about 75m and 30m in length and 100m and 250m in width, respectively. E experimental tidal flat is at the edge of the alluvial fan made by a small stream with 1.5km in length and it is a half of groundwater discharge area of the catchment. W experimental tidal flat is at the mountain slop foot with the twice average slope gradient of the E catchment and it is similar to the discharge area of the catchment.

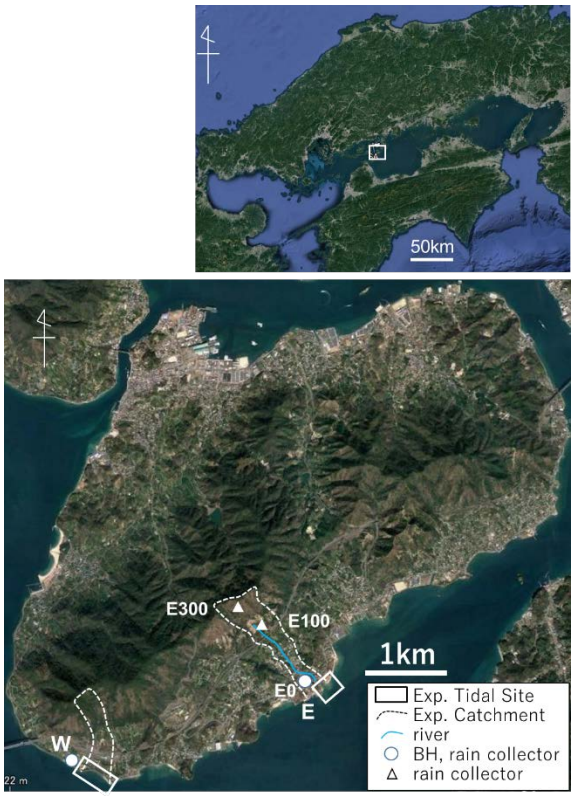

Fig.1 Study area and the experimental sites.

2.2 Field Observation

10 and 17 piezometers on two experimental tidal flats, which is composed of E site (100m x 30m) at the alluvial fan edge of an experimental catchment and W sites at the steep mountain slop foot (300m x 30m) were installed with the depth of 50cm, respectively. Pore water samples were collected in December in 2018 and July and December in 2019. Water temperature and electric conductivity (EC) were measured in situ, using the potable meter. In addition, water levels were monitored in 2017 and 2019, rain water and groundwater samples were collected monthly at each catchment.

The water budgets were estimated by the previous researches [21,22] in E catchment based on the river discharge and groundwater monitoring in 2003 and 2004. On the other hand, there is no stream discharge in W catchment.

2.3 Laboratory Analysis

These water samples were filtered using 0.2 μm cellulose ester filters in the field and stored in a freezer until analysis. The stable isotope ratio and nutrient concentration of water samples were analyzed, using the WS-CRDS method (Picarro Company, L2120-i) and a spectrophotometric auto-analyzing system (SWAAT; BL TEC K. K., Japan), respectively.

3. RESULTS AND DISCUSSION

3.1 Water budget

Table 1 Water Budget in each catchment.

	E catchment	W catchment
P (mm)	1100	1100
Ev (mm)	350[22] - 550[21]	550
Qr (mm)	250[21] – 435[22]	0
Qg (mm)	300[21] – 315[22]	550

Note: [21] using hydrological observation, and [22] using SWAT model.

Water budget is represented as Eq. (1),

$$P - Ev = Qr + Qg + \Delta \quad (1)$$

where P is precipitation, Ev is evapotranspiration, Qr is river discharge, and Qg is groundwater discharge, respectively. The water budgets in E catchment were estimated, using the hydrological observation and monitoring [21] and SWAT model analysis [22]. The water budgets in E and W catchments are shown in Table 1.

Based on the water budget, groundwater discharge in W is twice of E. The catchment area in E is twice of W, and the groundwater discharge volume in E is estimated to be similar to that in W. As the E tidal flat is a half of the discharge area of this catchment, the discharge volume in E site is a half of W tidal flat. If the groundwater discharges to the experimental tidal flat area (7,500m^2), annual groundwater discharge is estimated to be 8.68 m/yr or 23.9 mm/day in E, and 17.75 m/yr or 48.6 mm/day in W, respectively.

3.2 Spatial distribution of groundwater discharge

Figure 2a and 2b shows the distribution of EC in

pore water at E and W site, respectively. The average EC at E is 46 mS/cm and that at W is 25 mS/cm. The average groundwater discharge rate at E site was a half of that at W site, the trend of the EC distribution in pore water was similar to the trend of groundwater flux.

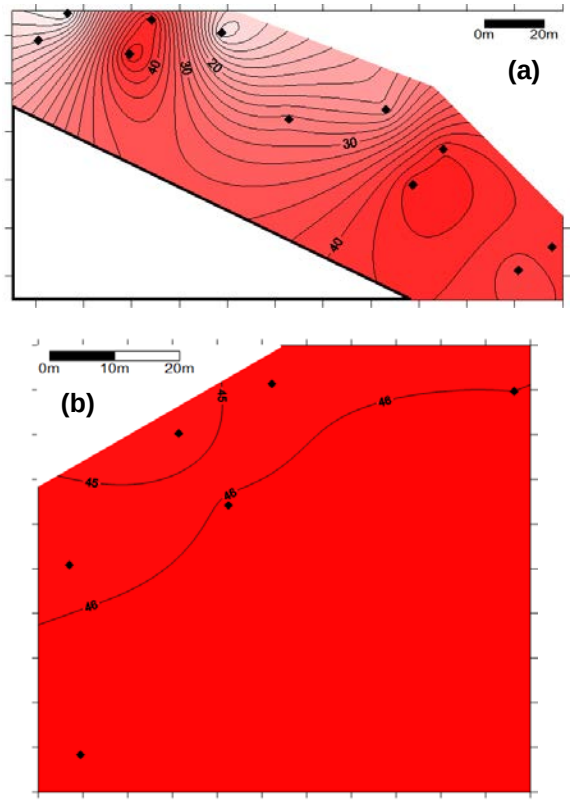

Fig.2 Spatial distributions of EC in pore water at W tidal flat (a) and E (b). The unit is mS/cm. ◆; piezometer plot.

Figure 3 shows the spatial distribution of groundwater contribution ratio (%) in pore water at W and E site. The ratio at W is around 60% in average and the range of from 10% to more than 95%, whereas the ratio at E is around 7% in average and the range from 5% to 10%, respectively. The ratio at W site is 8 times of that in E site. These difference could not explain only by the fresh groundwater flux described above. This means the sea water recirculation flux by the tidal pumping at E site would be around 4 times of that at W site. In general, this flux is related to the length of the tidal flat, especially the length at E was 2.5 times of that at W.

The distribution at W site is heterogeneous and the pore water with the ratio of 10% were found at 2 piezometers in 17 plots while that with more than 50% and 90% were found at 4 and 1 plots, respectively. On the other hand, the distribution at E site is homogeneous and the ratio continuously decreased from 10% near the land to 5% in the offshore. These comparative trends were shown obviously in the histogram (Fig. 4).

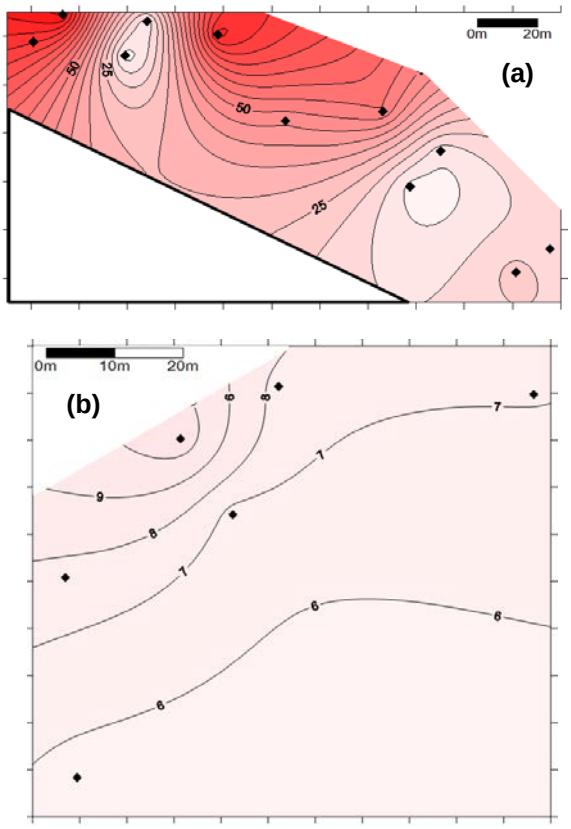

Fig. 3 Spatial distribution of groundwater contribution ratio (%) in pore water at W site (a) and E site (b). ◆; piezometer plot.

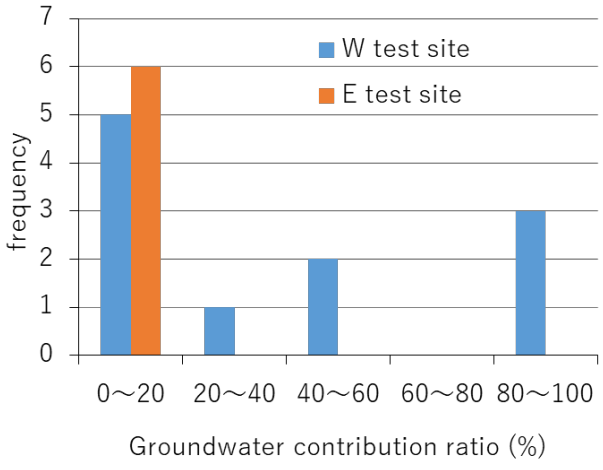

Fig. 4 The histogram of groundwater contribution ratio at E and W site.

3.3 Spatial distribution of nutrient discharge

Spatial distribution of NO_3-N concentration (mg/l) in pore water at W site (a) and E site are

shown in Fig. 5 (a) and (b), respectively. The lower areas of both catchments are covered by the citrus plantation, and dissolved nitrogen and phosphorus was contained so much in fresh groundwater by leaching of fertilizer component [21]. The concentration distributed the range from 0 mg/l to 7 mg/l at W tidal flat site, whereas it distributed the range from 0 mg/l to 0.2 mg/l. The maximum concentration at W was about 30 times of that at E. This means the attenuation rate is relatively small at W site because of the higher groundwater velocity, as compared at E. Especially, the concertation was maximum at the central part of W site.

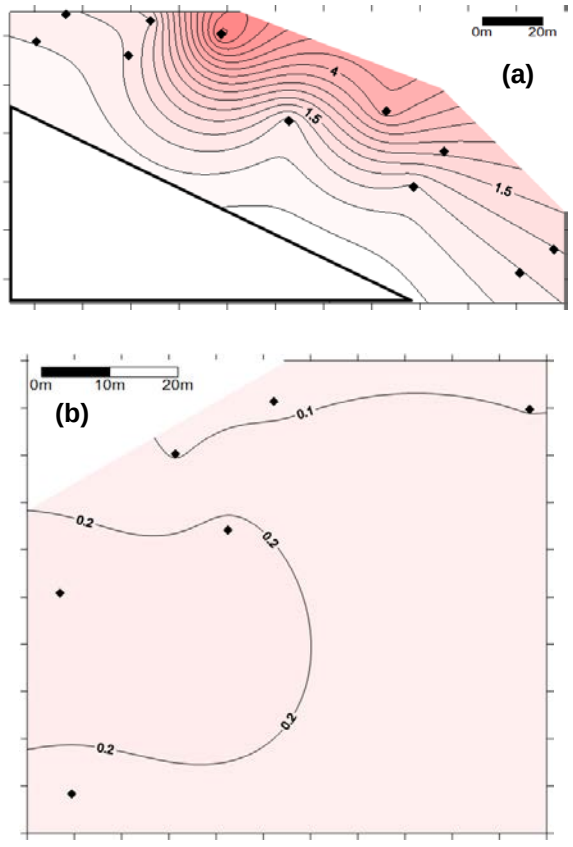

Fig. 5 Spatial distribution of NO_3-N concentration (mg/l) in pore water at W site (a) and E site (b). ◆; piezometer plot.

Figure 6 shows spatial distributions of SiO_2 concentration (mg/l) in pore water at W site (a) and E site (b). The concentration distributed the range from 3 mg/l to 17 mg/l at W site, whereas it distributed the range from 3 mg/l to 6 mg/l. The plots with high concentration indicated high contribution of fresh groundwater. The maximum concentration at W was about 3 times of that at E. This means recirculating seawater at E site contained relatively high concentration of SiO_2 because of the supply by the river. In addition, the variation of concentration was obviously smaller than NO_3^- concentration.

3.4 Temporal variation in pore water pressure and EC

Figure 7 shows the temporal variation in groundwater flux with tidal variation during 3 days. The range of tidal variation was 3.5m. The groundwater flux is maximum at the mid tide during the decreasing tide and minimum at the mid tide during the increasing tide. Figure 8 shows the temporal variation in EC of the pore water with tidal variation. The EC increased with the tidal level, and the tidal pumping effect was indicated [3,4]. But the variation range is only less than 1mS/cm with 34 mS/cm in the average.

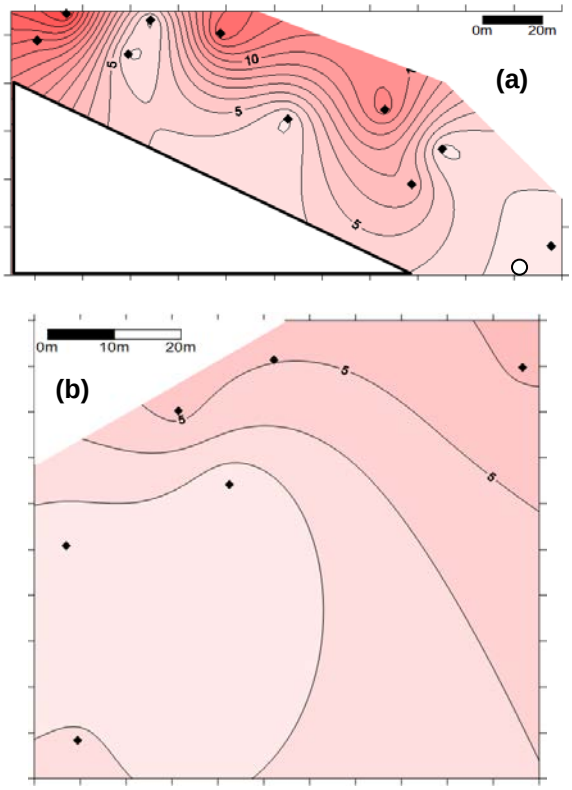

Fig. 6 Spatial distribution of SiO_2 concentration (mg/l) in pore water at W site (a) and E site (b). ◆; piezometer plot. ○; piezometer plot monitored water level and EC shown in Fig.7 and 8.

The groundwater flux was 2.5m/day in maximum and -4.0m/day in minimum. This maximum value was 100 times of the average flux estimated based on water budget. The negative value during the increasing tide indicated seawater recirculation. The sum for three days showed the positive value, while based on the huge difference between the average flux and maximum indicated also large recirculation and heterogeneous

distribution of SGD. This heterogeneous distribution at W site would contribute to the diversity of this ecosystem on the tidal flat. Recently, seagrass biomass is still active at W site as compared with that at E site.

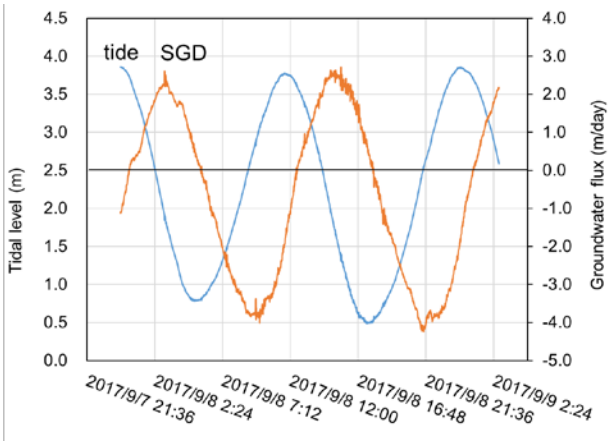

Fig. 7 Temporal variations in tidal level and groundwater flux at the eastern part of Site W (shown in Fig.6).

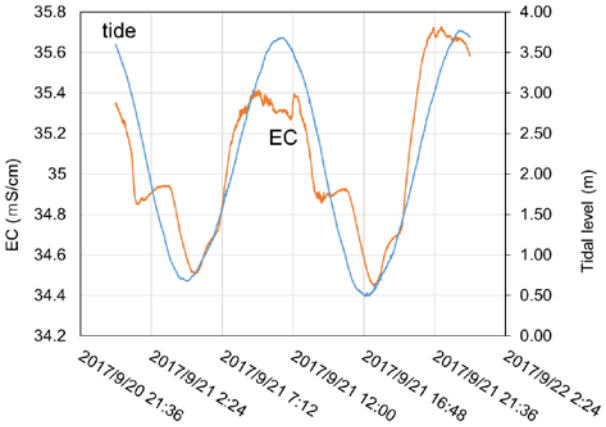

Fig. 8 Temporal variations in tidal level and EC at the eastern part of Site W (shown in Fig.6).

4. CONCLUDING REMARKS

This study examined to confirm spatial distribution in groundwater (SGD) on tidal flats with the area of around 100m square in a small and steep island.

1) Based on the water budget, the groundwater flux was estimated to be 8.68 m/yr or 23.9 mm/day in E, and 17.75 m/yr or 48.6 mm/day in W, respectively.
2) Spatial distributions of groundwater contribution ratio (%) in pore water at W was around 60% in average, which was 8 times of that in E site.
3) The NO_3-N concentration in pore water at W site was about 30 times of that at E because of the low attenuation rate with high groundwater velocity.
4) The temporal variation in groundwater flux with tidal fluctuation indicated 2.5m/day in maximum and -4.0m/day in minimum. This huge difference between the average flux and maximum indicated also large seawater recirculation and heterogeneous distribution of SGD. This heterogeneous distribution at this tidal flat would contribute to the activity of seagrass and diversity of ecosystem.

5. ACKNOWLEDGMENTS

This research was supported by JSPS KAKENHI Grant 18H04151 and 18H03411. We appreciate the reviewers and editors for their suggestions, and Ms. Morita and Mr. Hanioka for their cooperation.

6. REFERENCES

[1] Duffy J. E., Biodiversity and the functioning of seagrass ecosystems. Marine Ecology Prog. Ser., 311, 2006, pp.233-250.
[2] Taniguchi M., Burnett W. C., Cable J. E., and Turner J. V., Investigation of submarine groundwater discharge. Hydrol. Process., 16, 2002, pp.2115-2129.
[3] Burnett W. C., Aggarwal P. K., Aureli A., Bokuniewicz H., Cable J. E., Charette M. A., Kontar E., Krupa S., Kulkarni K. M., Loveless A., 2006. Quantifying submarine groundwater discharge in the coastal zone via multiple methods. Sci. Total Environ., 367, 2–3, 498–543.
[4] Burnett W. C., Dulaiova, H., Radon as a tracer of submarine groundwater discharge into a boat basin in Donnalucata, Sicily. Cont. Shelf Res., 26, 7, 2006, pp.862–873.
[5] Saito M., Onodera S., Guo X. Y., Seasonal variation of the ^{222}Rn concentration in the Central part of the Seto Inland Sea, Japan. Interdisc. Stud. Environ. Chem. Terrapub, 6, 2012, pp.339–344.
[6] Santos I. R., Burnett W. C., Dittmar T., Suryaputra I. G. N. A., Chanton J., Tidal pumping drives nutrient and dissolved organic matter dynamics in a Gulf of Mexico subterranean estuary. Geochim. Cosmochim. Acta, 73, 5, 2009, pp.1325–1339.
[7] Kim G., Kim J. S., Hwang D. W., Submarine groundwater discharge from oceanic islands standing in oligotrophic oceans: implications for global biological production and organic carbon fluxes. Limnol. Oceanogr., 56, 2, 2011, pp.673-682.
[8] Onodera S., Saito M., Hayashi M., Sawano M., Nutrient dynamics with interaction of groundwater and seawater in a beach slope of

steep island, western Japan. IAHS Publication, 312, 2007, pp.150-158.

[9] Climate Technology Centre and Network, Management of seagrass beds. https://www.ctc-n.org/technologies/management-seagrass-beds#:~:text=Degradation%20is%20due%20to%20smothering,Temperature%20increases.

[10] Rockström J., Steffen W., Noone K., Persson A., Chapin F. S., Lambin E. F., Lenton T. M., Scheffer M., Folke C., Schellnhuber H. J., Nykvist B., de Wit C. A., Hughes T., van der Leeuw S., Rodhe H., Sörlin S., Snyder P. K., Costanza R., Svedin U., Falkenmark M., Karlberg L., Corell R. W., Fabry B. J., Hansen J., Walker B., Liverman D., Richardson K., Crutzen P., Foley J. A., A safe operating space for humanity, Nature, 461, 2009, pp.472–475.

[11] Saito M., Onodera S., Jin G., Shimizu Y., Taniguchi M., Nitrogen dynamics in a highly urbanized coastal area of western Japan: impact of sewage-derived loads. Progress in Earth and Planetary Science, Volume 5, 2018, DOI: 10.1186/s40645-018-0177-6.

[12] Jin G., Onodera S., Saito M., and Shimizu Y., Sediment phosphorus cycling in a nutrient-rich embayment in relation to sediment phosphorus pool and release. Limnology, 2020, https://doi.org/10.1007/s10201-020-00627-x.

[13] Onodera S., Saito M., Yoshikawa M., Onishi K., Shimizu Y., and Ito H., Nutrient transport and surface water-groundwater interactions in the tidal zone of the Yamato River, Japan. IAHS Publication, 361, 2013, pp.204-211.

[14] Onodera S., Saito M., Sawano M., Hosono T., Taniguchi M., Shimada J., Umezawa Y., Lubis R. F., Buapeng S., and Delinom R., Effects of intensive urbanization on the intrusion of shallow groundwater into deep groundwater: Examples from Bangkok and Jakarta. Science of the Total Environment, 407, 2009, pp.3209-3217.

[15] Tomozawa Y., Onodera S. and Saito M., Estimation of groundwater recharge and salinization in a coastal alluvial plain and Osaka megacity, Japan using $\delta^{18}O$, δD, and Cl^-. International Journal of GEOMATE, Vol.16, Issue 56, 2019, pp.153-158.

[16] Rusydi A. F., Saito M., Ioka S., Maria R. and Onodera S., Estimation of ammonium sources in Indonesian coastal alluvial groundwater using Cl^- and GIS. International Journal of GEOMATE, Vol.17, Issue 62, 2019, pp.53-58.

[17] Nakada, S., Yasumoto, J., Taniguchi, M., and Ishitobi, T., Submarine groundwater discharge and seawater circulation in a subterranean estuary beneath a tidal flat. Hydrol. Process., 25, 17, 2011, pp.2755–2763.

[18] Shuler C. K., Dulai H., Leta O. T., Fackrell J., Welch E., and El-Kadi A. I., Understanding surface water–groundwater interaction, submarine groundwater discharge, and associated nutrient loading in a small tropical island watershed. Journal of Hydrology, 585, 2020, 124342.

[19] Zhu A., Saito M., Onodera S., Shimizu Y., Jine G., Ohta T., and Chen J., Evaluation of the spatial distribution of submarine groundwater discharge in a small island scale using the ^{222}Rn tracer method and comparative modeling. Marine Chemistry, 209, 2019, pp.25–35.

[20] Takeuchi T., Onodera S., Yamaguchi K. and Kitaoka K., Estimation of sedimentation rate and fresh-saline environment in a coastal alluvial plain, using boring cores of alluvium in the central part area of Seto Inland Sea, Japan. International Journal of GEOMATE, Vol.17, Issue 60, 2019, pp.70-75.

[21] Saito M., Onodera S., Okubo K., Takagi S., Maruyama Y., Jin G., and Shimizu Y., Effects of physical and morphometric factors on nutrient removal properties in agricultural ponds. Water Science & Technology, 72, 12, 2015, pp.2187-2193.

[22] Jin G., Shimizu Y., Onodera S., Saito M., and Matsumori K., Evaluation of drought impact on groundwater recharge rate using SWAT and Hydrus models on an agricultural island in western Japan. Proc. Int. Assoc. Hydrol. Sci., 371, 2015, pp.143–148.

6th Int. Conf. on Structure, Engineering & Environment (SEE), Kyoto, Japan, Nov.18-20, 2020, ISBN: 978-4-909106056 C3051

ASSESSMENT ON MICROPLASTICS CONTAMINATION IN FRESHWATER FISH: A CASE STUDY OF THE UBOLRATANA RESERVOIR, THAILAND

Pattira Kasamesiri[1], Charumas Meksumpun[2], Shettapong Meksumpun[3] and Chakhrit Ruengsorn[3]
[1]Faculty of Technology, Mahasarakham University, Thailand; Thailand; [2]Department of Fishery Biology, Faculty of Fisheries, Kasetsart University, Thailand; [3]Department of Marine Science, Faculty of Fisheries, Kasetsart University, Thailand

ABSTRACT

Microplastic pollution is now a global issue. Reservoirs are an enclosed aquatic environment at risk from accumulation of microplastics. Few studies have used fish species as bio-indicators to monitor microplastic contamination in reservoirs. Freshwater fish were caught by local fishermen from 10 stations around the Ubolratana Reservoir, Thailand in October 2018 and the abundance, size, color and shape of microplastic particles in their stomachs and intestines were investigated. Fourteen fish species were examined. Results showed that 96.4% of the fish had ingested microplastics at mean abundance of 2.92±1.30 particles per fish, with significant differences of abundance between species. Microplastic abundance was highest in carnivorous fish *Parambassis siamensis* (4.11±1.08 particles per fish). The most common size of ingested microplastics was over 0.5 mm (66.4%), with 51.0% as blue color and 98.2% fiber shaped. High levels of microplastics were ingested by fish located in the middle and lower parts of the reservoir. Results revealed that blue fiber microplastics dominantly observed in fish were derived from the breakdown of nets used for fishing activities.

Keywords: Microplastic pollution, Freshwater fish, Reservoir, Microplastic ingestion, Plastic waste

INTRODUCTION

In 1950, global plastic production was 2 million tons. This increased to 381 million tons in 2015. Seventy-five percent of primary plastic production ends up as waste [1], while over half of the polymers, synthetic fibers and additives produced are buried as landfill or discarded and washed into rivers and oceans [1]-[2]. Degradation or fragmentation of plastic waste generates microplastic pollution of the environment [2]-[3].

Microplastics are defined as small particles of plastic less than 5 mm in length, and further categorized according to their origin as primary and secondary. Primary microplastics are manufactured as small size for a specific purpose such as microbeads in cosmetics, exfoliating personal care or toothpaste [4], while secondary microplastics result from the breakdown of larger plastic items by sunlight, wind or waves [5]. Types of microplastics most commonly found on coastal beaches are low-density polyethylene (LDPE), polypropylene (PP) and polystyrene (PS) [5].

The direct effects of microplastics on aquatic animals are both physical and nutritional. Plastic ingredients and additives are indirectly transferred through aquatic food webs and impact food safety and human health [5]-[9]. Chemical substances added in plastic products to enhance polymer properties include diethylhexyl phthalate, dibutyl phthalate, diethyl phthalate and benzaldehyde [10]-[11]. These substances leach out from discarded microplastic waste into the environment as both aquatic and terrestrial pollution [12].

Microplastic contamination occurs in the oceans and also in freshwater. Nevertheless, research concerning microplastic pollution in freshwater systems and aquatic animals remains limited. High levels of microplastic pollution in lakes [13]-[14] and riverine fish [15]-[16] have been reported. Reservoirs are watershed areas that collect water from streams and rivers. They are closely connected to the land as important sources of plastic waste and microplastics [17]. Moreover, reservoirs comprise important fishery production habitats in South East Asia [18]. Therefore, pollution from microplastics may impact fisheries' products as a consumer health risk [18].

Here, the abundance, size, color and shape of microplastics ingested by freshwater fish in the Ubolratana Reservoir were quantified and assessed. Results will be useful for biomonitoring microplastic contamination in reservoirs and provide a database for fisheries to improve food security.

MATERIAL AND METHODS

Study Sites and Samples Collection

Study sites were located at the Ubolratana reservoir, northeast of Thailand. This man-made lake was opened in 1966 for electricity generation, flood control, irrigation, etc. The reservoir aggregate water

Table 1 Fish species habitats, feeding habits and abundance collected from 10 stations around the Ubolratana Reservoir.

Species	Habitat	Feeding habits	Total length (cm)	Weight (g)	Abundance
Puntioplites proctozysron	Benthopelagic	Omnivore	7.77±3.53	13.82±7.57	37
Cyclocheilichthys repasson	Benthopelagic	Omnivore	9.45±2.06	8.18±3.25	14
Parambassis siamensis	Demersal	Carnivore	4.81±0.64	1.40±0.61	18
Henicorhynchus siamensis	Benthopelagic	Herbivore	13.52±4.84	27.14±17.22	22
Pristolepis fasciatus	Demersal	Carnivore	12.43±1.13	44.28±10.53	7
Labiobarbus leptocheilus	Benthopelagic	Planktivore	11.00±0.71	10.80±0.84	5
Barbobymus goniontus	Benthopelagic	Omnivore	9.33±1.15	11.33±3.79	3
Rasbora aurotaenia	Benthopelagic	Planktivore	8.91±0.55	5.35±0.80	10
Clupeichtys aesarnensis	Pelagic	Planktivore	3.84±0.39	0.47±0.13	10
Mystacoleucus marginatus	Demersal	Carnivore	5.83±0.98	2.73±1.42	15
Osteochilus vittatus	Benthopelagic	Omnivore	18.41±4.53	45.72±21.16	8
Paralaubuca harmandi	Benthopelagic	Carnivore	10.64±3.45	4.86±2.29	7
Mystus mysticetus	Demersal	Carnivore	12.87±1.28	19.83±4.02	6
Hemibagrus spilopterus	Demersal	Carnivore	17.10±2.43	38.00±14.53	5

from the Nam Phong River, covered an area of two provinces and flow into the Chi River (the longest river of Thailand) with capacity 263,000 m^3 and 12,104 km^2 of catchment area. The multi-purpose reservoir was used for fisheries activity for longtime. The maximum yield in fisheries have been up to 2,480 ton/year in 1976 [19].

Fish samples were collected from ten sampling stations around the Ubolratana reservoir, Thailand (Fig. 1). Fish were caught by local fisherman using gill nets during the rainy season of August and October 2018. Fish samples were weighed and measured for total length to an accuracy of 0.1 g and 0.1 cm and then dissected to separate stomachs and intestines and stored at -20°C prior to examination for microplastics in laboratory.

Microplastic Extraction and Analysis

Fish stomach and intestine was defrosted and digested with 30% H_2O_2 in 50 ml Erlenmeyer flasks [20]. Volume of H_2O_2 was based on weight of stomach and intestine samples (approximately 30 ml/sample) and placed in an incubator at 65°C for 24 h. The separation of microplastics from extracted solution used a saturated NaCl solution (approximately 300 g/L) which filtered and added into the flasks then kept for 12 h at room temperature. Microplastics were floated by saline solution then the supernatant was pipetted and filtered through a glass microfiber filter (Whatman GF/C 1.2 μm pore size).

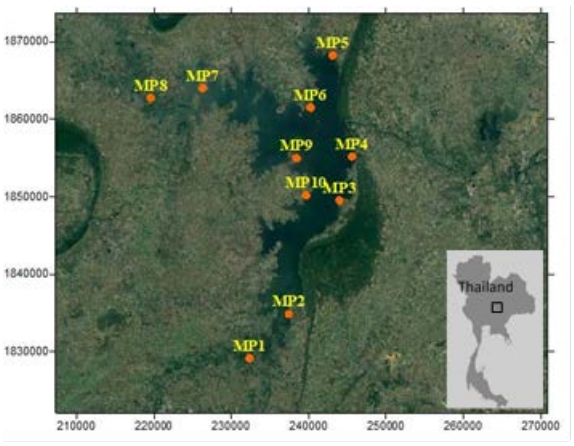

Fig.1 Location (UTM; 48Q) of the sampling stations in the Ubolratana reservoir, Thailand.

The numbers, colors, sizes and physical characteristics of microplastic particles on the glass fiber filter were observed under a stereomicroscope (Nikon SMZ745/745T). Microplastics were measured for their longest dimension and characteristics were divided into fibers, rods,

fragments, and pellets.

The abundance of microplastics between fish species and sampling stations were analyzed by Independent-Samples Kruskal-Wallis Test with significant difference was set as p-value less than 0.05.

RESULT AND DISCUSSION

Percent of Occurrence and Abundance of Microplastics in Fish

Fish sample 167 individuals were identified into 14 species (Table 1). A total of 488 microplastics particles were observed inside the stomach including intestine with 96.4% of fish samples (163 individuals). Ten fish species had 100 percent occurrence of microplastics in their gastrointestinal tract (Fig. 2). The percentage of occurrence microplastics ingested by fish was higher than the Chi river of Thailand (72.9% from 8 species, n=107) [16] and the Pajeu river, Brazil [22] (83% from 1 species, n=40) but similar to that the high level and biological risks of microplatics in Poyang Lake, China (90.9% from 1 fish species, n=11) [23].

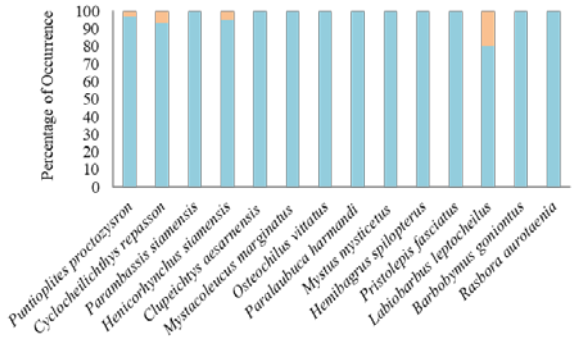

Fig. 2 The percentage of microplastics occurrence in fish gastrointestinal tract. Blue bar: ingested microplastics; Orange bar: not ingested microplastics.

The abundance of microplastics ingested by fish varied from 0 to 6 particles per fish with an overall average of 2.92±1.30 particles per fish, which lower than the Poyang Lake (0-18 particles/fish) [23] and Qinghai Lake (2-15 particles/fish) [24], China but higher than riverine fish of The Chi river, Thailand (1.76±0.58 particles/fish). There was significant difference in abundance of microplastics ingested by fish between sampling stations (Kruskal-Willis Test, p=0.016). The abundance of microplastics per fish varied among stations, the highest number of particles per fish was at MP3 (average 3.79±1.25 particles/fish) (Fig. 3A). The tourist spot (Bang Saen II Beaches) was located at MP3 (Fig. 1) that may cause source of microplastics. Meanwhile, station MP8 was located at upper part of reservoir had the lowed abundance of microplastics (average 2.20±1.24 particles/fish). The number of particles per fish between species was also significant difference (p=0.001) with the highest ingested microplatics in *Parambassis siamensis* (average 4.11±1.08 particles/fish) (Fig. 3B). *P. siamensis* is a demersal and carnivorous fish. There was significant difference between habitats (p=0.016) and feeding habits (p=0.002) related to abundance of imcroplastics ingested. The results showed that demersal and carnivorous had the highest abundance of microplastics particle of 3.49±1.32 and 3.29±1.33 particles per fish, respectively. The carnivorous fish ingested microplastics than other feeding habits, this difference to the riverine fish in Skudai River, Malaysia that herbivorous fish had highest microplastic ingestion (1.50±1.73 particles/fish) [25].

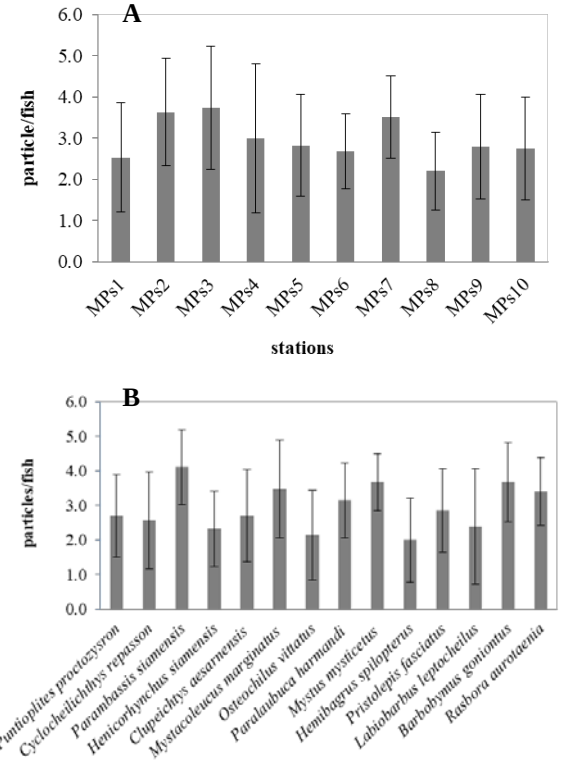

Fig.3 The mean abundance of microplastics between sampling stations around Ubolratana reservoir (A) and mean abundance microplastics in fish digestive tract by species (B). Error bar is ± SD.

Colors, Physical characteristics and size of Microplastic Particles

Four colors of microplastics were found in gastrointestinal tract of fish which compose of blue, black, transparent and red. The main colors of microplastics in fish samples was blue (51.0%) (Fig. 4A), concurrent with the former studies such as fish in Chi River, Thailand [16] and Skudai River, Malaysia [25]. The color proportion of microplastics in each fish species were similar (Fig. 5). Although

most of fish feed on resemble their prey [23],[26] but our results showed that blue microplastics was dominant color in all fish species. These may related to the microplastics abundance in fish environment [23] and there were unexpectedly ingested while fish feeding. Moreover, blue color was a favorite color of fishing net which was used in the Ubolratana reservoir.

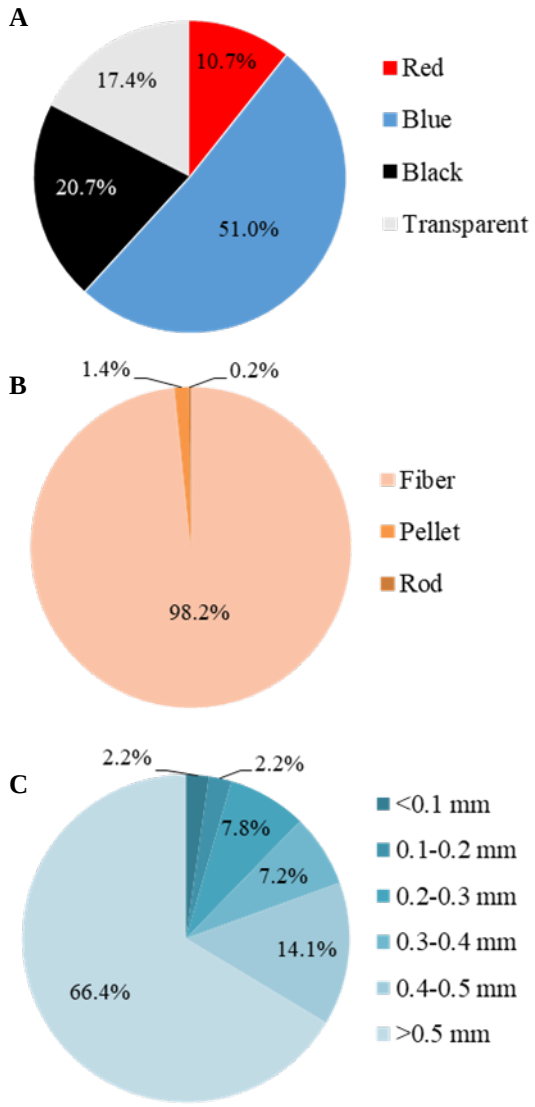

Fig. 4 Percentage of microplastics ingested by all fish samples base on color (A), shape (B) and size (C).

Three shapes of microplastics were found in fish. The common shape of microplastics ingested by fish was fiber (98.2%) followed by pellet and rod, respectively (Fig. 4B). Fiber character of microplastics were also a major shape in other reports such as in waters and sediments of Magdalena, Colombia [2] and Taihu Lake, China [14], in fish gut of Chi River, Thailand [16] and fish of Poyang Lake, China [23]. Source of fiber shape microplastics come from nylon rope, nylon line, fish cage, other fishing gear [27] and sewage from washing clothing made of woven synthetic textiles [2],[28].

Ingested microplastics size ranged between 0.03-4.77 mm. The dominant size-class was larger than 0.5 mm (66.4% of total plastic particles) (Fig. 4C). Microplastics fiber shape are usually classified into large size over 0.5 mm [16]. These size rage were similar to study in Poyang Lake, China found microplastics in fish gut larger than 0.5 mm, accounting for 82.1% of total plastic particles [23].

The dominant of color, shape and size in present study were blue fiber and larger than 0.5 mm. The result showed impact of plastic fishing gear which used in fisheries around reservoir to the abundance and physical character of microplastics. Damaged or unusable fishing gears disposal, net repairing and other fishing related activities increased abundance of microplastics as PA nylon in aquatic environments [27], finally could transport to aquatic organism like fish [13].

Freshwater fish collected in this study are commercial fish in local market of Thailand and some species were made into fishery products such as pickled fish. Thus, the potential consumer health risk can be higher when microplastics comtaminated in fish [9]. However, the monitoring and mitigation of microplastics pollution must be continue investigated and including the detrimental impact to aquatic ecosystem and human health.

CONCLUSIONS

The assessment on microplastics contamination can be used fish species as bioindicators. The abundance of microplastics ingested by fish in the Ubolratana reservoir has nearly reached to high-level contamination in freshwater fish compared to results of previous studies in freshwater systems. Opportunities to convey microplastics through the food chain must be concerning and monitoring. Physical chracters of microplastics indicate their origin as mainly from damaged fishing gear such as fish cages and gill nets.

ACKNOWLEDGMENTS

Laboratory operations were supported by the Research Unit of Excellence for Tropical Fisheries and Technology and Mahasarakham University. We would like to convey our special thanks to Sukhawit Noisena for assisting with field operations and ensuring project success.

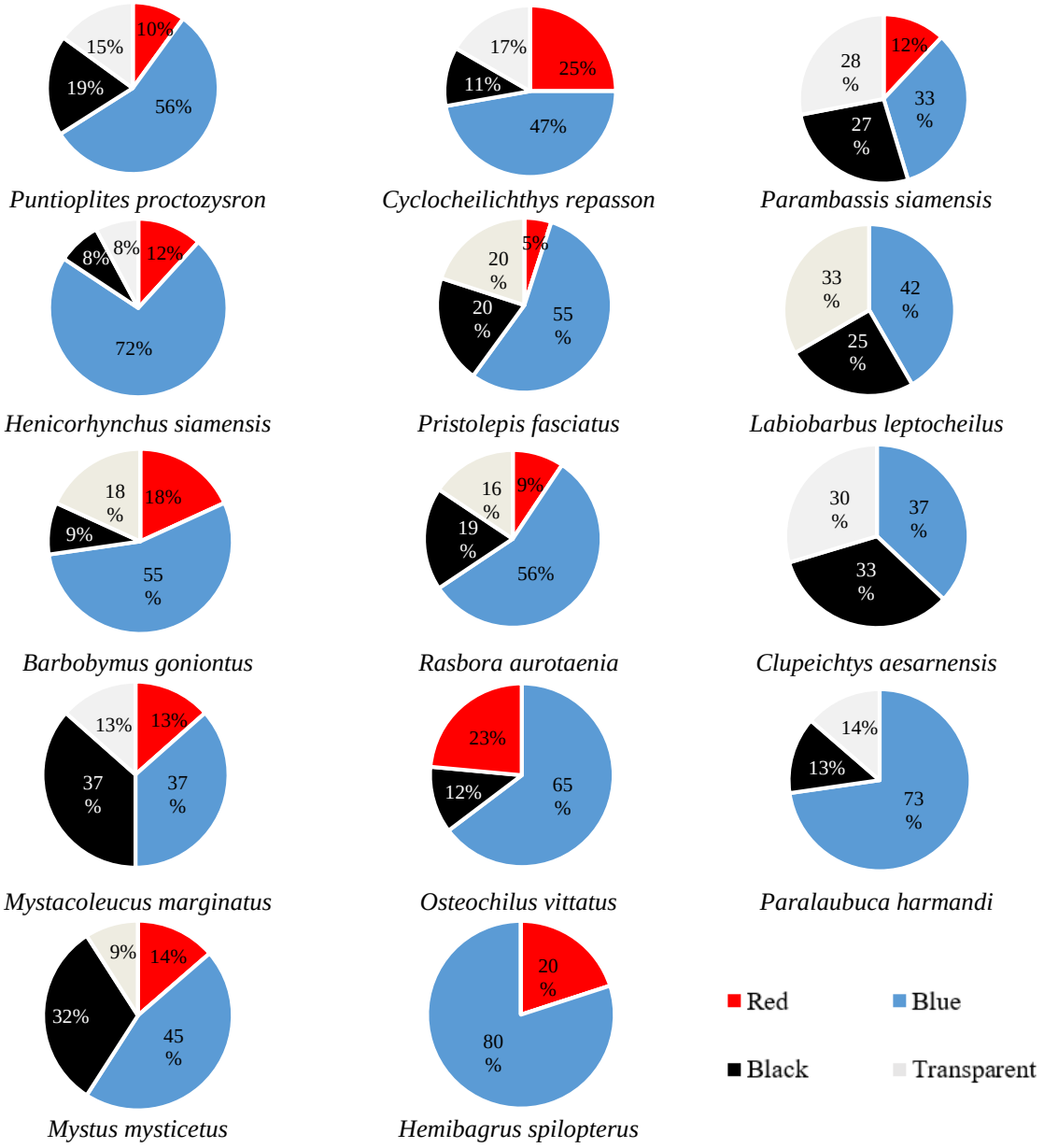

Fig. 5 Composition of microplastics particles colors in each fish species.

REFERENCES

[1] Geyer R., Jambeck J. R., and Law K. L., Production, use, and fate of all plastics ever made. Science Advances, Vol. 3, Issue 7, 2017, pp. e1700782.

[2] Silva P.M. and Nanny M.A., Impact of Microplastic Fibers from the Degradation of Nonwoven Synthetic Textile to the Magdalena River Water Column and River Sediments by the City of Neiva, Huila (Colombia). Water, Vol. 12, Issue 4, 2020, pp. 1210.

[3] Chen G., Feng Q. and Wang J., Mini-review of Microplastics in the Atmosphere and their Risks to Humans. Science of the Total Environment. Vol. 703, 2020, pp. 135504

[4] Lusher A., Hollman P. and Mendoza-Hill J., Microplastics in Fisheries and Aquaculture. FAO Fisheries and Aquaculture Technical Paper, Vol. 615, 2017, pp. 1-126.

[5] Efimova I., Bagaeva M., Bagaev A., Kileso A. and Chubarenko I.P., Secondary Microplastics Generation in the Sea Swash Zone with Coarse Bottom Sediments: Laboratory Experiments. Frontiers in Marine Science, Vol. 5, 2018, doi:10.3389/fmars.2018.00313.

[6] Chatterjee S. and Sharma S., Microplastics in Our Oceans and Marine Health. Field Actions Science Repports, Special Issue 19, 2019, pp. 54-61.

[7] Harmon S.M., Chapter8-The Effects of Microplastic Pollution on Aquatic Organisms, 1st

ed., Zeng, Ed. Elsevier Inc., 2018, pp. 249-270.
[8] Meeker J.D., Sathyanarayana S. and Swan S.H., Phthalates and Other Additives in Plastics: Haman Exposure and Associated Health Outcomes. Philos. Trans. R. Soc. Lond B. Biol. Sci., Vol. 364, Issue 1526, 2009, pp. 2097-2113.
[9] Barboza L.G.A., Vethaak A.D., Lavorante B.R.B.O., Lundebye A.K. and Guilhermino L., Marine Microplastic Debris: An Emerging Issue for Food Security, Food Safety and Human Health. Marine Pollution Bulletin, Vol. 133, 2018, pp. 336-348.
[10] Hahladakis J.N., Velis C.A., Weber R., Iacovidou E. and Purnell P., An Overview of Chemical Additives Present in Plastics: Migration, Release, Fate and Environmental Impact During Their Use, Disposal and Recycling. Journal of Hazadous Materials, Vol. 344, 2018, pp. 1799-199.
[11] Fries E., Dekiff J.H., Willmeyer J., Nuelle M.T., Ebert M. and Remy D., Identification of Polymer Types and Additives in Marine Microplastic Particles Using Pyrolysis-GC/MS and Scanning Electron Microscopy. Environmental Science: Processes & Impact, Vol. 15, 2013, DOI: 10.1039/c3em00214d.
[12] Schrank I., Trotter B., Dummert J., Scholz-Bottcher B.M., Loder M.G.J. and Loforsch C., Effects of Mocroplastic Particles and Leaching Additive on the Life History and Morphology of Daphnia magna. Environmental Pollution, Vol. 255, 2019, p. 113233.
[13] Free C.M, Jensen O.P., Mason S.A., Eriksen M., Williamson N.J. and Boldgiv B., High-Level of Microplastic Pollution in a Large, Remote, Mountain Lake. Marine Pollution Bulletin, Vol. 85, Issue 1, 2014, pp.156-163.
[14] Su L., Xue Y., Li L., Yang D., Kolandhasamy P., Li D. and Shi H., Microplastics in Taihu Lake, China. Environmental Pollution, Vol. 216, 2016, pp.711-719.
[15] McNeish R.E., Kim L.H., Barrett H.A., Mason S.A., Kelly J.J. and Hoellein T.J., Microplastic in Riverine Fish is Connected to Species Traits. Scientific Reports, Vol. 8, 2018, p.11639.
[16] Kasamesiri P. and Thaimuangphol W., Microplastics Ingestion by Freshwater Fish in the Chi River, Thailand. International Journal of GEOMATE, Vol. 18, Issue 67, 2020, pp. 114-119.
[17] Fischer E.K., Paglialonga L., Czech E. and Tamminga M., Microplastic Pollution in Lakes and Lake Shoreline Sediments – A Case Study on Lake Bolsena and Lake Chiusi (Central Italy). Environmental Pollution, Vol. 213, 2016, pp. 648-657.
[18] Fernanda C.H. and Furtado J.I., Reservoir Fishery Resources of South-East Asia. Bull.Fish. Res. Stn., Sri Lanka, Vol. 26, 1975, pp. 83-95.
[19] Smith M., Love D.C., Rochman C.M. and Neff R.A., Microplastics in Seafood and the Implications for Human Health. Curr. Environ. Health Rep., Vol. 5, Issue 3, 2018, pp. 375-386.
[20] Bhukaswan T. and Pholprasith S., The fisheries of Ubolratana Reservoir in the first ten years of impoundment. Proc.IPFC, Vol. 17, Issue 3, 1977, pp. 195–205.
[21] Jabeen K., Su L., Li J., Yang D., Tong C. and Mu J., Microplastics and Mesoplastics in Fish from Coastal and Fresh Waters of China. Environmental pollution, Vol. 221, 2017, pp. 141-149.
[22] Silva-Cavalcanti J.S., Silva J.D.B., de Franca E.J., de Araujo M.C.B., Gusmao F., Microplastics Ingestion by Common Tropical Freshwater Fishing Resource. Environmental Pollution, Vol. 221, 2017, 218-226.
[23] Yuan W., Liu X., Wang W., Di M. and Wang J., Microplastic Abundance, Distribution and Composition in Water, Sediments, and Wild Fish from Poyang Lake, China. Ecotoxicology and Environmental Safety, Vol. 120, 2019, pp. 180-187.
[24] Xiong X., Zhang K., Chen X., Shi H., Luo Z. and Wu C., Sources and Distribution of Microplastics in China's Largest Inland Lake-Qinghai Lake. Environmental Pollution, Vol. 235, 2018, pp. 899-906.
[25] Sarijan S., Azman S., Said M.I.M. and Lee M.H., Ingestion of Microplastics by Commercial Fish in Skudai River, Malaysia. Environmental Asia, Vol. 12, Issue 13, 2019, pp. 75-84.
[26] Alomar C., Sureda A., Capo X., Guijarro B., Tejada S. and Deudero S., Microplastic Ingestion by Mullus surmuletus Linnaeus, 1758 Fish and It Potential for Causing Oxidative Stress, Environmental Research, Vol. 159, 2017, pp. 135-142.
[27] Thushari G.G.N., Senevirathna J.D.M., Yakupitiyage A. and Chavanich S., Effects of Microplastics on Sessile Invertebrates in the Eastern Coast of Thailand: An approach to Coastal Zone Conversation. Marine Pollution Bulletin, Vol. 124, 2017, pp. 349-355.
[28] Browne M.A., Crump P., Niven S.J., Teuten E., Tonkin A., Galloway T. and Thompson R., Accumulation of Microplastic on Shorelines Worldwide: Sources and Sinks. Environmental Science & Technology, Vol. 45, 2011, pp. 9175-917.

6th Int. Conf. on Structure, Engineering & Environment (SEE), Kyoto, Japan, Nov.18-20, 2020, ISBN: 978-4-909106056 C3051

CHARACTERISTICS OF CULTURAL LANDSCAPE AS STREETSCAPE IN KUDOYAMA TOWN

Tomoko Miyagawa[1], Rena Ozaki[2], Kyota Matsuyama[3], Shinpei Yamamoto[4] and Masahiro Takasago[1]
[1] Faculty of Systems Engineering, Wakayama University, Japan; [2] Takara Standard CO., LTD., Japan; [3] Fukuvi Chemical Industry, [4]Kudoyama Town Office, Japan

Managing historic environment and cultural heritage in partnership with the community are becoming more important, due to the recent trend of shrinking society and limited resources. This study aims to clarify the characteristics of cultural landscape as streetscape forming townscape managed by the community in the town centre of Kudoyama, Wakayama Prefecture. This paper focuses on streetscape and site boundary objects as local resources. Field observations and literature reviews on cultural landscapes are used for study methods. From the results, characteristics of the town center of Kudoyama became clear as follows; the narrow and winding streets from the past times have been confirmed to form one of its characteristics of local resources in comparison with the old map of the year of 1767; many of the narrow streets connected to two main streets are not more than three meters; the differences of topography were 29.9 meters at the most within the size of 200 by 600 meters to create steep slopes and retaining walls made by stones or concrete; and site boundary objects to form streetscape, i.e., hedgerows, stone or concrete retaining walls, and Japanese style walls. As conclusion, the streetscape of town center of Kudoyama have unique characteristics and changing landscape by enclosure with narrow and winding streets as well as site boundary objects in undulating landforms.

Keywords: Partnership, Cultural landscape, Community, Local resources

INTRODUCTION

Management of Cultural Landscapes

Managing historic environment and cultural heritage in partnership with the community are becoming more important, due to the recent trend of shrinking society and limited resources. Working in partnership can promote the importance of 'viewing the landscape from a variety of perspectives' [1]-[2], which often has been discussed the differences of views and values between 'outsiders' and 'insiders' [3]. Working in partnership can also help to create its own network of people, knowledge and experience, as well as to diversify actions which may lead to increase other partners.

In terms of managing historic environment and cultural heritage, it would be necessary to understand a diversity and complexity from a wider scale [4], i.e., local resources managed by the community, and the local authority by being registered as cultural properties. Thus, this study tries to cover perspectives of community as living environment which also could form cultural landscape as streetscape.

Cultural Landscapes of Town Centre in Kudoyama

The town has a World Heritage Site, pilgrimage routes to Koyasan registered by the UNESCO, as a part of Sacred Sites and Pilgrimage Routes in the Kii Mountain Range in 2004, and 2016. Along with the world and national importance of heritage, the town has a townscape and landscape formed by its landforms surrounded by the rivers and mountains. The long-term plan of the town aims to foster local resource such as historic environment and creating opportunities for communication between residents and visitors to overcome structural changes of population [5]. Based on the questionnaire survey on the awareness and future images of the town to residents of town center in Kudoyama in 2016 responded by 108 people in total, it became apparent that 80 percent of residents are willing to welcome visitors, as well as nearly 70 percent of residents agreed on conserving historic buildings and townscape [6]. According to related research, townhouses and a part of local resources has been clarified [7]. However, there are other characteristics as streetscape. Therefore, this study focuses on streetscape and site boundary objects to clarify other characteristics of town center in Kudoyama.

The concept of local resources has been described by Miyayama and Kamihogi which can be divided into 'natural elements' and 'historic elements', and streets and landforms are in the category of 'natural elements' [8]. Streetscape in residential areas is formed by houses, exterior, parks

and streets as such, and within exterior, plantings such as hedgerows, gates, walls, and parking spaces are included, and in particular, plantings grow and changes by residents with their individuality [9].

The Aims and Methods of This Study

This study aims to clarify the characteristics of cultural landscape as streetscape forming townscape managed by the community from the perspectives on the cultural landscapes in the town centre of Kudoyama, Wakayama Prefecture. This paper focuses on streetscape and site boundary objects as local resources. This study undertook field observations including measuring widths of streets and lengths of site boundary objects by steps and literature reviews on cultural landscapes to study the methods. In terms of the analysis of streetscapes, this study tries to examine the width of streets and differences of inclination in slopes focusing on narrow streets connected by two major, wider streets running from the east to the west of the town center of the Kudoyama. This study also examines the lengths by steps and location of site boundary objects including retaining walls, i.e., hedgerows, stone or concrete walls, as well as Japanese style walls and iron fences. In terms of Japanese style walls, this study classified walls made by wood, clay, tiles, plaster, and stones which encloses houses and temples.

An Evaluation of Residents Concerning Townscape of Town Center in Kudoyama

An awareness survey to residents per household in town center of Kudoyama has been conducted in 2016, collecting 108 answers out of 270 houses at 40 percent [6]. From the results, 80 percent of residents are welcoming visitors for sightseeing to enjoy townscape, thus, residents are largely recognizing townscape as one of the characteristics of the town [6]. In terms of conservation of townscape in the future, residents value conservation of historic houses at 39 percent, while conservation of townscape as a whole town at 29 percent [6].

On the other side, the highest concern of residents was about streets at 46 percent [6]. The reasons for the concern about streets, 82 percent has been responded for the width of streets, and 8 percent for aging and slope of streets [6]. Particularly, the northern area of the town center has steep slopes with narrow width. Therefore, in terms of street width, the main street has 4.4 meters, while one of the narrowest streets has 1.04 meters [6].

From the above, residents are welcoming visitors and conservation of townscape has been largely recognized (Fig 1). The narrow and winding streets from the past times to form one of its characteristics of local resources, coincides to be a major concern for residents (Fig 2). Particularly, it addresses the issues of traffic and access, and risks in case of emergency.

Fig. 1 Townhouses creating streetscape of Kudoyama

Fig. 2 Streetscape with a narrow street and slopes

STREETSCAPES IN THE TOWN CENTRE OF KUDOYAMA

A Classification by The Width of Streets

In terms of the width of streets, it became clear that many of them are less than 2 meters at nearly 80 percent, while more than 2 meters at around 20 percent in total (Table 1, Fig. 3).

Table 1 A Classification by the width of streets [10]

Items	numbers	percentages
Less than 1m	6	19%
1m to 1.5m	9	29%
1.5m to 2m	9	29%
2m to 2.5m	4	13%
2.5m to 3m	1	3%
More than 3m	2	7%
Total	31	100%

A Comparison of Street Patterns

In comparison with the old map of the year 1767,

many of the narrow and winding streets remain in the similar pattern (Fig. 4).

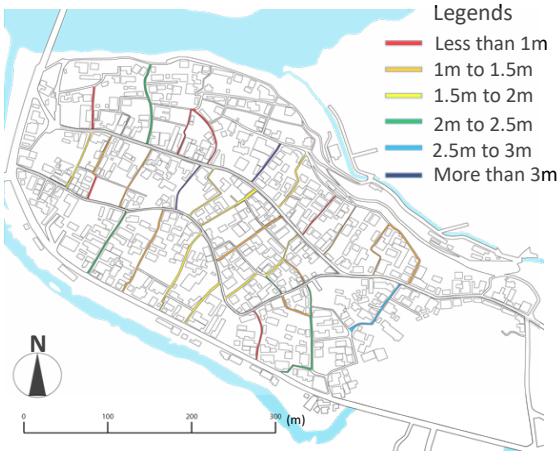

Fig. 3 The width of narrow streets (amended) [10]

Fig. 4 The old streets remained since 1767 (amended) [10]

The Topography Creating Slopes and Retaining Walls

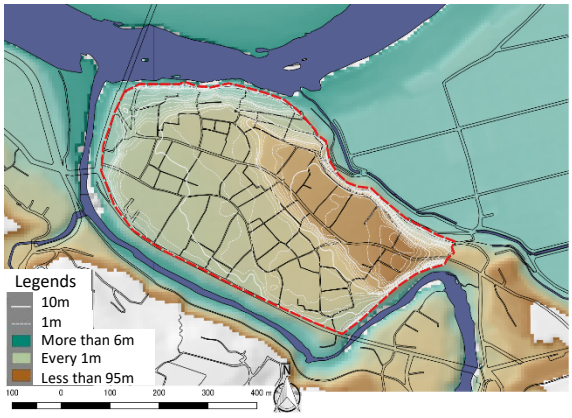

Fig. 5 The contour map (amended) [10]

Fig. 6 A narrow slope with stone walls [10]

The town is located between two rivers of the Kino and the Nyu which created river terraces, and the differences of topography were 29.9 meters at the most within the size of 200 by 600 meters to create steep slopes (Fig. 5). Due to the topography, houses are built on retaining walls made by stones or concrete which also create characteristics of streetscape, i.e., stone walls along the narrow slope (Fig. 6).

SITE BOUNDARY OBJECTS IN THE TOWN CENTRE OF KUDOYAMA

A Classification by Site Boundary Objects

Site boundary objects can be classified into seven items (Table 2). Concrete walls and concrete retaining walls are at nearly half of all; and retaining walls account for at 25 percent in total. The traditional styled objects were also found at 35.5 percent in total, i.e., hedgerows, stone walls and stone retaining walls, and Japanese style walls.

Table 2 A Classification of site boundary objects (amended) [11]

Items	numbers	percentages
Concrete walls	207	38%
Iron fences	102	18.5%
Hedgerows	52	9%
Japanese style walls	34	6%
Stone walls	21	4%
Stone retaining walls	91	16.5%
Concrete retaining walls	45	8%
Total	552	100%

A Japanese Style Walls

Many of them are constructed on its own. However, some houses and temples such as the Sanada Monastery, the Kayanoke House, and the

Fig. 7 Japanese style walls on the stone retaining walls [11]

Fig. 8 A Japanese style wall at the Sanada Monastery [11]

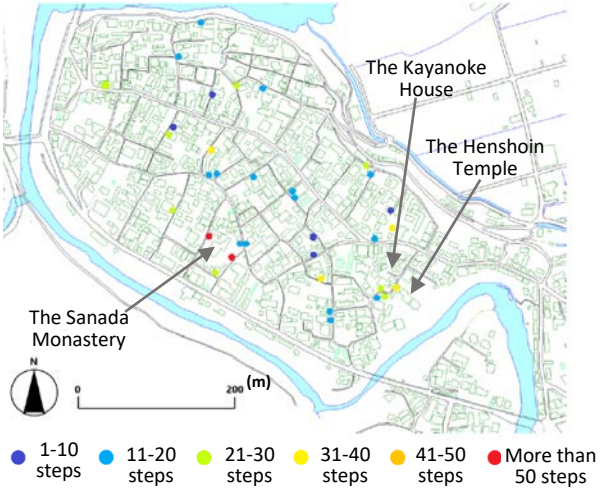

Fig. 9 Locations and lengths of Japanese style walls (amended) [11]

Henshoin temple have larger sites so that it creates continuous and longer Japanese style walls on stone or concrete retaining walls as well as having gardens on sites to be able to view trees over the walls (Fig. 7-9).

Stone Retaining Walls

Stone retaining walls has been confirmed up to 91 places in the town center of Kudoyama (Fig. 10). Many of them are located along narrow streets with smaller scale, thus, length is mostly within 30 steps [11]. Stone retaining walls are constructed on its own i.e., a foundation for houses (Fig. 11), as well as to be combined with other site boundary objects, such as with Japanese style walls (Fig.7). To highlight its characteristics with high walls, it is utilized into a place for the notice board along streets (Fig.12).

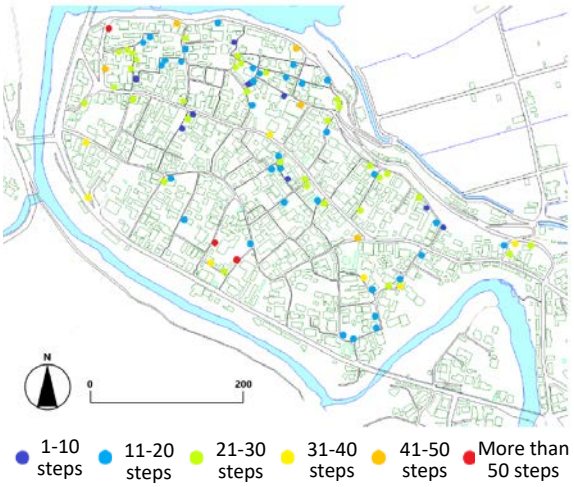

Fig. 10 Locations and lengths of Stone retaining walls (amended) [11]

Fig.11 A stone retaining wall as a foundation for a traditional house

Concrete Retaining Walls

Concrete retaining walls along streets can be confirmed at 45 places. Many of them are confirmed to be within 11 to 20 steps, in the case of construction

Fig.12 A stone retaining wall along streets utilized into a place for the notice board

for individual sites. However, there are some cases with more than 30 steps where the construction is shared with several sites to be a foundation for buildings or houses which create continuous walls (Fig.13). In addition, the height of walls may create impacts on landscapes by having majority of views (Fig.14) [11].

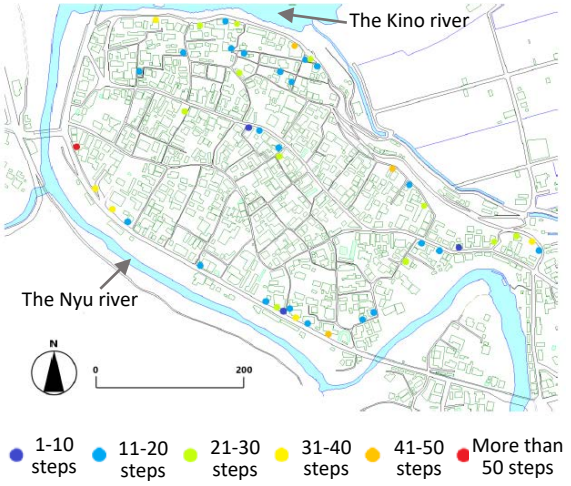

Fig. 13 Locations and lengths of concrete retaining walls (amended) [11]

Fig. 14 A concrete retaining wall along a road [11]

DISCUSSIONS

From the results, the pattern of some of the narrow streets are winding or joining to other narrow streets, which may create unique streetscapes but may also create difficulties in way finding particularly for visitors. Therefore, the old streets are also creating characteristics of streetscape in Kudoyama [10].

The other characteristics of streetscape is slopes created by topography in the town center of Kudoyama. In terms of topography, it is higher and steep in the north-eastern side, while the south-western side tends to be lower and gentle along the Nyu [10]. This may also be one of the reasons of having a significant amount of constructed retaining walls. For example, stone retaining walls has been constructed to reconcile undulations of its landform from the past times. Therefore, it tends to be concentrated in the edge of the town where a concentration of contours with a terraced landscape towards surrounding rivers, which is illustrated in the contour map showing, Fig.5. For concrete retaining walls, many of them are located around the edge of the town center, towards the Kino river and along a main road in parallel to the Nyu river. This is because of undulation of landforms, therefore, it is constructed on the places with differences in height in similar to stone retaining walls.

CONCLUSIONS

Based on survey and observed research, characteristics of the town center of Kudoyama became clear as follows; the narrow and winding streets from the past times have been confirmed to form one of its characteristics of local resources in comparison with the old map of 1767; many of the narrow streets connected to two main streets are not more than three meters; the differences of topography were 29.9 meters at the most within the size of 200 by 600 meters to create steep slopes and retaining walls made by stones or concrete; and site boundary objects to form streetscape, i.e., hedgerows, stone or concrete retaining walls, and Japanese style walls. To conclude, the streetscape of town center of Kudoyama have unique characteristics and changing landscape by enclosure with narrow and winding streets as well as site boundary objects in undulating landforms.

ACKNOWLEDGEMENTS

The authors would like to express our gratitude for the financial support provided to the cultural heritage utilization and community activation project from the Agency for Cultural Affairs.

REFERENCES

[1] Melnick R.Z., Protecting Rural Cultural Landscapes: Finding Value in the Countryside, Landscape Journal, Vol. 2, No. 2, 1983, pp. 85-96.

[2] Willemen L., Verburg P.H., Hein L., and Mensvoort M. E. F., Spatial characterization of landscape functions, Landscape and Urban Planning, Vol. 88, 2008, pp.34-43.

[3] Selman P., Chapter 6, Landscape and sustainability at the national and regional scales, in Landscape and sustainability, 2nd ed., Benson and Roe, Ed. Taylor and Francis, 2007, pp. 104-117.

[4] Roe M. and Taylor K., Chapter 1, New cultural landscapes: emerging issues, context and themes, in New Cultural Landscapes, Roe and Taylor, Ed. Routledge, 2014, pp.1-23.

[5] Planning Office, Kudoyama Town, The Fourth Long Term Comprehensive Plan of Kudoyama Town, <https://www.town.kudoyama.wakayama .jp/kikaku/sougoukeikaku/>, 2012, [Accessed 2019.10.15.] (in Japanese).

[6] Yokode Y., Study on the Consciousness of Residents and the actual situation of Unused, and under-used Lands in Town center of Kudoyama-cho, a master's thesis submitted to the School of Systems Engineering, Wakayama Univ., 2016, pp.1-49 (in Japanese).

[7] Miyagawa T., Yamaguchi S., Yoshino (Aoyama) S., Yamamoto S., and Takasago M., Characteristics of Cultural Landscape in the Gatewaytown of Kudoyama, in Proc. 9th Int. Conf. on GEOMATE, 2019, pp.792-797.

[8] Miyayama Y., and Kamihogi A., Study about the succession of Kyokaido road, looked at from the continuation situation of the road, maintenance and the use situation, Landscape Research, Vol.74, (5), 2011, pp.773-778 (in Japanese).

[9] Kamei Y., Sone Y., Ishii S., and Yokoyama R., A study on front yards and street-scapes in suburban housing development practices -the changing process of ready-built houses for sale in Japan part 2 -, Journal of Architecture and Planning, No.590, Apr., 2005, pp.9-15 (in Japanese).

[10] Ozaki, R., Research on Alleys in Oaza-kudoyama, Kudoyama-cho, a dissertation submitted to the Dept. of Env. Systems, Wakayama Univ., 2018, pp.1-40 (in Japanese).

[11] Matsuyama, K., Research on borders in town center of Kudoyama, Kudoyama town, a dissertation submitted to the Dept. of Env. Systems, Wakayama Univ., 2019, pp.1-39 (in Japanese).

6th Int. Conf. on Structure, Engineering & Environment (SEE), Kyoto, Japan, Nov.18-20, 2020, ISBN: 978-4-909106056 C3051

UTILIZATION OF ACTIVATED CARBON FROM PALM KERNEL SHELLS AS THE BIOADSORBENT OF LEAD WASTE

Muhammad Faisal[1], Asri Gani[1], Zahrul Fuadi[2]
[1]Department of Chemical Engineering, Universitas Syiah Kuala, Banda Aceh, Indonesia
[2]Department of Mechanical Engineering, Universitas Syiah Kuala, Banda Aceh, Indonesia

ABSTRACT

This research aimed to evaluate the use of palm kernel shells for activated carbon to adsorb lead (Pb) ions. The pyrolysis was performed on oil palm kernel shells at a temperature of 380°C to obtain charcoal which was reduced using a ball mill. The charcoal was then chemically activated with liquid smoke. Before and after activation, the sample of charcoal was assessed with scanning electron microscopy (SEM). The activated carbon was then used to adsorb Pb (II) ions in concentrations of 30, 60, 90, 120, and 150 mg/L. The adsorption process was performed in a batch reactor with contact times of 30, 60, 90, 120, 150, and 180 minutes at an agitation speed of 150 rpm. The initial concentration of Pb (II) ions and concentration after adsorption were determined with an atomic absorption spectrophotometer (AAS). Research has shown that initial concentrations and contact times affect the efficiency of Pb (II) removal. The highest adsorption efficiency (> 90%) was obtained at a contact time of 150 minutes and an initial concentration of 60 mg/L. Pb adsorption onto the activated carbon of palm kernel shells demonstrated best fit with both Langmuir and Freundlich isotherm models. Kinetics studies showed that the pseudo first-order reaction was more suitable ($R^2 = 0.9359$).

.

Keywords: Palm kernel shell charcoal, Pb (II), Activated carbon, Pyrolysis, Liquid smoke

INTRODUCTION

The continual expansion of industrialization has accelerated developments in the chemical industry, causing increased industrial waste—more and more is being discharged into the environment. Nature's capacity to tolerate the burden of waste is very limited, and it is believed that its normal self-purification systems have been exceeded. Among the wastes that pollute the environment and cause disturbing water pollution today are heavy metals, such as lead ions (Pb), commonly found in the industrial waste of manufacturers of batteries, paper, metallurgy, explosives, paints, and other colouring materials [1]–[3]. Pb (II) is a soft, blackish-brown metal that is easily extracted from mining. It comes from the earth's crust in the form of pure, organic, and inorganic material. Industrial processes play an important role in increasing the levels of this heavy metal.

Lead belongs to the group of toxic metals that are harmful to living things accumulatively and not easily degraded [4],[5]. Pb compounds can enter the human body through the respiratory and digestive tracts or through direct contact with the skin. According to the US Environmental Protection Agency (EPA), lead tolerance levels in drinking water and wastewater are 0.015 and 0.1 mg/L, respectively [6]. Levels of Pb higher than these limits are known to poison the human body both acutely and chronically. In addition, continuous Pb poisoning in childhood can cause neurotoxic disorders, cancer, and damage to the kidneys, pancreas, brain, and liver [7]–[9]. To avoid its harmful effects on living things, heavy metal concentration has to be reduced to a safe level by properly treating the waste before discharge into water systems.

There are several ways to remove heavy metals like Pb from wastewater, including precipitation and ion exchange, electrodialysis, evaporation, and absorption using activated carbon [10]. The most frequent problem in heavy metal waste treatment is its high cost, thus, effective and low-cost techniques are needed. One such technique is adsorption. The adsorption process occurs on the surface of the adsorbent material's pores, and the metal in the liquid undergoes a process of transferring metal mass from the liquid to the adsorbent's surface [11]. This is among the most frequently used methods for removing toxic metals from wastewater [12]. Adsorption is a physical–chemical process in which the adsorbates—in this case, the pollutants—accumulate on the surface of solids used as adsorbents. The process is suitable for wastewater with low metal concentrations, especially in industries with limited financial resources [13],[14]. Many types of adsorbent have been developed to remove Pb from wastewater, including zeolites [14],[15], Ethylene diamine tetra acetic acid **(**EDTA) magnetic graphene oxide [16], papaya seed [17], chlorapatite nanoparticles [18], montmorillonite

[19], *Areca catechu* shell [20], palm tree leaves [21], chitosan [22], modified bentonite and magnetic cellulose [23], charcoal from celery [24], rapeseed biomass [25], the bark of *Cordia macleodii* trees [26], and natural zeolite [27]. The challenge in adsorption technology is to select economical and efficient alternative adsorbents to minimize operating costs, especially in developing countries [28]. An alternate adsorbent that has been proposed is charcoal from oil palm shell pyrolysis. Before being used to adsorb heavy metals, the charcoal is activated chemically and physically. Several studies have shown that the activated carbon from the pyrolysis process is capable of removing heavy metals with fairly high removal efficiency [29]. This research aims to study the ability of activated carbon from pyrolysis of oil palm shells to remove Pb (II).

MATERIALS AND METHODS

Preparation of Activated Carbon from Oil Palm Shells

A pyrolysis reactor (stainless steel, homemade) with a height of 60 cm and an inner diameter of 40 cm was used to pyrolyze palm shells at 380°C. The temperature in the reactor was kept constant throughout the pyrolysis. The procedure for making charcoal and liquid smoke followed that in previous studies [30],[31]. Five kg of palm shells were loaded into the reactor, and the reactor was tightly sealed. A steam channel in the lid connected to the condenser unit condensed the vapor into liquid smoke. After the pyrolysis process was complete, the reactor was opened and the resulting charcoal was ground in a ball mill for 24 hours to reach nano size particles. The charcoal was then activated using the liquid smoke, previously purified by distillation, by immersing it in the liquid smoke solution for 24 hours. Then the activated carbon was filtered and washed with distilled water to a neutral pH before being dried in an oven dryer at a temperature of 105°C until the weight became constant. The surface morphology of the activated carbon was analysed using scanning electron microscopy (SEM) (JEOL-JSM 6510 LA, Shimadzu, Japan).

Adsorption Test

Carbon nanoparticles activated by liquid smoke were then used to adsorb Pb metal prepared from a lead sulphate ($PbSO_4$) solution. The initial concentration of Pb (II) varied from 30, 60, 90, 120, to 150 mg/L. On hundred ml of $PbSO_4$ was put into an Erlenmeyer and one gram of adsorbent was added and stirred at 150 rpm speed. The contact times between Pb (II) and adsorbent solutions were 30, 60, 90, 120, 150, and 180 min at room temperature. After the adsorption process was complete, the filtrate was separated by centrifuging. Pb (II) analysis was carried out using AAS (AA-7000, Shimadzu, Japan).

RESULTS AND DISCUSSION

Adsorbent Characteristics

Figures 1a and 1b show the results of SEM analysis of the palm shell carbon before and after activation. Surface morphology showed a better surface after activation by liquid smoke than before. The figures also show that the size of the activated carbon particles reached nanometres, that is, below 500 nm. Particles of the liquid smoke-activated carbon have a smaller size than that of NaOH-activated carbon particles under the same conditions and activation methods [29], demonstrating that activation in an acidic atmosphere reduced the size of the active carbon particles. Liquid smoke as an activator contains various chemical compounds, such as acetic acid, phenolic compounds, and other compounds with varying concentrations [32[,[33], allowing the adsorbent's surface to adsorb metal ions. In Figure 1, it can also be seen that the shape of the activated carbon surface was uneven but that nanometre sizes of the activated carbon dominated.

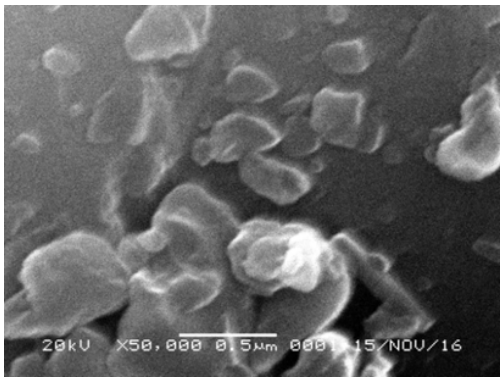

(a) Before activation

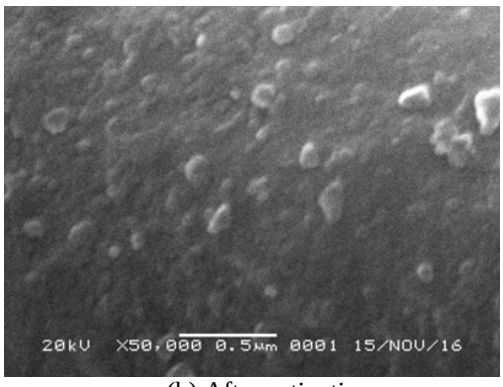

(b) After activation

Fig. 1 SEM analysis of the palm shell carbon before and after activation.

Effect of Contact Time and Initial Concentration on the Adsorption Efficiency of Pb (II)

Figure 2 shows the effect of contact time on the adsorption efficiency of Pb (II) at various initial concentrations. At 150 rpm agitation, an initial concentration of 30 mg/L and a contact time of 30 min, as shown in Figure 2**,** the adsorption efficiency was 75%. At the beginning of the adsorption of Pb (II) metal ions, the adsorbent surface had not absorbed much, so the adsorption process was less effective. This due to at a contact time of 30 min, the adsorbent and adsorbate had not fully bonded, resulting in fewer adsorbed ions. The adsorption efficiency increased to 92% at min 150.

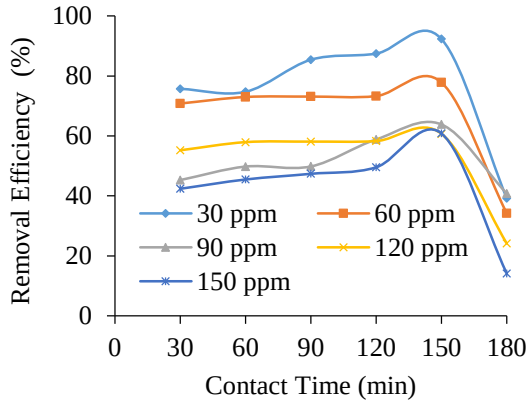

Fig. 2 The effect of contact time on the adsorption efficiency of Pb (II) at various initial concentrations.

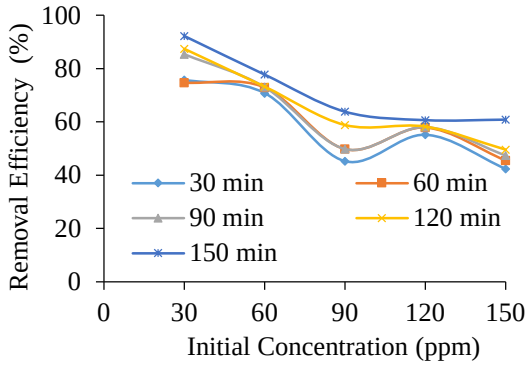

Fig. 3 The effect of initial concentration on the adsorption efficiency of Pb (II) at various contact times.

Figure 3 shows the effect of initial concentration on the adsorption efficiency of Pb at various contact times. At an initial concentration of 60 mg/L, the adsorption efficiency for contact times of 30, 60, 90, 150, and 180 mins were 70%, 72%, 73%, 73%, 77%, 93%, and 34%, respectively. The same trend was observed for all contact times (i.e., 30, 90, 120, and 150 min). The efficiency of adsorption decreased with increasing initial concentration. Low adsorption efficiency at 180 min was due to the saturation of the adsorbent's surface impeding further adsorption. At this point, the diffusion and adhesion of adsorbed solute molecules occurred more, thereby increasing the adsorption efficiency. The same trend has been reported in the literature for lead adsorption using zeolite-NaX [35]. The results of this study indicate that for all contact times, the greater the initial concentration, the smaller the absorption efficiency produced. Thus, in this study, the adsorption of Pb (II) was preferred at low initial concentrations.

Isotherm Studies

Changes in the adsorbate concentration by the adsorption process following the adsorption mechanism can be studied by determining the adsorption isotherm. Isotherm studies were carried out to determine the adsorption equilibrium, capacity, and mechanism. The Freundlich and Langmuir isotherm models are most commonly used to analyse equilibrium data. The Freundlich isotherm model is applied to multilayer adsorption with a heterogeneous distribution. The model provides a relationship between solid and liquid concentrations and is very helpful in connecting isotherm data collected in various concentrations.

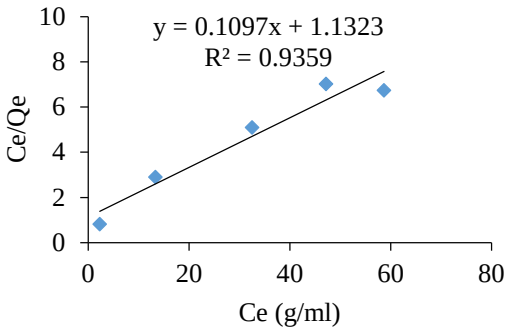

Fig. 4 Isoterm Langmuir.

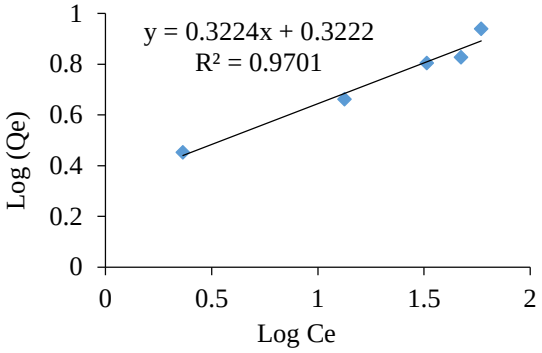

Fig. 5 Isoterm Freundlich.

The Langmuir isotherm model assumes monolayer adsorption with a homogenous distribution of energetic adsorption sites. The Langmuir and Freundlich adsorption isotherm models on Pb metal are shown in Figures 4 and 5, respectively. Figures 4 and 5 show that the R^2 values for Langmuir and Freundlich were 0.93 and 0.97, respectively. This indicates that the adsorption of Pb (II) metal using liquid smoke-activated charcoal from palm shells tended to follow the pattern of the two isotherms, namely the adsorption of monolayers on the adsorbent's outer surface and multilayer adsorption on heterogeneous surface sites. Table 1 shows the parameters and constants of the Langmuir and Freundlich isotherms. As can be seen from the Table 1, the Freundlich constant (K_F) representing adsorption capacity was 2.099 mg/g with adsorption intensity (n) of 3.101. The K_F obtained from this research was higher than the results of Lou et al. [23]. For the Langmuir isotherm, the adsorption ability (qm) of the activated carbon to adsorb Pb ions was 9.11 g/mg. This value was lower than that of previous studies using zeolite-NaX adsorbents [34]. The strength of the interaction between Pb (II) ions and the activated carbon is indicated by the value of K_L, which was 0.096. Previous studies reported that Pb (II) adsorption using chitosan-g-maleic anhydride-g-methacrylic acid copolymer tended to follow the Freundlich isotherm [22], whereas the adsorption of Pb (II) using adsorbents from rapeseed biomass tended to follow the Langmuir isotherm [25].

Table 1. Constant values of both Langmuir and Freundlich isotherm models of Pb (II) adsorption

Langmuir			Freundlich		
R^2	qm (mg/g)	K_L (L/mg)	R^2	n	K_F (mg/g)
0.935	9.11	0.096	0.970	3.101	2.099

In the Langmuir isotherm, to assess whether the adsorption process is favourable, irreversible, or unfavourable, the dimensionless separation factor (R_L) value can be used, which is calculated with the following equation:

$$R_L = \frac{1}{1 + K_L C_i}$$

where K_L = Langmuir constant and C_i = initial concentration.

A value of R_L between 0 and 1 indicates that the adsorption process is favourable. Adsorption is linear if the value of R_L = 1, irreversible if R_L = 0, and unfavourable if R_L > 1 [35]. Figure 6 shows the relationship between the initial concentration and separation factor values for Pb (II) adsorption.

As shown in Figure 6, the value of R_L at an initial concentration of 30 mg/L was 0.25, and it dropped to 0.05 at an initial concentration of 150 mg/L. The R_L values are between 0 and 1 for all initial concentrations, demonstrating that the adsorption process is favourable.

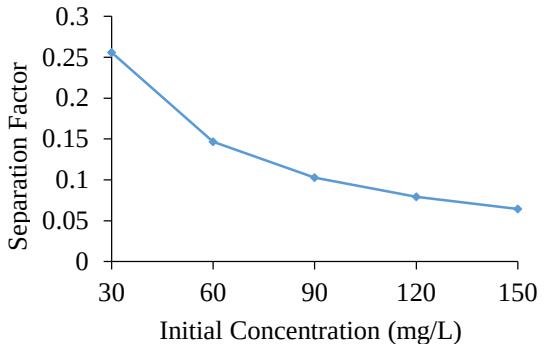

Fig. 6 The relationship between the initial concentration and separation factor for Pb (II) adsorption.

CONCLUSIONS

This research investigated the ability of adsorbents from palm kernel shell charcoal activated by liquid smoke to adsorb Pb (II) metal ions. The SEM test results showed that the activated adsorbents had better pore size for adsorption. At contact times of 30–150 min and initial concentrations of 30–150 mg/L, the efficiency of Pb (II) absorption ranged from 40% – 93%. At a contact time of 180 min, efficiency dropped dramatically as a result of the adsorbent's saturation. The best condition was achieved at 150 min contact time and an initial concentration of 30 mg/L. The results of the isotherm equilibrium analysis showed that the adsorption process was suitable for the Langmuir and Freundlich isotherm models.

.

ACKNOWLEDGMENTS

The work was financially supported by Universitas Syiah Kuala (Grant No. 289/UN11/SP/PNBP). We wish to thanks Sandi Putra Kelana and Dodi Eko Nanda for conducting experiments and data analysis.

REFERENCES

[1] Hanafiah, M.A.A.M., Ngah, W.S.W., and Ibrahim, S.C., Kinetics and Thermodynamic Study of Pb(II) Adsorption from Aqueous

Solution onto Rubber (Hevea brasi- liensis) Leaf Powder. Journal of Applied Sciences, Vol. 6, Issue 13, 2006, pp. 2762–2765.

[2] Paulino, A.T., Guilherme, M.R., Reis, A.V., Tambourgi, E.B., Nozaki, J., and Muniz, E.C., Capacity of Adsorption of Pb^{2+} and Ni^{2+} from Aqueous Solutions by Chitosan Produced from Silkworm Chrysalides in Different Degrees of Deacetylation. Journal of Hazardous Materials, Vol. 147, 2007, pp. 139–147.

[3] Saifuddin, N., and Raziah, A.Z., Removal of Heavy Metals from Industrial Effluent using Saccharomyces Cerevisiae (Baker's Yeast) Immobilized in Chitosan/Lignosulphonate Matrix. Journal of Applied Sciences Research, Vol. 3, Issue 12, 2007, pp. 2091–2099.

[4] Ince, O. K., Ince, M., Yonten, V., and Gok, A., A Food Waste Utilization Study for Removing Lead(II) from Drinks. Food Chemistry, Vol. 229, 2017, pp. 637–643

[5] Begum, A., Krishna, S.H., Khan, I., Ramaiah, M., Veena, K., and Vinuta, K., Nutrients and Heavy Metal Profile of Madivala Lake, Bangalore South, Karnataka. Rasayan Journal of Chemistry, Vol. 1, Issue 3, 2008, pp. 572-582.

[6] Guidelines for Drinking Water, US Environmental Protection Agency (US EPA), 2001.

[7] Zhou, Y., Zhang, L., and Cheng, Z., Removal of Organic Pollutants from Aqueous Solution using Agricultural Wastes: A Review. Journal of Molecular Liquids, Vol. 212, 2015, pp. 739-762.

[8] Dai, Y., Zhang, K., Li, J., Jiang, Y., Chen, Y., and Tanaka, S., Adsorption of Copper and Zinc onto Carbon Material in an Aqueous Solution Oxidized by Ammonium Peroxydisulphate. Separation and Purification Technology, Vol. 2, 2017, pp. 255-263.

[9] Sahu, M.K., Mandal, S., Dash, S.S., Badhai, P., and Patel, R.K., Removal of Pb (II) from Aqueous Solution by Acid Activated Red Mud. Journal of Environmental Chemical Engineering, Vol. 1, 2013, pp. 1315-1324.

[10] Zhu, Q., Zehuan, W. L., Ye, A.H., and Feng, X., Hydrothermal Synthesis of Silico-Manganese Nanohybrid for Cu(II) Adsorption from Aqueous Solution. Journal of Water Resource, Vol. 12, Issue 1, 2016, pp. 332-342.

[11] Qaiser, S., Saleemi, A. R., and Ahmad, M. M., Heavy Metal Uptake by Agro Based Waste Materials. Journal of Biotechnology, Vol. 10, Issue 3, 2007, pp. 411-419.

[12] Mahitti, U.F., Preparation and Use of Chemically Modified MCM-41 and Silica Gel as Selective Adsorbent for Hg (II) Ions. Journal of Hazardous Material, Vol. 154, 2008, pp. 578-587.

[13] Gupta, S.S. and Bhattacharyya, K.G., Immobilization of Pb (II), Cd (II) and Ni (II) Ions on Kaolinite and Montmorillonite Surfaces from Aqueous Medium. Journal of Environmental Management, Vol. 87, 2008, pp. 46-58.

[14] Salem, A., and Sene, R.A., Removal of Lead from Solution by Combination of Natural Zeolite-Kaolin-Bentonite as a New Low Cost Adsorbent. Chemical Engineering Journal, Vol. 174, 2011, pp. 619-628.

[15] Apiratikul, R., and Pavasant, P., Sorption of Cu $^{2+}$, Cd^{2+}, and Pb^{2+} Using Modified Zeolite from Coal Fly Ash. Chemical Engineering Journal, Vol. 144, Issue 2, 2008, pp. 245-258.

[16] Cui, L., Wang, Y., Gao, L., Hu, L., Yan, L., Wei, Q., and Du, B., "EDTA Functionalized Magnetic Graphene Oxide for Removal of Pb (II), Hg (II) and Cu (II) in Water Treatment : Adsorption Mechanism and Separation Property. Chemical Engineering Journal, Vol. 281, 2015, pp. 1–10.

[17] Garba, Z.N., Bello, I., Galadima, A., and Lawal, A.Y., Optimization of Adsorption Conditions using Central Composite Design for the Removal of Copper (II) and Lead (II) by Defatted Papaya Seed. Karbala International Journal of Modern Science, Vol. 2, Issue.1, 2016, pp. 20-28.

[18] Keochaiyom, B., Wan, J., Zeng, G., Huang, D., Xue, W., Hu, L., Huang, C., Zhang, C., and Cheng, M., Synthesis and Application of Magnetic Chlorapatite Nanoparticles for Zinc (II), Cadmium (II) and Lead (II) Removal from Water Solutions. Journal of Colloid and Interface Science, Vol. 505, 2017, pp. 824-835.

[19] Sani, H.A., Ahmad, M.B., Hussein, M.Z., Ibrahim, N.A., Musa, A., and Saleh, T.A., Nanocomposite of ZnO with Montmorillonite for Removal of Lead and Copper Ions from Aqueous Solutions. Process Safety and Environmental Protection, Vol. 109, 2017, pp. 97-105.

[20] Muslim, A., Aprilia, S., Suha, T.A., and Fitri, Z., Adsorption of Pb (II) Ions from Aqueous Solution Using Activated Carbon Prepared from Areca Catechu Shell: Kinetic, Isotherm and Thermodynamic Studies. Journal of the Korean Chemical Society, Vol. 61, Issue 3, 2017, pp. 89-96.

[21] Soliman, A.M., Hanan M ., Thiemann, T., Majedi, Y., Labata, F.T., and Nathir Al-rawashdeh, A.F., Removal of Pb (II) Ions from Aqueous Solutions by Sulphuric Acid-Treated Palm Tree Leaves. Journal of the Taiwan Institute of Chemical Engineers. Vol. 58, 2016, pp. 264–73.

[22] Lavanya, R., Gomathi, T., Vijayalakshmi, K., Saranya, M., Sudha, P.N., and Anil, S.,

Adsorptive Removal of Copper (II) and lead (II) using Chitosan-g-maleic Anhydride-g-Methacrylic Acid Copolymer. International Journal of Biological Macromolecules, Vol. 104, 2017, pp. 1495-1508.

[23] Luo, X., Lei, X., Xie, X., Yu, B., Cai, N., and Yu, F., Adsorptive Removal of Lead from Water by the Effective and Reusable Magnetic Cellulose Nanocomposite Beads Entrapping Activated Bentonite. Carbohydrate Polymers, Vol. 151, 2016, pp. 640-648.

[24] Zhang, T., Zhu, X., Shi, L., Li, J., Li, S., Lü, J., and Li, Y., Efficient Removal of Lead from Solution by Celery-Derived Biochars Rich in Alkaline Minerals. Bioresource Technology, Vol. 235, 2017, pp. 185-192.

[25] Morosanu, I., Teodosiu, C., Paduraru, C., Ibanescu, D., and Tofan, L., Biosorption of Lead Ions from Aqueous Effluents by Rapeseed Biomass. New Biotechnology, Vol. 39, 2017, pp. 110–124.

[26] Wanjari, A.K., and Chaudhari, U.E., Removal Of Cr (VI), Pb (II), Mn (II) And Bi (III) From Aqueous Solutions Using Granular Activated Charcoal Prepared From Cordia Macleodii Tree Bark. Rasayan Journal of Chemistry, Vol. 10, Issue 1, 2017, pp. 82-85.

[27] Utami, A.R., Sugiarti, S., and Sugita, P., Synthesis of NaP1 and Faujasite Zeolite from Natural Zeolite of Ende-NTT as Lead (Pb(II) Adsorbent. Rasayan Journal of Chemistry, Vol. 12, Issue 2, 2019, pp. 650 – 658.

[28] Yusoff, S. N., Kamari, A., Putra, W.P., Ishak, C.F., Mohamed, A., Hashim, N., and Isa, M.I., Removal of Cu (II), Pb (II) and Zn (II) Ions from Aqueous Solutions Using Selected Agricultural Wastes: Adsorption and Characterisation Studies. Journal of Environmental Protection, Vol. 5, 2014, pp. 289-300.

[29] Faisal, M., Gani, A., and Abubakar, Removal of Copper Ions from Aqueous Solution using Palm Shell Charcoal Activated by NaOH. International Journal of GEOMATE, Vol.15, Issue 48, 2018, pp.143-147.

[30] Faisal M., and Gani A. The Effectiveness of Liquid Smoke Produced from Palm Kernel Shells Pyrolysis as a Natural Preservative in Fish Ball. International Journal of GEOMATE, Vol. 15 Issue 47, 2018, pp. 145-150.

[31] Faisal, M., Gani, A.,Husni, Baihaqi, A., and Daimon, H., Pyrolysis of Oil Palm Kernel Shell into Liquid Smoke and Its Application to Control Anthracnose Disease on Chili (Capsicum annum L.). Journal of Engineering and Applied Sciences, Vol. 11, Issue 12, 2016, pp. 2583-2587.

[32] Faisal M., Chamzurni T., and Daimon H., A study on the Effectiveness of Liquid Smoke Produced from Palm Kernel Shells in Inhibiting Black Pod Disease in Cacao Fruit In Vitro. International Journal of GEOMATE, Vol. 14 Issue 43, 2018, pp. 36-41.

[33] Faisal, M., Gani, A., Husni and Daimon, H., A Preliminary Study of the Utilization of Liquid Smoke from Palm Kernel Shells for Organic Mouthwash. International Journal of GEOMATE Vol. 13, Issue 37, 2017, pp. 116-120.

[34] Pankaj K. Pandey, S.K. Sharma, S.S., and Sambi, Removal of lead(II) from Wastewater on Zeolite-NaX. Journal of Environmental Chemical Engineering, Vol. 3, Issue 4, 2015, pp. 2604–2610.

[35] Snoussi, Y., Abderrabba, M., and Sayari, A., Removal of Cadmium from Aqueous Solutions by Adsorption onto Polyethylenimine-Functionalized Mesocellular Silica Foam: Equilibrium Properties. Journal of the Taiwan Institute of Chemical Engineers, Vol. 66, 2016, pp.372-378.

6th Int. Conf. on Structure, Engineering & Environment (SEE),
Kyoto, Japan, Nov 18–20, 2020, ISBN: 978–4–909106056 C3051

EFFECT OF BIOAUGMENTATION AND PHYTOREMEDIATION ON DEGRADATION OF PARAQUAT IN CONTAMINATED SOIL

*Mullika Teerakun[1], Pensri Plangklang[2], Koson Rueangsan[3] Piyachat Wiriyaampaiwong[1] and Piyawadee Sarapirom[4]
[1]Faculty of Agricultural Technology, Kalasin University, Thailand; [2]Faculty of Technology, Khon Kaen University, Thailand; [3]Faculty of Engineering and Industrial Technology, Kalasin University, Thailand; [4]Faculty of Science and Technology, Rajabhat Mahasarakham University, Thailand

ABSTRACT

Paraquat degrading consortium was isolated from rhizosphere soil collected from the field with a history of paraquat application. Paraquat removal from soil with natural attenuation (NA), bioaugmentation (BA), and combined bioaugmentation and biostimulation (BAS) treatments were investigated in comparison to control (autoclaved soil without any treatment). The experiments were conducted with the initial paraquat concentration of 80 mg/kg soil. At day 60, paraquat removal of 44% was observed in NA treatment. Bioaugmentation with the isolated consortium (BA treatment) enhanced paraquat degradation in soil with the removal percentage of 76% while the BAS treatment increased the removal efficiency to 84%. The half-life of paraquat in soil with BA and BAS treatments were shorter than 20 days. Phytoremediation (PR) and combined bioaugmentation and phytoremediation (BAP) treatments were further investigated for bioremediation of paraquat in soil at the initial paraquat concentration of 80 mg/kg soil. The BAP treatments gave the higher paraquat degradation efficiency in comparison to the PR treatments in which the removal percentages of greater than 95% were achieved in BAP treatments with african sesbania (*Sesbania rostrata* Brem. and Oberm.), jack bean (*Canavalia ensifomis* (L.) DC.) or pinto peanut (*Arachis pintoi*).

Keywords: Pesticide, Bioremediation, Biodegradation, Rhizosphere remediation.

INTRODUCTION

Paraquat (1,1'-dimethyl-4,4'-bipyridinium) is a non-selective contact herbicide in the group of quaternary nitrogen compounds. It is a post-emergence herbicide that can disrupt the photosynthesis of the leaves when sprayed into the green plant tissue [1]. Paraquat is widely used in agricultural areas because it gives a rapid result, convenient to use, and low cost [2]. Based on the import statistics of pesticides in Thailand, paraquat is top ten rankings of imported substances. In 2019, paraquat was imported in second place with a high amount of 22,162,440.58 kg [3]. The increasing of paraquat usage causes dispersion and accumulation into the environment, which have both direct and indirect effects on living and human life. Paraquat is high water-soluble and high organic matter affinity, it can be easily spread and readily adsorbed to the organic matter in the environment. Since there have been reported that paraquat is extremely biologically active and toxic to plants and animals and very ecotoxic to the aquatic environment [4], the remediation of paraquat from contaminated environment is needed.

Bioremediation is a pollutant elimination technique using activities of living organisms such as microorganisms or plants. This technique has been used for the treatment of environmental contaminants with the advantages, compared to chemical and physical methods, of cost-effective, easy to maintain, and highly effective with low contaminant concentrations [5]. Bioaugmentation is one of bioremediation techniques that application of microorganisms to improve the biodegradative capacities of contaminated sites to accelerate the removal of undesired compounds [6]. This technique is adding indigenous or exogenous or genetically modified microorganisms that capable to degrade pollutants on contaminated media to enhance the rate of contaminant biodegradation in the affected soil or water because of the density of contaminant-specific degraders might have been artificially increased [7]. It is the most advantageous method for cleaning-up soil contaminated with pesticides [8]. The bioaugmentation found that significantly enhanced the degradation of pesticide compared with uninoculated soil, and the shortest half-life of pesticide was detected in the bioaugmentation treatment of soil [9-10]. One of bioremediation strategies is phytoremediation which using plants to removed, immobilized, or degraded contaminants from the environment [11]. It is an in situ, cost-effective, easy to adopt, eco-friendly approach for environmental remediation and has entered inactive developmental phase [12]. Some pesticides which

have been cleaned up by plants are DDT [13] and simazine [14]. Yoshitomi and Shann [15] reported that the increase in pyrene mineralization was obtained from the addition of corn root exudates. Several researches considered the rhizosphere as a treatment zone for contaminant degradation plants [16-18]. This research was therefore interested to combine the biological treatment method for paraquat removal. After the research completed, the effective method for treating paraquat in soil will be found and can be a guideline for the treatment of contaminated pollutants in the environment, especially the treatment of soil contamination with pesticides by biological methods. Moreover, the research team aims to make treatment process for degradation of environmental pollutants quickly and effectively.

MATERIALS AND METHODS

Soil Sampling

Soil samples were collected from the field with a history of paraquat application. The soil sample was collected at the depth of 0-15 cm from the surface level and sifted through a sieve of 2 mm to remove wood, stone, and grass. It was dried at room temperature until the moisture content was less than 10% and kept at 4°C until the usage to maintain the activity of microorganisms. The characteristics and compositions of the soil i.e., soil texture, organic matter content, and soil pH were analyzed. In the control treatment, the soil sample was sterilized by autoclave at 121°C 15 lb/in^2 for 15 minutes. The autoclave procedure was repeated three times with a 24-hour incubation period at room temperature in between [19].

Isolation of Paraquat Degrading Bacterial Consortium Microbial Community Analysis

Bacterial consortiums were isolated from rhizosphere soil which collected from the field with a history of using paraquat. The enrichment technique was applied to increase amount of bacterial consortiums. Ten-gram of rhizosphere soil was infused in mineral salt medium [20] supplemented with paraquat as nitrogen source. The sample was cultured in 250 mL Erlenmeyer flask at 30°C and 150 rpm. Sub-culturing was conducted every 7 days to obtain the bacterial consortium capable of paraquat degradation. The paraquat degradation efficiency was examined at the end of incubation for each sub-culture (7 days). The sub-culture was repeated until the paraquat degradation efficiency was higher than 50%. The obtained bacterial consortiums were then used in further experiments. The microbial community in the bacterial consortium was examined by Polymerase Chain Reaction Denaturing Gradient Gel Electrophoresis (PCR-DGGE) technique.

Bioremediation of Paraquat in Soil

Bioremediation of paraquat in soil with natural attenuation (NA), bioaugmentation (BA), combined bioaugmentation and biostimulation (BAS) were investigated in soil microcosms. Fifty grams of soil were placed in 240 mL glass bottles and mixed with paraquat at initial concentration of 80 mg/kg soil. The moisture content of the soil was adjusting to about 20% by sterile distilled water. In the BA and BAS treatment, the isolated bacterial consortium was added to the soil at the concentration of 100 g/kg soil. In the BAS treatment, glucose and KH_2PO_4, as biostimulant, were added to the soil in ratio 100:10:1 (C:N:P). The components in the glass bottle were mixed and the bottles were covered by the prior incubation at room temperature without light. The moisture content of the soil was examined every 3 days by comparing the bottle weight at day 0 and adjusted to 20% when the moisture content was lower than 10% by the addition of sterile distilled water. Soil samples were sacrificed at day 0, 3, 7, 14, 21, 28, 35, and 60 to extract the remaining paraquat in the soil using solid-liquid extraction method and analyze the concentration of paraquat by UV Spectrophotometer.

Phytoremediation of paraquat in soil was further investigated using five plants i.e., sunflowers (*Helianthus annuus*), marigold (*Tagetes erecta* L.), pinto peanut (*Arachis pintoi* Krapov. & W.C. Greg.), jack bean (*Canavalia ensifomis* (L.) DC.) and african sesbania (*Sesbania rostrata* Brem and Oberm.). These plants are rapid growth, easy to grow, and easy to maintain with a short life cycle. Besides, the combined bioaugmentation and phytoremediation treatments (BAP) was also investigated for the paraquat removal from soil. The seeds of 5 plant types were soaked in distilled water for 3 hours and then cultivate in soil in a seeding tray. It was nursed at room temperature for 10 days under natural light and daily watering to maintain constant soil moisture. The BAP experiment was assigned to 12 treatments and 3 replicates by Completely Randomized Design (CRD). In the phytoremediation treatment (PR), two kg of soil mixed with 80 mg/kg of paraquat was added into 8-inch diameter pot before planting with each of plant saplings. For the BAP treatments, the bacterial consortium was added to the soil at the concentration of 100 g/kg soil before planting. The pots were daily watering to control soil moisture at about 60% [21]. Then the samples were sacrificed on day 0, 5, 10, 15, 25, 35, and 45 to extract the remaining paraquat in the soil using solid-liquid extraction method and analyze the concentration of paraquat by UV spectrophotometer. Natural attenuation of autoclaved soil mixed with 80 mg/kg of paraquat was conducted as control.

Extraction and Analysis of Paraquat

The extraction of paraquat from soil samples was conducted with the modified method from Wong et al. [22]. Fifty-gram dry weight of soil and 100 mL methanol were put into 300 mL cover glass bottle for extraction at 150 rpm on the horizontal shaker for 4 hours. The extraction procedure was repeated 3 times. The extracted solution was collected, pooled together, and filtered through Whatman No. 42 filter paper. The extracted solution was subjected to methanol evaporation in a hot air oven at 80ºC for 24 h. The dried extract was dissolved with 1.0 mL deionized water and mixed with 3 mL of DI water and 1 mL of 1% $Na_2S_2O_4$ in 0.1 M NaOH solution. The supernatant was then analyzed for the concentration of paraquat using UV Spectrophotometer UV-1800 SHIMADZU (Japan) at the absorbance of 600 nm [23]. Paraquat concentration was calculated to compare with standard curve of paraquat concentration. The efficiency of paraquat extraction method was not less than 90%.

Statistical Analysis

The data were statistically analyzed by the variance analysis (ANOVA) with Duncan's New Multiple Range Test (DMRT). The SPSS 10.0 program was used for statistical analysis. $P<0.05$ was measured as statistically significant.

RESULTS AND DISCUSSION

Soil Properties

The physical properties of soil samples were determined and tabulated in Table 1. The result indicated that soil texture is loamy sand and color of soil is brown. The soil pH is 8.1 and the low organic matter content of 0.82% was observed in the soil.

Table 1 Properties of soil using in experiments**.**

Soil physicochemical properties	Values
Organic matter content (%)	0.82
Soil texture	Loamy sand
sand (%)	80.91
silt (%)	12.91
clay (%)	6.19
pH	8.10

Isolation and Identification of Paraquat Degrading Bacterial Consortium

The community structure of a bacterial consortium capable of degrading paraquat was analyzed by PCR-DGGE. The isolated consortium was exhibited a greater than 92% identity to the sequences deposited in the databases which were closet matched to 6 genera i.e., *Sphingomicrobium marinum* (97%), *Ferrovibrio xuzhouensis* (93%), *Azospirillum lipoferum* (93%), *Altererythrobacter xinjiangensis* (94%) *Xanthobacter autotrophicus* (92%) and *Azospirillum amazonense* (99%). In accordance with report of the researchers are found that microorganism i.e. *Sphingomicrobium* sp. [24], *F. xuzhouensis* [25], *A. lipoferum* [26], *X. autotrophicus* [27] capable of degrading recalcitrant natural, anthropogenic compounds, and different herbicides and pesticides.

Effect of Bioaugmentation on Paraquat Degradation in Soil

This research studied the addition of bacterial consortium on the efficiency of degradation of paraquat in soil. Fig. 1 shows the breakthrough curve of C/C_0 versus time and Table 2 shows the paraquat removal efficiency with various bioremediation techniques. Paraquat removal in the control (with autoclaved soil) was only 9%, while in the NA treatment was 44%. Results indicated that the indigenous microorganism has capability to degrade paraquat which can be the result of microbial adaptation to paraquat application in the field. BA treatment and BAS treatment resulted in a rapid decrease of the concentration of paraquat in soil. BAS was the most efficient treatment giving 84% of paraquat removal at day 60 of the experiment followed by BA treatment (paraquat removal 76%) and NA treatment (paraquat removal 44%), respectively (Table 2). The half-life of the paraquat in treatments BA and BAS were shorter than 20 days. This study indicated that the addition of bacterial consortium resulted in better efficiency of paraquat degradation. In addition, the efficiency of paraquat degradation increases with the addition of nutrients together with the addition of bacteria. These results agreed with the study of Dams et al. [28] who found that the bioaugmentation of *Sphingomonas chlorophenolica* ATCC 39723 into pentachlorophenol (PCP) contaminated soil accelerated the complete decomposition of contaminants. Elväng et al. [29] reported that complete degradation of 4-chlorophenol (4CP) contaminated soils occurred when *Arthrobacter chlorophenolicus* A6 was added. In addition, the maximum chlorobenzene removal from soil of 80% could be achieved with the addition of *Burkholderia* sp. strain PS14 [30].

Effect of Bioaugmentation and Phytoremediation on Degradation of Paraquat in Contaminated Soil

The efficiencies of paraquat removal from soil with PR and BAP treatments were investigated in his study. Percentage of paraquat removal was only 46% in the control treatment (soil without planting and without isolated consortium) while 51.43% of paraquat removal was observed in the treatment with the addition of isolated consortium.

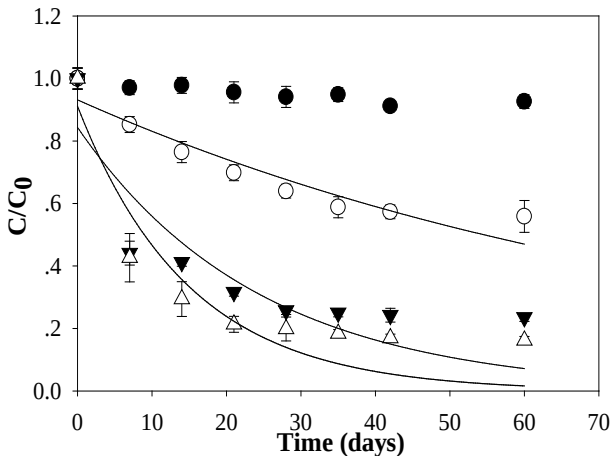

Fig. 1 The breakthrough curve for varying bioremediation method at NA: natural attenuation (○), BA: bioaugmentation (▼), BAS: combined bioaugmentation and biostimulation (△), control: autoclaved soil without any treatment (●) and initial paraquat concentration of 80 mg/kg.

Among the plants used for bioremediation treatments, african sesbania, jack bean, and pinto peanut possessed the high efficiency of paraquat remediation from with the removal percentages (in PR treatments) of greater than 64%.

BAP treatments gave higher paraquat degradation efficiency with the removal percentages of greater than 75% as compared to the PR treatments (removal percentages in the range of 64-89%). The BAP treatment with african sesbania showed the highest paraquat removal of 97.14%, followed by BAP treatment with jack bean (96.43%) and BAP treatment with pinto peanut (95.71%). The higher percentages obtained from BAP treatment with african sesbania, jack bean, and pinto peanut as compared to BA treatments indicated the improvement of paraquat degradation in soil by these three plants. Root exudate substances from these plants might support the growth and paraquat degradation activity of the augmented consortium as well as the indigenous microorganisms hence enhancing the paraquat degradation efficiency [31]. The root exudate, such as amino acids, sugars, and phenols can induce microorganisms to produce non-specific enzymes that can degrade contaminants into less toxic compounds [12]. These affected root surface properties or rhizosphere soil properties and increased contaminant availability through adsorption, and improved physical structure of the soil allowing more rapid and deeper penetration of water, nutrients, and microbes [12, 32].

Table 2 Effect of biological treatment process on the efficiency of paraquat degradation in contaminated soil.

Treatment	k (day^{-1})	$t_{1/2}$ (days)	r^2	paraquat removal at day 60 (%)*
Natural attenuation (NA)	0.011	63.0	0.89	44.12±5.09c
Bioaugmentation (BA)	0.042	16.5	0.86	76.47±1.27b
Combined bioaugmentation and biostimulation (BAS)	0.067	10.3	0.86	83.82±1.27a
Control	0.001	495	0.80	8.82±2.21d

*Different letters indicate significantly different results obtained by Duncan test ($p < 0.05$). k is the degradation rate constant, $t_{1/2}$ is half-life of paraquat.

Table 3 The effect of Combined bioaugmentation and phytoremediation by various plants on the degradation of paraquat in contaminated soil at day 45 of experiment.

Treatment	k (day^{-1})	$t_{1/2}$ (days)	r^2	paraquat removal at day 45 (%)*
Control (soil without plant and microbial consortium)	0.0153	45.29	0.99	46.43±2.47a
Soil with microbial consortium	0.0172	40.29	0.98	51.43±1.24b
Phytoremediation (PR)				
Sunflower	0.0284	24.40	0.98	72.14±3.71d
Marigold	0.0219	31.64	0.99	64.29±1.24c
pinto peanut	0.0366	18.93	0.97	82.86±2.14e
Jack bean	0.0401	17.28	0.96	88.57±1.24f
African sesbania	0.0405	17.11	0.96	89.29±2.14f
Combined bioaugmentation and phytoremediation (BAP)				
Sunflower with microbial consortium	0.0376	18.43	0.94	83.57±1.24e
Marigold with microbial consortium	0.0296	23.41	0.99	75.00±3.27d
pinto peanut with microbial consortium	0.0476	14.56	0.95	95.71±2.14g
Jack bean with microbial consortium	0.0480	14.44	0.94	96.43±2.47g
African sesbania with microbial consortium	0.0465	14.90	0.95	97.14±1.24g

*Different letters indicate significantly different results obtained by Duncan test ($p < 0.05$). k is the degradation rate constant, t1/2 is half-life of paraquat.

CONCLUSIONS

The efficiency of degradation of paraquat in soil by bioremediation technique found that BAS treatment was high efficiency in paraquat degradation (84%) in 60 days. The half-life for paraquat in soil from treatment BA and BAS were less than 20 days. The bioremediation efficiency of paraquat in contaminated soil showed that BAP could degrade paraquat up to 75%. BAP treatments with african sesbania, showed the highest paraquat degradation efficiency which was 97.14%, followed by using jack bean and pinto peanut which were 96.43 and 95.71, respectively. All the experimental groups including using phytoremediation with isolated bacteria consortium and the control group were significantly different ($p<0.05$). Using isolated bacteria consortium with phytoremediation showed higher paraquat degradation efficiency than that of phytoremediation as seen in the paraquat degradation percentage.

ACKNOWLEDGMENTS

The authors gratefully acknowledge the financial support provided by Kalasin University. The authors are grateful to the Research Group for Development of Microbial Hydrogen Production Process from Biomass, Khon Kaen University, and Department of Biotechnology, Kalasin University for providing the necessary laboratory facilities.

REFERENCES

[1] Dinis-Oliveira R.J., Remião F., Carmo H., Duarte J.A., Navarro A.S., Bastos M.L. and Carvalho F., Paraquat exposure as an etiological factor of Parkinson's disease, Neurotoxicology, Vol. 27, Issue 6, 2006, pp. 1110-1122.

[2] Maksymiv I., Pesticides: benefits and hazards, Journal of Vasyl Stefanyk Precarpathian National University, Vol. 2, Issue 1, 2015, pp. 70-76.

[3] The Office of Agriculture Regulation, Summary report of the top 10 hazardous substances imported in the year 2018, The Office of Agriculture Regulation, Department of Agriculture, Ministry of Agriculture and Cooperatives, 2018. http://www.doa.go.th/ard/?page_id=386 [accessed on June 13, 2019]

[4] Watts M., Paraquat, Pesticide Action Network Asia and the Pacific (PAN AP), 2011. http://wssroc.agron.ntu.edu.tw/note/Paraquat.pdf [accessed on June 19, 2019]

[5] Azubuike C.C., Chikere C.B., Okpokwasili G.C., Bioremediation techniques–classification based on site of application: principles, advantages, limitations and prospects, World Journal of Microbiology and Biotechnology, Vol. 32, Issue 180, 2016, pp. 1-18.

[6] Goswami M., Chakraborty P., Mukherjee K., Mitra G., Bhattacharyya P., Dey S. and Tribedi P., Bioaugmentation and biostimulation: a potential strategy for environmental remediation, Journal of Microbiology and Experimentation, Vol. 6, Issue 5, 2018, pp. 223–231.

[7] Nzila A., Razzak S.A. and Zhu J., Bioaugmentation: an emerging strategy of industrial wastewater treatment for reuse and discharge, International Journal of Environmental Research and Public Health, Vol. 13, Issue 846, 2016, pp. 1-20.

[8] Cycon M., Mrozik A. and Piotrowska-Segete Z., Bioaugmentation as a strategy for the remediation of pesticide-polluted soil: A review, Chemosphere, Vol. 172, 2017, pp. 52-71.

[9] Önneby K., Bioaugmentation for reduction of diffuse pesticide contamination. PhD thesis, Department of Microbiology, Swedish University of Agricultural Sciences, Sweden, 2013.

[10] Pimmata P., Reungsanga A. and Plangklang P., Comparative bioremediation of carbofuran contaminated soil by natural attenuation, bioaugmentation and biostimulation, International Biodeterioration and Biodegradation, Vol. 85, 2013, pp. 196-204.

[11] Etim E.E., Phytoremediation and its mechanisms: a review, International Journal of Environment and Bioenergy, Vol. 2, Issue 3, 2012, pp. 120-136.

[12] Cheema S.A., Khan M.I., Shen C., Tang X., Farooq M., Chen L., Zhang C. and Chen Y., Degradation of phenanthrene and pyrene in spiked soils by single and combined plants cultivation, Journal of Hazardous Materials, Vol. 177, 2010, pp. 384–389.

[13] Gao J., Garrison W., Hoehamer C.F. and Mazur C.S., Uptake and phytotransformation of o,p'-DDT and p,p'-DDT by axenically cultivated aquatic plants, Journal of Agricultural and Food Chemistry, Vol. 48, Issue 12, 2001, pp. 6121-6127, 2001.

[14] Wilson T.D., Lindsey S. and Schooler T.Y., A model of dual attitudes, Psychological Review, Vol. 107, Issue 1, 2000, pp. 101-126.

[15] Yoshitomi K.J. and Shann J., Corn (*Zea mays* L.) root exudates and their impact on 14C-pyrene mineralization, Soil Biology and Biochemistry, Vol. 33, Issue 12, 2001, pp. 1769-1776.

[16] Yang C., Wang Y. and Li J., Plant species

mediate rhizosphere microbial activity and biodegradation dynamics in a riparian soil treated with bensulfuron-methyl, Clean Soil Air Water, Vol. 39, Issue 4, 2011, pp. 338-344.

[17] Correa-Garcıa S., Pande P., Seguin A., St-Arnaud M. and Yergeau E., Rhizoremediation of petroleum hydrocarbons: a model system for plant microbiome manipulation, Microbial Biotechnology, Vol. 11, 2018, pp. 819–832.

[18] Hawrot-Paw M., Ratomski P., Mikiciuk M., Staniewski J., Koniuszy A., Ptak P. and Golimowski W., Pea cultivar Blauwschokker for the phytostimulation of biodiesel degradation in agricultural soil, Environmental Science and Pollution Research, Vol. 26, 2019, pp. 34594–34602.

[19] Zamani J., Hajabbasi M.A. and Alaie E., The effect of steam sterilization of a petroleum contaminated soil on PAH concentration and maize (*Zea mays* L.) growth, International Journal of Current Microbiology and Applied Sciences, Vol. 4, Issue 8, 2015, pp. 93-104.

[20] Ansari S.M., Dehghani M. and Samaei M.R., Isolation of atrazine degrading bacteria in semi-salinity medium, Journal of Health Sciences and Surveillance System, Vol. 4, Issue 3, 2016, pp. 121-128.

[21] Gadissa M., Woldemichael A. and Yimer F., Optimal soil moisture depletion levels for the production of *Vernonia* (*Vernonia galamensis* L.) and it's effect on growth, yield and yield components, Irrigation & Drainage Systems Engineering, Vol. 6, Issue 3, 2017, pp. 1-7.

[22] Wong Y.C., Norsyamimi N. and Wan-Nurdiyana W.A., Determination of paraquat (herbicide) residue level in sandy clay loam soil using high performance liquid chromatography, Journal of Basic and Applied Sciences, Vol. 9, 2013, pp. 566-577.

[23] Lima T.L., Nicoletti M.A., Munhoz C., De Abreu G.R., Magalhães J.Z., Ricci E.L., Waziry P.A.F., Alves da Costa J.N., Antônio A.C.N. and Fukushima A.R., Determination of paraquat in several commercially available types of rice, Food and Nutrition Sciences, Vol. 09, No.12, 2018, pp. 1368-1375.

[24] Stolz A., Molecular characteristics of xenobiotic-degrading Sphingomonads, Applied and Environmental Microbiology, Vol. 81, Issue 5, 2009, pp. 793-811.

[25] Song M., Zhang L., Sun B., Zhang H., Ding H., Li Q., Guo S. and Huang X., *Ferrovibrio xuzhouensis* sp. nov., a cyhalothrin-degrading bacterium isolated from cyhalothrin contaminated wastewater, Antonie van Leeuwenhoek, Vol. 108, Issue 2, 2015, pp. 377–382.

[26] Romeh A.A. and Hendawi M.Y., Bioremediation of certain organophosphorus pesticides by two biofertilizers, *Paenibacillus* (*Bacillus*) *polymyxa* (Prazmowski) and *Azospirillum lipoferum* (Beijerinck), Journal of Agricultural Science and Technology, Vol. 16, 2014, pp. 265-276.

[27] Sharma A., Bhatt P., Khati P. and Gangola S., Microbial degradation of pesticides for environmental cleanup, Bioremediation of Industrial Pollutants, Bharagava R.N. and Saxena G., Ed. Write & Print Publications, 2016, pp. 178-205.

[28] Dams R.I., Paton G. and Killham K., Bioaugmentation of PCP in two different soils by *Sphingomonas chlorophenolica* ATCC 39723, Pesticidas: Revista de Ecotoxicologia e Meio Ambiente, Vol. 16, 2006, pp. 111-124.

[29] Elväng A.M., Westerberg K., Jernberg C. and Jansson J.K., Use of green fluorescent protein and luciferase biomarkers to monitor survival and activity of *Arthrobacter chlorophenolicus* A6 cells during degradation of 4-chlorophenol in soil, Environmental Microbiology, Vol. 3, Issue 1, 2001, pp. 32-42.

[30] Rapp P. and Timmis K., Degradation of chlorobenzenes at nanomolar concentrations by *Burkholderia* sp. strain PS14 in liquid cultures and in soil, Applied and Environmental Microbiology, Vol. 65, Issue 6, 1999, pp. 2547-2552.

[31] Alvarez A., Yañez L.M., Benimeli C.S. and Amoroso M.J., Maize plants (*Zea mays*) root exudates enhance lindane removal by native Streptomyces strains, International Biodeterioration and Biodegradation, Vol. 66, 2012, pp. 14–18.

[32] Xu S.Y., Chen Y.X., Wu W.X., Wang K.X., Lin Q. and Liang X.Q., Enhanced dissipation of phenanthrene and pyrene in spiked soil by combined plants cultivation, Science of the Total Environment, Vol. 363, Issue 1-3, 2006, pp. 206-215.

6th Int. Conf. on Structure, Engineering & Environment (SEE), Kyoto, Japan, Nov.18-20, 2020, ISBN: 978-4-909106056 C3051

CHARACTERISTIC OF LIQUID SMOKE PRODUCED FROM SLOW PYROLYSIS OF CACAO POD SHELLS (*THEOBROMA CACAO L)*

Hera Desvita[1], Muhammad. Faisal[2], Mahidin[2], and Suhendrayatna[2]
[1]Doctoral Program, School of Engineering, Universitas Syiah Kuala, Indonesia
[2]Department of Chemical Engineering, Universitas Syiah Kuala, Indonesia

ABSTRACT

This study evaluated the characteristics of liquid smoke produced from cacao pod shells (*Theobroma cacao L)* through the slow pyrolysis process at various temperatures of 300, 340, 380 and 400 °C. Prior to chemical analyses, the liquid smoke was purified by distillation at 190 °C to remove tar and remaining carbon and some benzene compounds. The compounds contained in liquid smoke were then analysed using various analytical techniques. The results showed that temperature plays a significant role in the composition of liquid smoke. Results of Gas Chromatography Mass Spectrometry (GC-MS) analysis showed that the number of chemical compounds produced at pyrolysis temperatures of 300, 340, 380 and 400 °C were 9, 14, 10 and 18 compounds, respectively. Pyrolysis temperatures did not have significant effects on the pH (3-4) value of produced liquid smoke. Phenolic compounds, furan and ketone have been found to be the main components in liquid smoke. The highest amount of phenol (763.76 mg GAE) was found at 400°C.

Keywords: Cacao pod shells, Liquid smoke, Pyrolysis, Phenol

INTRODUCTION

Indonesia is a country with abundant natural resources across its provinces. Its tropical weather is ideal for growing cacao trees, especially in Aceh Province, where cacao is a main plantation product. Data from the Ministry of Agriculture showed that Aceh produced 42,180 tons of cacao in 2019 [1], and this large amount naturally leads to waste and environmental issues. Cacao beans are usually dried before being processed into food products such as chocolate powder, while the shells are discarded without any prior processing. The cacao shell biomass contains lignin (51.98%), cellulose (20.15%), hemicellulose (21.06%) and pectin (6%) [2],[3]. This high content of lignin, cellulose and hemicelluloses has the potential to be used as raw materials to produce liquid smoke.

In the past few years, liquid smoke has been developed from various biomass waste, such as oil palm shells [4]-[8], durian peel waste [9],[10], oil palm empty fruit bunches [11] and sawdust [12]. The resulting liquid smoke is used as a preservative in wood and food products. In general, hard-textured wood containing 50% cellulose, 25% hemicelluloses and 25% lignin [13] is used as liquid smoke material through a process called pyrolysis. Pyrolysis of wood or other biomass produces charcoal, tar and liquid smoke. The latter is essentially the smoke resulting from the decomposition of various compounds within the biomass, which is then condensated into liquid, hence the term liquid smoke.

Previous research stated that the degradation of biomass compounds, such as lignin, cellulose and hemicellulose, occurs at a temperature of 300-400°C, 260-350°C and 180-300°C, respectively [14]. Each temperature plays an important role in determining the liquid smoke content. Pyrolysis at a high temperature (above 400° C) will form toxic carcinogenic compounds such as PAH [15]. Hemicellulose degradation forms a number of carbonyl and acetic acid compounds as well as producing colours, while lignin degradation produces phenolic compounds that act as bacterial and flavouring agents [16,17]. There are several available studies about the content of liquid smoke produced by various types of biomass, such as oil palm fruit bunches [11], oil palm shells [4-8] and durian shells [9,10]. However, there is little literature about the characterization of liquid smoke from cacao pod shells. The objective of this research was to identify the components of liquid smoke produced from cacao pod shells at various pyrolysis temperatures.

METHODOLOGY

Three kilograms of cacao shells were fed into a stainless-steel pyrolysis reactor (60cm height, 40cm diameter and 5kg capacity) and processed at 300°C, 340°C, 380°C, and 400°C. The complete pyrolysis method has been identified in previous research [11]. The temperature and volume changes during pyrolysis were observed every five minutes. The crude liquid smoke was then distilled at 190°C to purify it from tar. A GC-MS (Gas

Chromatography-Mass Spectrometry) was used to analyse the compounds, while a spectrophotometer (Agilent Cary 60 UV-VIS) was used to analyse the phenol concentration.

RESULTS AND DISCUSSION

Pyrolysis Evaluation

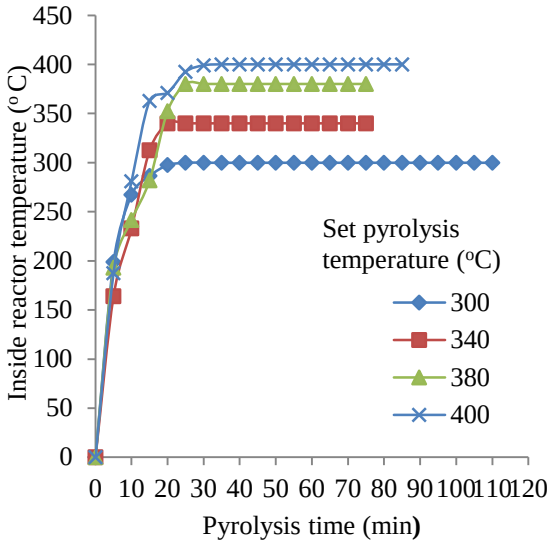

Fig 1. Correlation between pyrolysis time and the changes of inside temperature at various set pyrolysis temperatures.

The time required to reach the constant pyrolysis temperature was different for each set of temperatures, as can be seen in Figure 1, which shows that the pyrolysis temperature increases gradually. This results in the degradation of compounds within the cacao pod shells, such as hemicelluloses, cellulose and lignin. In our research, the temperature increased significantly to 277ºC within 10 minutes and continued to slowly rise until it reached the designated constant value. Our results are similar to those of Rahmat et al. [18], in which the temperature increased to 350ºC in 10 minutes. The constant pyrolysis temperatures of 300ºC, 340ºC, and 380ºC (same length of time) and 400ºC were achieved in 15, 20 and 35 minutes, respectively. In comparison, sawdust pyrolysis achieves the constant temperature of 450ºC in 25 minutes [18]; meanwhile, at >100ºC, the water content evaporates in 10 minutes, leading to an increase in liquid smoke volume. According to Ravendran et al. [19], raw material compound degradation was divided into five zones, namely (i) zone I at >100º C, where water content changes; (ii) zone II at 200-250°C, where compounds start to degrade; (iii) zone III at 250-350°C, where hemicellulose starts to decompose; (iv) zone IV at 350-500°C, where lignin and cellulose starts to degrade; and (v) zone V at <500º C, where lignin is degraded.

Liquid Smoke Production

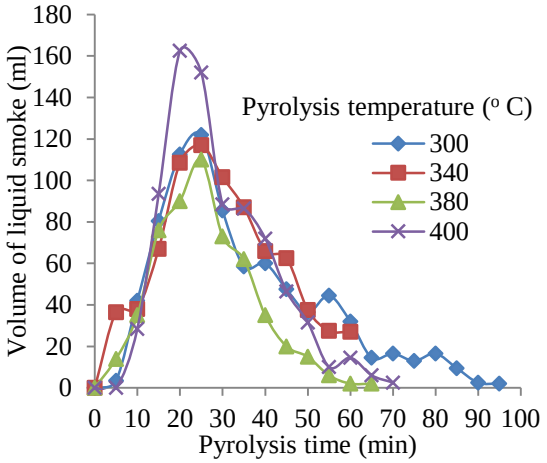

Fig 2. The correlation between pyrolysis time and liquid smoke volume resulted at various pyrolysis temperatures.

Figure 2 shows that maximum liquid smoke volume (162ml) was produced at 400ºC in 20 minutes. The resulting volume decreases during pyrolysis until it stops at 110 minutes (0ml) because all the cellulose, hemicellulose and lignin have decomposed completely. It also shows that the pyrolysis temperature influences the liquid smoke volume produced. The volumes resulting from 300ºC, 340ºC, 380ºC to 400ºC were quite similar at 801ml, 799ml, 795ml and 797ml, respectively. These numbers reflect those resulting from the work of Cao et al. [20], which used slow pyrolysis at 350ºC and 400ºC using corn cobs. In addition, Rahmat et al. [18] stated that the maximum liquid smoke volume resulting from sawdust at 450ºC in 10 minutes was 139ml, stopping at 90 minutes.

The pyrolysis duration of 20-30 minutes results in the maximum amount of liquid smoke volume before it starts decreasing, likely due to the decomposition of compounds contained within the cocoa shell. The degradation of organic compounds in the raw material is caused by the increase in the pyrolysis temperature [21]. The increase of temperature degraded cellulose, hemicellulose and lignin, which were then condensated into liquid smoke. According to Triastuti et al. [22], the liquid smoke volume results depend on the cooling system used, such as water, which accommodates the heat transfer. High temperature pyrolysis can cause a decrease in the resulting volume of liquid smoke because it leads to increased water temperature, causing the smoke to fail to condensate in completion.

The times required for pyrolysis at 300ºC, 340ºC, 380ºC and 400ºC were 100, 75, 75 and 85 minutes, respectively. The reason these durations were similar was likely due to the small differences in temperatures. A longer pyrolysis process results in less liquid smoke volume. According to Yokoyoma et al. [23], cellulose decomposes at 240-340ºC, hemicellulose at 200-260ºC and lignin at 280-500ºC.

Total Amount of Phenol

Phenol plays an important role in providing aroma and flavour as well as an antimicrobial agent. Phenol results from the thermal degradation of lignin and cellulose by aliphatic compounds [24]. Table 1 shows the spectrophotometer analysis of phenol produced from different pyrolysis temperatures.

Table 1. The content of Phenol

No.	Pyrolysis temperature (ºC)	Concentration (mg GAE)
1	300	242.96
2	340	192.51
3	380	363.68
4	400	763.76

Table 1 shows that the highest phenol concentration occurs at 763.76mg GAE (Gallic Acid Equivalent) at 400ºC pyrolysis temperature. A temperature of 340ºC results in a lower phenol concentration than that at 300ºC, while a temperature of 380ºC sees an increase in phenol concentration. This was likely due to lignin decomposition at 300-450ºC. A temperature of 400ºC (near the maximum temperature for lignin degradation) results in even higher phenol concentration. The research showed that liquid smoke resulting from the pyrolysis of oil palm fruit bunches at 420ºC contains 1.71% phenol [11]. The amount and quality of the resulting phenol depends on the amount of lignin content in the raw material as well as on the pyrolysis temperature [25].

GC-MS Analysis

Temperature plays an important role in the liquid smoke composition, and GC-MS analysis was carried out to determine its composition at different temperatures. The GC-MS test results can be found in Table 2-Table 5.

Table 2. GC-MS test on liquid smoke resulted from pyrolysis at 300 ºC.

No	Component	Area (%)
1.	2-furanmethanol , 2-furanmethanol ,3-furanmethanol	4.73
2.	Butyrolactone , Butanoic acid, 4-hydroxy, Butanoic acid, 4-hydroxy	16.54
3.	Heptane, 4-methyl- 2-Nonene, 3-methyl-, ®- 1-Butanol, 3-methyl-, carbonate	2.39
4.	Phenol	45.49
5.	2-Cyclopenten-1-one, 2,3-dimethyl- 2-Cyclopenten-1-one, 2,3-dimethyl- Cyclooctene	3.59
6.	Phenol, 2-methyl-p-Cresol, Phenol, 3-methyl-	4.87
7.	Phenol, 3-methyl, Phenol, 3-methyl p-Cresol	9.31
8.	Phenol, 2-methoxy-Phenol, 2-methoxy-Phenol, 2-methoxy	8.52
9.	Methenamine	4.55

Table 3. GC-MS test on liquid smoke resulted from pyrolysis at 340 ºC.

No	Component	Area (%)
1.	2-furanmethanol , 2- furanmethanol,3-furanmethanol	17.03
2.	Butyrolactone , Butanoic acid, 4-hydroxy, Butanoic acid, 4-hydroxy	5.47
3.	Phenol	29.78
4.	2-Cyclopenten-1-one, 2,3-dimethyl- 2-Cyclopenten-1-one, 2,3-dimethyl- Cyclooctene	4.80
5.	Phenol, 2-methyl-p-Cresol, Phenol, 3-methyl-	4.10
6.	Phenol, 3-methyl, Phenol, 3-methyl p-Cresol	8.02
8.	Phenol, 2-methoxy-Phenol, 2-methoxy-Phenol, 2-methoxy	14.06
9.	Methenamine	3.03
10.	2-Aminopyridine, Pyrazine, methyl- Cyclopropane, (3-chloropropyl)methylene	1.56
11.	2-Cyclopenten-1-one, 2-methyl-1-Pentyne, 2-Cyclopenten-1-one, 2-methyl-	4.25
12.	1-Butanol, 3-methyl-, carbonate, Propanoic acid, 2-methyl-, 3-methylbutyl ester, Diisoamyl ether	1.27

No	Component	Area (%)
13.	Phenol, 4-ethyl-Phenol, 3-ethyl-Phenol, 4-ethyl-	2.81
14.	1-Propanol, 2-amino- 1-Octadecanamine, N-methyl-2-Amino-1-propanol	1.44

Table 4. GC-MS test on liquid smoke resulted from pyrolysis at 380 ^{o}C

No	Component	Area (%)
1.	2-furanmethanol , 2-furanmethanol ,3-furanmethanol	13.42
2.	Butyrolactone , Butanoic acid, 4-hydroxy, Butanoic acid, 4-hydroxy	7.48
3.	Phenol	33.60
4.	2-Cyclopenten-1-one, 2,3-dimethyl- 2-Cyclopenten-1-one, 2,3-dimethyl- Cyclooctene	5.67
5.	Phenol, 2-methyl-p-Cresol, Phenol, 3-methyl-	7.15
6.	Phenol, 3-methyl, Phenol, 3-methyl p-Cresol	9.24
7.	Phenol, 2-methoxy-Phenol, 2-methoxy-Phenol, 2-methoxy	13.08
8.	Methenamine	3.52
9.	Phenol, 4-ethyl-Phenol, 3-ethyl-Phenol, 4-ethyl-	2.93
10.	2(1H)-Pyridinone 4-Methylcoumarine-6-(2-furylcarbon yl)oxy 2-Furancarboxylic acid, anhydride	3.73
11.	Phenol, 2-methyl-p-cresol-p-cresol	7.15

Table 5. GC-MS test on liquid smoke resulted from pyrolysis at 400 ^{o}C

No	Component	Area (%)
1.	2-furanmethanol , 2-furanmethanol ,3-furanmethanol	4.52
2.	Butyrolactone , Butanoic acid, 4-hydroxy, Butanoic acid, 4-hydroxy	5.98
3.	Phenol	49.87
4.	Phenol, 2-methyl-p-Cresol, Phenol, 3-methyl-	4.99
5.	Phenol, 3-methyl, Phenol, 3-methyl p-Cresol	5.81
6.	Phenol, 2-methoxy-Phenol, 2-methoxy-Phenol, 2-methoxy	6.56
7.	Methenamine	1.29
8.	2-Cyclopenten-1-one, 2-methyl- 1-Pentyne, 2-Cyclopenten-1-one, 2-methyl-	2.23
9.	2-Cyclopenten-1-one, 3,4-Pentadienal Cyclobutene	5.23
10.	2-Propanone, 1-(acetyloxy)- 2-Propanone, 1-(acetyloxy)- 2-Methyl-3-oxobutyronitrile	2.71
11.	Ethanone, 1-(2-furanyl)- 2-Furancarboxylic acid, 2-propenylester 2-Butynal	2.08
12.	Cyclopentene,Bicyclo[2.1.0]pentane, 2-Cyclopenten-1-one, 2-methyl-	1.58
13.	Pyrazine, trimethyl-Pyrazine, trimethyl-Pyrazine, trimethyl	0.58
14.	Butanoyl chloride Furan-2-carbonyl chloride, tetrahydro Butanoyl chloride	1.50
15.	2-Cyclopenten-1-one, 2,3-dimethyl-Cyclohexene, 1,2-dimethyl, 2-Cyclopenten-1-one, 2,3-dimethyl	1.64
16.	Terpinen-4-ol, Terpinen-4-ol, Terpinen-4-ol	1.05
17.	Creosol	1.38
18.	1,3-Benzodioxole, 4-methoxy-6-(2-p ropenyl) 1,3-Benzodioxole, 4-methoxy-6-(2-p ropenyl) 1,3-Benzodioxole, 4-methoxy-6-(2-propenyl)	1.01

Table 2-Table 5 shows that phenol was the most common component resulting from cacao shell pyrolysis at 300^{o}C, 340^{o}C, 380^{o}C and 400^{o}C at 45.49%, 29.78%, 33.60% and 49.87%, respectively. This result was slightly different from previous research [5],[9] on oil palm shell and durian shell pyrolysis, in which acetic acid was the most component produced. However, our result was in line with the research by Budagara et al. [25], where phenol was the most component found in coconut fibre pyrolysis. The liquid smoke produced from rice husks contains 85% phenol and its derivatives [26]. The GC-MS analysis on pyrolysis at 300^{o}C, 340^{o}C, 380^{o}C and 400^{o}C identified 9, 14, 11 and 18 compounds each. The compounds were phenol and its derivatives, ketone, furan and ester.

The largest amount of component in cacao shell liquid smoke was phenol and its derivatives such as phenol, 2-methyl-p-cresol, phenol, 3-methyl-; 1-propanol, 2-amino-1-octadecanamine, n-methyl-2-amino-1-propanol; and phenol, 4-ethyl-phenol, 4-ethyl. There are also a few other compounds such as hydrocarbon (2-cyclopenten, cyclopenten), furan (2-furanmethanol, 2-furanmethanol, 3-

furanmethanol) and ketone (2-cyclopenten-1-one, 2,3-dimethyl-2-cyclopenten-1-one, 2,3-dimethyl-cyclooctene; 2-cyclopenten-1-one, 2-methyl-1-pentyne, 2-cyclopenten-1-one, 2-methyl- and 2-cyclopenten-1-one, 2,3-dimethyl-cyclohexene, 1,2-dimethyl, 2-cyclopenten-1-one, 2,3-dimethyl). However, at the pyrolysis temperature of 400ºC, benzene compounds (1,3-benzodioxole, 4-methoxy-6- (2-propenyl) 1,3-benzodioxole, 4-methoxy-6- (2-propenyl) 1,3-benzodioxole, 4-methoxy-6- (2-propenyl)) were also produced, which are carcinogenic in nature and therefore cannot be used to preserve food products. The degradation of cellulose, hemicellulose and lignin compounds at various temperatures produces various components within the resulting liquid smoke. Research from Faisal et al. [9] showed that the pyrolysis of durian shells at 300ºC, 340ºC and 380ºC results in 18, 14 and 21 compounds, respectively, such as phenol, carboxylic acid, furan and lactone. These characteristics were found from GC-MS testing on liquid smoke that resulted from various raw materials such as oil palm fruit bunches [11], oil palm shells [6], durian shells [10] and rice hulls [26].

Liquid Smoke pH Value

The power of hydrogen (pH) shows the degradation of chemical compounds within the biomass that produces organic compounds within liquid smoke. Low pH in liquid smoke indicates good quality to be used as preservatives due to its effect on a product's shelf life and organoleptic value. Table 6 shows that liquid smoke's pH value before distillation was 6-4, which then decreases to 3 after distillation. Risfaheri et al. [27] showed that the pH value of liquid smoke produced from rice husks decreases after distillation because of the increasing number of compounds to be condensated. Saloko's research [28] showed that the liquid smoke produced from coconut shells has a pH value of 2.45 while Lombok's research [13] stated that its pre-distillation and post-distillation pH values are 4.28 and 4.10, respectively.

Table 6. The pH value of liquid smoke.

Pyrolysis temperature (ºC)	pH Liquid smoke	
	Before distillation	After distillation
300	6	3
340	6	3
380	4	3
400	4	3

CONCLUSION

Cacao shell liquid smoke produced at 400ºC pyrolysis contains a high concentrate of phenol (763.76mg GAE). For all pyrolysis temperatures, the GC-MS analysis showed that phenol is the main component in this liquid smoke. At temperatures below 400ºC, the liquid smoke did not contain benzene, while at temperatures above 400ºC, it did contain carcinogenic benzene. Higher pyrolysis temperatures result in less liquid smoke volume. Maximum volume was achieved in less than 30 minutes. The pH value was 3 (acidic), indicating that the liquid smoke has good quality.

ACKNOWLEDGEMENTS

The authors would like to appreciate Universitas Syiah Kuala for supporting this study.

REFERENCES

[1]Kementerian Pertanian., Rencana Strategis (Renstra) Kementerian Pertanian, 2019, pp. 1-364.

[2]Wijaya M., Muhammad W., and Wiharto M., Kandungan Selulosa Limbah Kakao dan Analisis Kandungan Kimia Asap Cair Kulit Kakao dengan Metode GC-MS. Jurnal Kimia dan Pendidikan Kimia, Vol. 2, 2017, pp. 66-71.

[3]Alemawor F., Dzogbefia V. P., Oddoye E. O., and Oldham J. H., Enzyme Cocktail for Enhancing Poultry Utilisation of Cocoa Pod Husk. Scientific Research and Essay, Vol. 4, Issue 6, 2009, pp. 555-559.

[4]Faisal M., Gani A., Husni., Baihaqi A., and Daimon H., Pyrolysis of Oil Palm Kernel Shell into Liquid Smoke and Its Application to Control Anthracnose Disease on Chili (Capsicum annum L). Journal of Engineering and Applied Sciences, Vol. 11, Issue 12, 2016, pp. 2583-2587.

[5]Faisal M., Gani A., and Husin., Utilization of Liquid Smoke from Oil Palm Kernel Shell to Preserve Mackerel. Rasayan Journal of Chemistry, Vol. 11, Issue 3, 2018, pp. 1120-1125.

[6]Faisal M., Gani A., Husni., and Daimon H., A Preliminary Study of the Utilization of Liquid Smoke from Palm Kernel Shells for Organic Mouthwash. International Journal of GEOMATE, Vol. 13, Issue 37, 2017, pp. 116-120.

[7]Faisal M., and Gani A., The Effectiveness of Liquid Smoke Produced from Palm Kernel Shells Pyrolysis as a Natural Preservative in Fish Ball. International Journal of GEOMATE, Vol. 15, Issue 47, 2018, pp. 145-150.

[8]Faisal M., Chamzurni T., and Daimon H., A study on the Effectiveness of Liquid Smoke Produced from Palm Kernel Shells in Inhibiting Black Pod Disease in Cacao Fruit In Vitro. International Journal of GEOMATE, Vol. 14, Issue 43, 2018, pp. 36-41.

[9]Faisal M., Sunarti A. R. Y., Desvita H., Characteristics of Liquid Smoke from the Pyrolysis of Durian Peel Waste at Moderate Temperatures. Rasayan Journal of Chemistry, Vol. 11, Issue 2, 2018, pp. 871-876.

[10]Faisal M., Gani A., and Mulana F., Preliminary Assessment of the Utilization of Durian Peel Liquid Smoke as a Natural Preservative for Mackerel [version 6; peer review: 2 approved]. F1000Research, 8 (240), 2019, pp. 1-9.

[11]Faisal M., Gani A., Mulana F., Desvita H., and Kamaruzzaman S., Effects of Pyrolysis Temperature on the Composition of Liquid Smoke Derived from Oil Palm Empty Fruit Bunches. Rasayan Journal of Chemistry, Vol. 13, Issue 1, 2020, pp. 514-520.

[12]Lingbeck J. M., Cordero P., O'Bryan C. A., Johnson M. G., Ricke S. C., and Crandall P. G., Functionality of Liquid Smoke as an All-Natural Antimicrobial in Food Preservation. Meat Science, Vol. 97, Issue 2, 2014, pp. 197-206.

[13]Lombok J. Z., Setiaji B., Trisunaryanti W., and Wijaya K., Effect of Pyrolysis Temperature and Distillation on Character of Coconut Shell Liquid smoke. Asian Journal of Science and Technology, Vol. 5, 2014, pp. 320-325.

[14]Yang H., Yan R.,, Chen H., Lee D. H., and Zheng C., Characteristics of Hemicellulose, Cellulose and Lignin Pyrolysis. Fuel, Vol. 86, Issues 12-13, 2007, pp. 1781-1788.

[15]Dong J., Cheng Z., and Li F., PAH's Emission from the Pyrolysis of Western Chinese Coal. Journal of Analytical and Applied Pyrolysis, Vol. 104, 2013, pp. 502-507.

[16]Vega R. C., Figueroa K. H. N., and Oomah B. D., Cococa (Theobroma Cacao L.) Pod Husk: Renewable Source of Bioactive Compounds. Trends in Food Science and Technology, Vol. 81, 2018 , pp. 172-184.

[17]Malarut J. A., and Vangnai K., Influence of Wood Types on Quality and Carcinogenic Polycyclic Aromatic Hydrocarbons (PAHs) of Smoked Sausages. Food Control, Vol. 85, 2018, pp. 98-106.

[18]Rahmat B., Pangesti D., Natawijaya D., and Sufyadi D., Generation of Wood-waste Vinegar and its Effectiveness as a Plant Growth Regulator and Pest Insect Repellent. BioResources, Vol. 9, Issue 4, 2014, pp. 6350-6360.

[19]Raveendran K., Ganesh A., and Khilar K. C., Pyrolysis Characteristics of Biomass and Biomass Components. Fuel, Vol. 75, Issue 8, 1996, pp. 987-998.

[20]Cao Q., Xie K. C., Bao W. R., and Shen S. G., Pyrolytic Behavior of Waste Corn Cob. Bioresource Technology, Vol. 94, Issue 1, 2004, pp. 83-89.

[21]Rahmat B., Kurniati F., and Hartini E., Mahogany Wood-Waste Vinegar as Larvacide for Spodoptera Litura. BioResources, Vol. 10, Issue 4, 2015, pp. 6741-6750.

[22]Triastuti W. E., Budhi P. A., Agustiani E., Hidayat R. A., Retnoningsih R., and Nisa A. A., Caracterization of Liquid Smoke Bamboo Waste with Pyrolysis Method. IPTEK Journal of Proceedings Series, Vol. 3, 2019, pp. 114-117.

[23]Yokoyama S., and Matsumura Y., The Asian Biomass Handbook: A Guide for Biomass Production and Utilization, The Japan Institute of Energy, 2008, pp. 1-50.

[24]Pino J. A., Characterisation of Volatile Compounds in a Smoke Flavouring from Rice Husk. Food Chemistry, Vol. 153, 2014, pp. 81-86.

[25]Budaraga K., Marlida Y., and Bulanin U., Liquid Smoke Production Quality from Raw Materials Variation and Different Pyrolysis Temperature. International Journal on Advanced Science, Engineering and Information Technology, Vol. 6, Issue 3, 2016, pp. 306-315.

[26]Sung W. C., Stone M., and Sun F. M., Analysis of Volatile Constituents of Different Temperature Rice Hulls Liquid Smoke. Chia-Nan Annual Bulletin, Vol. 33, 2007, pp.1-12.

[27]Risfaheri R., Hoerudin H., and Syakir M., Utilization of Rice Husk for Production of Multifunctional Liquid Smoke. Journal of Advanced Agricultural Technologies, Vol. 5, Issue 3, 2018, pp. 192-197.

[28]Saloko S., Darmadji P., Setiaji B., and Pranoto., Antioxidative and Antimicrobial Activities of Liquid Smoke Nanocapsules Using Chitosan and Maltodextrin and its Application on Tuna Fish Preservation. Food Bioscience, Vol. 7, 2014, pp. 71-79.

6th Int. Conf. on Structure, Engineering & Environment (SEE), Kyoto, Japan, Nov.18-20, 2020, ISBN: 978-4-909106056 C3051

A NUMERICAL SIMULATION OF DISASTER WASTE DISPOSAL IN WAKAYAMA CITY BY USING DHT MODEL

Soichiro ASAI[1], Tatsuya AKIYAMA[2], Hiroto TANOUCHI[3], and Nobuyuki EGUSA[4]

[1]Graduate School of Systems Engineering, Wakayama University, Japan; [2,3,4] Faculty of Systems Engineering, Wakayama University, Japan

ABSTRACT

We conducted a numerical simulation of disaster waste disposal by using a Dynamic Hauling/Transportation model (DHT model) in order to extract the factors to hinder the execution of a disposal management plan of Wakayama city government. The DHT model was developed for estimating number of days required for disaster waste disposal, following parameters are mandisopdatory as the model inputs; (1) disaster waste characteristics (distributions, volume and contents) in damaged area, (2) hauling/transportation route, (3) number/capacities of transportation vehicles, (4) maximum capacities at temporary storage / final disposal sites and (5) abilities of crushing/classification equipment. Almost all parameters were set by referring to a planning document of disaster waste disposal provided by Wakayama city and disposal guidelines published by Ministry of the Environment of Japan. Several parameters without description in these document/guideline, e.g. maximum capacities at temporary storage and distance of hauling/transportation route were estimated by using GIS. Severe shock and tsunami caused by Nankai Trough huge earthquake were adopted as external forces generating disaster waste. By assumption that parameters included in (3) and (5) could be critical parameters for a result of simulation, we performed sensitivity analysis of each parameter in them. As a result, abilities of several crushing / classification at temporary storages were the most sensitive parameters of all evaluated parameters. Therefore, augments of crushing/classification functions at temporary storage might be effective to shorten processing days for disaster waste disposal.

Keywords: Disaster waste disposal, Dynamic hauling/transportation model, Sensitivity analysis, Nankai Trough huge earthquake, Wakayama city

INTRODUCTION

An appropriate planning of disaster waste disposal is a great issue in a disaster recovery phase. Although it is therefore necessary to make appropriate assumptions about disasters and develop an ideal disposal management plan, it is generally difficult to formulate it with flexibility based on regional characteristics. This is particularly problematic other than large cities with vast population because of a lack of specialists and little financial leeway[1]. Wakayama city is also expected a huge amount of disaster waste generation caused by a Nankai Trough huge earthquake, a numerical system to support a waste disposal planning is effective in this regard.

Various investigations and studies have been conducted in order to establish efficient disaster waste treatment plans. Tanikawa et.al. [2] developed an accurate prediction method of the amount of disaster waste generation by considering material stocks of buildings and roads. Nasu et.al. [3] implied governments of several cities had been adopted inadequate assumption methods to estimate amounts of disaster waste generation. For instance, disaster waste amount caused by Tsunami shown in some waste disposal plans were calculated by using other disaster, e.g. strong earthquake without Tsunami. On the other hand, few researchers have addressed to develop numerical simulation models for disaster waste disposal management. Kayo et. al. 2011 proposed a simplified model to estimate financial/temporal cost for disaster waste disposal in Miyagi prefecture[4]. Sakaguchi et. al. 2018 developed a DHT model, which is a prototype of the numerical system to model all transport/hauling processes in the disposal plan. They also applied it for an actual city[5].

There remains a need for a lot of application of the numerical simulation such as the DHT model to evaluate actual disaster waste disposal plans published by a lot of governments. The amount and quality of disaster waste have great varieties depending on a target city, various patterns of transport/hauling processes also exist. Therefore, a model specialized and optimized for each target city is demanded in order to increase the number of applications. In this study, we have applied the DHT model targeting on Wakayama city as a new case study. In addition, we discussed to formulate a more appropriate planning than one proposed in this study through an evaluation about bottlenecks of disposal planning of Wakayama city.

Table 1 Input parameters of DHT model. Parameter is classified 1) type of set up by referring to official documents by governments, 2) type of set up by referring to environments of the Great East Japan Earthquake, 3) type obtained by GIS processes, 4) assumed value in this study originally. Subscripts shows i;SID , j: type of disaster waste(number of waste types were 6 in this study), k:toSID, l:link ID (number of links were 249 in this study), m: type of trailers (only 1 in this study)

kind	variable	Description	unit	value	type
Storages	SID	Storage ID	-	1 to 72	
	Vol_i	Facility storage volume	ton		3)
	$Su_{i,j}$,	Amount of disaster waste	ton		3)
	$Sa_{i,j}$	(untreated /treated)			
	$C\_R_{i,j,k}$	Proportion of the volume transported to multiple destination sites.	-		4)
Links	$frSID_l$,	Import SID	-		3)
	$toSID_l$	Export SID			
	$Dist_l$	Route length	km		3)
	Spd_l	Average speed	km /hour	30km/hour	4)
	$Load_l$	Loading time,	hour	30 minutes	1)
	$Unld_l$	Unloading time		20 minutes	1)
Transports	$TPNum_m$	Number of trailers	-	1245	4)
	$TPAbility_m$	Capacity of trailers	ton	10	1)
Classify	$CLNum_s$	Number of crushing / classification machines	-		2)
	$CLAbility_s$	Ability of crushing / classification machines	ton/hour		2)

METHOD

Model Summary

The DHT model is a kind of process-based, mass transfer and state change model, optimized for reproduction of disaster waste disposal. In actual disposal management, waste spread in damaged area generated by a catastrophic forcing are transported and hauled to each disposal facilities and storages step by step, aiming to disappear the waste from the area. In the model, all processes of them can be reproduced.

Figure 1 shows the general flow of disaster waste disposal. Reproduced processes in the model are followings; (1) Disaster waste generated in damaged area is transported to refuse collection places. In this phase, disaster waste is generally unsorted and many types of material are mixtures in it. (2) Then, this mixed disaster waste is transported from the collection places to primary temporary storages. (3) At the primary temporary storage, the disaster waste is separated based on material types. Here, crushing process is also installed generally in order to facilitate transportation, recycling and disposal. (4) Residual mixed waste generated by insufficient separate capability at the primary storages is transported to secondary temporary storages. (5) These transported residual mixed waste undergoes more advanced separation and crushing processes than the primary storages in the secondaries. (6) Disaster waste sufficiently separated and crushed in the primaries and secondaries are transported to disposal sites or recycling facilities based on the type of waste. (7) In these sites and facilities, disaster waste is completely disposed or recycled (e.g. landfill, recycling facility, incinerator). Concrete procedures of calculation in the model is shown in Sakaguchi et.al. 2018[5].

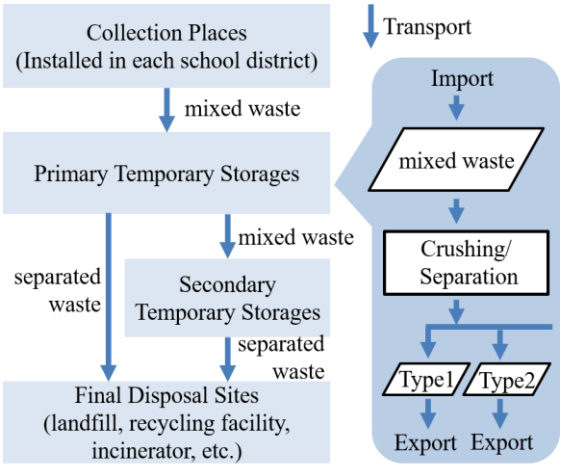

Fig. 1 General disaster waste management flow.

Parameters

Table 1 shows mandatory parameters in the DHT model. Although temporal flexibility of each parameter was necessary in order to reflect process changes accompany with disposal plan progression, each parameter value was fixed as initial values

during the simulation in this study. Additional function to adjust parameters even in a progression of analysis is necessary in future.

In this study, 1) the parameters were set basically by referring to official documents showing disaster waste planning published by Wakayama prefecture[6], Wakayama city[7] and Ministry of the Environment, Japan[8]. 2) Several other parameters without shown in these documents were set based on environmental value obtained by the Great East Japan Earthquake[9]. 3) In other parameters, especially location and capacity of each storage were estimated by GIS processes. 4) The other parameters impossible to obtain related information were set as reasonable values in our assumption.

Input and output

The input is spatial distributed disaster waste data, an arbitrary number of types and volume of disaster waste can be set in the model. Although a geospatial size of each input unit is also arbitrary, elementary school districts are often appropriate for the units because they have been adopted as the units for actual disaster waste disposal in previous managements. The output of the model is amount of each disaster waste type stored in each facility at each time step and required date to complete disaster waste disposal.

PROPERTIES OF TARGET AREA AND MODEL SET-UP

Study area and target disaster

Figure 2 shows the location and properties of a target area of this study. The target area was Wakayama city, Wakayama prefecture, Japan. Wakayama city is located in coastal area facing the Pacific Ocean, which has about 350 thousand of population and about 150 thousand of households. The city consists of 48 elementary school districts, total area size of it is 209 km^2. Especially industrial areas extend along the coast in the city.

A targeting disaster in this study was Nankai Trough huge earthquake, we took especially disaster waste generated by strong earthquakes and Tsunami into account. Wakayama city government inscribed in the report[9] that a vast area facing the Pacific ocean would be swallowed by the Tsunami, and most areas would receive a severe earthquake with a seismic intensity of 6 at least.

Transport and disposal network

Figure 2 also shows locations of collection places, primary and secondary temporary storages, disposal site and recycling facilities. Collection places were set as schoolyards of elementary schools, disaster waste generated in each district is firstly transported here. Information related with final disposal sites for combustible waste and incombustible waste were also mentioned in official documents[6], [7]. locations and capacities of disposal system of them were set by referring them. On the other hand, no detailed description related with recycling facilities were however shown in them. We therefore established recycling facilities for 4 materials (wood, concrete, metals and tsunami sediments) uniquely.

The guidelines of the Ministry of the Environment[7] noted a policy to set temporary storages. While referring to it, Candidates of primary or secondary temporary storages were raised by extracting open spaces (e.g. parks, parking lots and grounds) by GIS processes. Criterion to extract both types of storages were 1) exceeding 10,000 m^2 area size, 2) not located in riverside land to avoid secondary disaster caused by flooding, 3) not adjoined disaster base hospital. By these criterions, we obtained 13 sites as candidates of temporary storages. Then, the largest site of them were set as secondary temporary storages because of small distances between it and final disposal sites and recycling facilities. Finally, all candidate sites except

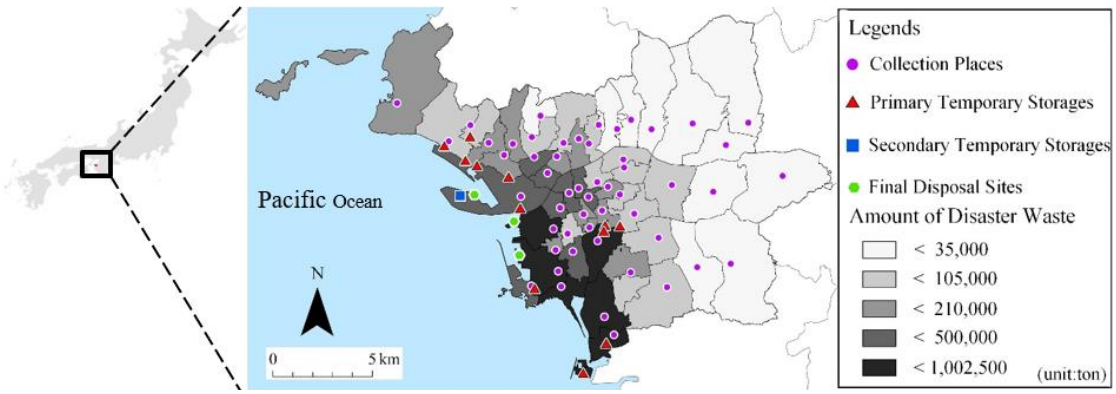

Fig. 2 The location of all sites and the amount of disaster waste in each school district.

chosen as secondary temporary storage were set as the primary storages.

As a result, there were 53 collection places, 12 primary temporary storages, 1 secondary temporary storage and 6 final sites (including final disposal sites and recycling facilities). Figure 3 shows the connection relationship of all sites. All collection places were connected to three primary temporary storages chosen in close order. Here, all distance between the collection places and primary temporary storages were calculated as them along roads. All primary temporary storages were connected to the secondary temporary storage. Secondary temporary storage was also connected to all final disposal sites. All connections were one-way from upstream to downstream. Transportation vehicles allocated links of completed disaster waste exporting were re-allocated for other links. A rule of the re-allocation is to priory for links of upstream, e.g. links from collection places.

Aiming at mitigation the burden on the damaged areas, an exportation from damaged municipalities to outside area is generally performed. In this study, however this kind of outside processing was not modeled because of facilitating interpretation of the results. This obvious limitation in this study could lead to results that the period required for waste disposal is calculated unfairly longer than actual.

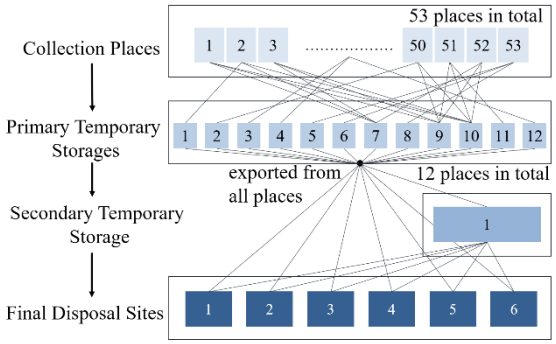

Fig. 3 Network structure in Wakayama city.

Capacity of each storage[7]

The capacity of each primary or secondary temporary storages was set as follows:

$$Cap = Area \times ASG \times SH / (1 + WSR) \quad (1)$$

Where, Cap is weight based capacity of each storage (t), $Area$ is area size (m^2). ASG is an apparent specific gravity (t/m^3), shown in table 2, respectively. SH is stacked height (m), the value was set on 5m as an empirical value. WSR is an indicator related to a vacant space without stacking with disaster waste to improve work efficiency, the value was also empirically set as 1.

Table 2 The value of the ASG

No	Type of waste	$\boldsymbol{ASG}$ (t/m^3)
1	Wood	0.55
2	Concrete	1.48
3	Metal	1.13
4	Tsunami Sediments	1.46
5	Combustible	0.4
6	Incombustible	1.1

Spatial-distributed input data creation

By allocating various types of waste generated both tsunami and earthquake forcing to each elementary school district, we created the spatial distributed data set of disaster waste as model input. Methods to estimate the amount of disaster waste was obtained by the Wakayama Prefecture's disposal management plan[6]. In this study, disaster waste was classified waste debris or tsunami sediment, both of them were calculated for each school district. The following assumptions were applied to calculate the amount of disaster waste. 1) Debris was generated only from buildings for housing, we ignored debris origin from road or other structures. 2) All buildings are wooden. 3) Despite of existence of various levels of destruction, only completely destroyed buildings are taken into the estimation. 4) Ages of buildings required to estimate durability of them were obtained by Japanese statistical survey 2018[10]. Eq. (2) show equations to calculate the amount of debris[5].

$$Q = s \times N \times q \quad (2)$$

Where Q is total amount of debris in each waste type(t), s is average gross floor area of building (m^2). N is number of buildings destroyed. q is debris generation per unit area of floor. In [6], q was although describes as different values based on debris types as respective (e.g. 0.194 (t/m^2) in combustibles), we used $q = 0.696$ (t/m^2) as total value of all debris types in order to estimate Q as the sum of all types. On the other hand, s and N were not shown in each disposal management plan, we replaced $s \times N$ with $TFA \times CDR$ as follows:

$$Q = TFA \times CDR \times q \quad (3)$$

Where, TFA is total floor area of each school district,

CDR is completely destroyed rate by tsunami or earthquake forcing. In areas with duplicated attacks both tsunami and earthquake forcing, CDR come a value as the sum of tsunami's CDR and earthquake forcing's CDR. If the total CDR exceeded 100% by this calculation, it was modified 100%. More detailed theory and procedures to estimate disaster waste amount by using CDR were described in some documents published by governments (e.g. [11]).

Finally, total debris amount of each school district was classified based on debris types. Some documents related with past disaster waste managements have indicated contents and volume of disaster waste, we adopted a ratio of constituent substances in debris obtained by a waste management of the Great East Japan Earthquake[5]. Table 3 shows the ratio of constituent substances and the amount of disaster waste generated by type in the entire Wakayama city. Total weight of Q exceeds 10 million ton, which is equivalent to total waste generation for 70 years in Wakayama city under non-disaster condition[7].

Table 3 Amount of the disaster waste

No	Type of waste	Ratio (%)	Amount (million ton)
1	Wood	4.5	5.627
2	Concrete	43.2	54.182
3	Metal	5.5	6.877
4	Tsunami Sediments	17.0	21.330
5	Combustible	14.9	18.755
6	Incombustible	14.9	18.755
	Total	100.0	125.526

The amount of tsunami sediment was calculated as follows:

$$Sd = A_{tus} \times d \times k \quad (4)$$

Where Sd weight of tsunami sediment in each school district(t), A_{tus} is area size of inundation (m^2), d is average depth of inundation(m). k is conversion factor from inundation depth to deposition amount per unit area by empirical rule[6]. Finally, Total weight of Sd exceeds 2 million ton.

An estimated amount of disaster waste (sum of Q and Sd) at each school district was also shown in figure 2. Larger proportion of disaster waste was generated in the coastal area, the impact of the tsunami was strongly shown.

RESULTS

Figure 4 represents the time series of the disaster waste amounts in each phase estimated by an analysis under the above condition. A period to disappear disaster waste from all collection places was 22.7 years, which is the same as a period from disaster forcing to export disaster waste from all primary temporary storages. Finally, it was demanded 22.8 years to complete disposal process for all disaster waste.

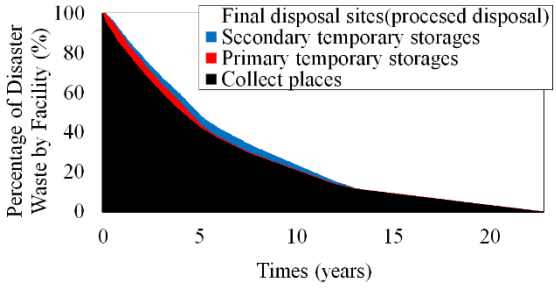

Fig.4 A time series of the disaster waste amounts of collection places, primary and secondary temporary storage, processed in final disposal sites in total.

Periods required under ideal conditions without bottlenecks in transportation or separation could be simply estimated by dividing of each types of disaster waste amount by ability of disposal site for each type, the longest of them was calculated as 8.4 years. This period is much smaller than the period obtained by the numerical simulation in this study.

Figure 5 shows utilization rate of primary and secondary temporary storages, it was shown that especially secondary temporary storages were mostly vacant trough the disposal period. In addition, primary temporary storages were also un-used efficiently especially mid to late in disposal. These results suggested that enhancement and optimization for transportation and separation were critical issues for efficient disaster waste disposal planning. On the other hand, it was also shown that fundamentally enhancements of function final disposal sites were also necessary for further shorten of date to complete all disposal process.

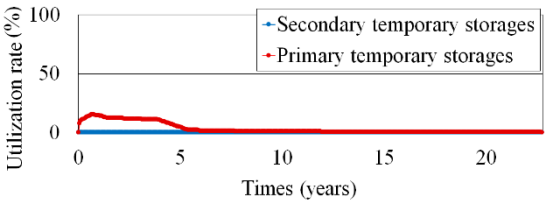

Fig.5 Utilization rate of primary and secondary temporary storages in whole disposal period.

CONCLUSION

In this study, the DHT model was applied to Wakayama city to simulate a disposal process of disaster waste caused by the Nankai Trough Earthquake. Although the process of collection/transportation was modelled based on reasonable ideas, temporal storages were not utilized well chronically. In this case, this surplus caused inefficiency of the entire processes and a delay the processing period. This result suggested that enhancement and optimization for transportation and separation were critical issues for efficient disaster waste disposal planning in Wakayama city. One of the notable limitation of this study is not to reflect outsourcing outside the disaster area. The outsourcing might be effective for further shortening the processing time if these kind of enhancement and optimization had been well-performed. Development of methods for enhancement and optimization are considerable issue in order to improve convenience of the DHT model, we plan to work on this in the future.

ACKNOWLEDGMENTS

This research was performed by the Environment Research and Technology Development Fund "JPMEERF20201004" of the Environmental Restoration and Conservation Agency of Japan. Hiroaki TANIKAWA provided a distributed TFA data usable in GIS.

REFERENCES

[1] Ministry of the Environment, Discussion of the status and promotion of disaster waste management plan development, 2020, https://www.env.go.jp/recycle/waste/disaster/earthquake/committee2/r1-02/R1_2_02_-keikakusakutei.pdf, Accessed 2020/6/23

[2] Hiroki T., Shunsuke M., and Cherry M.L., Estimates of Lost Material Stock of Buildings and Roads Due to the Great East Japan Earthquake and Tsunami, Journal of INDUSTRIAL ECOLOGY, Vol.18, Issue 3, 2014, pp.421-431.

[3] Yuta N., Akifumi N., Syuiti Y., Yugo Y., Mineo T. and Noboru Y., Analysis on Intensity of Waste Generation in Prefectural Disaster Waste Disposal Plans and Influence in Existing Plan in Wakayama Prefecture, Journal of Japan Society of Civil Engineers, Ser. G (Environmental Research), 2019 Volume 75 Issue 6 Pages II_261-II_271.

[4] Chihiro K., Koichi T., Tomonori I., Kazuto E., Masato Y., Development of Support Tool for Seismic Disaster Waste Treatment Planning - Waste Distribution Planning Model by Time and Cost Optimization -, The 22nd Annual Conference of Japan Society of Material Cycles and Waste Management, 2011.

[5] Naoya S., Hiroto T., Nobuyuki E. and Yoshikazu O., Development of a Disaster Waste Disposal Planning Model Aiming at Supporting of Appropriate Decision of Disaster Waste Treatment, Journal of Japan Society of Civil Engineers, Ser. G (Environmental Research), Vol.74, Issue 5 ,2018, pp. I_195-I_202.

[6] Wakayama prefecture, Wakayama accident treatment of waste plan, 2015, https://www.pref.wakayama.lg.jp/prefg/031800/saigaikeikaku/saigaikeikaku.html, Accessed 2020/6/23.

[7] Wakayama city, Disaster waste disposal management plan for Wakayama city, 2017, http://www.city.wakayama.wakayama.jp/kurashi/gomi_kankyo/1001113/1001251/1018288/1018258.html, Accessed 2020/6/23.

[8] Ministry of the Environment, Guideline for disaster waste management, pp. Teq 14-4 - Teq 18-3, 2014, http://kouikishori.env.go.jp/guidance/download/, Accessed 2020/4/23.

[9] Okumura Corporation, Entrusted with the crushing and sorting of disaster waste in the Yamada area performance report, 2014.

[10] Statistics Bureau of Japan, Housing and Land Survey 2018 (e-stat), https://www.e-stat.go.jp/en/stat-search/files?page=1&layout=datalist&toukei=00200522&tstat=000001127155&cycle=0&year=20180&month=0&tclass1=000001129435&tclass2=000001129436&stat_infid=000031865682, Accessed 2020/06/29.

[11] Tokyo Metropolitan of Government Disaster Prevention Information, Damage assumption in Tokyo by Nankai Trough disastrous earthquakes (It's published on May 14, 2013.), pp.3-7, 2013, https://www.bousai.metro.tokyo.lg.jp/_res/projects/default_project/_page_/001/000/402/part3-4-2.pdf, Accessed 2020/4/23.

6th Int. Conf. on Structure, Engineering & Environment (SEE)
Kyoto, Japan, Nov.18-20, 2020, ISBN: 978-4-909106056 C3051

ENERGY POLICY, CORPORATE STRATEGY, AND CONSUMER BEHAVIOUR IN JAPAN

Hisatoshi Tanaka[1], Atsushi Nakashima[2] and Nabil Maghrebi[3]
[1]Graduate School of Systems Engineering, Wakayama University, Japan;
[2]Graduate School of Systems Engineering, Wakayama University, Japan;
[3]Graduate School of Economics, Wakayama University, Japan

ABSTRACT

Natural disasters in Japan have had a significant impact on the Japanese people's relationship with nature and their convictions about social and economic life. However, the devastating nuclear accident caused by the Great East Japan Earthquake in March 2011 led to a drastic change in Japan's nuclear policy. This new energy crisis has indeed forced a fundamental rethink of Japan's energy strategy, while at the same time calling into question the importance of non-renewable energy sources. As a result, there has been a growing interest in renewable energy as a means of achieving sustainable economic and social systems. Despite the promises of clean energy, there are also various constraints on the operation of renewable energy. The recent social trends are reshaping global energy policy based on the SDGs and ESG perspectives. This study examines the relation between energy policy and corporate strategy as well as consumer behaviour in Japan based on evidence from related literature. It argues that an effective energy policy solution lies in raising awareness not only about structural changes in energy demand and supply, but also about the technical and social challenges. It considers also the strategic role of Japan's energy policy in providing viable solutions to these serious challenges.

Keywords: Natural energy, Energy policy, Geothermal resources, Energy self-sufficiency rate

INTRODUCTION

It has been said that Japan is a "resourceless country". However, there are actually many active volcanoes and it is blessed with geothermal resources. On the other hand, most of the land suitable for geothermal power is designated as a national park. As a result, development has long been severely restricted by law. It was also necessary to consider the impact of pumping large amounts of hydrothermal water from the ground on the source of the hot springs.

However, Japan's Ministry of the Environment has eased restrictions on nature parks. Furthermore, the New Energy and Industrial Technology Development Organization (NEDO) is aiming to expand the introduction of geothermal power. The system has been put in place to resolve the issues.

As the use of natural energy is desirable for environmental reasons, the introduction of geothermal power generation is expected to accelerate in the future. It would significantly change the nature of Japan's energy policy. Thus, this study explores the possibility of geothermal power generation in Japan based on data from the Ministry of the Environment, NEDO and the Agency for Natural Resources and Energy.

THE IMPORTANCE OF ENERGY POLICY

Looking back at the history of Japan's energy policy, the procurement of resources from overseas has been at the mercy of international conditions and the international economy. In the case of Japan, it is dependent on Middle Eastern oil-producing countries for much of its oil, and there was a time in the 1970s when it was on the verge of "losing its oil"[1]. In the background, geopolitics is involved, further exacerbating the problem. Even in recent years, the risk of terrorism has increased and made the sea routes for oil transport by tankers, such as the Strait of Hormuz, the Strait of Malacca and the South China Sea, extremely vulnerable [2]-[4]. As the recent international situation shows, the resource issue is not a simple one. As economist David Ricardo advocated the principle of world trade, every country should have benefited from free trade [5], [6]. In reality, however, due in part to speculation in financial and commodities markets, the division of labor in the world has rather increased, making it more difficult to import resources freely. In order for Japan to maintain and develop its domestic economy in the future, it is necessary to achieve domestic energy self-sufficiency.

The 1973 oil crisis exposed the weakness of Japan's resource base and the danger of its dependence on foreign countries. At the time, Japan launched a series of new energy policies, including a review of coal, promotion of nuclear power, and consideration of environmental issues through the Sunshine Plan. They have been followed by the Moonlight Plan and the new Sunshine Plan, which has been carried over into today's Basic Energy Plan [7]-[9].

After the Fukushima nuclear disaster in March 2011, Japan's power companies faced two issues regarding the safety and economy of nuclear power faced. The former were the technical challenges associated with power generation, such as air and water pollution and radiation. The latter were the economic and other issues such as electricity prices, dividend rates on shares for investors, and funding for businesses to prepare for the future. This was a major challenge. The Fukushima nuclear disaster has shown the Japanese people that no matter how advanced the technology is, it is difficult to meet the demands of both safety and economy.

Japan's energy self-sufficiency rate was 20.3% (2010) before the Fukushima nuclear accident. However, due to the shutdown of nuclear power plants after the accident, the rate of 9.6% (confirmed in 2017 in "General Energy Statistics") (value) [10].

As a result, Japan's energy policy has set four goals: (1) to innovate in safety, (2) to ensure technological self-sufficiency and diversity of energy choices in addition to resource self-sufficiency, (3) to take up the challenge of "decarbonization," and (4) to reinforce Japan's industrial competitiveness in addition to controlling costs.

In Japan, thermal power generation was promoted as a substitute for nuclear power. However, this was a retrograde step in terms of global warming. For this reason, rather than increasing thermal power generation, a switch to renewable energy sources, which use natural energy it became necessary.

Amid concerns about declining global economic growth rates, a broader focus on the use of renewables could influence the development of the country's long-term energy supply and demand outlook. In order to decommission nuclear power plants in Japan in the future, it will be necessary to make use of enough renewable energy sources to replace them It is considered to be one of the conditions. For this reason, domestic geothermal resources have been given an important place in Japan's "Basic Energy Plan"[7].

GEOTHERMAL POWER GENERATION

Modern society has been using fossil fuels to expand its economy since the "industrial revolution" of the mid-18th century. However, the negative aspect of this has manifested itself today in the form of global warming. Therefore, since the 1992 Earth Summit (United Nations Conference on Environment and Development), natural alternatives to fossil fuels in energy use have been suggested.

It is noted that in Japan, geothermal power is expected to be an environmentally friendly energy source. Unlike solar and wind power, which are constrained by natural and geographic conditions, geothermal power is considered to be capable of generating electricity consistently throughout the year.

Geothermal power generation in Japan has a long history, with the first successful geothermal power plant in Japan in 1925. However, no progress has been made since then. The first full-scale geothermal power plant in Japan started operation in 1966. The oil crisis of the 1970s led to the development of domestic geothermal research and development, encouraged by the Sunshine Plan, an alternative energy policy [11].

Table 1 Geothermal resources (in terms of electricity) in major countries

Country.	Amount of geothermal resources (in terms of electricity)	Geothermal energy generation capacity	Percentage used for power generation (%)
USA	30,000	3801.00	12.67
Indonesia	27,790	1945.50	7.00
Japan	23,470	536.00	2.28
Philippines	6,000	1927.90	32.13
Mexico	6,000	950.60	15.8
Iceland	5,800	753.00	12.98
New Zealand	3,650	996.00	27.29
Italy	3,270	767.20	23.46

Source: Prepared by the author based on materials from NEDO and other organizations.

・Most recent data: 2018

・Units are megawatts (MW)

・Based on geothermal power generation capacity in each country at the end of each year

In countries with active volcanoes, geothermal resources are being actively developed and used. Table 1 shows the geothermal resources of major countries with active volcanoes in 2018. It is clear that Japan's geothermal power potential is among the highest in the world [12]. Japan's geothermal power potential is one of the best in the world. However, only a little more than 2% of the potential electricity is actually used for power generation, highlighting that the country is not making effective use of its own

resources.

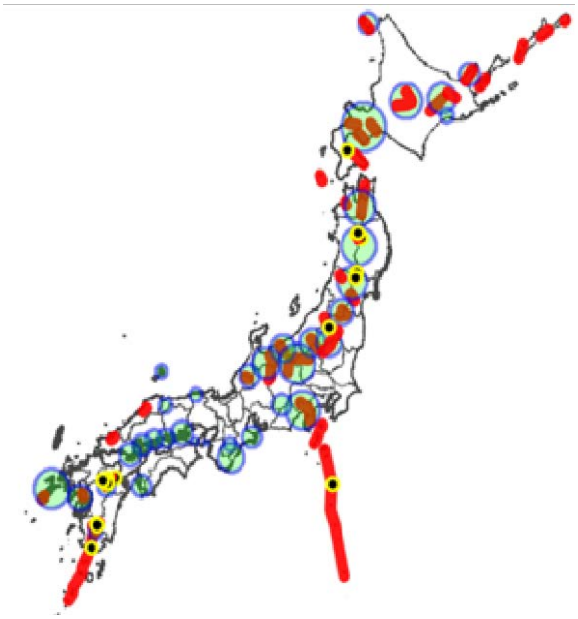

Fig. 1. Location of active volcanic belts, national parks, and geothermal power plants in Japan Source: author's drawing on a white map of Japanese Geographical Survey Institute.

Given the prevailing conditions of the energy sector, the Japanese government has announced a goal of increasing geothermal power generation to approximately 1.5 GW by 2030, but currently it is only 536.00 MW, which is a huge gap [13]. Fig. 1 shows a simple map of Japanese active volcanic belts, national parks, and geothermal power plants based on data from government agencies. The red zone is a geothermal potential area with a series of active volcanoes. The blue area is a national park. The black dots represent the current locations of geothermal plants. Most of the geothermal potential areas are designated as national parks, and for a long time, the law has been strictly enforcing development it has been limited. However, the Ministry of the Environment eased regulations on nature parks in March 2012 and a feed-in tariff system was introduced in July 2012 to promote the use of geothermal energy [14].

As can be seen from the map, it is clear that the areas where geothermal energy can be used are unevenly distributed. Given the disparities in the distribution of potential geothermal plants, it may be difficult to serve the diverse regional needs based on this natural energy resource.

Table 2 shows the evolution of the power supply mix in Japan from 2014 to 2019. The decrease in the percentage of thermal power generation was due to the restart of nuclear power plants that had been shut down following the Fukushima nuclear accident and the increase in the amount of solar power generation. Geothermal power generation has hardly increased and remains at rather low rates.

In order to reduce the proportion of thermal and nuclear power generation on the premise of environmental protection, other sources of renewable energy, especially the question of whether the proportion of geothermal power generation can be increased has emerged as a difficult challenge.

Table 2 Trends in power supply composition in Japan

power source	2014	2015	2016	2017	2018	2019
fire power	87.90%	85.70%	83.60%	80.80%	77.90%	75.00%
nuclear power	0.00%	0.40%	1.70%	2.80%	4.70%	6.50%
hydraulic power	8.00%	8.60%	7.60%	7.60%	7.80%	7.40%
solar power	1.90%	3.00%	4.40%	5.70%	6.50%	7.40%
biomass	1.50%	1.50%	1.90%	2.00%	2.20%	2.70%
wind power	0.47%	0.50%	0.54%	0.61%	0.69%	0.76%
geothermal energy	0.24%	0.25%	0.22%	0.21%	0.22%	0.24%

Source: Compiled by the author based on "Power Survey Statistics" by the Ministry of Economy, Trade and Industry and the Agency for Natural Resources and Energy.

Thus, in the case of geothermal power, it is undoubtedly costly to install and maintain the equipment, but theoretically the energy resource itself is cost-free. However, it is undeniable that there are many areas where geothermal power generation is not possible due to geographical conditions. Therefore, measures are needed to address the vulnerability of the power source. As a countermeasure, if it is possible to combine multiple types of natural energies, it will be possible to increase the amount of electricity generated in Japan as a percentage of the total amount of electricity. The percentage of renewable energy could be increased. Naturally, this can be increased from 18.5% in the fiscal year 2019 [15], [16].

CORPORATE STRATEGY AND CONSUMER BEHAVIOUR

In order to utilize renewable energy, the cooperation of Japanese companies is essential, both in terms of funding and technology. However, it has become apparent that the influence of Japanese companies is declining in global terms [17]. This is due to the rise of companies seeking to go borderless and the speed of business in the world. This is due to the fact that Japanese companies' business models to date have focused on regional rather than global strategies, and that they have focused on internal matters rather than negotiations with their counterparts [18]-[20].

The slowness of management decisions and decision-making was particularly critical. It has been pointed out by foreign countries that Japan's social structure and various regulatory issues have not changed much, which has greatly delayed the flow of electricity liberalization [21]. In addition, Japan's energy policy is based on the premise of maintaining and restarting nuclear power plants even after the Fukushima nuclear accident. On the other hand, the approval of full liberalization of electricity in April 2016 is a small step forward after a long monopoly on the supply and sale of electricity by power companies.

If we look at the Japanese energy industry, especially the power industry, there is a need to review market needs in light of changing demographics, consumer behaviour, and a shrinking market. Furthermore, it will be difficult to survive without rationalization and economies of scale, through strategic capital investment in ICT and AI, and outsourcing to reduce fixed costs. It is imperative also that energy consumption is rationalized through more responsible consumer behaviour and energy education.

CONCLUSION

One of the main characteristics of Japan is that it is a country with little natural resources, yet it imports and consumes a large amount and variety of resources. In other words, the resources of developing countries are being used unconsciously, and the natural environment of the target country is being destroyed. An efficient energy policy that reflects the demographics and environmental needs is thus warranted.

Japan has already transitioned to a steady-state economy, and the demand for energy is expected to decline as the population declines [22], [23]. However, energy independence, energy decentralization and responsible corporate strategy are needed to mitigate for future risks and achieve meaningful reductions in carbon dioxide emissions. It is research and development in geothermal energy that may contribute significant toward a more sustainable energy environment.

REFERENCES

[1] Agency for Natural Resources and Energy., What happens when the oil stops? ～Learning from History, A Risk to Japan's Energy Supply? , 2019.

[2] Cabinet Office, Government of Japan, Government Efforts to Ensure the Safety of Japanese Ships in the Middle East, 2019.

[3] Japan Ministry of Defense. Government Efforts to Ensure the Safety of Japanese Ships in the Middle East, 2019.

[4] Ministry of Foreign Affairs of Japan, Government Efforts to Ensure the Safety of Japanese Ships in the Middle East, 2019.

[5] Ministry of Economy, Trade and Industry, The benefits of free trade: a trade white paper, 2017.

[6] David Ricardo, Takuya Hatori et al., Principles of Economics and Taxation, Iwanami Bunko, Vol. 1, 1987.

[7] Agency for Natural Resources and Energy, Basic Energy Plan, 2020.

[8] Agency for Natural Resources and Energy (ed.). Sunshine Project, New Energy Handbook, March 1999, pp. 221-228.

[9] Agency for Natural Resources and Energy supervised, resource and energy yearbook 1999/2000, 1999, pp. 642-645.

[10] Ministry of Economy, Trade and Industry, Total Energy Statistics, 2019.

[11] Agency for Natural Resources and Energy., Japan's 150-year history of energy, 2019.

[12] Japan Meteorological Agency and Volcano-logical Society of Japan. 2020.

[13] Japan Oil, Gas and Metals National Corporation.2020.

[14] New Energy Subcommittee, Current Status and Issues of Geothermal Power, 2020.

[15] Annual Report on Energy in 2019., Energy White Paper 2020, 2020

[16] Institute for Sustainable Energy Policies. Renewable Energy White Paper 2020, 2019.

[17] Economic and Social Research Institute, Cabinet Office, Government of Japan, Structural Problems and Deregulation, 2019.

[18] Forbes Global 2000, 2019.

[19] Kazuhiro Asakawa., Introduction to Global Management, Nihon Keizai Shimbun, 2003.

[20] Ministry of Health, Labour and Welfare, Characteristics of Japanese Society in International Comparison, 2019.

[21] Ministry of Economy, Trade and Industry, The potential for trade in services, 2016.

[22] Research Institute of Economy, Trade and Industry, 2020.

[23] Bank of Japan, HP, 2020.

6th Int. Conf. on Structure, Engineering & Environment (SEE), Kyoto, Japan, Nov.18-20, 2020, ISBN: 978-4-909106056 C3051

IMPACT OF CITRUS AGRICULTURE ON THE QUALITY OF WATER RESOURCE IN A SMALL STEEP ISLAND, SETO INLAND SEA, JAPAN

Sharon Bih KIMBI [1], Shinjo NOZAKI[1], *Shin-ichi ONODERA[1], Yusuke TOMOZAWA[1], Kungyang WANG[1], Anna RUSYDI[1], Mitsuyo Saito[2]

[1]Graduate School of Integrated Arts and Sciences Hiroshima University, Japan
[2]Graduate School of Environmental and Life Science, Okayama University, Japan

ABSTRACT

Groundwater is the major source of water for domestic, agricultural and industrial purposes and its exploitation for agricultural purposes has increased significantly in the past decades especially in Asian countries. This paper investigates the groundwater resources of osakishimojima for its quality and possible effects of agricultural activities on the resources. Fifty-one groundwater samples were collected and analyzed for major ions and nutrients using an ion chromatography and automated nutrient analyzer respectively. Results suggested that groundwater quality is strongly influenced by water rock interaction and by the dominant citrus fruit cultivation in the area. The groundwaters are freshwaters (TDS<500 mg/l) and are mainly: Ca + Mg-HCO3, Ca + Mg-NO3 + Cl - and Ca-Cl water types. High concentrations of nitrate (91%) and phosphate phosphorus (53.1%) were observed in the shallowest wells suggesting inputs from heavy application of NPK fertilizers. Thus, proper groundwater management strategies are necessary to sustainably protect this valuable resource.

Keywords: Agriculture, Groundwater Quality, Contamination, Small Island, Seto Inland Sea

INTRODUCTION

Groundwater is the major source of water for domestic, agricultural and industrial purposes in many countries. Water quality is the critical environmental determinant that influences the agricultural production in any economy that solely depends on it [1]. In Asian countries, exploitation of groundwater has increased greatly over the past few decades where it is used for agricultural and drinking purposes [2]. Elevated levels of contaminants such as nitrate and phosphate in water sources can be associated with rapid population growth, agriculture, industries and domestic waste. Findings from [3] show that, agriculture is recognized as a major source of water pollution, which is also the most difficult to eliminate due to its spatial character.

A number of factors controlling groundwater quality have been documented by [4] which include; rainfall, topographic relief, mineral dissolution, mineral solubility, ion exchange, oxidation, reduction, natural and anthropogenic activities such as geological structure and mineralogy of the watersheds and aquifers, the residence time, poor sanitary conditions, application of fertilizers and pesticides for higher crop yields. Therefore, it is most essential to monitor the quality of water. Previous studies have been conducted on groundwater quality assessment in many parts of Japan such as estimation of sedimentation rate and fresh-saline environment in coastal alluvial plain using boring cores of alluvium in the central part area of Seto Inland Sea[5], suitability of groundwater for agriculture in Northwest Honshu island [6] and estimation of groundwater recharge and salinization in a coastal alluvial plain and mega city[7].

The present study investigates groundwater quality in osakishimojima, a small island located along the stretches of the Seto inland in Hiroshima prefecture located in western Japan (Fig. 1). Osakishimojima like the many small island in the Seto inland sea is currently a rural area suffering from depopulation and population aging [8] as well as a high rate of rural exodus. Citrus agriculture is well practiced in this area all through the year in different scale. Nevertheless, unlike the big islands of Miyajima and Ninoshima, osakishimojima has experienced little or no significant human environment impact over the years. This relatively pristine condition is ideal for studying the nature of the groundwater environment. The inhabitants of osakishimojima equally rely solely on Kure regional water supply

system which is over 100km away from Kubi village. Thus, in an advent of a natural disaster such as the devasting flood which occurred in June 2018, contaminating the pipelines with mud and sediments, the villagers were without access to safe drinking water for over 10 days having to turn to their untested sources of groundwater for drinking and other uses. The villagers were then motivated to seek out other sustainable water resources of drinking water for future use and guide against being without a reliable source of water supply in the future.

On this note, the groundwater sources of osakishimojima were being analyzed for their quality and the study seeks to provide baseline information on the effects of citrus farming on the groundwater quality with emphasis on nitrates and phosphates as the major contaminants. The assessment of water quality in the study area is one of the important tools for sustainable development and will provide decisive information for water resources management.

METHODS

Study Area

Osakishimojima is one of more than 700 islands located in the center of the Seto inland sea in japan, about 10km off the coast of Kure city. Its surface area is about 43km^2 with geographic coordinates 34°10'24"N and 132°50'3"E (Fig. 1) with a dwindling aging population of about 3,000 people. It is a modest-sized island large enough to be lined with steep mountains and narrow valleys yet small enough to be tucked away amid a cluster of other islands. The topography of the area is low land to shore.

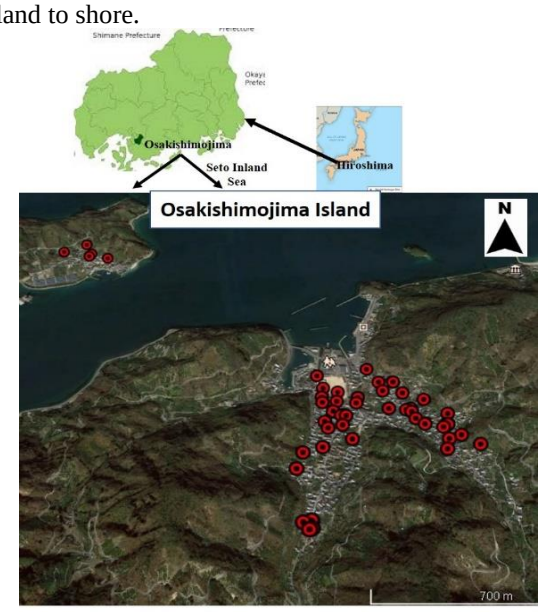

Fig. 1 Location of Osakishimojima in Hiroshima Prefecture and sampling points

Geology

Osakishimojima is one of the Archipelago in the middle of the Seto inland sea located in the western region of Japan (Fig. 2). It is made up of late Cretaceous Hiroshima granitic rocks which widely intrude into the remote islands of the Seto island sea. It equally comprises of late Cretaceous rhyolite- dacitic rocks outcrop and a mélange matrix of Early to Middle Jurassic accretionary complexes associated with Triassic chert block and Carboniferous to Permian limestone which underlay the island [9].

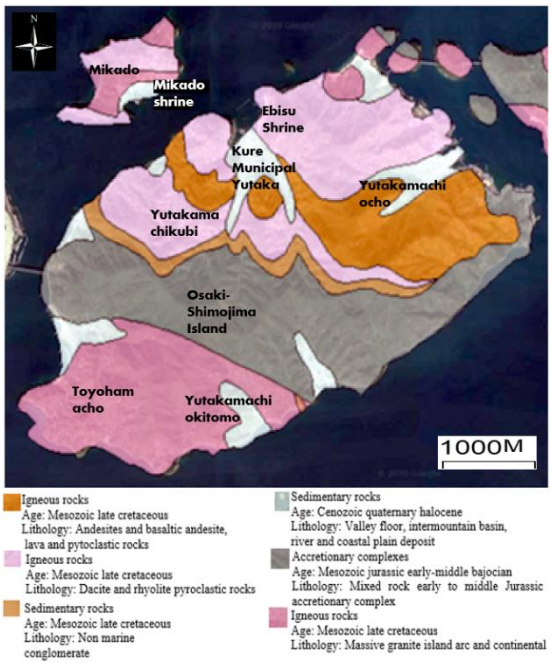

Fig. 2 Geology of Osakishimojima Island modified from [10]

Land-uses

Osakishimojima is known to be one of the most interesting islands in the Seto inland sea. Renowned for its well-preserved edo period architecture of Mitarai it can easy be visited as a day trip. Dominated by forest, the island has a well-drained soil, which makes it perfect to grow citrus. The island is famous for its rich cultivation of Mikan (Japanese mandarin) and lemon. The land-use of Osakishimojima island is portrayed in Fig 3. In the past when the inland sea was the superhighway of Japan, it was very busy and prosperous but since the advent of powered ships, railways and finally roads, it lost its prosperity and is now little more than a fishing village with an ageing population.

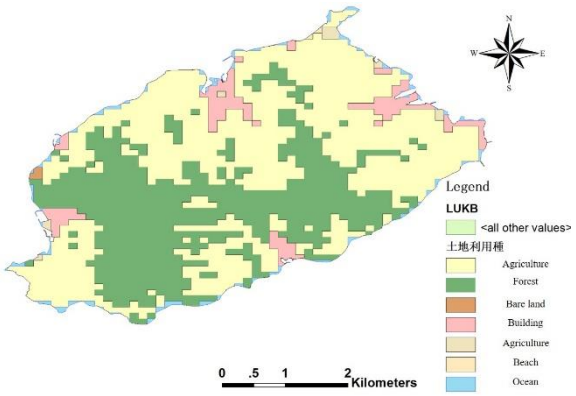

Fig. 3 land-use types of Osakishimojima and sampling locations.

Because of its sheltered location and gentle climate, osakishimojima is Japan's citrus island taking advantage of the calm air, strong sunlight, light rainfall, and good mountain drainage, which is so important for citrus orchards cultivation.

Sample Collection

Fifty-one water samples (49 wells, 1 stream and 1 spring) were collected during the month of October 2019 from representative sites in the village of Mikado and Kubi located in osakishimojima island. Sampling points are indicated in (Fig. 1). Samples of each point were collected in acid washed 250ml polyethylene bottles after rinsing at least three times with the sample water and preserved airtight to avoid evaporation. Physicochemical parameters including pH, electrical conductivity (EC), dissolved oxygen (DO), and water temperature were measured in situ using portable devices. The values of these parameters were recorded after they were stabilized. TDS was calculated from EC by an empirical formula TDS= 0.64*EC as described by [11]. Samples were filtered through a 0.2 µm polytetrafluoroethylene filter and preserved at 4˚C in a refrigerator. Alkalinity measurements were carried out by acid titration with 0.02N H_2SO_4 added to each sample to reach its titration end point within 24 hours of sample collection.

Parameters and Chemical Analysis

Concentrations of major ions in water samples were determined in the Laboratory of Biogeochemistry at the University of Hiroshima, Japan. Analyses for major ion chemistry included sodium (Na^+), potassium (K^+), calcium (Ca^{2+}), magnesium (Mg^{2+}), chloride (Cl^-), nitrate (NO_3^-) bicarbonate (HCO_3^-) and sulfate (SO_4^{2-}) by ion chromatography while the concentrations of phosphate and ammonia species were determined with a continuous flow automated nutrient analyzer. Each sample was filtered using a 0.2 µm polytetrafluoroethylene filter and subjected to 10 times and 5 times dilution using distilled water before analyzing for the major ions. The investigation of phosphate (PO4-P) sources was conducted to determine the relationship between PO4-P and Cl- and their respective contribution to groundwater contamination. Analytical precision for cations (Na^+, K^+, Mg^{2+}, and Ca^{2+}) and anions (Cl^-, NO_3^-, SO_4^{2-} and HCO_3^- was checked using ionic balance error (IBE).

RESULTS AND DISCUSSION

General Groundwater Chemistry and Hydrochemical facies

General groundwater chemistry

The physiochemical parameters and statistical summary for all 51 water samples collected from osakishimojima are presented in Table 1. Physical parameters such as pH, DO and EC often give us the preliminary information that is required in any groundwater study. pH is a negative logarithm of the hydrogen ion concentration in an aqueous solution and its temperature dependent thus measurements should be taken in-situ alongside temperature. Thou pH has no direct effect on human health, it is closely related to other chemical parameters. The hydrogen ion can disrupt mineral structures so that they contribute dissolved constituents to groundwater i.e. the lower the pH, the higher the TDS in the water [12]

Table 1: Statistical analysis of various chemical parameters

Parameters	Min	Max	Mean	ST. Dev
EC	22.6	543	281.7	115.6
TDS	14.46	347.5	180.3	74
DO	4.2	10.2	8	1.4
pH	6.02	7.4	6.5	0.3
Temp	11.7	20.6	15.6	1.8
Na^+	2.55	39.1	14.5	7.9
K^+	0.45	13.8	4.4	2.7
Ca^{2+}	5.92	86.3	30.7	14.4
Mg^{2+}	2.03	31.2	10.7	5.7
NH_4^+	-0.09	3.4	0.5	0.8
HCO_3^-	0	139.9	55.8	25.9
NO_3^-	5.4	92.2	34.6	21
PO4-P	0	3.2	0.6	0.7
SO_4^{2-}	7.6	95.4	41.7	22.1
Cl^-	1.94	48.6	14.1	8.9

Note: Ionic concentrations, TDS and DO: mg/l, EC: µS/cm, Temp: ^{O}/C

The pH values for the study area ranged from 6.02 to 7.4 with a mean value of 6.5 (Table 1) thus, the groundwater of this area is generally neutral. The maximum depth to the water table (12 m) was relatively low, suggesting an existence of a shallow aquifer system for the water sources that were observed. The water temperature ranged from 11.7 to 20.6 °C with mean value of 6.5 °C. The relatively low temperatures recorded in water samples may indicate their recharge under recent climatic conditions.

Groundwaters in the study area have pH values slightly out of the World Health Organization [14] guideline limit (6.5–8.5) for drinking water with only 41% within the acceptable limit making them neutral slightly acidic meanwhile 58% of the samples were slightly acidic. EC is a measure of the salt content of water in the form of ions. It is based on the flow of electrical current through the sample, the higher the salt content the greater its flow of electrical current. The EC of the groundwater varies between 22.6 to 543µS/cm with the mean value of 281.7µS/cm. The obtained electrical conductivity (EC) values of groundwater samples ranged from 22.6 to 543 µS/cm (Tables 1). Concentration of total dissolved solids (TDS) in groundwater ranged from 14.46 to 347.5mg/l (Tables 1). However, [14] categorized water based on TDS concentration into four groups which are represented as fresh (TDS < 1000 mg/L), brackish (> 1000 mg/L), saline (> 10,000 mg/L) and brine (100,000 mg/L). Based on this classification, all the groundwater samples fall in fresh category. The concentrations of dissolved major cations and anions vary spatially.

Hydrochemical facies *definition*

The chemical composition of groundwater is primarily dependent on the geology as well as the geochemical processes and anthropogenic activities which take place within the aquifer system. Ionic concentrations of major cations and ions plotted on the Piper trilinear diagram [15] which provides useful information on their chemical properties. The meq/l concentrations of major ions plotted on a pie chart (Fig. 4) showed that Ca^{2+} and HCO_3^- were the major ions in waters followed by Na^{2+} and SO_4^{2-}. Based on their ionic concentrations and relative proportions. Three types of water have been identified (Fig. 3): Ca + Mg-HCO3, Ca + Mg-NO3 + Cl or Ca + Mg-NO3 + SO_4^{2-}, and Ca-Cl. Majority of the water samples (68 %) belonged to the mixed Ca + Mg-HCO3 water type. This type indicates mineral dissolution possibly secondary carbonate and silicate minerals with enough recharge from freshwater. Minor representations of Ca + Mg-NO3 + Cl (31%) and Ca-Cl (1 %) may suggest the mixing of freshwater with water from contaminated sources.

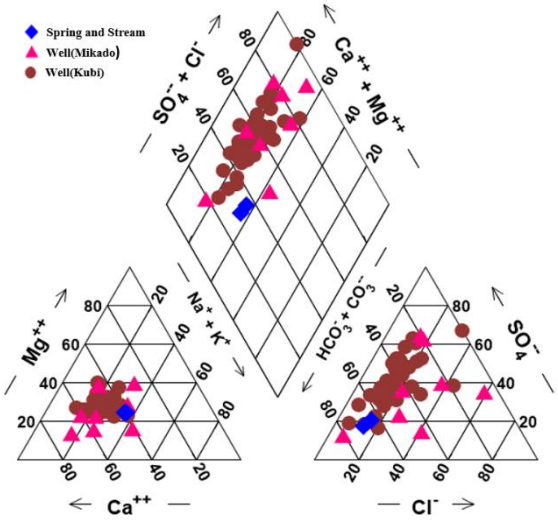

Fig. 4 Piper trilinear diagram showing the main Hydrochemical facies of groundwater in Osaki-shimojima

The order of dominance of ionic species in the groundwater of the study area. The order of $Ca^{2+} > Na^{2+} > Mg^{2+} > K^+$ for the cations and $HCO_3^- > SO_4^{2-} > NO_3^- > Cl^-$ for the anions. $(Ca^{2+} + Mg^{2+})$ dominates $(Na^+ + K^+)$, and $(CO_3^{2-} + HCO_3^-)$ exceeds $(SO_4^{2-} + Cl^-)$. The high concentration of Ca^{2+} and HCO_3^- may suggests that process such as chemical weathering occurs within the aquifer system.

Mechanisms controlling water chemistry

The geochemical process occurring within the groundwater and reactions with aquifer minerals have a profound effect on water quality. These geochemical processes are known to be responsible for the seasonal and spatial variations in groundwater chemistry. The Gibbs diagram [16] was used to provide information on the mechanisms that controls the chemistry of the water sources. The Gibbs's plot (Fig. 5) revealed that majority of the data (98%) points plotted in the domain of water-rock interaction suggesting that chemical weathering of rock forming minerals is apparently the dominant process influencing the hydrochemistry of the aquifer in the study area.

The interaction between rocks and water results in leaching of ions into the aquifer which subsequently influences the groundwater chemistry.

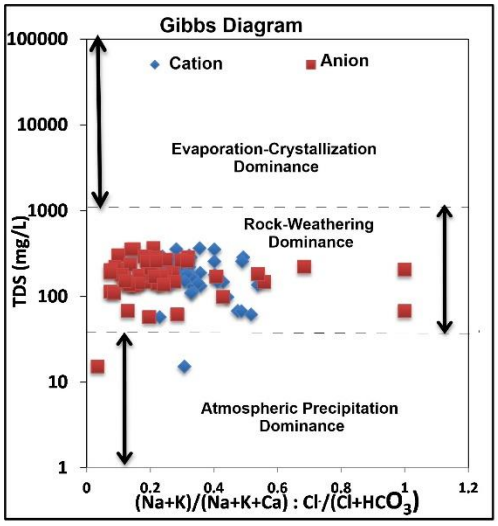

Fig. 5 Gibbs plots indicating water-rock interaction as the major process regulating the chemistry of waters in osaki-shimojima

Contamination of Groundwater

Phosphates and nitrates are useful nutrients for plant growth but when they become too concentrated in our water system, they become dangerous to both humans and their environment. Leaching of Nitrogen and Phosphorus from arable fields to groundwater occurs as a result of high amounts of these nutrients applied in the form of natural and mineral fertilizers needed by plants [3].

Nitrate Contamination

According to Berner [17], there exist three sources of nitrogen in water; biological fixation, precipitation, and the application of fertilizers however humans significantly affect nitrogen load in the environment. Anthropogenic sources of nitrogen have been classified into three classes by [18] and they include (1) point source including industrial sewage, refuse dumps discharged directly into the surface water, (2) diffuse source including runoff and leaching from rural and urban land, and (3) precipitation. Generally, lithologic source for NO_3^- in natural waters is unlikely and atmospheric input is not often considered to be a major source of NO_3^- concentrations in groundwater [19]. Based on the premises that (Nitrogen, Phosphorous, and Potassium: (NPK), fertilizer is highly used during agricultural activities, and domestic wastes are often rich in chloride, a strong and weak correlation between any pair of these element shall be indicative of anthropogenic and non-anthropogenic inputs, respectively[20].

The warm weather, low rainfall and volcanic soils of osakishimojima have promoted the growth of intensive citrus fruit dating back to the 1930's. In order to maintain and increase crop yield, chemical fertilizers and pesticides are usually applied to the trees. Equally some organic citrus farmers whose orchards are near the sea spray their orchards with diluted salty sea water to ward off pests and fungus. Figure 6 indicates that there exists a weak negative correlation between NO_3^- and Cl^-. Hence, the agro-industrial activities of the study area could be the main source of groundwater contaminated alongside lithologic effects. This contamination of NO_3^- in most groundwaters may equally be driven by the process of leaching of percolating rainwater. This result was in disparity with those of [21] who observed that, groundwater analysis of samples from Indramayu exhibited higher NH_4^+-N concentrations as oppose to NO_3N.

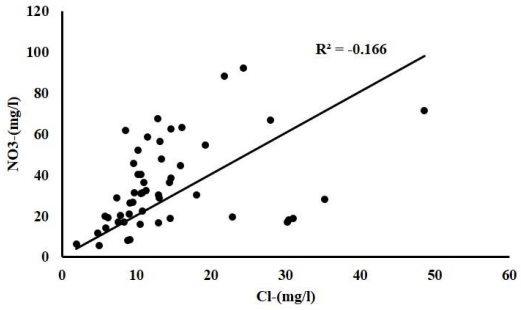

Fig. 6 Scatter plot of NO_3^- versus Cl^- in groundwaters

Elevated concentrations of nitrates have undesirable effects when present in drinking water. Table 2 characterizes water samples bases on the desirable limit set by WHO [13]

Table 2: Summary of WHO limit for NO_3^-N (10mg/l) and PO4-P (0.03mg/l) concentrations in water samples of osakishimojima.

Parameter	Pollution grade	No of Wells	% of Sample	Pollution Status
NO_3^- (mg/l)	<10	4	7.84	No Pollution
	10-50'	35	68.63	Pollution
	50-70'	9	17.65	Pollution
	>70	3	5.88	Pollution
PO4-P(mg/l)	<0.03	23	46.94	No Pollution
	>0.03	26	53.06	Pollution

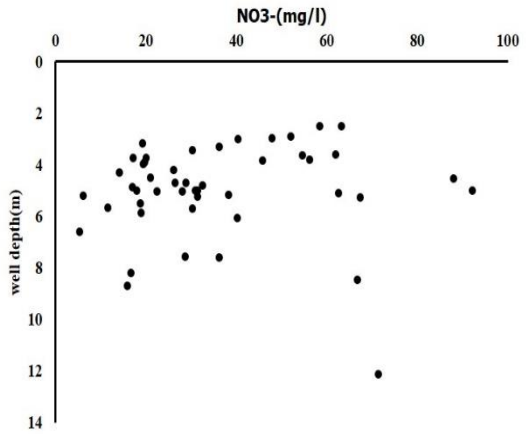

Fig. 7 Plot of depth of wells versus nitrate concentrations in groundwaters

Figure. 7 shows a plot of NO_3^-N against depth. The concentration of nitrates is significantly homogenous spanning from 2m to 13m of the aquifers thou decreasing with depth. Such a distribution clearly indicates that nitrate species in most of the considered groundwaters are of superficial origin (anthropogenic). This is indicative of the unconfined nature of the system and shallow groundwater resources (open wells, springs and streams) are more vulnerable to nitrate contamination due to natural N-fixing under aerobic conditions.

As earlier mentioned, the most common land use in the study area is agro-industrial cultivation which is usually accompanied by large applications of fertilizers and pesticides. Nevertheless, other factors responsible for high nitrate concentrations in other basins have been known to include soil leaching and nitrogenous organic waste, poor well completion improper waste disposal, handling and applications of organic and inorganic fertilizers [22]-[23].

Phosphate phosphorus contamination

Phosphorus is a soluble agricultural chemical that may be moved from point of application by surface run off or moved out of the soil surface layer with percolation [6]. The increase of PO_4^-P in groundwater may equally be due to a high exchange of water which has been documented in sand flats by [24]. Phosphate phosphorus concentration in ground water of the study area was varied with depth (Fig. 8). In present investigation the concentration of phosphate has been found to be more than the permissible limit in fifty-three (53.1%) water samples out of forty-nine water samples (Table 2). The PO4-P for water sources ranged from 0 to 3.2mg/l with a mean of 0.6mg/l. Thirty samples were within the depths of 4-5m, six samples fell between 6-7m, eight samples within 5 and one sample at 12m (Table 2).

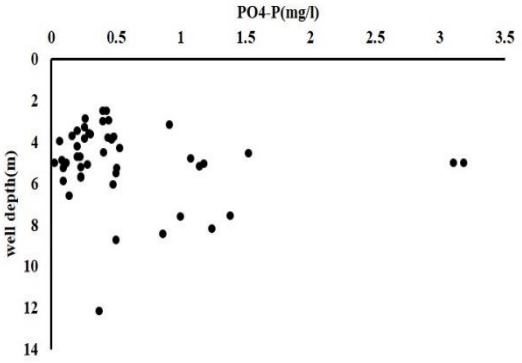

Fig. 8 Plot of depth of wells versus PO_4^-P concentrations in groundwaters.

According to WHO [13] the recommended value of phosphorous in drinking water is 0.3mg/L. Consumption of water with phosphate more than permissible limit causes disease of the kidney and osteoporosis in human being [25]. Our findings indicated that concentration of PO4-P was high in groundwater, thus poses a future risk of eutrophication of surrounding water bodies such as Japan Sea.

CONCLUSION

This paper presented an analysis of water chemistry results to identify the effects of agriculture on the groundwater quality in osakishimojima, a small island in western japan. According to the results, groundwater quality in osakishimojima is strongly influenced by rock water interactions and anthropogenic activities (linked to agriculture). The groundwaters are freshwaters (TDS<500 mg/l) and are mainly: Ca + Mg-HCO3, Ca + Mg-NO3 + Cl^- and Ca-Cl water types. Chemical content of groundwaters is primarily controlled by low temperature and water–rock interaction. However, high values of NO3 and PO4-P(mg/l) in most of the well samples render them unsafe for drinking and domestic purposes. Overall, groundwater quality in osakishimojima is impeded by anthropogenic activities, and proper groundwater management strategies are necessary to sustainably protect this valuable resource. Nevertheless, there is a need to extensively carry out studies on the types of contamination and its relationship with the environmental conditions in the area.

ACKNOWLEDGMENTS

The authors acknowledge the Graduate School of Integrated Arts and Sciences, Hiroshima University

for facilitating this research. We would also like to express our gratitude for the valuable comments provided by reviewers and the editor of GEOMATE. The authors wish to acknowledge Google Earth engine for facilitating the access to archive of publicly available satellite imagery.

REFERENCES

[1] Islam M.M., Azad A.K., Ara M.H., Rahman M., Hassan N., Swarnokar S.C., and Rabeya, I., Environmental Study on a Coastal River of Bangladesh with Reference to Irrigation Water Quality Assessment: A Case Study on Shailmari River, Khulna. Journal of Geoscience and Environment Protection, 4, 2016, pp. 41-64.

[2] Gupta S., Kumar A., Ojha C.K., and Seth G., (2004) Chemical analysis of groundwater of Sanganer Area, Jaipur in Rajasthan. J Environ Monit Assess 102, 2004, pp.179–200.

[3] Billen G., Garnier J., and Lassaletta L., The nitrogen cascade from agricultural soils to the sea: modeling nitrogen transfers at regional watershed and global scales. Philosophical Transactions of the Royal Society B, 368,2013, pp.1–13.

[4] Sappa G., Ergul S., Ferranti F., Sweya L.N., and Luciani G., Effects of seasonal change and seawater intrusion on water quality for drinking and irrigation purposes, in coastal aquifers of Dares Salaam, Tanzania. J Afr Earth Sc 105, 2015, pp 64–84.

[5] Takeuchi T., Onodera S., Yamaguchi K. and Kitaoka K., Estimation of sedimentation rate and fresh-saline environment in a coastal alluvial plain, using boring cores of alluvium in the central part area of Seto Inland Sea, Japan. International Journal of GEOMATE, Vol.17, Issue 60, 2019, pp.70-75.

[6] Mitra B.K., Sasaki C., Enari K., Matsuyama N., and Pongpattanasiri S., Suitability Assessment of Shallow Groundwater for Irrigation in Sand Dune Area of Northwest Honshu Island, Japan. International Journal of Agricultural Research, 2, 2007, pp.518-527.

[7] Tomozawa Y., Onodera S. and Saito M., Estimation of groundwater recharge and salinization in a coastal alluvial plain and Osaka megacity, Japan using δ18O, δD, and Cl-. International Journal of GEOMATE, Vol.16, Issue 56, 2019, pp.153-158.

[8] Masato O., and Atushi T., A study of economic valuation of a passenger boat line in deficit - Case study of rapid boat between the osaki-kamijima island and the mainland in japan. Journal of the eastern asian society for transport studies, vol. 11, 2015.

[9] Ohta A., (2018) Evaluation of straightforward and rapid multi-element analyses of stream sediments for geochemical mapping in the remote islands of Japan,Seto Inland Sea region. Bulletin of the Geological Survey of Japan, vol. 69 (1), 2018 Bull. Geol. Surv. Japan, vol. 69 (1),2018, pp. 1–30.

[10] National Institute of Advance Industrial Science and Technology (AIST)., Geological Survey of Japan, https://www.gsj.jp/Map/EN/geology4-13.html, 2020.

[11] Sajil-Kamar P. J., Interpretation of Groundwater Chemistry using Piper and Chadha's Diagram: A Comparative Study from Perambular Taluk. Elexir Geoscience 54, 2013, pp. 12208-12211.

[12] Vetrimurugan E., and Elango L., Groundwater Chemistry and Quality in an Intensively Cultivated River Delta. Water Qual Expo Health 7, 2015, pp.125–141.

[13] WHO., Guidelines for drinking water quality, Geneva: World Health Organization, 2004.

[14] Freeze R. A., and Cherry J. A., Groundwater.Englewood Cliffs: Prentice Hall. 1979, pp. 604.

[15] Piper, A.M., A Graphic Procedure in the Geochemical Interpretation of Water- Analyses. Eos, Transactions American Geophysical Union, 25, 1994, pp.914-928.

[16] Gibbs R.J., Mechanisms controlling world water chemistry. Science 17, 1970, pp.1088–1090.

[17] Berner E. K., and Berner R. A., The global water cycle: Geochemistry and environment. Englewood Cliffs:Prentice Hall.1987.

[18] Kumar S. C., and Anderson H. W., Nitrogen isotopes as indicators of nitrate sources in Minnesota sand plane aquifers. Groundwater, 31, 1993, pp. 260–271.

[19] Tamma R.G., Srinivasa R.Y., Mahesh J., Surinaidu L., Dhakate R., Gurunadha R.V.V.S., and Durga P.M., (2015) Hydrochemical assessment of groundwater in alluvial aquifer region, Jalandhar District, Punjab, India. Environ Earth Sci 73, 2015, pp. 8145–8153.

[20] Alemayehu T., Dietzel M., and Leis A. (2010). Geochemical evolution of groundwater quality in shallow and deep wells of volcanic aquifer in Axum, Ethiopia. In Proceeding of XXXVIII IAH Congress, Krakow-Poland. ISSN0208-6336.

[21] Rusydi A. F., Saito M., Ioka S., Maria R. and Onodera S., Estimation of ammonium sources in Indonesian coastal alluvial groundwater using Cl- and GIS. International Journal of GEOMATE, Vol.17, Issue 62, 2019, pp.53-58.

[22] Alagbe S.A., Preliminary evaluation of hydrochemistry of the Kalambaina Formation, Sokoto Basin, Nigeria. Environ. Geol., 51, 2006, pp. 39-45.

[23] Edet A.E., and Okereke C.S., Hydrogeological and hydrochemical character of the regolith aquifer, northern Obudu Plateau, southern Nigeria. Hydrogeol. J. 13(2),2015, pp. 391-415.
[24] Ullma T., Croog V., Harpaz N., Sachar D., and Itzkowitz S., Progression of flat low-grade dysplasia to advanced neoplasia in patients with ulcerative colitis Gastroenterology Vol 125, Issue 5, 2003, pp.1311-1319.

[6th] Int. Conf. on Structure, Engineering & Environment (SEE), Kyoto, Japan, Nov.18-20, 2020, ISBN: 978-4-909106056 C3051

ECOSYSTEM-LEVEL WET TEST OF CAFETERIA DRAINAGE USING MICROCOSM SYSTEM

Kazuhito Murakami[1], Kakeru Ruike[2], Tomomi Tsuchiya[1,3], Kazuhi Obata[1,4], Ryuhei Inamori[2] and Yuhei Inamori[2]

Faculty of Advanced Engineering, Chiba Institute of Technology, Japan; [2]Bio-Eco Engineering Research Institute, Foundation for Advancement of International Science, Japan, [3]Kato Construction Co., Ltd., Japan, [4]BML Inc., Japan

ABSTRACT

In Japan, the introduction of the WET (Whole Effluent Toxicity) test is under processing in consideration, but this test may be different from the actual ecosystem phenomena because it is a single species test in spite of the natural ecosystem consists of multi species biota. In this study, we developed the WET test using microcosm (M-WET) which is a simulated ecosystem model and consisted of several species of producer, consumer and decomposer. Both the number of organisms as structural parameter and DO as functional parameter after cafeteria drainage addition were analyzed by branched-type ANOVA, and the microcosm no observed effect concentration (m-NOEC) and toxicity unit (TU) were calculated. As result, the m-NOEC of cafeteria drainage was calculated as 5% and the TU was as 10, and assessed that the cafeteria drainage was discharged safely. It is important to assess the complex influences of chemical agents, such as surfactants, medicines and so on, to the environment. To conduct such comprehensive assessments, M-WET tests should be used to examine drainage with collecting total toxicity test data through single-species tests of chemical contaminants in environmental water.

Keywords: Microcosm, Whole effluent toxicity (WET) test, Branched-type ANOVA, Cafeteria drainage, m-NOEC

INTRODUCTION

Currently, introduction of WET (Whole Effluent Toxicity) test is being considered in Japan, but it is difficult to believe that the actual ecosystem can be represented by the test method by current single species as typified by small crustaceans *Daphnia magna* as primary consumer and small fish *Danio rerio* as secondary consumer [1][2]. Therefore, by introducing microcosms, which is a simulated ecosystem including producers, predators, and decomposers, into the WET test, more realistic evaluation can be considered possible [3].

In this study, we conducted WET test, which is a method of managing the influence on ecological systems for actual drainage, with a microcosm, which is a model ecosystem that imitates natural ecosystem to calculate the microcosm no observed effect concentration (m-NOEC) and toxicity unit (TU) from the experimental results.

NECESSITY OF MICROCOSM TEST FOR WET

Impact assessments at the ecosystem level utilizing aquatic model ecosystems, including a microcosm, are well understood, but focus on the WET test method utilizing a microcosm as a wastewater management method is needed. In parallel with a single-species test using species belonging to different niches, such as fish, crustaceans, and algae, microcosm tests are positioned as multiple-species tests. They may be correlated with natural ecosystems, and it is essential to construct these systems as comprehensive test methods based on ecological impact assessment.

The WET test is a method that evaluates toxicity, including multiple effects, because it is targeted at test waters containing multiple chemical substances rather than being used for evaluations of the toxicity of individual chemical substances [1][2]. However, although we use individual species (fish, crustaceans, and algae) located in different niches in the food chain for the assay, it is a single-species test only. It is not a test method that accounts for material cycles, energy flow, or biological interactions, which are the basic elements of natural ecosystems [4]. The microcosm is a system that includes multiple species in coexistence and contains material circulation, energy flow, and biological interactions [5][6]. Therefore, the microcosm makes it possible to evaluate the risks associated with added chemical substances at the ecosystem level. The safety factors for the ecological effects of chemical substances obtained by the microcosm test were supported by

the high correlation observed between the microcosm test and mesocosm (natural ecosystem) test obtained from the Environmental Research Comprehensive Promotion Fund (2009–2011) and the New LRI (2012–2014) [4]. Therefore, we determined that it is possible to use the microcosm test to evaluate the effects of chemical substances in an ecosystem with higher precision and with less dispersion than in the conventional single-species tests, such as the HC5 method. Consequently, it is possible to calculate more realistic values of the PNOEC for natural ecosystems using the microcosm.

Microcosms are highly correlated with natural ecosystems and can be regarded as models containing the basic components and characterized by the basic principles of natural ecosystems [7]. From this fact, it is considered that a more realistic estimate of the NOEC can be obtained using a microcosm as compared with the current single species test that does not account for material cycling, energy flow, or biological interactions [8]. In the ecosystem impact assessment of wastewater containing various chemical substances, comprehensive tests were conducted to introduce the ecosystem model, a multiple-species test with a food chain and energy flow, simultaneously with the single-species test. A series of test methods were constructed, making it possible to evaluate the degradability and persistence of chemical substances contained in wastewater and the collapse and restoration of ecosystem functions [9]. The microcosm test can be performed at a lower cost than the WET test with commonly used single species (fishes, crustaceans, and algae).

The microcosm has already been subcultured for nearly 40 years and is easy to use by researchers accustomed to environmental microorganism testing who can master the microbial culturing procedures. It is also easy to use after short-term training. Additionally, a series of tests are possible without using expensive culturing tools or measurement instruments. The position of the microcosm test within the WET test is shown in Fig.1. The foundation of a certain ECETOC method and the HC5 method conventionally includes the evaluation of independent chemical substances in toxicity tests using single species, and the current WET test also uses single species for toxicity tests on the composition of chemical substances. The interactions between species constitute the ecosystem and drive the cycling of materials and energy flow; no single species is able to exist alone. It is therefore insufficient to evaluate the influence of added chemical substances at the ecosystem level using a single-species test. However, the model ecosystem consists of combinations of species, and multiple microcosm tests contain the basic elements of ecosystems, such as biological interactions, cycling of materials, and energy flow between

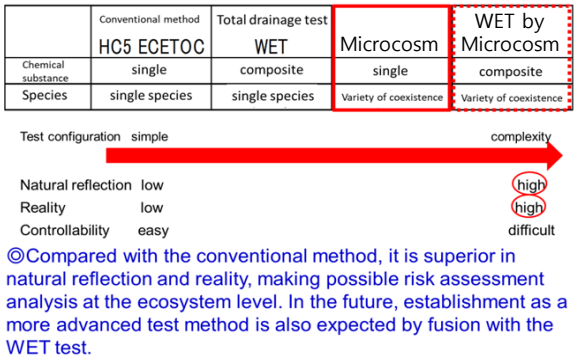

Fig.1 Placement of microcosm test for WET

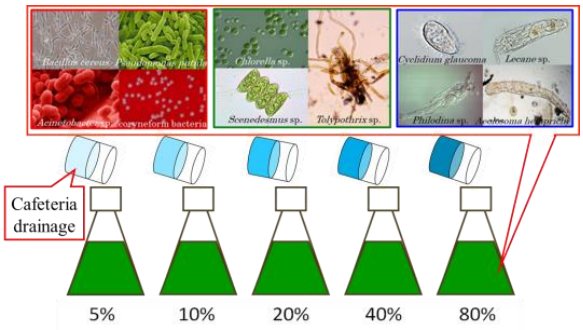

Fig.2 Addition procedure of test effluent

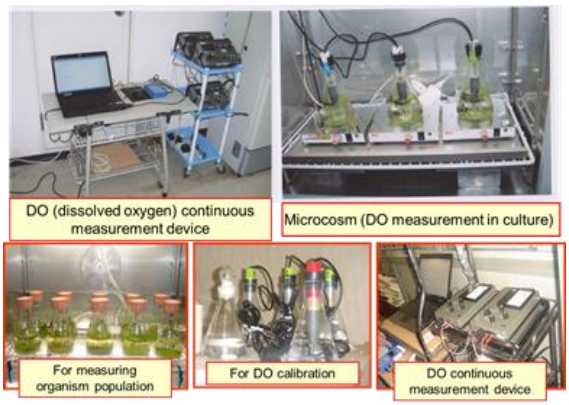

Fig.3 Microcosm N-system apparatus

biological species.

Using the microcosm, it is possible for impact assessments at the ecosystem level to reflect the natural ecosystem, advancing the WET test as well evaluating single chemical substances.

MATERIALS AND METHODS

Microcosm

A gnotobiotic-type flask-size microcosm system (N-system) [3][5][6] applied in this study consisted of combination of several species of four dominant bacteria as degraders, *Bacillus cereus*, *Pseudomonas putida*, *Acinetobacter* sp., coryneform bacteria, two green algae *Chlorella* sp., *Scenedesmus quadricauda*

and one filamentous alga *Tolypothrix* sp as producer, and one species of protozoan ciliates *Cyclidium glaucoma*, two metazoan rotifer *Lecane* sp., *Philodina erythrophthalma* and one metazoan oligochaeta *Aeolosoma hemprichi* as consumer. Since this microcosm is a model microbial ecosystem with high stability and reproducibility, it is suitable for experiment [3]. The biomass (individual number) of each microorganism in the stationary phase are maintained about 1.1×10^6 N/ml in bacteria, 1.1×10^5 N/ml in *Chlorella* sp., 5.3×10^3 N/ml in *Scenedesmus quadricauda*, 8.0×10^2 cm/ml in *Tolypothrix* sp., 6.0×10^1 N/ml in *Cyclidium glaucoma*, 1.3×10^2 N/ml in *Lecane* sp., 1.1×10^1 N/ml in *Philodina erythrophthalma*, and 6.0 N/ml in *Aeolosoma hemprichi*, respectively.

Preparation of Test Effluent

According to the testing procedure described in the 1997 Sewage Examination Method (Japan Sewage Works Association, Volume III Biological Examination, Chap.1 Biological Examination, Sect.10, Ecosystem Impact Assessment Testing) [10], the ratio of TP medium and test effluent should be set to 0, 25, 50, 75, or 100 %. Remove contaminants by filtering with a 0.45 μm size mesh filter, and add the filtrate to the microcosm. The time of addition is during the stationary phase (16th day of cultivation). The water quality of the test effluent should be analyzed if necessary. The procedures of microcosm-WET test are shown in Fig.2.

Addition of Test Effluent

Addition of test effluent to the microcosm is conducted on the 16th day, when the microcosm has reached a stationary phase. For experiments in which chemical substances were added on the 16th day, the effect of the test effluent on the microcosm and the constituent microbiota may or may not allow for the retention of species diversity (*i.e.*, a stable ecosystem may or may not be recovered). The structural parameter (microbial population) and the functional parameter (P/R ratio) should be measured to evaluate the effects of the test effluent.

In the conventional microcosm experiments, chemical addition is usually performed on the 16th day after the cultivation began, when the system stabilizes. In the WET test using the microcosm, the medium in the flask must be exchanged for wastewater, which is then added. At that time, it is necessary to separate the organisms and the culture medium, and a fresh medium containing wastewater is added instead of the extracted medium. The addition of the attached microcosm standard medium increases the number of individuals in the steady state. This is because organic substances that feed microorganisms are already consumed. In this case, it is impossible to compare it with the non-additive system (control), so an appropriate medium was developed with reference to the amount of organic matter added at the time of wastewater addition.

Substance Concentration

Addition of a substrate was conducted by replacing the culture medium in the flask with wastewater. A fresh medium containing wastewater was added as a substitute for the extracted medium. However, when the standard microcosm medium was added as a new medium, the number of individuals in the steady state increased. Therefore, as a new medium, the amount of peptone in the medium was adjusted to 0, 5, 10, 20, and 40 mg/l and then added into the medium. The impact of each culture medium was assessed from both the P/R ratio as the functional parameter and the abundance of microbiota as the structural parameter in the microcosm. The environmental impact and ecological risk were estimated by comparing the treated microcosms with the no-addition system (control) in both assessment methods. With respect to the structural parameters, the abundance of *Cyclidium glaucoma*, a ciliate primary predator, was greatly increased by increasing the amount of peptone in the medium; there was no major change in the abundance of other species in the microcosm. From the P/R ratio, which is the functional parameter, no change was observed when compared to the no-addition system (control) as shown in Fig. 9.4. From this, the system was considered stable unless wastewater was added. Statistical analysis of the DO concentration was performed. The slope (a) and the coefficient of variation (cv) were obtained assuming that the microcosm was normally distributed. If they fell within the range of $\pm$ 34.13 % for each, it was considered that there was no influence. Since the range of $\pm$34.13 % of the slope of the DO was $0.0028 \leqq a \leqq 0.0056$, it was considered as having no influence on the medium containing only 2 mg/l. Additionally, since the range of $\pm$34.13 % of the coefficient of variation of the DO was $0.10 \leqq cv \leqq 0.20$, it was considered as having no effect on the medium containing 0 to 20 mg/l. Therefore, a medium containing 2 mg/l of peptone was considered appropriate for adding wastewater in the microcosm-WET test [9][11].

Microcosm WET Test

As shown in Fig.3, for microcosm culture, 200 ml of TP medium adjusted to a concentration of 100 mg/l of polypetone was placed in a 300 ml volume Erlenmeyer flask, inoculated with 10 ml of subcultured microcosm as a seed, 25 °C, 2,400 lux (bright 12 hr./dark 12 hr.) and without shaking.

Treated water of cafeteria drainage from the wastewater treatment facility in the university campus filtered using a membrane filter with a caliber of 0.45 μm. Thereafter, on the 16th day, which is the stable period of the microcosm, it was added to have concentrations of 0, 5, 10, 20, 40 and 80%.

Assessment Method

Impact risk assessment of each concentration was estimated from the DO change in the microcosm was continuously measured sequentially by the DO meter, and the transition (functional parameter) of P (production), R (respiration) and P/R ratio was obtained.

Simultaneously, sampling was started from the microcosm on 0, 2, 4, 7, 14, 16, 18, 20, 23 and 30 days after the start of culture, and plankton was sampled under a light microscope using a plankton counter and the transition (structural parameter) of the number of organisms constituting microorganisms was observed. Also, "Branched-type ANOVA" was performed on the change over time of functional parameters and structural parameters. As shown in Fig.4, in the branched-type ANOVA evaluation was performed from two items, "group" which is the variance analysis by all the values of each system and "interaction" which is an analysis of variance over time [3].

In the functional/structural parameter, the highest concentration among the concentrations not affected as a result of the branched-type ANOVA was taken as the maximum no-effect concentration (m-NOEC), and the toxicity unit (TU) was calculated from the following equation (1). The safety factor is proposed as 200 by the former investigation [4][12].

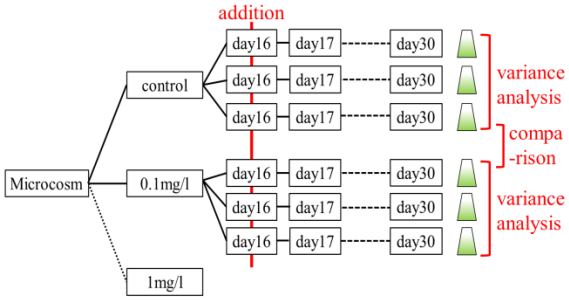

Fig.4 Outline of branched-type ANOVA

$$\text{Toxicity unit (TU)} = 100 / (\text{m-NOEC} \times 200) \quad (1)$$

RESULTS AND DISCUSSION

Water Quality of Cafeteria Drainage

The water quality of the treated water from the treatment facility as tested drainage effluent in the university campus was pH: 7.18-7.21, COD: 15.2-17.2 mg/l, T-N: 2.68-12.4 mg/l, T-P: 0.13-0.98 mg/l, SS: 9.40-18.5 mg/l, Cl^-: 14.2-15.7 mg/l, respectively.

Functional Parameter Analysis

Time course of DO and P/R ratio (functional parameter) in microcosm under each test condition were shown in Fig.5. In the evaluation by DO and P/R ratio (functional parameter), the amplitude of DO decreased as the added concentration became higher, and the activity in the microcosm was lower. It is thought that residual chemical substances are contained in the cafeteria drainage. However, the P/R ratio was stable around 1 at all added concentration. This is probably because the activities of phytoplankton and zooplankton have both

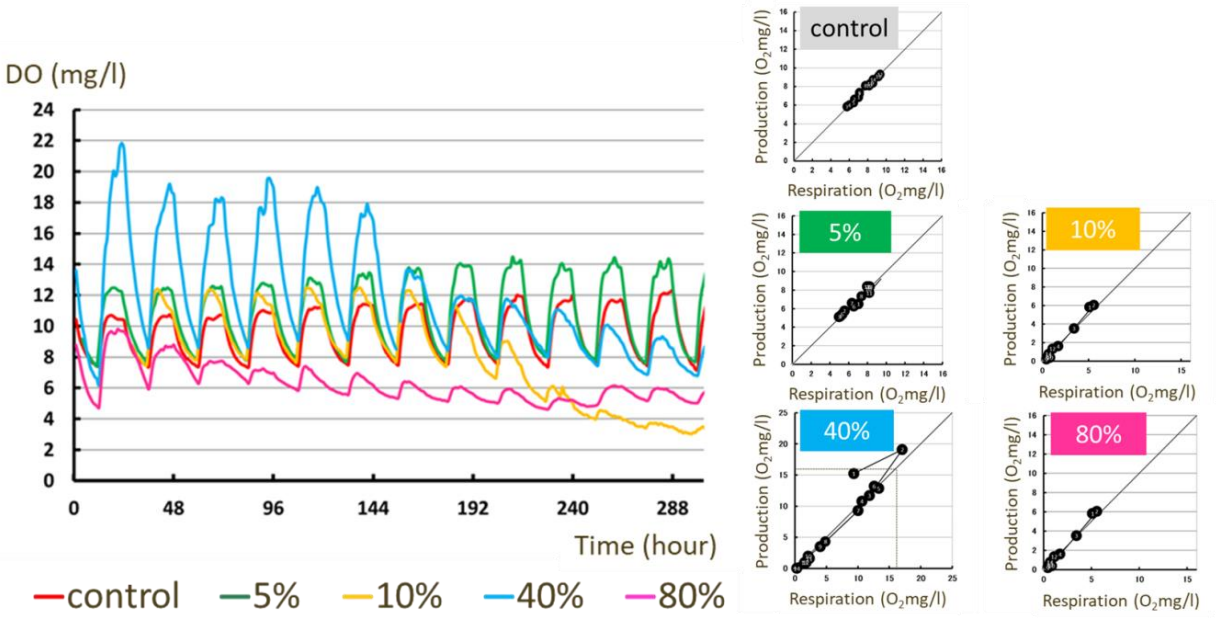

Fig.5 Time course of DO and P/R ratio (functional parameter) in microcosm under each test condition

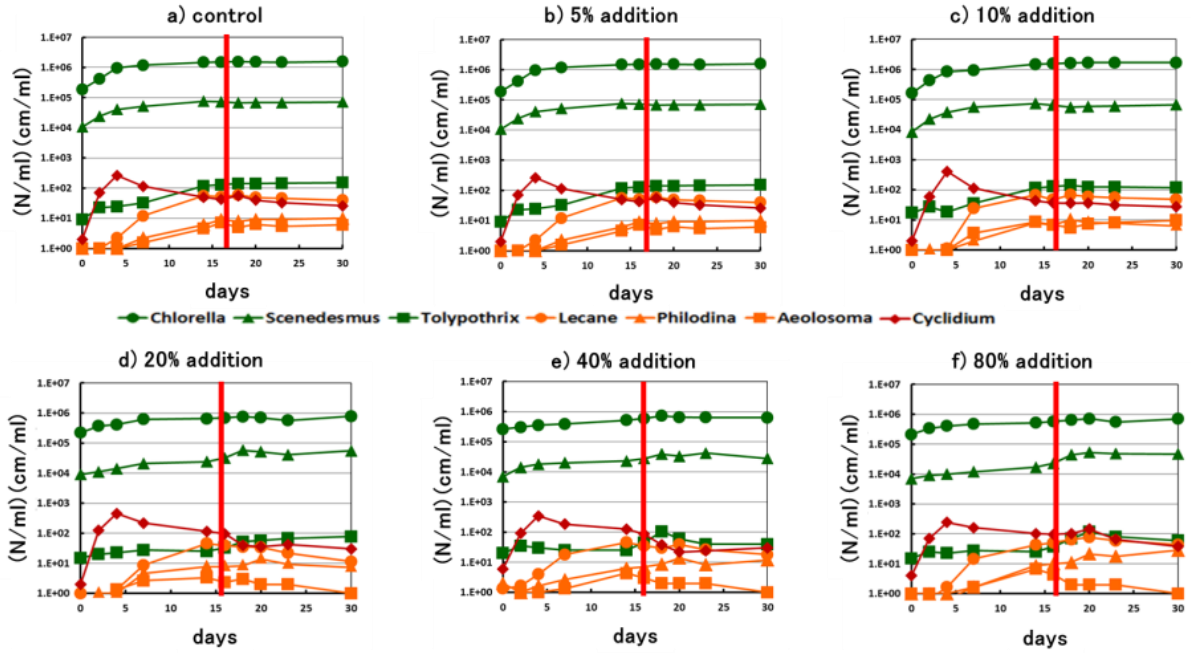

Fig.6 Time course of individual number of microorganism (structural parameter) in microcosm under each test condition

decreased. In functional parameters, the P/R ratio, respiration, and production were tested by branched-type ANOVA and the presence or absence of influence was determined. As a result, m-NOEC was evaluated to be less than 5 %.

Structural Parameter Analysis

Time course of individual number of plankton (structural parameter) in microcosm under each test condition were shown in Fig.6. Two zooplankton species (*Lecane* sp. and *Aeolosoma hemprichi*) decreased in 20, 40, 80% addition system in the evaluation by the number of individuals (structural parameters), but did not exterminate. It was considered that these were influenced by chemical substances remaining in effluent as well as functional parameters. However, since all the microorganisms did not exterminate but coexisted, the ecosystem in the microcosm was maintained. There was no influence in 5 and 10 % addition system.

Statistical Analysis for Ecotoxicological Assessment

In the evaluation by DO and P/R ratio (production/respiration ratio) as the functional parameter, the amplitude of DO decreased as the added concentration became higher, and the activity in the microcosm became lower. It is thought that residual chemical substances were contained in the drainage. However, the P/R ratio was stable around 1 at all added concentration. This is probably

Table 1 Summary of evaluation result

	5%	10%	20%	40%	80%
Function parameters	×	×	×	×	×
Structural parameters	○	○	×	×	×
Evaluation	×	×	×	×	×

○・・No effect ×・・Effected

because the activities of phytoplankton as producer and zooplankton as consumer have both decreased. For the functional parameters, the P/R ratio was significant-tested by branched-type ANOVA, and the influence was determined. Based on the statistical processing result of the functional parameters, m-NOEC which is the maximum no-effect concentration was evaluated to be present in a range lower than 5% as shown in Table 1. The toxicity unit (TU) was calculated as 100 / (0.05 × 200) = 10. Here, 200 is the safety factor for microcosm test. This value means that 10 times dilution is necessary to discharge safety to the environment, but 10 times dilution is expected after discharge by natural purification. Considering the above, the cafeteria drainage in the university campus was evaluated as being properly treated.

It is important to assess the complex influences of chemical agents, such as surfactants and medicines, on the environment. To conduct such comprehensive assessments, microcosm-WET tests should be used to examine drainage by collecting total toxicity test data through single-species surveys of chemical contaminants in environmental water. It is thought that more details for high-risk materials can be analyzed by the microcosm-WET test with a

general comparison analysis. Additionally, because the microcosm-WET test offers high precision at a low cost, and it is expected that the correlation between the natural ecosystem and the microcosm is high, the estimated NOEC is more realistic than that derived from single-species tests, and the prediction of the behavior of the natural ecosystem is more practically enabled.

It can also be expected that wastewater management can greatly contribute to the remediation of the environmental impacts of effluents by introducing the microcosm-WET test of the Ministry of the Environment, Japan.

CONCLUSIONS

A gnotobiotic-type flask-size microcosm system (N-system) was applied to assess the whole effluent toxicity (WET) of cafeteria drainage, which consisted of several species of four dominant bacteria as decomposer, two green algae and one filamentous alga as producer, and one species of protozoan ciliates, two metazoan rotifer and one metazoan oligochaeta as consumer.

In the evaluation by DO and P/R ratio (production/respiration ratio) as the functional parameter, the amplitude of DO decreased as the added concentration became higher, and the activity in the microcosm became lower. It is thought that residual chemical substances were contained in the drainage. However, the P/R ratio was stable around 1 at all added concentration. This is probably because the activities of phytoplankton and zooplankton have both decreased.

In the functional parameters, the P/R ratio was significant-tested by branched-type ANOVA, and the influence was determined. Based on the statistical processing result of the functional parameters, m-NOEC (microcosm No Observed Effect Concentration) was evaluated to be in the range lower than 5 %.

The toxicity unit (TU) was calculated as 100 / (0.05 × 200) = 10, and the cafeteria drainage from the university treatment facility was evaluated as being properly treated.

From above, microcosm WET test is considered to be essential for ecosystem-level environmental impact risk assessment of various drainage.

ACKNOWLEDGEMENT

Special thanks to late Dr. Yasushi Kurihara, emeritus professor of Tohoku University, and Dr. Katsura Sugiura, emeritus professor of Sagami Women's University, for their kind and essential discussion in microcosm experimental method.

REFERENCES

[1] United States Environmental Protection Agency, Method Guidance and Recommendations for Whole Effluent Toxicity (WET) Testing, 40 CFR Part 136, EP 821-B-00-004, 2000.

[2] Tatarazako N., The Newest Domestic and Overseas Trend of Assessment and Regulation of Effluent Water using Bioassay –Overseas Operation Case to Japanese WET Test Introduction", Tokyo, NTS, 2014. 322pp. (in Japanese)

[3] Inamori Y., ed,, Microcosm Manual for Environmental Impact Risk Assessment: From Chemicals to Whole Effluent Toxicity (WET), New York, Springer, 2019, 258pp.

[4] Inamori Y., Murakami K., Kakazu K., Inamori R., Kanzo Y., Shibata K., Amemiya T. and Sugiura K., Development of Environmental Impact Risk Assessment Method using Microcosm for OECD Standard Test, Proceedings of 20th Symposium on Japan Society of environmental Toxicology in Toyama, 2014. (in Japanese)

[5] Kurihara Y., Finite Ecology –A System of Stability and Coexistence-, Tokyo, Iwanami Shoten, 1975, 187pp. (in Japanese)

[6] Kurihara Y., Stability in Ecological Microcosm, Proceedings of Japan Academy, Series B, Physical and Biological Sciences, Vol.80, No.7, 2004, pp.327-335.

[7] Beyers R. J., and Odum H. T., Experimental Microcosms, New York, Springer-Verlag, 1993, 545pp.

[8] Graney, R. L., Kennedy, J. H. and Rodjers, J. H. Jr., Aquatic Mesocosm Studies in Ecological Risk Assessment, Boca Raton, CRC Press, Lewis Publishers, 1994, 736pp.

[9] Tsuchiya T. and Murakami K., Ecosystem Level Whole Effluent Toxicity Test using Microcosm System, Papers on Environmental Information Science, Vol.33, 2019, pp.31-36. (in Japanese)

[10] Japan Sewerage Works Association, Wastewater Examination Method -FY2012-, Tokyo, 2012, 819pp. (in Japanese)

[11] Tsuchiya T., Murakami K., Inamori R. and Inamori Y., Development and Verification of Microcosm-WET Test on Basal Medium Concentration, Proceedings of IWA World Water Congress & Exhibition 2018, Tokyo, 2018, online.

[12] Sugiura K., Effects of Chemicals on Microcosms: Comparison with the NOECs in Experimental and Natural Ecosystems, Japanese Journal of Environmental Toxicology, Vol.13, 2010, pp.13-22.

6th Int. Conf. on Structure, Engineering & Environment (SEE), Kyoto, Japan, Nov.18-20, 2020, ISBN: 978-4-909106056 C3051

RIVER ENVIRONMENT EVALUATION BY WATER QUALITY, ATTACHED DIATOM AND MACROBENTHOS IN BOSO PENINSULA, JAPAN

Kazuhito MURAKAMI[1], Haruna NIIDA[1],Tsuyoshi DOYAMA[1] and Kenji WATANABE[2]
[1]Chiba Institute of Technology, Japan,
[2] Tokyo Metropolitan Kohoku High School, Japan

ABSTRACT

To evaluate river environment in Boso peninsula of Japan, Koito river (FY2009), Obitsu river (FY2010), Yoro river (FY2011), Inba marsh inflow and outflow rivers (Shinkawa river, Hanami river, Kashima river) (FY2012, 2016), Tega marsh inflow and outflow rivers (Ohori river, Ohtsu river, Someiiriotoshi, Tega river) (FY2013), Kuriyama river (FY2013), Isumi river (FY2014), Sakuta river (FY2015), Ichinomiya river (FY2016), Minato river (FY2017), Kamo river (FY2018), Maruyama river (FY2019), Murata river (FY2019), and their watershed were researched their water quality, attached diatom and macrobenthos. The survey were carried out four times a year at each of three to seven points of each river seasonally. BOD (water quality), DAIpo (attached diatom) and ASPT (macrobenthos) were measured and calculated. The Boso peninsula was shown to be divided into three areas: the Northwestern (urban area), the Northeastern part (plains), and the Southern part (hilly area). The Northwestern part (urban area) and Northeastern part (plains) were evaluated as "polluted", and the Southern part was evaluated as "clean", and it was shown that rich nature was left in the Boso hills. Note that, there was the great gap between the evaluation by macrobenthos and attached diatom. The Northwestern part, where large cities are gathered, were evaluated as "polluted". Despite the large city does not exist, the Northeastern part was assessed as "polluted". It was considered due to nonpoint sources from huge paddy fields along Kujyukurihama coastal line. ECI_{eco} as the overall index, which comprehensively evaluates attached diatoms and benthos, evaluated the hilly area as clean.

Keywords: River environment, Water quality, Attached diatom, Macrobenthos, Boso peninsula

INTRODUCTION

Utilization of biological indicators for water environmental evaluation is different from water quality indicator by chemical analysis. It has the advantage of reflection a relatively long-term environmental change and easy to convert as an influence to human. On one hand, there is a big problem that they require skill in the classification, identification and counting and susceptible to the influence of analysis of individual differences and method of investigation.

In Japan, when evaluating rivers, chemical water quality survey is main investigation but biological water quality survey is not, as well as in Chiba Prefecture. Then, it is thought that comprehensive biological water quality survey in Chiba Prefecture will be possible by using attached diatom as a producer and benthos as higher-end consumers [1].

In this study, the river environment evaluation using the biological index was carried out for the river which flows down the Boso Peninsula, and the river environment map in the Boso Peninsula was made, and it aimed at the construction of the bio-environment information of Chiba Prefecture at the same time. Also, ECI_{eco} (Environmental Condition Index of Ecosystem) was devised and calculated. It is indicators that express attached diatom and benthos integrally.

RESEARCH METHODS

Rivers to survey

Fig.1 shows the survey river. To evaluate river environment in Boso peninsula of Japan, ①Koito river (FY2009), ②Obitsu river (FY2010), ③Yoro river (FY2011), ④Inba marsh inflow and outflow rivers (Shinkawa river, Hanami river, Kashima river) (FY2012, 2016), ⑤Tega marsh inflow and outflow rivers (Ohori river, Ohtsu river, Someiiriotoshi, Tega river) (FY2013), ⑥Kuriyama river (FY2013), ⑦Isumi river (FY2014), ⑧Sakuta river (FY2015), ⑨Ichinomiya river (FY2016), ⑩Minato river (FY2017), ⑪Kamo river (FY2018), ⑫Maruyama river (FY2019), ⑬Murata river (FY2019), and their watershed were researched their water quality, attached diatom and macrobenthos. It was carried out four times a year at each of three to seven points of each river by season.

Water quality survey

The surface water was collected with a heyroth water sampler and measured BOD according to JIS-

K0102 [2] of the factory wastewater test method and the ocean observation guidelines [3].

Attached diatom

Attached diatom was collected using a quadrate frame of 5 cm × 5 cm from the bottom of the river, and we classified, identified, and counted using a biological microscope (Nikon Ecripse E 800).

DAIpo (Diatom Assem blage Index to organic water pollution) and RPId (River Pollution Index based on DCI) were calculated, and the river environment was evaluated.

DAIpo

It is an organic pollution index based on attached diatom community, and it is used as a biological index for organic contamination common to still water areas (lakes) and running water areas (rivers) [4].

We calculated Eq. (1) after identifying what species category the attached diatom belongs to.

$$DAIpo = 50 + 0.5(A - B) \quad (1)$$

Here,

A: The sum of the relative frequency (%) of all good clear water species at the survey site

B: The sum of the relative frequency (%) of all good pollution species at the survey site

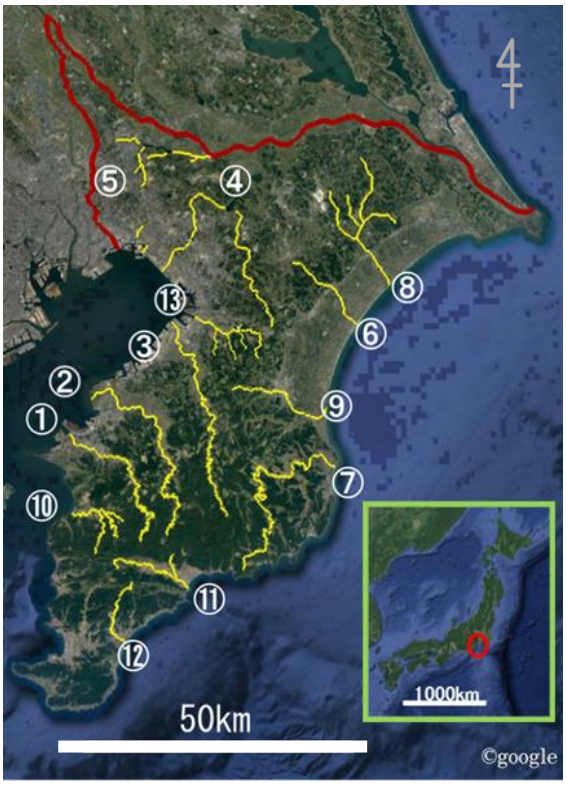

Fig. 1 Survey rivers in this study

Table 1 shows the relationships between DAIpo, BOD, and pollution class

RPId

RPId is a river total evaluation value based on DAIpo, which is possible to compare the pollution of rivers different flow path length [4]. It was calculated the area of the trapezoid created by plotting the value of DAIpo on the graph and drawing a perpendicular from the plot and flow path length, and calculated from Eq. (2)

$$RPId = S/L \quad (2)$$

Here,

S: The area of figure consisting of DAIpo (horizontal axis) at each survey site flow path channel length (vertical axis) of the survey river

L: The flow path length of the river surveyed (Distance between the most upstream point and the most downstream point among the surveyed points)

Benthos

The benthos was collected using D-frame net or Ekman-Birge bottom sampler, and classified, identified, and counted using a substantive microscope (Nikon smz445). The ASPT (Average Score Per Taxon) value from the BMWP score (Biological Monitoring Working Party score) was calculated, and the river environment was evaluated [5][6].

ASPT

After classifying and identifying benthos into families, we applied those benthos to a score table that classified the benthos of the 62 families into scores of 1-10 [7]. ASPT was calculated by Eq.(3).

$$ASPT = TS / TF \quad (3)$$

Table 1 Relationship between DAIpo, BOD, and pollution class

DAIpo	BOD	The pollution class
100~85	0~0.0625	Destitute water
85~70	0.0625~1.25	B-Oligosaprobic water
70~50	1.25~2.5	α-Oligosaprobic water
50~30	2.5~5.0	B-Mesosaprobic water
30~15	5.0~10.0	α-Mesosaprobic water
15~0	>10	Palysaprobity water

Table 2 Evaluation of water environment by ASPT value (provisional)

ASPT value	Expression(Provisional)
≧7.5	Clear water
6~7.4	Somewhat clean water
5~6	Somewhat polluted water
<5	Polluted water

Table 3 Evaluation of water environment by ECI_{eco}

ECI_{eco}	Expression
9～10	Clean water
8～9	
7～8	
6～7	
5～6	
4～5	
3～4	
2～3	
1～2	
0～1	Polluted water

Here,
TS: Total BMWP score of appeared benthos
TF: Total family number of appeared benthos

The survey point is evaluated from 1 to 10 points by the ASPT value (Table 2).

ECI_{eco}

As the overall index, ECI_{eco} (Environmental Condition Index of Ecosystem) was calculated by DAIpo (attached diatom) and ASPT value (benthos) [8]. ECI_{eco} expresses biological interaction as the multiplication of each pollution class. ECI_{eco} was devised as an index that comprehensively expresses both. Each evaluation result is converted into 10 classes and calculated. ECI_{eco} was calculated from Eq. (4).

$$ECI_{eco} = (C_{diatom} \times C_{benthos})^{1/2} \quad (4)$$

Here,
C_{diatom} : Evaluation classification based on DAIpo
$C_{benthos}$: Evaluation classification based on ASPT value

The result of 10 is clean and 0 is dirty (Table 3).

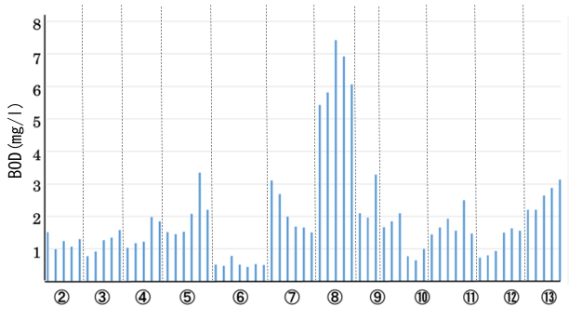

Fig.2 BOD of each river (The numbers below correspond to Fig.1.)

RESULTS

Water quality

Figs.2 and 3 show the result of BOD and environmental condition map of Boso peninsula based on BOD.

From Fig.2, BOD was highest in the Sakuta river ⑧ and lowest in the Kuriyama river⑥ in the Boso Peninsula. From Fig.3, urban and plain area were evaluated as “slight clean” by BOD.

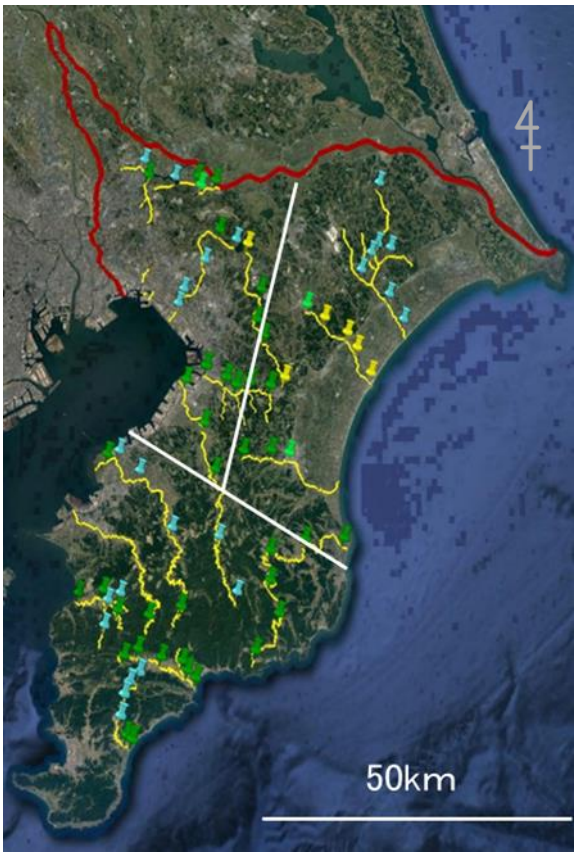

Fig.3 Environmental condition map of Boso peninsula based on BOD, divided into three areas.

Attached diatom

Figs.4 and 5 show the result of RPId and environmental condition map of Boso peninsula based on attached diatom.

The Boso peninsula was shown to be divided into three areas, that is the Northwestern (urban area), Northeastern (plains) and Southern parts (hilly area) [9]. The Northwest (urban area) and the Northeast (plains) were estimated as "dirty" and the South (hilly area) was estimated as "clean", and it was shown that rich nature was left in the Boso hills. The Minato river ⑬, which flows down the southern part of the Boso Peninsula, was evaluated as ß-Oligosaprobic water (clean) only in the Boso Peninsula.

Benthos

Fig.6 shows environmental condition map of Boso peninsula based on benthos.

Like attached diatoms, the Boso peninsula was shown to be divided into three areas, that is the Northwestern (urban area), Northeastern (plains) and Southern parts (hilly area) [9]. In addition, there was the great gap between the evaluation benthos and attached diatom.

As for benthos, it was shown that the southern part was further divided into the southwestern part and the

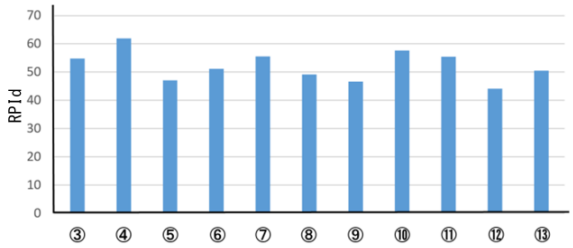

Fig.4 RPId value in each research point (The numbers below correspond to Fig.1.)

southeastern part. The southwestern part was in the mountains and the river mouth was also rich in nature. The southeastern part was evaluated somewhat polluted water to polluted water, because the residential area and the fields were expanding along the river mouth, it was the effect of domestic wastewater and agricultural wastewater.

ECI_{eco}

Figs.7 and 8 shows the result of ECI_{eco}.

The results of ECI_{eco} showed that the values in the south (hilly area) were higher than those in the northeast (plains) and northwest (urban areas). The comprehensive evaluation of attached diatoms and benthos also showed that the southern part (hilly area)

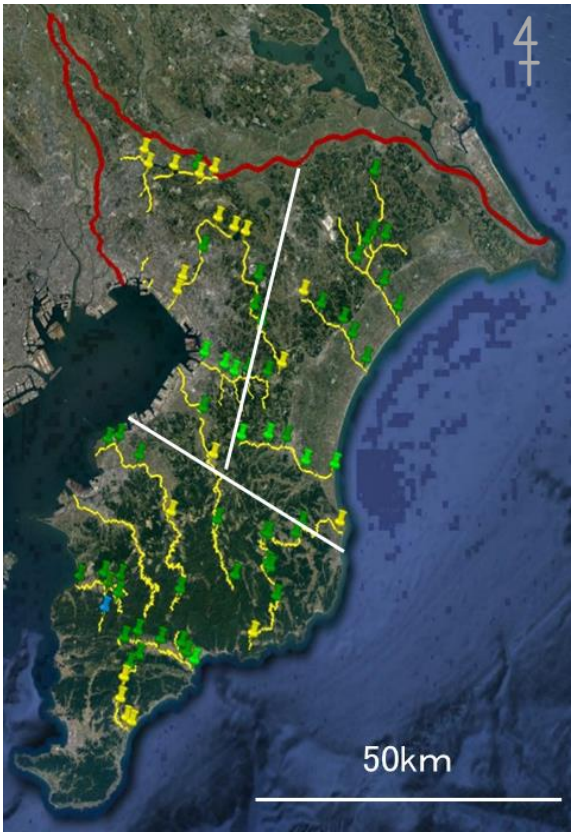

Fig.5 Environmental condition map of Boso peninsula based on attached diatom, divided into three areas.

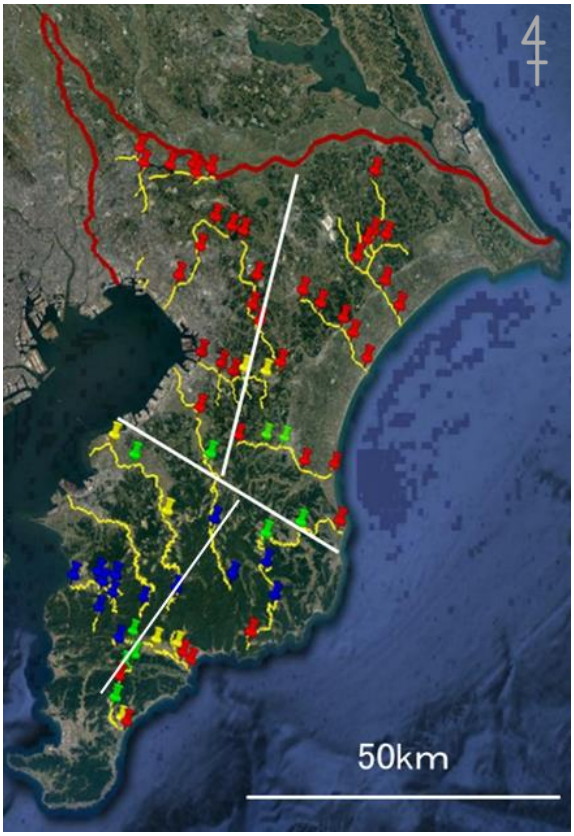

Fig.6 Environmental condition map of Boso peninsula based on benthos, divided into four areas.

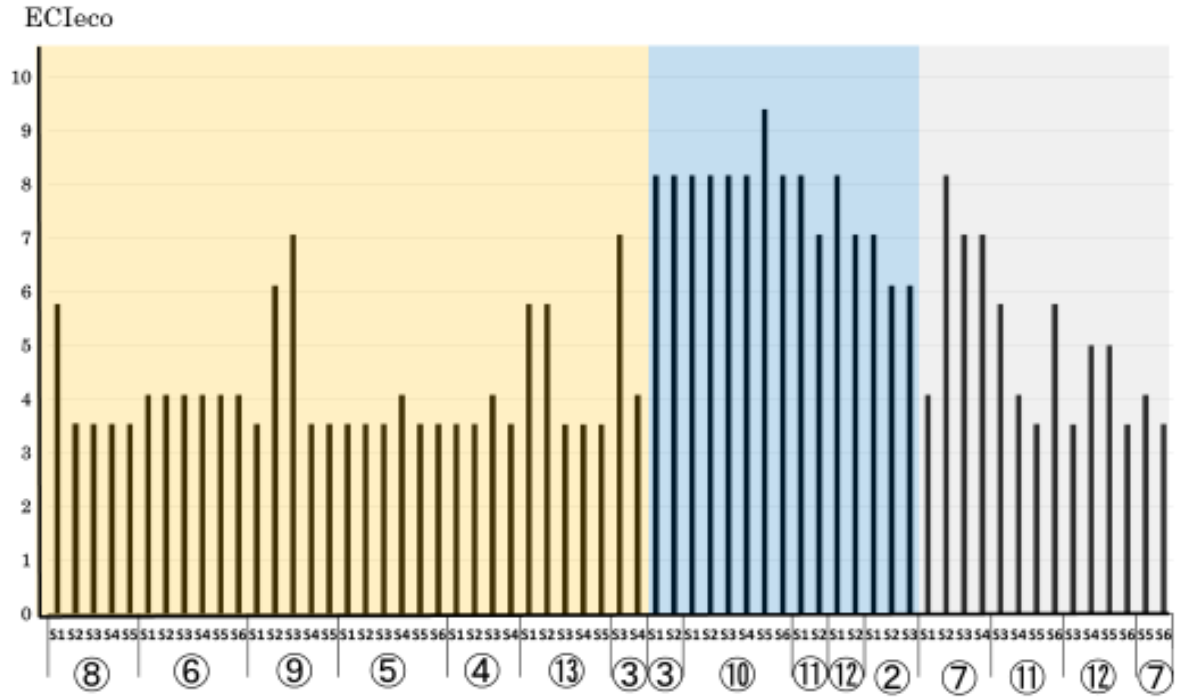

Fig.7 ECI_{eco} in each research point (The numbers below correspond to Fig.1.)
yellow: North part (plains and urban area), blue: hilly area, white: coastal area

was clean. For each river, many rivers had lower values from upstream to downstream, and it was shown that there is a tendency for pollution especially from upstream to downstream in the south (hilly area).

DISCUSSION

The river environment map of the Boso Peninsula

The Northwest (urban area), where many large cities are gathered, were evaluated as "polluted". It was considered due to the pollution caused a vibrant urban economy. Despite the big city does not exist, Northeast (Plains) was assessed as "polluted". It was considered nonpoint sources from paddy fields along Kujyukuri because fluctuation of pollution connected farm work. BOD becomes somewhat clean reputation in the Northwest (urban areas), and Northeastern (Plains), and BOD and biological indicators were not consistent. The water quality is evaluated from instantaneous sampling, however, biological indicators are for the evaluation of long-lasting water quality of river. Attached diatoms reflect the water quality, and benthos reflect the sediments pollution condition.When the water quality was improved, the quality of the water changed immediately but the bottom sediment took a long time to improve, so the evaluation results were different. Therefore, it may show improvement from pollution state.

Furthermore, ECI_{eco} as the overall index was shown to be lower in the downstream. ECI_{eco} resulted closer to DAIpo than ASPT value but, the trend was similar to ASPT value. Also, it was not evaluated as "Polluted water". The value exceeded 3 at all points. Therefore, there are no rivers that are rated "dirty" in the Boso Peninsula. It seems to be in the range of a little dirty to a little clean.

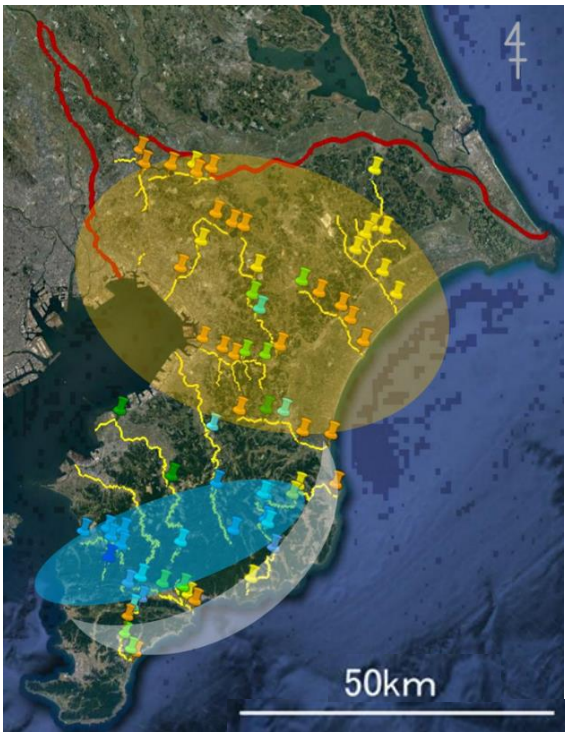

Fig.8 Environmental condition map of Boso peninsula based on ECI_{eco}, divided into three areas.

In the future, using assessment by existing individuals, population and water quality and DNA analysis (eDNA), more detailed environmental assessment will be conducted considering quality/quantity of existing creature and construction/structure/function of ecosystem. While continuing to accumulate data, it try to create new indicators that comprehensively evaluate water quality, attached diatoms, and benthos.

CONCLUSIONS

1) The Boso peninsula was shown to be divided into three areas of the Northwestern (urban area), Northeastern (plains) and Southern parts (hilly area)
2) The Northwestern part (urban area) and the Northeastren part (plains) were estimated as "dirty" and the Southern part (hilly area) was estimated as "clean", respectively.
3) There was the great gap between the evaluation by benthos and attached diatom as biological indicators, and from this reason, it is necessary to evaluate both indicators comprehensively.
4) ECI_{eco} as the overall index, which comprehensively evaluates attached diatoms and benthos, also evaluated the hilly area as clean. It was shown that there is a tendency for pollution from upstream to downstream.

ACKNOWLEDGMENTS

In carrying out this research, many graduate students of our laboratory made much efforts to provide useful discussion. We would like to express our sincere gratitude for their kindly and serious cooperation.

REFERENCES

[1] Tanida K. , Indicators Biology of River Environment, Hokuryukan, 2010, 197pp. (in Japanese).
[2] Japan Standards Association, Factory Wastewater Test Method JIS-K0102, 1993, 593pp. (in Japanese).
[3] JMA, Manual on Oceanogaphic Observation, Meteorological Business Support Center, 1999, 252pp. (in Japanese).
[4] Watanabe T., Ecology of Freshwater Diatom, Uchidaroukakuho, 2005, 666pp. (in Japanese).
[5] Environmental Management Bureau, Search for river creatures, Ministry of the Environment, Japan, 2017, 34pp. (in Japanese).
[6] Environmental Agency Water Quality Conservation Bureau, Survey manual for assessing river water environment using large benthic animals, Environment Agency, 1992, .21pp. (in Japanese).
[7] Environmental Management Bureau, Manual for Water Quality Assessment by Aquatic Organisms -Japanese version ASPT method-, Ministry of the Environment, Japan, 2017, 33pp. (in Japanese).
[8] Murakami K., Gomyo M., Agatsuma S., Amano Y.,Inoue-Kohama A., Environmental Condition Index for Estimation on Eutrophic State of Enclosed Aquifer Ecosystem, Journal of GEOMATE, Vol.5, Issue 2, 2013, pp.706-711.
[9] Murakami K., Doyama T., Niida H., Watanabe K., Evaluation of River Environment by Biological Indicators in Boso Peninsula, Proceedings of 17th World Lake Conference (Ibaraki-Kasumigaura 2018), 2018, pp.942-944.

6th Int. Conf. on Structure, Engineering & Environment (SEE), Kyoto, Japan, Nov.18-20, 2020, ISBN: 978-4-909106056 C3051

IDENTIFYING IMPACTS OF DENSITY-DRIVEN FLUCTUATION TO GROUNDWATER CAUSED BY SALTWATER INTRUSION

Theara Seng[1], Junichiro Takeuchi[1] and Masayuki Fujihara[1]
[1]Graduate School of Agriculture, Kyoto University, Japan

ABSTRACT

Engineering knowledge on soil and water is crucial for sustainable water resources management. Saltwater intrusion due to such as storm surges or high tide often causes salt damage to crop farmlands. To prevent losses, it is recommended to leach salt by freshwater; however, this activity might create a density-driven flow of salinity into groundwater, and finally, it has possibility to get saltwater to spread widely in downstream. This study aimed to analyze the impact of saltwater intrusion on groundwater flow by laboratory experiments. The technique was to verify the oscillatory phenomena of vertical intruding saltwater into horizontally flowing groundwater. To find out the qualitative difference of saltwater intrusion under various conditions, a laboratory-scale of aquifer flow model was set up. The oscillatory flow could be estimated by the proposed Rayleigh number which comes from different saltwater concentrations, basal groundwater flow rate and so on. According to the photography results, oscillatory flow occurred, and its variation could be evaluated by the Rayleigh number, whereas the increase of basal groundwater flow rate tends to reduce the side effects of salinity intrusion.

Keywords: Saltwater Intrusion, Density-driven Flow, Rayleigh Number

INTRODUCTION

Density-driven flow of fluids usually caused by density difference due to instability of fluids caused by solutes and/or heat, resulting the changes in flow behaviors of solute and/or heat. When this phenomenon happens in groundwater, it will contribute a significant impact on solute and/or heat transports. For these reasons, it is important to comprehensively observe the condition for occurrence of density-driven flow and to identify its dynamics to sustainably manage water resources.

Density-driven flow comes from different sources for both natural and human activities. Saltwater intrusion in coastal regions is a specific case, caused by high tides, storm surges, and saltwater wedge which is formed by density gradient of seawater and freshwater [1]. Dumping sites and chemical from industrial wastes also can be sources of contaminant leakage to the groundwater. In a case of dense non-aqueous phase liquids (NAPLs) leaking from these sites move downward straightly and disperse widely to the flow. In contrast, light NAPLs will cause the sump on the water table [2].

In some cases, density-driven flow also associates with temperature difference. Holzbecher [3] showed that flow instability emerges under specific conditions. When cold water intrudes from ground surface into shallow groundwater, the groundwater flow rate and the Rayleigh number were found by numerical experiments to be conditions for the onset and decay of thermal convection phenomena [4]. Momii [5] reported that saltwater density effect causes oscillatory phenomena of vertical intruding saltwater into horizontal groundwater flow through laboratory experiment. Kawabata [6] investigated these phenomena through numerical approach, in which the dispersion was treated as a constant scalar. Their results illustrated that the oscillatory flow pattern depends on three parameters including Rayleigh number, basal groundwater flow, and saltwater intrusion rate. Three types of saltwater intrusion were found: rapid convergence without oscillation, oscillation, and oscillatory convergence. It is also concluded that some bifurcations occur relative to given basal groundwater flow rate. But they considered that the basal flow rate is another parameter that changes flow regime except for the Rayleigh number because they adopted the constant dispersion coefficient. The dispersion coefficient is a tensor and it depends on the flow rate [7]. Hence, it is considered that the basal flow rate needs to be included in the Rayleigh number.

Kawabata [8] extended investigation on saltwater intruding behaviors through laboratory experiments by using lab-scale groundwater flow tank. The results from photography and measurement of electrical conductivity indicated oscillatory flow and its variation caused by the Rayleigh number whereas periodic pattern happened for the numerical model which meticulous investigation is needed. Further, a study of the stability of density-driven flows in saturated homogeneous porous media by Musuuza [9] suggested that dispersion has a significant effect on flow states, in which varying degrees of instability can be seen by different assumptions of dispersion. Holzbecher [10] proposed the mixed convection number instead of the Rayleigh number to evaluate

the stability of groundwater flow with a heat source. In the equation of the mixed convection number, groundwater flow velocity is included explicitly, which implies flow instability depends on the flow velocity. In a case of instability caused by saltwater concentration, the dispersion depends on the flow velocity [7], and hence flow velocity needs to be considered in the Rayleigh number, in which flow velocity is not included normally. For this reason, this study is intended to propose a new Rayleigh number taking flow velocity into consideration explicitly and verify the availability of it through laboratory experiments.

GOVERNING EQUATIONS

The governing equations for groundwater flow and solute transport are based on the one from Holzbecher [1]. The domain is considered to be a vertical two-dimensional coordinate system where x and z are the horizontal and vertically upward axes, respectively.

The mass balance of fluid with variable density in porous media under assumptions that water is incompressible, the aquifer is rigid, and there is an absence of sources or sinks, is represented as follows when the Oberbeck-Boussinesq approximation is applied to:

$$\nabla \cdot \boldsymbol{v} = 0 \tag{1}$$

with generalized Darcy's Law

$$\boldsymbol{v} = -\frac{\boldsymbol{\kappa}}{\mu}\left(\nabla p + \rho g \nabla z\right) \tag{2}$$

where ρ is the density of the fluid, $\boldsymbol{v} = (u, w)^T$ is the Darcy velocity of the fluid, u and w are vector components of x and z directions, respectively, $\boldsymbol{\kappa}$ is the intrinsic permeability tensor of the porous medium, μ is the viscosity of the fluid, p is the pressure, g is the gravitational acceleration. Here, the porous medium is assumed to be isotropic, and $\boldsymbol{\kappa}$ becomes a scalar κ.

The transport equation for salinity simplified by Oberbeck-Boussinesq approximation is represented as follows,

$$\frac{\partial(\phi R c)}{\partial t} = \nabla \cdot \left(\phi \boldsymbol{D} \nabla c\right) - \nabla \cdot \left(\boldsymbol{v} c\right) \tag{3}$$

where ϕ is the porosity of the porous media, t is the time, R is the retardation factor, $\boldsymbol{D}$ is the dispersion tensor, and c is the salinity.

The dispersion tensor is implemented according to Scheidegger's law,

$$\phi \boldsymbol{D} = \phi D_m \boldsymbol{I} + (\alpha_L - \alpha_T)\frac{\boldsymbol{v}\boldsymbol{v}^T}{|\boldsymbol{v}|} + \alpha_T |\boldsymbol{v}| \boldsymbol{I} \tag{4}$$

where $\boldsymbol{I}$ is an identity matrix, D_m is the molecular diffusion coefficient, and α_L and α_T are longitudinal and transverse dispersion lengths, respectively.

In this study, the stream function is used to describe flow for 2D situation with,

$$(u, w)^T = \left(\frac{\partial \psi}{\partial z}, -\frac{\partial \psi}{\partial x}\right)^T \tag{5}$$

By substituting Eq. (5) into Eq. (2) after curl is applied to the both sides of Eq. (2), the governing equation for the stream function is derived.

$$\frac{\partial}{\partial x}\left(\frac{\mu}{\kappa}\frac{\partial \psi}{\partial x}\right) + \frac{\partial}{\partial z}\left(\frac{\mu}{\kappa}\frac{\partial \psi}{\partial z}\right) = g\frac{\partial \rho}{\partial x} \tag{6}$$

Here, it is assumed that the domain is homogeneous, and the retardation factor R is unit.

To evaluate the Rayleigh number Ra, the dimensionless forms of the governing equations for groundwater flow with variable density is derived by substituting the following dimensionless variables into Eqs. (6) and (3): $X = x/H$, $Z = z/H$, $\Psi = \psi/D_0$, $U = uH/D_0$, $W = uH/D_0$, and $T = tH^2/D_0$.

$$\frac{\partial}{\partial X}\left(\frac{\partial \Psi}{\partial X}\right) + \frac{\partial}{\partial Z}\left(\frac{\partial \Psi}{\partial Z}\right) = Ra\frac{\partial C}{\partial X} \tag{7}$$

$$\frac{\partial C}{\partial T} = \nabla_x \cdot \left(\frac{\phi}{D_0}\boldsymbol{D}\nabla_x C\right) - \boldsymbol{V} \cdot \nabla_x C \tag{8}$$

with

$$C = \frac{c - c_{\min}}{c_{\max} - c_{\min}},\ \rho = \rho_f + \Delta\rho C,\ Ra = \frac{\Delta\rho g \kappa H}{\mu D_0} \tag{9}$$

$$\nabla_X = \left(\frac{\partial}{\partial X}, \frac{\partial}{\partial Z}\right)^T,\ \boldsymbol{V} = (U, W)^T = \left(\frac{\partial \Psi}{\partial Z}, -\frac{\partial \Psi}{\partial X}\right)^T \tag{10}$$

where X and Z are the dimensionless coordinates for x and z, respectively; Ψ is the dimensionless stream function; Ra is the Rayleigh number; U and W are the dimensionless velocities; C is the dimensionless (normalized) salinity; H is the representative length, which is given as the height of an objective domain in Holzbecher [1], but is given as the vertical thickness of the saltwater thickness here; the saltwater density $\rho = \rho(C)$ is assumed to be proportional to C, where ρ_f is freshwater density, $\Delta\rho$ is the difference of density between saltwater ($\rho_s = \rho(1)$) and freshwater ($\rho_f = \rho(0)$); $c_{\max}$ and $c_{\min}$ are the maximum and minimum salinity in the domain, respectively. Regarding the representative dispersion coefficient D_0, it is defined as follows to evaluate whether the intruding saltwater shows instability or not, using the basal groundwater velocity $\boldsymbol{v}_0$.

$$D_0 = \alpha_L |\mathbf{v}_0| \tag{11}$$

By using Eq. (11) and variables Eq. (12), the Rayleigh number is represented in this study as follows.

$$K = \frac{\rho_f g \kappa}{\mu}, \quad \gamma = \frac{\rho_s}{\rho_f} \tag{12}$$

$$Ra = \frac{(\gamma - 1) KH}{\alpha_L |\mathbf{v}_0|} \tag{13}$$

where K is the hydraulic conductivity of the domain, and γ is the specific weight.

Boundary and Initial Conditions

The boundary conditions for the groundwater flow and the salt transport governed by Eqs. (6) and (3), respectively, are provided in Figure 1. In this study, unconfined groundwater flow is considered. The objective domain is the one under water, and the saltwater intrusion zone is on the upstream of the top boundary. Respective to the stream function, the top and bottom are set as Dirichlet-type boundary condition whereas the both sides of the domain are set as Neumann-type. The basal flow rate and the saltwater intrusion rate are represented by ψ_{top} and ψ_{ent}, respectively.

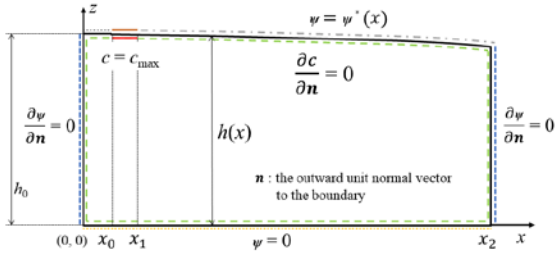

Fig. 1 Boundary conditions of the objective domain.

Constant values ψ_{top} and $\psi_{top} + \psi_{ent}$ are given to the top except for the saltwater intrusion zone, and the following function is given to saltwater intrusion zone.

$$\psi = \psi^*(x) = \begin{cases} \psi_{top} & 0 < x < x_0 \\ \psi_{top} + \dfrac{x - x_0}{x_1 - x_0} \psi_{ent} & x_0 < x < x_1 \\ \psi_{top} + \psi_{ent} & x_1 < x < x_2 \end{cases} \tag{14}$$

Groundwater flows freely across both side boundaries not for the top and bottom. As an initial condition for stream function, a flow without any salt intrusion is given such that $c = 0$.

LABORATORY EXPERIMENTS

Laboratory Approach

Figure 2 shows the schematic diagram of the experimental setup. The experiments are conducted in a flow tank with internal dimensions of 165 cm length, 54 cm height, and 5 cm width shown in Fig. 3. To model the aquifer, the flow tank is filled with homogeneous glass beads with a diameter of 2.0 mm up to the height of about 45 cm. Freshwater is released to flow from left side to the right side, and saltwater intrudes via the saltwater tank which is placed on the upstream of the top of the flow tank. The water levels in the left and right sections, which are separated by perforated acrylic sheets with wire nets, are controlled by the adjustable drainage pipe in each section.

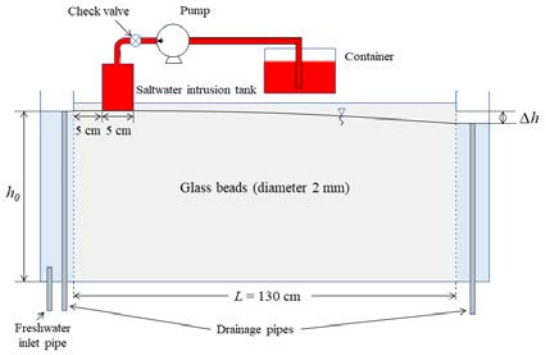

Fig. 2 Schematic diagram of experimental setup.

The saltwater tank is packed with 1 mm glass beads and its bottom is perforated and covered with non-woven fabric. Saltwater is pumped from a tank that contains commercial salt solution dyed with red food color (New Coccine Red No. 102, Kiriya Chemical), whose concentration is set as 1.5 g per 3 L according to Luyun Jr. [11]. The behavior of saltwater intrusion is monitored by two fixed cameras to photograph every fixed time step. One camera is used to take fixed photos and another one is used to take to whole video of the experiments.

Fig. 3 Appearance of the flow tank.

Experimental Setting

The Rayleigh number *Ra* can be calculated using Eq. (13) with the hydraulic conductivity *K*, which is estimated from measured flow volume Q_f as follows.

$$K = \frac{2Q_f L}{b(2\Delta h h_0 - \Delta h^2)} \quad (15)$$

where L is the length of the flow tank, b is the width of the tank, h_0 is the water level at the upstream end, and Δh is the water level difference of the upstream and downstream ends. The dispersion length α_L is given as 2 mm according to Luyun [10].

Experimental condition to be specified for the verification of oscillation occurrence in the case of relatively high Rayleigh numbers, four kinds of relative saltwater density are prepared: $\gamma=\rho_s/\rho_f$ = 1.006, 1.012, 1.024, 1.048. These conditions will yield the values of Rayleigh number corresponding to changes in the basal groundwater flow rate. In each experiment, the difference of water level between the left and right sections Δh are adjusted as 1.5, 2.5, and 3.5 cm in each saltwater density using the drainage pipes in order to make a hydraulic gradient. The upstream water level is fixed as 40 cm in all conditions. The groundwater rate Q_f from flow tank is measured in each experiment to calculate the value of the hydraulic conductivity K and the basal groundwater velocity $\boldsymbol{v}_0$. Saltwater intrusion rate Q_s is decided based on the measured groundwater rate to keep the same shape of streamlines through experimental conditions. To do so, the saltwater intrusion rate is set as 1/20 of the measured groundwater rate.

EXPERIMENTAL RESULTS

Essentially, the Rayleigh number varies depending on the location in the experimental tank as defined in Eq. (9) or (13), because H and $\boldsymbol{v}_0$ vary along flow down. From some preliminary experiments, it was observed that oscillatory flow began when the vertical thickness of the saltwater plume was about 15 cm, which is also shown in the following figures. Therefore, H and $|\boldsymbol{v}_0|$ are given as 15 cm and $Q_f/(h_0 b)$, respectively, in this study to evaluate a representative Ra in experimental conditions.

A Case of Δh = 2.5 cm

From the numerical results found by Kawabata [5], the patterns of intruding saltwater were classified into 3 types: rapid convergence without oscillation (Type I), oscillation (Type II), and oscillatory convergence (Type III). According to the classical analysis of Holzbecher [1], it is indicated that the saline conduction state becomes unstable if $Ra > 4\pi^2$, which is a threshold of stability, or occurrence of density-driven flow, and which is applicable to a saltwater case. In the current study, Figs. 4 (b1) through (b4) shows the photography results of the behaviors of saltwater intrusion in the cases of γ = 1.006, 1.012, 1.024, 1.048 (with Ra = 20.30, 40.61, 81.21, 162.42), and Δh = 2.5 cm, respectively.

Figure 4 (b1) shows saltwater intrusion under a low salinity with γ = 1.006. It is found from this figure that intruding saltwater almost not downward but in the right direction. It is observed that saltwater didn't develop any more pattern after sufficiently long-time elapse, although some disturbances were observed when the Rayleigh number is lower than threshold value. On the other hand, from Figs. 4 (b2) – (b4) which are corresponding to γ equal to 1.012, 1.024 and 1.048, respectively, it indicates that saltwater intrusion visually developed with oscillation like Type II of numerical experiments by Kawabata [5]. From the beginning of intrusion, the saltwater gradually moved downward and started to develop an oscillatory flow after 15 minutes until the saltwater in the tank became empty. These evidences show that salinity distributions get to an unsteady state in a high enough Rayleigh number regime in which Ra exceeds the threshold value. Figure 4 (b4) displays the salinity distribution under a high saltwater density with γ = 1.048 and also exhibits in a relatively high Rayleigh number. It is visible that the intruding saltwater originally penetrated almost downward direction, then after 10 minutes it became oscillating until saltwater reach the bottom and to the rightest end of the tank. However, after long-time elapse, the intruding pattern stopped oscillate and it became almost steady convergent at the end. This is because no freshwater exists under the saltwater after the saltwater reached the bottom. To summarize, all the results in Figs. 4 (b1) – (b4) reveal that in a mild flow regime of the basal groundwater in which Δh = 2.5 cm, salinity varies with oscillation in case of high Rayleigh number ($Ra > 4\pi^2 \cong 39.48$) whereas it does without oscillation in case of low Rayleigh number (Ra < 39.48). It is considered that the oscillation occurs as a bifurcation with increase of the Rayleigh number.

Cases of Δh = 1.5 cm and 3.5 cm

The Rayleigh number causes different saltwater intrusion patterns as discussed in the previous section. In this section, we will discuss on the consequences of changing the horizontal flow rate of groundwater from lower to higher flow rates.

Figures 4 (a1) – (a4) shows the result of saltwater intrusion by changing to a lower horizontal flow rate at which the difference of water level between both sides of the tank is Δh = 1.5 cm. The resulted Rayleigh number corresponding to each specific weight of saltwater are Ra = 39.74, 79.48, 158.97, and 317.93, respectively. From Fig. 4 (a1), it is found that salinity distribution almost flow horizontally; however, its streamlines is slightly downward than in case of Δh = 2.5 cm. Additionally, since the Ra = 39.74, which is nearly approach to the threshold value, the intruding

saltwater seems to have a small degree of oscillations after a long-time elapse. When the *Ra* increase to twice, Fig. 5 (a2) is observed to disperse steeper than previous case, and it started to oscillate after 15 min of intrusion. This case is similar to the case in Fig. 4 (b3) which is identified as Type II pattern. On the other hand, saltwater intrusion converges to a steady state when the *Ra* is increase to 158.97 and 317.93 as shown in Figs. 5 (a3) and (a4). This occurrence is thought to be the same reason with the case of Δh = 2.5 cm and Ra = 162.42. However, since the groundwater flow rate is slower than the case of Δh = 2.5 cm, and which leads to the higher Rayleigh numbers, it is obvious that salinity is finally submerged to the bottom of the tank. It is investigated from these results that the low flow of the basal groundwater makes the Rayleigh number high, and that the oscillatory flow occurs even in low concentration of saltwater. Figures 4 (c1) – (c4) shows the behavior of intruding salinity when the basal groundwater flow rate is increased higher by changing the difference of water level up to 3.5 cm. As the horizontal flow rate increases while keeping constant the specific weight of saltwater, there is a proportional decrease of the Rayleigh number. The resulting *Ra* are 14.59, 29.19, 58.37, and 116.74, respectively.

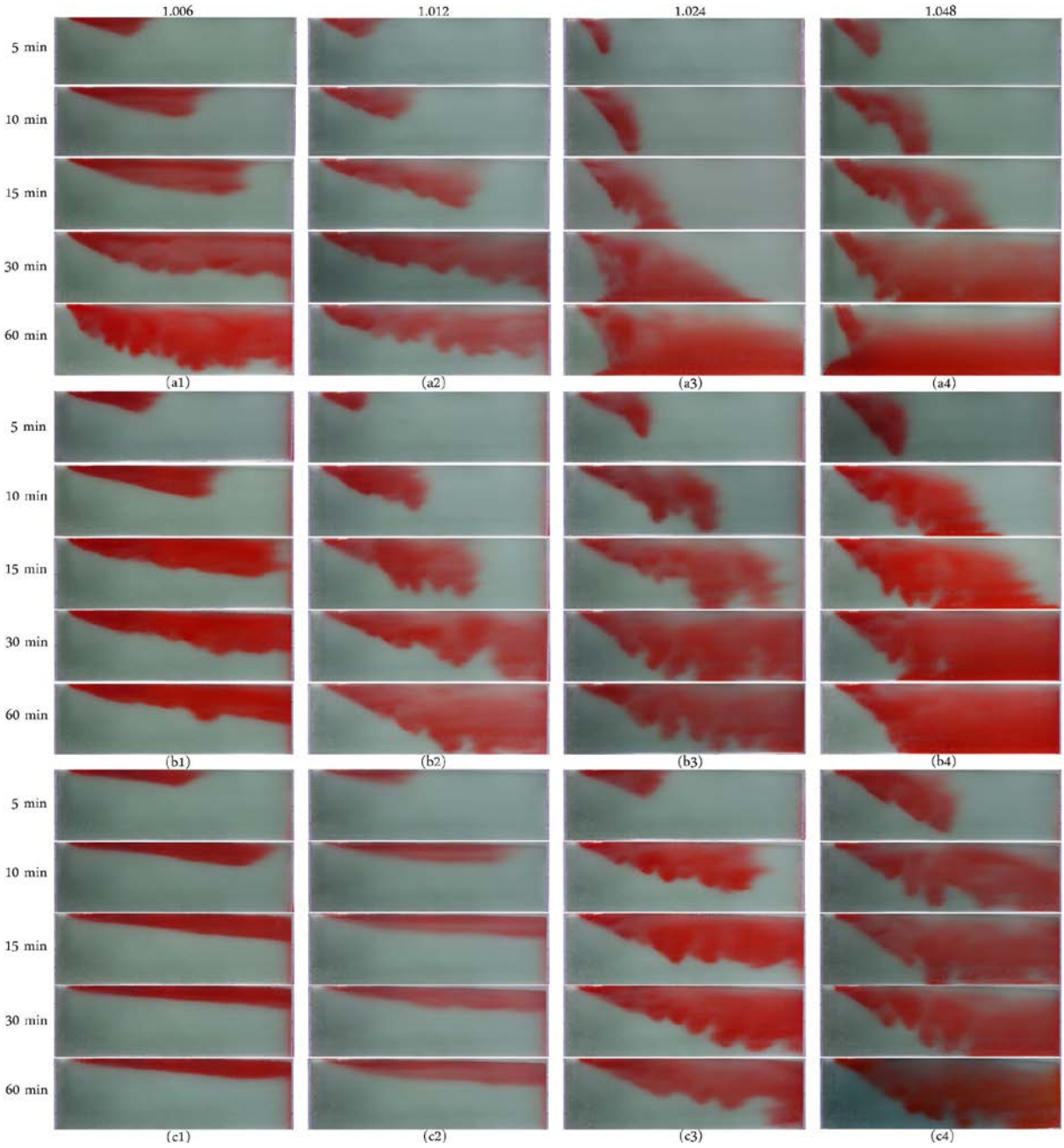

Fig. 4 Photography of time variation of salinity distribution

(a1) – (a4): Δh = 1.5 cm, (b1) – (b4): Δh = 2.5 cm, (c1) – (c4): Δh = 3.5 cm

From Figs. 4 (c1) – (c2), it is observed that saline water moved almost horizontally to the right exit of the tank when the flow is in the relatively low Rayleigh number regime. This can be inferred that impact of less dense saltwater intrusion is considerably not significant in the high basal groundwater flow. However, the oscillatory pattern can be found when the Rayleigh number is higher than the threshold. Figure 4 (c3) indicates an oscillatory flow of salinity distribution which is similar to the cases of Figs. 4 (a1), (b2), and (b3). Furthermore, the oscillatory convergence pattern is expected from Fig. 4 (c4) in a case of the relatively high Rayleigh number and when time elapse is long enough.

CONCLUSIONS

In this study, oscillatory flow behaviors of vertically saltwater intrusion into horizontally flowing groundwater are investigated through laboratory experiments. The proposed Rayleigh number which is associated with the saltwater density, the hydraulic conductivity, the height of a domain, the dispersion length, and the basal groundwater flow rate was varied to identify the impacts of the density-driven flow to groundwater.

From the obtained results, the proposed Rayleigh number can estimate the occurrence of oscillatory flow compare to the threshold value without considering other parameters separately. The photography results showed that the intruding saltwater flows down spreading widely because of its instability when the Rayleigh number exceeds the threshold value. It will cause significant impact on the downstream.

ACKNOWLEDGMENTS

This research was partially funded by Grant-in-Aid for Scientific Research(B) JP20H0310.

REFERENCES

[1] Holzbecher E., Modeling Density-Driven Flow in Porous Media. Springer, 1998, pp. 1-47.

[2] Tamai Y. and Honma S., Experiments and Analysis on the Simultaneous Seepage of Pore-Water and Oils in Soils, Proceeding of the School of Engineering of Tokai University, 2012, pp. 217-224.

[3] Holzbecher E. and Yusa Y., Numerical Experiments on Free and Forced Convection in Porous Media. International Journal of Heat and Mass Transfer, Vol. 38, Issue 11, 1994, pp.2109-2115.

[4] Takeuchi J., Kawabata M., and Fujihara M., Numerical Analysis on the Occurrence of Thermal Convection in Flowing Shallow Groundwater, International Journal of GEOMATE, Vol. 11, Issue 27, 2016, pp. 2688-2694.

[5] Momii, K., Study on Solute Dynamics in Groundwater and Lake as Agricultural Water Resources. Proceedings of Annual Symposium, Applied Hydraulics Division, JSIDRE, 2013, pp.68-71. (in Japanese)

[6] Kawabata M., Takeuchi J., and Fujihara M., Numerical Analysis of Density-Driven Fluctuation in Groundwater Caused by Saltwater Intrusion, Jurnal Teknologi, Vol. 76, No.15, 2015, pp.7-12.

[7] Bear J. and Verruijt A., Chap. 6 Modeling Groundwater Pollution, Modeling Groundwater Flow and Pollution, D. Reidel Publishing Company, 1994, pp.153-195.

[8] Kawabata M., Analysis and Verification of Density-driven Fluctuation Caused by Saltwater Intrusion into Groundwater. Master's Thesis, Kyoto University, 2017.

[9] Musuuza J.L., Radu F.A., and Attinger S., The effect of dispersion on the stability of density-driven flows in saturated homogeneous porous media, Advances in Water Resources, Vol. 34, Issue 3, 2011, pp.417-432.

[10] Holzbecher E., Chap.10 The Mixed Convection Number for Porous Media Flow, Emerging Technologies and Techniques in Porous Media, Ed. Ingham D.B., Bejan A., Mamut E., Kluwer Academic Publishers, 2003, pp.169-182.

[11] Luyun R.A.Jr., Effects of Subsurface Physical Barrier and Artificial Recharge on Seawater Intrusion in Coastal Aquifers. Doctoral Dissertation, Kagoshima University, 2010.

6thInt. Conf. on Structure, Engineering & Environment (SEE), Kyoto, Japan, Nov.18-20, 2020, ISBN: 978-4-909106056 C3051

CHARACTERIZATION OF GROUNDWATER POLLUTION SOURCES BY KRIGING BASED LINKED SIMULATION OPTIMIZATION

Anirban Chakraborty[1]and Om Prakash[1]

[1]Department of Civil and Environmental Engineering, Indian institute of Technology Patna, Bihta, Patna, India 801106.

ABSTRACT

Often untreated wastes are buried underground as convenient method of disposal. These clandestine disposal methods are adopted to offset the cost incurred in proper waste management. Though there might be short term economic gain to the disposer but the long-term impact of such disposal manifests in form of groundwater pollution, which if left unchecked would potentially pollute the entire aquifer. Any contaminated aquifer treatment technique requires prior information about the pollutant sources characteristics. Thus, characterization of unknown groundwater pollution sources becomes imperative in remediation process. The first step involves the identification of number of sources and their locations. In a clandestine scenario the entire study area is treated as a potential source and the search for the actual source can be extensively rigorous in space and time. To overcome this challenge a kriging based zoning is adopted to narrow down the search space for the actual sources in a limited data availability scenario. A comparative analysis of two methods is presented; first method where only (Simulated Annealing based Linked Simulation Optimization) SALSO is used, and second method where kriging based zoning plus SALSO is adopted for pollution source characterization. It is found that kriging method clubbed with SALSO gives significantly better results compared to initial results. A boundary of Indian Institute of Technology Patna with hypothetical hydro-geological parameters is used to test the developed method. The location of the pollutant sources is easily identified when a kriging based Simulated Annealing Linked Simulation Optimization (KSALSO) method is adopted.

Keywords: Linked simulation optimization; *Groundwater pollution source identification*; *Simulated annealing*; *Kriging*

INTRODUCTION

Groundwater is one of the most important sources of drinking in many parts of the world. Groundwater pollution is the biggest threat to sustainability of groundwater resources and even more difficult to detect. Clandestine dumping of toxic wastes underground to offset the cost incurred in proper waste management has further complicated the scenario. Finding such sources of pollution is highly challenging due to their untracebility. Presences of such pollutant sources are unknown until pollution is first detected in some sparsely located wells. In designing an effective remediation strategy for these polluted aquifers, accurate knowledge of pollution source characteristics in terms of their numbers, their locations with release flux histories are most vital. It may be possible to decipher the number of sources from the pattern of land use, but the greatest challenge is to estimate the history of release flux and location of these pollution sources.

Various methods have been developed to identify the unknown pollution source characteristics. [1] developed a nonlinear regression model to identify the release flux histories of groundwater pollution sources. Linked Simulation Optimization (LSO) models are very popular in identifying the release histories of pollution sources [2]-[5]. Surrogate models are efficiently used to recover the release histories of groundwater pollution sources when locations of sources are well known [6]-[7]. These methods are valid for only some simple case studies, which cannot be used for complex scenarios of source identification problems involving clandestine sources.

There are very few methods which simultaneously identify the locations and release flux histories of groundwater pollution sources [8]-[9]. One of the biggest limitations of these methods are that these methods assume the location of the sources to be anywhere in the study area, which makes these methods computationally expensive. However, these developed methods fail to yield any fruitful result when the study area is large and there is no initial guess about the number of sources and their location. In such scenarios the number of possibilities to be evaluated in LSO is very large and may not converge to an optimal solution. [10] used a geo-statistical kriging method to identify the number

of sources and their locations using pollutant concentration measurement from a sequentially designed monitoring network.

In order to reduce the computational burden and accurately identify groundwater pollution sources, a KSALSO methodology is proposed. This interpolation technique termed as kriging method is applied to determine the pollutant concentration profile over the study area. This concentration profile gives an overview of location of pollutant sources which reduces the area of search. Thereafter, LSO method is used after kriging interpolation for source identification. Here, Simulated Annealing (SA) is used as optimization algorithm. A comparative study is also presented between the developed KSALSO model and conventional SA based SALSO technique in identifying unknown source characteristics.

METHODOLOGY

In order to estimate Location and Release Flux histories (LRF) of these pollutant sources, two different pathways are adopted. In the first case conventional SALSO is used. Conventional SALSO was mostly used previously to identify the release flux histories of pollutant sources. In the current study, SALSO methods are used to identify both location and release flux histories. Here, a newly developed KSALSO method is implemented for simultaneous identification of LRF of pollutant sources. The search space for the sources is narrowed down by kriging based pre-processing to reduce the computational budget.

Linked Simulation-Optimization

Linked Simulation Optimization (LSO) is widely used in groundwater pollution source identification problems. The proposed methodology uses meta-heuristic optimization algorithm clubbed with a simulation model (Eq.(1) & Eq.(2)) to reconstruct LRF of pollutant sources.

$$k_i \nabla^2 h + R_h = S_s \frac{\partial h}{\partial t} \quad (1)$$

Eq. (1) represents groundwater flow equation and is based on Darcy's law. The hydraulic head is denoted by h; k_i is the hydraulic conductivity in *i* th direction R_h is the storitivity of the aquifer; *t* is the elapsed time.

$$\frac{\partial C}{\partial t} = D_{i,j} \nabla^2 C - \frac{\partial h}{\partial t} \nabla c + C_s q_s \quad (2)$$

Eq.(2) simulates the transport of pollutant in groundwater system. *C* represents the concentration of pollutant sources; $D_{i,j}$ is the disversivity coefficient at *i, j*; the term $C_s q_s$ represents the source sink mixing in groundwater system;

In LSO approach, the residual error between simulated and observed pollutant concentration values are minimized in Eq. (3). Simulation model replicates flow and pollutant transport in groundwater system [10]. The unknown LRF are considered as explicit unknown decision variables. For different combinations of source numbers, locations and fluxes, simulation model is solved iteratively, such that the optimal solution represents the best estimate of the unknown decision variables. SA is used to solve the optimization problem. In LSO method, location and release flux histories (LRF) of pollutant sources are estimated by formulating optimization problem.

$$F = Min \sum_1^4 \sum_1^6 (Cobs_{iob}^k - Cest_{iob}^k) \quad (3)$$

Subjected to,

$$L_{min} \leq L \leq L_{max}; \quad (4)$$

In Eq. (3) objective function is minimized at any arbitrary location *iob* and time *k;* $Cobs_{iob}^k$ is the observed concentration and $Cest_{iob}^k$ is the simulated concentration at measurement time step *k* at location *iob;* $Cobs_{iob}^k$ is obtained from sampling an observation well; and *;* $Cest_{iob}^k$ is obtained from Eq. (5);

$$Cest_{iob}^k = f(L, F, H) \quad (5)$$

L is the location (grid) of pollutant sources and it depends on the study area and constrained by Eq. (4), *F* is the release concentration of the sources and *H* represents the hydrogeological characteristics of the polluted aquifer study area. In the optimization formulation *L* and *F* are the decision variables. The SALSO method links the simulation model to the SA optimization algorithm. SALSO approach incorporates the groundwater flow and pollutant transport simulation models as set of binding constraints in the optimization formulation which is solved iteratively.

Description of Kriging

Kriging is popular interpolation technique, which is applied in the developed methodology to identify the groundwater pollution source locations to reduce the computational burden in identifying the LRF. In geo-statistics, kriging or Gaussian regression is originally an interpolation procedure for which the interpolated values are determined by a Gaussian mechanism controlled by prior covariance [8]. Application of Geo-statistics is very common in the field of pollution [9]. Kriging as a tool is often used

to determine the quality of groundwater with the help of intensity profile. The approach is commonly used in the spatial analysis context and in machine experiments.

Generally, L values of the pollutant source depend on the size of the study area chosen. If the study area is large, the variable L increases the computational burden as more number of source combination scenarios need to be evaluated to find the optimal result. In order to avoid the excessive load in computing, Ordinary Kriging (OK) is incorporated as a preprocessor. This preprocessor tool is used to reduce the load on optimization. The OK equation is stated in Eq. (6).

$$G(L_0) = F(L_0) + \mu \quad (6)$$

$G(L_0)$ is the concentration obtained by OK; $F(L_0)$ is the unknown concentration value interpreted by combined neighborhood function at the location L_0; and the μ is the standard normalized error occurred at same location (Eq. 6).

Kriging Based Zoning of KSALSO Method

The proposed methodology (KSALSO) uses two step processes. In the 1st step, pollutant concentration data from monitoring wells are collected. From these concentration data, a kriging interpolation is carried out to generate concentration profile over the entire study area, which is further used as input for the source identification model. In this 2nd step, higher concentration region is designated as potential source location zones (Eq. 7) for LSO model. If,

$$G^{max}(L_{max}) \gg G^{min}(L_0); \quad (7)$$

$G^{max}(L_{max})$ is the maximum concentration obtained after creating the variogram at location L_{max}, L_0 is reduced potential grid after Kriging based zoning; L_0 is not considered as a potential source location in LSO. After OK the L_{max}^T variable is deduced. L_{max}^T is maximum length of study area of KSALSO method;

$$L_{max}^T \leq L_{max}; \quad (8)$$

Eq. (4) is replaced by Eq. (8) to forms Eq. (9).

$$L_{min} \leq L \leq L_{max}^T; \quad (9)$$

These variable L_{max}^T become the final constraint of the optimization. Thus, the search space is reduced from entire study area to smaller region for actual source locations in LSO. The schematic chart representing the flow of developed KSALSO is given in Fig. 1.

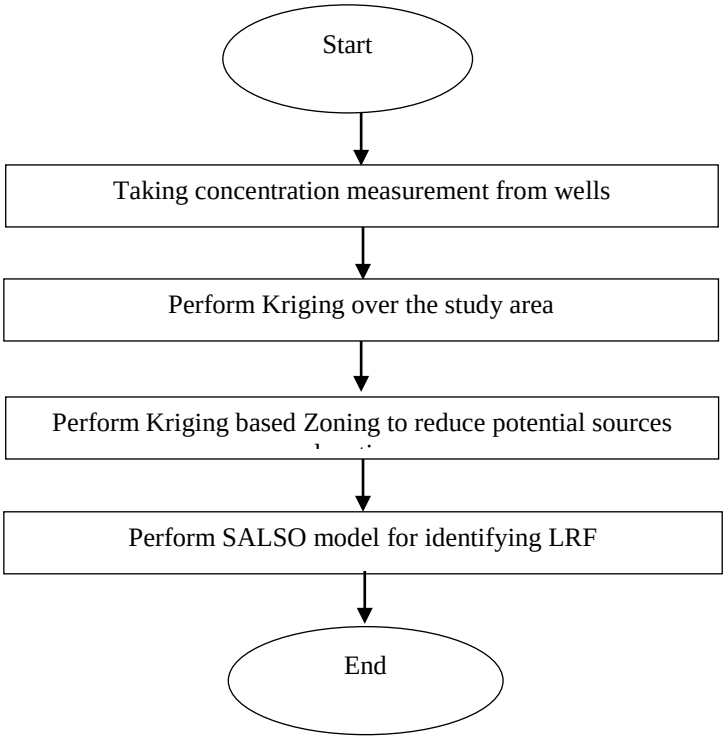

Figure 1: Flowchart of KSALSO

PERFORMANCE EVALUATION

Table 1: Hydro-geological parameters of study area

Name of the parameter	Unit	Value
Length of the area	m	5410
Breadth of the area	m	3628
Thickness of the area	m	30.6
Length of the grid	m	50
Breadth of the grid	m	50
Thickness of the grid	m	30.5
Hydraulic conductivity	m/s	21.34
Horizontal anisotropy	Unit less	0.8
Size of stress period	Days	365
Porosity	Unit less	0.3
Source grid	-	(16,7), (20,6)
Well Number	-	16

In order to test the performance of the developed methodology, site of Indian Institute of Technology Patna is chosen. The location of the site is 25.5357° N, 84.8512° E (Fig. 2). It is assumed that there are two pollutant sources and there are sixteen points where the concentration data is recorded. The hydro-geological parameters of the study area are given in table 1. It is assumed that all these sixteen observation locations are impacted by pollution coming from two point sources. It is assumed that

pollutant is conservative, and the sources are active for seven stress periods. Each stress period is of one year. Source fluxes remain constant throughout each stress periods.

A three-dimensional unsteady transient pollutant transport model was developed to estimate the fate and transport behavior of polluted aquifer. It was assumed that the initial concentration is zero. The simulation is performed with the implicit assumption that the starting time of these sources are known. In the LSO model SA is used as optimization algorithm to estimate the source flux release history and source locations using pollutant concentration measurements from few monitoring locations. The fundamental idea of SA comes from thermodynamics. Groundwater pollution source identification problems are categorized as multivariate optimization problem. The non-linearity phenomenon makes the solution more complex. The formulation of such complex problem has multiple local optima. SA works efficiently in getting out from this trap of local optima. Using hill-climbing moves to avoid local optima makes SA is effective in solving problems of non-convex optimization. The simplicity of application to the complex problem and convergence to an optimum global solution extends the competency to solve the ill-posed inverse problems, as in the case with the problem.

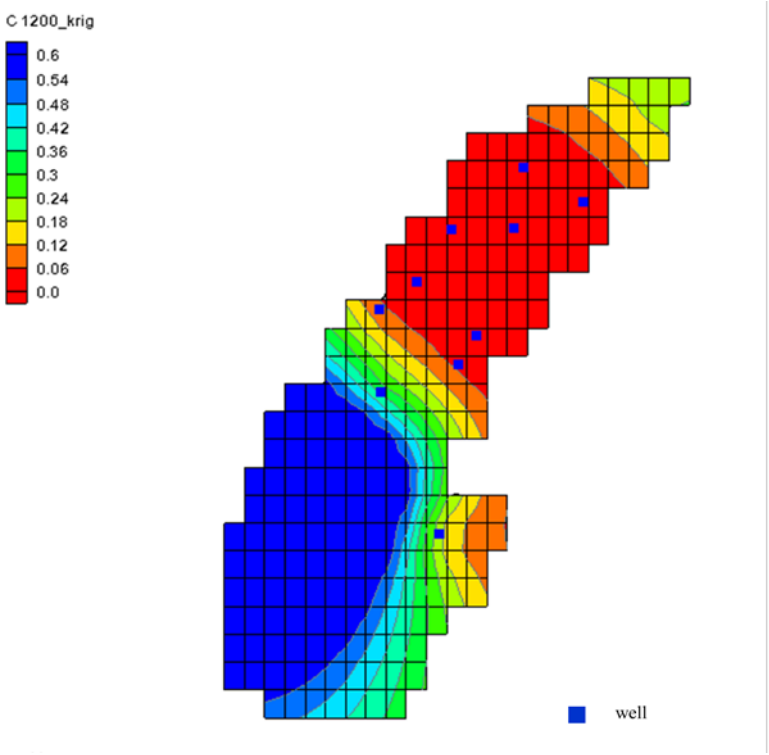

Figure 2: Plan view and interpolated concentration in the study area

From Fig. 2, the likelihood of sources to be present are in the higher concentration zone which is denoted by deep blue color. By kriging, the potential source locations are reduced from 108 active grids to 36 active grids (refer: table 2). Thereafter, SALSO model is applied to identify the sources characteristics in the limited search area. Basically, Kriging based zoning method helps SALSO method to perform in reduced search area for location of pollutant sources, which invariably decreases the plausible number of source characters' combinations to be evaluated in the SA optimization algorithm in search for the optimal LRF.

Table 2**:** Comparison of optimization parameters between SALSO and KSALSO

Method	Number of decision variables	*L*	Source location combinations for search
SALSO	18	108	5778
KSALSO	18	36	630

In this study area, the maximum number of sources are two. Total number of stress period for each sources are seven. So, the number of variables to be estimated is eighteen ($2 \times 2 + 7 \times 2$). The description of and *L* variable is given in table 2.

RESULTS AND DISCUSSIONS

The identified source characteristics result is given in table 3 and Fig. 3. In case of KSALSO, out of two sources, location of one source matches exactly with the actual location of the source, and the location of other sources is slightly shifted (one grid shift) from the actual source location of the second source. The location is expressed in terms of grids.

The release flux histories are also presented in the Fig. 3, where X dimension represents the stress period and Y dimension represent the release history of each sources. It is observed from Fig. 3 that KSALSO method give better recovery of release flux of the identified sources compared to SALSO.

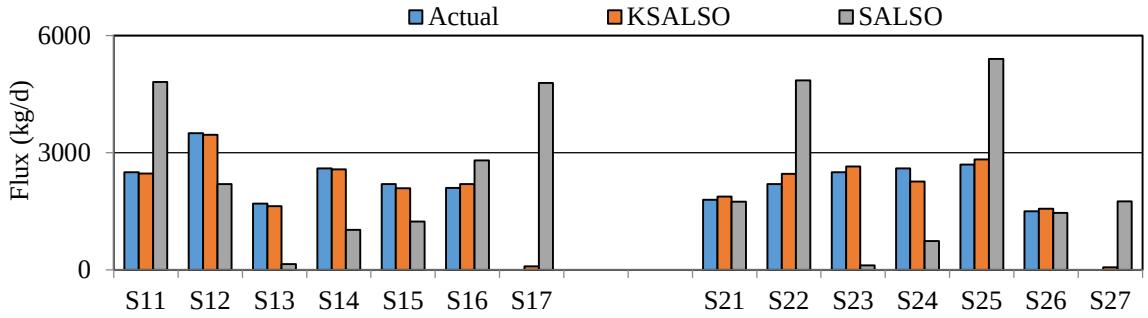

Figure 3: Release flux histories of identified sources

A comparative study is also presented between developed KSALSO method and conventional SALSO methods. From the table 3, it is obvious that KSALSO give significantly superior result than that of SALSO in terms of identifying location of the pollutant sources. KSALSO method converged with less number of iteration compared to SALSO method. That is why elapsed time for completing KSALSO method is also lower than that of SALSO method.

Table 3: Characteristics of identified sources

Characteristics	Actual	KSALSO	SALSO
Co-ordinates (S1)	(16,7)	(16,7)	(12,8)
Co-ordinates (S2)	(20,6)	(21,6)	(18,8)
Time taken (sec)	-	31294	591432

Computational time taken by the developed method KSALSO, and the conventional method SALSO are analyzed to estimate the efficiency in using kriging for potential source location zoning. From the estimates it is seen that performance of KSALSO model is superior in efficiency and reduces the computational burden by 97.40%.

By comparing the breakthrough curves, the accuracy of the estimated source fluxes using both KSALSO and SALSO methodology is examined in Fig 4. Estimated source flux values for producing the breakthrough curves are used in a forward simulation for both KSALSO and SALSO method. The concentration versus observation location is generated at 1200 days after pollution started. Those values are compared with the actual concentration at same time and it is found that KSALSO gives greater accuracy in recovery of breakthrough curve than that of SALSO method.

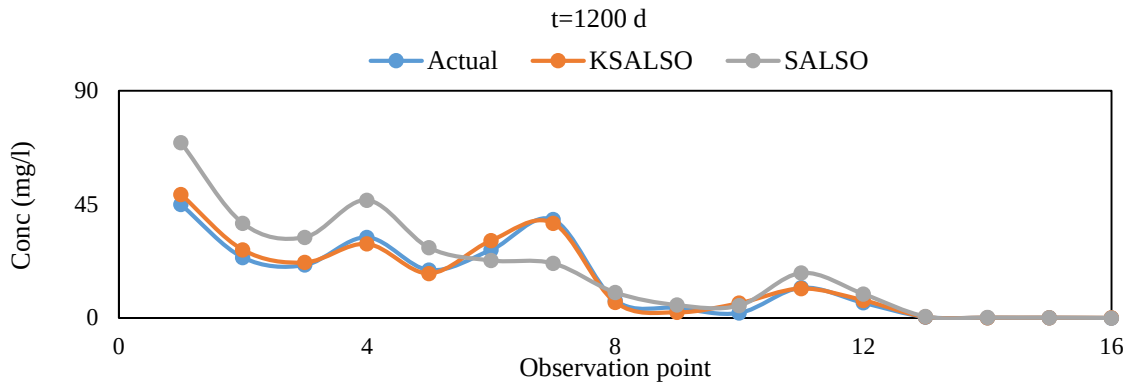

Figure 5: Breakthrough curve comparison

CONCLUSIONS

KSALSO is significantly more efficient than SALSO in identifying the sources characteristics. The location of each sources are identified with 90% precision. The recovery of flux histories are also satisfactory (87% precision). KSALSO method works 97% faster than conventional SALSO method, which is a major advantage of developed KSALSO method. One of the major challenges in groundwater pollution is to identify the locations of pollution sources. The proposed methodology is able to relax this difficulty. The number of sources is not taken as unknown explicit variable in this developed methodology.

REFERENCES

[1] Gorelick, S. M., Evans, B., &Remson, I. (1983). Identifying sources of groundwater pollution: An optimization approach. *Water Resources Research*, *19*(3), 779-790.

[2] Mahar, P. S., & Datta, B. (2000). Identification of pollution sources in transient groundwater systems. *Water Resources Management*, *14*(3), 209-227.

[3] Guneshwor, L., Eldho, T. I., & Kumar, A. V. (2018). Identification of groundwater contamination sources using mesh-free RPC simulation and particle swarm optimization. *Water resources management*, *32*(4), 1517-1538.

[4] Prakash, O., & Datta, B. (2014). Multiobjective monitoring network design for efficient identification of unknown groundwater pollution sources incorporating genetic programming–based monitoring. *Journal of Hydrologic Engineering*, *19*(11), 04014025.

[5] Prakash, O., & Datta, B. (2015). Optimal characterization of pollutant sources in contaminated aquifers by integrating sequential-monitoring-network design and source identification: methodology and an application in Australia. *Hydrogeology Journal*, *23*(6), 1089-1107.

[6] Xing, Z.X., Qu, R.Z., Zhao, Y., Fu, Q. , Ji, Y. , Lu, W.X , 2019. Identifying the release history of a groundwater pollution source based on an ensemble surrogate model. *J. Hydrol*. 572, 501–576.

[7] Zhao, Ying, et al. "Identifying Groundwater Contaminant Sources Based on a KELM Surrogate Model Together with Four Heuristic Optimization Algorithms." *Advances in Water Resources* (2020): 103540.

[8] Sophia, L., & Bhattacharjya, R. K. (2020). A GA Based Iterative Model for Identification of Unknown Groundwater Pollution Sources Considering Noisy Data. In *Nature-Inspired Methods for Metaheuristics Optimization* (pp. 303-321). Springer, Cham.

[9] Ayvaz, M. T. (2010). A linked simulation–optimization model for solving the unknown groundwater pollution source identification problems. *Journal of Contaminant Hydrology*, *117*(1-4), 46-59.

[10] Prakash, O., & Datta, B. (2013). Sequential optimal monitoring network design and iterative spatial estimation of pollutant concentration for identification of unknown groundwater pollution source locations. *Environmental monitoring and assessment*, *185*(7), 5611-5626.

[11] Cressie, N. (1990). The origins of kriging. *Mathematical geology*, *22*(3), 239-252.

[12] Zheng, C. (1992). *MT3D:* A modular three-dimensional transport model for simulation of advection, dispersion and chemical reactions of contaminants in groundwater systems. *SS Papadopoulos & Associates.*

6th Int. Conf. on Structure, Engineering & Environment (SEE), Kyoto, Japan, Nov.18-20, 2020, ISBN: 978-4-909106056 C3051

THE KUMAMOTO EARTHQUAKE'S CREATIVE RECONSTRUCTION EFFORT LED BY A DIVERSE RANGE OF ORGANIZATIONS

Reiko MACHIDA[1], Eri OTSU[2] , Hiroko SHIMA[2], Hitomi YaGI[2] ,Katusunori MOCHIZUKI[3]
Junya MACHIDA[4],Hijiri SHIMOJIMA[1] and Naomasa HONDA[1]

1 Department of Regional Regeneration Science, Tokyo University of Agriculture, Japan
2 Institute of GIAHS Life Aso, Japan**,** 3 Institute of YUHUIZUM, Japan
4 Co. Environment Design, Japan

ABSTRACT

This study analyzed the creative reconstruction efforts led by a diverse range of organizations from the Kumamoto earthquake in the Aso region in chronological order. In addition, this study was aimed to clarify the efforts of the residents and communities of the Aso region ranging from disaster relief to tourism and various forms of exchange. These efforts utilized the unique human networks and organizations during the period for ensuring survival (10 days after the earthquake) and the period for securing living conditions (1 month after the earthquake) and also provided quick support where the government could not reach. Furthermore, we clarified how the unique efforts undertaken by each subject has made it easier to continue the relief effort and how they developed into tourism, exchange and disaster prevention education programs reviewing local communities

Keywords: Kumamoto Earthquake, Aso, reconstruction, tourism,

INTRODUCTION

The Aso area is located in the northwestern part of Kyushu. The main topographic feature of Aso is the huge caldera which was created by four volcanic eruptions with pyroclastic flows. The vast grassland landscape spreads over the central cone and the top of the caldera. In Japan, the designation of national parks started in 1929 and 5 years later Aso was designated as a national park in 1934.The grasslands of Aso were certified as Globally Important Agricultural Heritage Systems (GIAHS) in 2013, and they were also certified as Geoparks in 2014. The grasslands of Aso have been managed by local agricultural activities such as controlled burning, mowing and pasturage.

Tourism is one of the main industries of the Aso region. The number of tourists who visited the Aso area in 2012 was 16,559,613, which was the highest number in the whole of Kumamoto prefecture[1].

The Kumamoto Earthquake struck the Aso area of Kumamoto Prefecture on April, 14 and April 16 in 2016, killing at least 20 people. The earthquake with a Magnitude of 7.3 triggered a sediment disaster in the mountain slope. The sediment disaster was further aggravated by the subsequent torrential rainfalls (19-25, June 2016). The sediment disaster caused ground cracks and sediment movement cracks across the grasslands. As a result, road and rail transportation was shut down. Also, some tourist facilities were closed down since the hot springs ran dry.

Kumamoto Prefecture formulated a policy for the disaster recovery called "Build Back Better"[2] which aimed to not only restore the area to its former condition, but to rebuild it to a state better than before so that it would lead to further development in the future.

Learning from the Great East Japan Earthquake, Yamakawa (2018) [3]. points out that "Build Back Better" is important not only as infrastructure development, but also as support for the affected people and the local communities.

According to the overview of "Build Back Better" of the Great East Japan Earthquake, which supported the affected people and local communities in Minami-sanriku Town, Miyagi Prefecture, it has been reported that the network of people, organizations, and regions before the earthquake had transformed into supporting the victims and developing tourism[4].. In Miyako City, Iwate Prefecture, various forms of tourism utilizing resources that will remain in the region after the disaster have led to regional revitalization[5]. In addition, visitors to the Sanriku Reconstruction National Park Tanesashi Coast Michinoku Shiokaze Trail have been effectively increasing their degrees of attachment to the area and their intentions to revisit thanks to their interactions with local residents[6]. There has also been raised awareness and formulations of networks through volunteer tourism to the disaster-stricken areas. Even more importantly, new leaders of the regional development are being trained through these reconstruction activities.

During "Build Back Better", the creative recovery effort a diverse group of actors which included the Grassland Restoration Committee, grassland conservation volunteer groups, accommodation providers and residents strove to provide disaster relief to the victims and to revive the local community using the preexisting networks.

For example, the Grassland Restoration Committee and the grassland conservation volunteer group "NPO Aso Greenstock" provided immediate support to the livestock farmers by repairing the pastures and thereby restoring their livelihoods. These activities then developed into various tourist and exchange projects.

The accommodation facility "Namino Yasuragi Exchange Center", which provided environmental education programs before the earthquake, urgently set up evacuation centers and provided mental care for infants and their mothers. Once the support programs were no longer needed, they were turned into disaster prevention education programs.

In addition, a group of young disaster volunteers together with local residents have contributed to the revitalization of the community by organizing sightseeing tours for reconstruction and opening a community cafe (GIAHS Cafe) that also functions as a shelter.

The supporting measures of "Build Back Better" were split into categories based on time periods such as the time to secure survival (10 days after the disaster), the time to secure living conditions (one month after the disaster), the time to secure livelihood (three months from the time of the disaster), and the time until the resumption of business activities[7].

The purpose of this study was to analyze the sequence of efforts of the local residents, communities, organizations from the immediate support of the victims to the reconstruction efforts through tourism and exchange.

METHOD

The local residents were able to overcome after the disaster by the reconstruction assistance from the grassland conservation volunteers, and support for infants form exchange facilities. In addition, the local residents succeeded in the reconstruction and revitalization of the local community through the reconstruction assistance form divers range of organizations and the collaboration between the local residents and the Kumamoto earthquake volunteers.

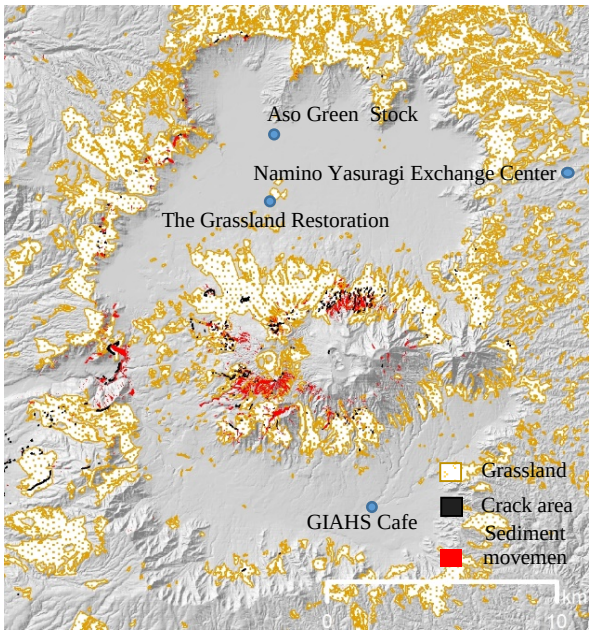

Fig.1 Research Area

Table 1 The interview survey of subsequent creative reconstruction effort

Interviewee	Context	Pre-earthquake activities	Creative reconstruction effort
The Grassland Restoration Committee	Various members (livestock farmer, government, volunteers and academic expert)	Discussions for restoration and conservation of the grassland	The disaster support for livestock farmer
Aso Green Stock	NPO	Support the grassland maintenance tasks such as the controlled burning	①The disaster support for livestock farmer ②Plan of sightseeing tours
Namino Yasuragi Exchange Cente	Accommodation and training facility	Providing environmental education programs	A shelter for mothers with infants and toddlers.
GIAHS CAFÉ	Inhabitant	Earthquake volunteer	①Opening a community cafe that also functions as a shelter ②Plan of a restaurant bus
GIAHS CAFÉ	Inhabitant	Vegetable pastry chef in another city	① Participation as a vegetable sweets pâtissier in a "restaurant bus ②Management of GIAHS Café

By clarifying the reconstruction assistance of the organizations that played a leading role in creative reconstruction in chronological order using the time frames, it is possible to clarify the efforts of reconstruction support from the immediate support of the victims to the reconstruction efforts through tourism and exchange.

This study conducted the interview survey with the Grassland Restoration Committee, the core leadership group a local collaboration and exchange, The Aso Green Stock, Namino Yasuaragi Exchange Center specialties in infant support and urban rural migrated volunteers to support the revitalization of local community.

The question topics were as follows: relationship between activities before and after the earthquake,the reconstruction assistance and the implementation periods following the Kumamoto Earthquake, the support activities, methods of information distribution and funding. The interview surveys were conducted on May 4, 2017, September 12, and September 13, 2017, and September 8, 2018. In addition, literature surveys related to the reconstruction from the Kumamoto Earthquake were carried out using the written reports of Aso Green Stock and the Grassland Restoration Committee.

This study analyzed the recovery efforts of the grassland conservation volunteers, the exchange center, and the collaboration between local residents and earthquake volunteers in a chronological order using the following time frames, on a time series basis: the time to secure survival (10 days after the disaster), the time to secure living (one month after the disaster), the time to secure livelihood (three months from the time of the disaster), and the time to make a forecast for the business resume.

RESULTS

The Grassland Restoration Committee

The Act for the Promotion of Nature Restoration in 2003 established the system to restore the lost natural environment in collaboration with various bodies. Under this law, The Grassland Restoration Committee discusses the conservation of grasslands with various members from local people, government, volunteers and academic experts totaling 224 members since 2015.

The Grassland Restoration Committee was established as the fund for the restoration of the grasslands in Aso since2011. The fund is used for the promotion of livestock and for the restoration of grassland.

Although the improved grasslands were subjects of the National Disaster Assistance of the Kumamoto Earthquake, the Wild grasslands mainly composed of Nezasa and Susuki plants which have been managed by controlled burning, mowing and pasturage were not eligible for the National Disaster Assistance. This made it difficult for livestock farmers to foresee the resumption of the livestock industry.

Therefore, the Grassland Restoration Committee conducted an emergency questionnaire to the livestock farmers on the disaster support, immediately after the Kumamoto Earthquake[8].

On June 15, about two months after the earthquake the Grassland Restoration Committee has restored a pasturage road in Nishimura village, which was damaged by surface ruptures. On June 17 damaged water wells, feeders and farm fences were repaired or replaced.

Three months after the Kumamoto Earthquake, on July 19 new water tanks were installed in the grasslands of Minami-Aso Village.

Also, 11 months after the Kumamoto Earthquake, the Grassland Restoration Committee carried out supporting activities in order to restart the fire controlled burning for the livestock farmers on the grasslands where the land had been damaged by surface ruptures The methods of information of the Grassland Restoration Committee was the mass media such as the newspapers and the report of the Grassland Restoration Committee.

These creative reconstruction efforts were financed by the fund of the Grassland Restoration Committee.

Aso Green Stock

The decline of the livestock industry and the increasingly aging population, the landscape management of grasslands has become increasingly difficult. To address the shortage of manpower, the volunteer activity in Aso attracted a lot of motivated people outside of Aso since 1990’s. A volunteer group was founded to support the controlled burning work under the name Aso Green Stock in 1995.Also, approximately 960 volunteers carry out maintenance tasks such as the controlled burning together with the local inhabitants presently.

Aso Green Stock implemented three projects as emergency support for the livestock farmers.

Firstly, it supported the resumption of the fire controlled burning in the ruptured grassland areas. Secondly, it repaired the grassland roads that were damaged by the earthquake. Thirdly, it raised fences for preventing cattle and horses from slipping into the cracks across the grasslands. It also repaired the barns and cattle sheds damaged by the earthquake.

3 days after the Kumamoto Earthquake, on April 19th, Aso Green Stock surveyed the area struck by the disaster and assessed the extent of damage to the

grasslands.

11 days after Kumamoto Earthquake, the Aso Green Stock started raising funds for the affected livestock farmers. The donations have reached approximately 2.8 million yen in four months.

Aso Green Stock organized sightseeing tours and exchange opportunities in order to facilitate constructive participation efforts. These tours included grassland management experiences, barbecues and visits to the local hot springs. The tours began in Oct, 2016; buses departed from the cities of Fukuoka and Kumamoto in Kyushu. In total, 119 people have participated in these events.

These creative reconstruction efforts for Aso Green Stock were financed by donations from the Kirin Kizuna Project and by Coca-Cola.

Fig. 2 The controlled burning

Aso Green Stock used postal mail and social media platforms such as Facebook to share information with its members about the reconstruction support.

As a result of the aforementioned efforts, the partnerships with the volunteers of the grassland preservation before the Kumamoto Earthquake have led to the swift recovery of the livestock farmers following the earthquake.

After 6 months, the disaster support activities of the grassland volunteers have successfully developed into various tourist and exchange projects.

NAMINO YASURAKI EXCHANGE CENTER

The Namino Yasuragi Exchange Center was opened in 2002 as an accommodation and training facility and to serve as a venue of interaction between urban and rural areas. The Exchange Center has also been providing environmental education programs such as camps and nature watching programs.

During times of disasters, mothers in evacuation centers often worry about the noise of their children crying and bothering other evacuees which causes them great stress. To tackle this problem, immediately after the Kumamoto earthquake, the Namino Yasuragi Exchange Center opened up as a shelter for mothers with infants and toddlers.

To support the victims, they lent the facility's baths and launderettes to families with infants. In addition, they provided updated information on baths, launderette facilities and road traffic information in Aso, based on the information published by the city.

The Namino Yasuragi Exchange Center initiated a program called: "Playing and Healing – Recovery Starting with the Hearts of Mothers and Children", which provided mental care. The program drew on the actual experiences gained from the earlier environmental education programs. It started 5 days after the Kumamoto earthquake and ran for 18 days between 2016, April 19 and May 8. The activities included reading sessions, hardcover and paperback rentals, creating chalk art works, yoga, head massages and chiropractic sessions for mothers.

They held "Play Activities" every Saturday from May 8th to July 2016 and they held "Healing Activities" twice a month from September 2016.

From May 2016 they opened a recycling shop for home appliances such as refrigerators and washing machines, and storage furniture in collaboration with a logistics company.

From July, 2016 they held disaster prevention workshops in collaboration with NPOs specializing in disaster prevention.

2 years and 5 months after the earthquake, since local residents and children's level of interest towards disaster prevention was still high, they held a disaster prevention workshop in collaboration with universities. The workshop featured the following contents: introduction of the local community's mutual assistance during the Kumamoto earthquake, explanation of the characteristics of the sediment disaster in the Aso area, preparation of emergency food, proposed emergency action plan utilizing Aso region's hazard map and 3D topographic models.

The methods of information was the web site of the Namino Yasuragi Exchange Center and social media platforms such as Facebook. These creative reconstruction efforts were financed by several grants.

GIHAS CAFÉ

GIAHS Cafe is a community cafe established by a female farmer living in the Aso area who was previously actively involved in the efforts to recognize the Aso area as a Globally Important Agricultural Heritage System.

The concept of GIAHS Cafe is to serve as a hub for local communication in daily life and to function as a shelter at times of disaster.

The interview subject is a person who participated as an earthquake volunteer at the evacuation center immediately after the Kumamoto earthquake, and visited Minamiaso Village.

She sympathized with the concept of the GIAHS cafe and moved to Minamiaso village four months after the earthquake to open GIAHS cafe.

A workshop was held to remodel the venue for the opening of the GIAHS cafe. The renovation workshop was attended by more than 30 people in their 20s and 30s who participated as volunteers. At the renovation workshop, the walls and the ceiling of the barn were painted.

In order to allow the GIAHS Café to function as a shelter during times of disaster, it was equipped with a biomass toilet, a solar power generator, a pellet stove, and a pellet fired pizza kiln.

The other interviewee was working outside Minamiaso as a vegetable sweets pastry chef.

Her opportunity to move to Minamiaso village came about when she participated as a vegetable sweets pâtissier in a "restaurant bus" ran by a female farmer in Minamiaso village in May 2017.

The idea of the restaurant bus came from female farmers and young people who moved to Kumamoto after the earthquake[8].The restaurant bus was set up in collaboration with the East Food Society and WILLER Co., Ltd., which creates local attractions using the restaurant bus. The restaurant bus is an open-top double-decker bus with a kitchen on the first floor and a dining room on the second floor. The course of the restaurant bus tour ran around farm lands, sake breweries, and brewery cellars which were recovering from the disaster. The restaurant bus successfully connected the landscape, food and people creating local production for local consumption in the Aso area. Two years have passed, GIAHS Cafe is holding workshops sharing life related techniques and wisdom with residents.

The subsequent creative reconstruction effort led by a diverse range of organizations

The following three points can be considered as results of the creative reconstruction effort led by the organizations.

The first key to success was that each body utilized its networks and facilities to support subjects that typically lack support at times of disasters such as supporting infants who are highly vulnerable or supporting the grasslands that couldn't qualify for government aid. The other crucial point was taking quick action that led to the speedy recovery.

They secured living conditions within the first month of the earthquake and secured livelihood within three months.

Table 2 The subsequent creative reconstruction effort led by a diverse range of organizations

Interviewee	Context	Time to secure survival (10 days after the disaster)	Time to secure living conditions (one month after the disaster)	Time to secure livelihood (three months from the disaster)	The time until the resumption of business activities	Transmission of information	Fund
The Grassland Restoration Committee	Various members for the conservation of the grassland in Aso	Questionnaire to the livestock farmers on the disaster support	Coordination of disaster support	Restored a pasturage road/ Damaged water wells, feeders and farm fences were repaired or replaced/ New water tanks were installed	Supported activities in order to restart the fire controlled burning on the grasslands where the land had been damaged by surface ruptures	Newspapers and the report of the Grassland Restoration Committee	Fund of the Grassland Restoration Committee
Aso Green Stock	NPO (Support the controlled burning with the local inhabitants by volunnteers)	Survey of the area struck by the disaster and assessed the extent of damage to the grasslands/ Started raising funds for the affected livestock farmers.	Fundraising/ Coordination of disaster support	Restored a pasturage road/ Damaged water wells, feeders and farm fences were repaired or replaced/ New Barn were installed	Sightseeing tours and exchange opportunities in order to facilitate constructive participation efforts	Postal mail and social media platforms such as Facebook	Donations from the members and the Company
Namino Yasuragi Exchange Cente	Accommodation and training facility	Opened up as a shelter for mothers with infants and toddlers/ Lending the facility's baths and launderettes to families with infant/	"Playing and Healing – Recovery Starting with the Hearts of Mothers and Children", which provided mental care.	Opened a recycling shop for home appliances	A disaster prevention workshop in collaboration with universities.	The website of Namino Yasuragi Exchange Cente and social media platforms such as Facebook	Several grants
GIAHS CAFÉ	Inhabitant	An earthquake volunteer at the evacuation center	An earthquake volunteer at the evacuation center	A workshop for the opening of the GIAHS cafe	Open of the GIAHS café/ Plan of the restaurant bus	Social media platforms such as Facebook	Donations from the members and the Company
					Participation of the restaurant bus		

Second, each body continued its activities from the stages of securing survival to securing livelihood. During this process the activities have expanded into new forms such as tourism and disaster prevention education, where creative reconstruction activities were proposed and implemented by local residents. These creative reconstruction efforts also served as triggers to young migrants and led to the revival of the local community.

Thirdly, each body independently disseminated information through social media and other channels to raise awareness and gain support for the creative reconstruction.

CONCLUSION

This study analyzed the creative reconstruction efforts led by a diverse range of organizations from the Kumamoto earthquake in the Aso region in chronological order. In addition, this study was aimed to clarify the efforts of the residents and communities pp.333-336of the Aso region ranging from disaster relief to tourism and various forms of exchange.

These efforts utilized the unique human networks and organizations during the period for ensuring survival (10 days after the earthquake) and the period for securing living conditions (1 month after the earthquake) and also provided quick support where the government could not reach.

Furthermore, we clarified how the unique efforts undertaken by each subject has made it easier to continue the relief effort and how they developed into tourism, exchange and disaster prevention education programs reviewing local communities.

Therefore, we can conclude that the characteristics of the creative reconstruction effort of the Aso area are that the prompt support was based on leveraging the preexisting strengths of each entity, and the efforts were linked to tourism, exchange and other activities which resulted in providing new value and appeal to the Aso region.

The research subject is one of the key people or platforms in the Aso area. New proposals for creative reconstruction efforts built upon the cooperation of each entity is a topic of further interest.

ACKNOWLEDGMENTS

This work was supported by JSPS KAKENHI Grant Number JP17K02130 and JP19H02981 , the Strategic Research Project of Tokyo University of Agriculture.

REFERENCES

[1] The Ministry of Environment., The number of users in National Park,2015 https://www.env.go.jp/park/doc/data/

[2] Kumamoto Prefecture., Revival plan from 2016 Kumamoto earthquake, https://www.pref.kumamoto.jp.e.qp.hp.transer.com/kiji_16643.html

[3] YAMAKAWA Mitsuo., East Japan Great Earthquake Disaster and Socio-economic Reconstruction Paradigm Putting the Kumamoto Earthquake in Range, Annals of the Japan Association of Economic Geographer, Vol.64, 2018,pp.129-137

[4] SANO Hiroyoshi., The Network on Tourism toward the East Japan Earthquake Disaster Reconstruction in Minami-sanriku Town, Proceedings of Japan Institute of Tourism Research Annual Conference Vol.26,2011, pp.329-332.

[5] KAIZU Yurie., Empirical studies of earthquake reconstruction assistance through eco-tourism in Miyako city, Iwate, From over thousand years treasure hunting to Ecotourism, The journal of the Tourism Research, Vol24(1) , 2012 , pp.41-44.

[6] YAMAMOTO Kiyotathu,The Influence of Contact with Local People upon the Tourists' Consciousness of Tourism in a Natural Sightseeing Spot : A Case of Urabandai, Fukushima, Proceedings of Japan Institute of Tourism Research Annual Conference Vol.26,2011, pp.329-336..

[7] Cabinet Office of Japan, The Hand book of Disaster Management, bousai.go.jp/kaigirep/houkokusho/hukkousesaku/saigaitaiou/output_html_1/images/dept/cao_fukkou/handbook.pdf

[8] OTSU Eri., Grass Root Activities in Aso before and after the Big Earthquake, Journal of rural planning 35(3),369-374

[9] Hossain M.Z. and Awal A.S.M.A., Experimental Validation of a Theoretical Model for Flexural Modulus of Elasticity of Thin Cement Composite, Const. Build. Mat., Vol.25, No.3, 2011, pp.1460-1465.

6th Int. Conf. on Structure, Engineering & Environment (SEE), Kyoto, Japan, Nov.18-20, 2020, ISBN: 978-4-909106056 C3051

ASSESSMENT OF HABITAT SUITABILITY AREA OF ENDANGERED SPECIES USING MAXENT BY LAND USE CHANGE IN FUKUSHIMA PREFECTURE, JAPAN

Hideyuki Ito[1], Hiromu Tomita[2], Makoto Ooba[3] and Takahiro Fujii[4]
[1,4]College of Science and Technology, Nihon University, Japan; [2]Fujita Road Construction, Japan;
[3]National Institute for Environmental Studies, Japan

ABSTRACT

Fukushima prefecture in Japan is the third largest of Japan's 47 prefectures and stretches over 150 kilometers from the Pacific coast into the mountainous interior of northeastern Honshu. Fukushima prefecture is abound with rich nature such as Mt. Bandaisan, Lake Inawashiro and Bandai highlands including beautiful ponds and lakes. However, the number of endangered species in Fukushima has been increasing since the 1970's because the area of nature environment has been decreasing and then various habitat for valuable living organisms have been destroyed by rapid urbanization and infrastructure developments.
Therefore, in this research, we analyzed the time-series change of amount of habitat area for four endangered species (*Aquila chrysaetos, Accipiter gentilis, Macaca fuscata* and *Ursus thibetanus*) using MaxEnt (Maximum Entropy Modeling) software for modeling species distributions. As the result, it was concluded that total habitat possibility area for only Golden eagle was increased slightly but the one of other species was decreased.

Keywords: MaxEnt, GIS, Endangered Species, Green Area

INTRODUCTION

Fukushima prefecture in Japan is the third largest of Japan's 47 prefectures and stretches over 150 kilometers from the Pacific coast into the mountainous interior of northeastern Honshu. Fukushima prefecture is abound with rich nature such as Mt. Bandaisan, Lake Inawashiro and Bandai highlands including beautiful ponds and lakes. However, the number of endangered species in Fukushima has been increasing since the 1970's because the area of nature environment has been decreasing and then various habitat for valuable living organisms have been destroyed by rapid urbanization and infrastructure developments.

For the changes in land use, a lot of existing researches have analyzed the area and green coverage depending on the land use classification. A study by Hashimoto et al. [1] on umbrella species, which need large habitats satisfying specific conditions, elucidated their winter habitat preferences in the Lake Inba basin. Field research has also been conducted on raptors by evaluating the effects of environmental factors on the birds using the jackknife method. Ikemi et al. [2] performed quantitative analysis regarding the impact of artificial landform changes on biodiversity through a time-series analysis of land use changes. Harada et al. [3] conducted quantitative analysis on the extent of degradation of a forest environment through a count of each type of tree. Iwasaki et al. [4] reported on the changes in land use up to the 1980s and on their relationship with the increased damage to agricultural products caused by the expansion of the habitat of Japanese macaques. Li et al. [5] researched the impact of environmental variables and land use in Nagoya City on the habitat of tanuki (raccoon dogs) and Japanese weasels using Maxent analysis, albeit without performing a broad-based analysis. Matsuura et al. [6] created vegetation models, etc., for the Yatsu Higata tidal flats and estimated the environment required by the gray-faced buzzard eagle. However, the gray-faced buzzard eagle also lives in habitats such as mountains, under conditions different from those of tidal flats. Such habitats were not estimated in this research and require further study. Kamata et al. [7] proposed methods of forest zoning on the basis of land productivity and mountain disaster risks. However, it is also necessary to perform analysis from the viewpoint of wildlife habitats. Miyamoto [8] indicated the focal points to propose Marine Protection Area by applying MaxEnt to Emperor Seamount Chain using limited data. Pan et al. [9] estimates the suitable habitat area of Chinese Alligator that is a critically endangered crocodilian and predicted its distribution in Anhui Province, China by MaxEnt. West et al. [10] developed a presence-only model of invasive cheat grass (*Bromus tectorum*) distribution in Rocky Mountain National Park, Colorado, USA in from 2007 through 2013 with limited data to compare with the result of GLM (Generalized Linear Model). Remya et al. [11] represented current and future habitat suitability distribution of *Myristica dactyloides Gaertn*, a

medicinally and ecologically important tree species by MaxEnt in order to implement sustainable conservation or adaptation strategy. Pratumcharta et al. [12] predicted the distribution of *B. s. goniomphalos* in Thailand on the basis of environmental and climatic factors and also indicated that altitude, land cover, normalized difference vegetation index (NDVI), precipitation in the driest month, land surface temperature and soil pH affected its distribution.

Previous researches encompassed the evaluation of lands and forests by GIS, as well as the evaluation of habitats for target species by MaxEnt. However, there are few studies on the impact of urban development, including transportation infrastructure development, over time and in a wide area within wildlife habitats.

Therefore, in this research, we analyzed the time-series change of amount of habitat area for four endangered species (*Aquila chrysaetos*, *Accipiter gentilis*, *Macaca fuscata* and *Ursus thibetanus*) using MaxEnt (Maximum Entropy Modeling) software for modeling species distributions.

DATA

The wildlife habitat data used in MaxEnt were obtained from the Red Data Book[13], [14] compiled in 2002, plotted in QGIS, then converted into CSV data so as to be usable in MaxEnt. Having examined various habitat data, these were found to be the most suitable for analysis and further use. Further, because these habitat data were gathered in a mesh of 10km x 10km, at the time of plotting, the points were placed in the land use category that occupied the largest portion of the mesh.

Table 1 is a list of the environmental variables used in MaxEnt. According to the Digital National Land Information [15], seven environmental variables were used and arranged by QGIS in MaxEnt: land use subdivision data on Fukushima Prefecture from 1976, 1987, 1991, 2006, 2009 and 2014; average elevation in 2009; average inclination angle in 2009; annual average temperature, annual average precipitation, and annual deepest snow cover calculated from the average of the past 30 years; road edge data created from 2015 to 2016 by the Geographical Survey Institute of Japan (GSI) [16]. Road edge data were obtained by calculating distance from the road with the raster distance tool in QGIS and digitizing it for analysis.

Figure 1 shows the analyzed target species. The target species were selected from the Fukushima Red Data Book I [13] and II [14] (created in 2002). The selection criteria were: habitat conditions considered to be related to each environmental variable used in the study, species with a large habitat (due to the use of a 10km x 10km mesh data), and the condition that the Fukushima Red Data Book I [13] and II [14] recorded sufficient habitat data. As for the number of habitat data, to obtain a uniform degree of accuracy, we selected those with 15 or more meshes indicating confirmed habitat.

As a result, the golden eagle (*Aquila chrysaetos*) and the northern goshawk (*Accipiter gentilis*), two raptors with a particularly large habitat which are Category I threatened species, were selected among birds. Two vulnerable species, the Japanese macaques (*Macaca fuscata*) and the Asian black bear (*Ursus thibetanus*) were selected among mammals. Japanese macaques and black bears are vulnerable species, and although their conservation priority was not especially high in 2002, they were selected due to the increasing necessity of measures for conservation and animal protection which were expected in the future.

The land use classification of each period was used Digital National Land Information [15]; land use subdivision meshes have different land use categories from year to year. In light of the need to unify land use classifications in order to perform analysis over time, a new classification has been created, integrating land use into 9 categories: rice fields, other agricultural land, forests, wastelands, Buildup Area, main line traffic sites, other land, rivers and lakes, and seaside areas.

Table 1 Data sets input into MaxEnt

Data	Mesh size	Year	Source
Land use	100m	2014	Geospatial Information Authority of Japan
		2009	
		2006	
		1997	
		1991	
		1987	
		1976	
Average slope angles	10m	2009	
Average altitudes	10m	2009	
Average rainfall amount	1 km	2010	
Annual average temperature	1 km	2010	
Deepest snowfall in the year	1 km	2010	
Distance from nearest road	-	2016	

Fig. 1 Target species

RESULTS

Comparison result of area of each land use

In Table 2, land use areas are compared according to land use in Fukushima prefecture. Rice fields decreased uniformly, and other agricultural land, despite showing a growing trend from 1976 to 1997, decreased thereafter, resulting in a total area that was only 0.3% larger in 2014 than in 1976. Forests decreased almost uniformly from 1976 to 2006, but recovered remarkably in 2009. Although the results of conservation activities such as afforestation can be taken into account, it may be supposed that the number of high-quality forests is decreasing due to the decline of forestry. Wastelands decreased almost uniformly, and showed a significant decrease between 1976 and 2014 as well. Buildup Area increased almost uniformly. The land that is considered unsuitable as a wildlife habitat, such as Buildup Area, main line traffic sites, and other land increased by 82.7% between 1976 and 2014. The green ratio, including rice fields, other agricultural land, forests, and wastelands, decreased by 2.9% between 1976 and 2014. As for the reason of the significant decrease in the number of main line traffic sites in 2009, it is likely due to the fact that since 2009 roads and railways have been divided into two categories of land, whereas until 2009 there was only one category for both. Furthermore, in this land use subdivision mesh, the land use category that occupies the largest area in a 100m x 100m mesh constitutes the land use of that entire mesh. Thus, for example, even if the traffic land itself has not decreased, new buildings may have been constructed in the surroundings, occupying the largest area in the mesh, and determining the land use to be changed from traffic land to buildup Area.

Analysis results of suitable habitat area

Figure 2 shows the result of suitable habitat area of four target species by MaxEnt in 1976 and 2014. The map of habitat suitability for the target species being expressed as a value from 0 to 1. Habitat suitability increases as the color changes from blue to green, yellow, orange, and red. White dots are habitat plot data confirming location of the target species.

In the case of the Golden eagle, the suitable habitat mainly extends in the southwest and north, such as Oze National Park and Aizukomagatake, which is blessed with a rich natural environment. In a comparative evaluation of suitable habitats in 1976 and 2014, almost no significant change was found in the habitat suitability map.

The habitat suitability map for northern goshawks shows that there are many suitable habitats in the mountains, northern areas, etc., between Hamadori located in the east area and Nakadori in the central area in Fukushima prefecture. The most remarkable change in the habitat suitability map between 1976 and 2014 was found in Nakadori, Fukushima Prefecture, where habitats with a low degree of suitability are extending gradually. Further, the same tendency is seen in the Aizu region and the nearby mountainous areas, which can be said to be greatly affected by recent urban development.

The suitable habitats for Japanese macaque were found in the northern part of Hamadori and in the northern and southwestern parts of Lake Inawashiro (black part in the center). In the case of Japanese macaques, yellow moderate-degree habitat suitability was found often, whereas red and orange—indicating highly suitable habitats—were rarely seen. Since Japanese macaques may appear in urban areas in search of food, their habitat is considered to be widely distributed. Comparing the map between 1976 and 2014, no significant change was found in the habitat suitability map, but there is a tendency toward the shrinking of suitable habitats in the mountains due to the opening of expressways.

The habitat suitability map of Asian black bear shows suitable habitats in the northern and southwestern parts in Fukushima prefecture. It was found that suitable habitats in the northern and southwestern parts of Fukushima prefecture have decreased due to environmental changes as a consequence of deforestation due to a high contribution ratio related to forest land.

Table 2 Comparison result of area of each land use

(1,000ha)

Land use	1976	1987	1991	1997	2006	2009	2014	Comparison between 1976 and 2014 (%)
Rice fields	162.1	157.0	155.0	149.0	149.0	146.8	145.2	-10.4%
Other agricultural land	89.6	96.6	96.5	103.0	95.2	87.4	89.9	0.3%
Forests	1002	997	992	972	971	1015	1009	0.7%
Wastelands	41.4	33.2	32.9	31.0	31.2	15.3	13.7	-66.9%
Buildup Area	36.5	43.0	42.8	54.8	57.3	62.6	63.2	73.2%
Traffic sites	1.6	2.5	6.6	8.1	10.5	1.3	5.4	237.5%
Rivers, Lakes and Ponds	35.1	35.2	35.0	40.9	36.4	30.1	33.6	-4.3%
Coastal Area	14.2	2.8	2.7	18.2	25.2	2.6	1.9	-86.6%
Others	9.3	12.5	16.1	18.8	26.8	18.1	18.0	93.5%

The result of Golden eagle had an AUC of 0.775,

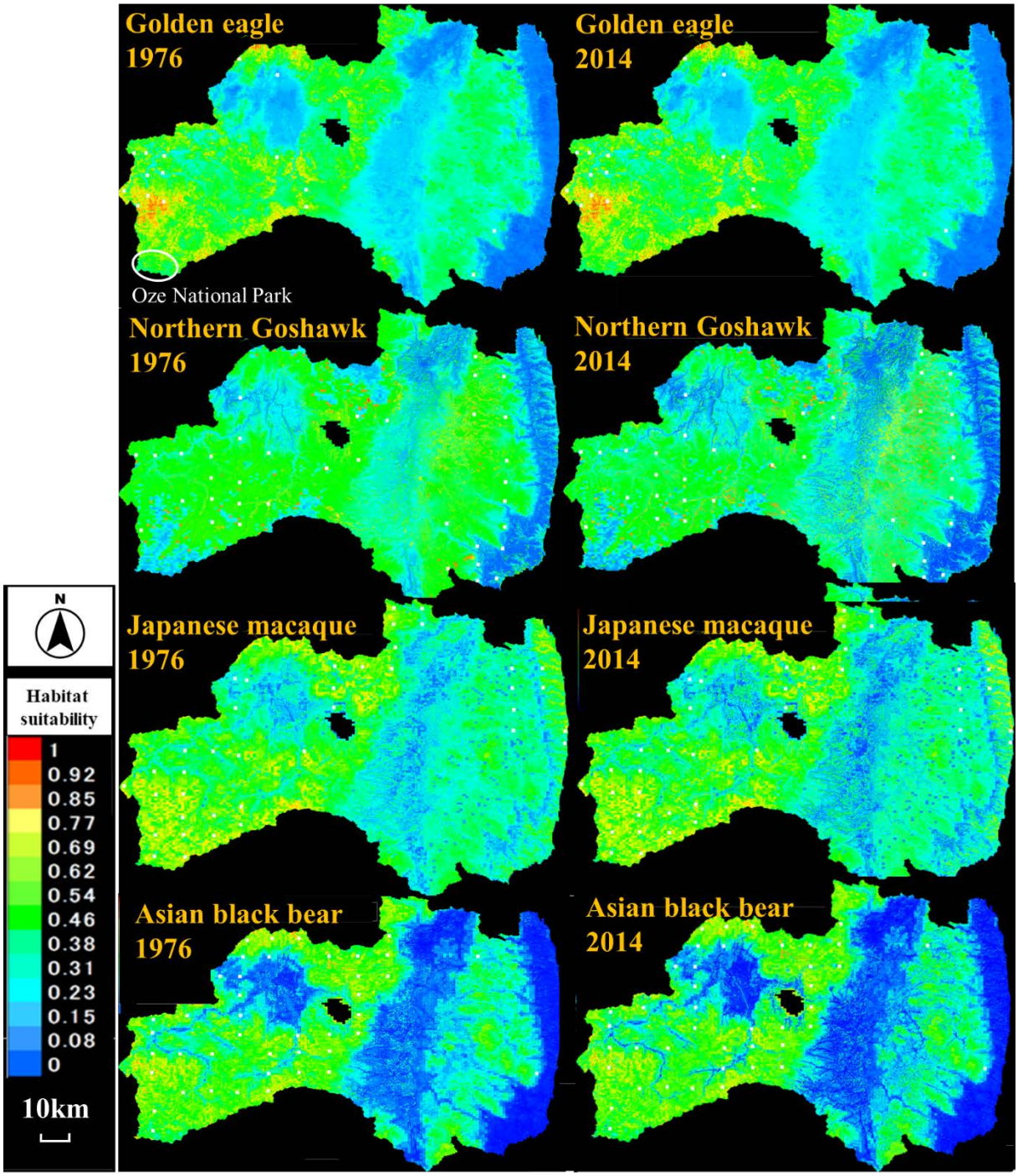

Fig. 2 Suitable habitat area estimated by MaxEnt

Result of AUC and Contribution Rate

Table 3 shows the Area Under the Curve (AUC) and contribution rate of respective environmental factors of each species. A model with AUC value exceeding 0.7 is considered as a good model, and the closer to 1 is better model.

which was a good result. Regarding the contribution ratio of Golden eagle, the land use contribution ratio for the golden eagle was found to be very low at 0.6%, and each environmental variable exerts an impact on the Golden eagle, and it is understood that the average slope angles and average altitude have a large impact. These two environmental factors influences may be high because the Golden eagle lives and nests on rocky spots such as steep cliffs in mountainous area.

On the other hand, the land use contribution ratio was only 0.6%. Therefore, the impact of land use is not particularly significant. The highest contribution ratio is that of other agricultural land.

The AUC of the Northern goshawk was 0.765, which was a good result. The contribution ratio of land use and average altitude for Northern goshawks were as high as 49.5% and 33.2% respectively. The detail land use contribution ratio of Northern goshawk is shown in Figure 3. Figure 3 is the contribution ratio showing which land uses are likely to influence habitat suitability, and the likeliness of habitat suitability itself. As raptors such as the northern goshawk catch their prey in grasslands, paddy fields, wetlands, etc., with good visibility, the contribution ratio of rice fields, other agricultural lands, and wastelands were high. In contrast, forests reduce the range of vision and obstruct flight, resulting in a low contribution ratio.

The AUC of Japanese macaque was 0.766, which was a good result. The highest contribution ratio for Japanese macaques was temperature, followed by the angle of inclination. In the case of Japanese macaques, it was found that all environmental variables had a certain degree of contribution. Consequently, habitat suitability tended to be high only in areas where all environmental factors were well-balanced.

The AUC for the black bear was 0.809, the highest among the four target species. In the case of the black bear, the contribution ratio is high for temperature, land use, and snowfall. This suggests that the black bear is easily affected by environmental factors related to temperature.

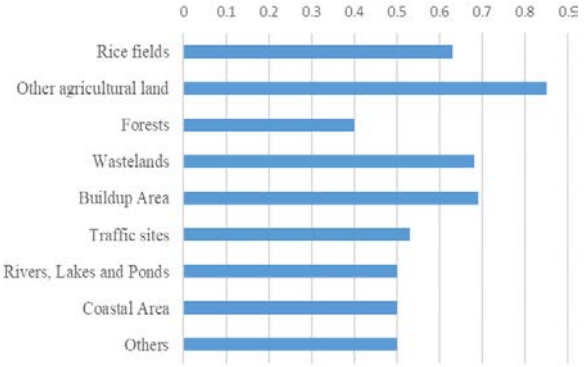

Fig. 3 Response curve on each land use of Northern goshawks

Result of time-series change of potential suitable habitat area

Table 4 and Figure 4 show numerical values corresponding to the changes in potential suitable habitat areas in Fukushima Prefecture over time for each four species. From the data in the ASC file obtained by MaxEnt analysis, data evaluating suitable habitats at a ratio of 0 to 1 were extracted and used to define potential suitable habitat area by multiplying the numerical values by the area of each mesh (100m x 100m mesh). As a result, a comparison between 1976 and 2014 confirmed a decrease in habitability areas by 3.57% for the Japanese macaque, by 7.44% for the northern goshawk, and by 1.92% for the black bear. The habitability areas for the golden eagle were

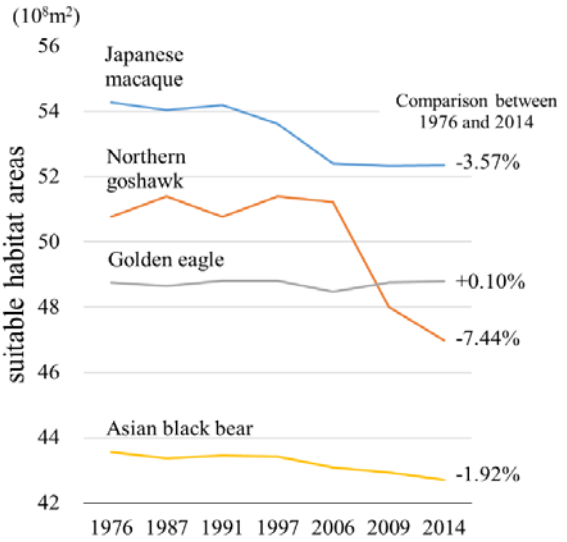

Fig. 4 Suitable habitat areas response curve on each land use of Northern goshawks

Table 3 AUC and contribution rate of respective environmental factors

	AUC	Land use (%)	Average rainfall amount (%)	Annual average temperature (%)	Average altitudes (%)	Average slope angles (%)	Deepest snowfall in the year (%)	Distance from nearest road (%)
Golden eagle	0.775	0.6	0.8	1.8	32.7	52.0	0.3	11.9
Northern goshawk	0.765	49.5	5.2	0.0	33.2	1.2	10.8	0.1
Japanese macaque	0.766	15.3	6.6	28.2	5.1	23.3	11.9	9.7
Asian black bear	0.809	18.2	1.5	48.2	0.6	9.9	18.2	3.4

Table 4 Result of potential suitable habitat area between 1976 and 2014

	1976	1987	1991	1997	2006	2009	2014	Comparison between 1976 and 2014
Golden eagle	48.75	48.65	48.81	48.80	48.47	48.75	48.80	0.10%
Northern goshawk	50.76	51.40	50.76	51.40	51.22	48.01	46.99	-7.44%
Japanese macaque	54.28	54.04	54.18	53.61	52.40	52.33	52.35	-3.57%
Asian black bear	43.55	43.37	43.46	43.42	43.08	42.93	42.72	-1.92%

found to have increased by 0.1%. The results suggest that a decrease in suitable habitats for wildlife due to urban development and transportation infrastructure maintenance has become increasingly likely.

CONCLUSIONS

In this research, MaxEnt was used to analyze the suitable and potential habitat area of four endangered species in Fukushima prefecture over time, demonstrating the impact of rapid urbanization and infrastructure developments and the tendency for suitable habitats to decrease for species other than the golden eagle. Thus, it was cocluded that the habitat for various species including endangered species needs to protect from the point of view of the harmony of environment conservation and human activity.

For further research, it is necessary to improve the accuracy of the plot data for habitat places by collecting more data and by including other environmental variables for MaxEnt.

REFERENCES

[1] Hashimoto D. and Hasegawa M., Habitat preference and species distribution modeling of raptorial birds inhabiting Inbanuma-lake during winter season, Report of the Chiba Biodiversity Center (7), 2014, pp.65-78.

[2] Ikemi H., Esaki T., Mitani Y. and Tran T. A., Spatial Distribution of Human Impacts on Terrain Based on Land-use Change Analysis : Development and GIS Analysis of Land-use Maps since 1900 in the Fukuoka Prefecture Area, Engineering Geology, Japan, 52(3), 2011, pp.97-108.

[3] Harada I., Matsumura T., Hara K., and Kondoh A., Spatial analysis of changes in Japanese forests during the process of modernization, Landscape and Ecological Engineering, 16(1), 2011, pp.17-32

[4] Iwasaki N., and Sprague D., A study of the land use history in the Japanese macaque habitat expansion area of the Boso Peninsula, Japan, Journal of Rural Planning Association, 24, 2005, p.1-6.

[5] Li R., Ooba M., Hayashi K., Noro T., Dhakal, A., "The potential distributions of mammalian with land use changes by the MaxEnt model - case of Nagoya city", ISETS'13, 2013, pp.13-15.

[6] Matsumura T., Yokohari M., and Azuma A., Identification of potential habitats of Gray-faced Buzzard in yatsu valleys based on DEMs and vegetation data, Proceedings of Japanese Institute of Landscape Architecture, 65(0), 2002, pp.39-39.

[7] Kamada M., Sanpei R., and Oka K., Method for forest zoning in broad area based on the evaluation of land-productivity and mountain hazard, Landscape and Ecological Engineering, 18(2), 2013, pp.109-122.

[8] Miyamoto M., Attempts to estimate habitat of cold-water corals, Aquabiology, Vol.35(5), 2014, pp.461-468.

[9] Pan T., Wang H., Duan S., Ali I., Yan P., Cai R., Wang M., Zhang J., Zhang H., Zhang B. and Wu X., Historical population decline and habitat loss in a critically endangered species, the Chinese alligator (Alligator sinensis), Global Ecology and Conservation, Vol.20, 2019, e00692.

[10] West M. A., Kumar S., Brown S. C., Stohlgren J. T. and Bromberg J., Field validation of an invasive species MaxEnt model, Ecological Informatics, Vol.36, 2016, pp.126-134.

[11] Remya K., Ramachandran A. and Jayakumar S., Predicting the current and future suitable habitat distribution of Myristica dactyloides Gaertn using MaxEnt model in the Eastern Ghats, India, Ecological Engineering, Vol.82, 2015, pp.184-188.

[12] Pratumcharta K., Suwannatrai K., Sereewong C., Thinkhamrop K., Chaiyos J., Boonmars T. and Suwannatrai T. A., Ecological Niche Model based on Maximum Entropy for mapping distribution of Bithynia siamensis goniomphalos, first intermediate host snail of Opisthorchis viverrini in Thailand, Acta Tropica, Vol.193, 2019, pp.183-191.

[13] Fukushima prefecture, Japan, Red Data Book Fukushima Ⅰ (Plants, Insects and birds), http://is2.sss.fukushima-u.ac.jp/fks-db/txt/51603.002/thumb/00000_01.jpg

[14] Fukushima prefecture, Japan, Red Data Book Fukushima Ⅱ (freshwater fishes, amphibians, reptiles and mammals), http://is2.sss.fukushima-u.ac.jp/fks-db/txt/51603.003/index.html

[15] Ministry of Land, Infrastructure, Transport and Tourism, digital national land information, http://nlftp.mlit.go.jp/ksj/

[16] Geospatial Information Authority of Japan, base map information, http://fgd.gsi.go.jp/download/menu.ph

6th Int. Conf. on Structure, Engineering & Environment (SEE), Kyoto, Japan, Nov.18-20, 2020, ISBN: 978-4-909106056 C3051

HEAVY METALS EXPOSURE AND RISK ASSESSMENT OF COOKED RICE FROM THE FIELD NEAR THE OLD DUMPSITE IN INDONESIA

Fajri Mulya Iresha[1,2], Suphia Rahmawati[2], Dhandhun Wacano[2], Kasam[2], Ratna Kartika Sari[2], Minoru Yoneda[1]
[1]Graduate School of Engineering, Kyoto University, Japan; [2]Faculty of Civil Engineering and Planning, Universitas Islam Indonesia, Indonesia

ABSTRACT

The lack of implementation of spatial planning and landfill site planning in several areas of Indonesia in the past has led to the case of the rice field directly bordering the open dumping site. High intensity of rainfall, leachate-contaminated irrigation, and the open dumping site with steep slopes create a high risk of rice pollution. This study aims to identify the concentrations and the exposure of heavy metals consist of Cr, Cd, Cu, Fe, Mn, Zn, and Pb in the cooked rice which is consumed by residents around the open dumping site, the rice, and the water using for rinse the rice. In this research, rice also compared between two zones which are upstream site zone and downstream site zone. Thus, applicable quality standards and analysis of estimated metal intake will be conducted. The results of this work demonstrate the heavy metals in the downstream zone concentrations are higher than the upstream zone. Besides, there are several samples whose exceeds the quality standard. Based on the test results obtained heavy metal concentrations in rice samples are higher than heavy metal concentrations in cooked rice. The higher Pb content in adult (Risk Quotient (RQ) value > 0.2) and Cr content in children (Excess Cancer Risk (ECR) value > 10^{-3}) suggest the risk of the health of the people near the site.

Keywords: Exposure, Heavy Metals, Open Dumping, Rice, Risk Assessment

INTRODUCTION

Every day, human activities produce waste. Almost all sectors of human activity always produce waste. With the increase in the number of residents will increase the percentage of the amount of solid waste. With the times will change lifestyle patterns. With these changes will also affect the increase in the amount of waste generated. Whether it is domestic, electronic, industrial waste and others. In Indonesia, the percentage of waste transported to the landfill is still very high without prior treatment, such as the sorting of solid waste from a waste source. So that with a large amount of garbage transported to the landfill, over time, the solid waste will continue to accumulate in the landfill without any management [1].

The Gunung Tugel dumpsite operated in 1983 and was closed because it was considered to have been overloaded. In 2016, therefore the Gunung Tugel dumpsite was no longer used. However, the Gunung Tugel dumpsite is still prone to landslides and garbage fires that occur every dry season. The Gunung Tugel dumpsite itself now has a land area of 5.3 hectares by accommodating waste from Purwokerto with a more significant percentage of organic waste. Every day, the Gunung Tugel dumpsite can provide 300-350 m^3 of garbage.

The Gunung Tugel dumpsite uses an open dumping method in which existing waste was not being processed. With the application of the open dumping method, it was high possibility that leachate originating from the degradation of the waste from the landfill will enter the soil pores, which then will subsequently enter to the groundwater. With the groundwater that has been contaminated with leachate even with slow groundwater flow, the heavy metal pollutants will still be exposed to the environment around the Gunung Tugel dumpsite [2].

Heavy metals that are in the soil can be sourced from nature and also anthropogenic. In soils that are still not utilized, heavy metals can be contained in soil parent materials, geochemical and pedological processes in soil formation [3]. Ballistic soil naturally contains heavy metals Cu, Zn, Ni, and Cr . In anthropogenic processes, heavy metals can enter through the addition of chemicals such as pesticides and also the use of fertilizers, motor vehicle pollution [4, 5].

Around the Gunung Tugel dumpsite, there is a rice farm owned by residents with an irrigation channel just below the landfill. Rice produced from rice fields around the Gunung Tugel dumpsite will be consumed by themselves for daily food by residents around the Gunung Tugel dumpsite. The presence of heavy metals in the environment, such as in soil and irrigation, can be hazardous to human

health. There is other study in the open dumping site that found the concentration of heavy metals in soil and water around the landfill were higher than the permissible limit because of the leachate migration [6]. Even some plants those are in the landfill could be a promising trace metals contamination indicator for heavy metals [7]. For rice plant, also can adsorb the heavy metals so that there is high content in the rice grains and cause the risk for the human health [8]. The entry of heavy metals from the environment into the food chain can cause the concentration of heavy metals that are higher and higher, because of difficulty nature heavy metals properties to decompose and to be deposited on the surface of the soil that can be absorbed by the surrounding organisms.

Therefore, to identify whether the Gunung Tugel dumpsite has a role in the entry of heavy metals in an agricultural land owned by residents around the landfill or not. So, this research was conducted to identify the magnitude of the concentration of heavy metal content contained in water, rice and also in the cooked rice consumed by residents from the rice field around the Gunung Tugel dumpsite.

MATERIALS AND METHODS

Location

This study was conducted at the Gunung Tugel Dumpsite, Banyumas Regency, Central Java. The local government closed this site approximately in 2016. The object of research carried out consisted of the water using for rinse the rice, the rice itself and the cooked rice. The rice was used for research originating from rice fields belonging to residents around the landfill, and they consumed it directly. For the water using for rinse the rice, the residents are devided into two groups, who use of tap water from local water company and from ground water. The map of research locations can be seen in Fig. 1.

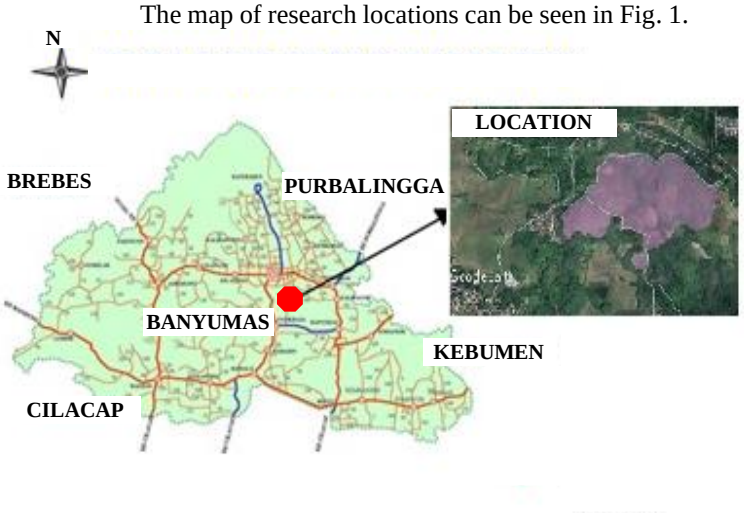

Fig.1 Location of Gunung Tugel Dumpsite

The location of the rice and water sampling in this study was divided into two zones for each test sample. The first zone is the paddy field zone with irrigation flow before the landfill landslide occurred. The second zone is the paddy area zone with irrigation flow after landfill landslide. The water sampling zone was also divided into two zones. The first and second zones are based on the residence of the rice field owner at the location of the rice sampling point (See in Fig.2). For the rice and the water samples in zone 1, there are eight sampling points for each house and rice field. For the second zone, there are three sampling points for each house and rice field. In this study, the number of 12 sample points was based availability of the farmers in the fields and the using water in the rice fields is from the irrigation flow which contaminated with leachate especially within and after zone 2 of rice field .

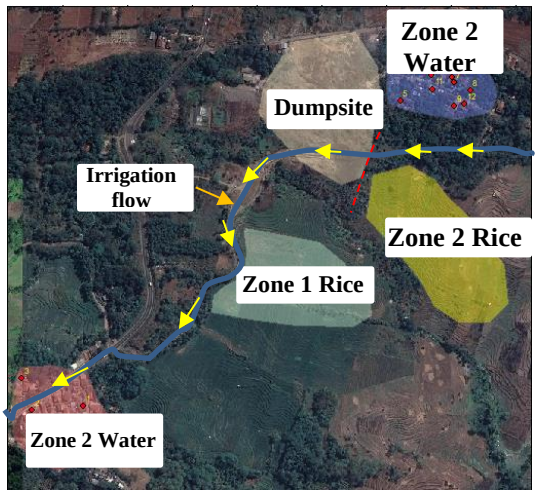

Fig. 2 Water and Rice Sampling Location

Sample Preparation and Laboratory Analysis

The rice is taken from the rice field around the Gunung Tugel Dumpsite, and residents themselves consume the rice. The water sample taken in this study is from the well water or tap water that is used by residents to cook the rice every day.

The sampling method used in this study is stratified Sampling method. Considerations taken in the sampling of rice and water in the form of residents around the Gunung Tugel Dumpsite who have rice fields, consume rice from the harvested rice fields around the landfill and live around the site. Samples taken in the form of rice and water are used for cooking rice at the Gunung Tugel Dumpsite. A sampling of the water is done based on SNI 6989: 58: 2008 Concerning Groundwater Sampling Methods .

Physical observations carried out in the form of conditions from topography, irrigation flow for

irrigating rice fields. Then the primary data is also in the way of data from the results of heavy metal tests. Interviews and questionnaires to residents of rice fields around the Gunung Tugel dumpsite are also conducted. Interview data were made in the way of how many times people consume rice in a day, how many times people cook rice in one day, how many times people rinse rice, what kind of water is used.

For the equipment or detecting the heavy metals this research use Flame-Atomic Absorption Spectroscopy (AAS) instruments. Samples that have been taken from the field will be tested and analyzed in the Environmental Engineering Laboratory of the Universitas Islam Indonesia. Samples that were tested were carried out in destruction process until the volume decreased up to 10 ml and then extracted to 25 ml. In testing, this sample is carried out under applicable Indonesia National Standard and no modification of sample testing. In the metal test, the sample was added with a 65% concentrated nitric acid.

Data Analysis

Exposure analysis or usually referred to as exposure assessment or commonly also called contact assessment which aims to identify the path of heavy metal exposure through food or risk agents so that the amount of intake received by potentially risky individuals can be calculated. By using the calculation formula as follows [9].

Intake Exposure (I_{nk})

$$I_{nk} = \frac{C \times R \times fE \times Dt}{Wb \times t\,avg} \quad (1)$$

Risk Quotient (RQ)

$$RQ = \frac{I_{nk}}{RfD} \quad (2)$$

Excess Cancer Risk (ECR)

$$ECR = I_{nk} \times SF \quad (3)$$

Notes :

Table 1 Description of Variables in Formulas

Symbol	Definition
I_{nk}	Total concentration of risk agents (mg / kg.day)
C	Concentration of risk agents in clean water / drinking or food (mg / kg)
R	The rate of consumption or the amount of weight of food that enters the human body (g / day)
fE	The duration or number of days a year occurs (days/years)
Dt	The duration or number of years the exposure occurred (years).
Wb	Human weight (kg)
tavg	The average period for carcinogenic and non-carcinogenic effects (days). For non-carcinogenic (30 years x 365 days) for carcinogenic (70 years x 365 days)
RQ	Risk agent reference value in ingestion exposure
RfD	The dose/concentration of daily non-carcinogenic risk agent exposure is estimated to have no detrimental effect even though the exposure occurs throughout life (for life)
ECR	The magnitude of the risk expressed infractions multiples of rank 10 - (exponents)
SF	The reference value of risk agents with carcinogenic effects

Based on the Risk Quotient (RQ), it is found that there are health risks stated if the RQ value > 1. Assume that there is other paths of exposure, especially from drinking water and vegetables, so that RQ < 0.2 is thought to be acceptable. Based on the value of Excess Cancer Risk (ECR) Risk level is expressed in exponent numbers without units (example: 1.3E-4). The level of risk is said to be acceptable or safe if the ECR ≤ E-4 (10^{-4}) based on guidelines for Environmental Health Risk Analysis issued by the Indonesian Ministry of Health and Health in 2012. The level of risk is said to be unacceptable or unsafe if ECR> E-4 (10^{-4}).

RESULT AND DISCUSSION

Heavy Metals in the Water Used for Rinsing the Rice

The concentrations of heavy metals in the water used for rinsing the rice for Gunung Tugel dumpsite followed the decreasing order of Fe > Mn > Zn > Cr > Pb > Cd > Cu. Based on the AAS, Cr, Cd, Fe, and Zn test results exceed the quality standards at all sampling points. The rest, other heavy metals namely Mn, Pb, and Cu exceed quality standards at several points (See Fig. 1 & Fig. 2).

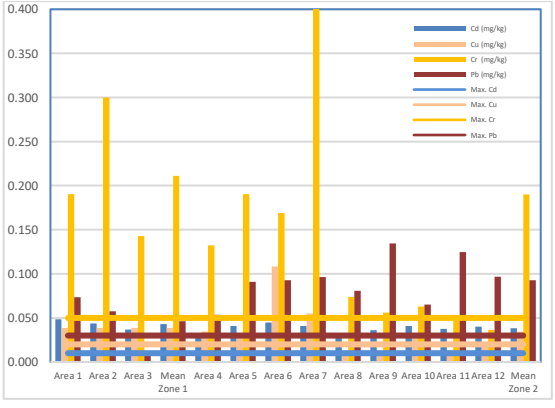

Fig. 3 Concentration of Cd, Cu, Cr & Pb in the Water

The amount of Pb in tap water caused by pipes used to distribute the water, are made from polyvinyl. This plastic containing Pb stearate. It shows the occurrence of Pb leaching into the water when water is overnight in the water pipe. For Fe, Zn and Mn are naturally present in the environment and at specific concentrations also needed by the body. The rest, such as Cu, Cd, Cr may be present because of seepage of leachate into wells for those whose source of water is from well water, and also seepage of leachate water to piped water network for those whose source of water is from tap water.

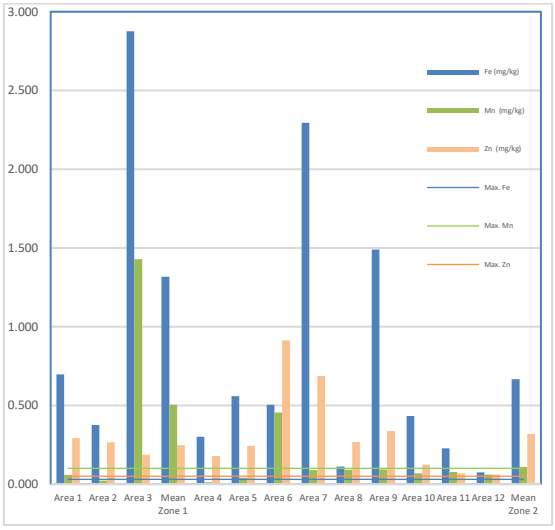

Fig. 4 Concentration of Fe, Mn, & Zn in the Water

Heavy Metals in the Rice

The concentrations of heavy metals in the rice for Gunung Tugel dumpsite followed the decreasing order of Fe>Cu>Zn>Mn>Pb>Cr>Cd. Based on the results of the AAS test, concentrations of Mn, Cr, and Zn did not obtain a single rice sampling point that exceeded the maximum allowable value. For the concentrations of Cu, Pb, Fe, and Cd, there are several sampling points whose values exceed the quality standard (See Fig. 3 & Fig. 4). Pb, found in the most sampling points that exceeded the quality standard is likely to occur due to the location of paddy fields in zone 2 close to the landfill with irrigation flow entering zone 2 being

hit by a landslide from landfill so that leachate containing heavy metals Zn, Cu, Fe, Co, Mn, Hg, Cd, Pb, and Cr [10]. Entering the irrigation channel and mixed with irrigation water, but apart from coming from irrigation water that has been buried by landslides.

There is also a possibility that is caused by the use of pesticides and TSP fertilizer used by farmers. Excessive use of pesticides can also contribute to the accumulation of heavy metals in agricultural land. In a study, it was found that the pesticides contained heavy metals As, Cu, Zn, Mn, Hg, and Pb with Pb metal content had a higher concentration compared to other heavy metals which are around 11 - 60 ppm [11].

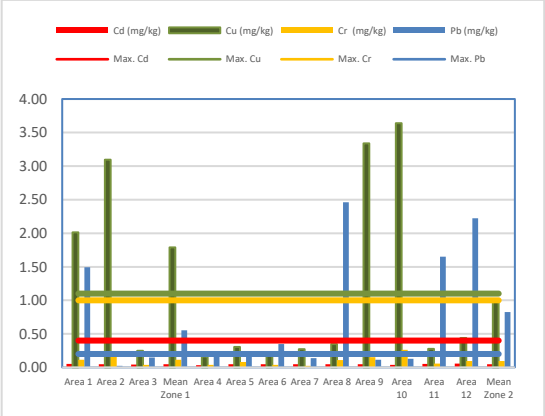

Fig. 5 Concentration of Cd, Cu, Cr & Pb in the Rice

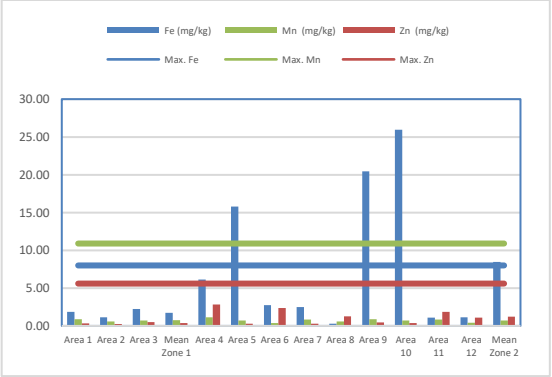

Fig. 6 Concentration of Fe, Mn, & Zn in the Rice

Heavy Metals in the Cooked Rice

The concentrations of heavy metals in the cooked rice for Gunung Tugel dumpsite followed the decreasing order of Zn>Pb>Fe>Cu>Mn>Cr>Cd. Based on the results of the AAS test, the Pb concentration exceeds the quality standard that have been set at all sampling points. This can be possible in the cooked rice accumulation of Pb metal from water and also cooked rice. It was found that the concentration of Pb in zone 1 is higher than the concentration of Pb in zone 2. It can be said that the accumulation of rice by heavy metals Pb occurs because there is already Pb metal in rice and accumulates with Pb metal in hydrolyzed water entirely when cooking rice so hydrolyzed water will make the heavy metal enter and be absorbed entirely into cooked rice. And there is also a possibility because of the tools used to cook rice. For the concentration of Cd and Zn, several sampling points exceed the quality standard. As for the

concentrations of Fe, Mn, Cr, and Cu, no concentrations at all were found that exceeded the quality standard at all sampling points.

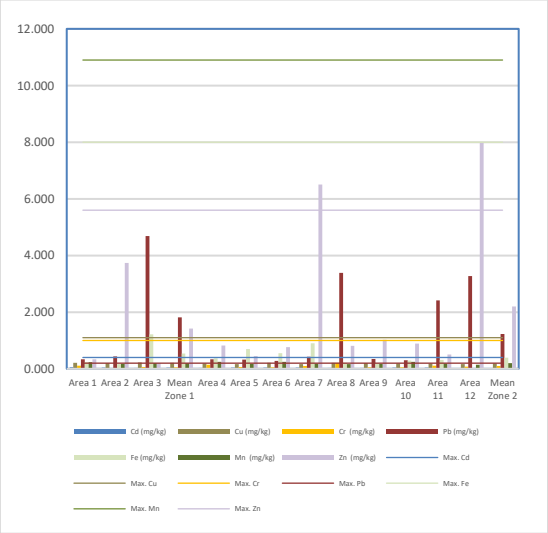

Fig. 7 Concentration of Heavy Metals in the Cooked Rice

Estimation of Heavy Metal Intake

The path of heavy metal intakes can come from various kinds, but in this study rice consumption is the primary intake of heavy metals into the human body [12]. Heavy metal intake is estimated by the level of daily consumption with the metal content in rice [13].

Based on the results of interviews with residents of agricultural land owners who are used for sampling it is estimated that in 1 day adults will consume 170 g of rice / person / day, with an estimated adult weight of 55 kg and for children of 15 kg of the estimate based on Technical Guidelines for Environmental Health Risk Analysis for 2012. Duration time (Dt) for non-carcinogenic intakes is estimated for 30 years for adults, and six years for children and carcinogenic Dt intakes for 70 years it is based that for carcinogenic the effect that can be caused to be a symptom of cancer requires a long duration to the symptoms of cancer, the value is taken based on the 2012 Technical Guidelines for Environmental Health Risk Analysis—used as an evaluation of daily intake and hazard quotient. In calculating the estimated intake is done by calculating the intake or exposure analysis and also calculating the risk characteristics.

In this study, the path of exposure comes from oral exposure (rice consumed by residents around the Gunung Tugel Dumpsite) in the Guidelines for Environmental Health Risk Analysis [14], Ministry of Health 2012 called intake ingestion. In the estimation of intake estimates based on the Environmental Health Risk Analysis Guidelines, the Ministry of Health 2012 with reference Dose (RfD) and Slope Factor (SF) values obtained from USEPA, WHO and USDOE IRIS (Integrated Risk Information System) 2011. Exposure analysis is an evaluation of exposure to the organism, system, or sub/population, and this exposure analysis is step 4 of Environmental Health Risk Analysis (EHRA). While the calculation of risk characteristics itself is a qualitative and quantitative calculation which includes the probability of potential adverse effects from exposure to organisms, systems, or sub-populations to determine the level of risk whether risk agents at certain concentrations will pose a risk of causing harm to the health of the community or not.

Based on the calculation results in Fig. 6, it is found that the concentrations of heavy metals Cr, Cu, Mn, Fe, Zn, Cd have a safe risk value because they have an RQ value of ≤ 0.2. While for heavy metals Pb metal for adults, has a risk level value which is not safe with an RQ risk level value > 0.2. The level of risk for carcinogenic effects is expressed as Excess Cancer Risk (ECR). The level of cancer risk is acceptable or safe if the ECR value is ≤ E-4 (10^{-4}) and is declared unacceptable or unsafe if the ECR value> E-4 (10^{-4}). Based on the Fig. 7 obtained for heavy metal Cd, children have the potential to become cancerous cases because they have an ECR value> E-4 (10^{-4}).

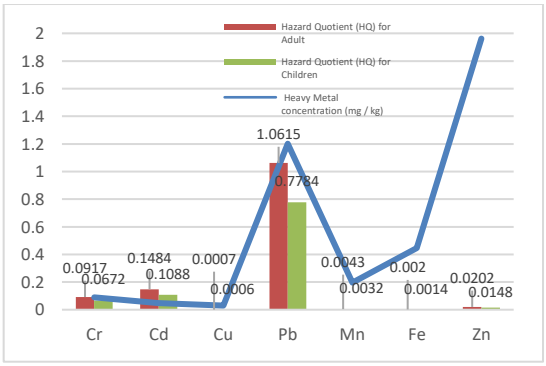

Fig. 8 The level of Risk Quotient from all Heavy Metals

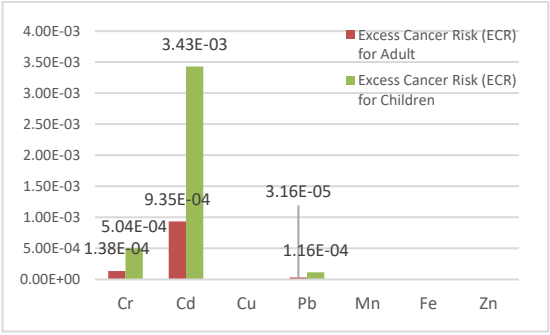

Fig. 9 The level of Excess Cancer Risk (ECR) from All Heavy Metals

CONCLUSION

It was found that the concentration of heavy metals in upstream zone (zone 2) has an average higher than downstream zone (zone 1). This is following the division of zones wherein zone 2, the distance is closer to the landfill than zone 1 and according to the direction of the contaminant flow it is directly flow to zone 2.

Based on the established quality standards for the water, rice and cooked rice test samples obtained consecutively the concentration of Cu, Cr, Cd, Pb, Zn, Mn, and Fe are 33%, 28%, 58%, 78%, 39%, 6%, 42% of sample points that exceed the quality standard of the total sample size. Based on the test results obtained heavy metal concentrations in rice samples are higher than heavy metal concentrations in rice.

Obtaining the result of the calculation of risk characteristics (RQ) on the prediction of adult Pb metal risk having an RQ value> 1, it can be concluded that there is a potential risk which is necessary to control, and obtaining an ECR value for the metal Cd of children> 10^{-4} , it can be concluded that there is a potential to be a symptom of cancer.

ACKNOWLEDGEMENTS

The authors would like to acknowledge Directorate of Research and Community Service, Islamic University of Indonesia and Environmental Risk Analysis Laboratory of Kyoto University for the funding the research. Also, for Universitas Islam Indonesia and students from the Banyumas landfill group 2019. We also thank to Development Planning Agency at Sub-National Level of Banyumas Regency for the support of the current condition data of the site and the permission for the sampling activity.

REFERENCES

[1] Tchobanoglous G., Theisen H., dan Vigil S. A., Integrated Solid Waste Management, United States : McGraw Hill International, 1993.

[2] SEPA, The Geological Barrier, Mineral Layer and the Leachate Sealing and Drainage System, Framework for Risk Assessment for Landfill Sites, 2002.

[3] Hardy M. and Cornu S., Location of natural trace elements in silty soils using particle-size fractionation. Geoderma, Vol. 133, Issue 3-4, 2006, pp. 295-308.

[4] Mortvedt J.J. and Beaton J.D., Heavy metal and radionuclide contaminants in phosphate fertilizers. Scope-scientific Committee on Problems of the Environment International Council of Scientific Unions, Vol. 54, 1995, pp. 93-106.

[5] Chancy, R.L., Reeves, P.G. and Angle, J.S., Rice plant nutritional and human nutritional characteristics role in human Cd toxicity, In Plant Nutrition, Dordrecht, Springer, 2001, pp. 288-289.

[6] Alam R., Ahmed Z. and Howladar M.F., Evaluation of heavy metal contamination in water, soil and plant around the open landfill site Mogla Bazar in Sylhet, Bangladesh. Groundwater for Sustainable Development, Vol. 10, 2020, p. 100311.

[7] Bakar, A.A., Yoneda, M., Thuong, N.T. and Mahmood, N.Z., Development of assessment for potentially toxic element contamination indicator in closed landfills and prospective geostatistical analysis. International Journal of GEOMATE, Vol. 17, Issue 60, 2019, pp. 136-143.

[8] Kasam, Rahmawati S., Mulya Iresha, F., Wacano, D., Farida Fauziah, I. and Afif Amrullah, M., Evaluation of Heavy Metal Exposure to Soil and Paddy Plant around the Closed Municipal Solid Waste Landfill: Case Study at Gunung Tugel Landfill, Banyumas-Central Java. MS&E, Vol. 299, Issue 1, 2018, p. 012012.

[9] Agency for Toxic Substances and Disease Registry. Toxicological Profile For Cadmium. United State : Department Of Health And Human Services Public Health Service, 2012.

[10] Irhamni I., Serapan Logam Berat Esensial dan Non Esensial pada Air Lindi TPA Kota Banda Aceh Dalam Mewujudkan Pembangunan Berkelanjutan. Jurnal Serambi Engineering, Vol. 2, Issue 1, 2017.

[11] Senesil G.S., Baldassarre G., Senesi N. and Radina B., Trace element inputs into soils by anthropogenic activities and implications for human health. Chemosphere, Vol. 39, Issue 2, 1999, pp. 343-377.

[12] Liu J., Hong Zhang, X., Tran, H., Wang Qiu, D., Zhu Nian, Y., Heavy Metal Contamination and Risk Assesment in Water, Paddy Soil, and Rice Around and Electroplating Plant. Environmnetal Science Pollution Research. Vol. 18, 2011, pp. 1623-1632.

[13] Shimbo S., Zhang Z.W., Watanabe T., Nakatsuka H., Matsuda-Inoguchi N., Higashikawa K. and Ikeda M., Cadmium and lead contents in rice and other cereal products in Japan in 1998–2000. Science of the total environment, 281(1-3), 2001, pp.165-175.

[14] Kementrian Kesehatan. Pedoman Analisis Risiko Kesehatan Lingkungan, 2012.

6th Int. Conf. on Structure, Engineering & Environment (SEE), Kyoto, Japan, Nov.18-20, 2020, ISBN: 978-4-909106056 C3051

DEVELOPMENT OF AN INTERACTIVE AND VISUALIZATION SYSTEM FOR DETERMINING CLIMATE RISK

Makoto Ooba[1], Takuya Togawa[1], Ronald Canero Estoque[1], Shogo Nakamura[1], Takashi Tsuji[1], Akira Yoshioka[1] and Yasuaki Hijioka[1]
[1]National Institute for Environmental Studies, Japan

ABSTRACT

In its Fifth Assessment Report, the Intergovernmental Panel on Climate Change reported the seriousness of climate change and its future effects. Human society faces certain inevitable consequences without a plan for adapting to global climate change. A multi-sector collaboration to plan local adaptation is necessary because climate change affects many sectors. Extreme rain events (hazard) may enhance the risk of river floods and are related to river management, residential evacuation, traffic control, etc. To promote a multi-sector approach for adaptation planning, a visualization system for mapping climate change risk (Vulpes) was developed to suggest adaptation policies at the local governmental level. The authors also developed an interactive method, i.e., organizing workshops regarding local adaptation to climate change using the system. Such workshops have been conducted for local policy makers as well as the staff of the regional center of climate change adaptation. These workshops showcase the decrease in disaster risk, or changes in the ecosystem and the socio-economic system resulting from regional climatic changes.

Keywords: Climate change, Adaptation, Multi-sector approach, Workshop, GIS (Geographical information system)

INTRODUCTION

Around the world, including Japan, there is increasing attention on risk assessment to climate change. Climate change can impact not only one sector, but several sectors simultaneously. For example, an extreme rain event can cause not only river flooding but also related disturbances such as runoff of river water into agricultural land and residential areas, as well as traffic hazards that may cause serious disruption to the supply chain. The Ministry of Environment of Japan (MOEJ) started the promotion of local adaptation planning for climate change at municipalities-level within Japan, and the National Institute for Environmental Studies (NIES) conducts several studies and provides information for the planning via A-PLAT [1] within Japan, as well as for the Asia-Pacific region via AP-PLAT [2]. However, climate risk information is still limited, especially on a detailed geographical scale, to be helpful for local assessment by municipalities. In addition, at the municipality level, human resources are also found to be lacking. While local governmental bodies have conducted miscellaneous environmental tasks, climate risk assessment is not a high priority in local administration.

Visualization is a key factor in assessment and recognizing climate risks that impact wide sectors. Various data (biodiversity, ecosystem, and infrastructure) and high geographical resolution (km-level) may aid visualization of the current and future risk and geographical extent of disaster. Moreover, there is need for an interactive method to assess climate risk, such as workshops for local adaptation to climate change.

The impact chain method is a major candidate among the many assessment methods for risk. Rather than a rigorous analysis of causal factors and their relationship in the impact process under climate change, the impact chain method provides a qualitative assessment of risk through visualization of the causal chain. GIZ [3] published a guidebook on the development of the impact chain. In addition to related quantitative assessment (calculation of indicators and their integration), they recommended risk communication, specifically by conducting workshops with policy makers, administrators, specialists, and stakeholders.

In this paper, first, climate risk is defined, after which the interactive and the visualization systems are explained. Then, workshops for creating impact chains with policy makers are described. Finally, we suggest the direction of risk assessment using the interactive method.

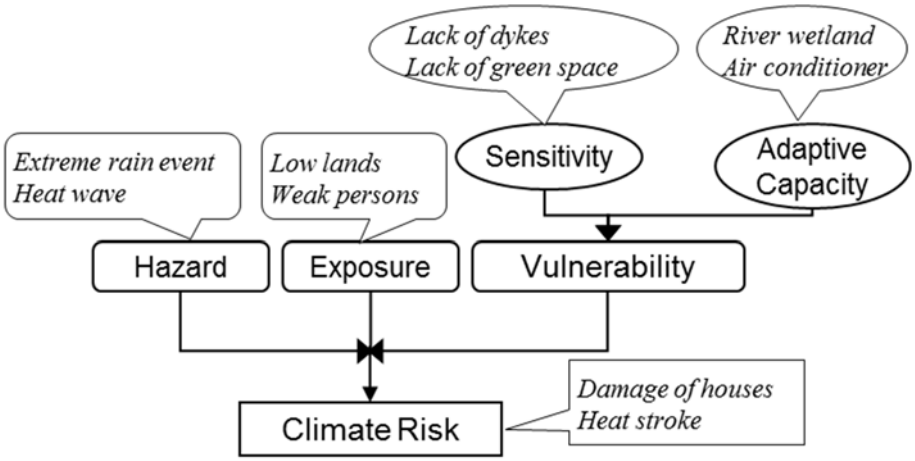

Fig. 1 The definition of risk for climate change and components with examples (balloons)

METHODS

Concept of Climate Risk

In this paper, climate risk is defined as per the definition of IPCC AR5 (Fig. 1, [4]).

The risk consists of three risk components: hazard (such as an extreme event: heavy or extensive precipitation, very hot summer days, etc), exposure (people, land, and goods), and vulnerability.

Vulnerability is further divided into two risk factors: sensitivity (lacking adjustment or coping) and adaptation capacity.

Visualization System

More detailed information such as higher geographical resolution, larger amounts of data, and increased multiple simulation of models (agricultural, ecological, and geographical models) are helpful for

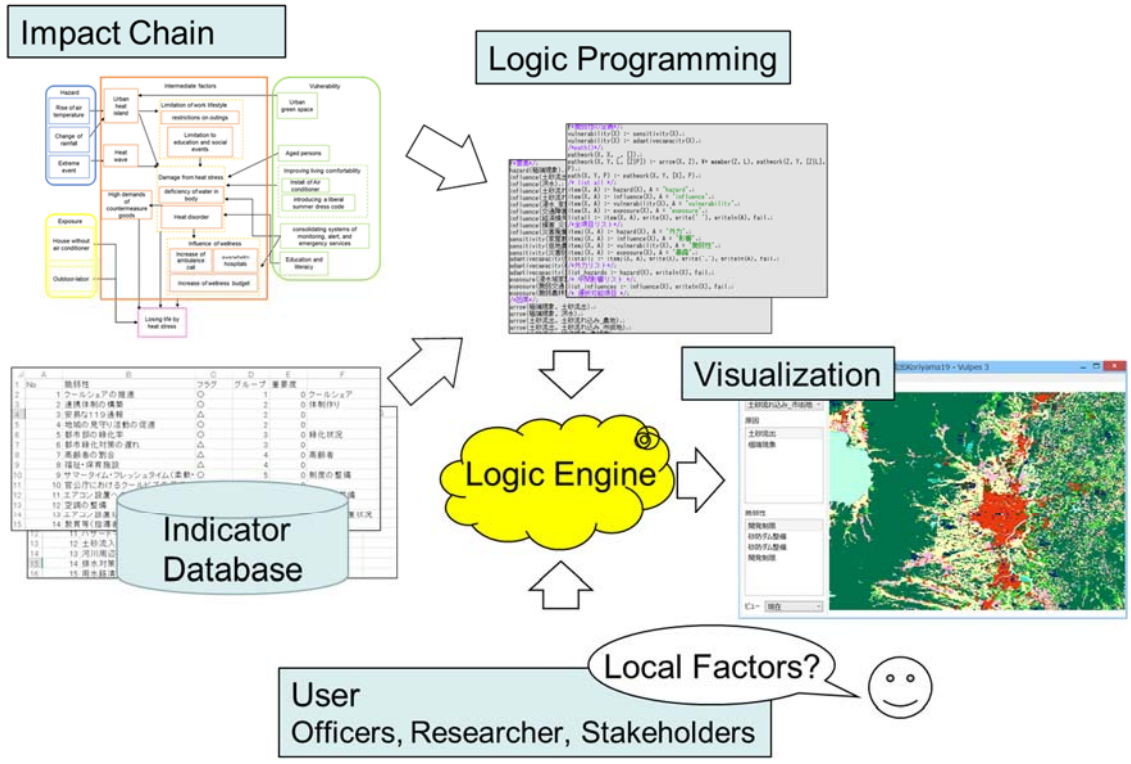

Fig. 2 The system for visualization of climate risk (Vulpes: Vulnerability Pluralistic Evaluation System)

the assessment of climate risk for multiple sectors. Visualization of these data may also enhance non-specialists' imagination and interest in risk. The Vulnerability Pluralistic Evaluation System (Vulpes) was developed based on logic programming and the Geographical Information System (GIS) system. Vulpes can load the impact chain that is coded by logic programming and conduct an inference according to the chain, and indicate geographical result on the GIS pane.

Interactive Risk Assessment

GIZ proposed assessment methods by using the impact chain in nine steps [3]: (1) Preparation for assessment; (2) Development of the impact chain; (3) Identification and selection of risk indicators; (4–7) Data acquirement, estimation of the indicators, and integration; (8) Indication and interpretation of results; and (9) Identification of adaptation. Step (2) was directory adopted, while the other steps were refereed to our methodology due to limitation of the workshop time schedule.

Two types of workshops were held in 2019: one for the staff of regional adaptation centers (prefectural level) and the other for environmental policy officers of the municipality. Each workshop had approximately 20 attendees who were divided into three work groups.

In each group, a diagram of the impact chain was developed by identification of the intermediate factors and risk complements with deep discussions led by a facilitator. Prior to the group work, information on local adaptation based on our system and a workshop tutorial were presented.

RESULTS AND DISCUSSION

Our assessment system for climate risk can manage various types of data and actual diagrams of impact chain programmed by Prolog (Fig. 2).

In our workshops for development of impact chains, natural disaster, water resources, and agriculture were covered. Heat shock in urban areas was also discussed by a group in a workshop with environmental policy officers of municipality (Fig. 3). A diagram of impact chain consists of three risk components (hazard, exposure, and vulnerability) and intermediate factors. An intermediate factor is corresponded to one or more vulnerability factors and they can be grouped as: indoor living

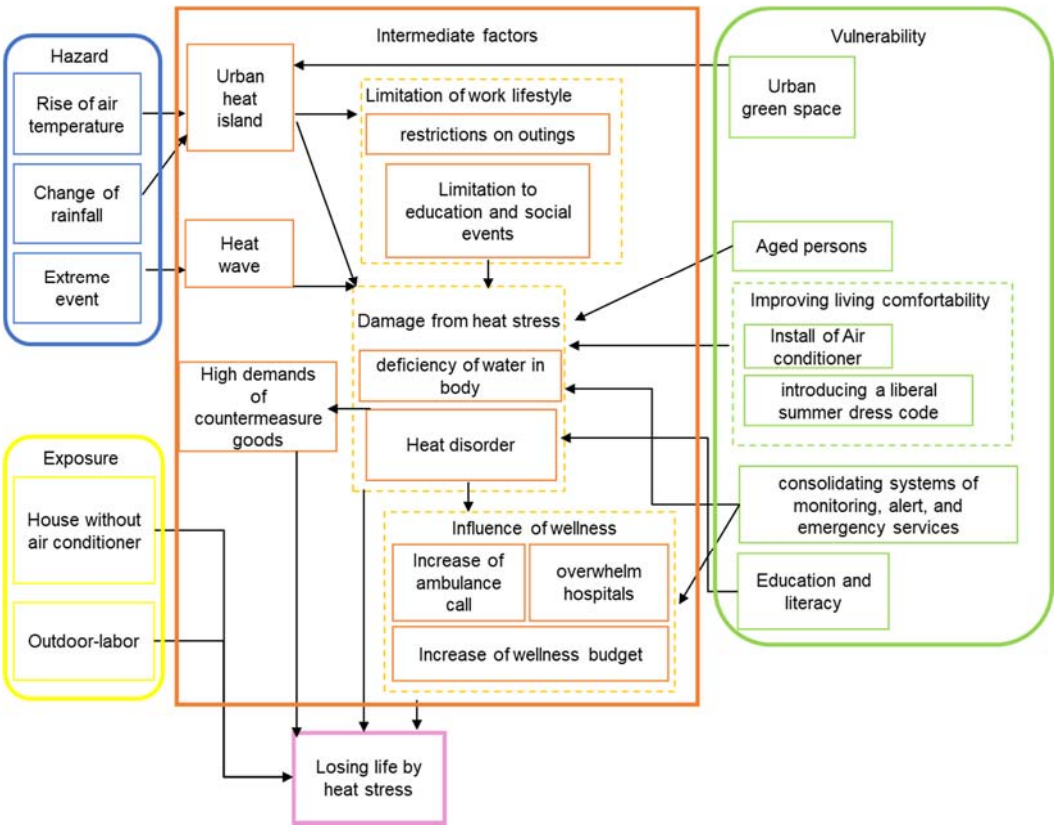

Fig. 3 An example diagram of impact chain for heat health risk developed by the workshop

comfortability (air conditioner and introducing a liberal summer dress code), care of weak person to heat (such as an elderly person), monitoring and alert system for heat shock, consolidation of emergency medical service, and mitigation of urban heat island. Some factors were previously considered by the group, and adaptation policies were implemented to examine their vulnerability (living comfortability and alert system). However, other groups were not well recognized, and the attendees confirmed the need to install additional effective adaptation policies. Several adaptation policies needed the collaboration of wide-ranging sectors, for example, by extending and rearranging urban green spaces and preventing urban heat islands, which must be implemented by related sections of administrators (agricultural manager, urban planner, environmental officer, etc.), science advisors (urban meteorology, conservational ecology, etc.), and local residents.

CONCLUSION

Visualization of climate risk has strong appeal. The system for visualization of local data and impact chain (Vulpes) was well accepted even by non-specialists in the workshops. Deep discussions for planning adaptation are also effective in considering the intermediate effects of climate change and final risk, and the workshop for developing the impact chain is a significant tool to enhance deep discussions. In the workshop for officers of the municipality, fifty three factors of intermediate effect and forty two indicators of vulnerability were originally listed from the limited time (less than two hours).

The current version of Vulpes is not automatically connected between development of impact chain in workshops and indication of risk assessment: a diagram of the impact chain is manually coded and input into the Vulpes system. However, the forthcoming version of Vulpes will support real-time development of the diagram and display the assessment results in the GIS pane. This full interactive system may accelerate deep discussions of climate risk.

ACKNOWLEDGMENTS

This study was supported by the Environment Research and Technology Development Fund (2-1708 and 2-2009, MOE, Japan). I also thank the research team of E-konzal corporation.

REFERENCES

[1] Ministry of the Environment Government of Japan (MOEJ) and National Institute for Environmental Studies (NIES), Climate Change Adaptation Information Platform (A-PLAT), 2018.http://www.adaptation-platform.nies.go.jp/en/index.html

[2] Ministry of the Environment Government of Japan (MOEJ) and National Institute for Environmental Studies (NIES), Asia-Pacific Climate Change Adaptation Information Platform (AP-PLAT), 2018. http://www.adaptation-platform.nies.go.jp/en/ap-plat/index.html

[3] GIZ, EURAC and UNU-EHS. Climate Risk Assessment for Ecosystem-based Adaptation – A guidebook for planners and practitioners. GIZ, 2018. Bonn.

[4] Intergovernmental Panel on Climate Change, IPCC Fifth Assessment Report, WG2 Impacts, Adaptation, and Vulnerability, 2014. https://www.ipcc.ch/report/ar5/

6th Int. Conf. on Structure, Engineering & Environment (SEE), Kyoto, Japan, Nov.18-20, 2020, ISBN: 978-4-909106056 C3051

MEASURING TOD READINESS OF THE BANDAR LAMPUNG CITY

Aleksander Purba[1], Aken Andha Runiawan[2], Rahayu Sulistyorini[3], Shahnaz Nabila Fuady[4], Lusmeilia Afriani[5], Dikpride Despa[6], Ratna Widyawati[7], and Rosalia Dwi Werena[8]
[1,5,6,7,8]Engineering Faculty, the University of Lampung, Indonesia
[2,3,4]Urban and Regional Planning Study Program, Institut Teknologi Sumatera, Indonesia

ABSTRACT

Referring to the Bandar Lampung City Regulation Act No. 10/2011 concerning Regional Spatial Planning (2011-2030) emphasized that city government will develop an integrated activity center area at the mass public transportation node through the concept of Transit Oriented Development (TOD) in Bandar Lampung City. In article 20 explained more details of TOD location will be built and developed in the area of the transit station Tanjung Karang. In preparing the development of the TOD area in the primary center, city government will prepare the integration of bus services that implicates also on the provision of facilities for pedestrian. The steps undertaken by city government are based on Ministerial Regulation Act of ATR/BPN No. 16/2017 concerning Guidelines for Development of Transit-Oriented-Development which generally regulates the procedures for developing transit-oriented areas based on specific criteria and characteristics. This paper explores the readiness of the Tanjung Karang transit station as a TOD area using Calthorpe scheme, Indonesian guidelines and ITDP standard. Measurement results indicate, the Tanjung Karang station not yet functioning as TOD. The main variables i.e. walk, cycle, connect, transit, mix, densify, compact, and shift has been stated in the city Act, but there is no implication in the field within surrounding area after almost ten years planned.

Keywords: TOD, Readiness, Procedure, Implication, Tanjung Karang

INTRODUCTION

Currently, the Indonesian Government has begun to implement more innovative strategies in addressing rapid motorization issues in major cities such as expressed by capital Jakarta by integrating land development along MRT line. One of the innovations applied is the Transit Oriented Development (TOD) concept as a transit-based development strategy. Transit Oriented Development is at the very heart and soul of sustainability, and brings together compact, walkable communities with high quality rail systems. This creates low carbon lifestyles by enabling people to live, work, and play without depending on a car for mobility. This type of lifestyle can reduce energy consumption and driving by up to 85% [1]. Based on long experiences in developed cities of developed countries, there are a number of factors driving the trend toward TOD. They are rapidly growing, mind-numbing traffic congestion nation-wide, growing distaste for suburbia and fry-pit strip development, growing desire for quality urban lifestyle, growing desire for more walkable lifestyles away from traffic, changes in family structures: more singles, empty-nesters, growing national support for smart growth, respectively. TOD means integrated urban places designed to bring people, activities, buildings, and public space together, with easy walking and cycling connection between them and near-excellent transit service to the rest of the city. It means inclusive access for all to local and citywide opportunities and resources by the most efficient and healthful combination of mobility modes, at the lowest financial and environmental cost, and with the highest resilience to disruptive events. Inclusive TOD is a necessary foundation for long-term sustainability, equity, shared prosperity, and civil peace in cities [2]. The Bandar Lampung city itself embarked on an implementation step towards a transit-oriented city through City Act's No. 10/2011 enacted Regional Spatial Planning for period of 2011-2030 [3]. In article 20 mentioned more detail that the area of TOD will be built and developed in Tanjung Karang station and surrounding areas. This paper explores the extent of TOD's achievement of readiness, after a ten-year planning process since being declared by the city government. This kind of step needs to be conducted due to understanding the degree to which transit corridors and station areas are potential places for TOD helps public agencies implement TOD. To date, the Metropolitan Council does not have a system for evaluating the potential for TOD along transit corridors and within station areas. Instead, TOD evaluation is typically performed on a project-by-project basis without considering the existing corridor and station area [4].

METHODOLOGY

Bandar Lampung is the capital and largest city of the Indonesian province of Lampung. Located on the southern tip of Sumatra, Bandar Lampung was originally called Tanjungkarang–Telukbetung, since it was a unification of two major settlements in Lampung, before being renamed in 1983. Bandar

Lampung or Tanjung Karang has become the third-densest city in Sumatera, after Medan and Palembang. The city's area is about 169.21 km², with an estimated population of 1,015,910 as of 2017. Hence, the average density is 5,151 people/km^2; the densiest area is located in the Tanjung Karang Timur district with density of about 24,549 people/km^2, while the Sukabumi district has density of 1,235 people/ km^2. According to these figures, the Tanjung Karang Timur district is near five times denser than the city average density and almost twenty times higher compared to the lowest figure. Tanjung Karang station itself is the terminus of the railway service from Palembang, Baturaja, Blambangan Umpu and Kotabumi although the railway track continues all the way until Panjang harbor and Tarahan coal offloading point at the southern end of the city. The research scope includes a transit station with a radius of 1 km as shown in Figure 1. Primary data collection through field observation and interview with a number stakeholder include railway operator, city bus operator, city officers, and land developers. Each country may have different ways in terms of TOD standard and how elements or attributes are set and measured. In Indonesia, the steps undertaken by city government are based on Ministerial Regulation Act of ATR/BPN No. 16/2017 concerning Guidelines for Development of Transit-Oriented-Development which generally regulates the procedures for developing transit-oriented areas based on specific criteria and characteristics [5]. According to Calthorpe [6], the concept of TOD is simple: moderate and high-density housing, along with complementary public uses, jobs, retail and services, are concentrated in mixed-use developments at strategic points along the regional transit system. In summary, the principles of TOD are to:

- Organize growth on a regional level to be compact and transit-supportive;
- Place commercial, housing, jobs, parks, and civic uses within walking distance of transit stops;
- Create pedestrian-friendly street networks which directly connect local destinations;
- Provide a mix of housing types, densities, and costs;
- Preserve sensitive habitat, riparian zones, and high quality open spaces;
- Make public spaces the focus of building orientation and neighborhood activity; and
- Encourage infill and redevelopment along transit corridors within existing neighborhoods

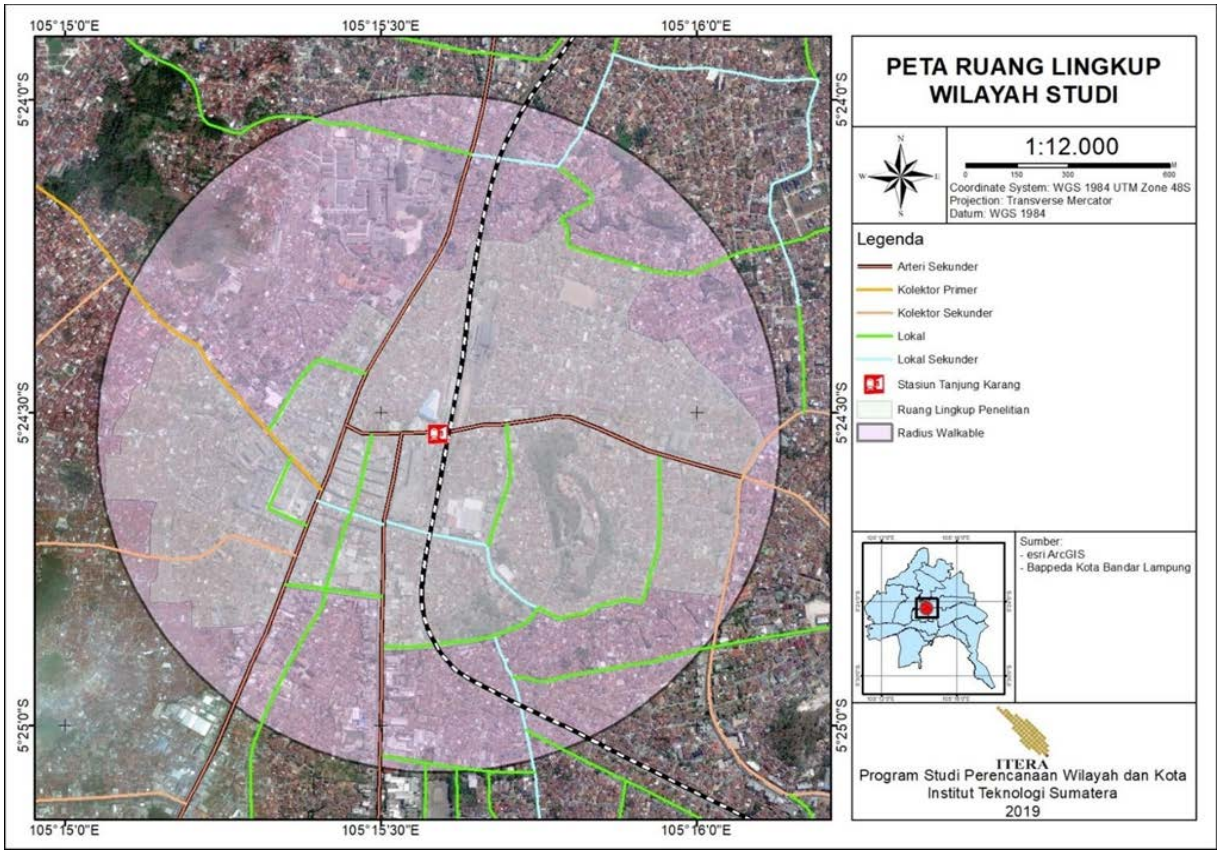

Fig. 1. Transit station and surrounding areas

Several years later after the Calthorpe's concept, the Institute for Transportation and Development Policy (ITDP) developed TOD standard regarding Principles of Urban Development for Transport in Urban Life, and identifies the key concrete objectives that are essential to implementing these principles in urban development. Hence, the TOD standard is a unique assessment tool available to score the plans and products of urban development according to their adherence to the TOD principles and implementation

objectives [7]. Furthermore, we perform syntheses and simplification of variables and indicators and combined into the tool for measuring TOD readiness as shown in Table 1.

Table 1 TOD-forming variables

Source	Element	Variable	Indicator
Calthorpe (1993)	function	compact and transit-supportive	planning policy
		surrounding area within walking distance of transit stops	function performs
		street networks directly connect local destinations	function performs
		mix of housing types	type of housing
		high quality open spaces	function performs
		public spaces the focus of building orientation and neighborhood activity	planning policy
		infill and redevelopment along transit corridors within existing neighborhoods	planning policy
Regulation Act of ATR/BPN No. 16/2017	location	transit	transit stop
			intramode and intermode
			transit services
		disaster	vulnerability and disaster mitigation
		directions in development	compliance with spatial development
		secure	interference to state-owned vital installations
ITDP (2017)	physical environment	walk	walkways (3 points)
			crosswalks (3 points)
			visually active frontage (6 points)
			physically permeable frontage (2 points)
			shade & shelter (1 point)
		cycle	cycle network (2 points)
			cycle parking at transit stations (1 point)
			cycle parking at buildings (1 point)
			cycle access in buildings (1 point)
		connect	small blocks (8 points)
			prioritized connectivity (2 points)
		transit	walk distance to transit
		mix	complementary uses (8 points)
			access to local services (3 points)
			access to parks and playgrounds (1)
			affordable housing (8 points)
			housing preservation (3 points)
			business services preservation (2 points)
		densify	non-residential density (7 points)
			residential density (8 points)
		compact	urban site (8 points)
			transit options (2 points)
		shift	off-street parking (8 points)
			driveway density (1points)
			roadway area (6 points)

RESULT AND DISCUSSION

Functions of the Surrounding Area

The function of the TOD in terms of compact and transit-supportive has been stated in the City Act document, but has not yet seen the implementation plan in the surrounding areas including the redevelopment plan of the pedestrian path to the transit station. Though, for station areas, strategies to promote TOD could therefore focus on increasing density and improving walkability to match their already high mix. The characteristics of station areas suggest a different set of strategies. Their urban density is relatively high, but their transportation supply is relatively low, suggesting that improving the transit dimension is a more logical strategy to promote TOD there [8]. Based on field identification,

Tanjung Karang station categorized as urban TOD model, since the high-intensity commercial functions already exist around the area. This type of development includes the redevelopment site where buildings around the relatively are old and supporting facilities require a massive revitalization. In different cases, the condition of Tanjung Karang also experienced other areas relatively developed by City Region Arnhem and Nijmegen, where urban development has high TOD levels, but has poor transit connections/the TOD levels are high but train connections are further away than 800 m [9]. The street networks directly connect local destinations is not yet available in terms of length and its quality as shown in Fig. 2. Referring to case study in Brisbane, Australia, in comparison to people living in areas classified as residential TODs, people who reside in non-TOD clusters were significantly less likely to use public transport (PT) (1.4 times), and active transport (4 times) compared to the car. People living in areas classified as potential TODs were 1.3 times less likely to use PT, and 2.5 times less likely to use active transport compared to using the car. Only a little difference in mode choice behaviour was evident between people living in areas classified as residential TODs and activity centre TODs [10]. The Brisbane experience also takes place in Washington, D.C. and Baltimore metropolitan areas: results indicate that people living in TOD areas tend to drive less, reducing their VMT by around 38% in Washington, D.C. and 21% in Baltimore, compared to the residents of the non-TOD areas even with similar land use patterns [11].

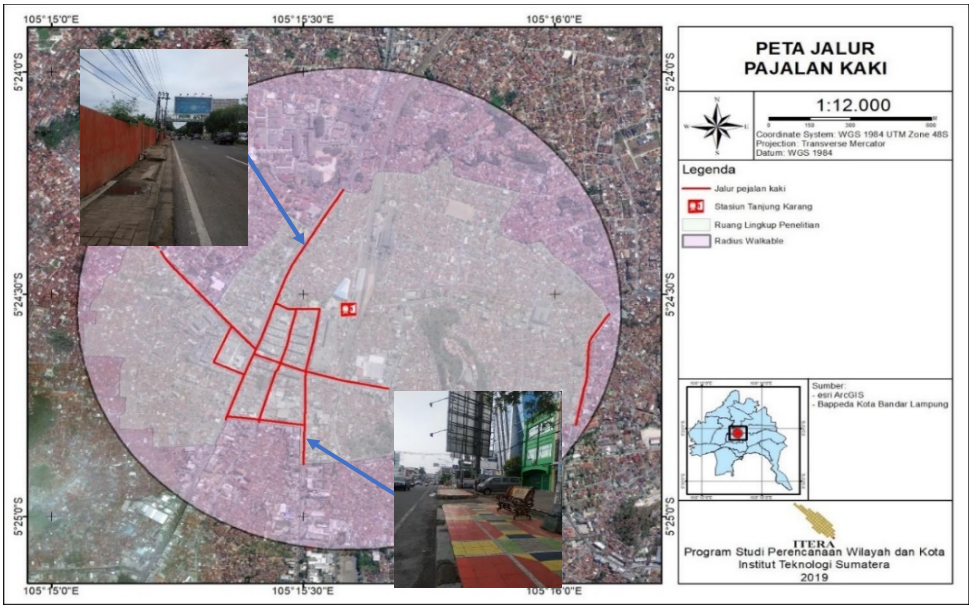

Fig. 2 Pathway network

Related to the existence of mix of housing types in the study area has not been seen and not yet available a high quality open spaces around the station. According to available documents and interview with city officials the redevelopment along transit corridors within existing neighborhoods does not include a priority plan for the next few years. Referring to Carlton and Fleissig [12], because TOD planning is so often formulaic and based on templates, land use plans may describe visions that do not match market conditions. Unsophisticated landowners may hold onto land in spite of reasonable purchase offers because they expect impending development will increase their value.

Then, unrealistic prices can lead to frozen land markets, an inability to accumulate lots necessary for development, and stalled TOD investment. On the other hand, delaying longer implementations can result in higher land prices, such as other city experiences where TOD projects tend to cause an increase in land value leading to gentrification and displacement. As a result, prioritizing social equity as a key component of TOD implementation is an essential pathway for achieving equitable solutions to such projects [13]. Table 2 shows the readiness level of Tanjung Karang station referring to Calthorpe scheme.

Table 2 Readiness level (Calthorpe)

Variable & Indicator	Readiness level	
	yes	no
1. transit-supportive		x
2. walking distance to transit stops		x
3. street connect destinations		x
4. mix housing		x
5. high quality open space		x
6. building orientation		x
7. redevelopment along transit corridor		x

TOD Location

As stated by Ministerial Regulation Act of ATR/BPN No. 16/2017, the location or surrounding area of TOD required satisfy the criteria and meet the requirements. They are transit, disaster, direction in development, and secure, respectively. Transit variable means that the Tanjung Karang has been designated as a transit station in the city Act document even though it is not fully ready to run its functions due to various supporting facilities as a transit station is very limited after ten years of initial planning. In the opinion of related stakeholders, the station is relatively safe against possible disaster and secure against criminality. As mentioned previously the Tanjung Karang station has been designated as a transit-oriented development area in the city Act document. This means that land developers and railway operators must follow the instructions in the document when developing projects around the station. Referring to experiences in other cities, centralizing housing and jobs along transitway corridors is the best strategy to follow if increasing regional accessibility is the goal. Particularly a strategy that focuses on targeted jobs centralization along transitway corridors would have significant payoffs. With a joint population and jobs centralization along transitway corridors, increases in accessibility as large as 7% are possible; by focusing on jobs centralization alone gains of 4.5% can be achieved [14]. Since those variables the readiness of TOD are widespread application, the end result is as seen in Table 3.

Table 3 Readiness level related location

Variable & Indicator	Readiness level	
	yes	no
1. transit		
a. Transit stop	√	
b. intramode and intermode		x
c. transit services		x
2. disaster	√	
3. directions in development	√	
4. secure	√	

Physical Environment

The ITDP method relatively easier to implement since most of variables can be measured and observed in the TOD region although the final value set is not fully objective depend on the observation of someone which can differ from others for the same variable. Table 4 shows the results of the TOD assessment readiness referring to the ITDP method that emphasizes the physical environment element.

Table 4 Readiness level of TOD (ITDP)

Variable	Indicator	Score	Max Score	Readiness Level	
				yes	no
1. Walk	a. walkways	0	3		x
	b. crosswalks	0	3		x
	c. visually active frontage	2	6		x
	d. physically permeable frontage	0	2		x
	e. shade & shelter	0	1		x
2. Cycle	a. cycle network	0	2		x
	b. cycle parking at transit stations	0	1		x
	c. cycle parking at buildings	0	1		x
	d. cycle access in buildings	0	1		x
3. Connect	a. small blocks	0	10		x
	b. prioritized connectivity	1	5		x
4. Transit	a. walk distance to transit				
5. Mix	a. complementary uses	3	8		x
	b. access to local services	1	3		x
	c. access to parks & playgrounds	0	1		x
	d. affordable housing	1	8		x
	e. housing preservation	0	3		x
	f. business services preservation	0	2		x
6. Densify	a. non-residential density	3	7		x
	b. residential density	2	8		x
7. Compact	a. urban site	1	8		x
	b. transit options	1	2		x
8. Shift	a. off-street parking	2	8		x
	b. driveway density	1	1	√	
	c. roadway area	3	6		x
	Total	21	100		

As seen in table 4, there are no variables in the study area that meet the requirements if TOD readiness measured based on the ITDP scheme. The city bus services are already available since a few years ago and pass the transit station, but service quality of the bus is not reliable and without timetable. Ideally, as Pavneet stated, comprehensive planning funded through the program must examine ways to improve economic development and ridership, foster multimodal connectivity and accessibility, improve transit access for pedestrian and bicycle traffic, engage the private sector, identify infrastructure needs, and enable mixed-use development near transit stations [15]. Moreover, as the project was launched as a bicycle lane, cyclists were expecting permanent infrastructure in the city center, while the purpose of the project was leisure rather than transport. City officials tend to use the apparent a-political technical solutions in order to gain legitimacy, placate social demands and minimize political debates, as experienced by Curitiba [16].

CONCLUSION

This paper explores a number of variable in order to measure the TOD readiness of Tanjung Karang transit station using Calthorpe method, Indonesian guidelines and ITDP scheme. As the result of measurements vary, although the conclusion is the same: Tanjung Karang Transit station not yet functioning as TOD based on ITDP standard as measurement tool commonly used in many countries. The main variables i.e. walk, cycle, connect, transit, mix, densify, compact, and shift has been stated in the city Act, but there is no implication in the field within surrounding area after almost ten years planned. Issues related to land-use and transport integration are one of critical issues due to rapid motorization and as suggested by Papa and Bertolini [17], strengthening the relationship between the railway network and land uses is an effective measure for increasing cumulative rail-based accessibility; improving railway network connectivity is also important, but just increasing densities is not. A key role is played by the correlation between railway system connectivity values and land use densities, what we term the TOD degree of the urban structure. Planners wishing to enhance the cumulative rail-based accessibility of an urban area should primarily focus on transport and land use interventions that improve this correlation. The condition of Tanjung Karang station was experienced by Beijing several years ago, related to policy at a higher level of government which several aspects of urban planning and development policies in Beijing still prevent TOD from reaching a higher potential. First, station orientation cannot be detected among land parcels leased before station construction, partially because developers tend to avoid the risk associated with station location change. In addition, station impacts are not significant in the new suburbs, partially because of the municipal government's under-investment in transit and social services in suburbs. Furthermore, the Beijing city government does not have an explicit policy statement to encourage higher density around transit stations [18].

REFERENCES

[1] Transit Oriented Development Institute, US High Speed Rail Association. Available at: http://www.tod.org/sustainability.html

[2] Institute for Transportation and Development Policy. Available at: https://www.itdp.org/library/standards-and-guides/tod3-0/what-is-tod/

[3] City Act No. 10/2011. Available at: https://peraturan.bpk.go.id/Home/Details/114606/perda-kota-bandar-lampung-no-10-tahun-2011 (*in Indonesian*)

[4] Frank, A., Joanne Cho, Y.J., Andrew, D., Ashley, H., and Reed, S., THE TOD EVALUATION METHOD Evaluating TOD on Station Area and Corridor Scales, University of Minnesota Humphrey School of Public Affairs, 2018, pp. 1-106.

[5] Ministerial Regulation Act of ATR/BPN No. 16/2017. Available at: https://www.atrbpn.go.id/Publikasi/Peraturan-Perundangan/Peraturan-Menteri-ATR-Kepala-BPN/peraturan-menteri-agraria-dan-tata-ruang-kepala-badan-pertanahan-nasional-republik-indonesia-nomor-16-tahun-2017-70794 (*in Indonesian*)

[6] Calthorpe, P., The Next American Metropolis: Ecology, Community, and the American Dream, Princeton Architectural Press, New York, 1993, pp. 1-175.

[7] Institute for Transportation and Development Policy. Available at: https://www.itdp.org/library/standards-and-guides/tod3-0/the-tod-standard-scorecard/

[8] Lyu, G., Bertolini, L., and Pfeffer, K., Developing a TOD typology for Beijing metro station areas, J. of Transport Geography, Vol. 55, 2016, pp. 40–50.

[9] Singh, Y. J., Fard, P., Zuidgeest, M., Brussel, M., and Maarseveen, M., Measuring transit oriented development: a spatial multi criteria assessment approach for the City Region Arnhem and Nijmegen, J. of Transport Geography, Vol. 35, 2014, pp. 130–143.

[10] Kamruzzaman, M., Baker, D., Washington, S., and Turrell, G., Advance transit oriented development typology: case study in Brisbane, Australia, J. of Transport Geography, Vol. 34, 2014, pp. 54–70.

[11] Nasri, A., and Zhang, L., The analysis of transit-oriented development (TOD) in Washington, D.C. and Baltimore metropolitan areas, J. of Transport Policy, Vol. 32, Issue C, 2014, pp. 172-179.

[12] Ian, C., and William, F., Steps to Avoid Stalled Equitable TOD Projects, Living Cities, 2014, pp. 1-45.

[13] Beryl O., Measuring Equity in Transit-Oriented Development: Application to Affordable Housing, Sustainable Development: International Policy and Management, Washington, DC, 2015, pp. 1-115.

[14] Tilahun, N., and Fan, Y., Transit and job accessibility: an empirical study of access to competitive clusters and regional growth strategies for enhancing transit accessibility, J. of Transport Policy, Vol. 33, 2014, pp. 17-25.

[15] Pavneet, K., Assessing Richmond Transit Network Plan for Transit Oriented Development. Greater Richmond Transit Company (GRTC), 2017, pp. 1-82.

[16] Duarte, F., Procopiuck, M., and Fujioka, K., No bicycle lanes! Shouted the cyclists. A controversial bicycle project in Curitiba, Brazil, J. of Transport Policy, Vol. 32, 2014, pp. 180–185.

[17] Papa, E., and Bertolini, L., Accessibility and Transit-Oriented Development in European

metropolitan areas, J. of Transport Geography, Vol. 47, 2015, pp. 70–83.

[18] Yang, J., Quan, J., Yan, B., and He, C., Urban rail investment and transit-oriented development in Beijing: Can it reach a higher potential? J. of Transportation Research Part A: Policy and Practice, Vol. 89, 2016, pp. 140–150.

6th Int. Conf. on Structure, Engineering & Environment (SEE), Kyoto, Japan, Nov.18-20, 2020, ISBN: 978-4-909106056 C3051

SPATIAL VARIATIONS OF WATER QUALITY IN ACIDIC RIVER BASINS OF NORTHEAST JAPAN

Takeshi Saito[1] and Naoki Watanabe[2]
[1]Graduate School of Science and Engineering, Saitama University, Japan; [2]Research Institute for Natural Hazards and Disaster Recovery, Niigata University, Japan

ABSTRACT

In Japan, there are some environmental issues related to acid mine drainage (AMD) and acidic hot springs generally characterized by low pH values and relatively high concentrations of harmful elements such as As (arsenic) and Pb (lead). In this study, spatial variations of water quality parameters especially including pH and concentrations of harmful elements were investigated in the Sukawa river basin (Yamagata Prefecture) and the Tamagawa river basin (Akita Prefecture) that are located in volcanic areas of Northeast Japan. In the Sukawa river basin with no specific neutralization treatments, the pH values ranged from 1.93 to 6.72 were observed from the upstream to downstream, while in the Tamagawa river basin with neutralization treatment using limestone, the pH values showed 1.2 to 6.93 from the upstream to downstream. The river acidity and concentrations of As, Pb, and Zn (zinc) as harmful elements were markedly improved due to the dilution by the mixing with other rivers and the associated coprecipitation with Fe (iron) and Al (aluminum) hydroxides. Especially, effect of the neutralization on the improvement of water quality was probably more significant in the Tamagawa river basin.

Keywords: Water quality, pH, Harmful elements, Acidic river basins, Northeast Japan, Neutralization

INTRODUCTION

Acid mine drainage (AMD) is generally characterized by low pH values and relatively high concentrations of harmful elements. Especially in Japan, there are also many acidic hot springs which represent almost the same characteristics with the AMD. These acidic waters are typically produced by the natural oxidation of sulfide minerals and often contain harmful elements such as As (arsenic) and Pb (lead) [1-3].

In the acidic river basins which are formed by receiving the acidic waters, there are some possible negative impacts on surrounding natural environment and human activity including the degradation of infrastructures, the incompatibility for agricultural water usage, and adverse effect on the biosphere. Therefore, large-scale water treatments are sometimes applied in the upstream of the acidic river basins. For example, in the Kusatsu hot spring as one of the most famous acidic hot springs in Japan located in the upstream of the Agatsuma river basin (Gunma Prefecture), neutralization treatment using limestone has been applied over 50 years [4, 5]. The positive effect of the treatment on the river acidity and concentrations of harmful elements was clearly observed in a previous study [6].

The neutralization treatment is essential to reduce the acidity and concentrations of harmful elements, however, the treatment needs a high cost and one of the most effective and common neutralizers is limestone, which is a limited natural resource. Therefore, the authors are trying to find appropriate alternative neutralizers selected from waste materials. It is highly important to investigate and clarify spatial variations of water quality in acidic river basins as fundamental knowledge to develop effective alternative neutralizers when they are applied to acidic rivers. The objective of this study is to investigate spatial variations of water quality parameters especially including pH and concentrations of harmful elements in the Sukawa (Yamagata Prefecture) and Tamagawa (Akita Prefecture) river basins which are famous acidic river basins located in volcanic areas of Northeast Japan.

MATERIALS AND METHODS

Study Areas

The Sukawa river basin in Yamagata Prefecture and the Tamagawa river basin in Akita Prefecture which are located in volcanic areas of Northeast Japan were selected for investigating spatial variations of water quality (Fig. 1).

In the Sukawa river basin, a total of 8 sampling locations were selected. Field investigation was performed in November 2018 and May 2019. In the Tamagawa river basin, a total of 10 sampling locations were selected. Field investigation was

carried out in July 2018. These sampling locations are shown in Fig. 1.

Field investigation and water quality analysis

In-situ measurements of water temperature, pH, and electric conductivity (EC) were conducted using a portable analyzer (WM-32EP, DKK-TOA CORPORATION, Japan) calibrated precisely before each field investigation.

The river water was immediately filtered using a 0.20 μm membrane filter (DISMIC-25CS, Toyo Roshi Kaisha, Ltd., Japan) and the following water quality parameters were analyzed in the laboratory. Major cations (Na^+, NH_4^+, K^+, Mg^{2+}, and Ca^{2+}) and anions (F^-, Cl^-, NO_3^-, and SO_4^{2-}), dissolved inorganic carbon (DIC), and heavy metals and other trace elements including harmful elements (Li, Al: aluminum, Si, Cr, Mn, Fe: iron, Ni, Cu, Zn: zinc, As, Se, Sr, Cd, and Pb) were analyzed using an ion chromatograph (ICS-1500, Nippon Dionex K.K., Japan), TOC (total organic carbon) analyzer (TOC-V CSH, SHIMADZU CORPORATION, Japan), and ICP (inductivity coupled plasma)-MS (mass spectrometer) (ICPM-8500, SHIMADZU CORPORATION, Japan) or atomic absorption spectrophotometer (AA-6200, SHIMADZU CORPORATION, Japan), respectively. For the DIC, there are mainly three chemical forms of H_2CO_3, HCO_3^-, and CO_3^{2-}. Because the relative abundance ratios depend highly on the pH in water [7], the concentration of HCO_3^- was estimated using pH, ionic strength, activity coefficient, and equilibrium constant in this study.

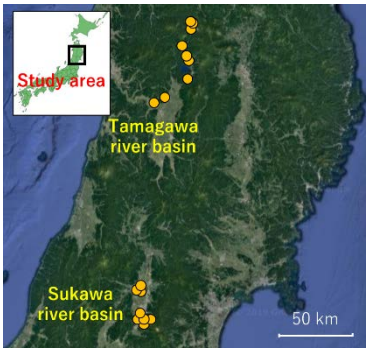

Fig. 1 Study areas of the Sukawa river basin in Yamagata Prefecture and the Tamagawa river basin in Akita Prefecture, Northeast Japan. Orange circles show water sampling locations. The base map was downloaded from Google Maps.

RESULTS AND DISCUSSION

Spatial variations of water quality in the Sukawa river basin

The Zao hot spring as one of the most famous acidic hot springs in Japan is in the upstream of the Sukawa river. For the discharged water from the Zao hot spring, the pH and EC values in November 2018 were 1.93 and 5730 μS/cm, respectively. A closed sulfur mine is located in the upstream of the Zaougawa river that is also an acidic river. These two acidic rivers discharge to the mainstream of the Sukawa river and it (the mainstream) finally flows into the Mogami river which is one of the biggest rivers in Japan. Even under these acidic conditions, there are no specific neutralization treatments applied in the Sukawa river basin. In the following section, variations of water quality along the Sukawa river basin are discussed based on the data of 5 sampling locations as shown in Fig. 2.

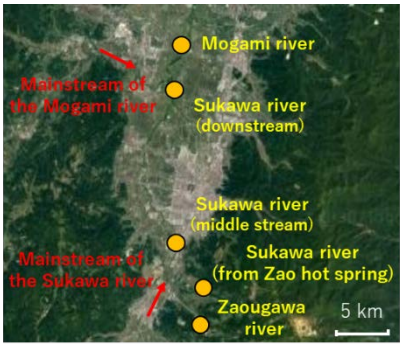

Fig. 2 Study area of the Sukawa river basin. Orange circles show water sampling locations. The base map was downloaded from Google Maps.

Figure 3 shows variations of pH, EC, and concentrations of Fe, Al, As, Pb, and Zn as water quality parameters from the upstream to downstream along the Sukawa river basin. In the mainstream of the Sukawa river before discharge of the acidic water from the Zao hot spring and the Zaougawa river, the pH and EC values in November 2018 were 6.18 and 242 μS/cm, respectively (not shown in the Fig. 3). After the inflow of the acidic water, the pH dramatically decreased to 2.95 and the EC increased to 748 μS/cm at the sampling location as “Sukawa river (middle stream)” in Fig. 3. In the downstream of the Sukawa river (shown as “Sukawa river (downstream)” in Fig. 3) before flowing into the Mogami river, the pH still showed a slightly acidic value of 5.40 and the EC value was 353 μS/cm. Finally, the pH showed an almost neutral value of 6.72 and the EC value was 165.5 μS/cm after flowing into the Mogami river at the sampling location as “Mogami river” in Fig. 3.

For behaviors of harmful elements, As was detected only in the Zaougawa river, however,

relatively high concentration of Zn was found at almost all the sampling locations. The Zn concentration gradually decreased with decrease in both Fe and Al concentrations. Especially in the downstream of the Sukawa river, all these elements showed significantly low concentrations at the sampling location as “Sukawa river (downstream)” in Fig. 3. Saito and Watanabe (2020) [6] investigated variations of water quality along the Agatsuma and Nagase (Fukushima Prefecture) river basins as famous acidic river basins in Japan. This previous study suggested that harmful elements such as As and Pb were probably coprecipitated with the Fe and Al hydroxides due to increase in the pH values. Because the Fe hydroxides were at least found in the river bed of the Sukawa river basin, harmful elements including Zn were suggested to be coprecipitated with the hydroxides. Finally, at the sampling location as “Mogami river” in Fig. 3, all these elements were not detected.

Considering all observation results, the river acidity and concentrations of harmful elements in the Sukawa river basin were significantly improved due to the dilution by the mixing with other rivers and the associated coprecipitation with Fe and Al hydroxides without specific neutralization treatments.

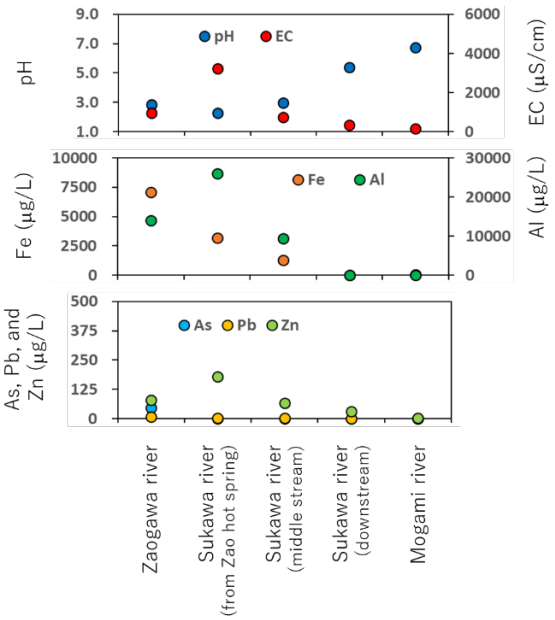

Fig. 3 Variations of pH, EC, and concentrations of Fe, Al, As, Pb, and Zn from the upstream to downstream along the Sukawa river basin. Water sampling locations correspond to Fig. 2.

Spatial variations of water quality in the Tamagawa river basin

The Tamagawa hot spring as the strongest acidic hot spring in Japan is located in the upstream of the Tamagawa river basin. Based on a previous study, the pH value is usually around 1.2 [8]. The discharged acidic water flows into the Shibukuro river and the water in the Shibukuro river is continuously neutralized using limestone. In the following section, variations of water quality along the Tamagawa river basin are discussed based on the data of 7 sampling locations as shown in Fig. 4.

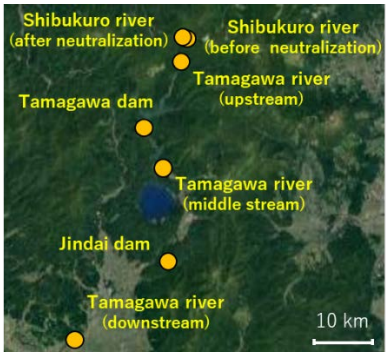

Fig. 4 Study area of the Tamagawa river basin. Orange circles show water sampling locations. The base map was downloaded from Google Maps.

Figure 5 shows variations of pH, EC, and concentrations of Fe, Al, As, Pb, and Zn as water quality parameters from the upstream to downstream along the Tamagawa river basin. Before the neutralization treatment, the pH and EC values in July 2018 were 2.42 and 2100 μS/cm, respectively, at the sampling location as “Shibukuro river (before neutralization)” in Fig. 5. After the neutralization treatment, the pH increased to 2.99 and the EC slightly decreased to 1421 μS/cm at the sampling location as “Shibukuro river (after neutralization)” in Fig. 5. Finally, the pH showed an almost neutral value of 6.93 and the EC value was 68.5 μS/cm in the downstream of the Tamagawa river (at the sampling location as “Tamagawa river (downstream)” in Fig. 5) before flowing into the Omono river which broadly flows in Southern Akita Prefecture.

Harmful elements, As, Pb, and Zn were detected with high concentrations in the upstream of the Tamagawa river before flowing into the Tamagawa dam (shown as “Tamagawa dam” in Fig. 5). The neutralized acidic water is sufficiently mixed in the dam and the water in the dam is gradually released to the Tamagawa river. Therefore, these harmful elements were not generally detected. Also, Fe and Al were not detected even at the sampling location as “Tamagawa river (middle stream) in Fig. 5”. As previously discussed, in the Sukawa river basin, Zn as one of harmful elements might be coprecipitated

with Fe and Al hydroxides due to increase in the pH values. In the Tamagawa river basin, at least Fe hydroxides were clearly found in the river bed before flowing into the Tamagawa dam. Harmful elements, As, Pb, and Zn were also suggested to be coprecipitated with the hydroxides.

As observed in the Sukawa river basin, the river acidity and concentrations of harmful elements were clearly improved by the dilution effect and the related coprecipitation with the Fe and Al hydroxides. Especially, effect of the neutralization on the improvement of water quality was probably more significant in the Tamagawa river basin.

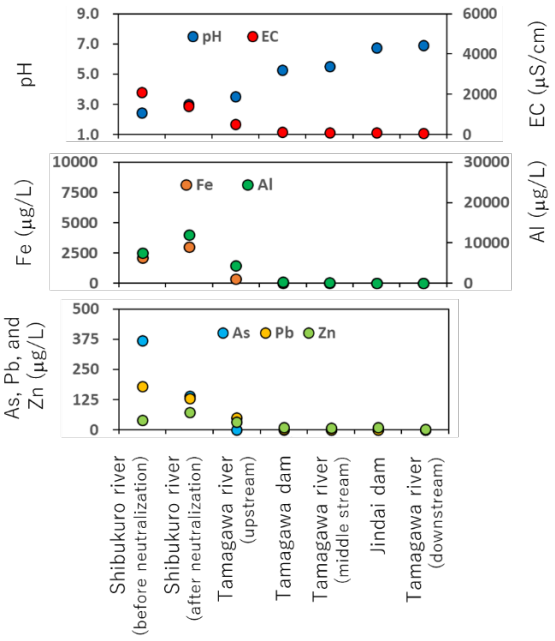

Fig. 5 Variations of pH, EC, and concentrations of Fe, Al, As, Pb, and Zn from the upstream to downstream along the Tamagawa river basin. Water sampling locations correspond to Fig. 4.

CONCLUSIONS

Spatial variations of water quality parameters including pH and concentrations of harmful elements were investigated in the Sukawa river basin in Yamagata Prefecture and the Tamagawa river basin in Akita Prefecture which are located in volcanic areas of Northeast Japan.

In the Sukawa river basin with no specific neutralization treatments applied, observed pH values were in the range of 1.93 to 6.72 from the upstream to downstream. Harmful elements, As and Pb, which are regulated by environmental criteria, were not detected, however, relatively high concentration of Zn was detected. The river acidity and the Zn concentration were significantly improved due to the dilution by the mixing with other rivers and the associated coprecipitation with Fe and Al hydroxides in the river basin.

In the Tamagawa river basin with neutralization treatment using limestone, the pH values ranged from around 1.2 to 6.93 were observed from the upstream to downstream. Harmful elements, As, Pb, and Zn were detected with high concentrations in the upstream of the river basin. Similarly observed in the Sukawa river, the river acidity and concentrations of As, Pb, and Zn were clearly improved by the dilution effect and the related coprecipitation with the Fe and Al hydroxides. Especially, effect of the neutralization on the improvement of water quality was probably more significant in the river basin.

ACKNOWLEDGMENTS

This study was supported from a Grant-in Aid for Scientific Research (no. 26889015) by the Japan Society for the Promotion of Science, a research grant by JFE 21st Century Foundation, ISIJ Research Promotion Grant by the Iron and Steel Institute of Japan, and the Collaborative Research Project (2017-17, 2018-13-, 2019-15, and 2020-12) by the Research Institute for Natural Hazards and Disaster Recovery, Niigata University, Japan. Water quality analysis was partly conducted by the support from Joint Research Grant for the Environmental Isotope Study of Research Institute for Humanity and Nature (RIHN), Japan. The authors deeply appreciate Professor Ichiro Tayasu, Dr. Ki-Cheol Shin, and Dr. Shiho Yabusaki all of RIHN for supporting the water quality analysis.

REFERENCES

[1] Akcil A. and Koldas S., Acid Mine Drainage (AMD): Causes, treatment and case studies. Journal of Cleaner Production, Vol. 14, Issue 12-13, 2006, pp.1139-1145.

[2] Herrera S.P., Uchiyama H., Igarashi T., Asakura K., Ochi Y., Ishizuka F. and Kawada S., Acid mine drainage treatment through a two-step neutralization ferrite-formation process in northern Japan: Physical and chemical characterization of the sludge. Minerals Engineering, Vol. 20, Issue 14, 2007, pp.1309-1314.

[3] Nieto J.M., Sarmiento A.M., Olías M., Canovas C.R., Riba I., Kalman J. and Dlvalls T. A., Acid mine drainage pollution in the Tinto and Odiel rivers (Iberian Pyrite Belt, SW Spain) and bioavailability of the transported metals to the Huelva Estuary. Environment International, Vol. 33, Issue 4, 2007, pp.445-455.

[4] Kikawada Y., Kawai S., Shimada K. and Oi T., Arsenic originating in Kusatsu hot springs, Gunma, Japan, and arsenic pollution status of

Kusatu rivers. Journal of Disaster Research, Vol. 3, Issue 4, 2008, pp.261-269.

[5] Mitsuya D., Hayashi T., Wang Y., Tanaka M., Okai M., Ishida M. and Urano N., Isolation of aquatic yeasts with the ability to neutralize acidic media, from an extremely acidic river near Japan's Kusatsu-Shirane Volcano. Journal of Bioscience and Bioengineering, Vol. 123, Issue 1, 2017, pp.43-46.

[6] Saito T. and Watanabe N., VARIATIONS OF WATER QUALITY ALONG ACIDIC RIVERS IN VOLCANIC AREAS OF EASTERN JAPAN. International Journal of GEOMATE, Vol. 19, Issue 71, 2020, pp.36-41.

[7] Weathers K.C., Strayer D.L. and Likens G.E., Fundamentals of Ecosystem Science. Academic Press, New York, USA, 2013.

[8] Sasaki S., Narita, S., Kikuchi, Y. and Fuda, K., Intake of As and Cr Atoms into Schwertmannite-Like Sediment at the Neutralization Treatment Plant for Tamagawa Hot Spring Acidic Water. Journal of Japan Society on Water Environment, Vol. 36, Issue 5, 2013, pp.137-141 (in Japanese with English abstract).

6th Int. Conf. on Structure, Engineering & Environment (SEE), Kyoto, Japan, Nov.18-20, 2020, ISBN: 978-4-909106056 C3051

OIL/WATER SEPARATION TECHNIQUES USING HYDROPHOBIZED/OLEOPHILIZED GRAINS: A REVIEW OF RECENT STUDIES

Akihiro Matsuno[1], Zafar Muhammad Junaid[1], Takeshi Saito[1], Huyen Thi Thanh Dang[2], Pham Thanh Huyen[3], Tran Thi Viet Nga[2] and Ken Kawamoto[1,2]
[1]Graduate School of Science and Engineering, Saitama University, Japan; [2] National University of Civil Engineering, Vietnam; [3] Hanoi University of Science and Technology, Vietnam

ABSTRACT

Many domestic sources and industries such as foods, textiles, metal industries, petrochemicals, and mining produce massive volume of oily wastewater all over the world. Especially, the insufficient treatment of oily wastewater in developing countries lead a serious environmental pollution. To treat oily wastewater, many techniques such as flotation, chemical coagulation, biological treatment, filtration and membrane separation, and adsorption have been developed. Among them, the oil/water separation techniques based on adsorption and filtration utilizing natural hydrophilic sands and hydrophobized/oleophilized grains are worth being paid attention due to the ease of application and cost effectiveness. In this review, we have summarized the recent studies on the adsorption- and filtration-based oil/water separation utilizing natural hydrophilic sands and grains coated/modified with hydrophobic/oleophilic substances and compared the treatment performance, categorizing types of grains, coating substances, used oil, and testing methods. Prospects and challenges on the oil/water separation studies are also given.

Keywords: Oily wastewater, Oil/water separation, Hydrophobized/oleophilized grains, Adsorption, Filtration

INTRODUCTION

The discharge of massive volumes of oily wastewater due to the rapid industrialization, unplanned urbanization, and agricultural development over the last few decades has led to serious impact to environment and human health [1]. Especially, insufficient treatment and inadequate disposal of oily wastewater generated from human activities and industries such as petrochemical, food processing, textiles, and metal industries, mining, biopharmaceuticals, and oil and gas refineries as well as oil-spill accidents are causing serious water pollution in developing countries. These negative phenomena in endangering aquatic life significantly affect human health, living nature, and natural environment, finally induces substantial economic losses [2].

In general, oil (as well as grease) in wastewater exists as various forms such as free and floating oil, dispersed oil (emulsified with surfactant and/or mechanically), and dissolved oil. The concentrations in oil and grease in wastewater are highly dependent on the sources of wastewater. Typical concentration of oil and grease in untreated domestic wastewater ranges 50 - 150 mg/L [3]–[4]. On the other hand, it has been well known that industrial activities generate wide range of oil and grease concentrations: e.g., oilfield-produced water contains 2 - 565 mg/L, wastewater generated from vegetable oil factories contains 480 - 7,782 mg/L, and wastewater/fluids from metalworking contain 20 - 200,000 mg/L [5]. Thus, the treatment of oily wastewater has been obliged all over the world and permissible levels of oil and grease are regulated before discharging the treated effluents to the environment. For example, Water Pollution Prevention Act (1970) of Japan regulates the maximum permissible levels of treated water discharge are 5 mg/L for mineral oil and 30 mg/L for animal and vegetable oil. In Vietnam, the permissible levels of animal and vegetable oil and grease in domestic wastewater range between 10 - 20 mg/L in QCVN 14:2008/BTNMT, depending on the destination of discharge.

In recent years, many techniques of oily wastewater such as flotation, coagulation, chemical treatment, gravity separation, biological treatment, filtration and membrane separation, and adsorption have been developed [6]. Among of them, the oil/water separation techniques based on adsorption and filtration have been progressed by using various types of materials such as membrane, mesh, film, porous media, grains (powders), and so on. For the oil/water separation, not only using natural hydrophilic/oleophobic (vice versa natural hydrophobic/oleophilic) materials but also the synthetic materials with hydrophobic/oleophilic substances can be applied to improve the surface hydrophobicity/oleophilicity [7]–[10]. Although various types of oil/water separation techniques have

been reported, the further development of cost-effective and environmentally friendly (e.g., use of recyclable/reusable materials) methods are required especially to treat large volumes of oily wastewater with high efficiency [11].

Among the oil/water separation techniques based on adsorption and filtration, the utilization of natural hydrophilic sands and hydrophobized/oleophilized grains are of the most interest due to the ease of application and their cost effectiveness. In this study, we especially reviewed on the recent progress on the utilization of natural hydrophilic sands and hydrophobized / oleophilized grains for the oil/water separation techniques and compared the treatment performance, categorizing types of grains, coating substances, used oil, and testing methods.

METHODOLOGY

Data review was based on the keywords such as oil/water separation, oily wastewater, hydrophobicity (oleophilicity), hydrophilicity (oleophobicity), hydrophobized/oleophilized grains, adsorption, and filtration. Tens of journal papers, books, and reports published in English after 2000's were searched in this study [e.g., Web of Science™ (Clarivate Analytics)]. After checking the searched literatures from the viewpoint of the utilizations of hydrophobized/oleophilized grains for the oil/water separation have been chosen, a total of 11 literatures was selected to summarize and compare the data.

RESULTS AND DISCUSSION

Table 1 summarizes the oil/water separation techniques utilizing natural hydrophilic sands and hydrophobized/oleophilized grains, categorizing types of grains, coating substances, measured contact angle of water in air (CA_a) and contact angle of oil in water (CA_o), used oil and concentration (or oil/water ratio), testing methods, and separation efficiency and/or separation capacity. The oil/water separation techniques are classified into two types: one is the adsorption-based technique and the other is the filtration-based technique.

Types of Grains and Measured Contact Angles

For both adsorption-based and filtration-based oil/water separation techniques, sand materials were generally used for the oil/water separation techniques except for [22]. This is because the sand materials are easy-available, low-cost, and nontoxicity to environment [16]. Among of the sand materials, quartz sand was commonly used for fabricating hydrophobicity/oleophilicity on the grain surface [13], [15], [20], [21], and natural desert sand was used for the filtration-based oil/water separation due to its surface hydrophilicity/oleophobicity [17]– [19]. The tested grain sizes ranged < 1 mm and mostly around 0.2 mm that is a typical boundary between fine sand and medium sand in the fields of Geotechnical Engineering and Soil Science.

CA_a is used to characterize the hydrophobicity/oleophilicity of grain surface and CA_o is used to characterize the hydrophilicity/ oleophobicity of grain surface. The relationship between measured CA_a/CA_o and the grain size are plotted in Fig. 1. The contact angles with > 150º are identified as materials with "superhydrophobic/ superoleophilic" surface or "superhydrophilic/ superoleophobic" surface [23]. The measured CA_a and CA_o were dependent on the tested oils, but, most of the tested grain surfaces became > 150º, indicating that the tested grains were categorized as "superhydrophobicity / superoleophilicity" or "superhydrophilicity /superoleophobicity". However, it has been reported that the grain size and geometry affected the water repellent characteristics of hydrophobized grains [24]. Thus, the effects of grain size geometry on the surface are needed to assess carefully for selecting suitable materials for the oil/water separation techniques.

Used Oils for Oil/Water Separation Studies

As shown in Table 1, various types of oils such as gasoline, diesel, crude oil, vegetable oils (soybean cotton seed, rapeseed and so on) including so-called volatile organic compounds (VOCs) such as petroleum ether, hexane, and chloroform were used depending on the purposes of studies. Besides, both "oil in water" and "water in oil" were used and both concentration (given in mg/L or mL/L in Table 1) and oil/water ratio (given in O/W in Table 1) were used in the oil/water separation studies

Testing Methods and Separation Efficiency for Oil/Water Separation Studies

Basically, all reported studies on both adsorption-based and filtration-based gave a good oil/water separation performance. For the adsorption-based techniques using batch and mixing methods, the adsorption/adhesion capacities ranged between 110 to 500 mg/g. Atta [14] reported that the adsorption capacity of crude oil was increased from 160 (uncoated silica particles) to 500 mg/g after the coating of grain surface. Bigui [15] reported that the adsorption capacities of hydrophobized quartz sands increased 54% for engine oil and 45% for rapeseed oil compared to those of uncoated quartz sands. For the filtration-based techniques, the gravity-driven method was commonly used to assess the separation efficiency and capacity. The separation capacity was validated based on the performance under repeated separation tests (i.e., cycles).

Table 1 Oil/water separation techniques utilizing natural hydrophilic sands and hydrophobized/oleophilized grains.

Grains/sands (size in mm)	Coating substances	CA_a / CA_o (°)	Used oil*	Oil concentration or O/W	Method	Separation efficiency (in %) and/or separation capacity**	Ref.
Adsorption-based							
Silica particles (~0.4)	1,7-octadiene monomer	CA_a = 129-144	Motor oil, crude oil, kerosene	20 g/L (in water)	Batch (4 g solid to 80 mL oil)	> 99 % 330-500 mg/g	[12]
Quartz sand (0.55-0.83)	ODTS, ZnO nanoparticles	CA_a = 150-154	Engine oil, rapeseed oil, and so on	N.C.	Mixing (10 g solid to 5 mL oil)	96.5-99.7 % 180-380 mg/g	[13]
Sand (0.1-0.25)	TEOS, VTS	CA_a = 140-170	Crude oil	20 mL/L (in seawater)	Mixing (Sand : oil = 1:1, 1:2, 1:10)	80-92 % (Coating substances: sand = 1:2)	[14]
Quartz sand (0.6-0.9)	Chitosan, SiO_2 nanoparticles	CA_o = 152	Engine oil, rapeseed oil	N.C.	Mixing (20 g solid to 100 mL oil)	~ 280 mg/g (Engine oil) ~ 110 mg/g (Rapeseed oil)	[15]
Filtration-based							
Sand (0.1-0.5)	ODTS	CA_a = 155	Hexadecane, chloroform	O/W = 5:3 (in volume)	Gravity-driven with vacuum (Oil: chloroform)	High separation capacity was kept even after 5 cycles of separation	[16]
Desert sand (0.13-0.27)	(Non-coating)	CA_o = 146-152	Decane, sesame oil, crude oil, diesel oil, and so on	N.C.	Gravity-driven (Oil: petroleum ether)	High separation capacity depending on the thickness sand layer	[17]
Desert sand (> 0.05)	(Non-coating)	CA_o = 112*** (CA_a = 0)	Diesel, petroleum ether, and so on	O/W = 50:1 (in volume)	Gravity-driven (Porosity: 79.6%)	> 99.8% (Separation capacity was maintained even after 10 cycles of separation)	[18]
Desert sand (0.1-0.2)	$Cu(OH)_2$ nano-needles	CA_a = 158	1,2-dichloroethane	O/W = 2:1 (in volume)	Gravity-driven	Up to 99.5 %	[19]
Quartz sand (0.55-0.83)	IDT, 3-MPS	N.D.	Gasoline engine oil	17.3 mg/L (in water)	Steady effluent flow rate	74-87 % (in the first 9 hours)	[20]
Quartz sand (0.1-0.3)	HMDS (nano silica)	CA_o = 154	Xylene, chloroform, diesel oil	O/W = 1:1 (in weight)	Gravity-driven	97-98 % (96 % even after 50 cycles of separation)	[21]
Quartz sand (0.6-0.9)	Chitosan, SiO_2 nanoparticles	CA_o = 152	Engine oil	O/W = 1:19 (in weight)	Gravity-driven (Porosity: 45%)	~ 100 %	[15]
Waste brick grains (0.1-0.4)	(Non-coating)	CA_o = 146	Soybean oil, hexane, and so on	N.C. (water-in-oil and oil-in-water emulsions)	Gravity-driven (Porosity: 47%)	~ 98 % (Separation capacity was kept even after 10 cycles of separation)	[22]

Note: *Used oil including volatile organic compounds (VOCs). **Capacity: Adsorbed amount of oil / grains (g/g) was given for the adsorption-based technique. Applicable range and observed performance of oil/water separation were given for the filtration-based technique. ***CA_o was read by the figure in the literature.

[Abbreviations] CA_a: Contact angle of water in air (°), CA_o: Contact angle of oil in water (°), HMDS: 1,1,1,3,3,3-hexamethyldisilazane, IDT: Isopropyl dioleic (dioctylphosphate) titanate, N.C.: Not controlled (used as it) or not clarified, N.D.: Not determined, ODTS: Octadecyltrichlorosilane, O/W: Oil/water ratio, TEOS: Tetraethoxysilane, VTS: Vinyltrimethoxysilane, 3-MPS: 3-methacryloxypropyltrimethoxysilane

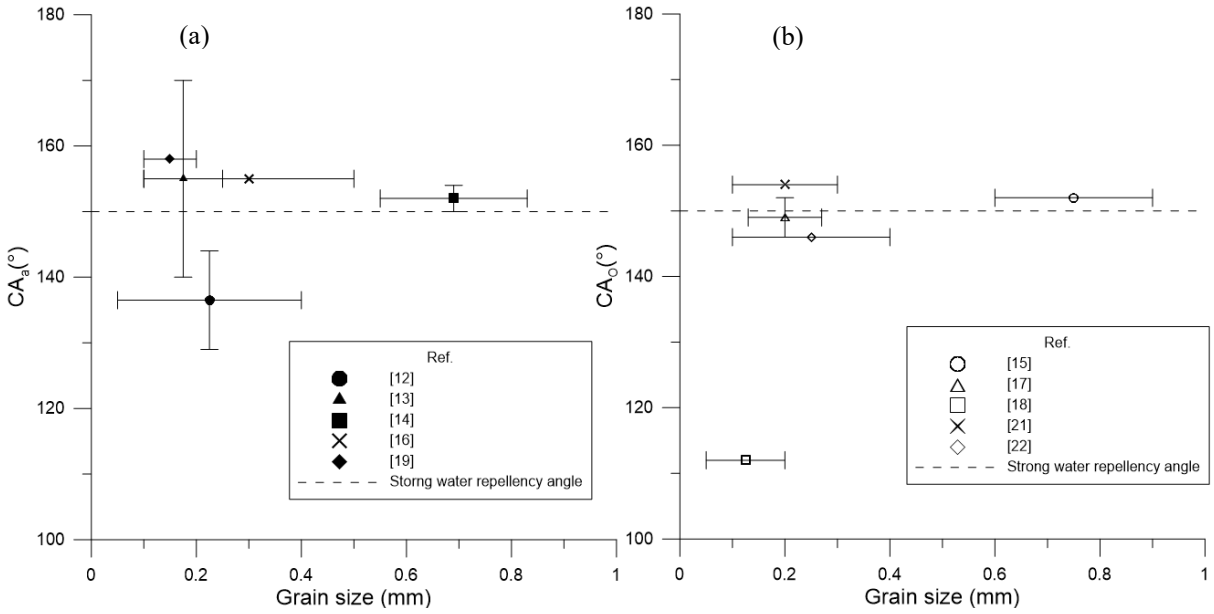

Fig. 1 Relationship between grain size and (a) contact angle of water in air (CA_a) and (b) Contact angle of oil in water (CA_o).

CONCLUSIONS AND PROSPECTS

In this paper, recent studies and progress on the oil/water separation techniques based on adsorption and filtration utilizing natural hydrophilic sands and hydrophobized/oleophilized grains were reviewed. All reviewed literatures performed well and gave high oil/water separation efficiency and capacity through the laboratory tests. Most of the studies used sands as tested grains. It is worth to note that Li [22] used the grains from waste clay brick (origin from construction waste). In addition, Shi [25] utilized waste brick powders for coating membrane for the oil/water separation. Junaid [26] assessed the water repellency for hydrophobized autoclaved aerated concrete grains originated from the scrap of construction materials. Those harmless waste materials and industrial by-products should be encouraged to utilize for the oil/water separation techniques from the viewpoints of reuse and recycle of waste, sustainability, and green development.

With regard to the practical applications of tested studies to the actual treatment of oily wastewater, not only the assessment of the grain size and coating substances but also the examination of suitable packed density (porosity) and flowing conditions of oily wastewater such as line velocity, hydraulic retention time, and mass transport analysis under continuous flowing condition are important. Further studies and challenges are necessary to evaluate the performance of oil/water separation techniques utilizing those natural hydrophilic sands and hydrophobized/oleophilized grains fully considering the packed density and flowing conditions.

ACKNOWLEDGMENTS

This research was supported by JST-JICA Science and Technology Research Partnership for Sustainable Development (SATREPS) project (No. JPMJSA1701).

REFERENCES

[1] Shamaei L., Khorshidi B., Islam M. A., and Sadrzadeh M., Industrial Waste Lignin as an Antifouling Coating for the Treatment of Oily Wastewater: Creating Wealth from Waste, Journal of Cleaner Production, Vol. 256, 2020, pp. 120304.

[2] Yong J., Huo J., Chen F., Yang Q., and Hou X., Oil/Water Separation Based on Natural Materials with Super-Wettability: Recent advances, Journal of Physical Chemistry Chemical Physics, Vol. 20, Issue 39, 2018, pp. 25140–25163.

[3] Crites R., and Tchobanoglous G., Small & Decentralized Wastewater Management Systems (1st Edition), Series: McGraw-Hill Series in Water Resources and Environmental Engineering, McGraw-Hill Science/Engineering/Math, USA, 1998, pp. 169-239.

[4] Tchobanoglous G., Burton F. L., and Stensel H.D., Wastewater Engineering: Treatment and Reuse (Fourth Edition), McGraw-Hill Series in Civil and Environmental Engineering, Metcalf & Eddy, Inc., USA, 2002, pp. 153-213

[5] Pintor A. M. A., Vilar V. J. P., Botelho C. M. S., and Boaventura R. A. R., Oil and Grease Removal from Wastewaters: Sorption Treatment as an Alternative to State-of-the-Art Technologies. A

Critical Review, Chemical Engineering Journal, Vol. 297, 2016, pp. 229–255.
[6] Jafarinejad S., Treatment of Oily Wastewater, Publication of Petroleum Waste Treatment and Pollution Control, 2017, pp.185-267.
[7] Xue Z., Cao Y., Liu N., Feng L., and Jiang L., Special Wettable Materials for Oil/Water Separation, Journal of Materials Chemistry A, Vol. 2, Issue 8, 2014, pp. 2445–2460.
[8] Wang B., Liang W., Guo Z., and Liu W., Biomimetic Super-Lyophobic and Super-Lyophilic Materials Applied for Oil/Water Separation: A New Strategy beyond Nature, Journal of Chemical Society Reviews, Vol. 44, Issue 1, 2015, pp. 336–361.
[9] Zhang Y., Zhang Y., Cao Q., Wang C., Yang C., Li Y., and Zhou J., Novel Porous Oil-Water Separation Material with Super-Hydrophobicity and Super-Oleophilicity Prepared from Beeswax, Lignin, and Cotton, Journal of Science of the Total Environment, Vol. 706, 2020, pp. 135807.
[10] Zhao B., Ren L., Du Y., and Wang J., Eco-Friendly Separation Layers based on Waste Peanut Shell for Gravity-Driven Water-in-Oil Emulsion Separation, Journal of Cleaner Production, Vol. 255, 2020, pp. 120184.
[11] Gupta, R.K., Dunderdale G.J., England M.W, and Hozumi A., Oil/Water Separation Techniques: A Review of Recent Progresses and Future Directions. Journal of Materials Chemistry A: Materials for Energy and Sustainability, Vol. 5, 2017, pp. 16025-16058.
[12] Akhavan B., Jarvis K., and Majewski P., Hydrophobic Plasma Polymer Coated Silica Particles for Petroleum Hydrocarbon Removal, Journal of ACS Applied Materials and Interfaces, Vol. 5, Issue 17, 2013, pp. 8563–8571.
[13] Jianlin L., Xiaofei Z., Hongwei Z., Fuping W., Bigui W., and Qing C., Superhydrophobic Coating on Quartz Sand Filter Media for Oily Wastewater Filtration, Journal of Colloids and Surfaces A: Physicochemical and Engineering Aspects, Vol. 553, Issue June, 2018, pp. 509–514.
[14] Atta A. M., Abdullah M. M. S., Al-Lohedan H. A., and Mohamed N. H., Novel Super-hydrophobic Sand and Polyurethane Sponge Coated with Silica/Modified Asphaltene Nanoparticles for Rapid Oil Spill Cleanup, Journal of Nanomaterials, Vol. 9, Issue 2, 2019, Article Number 187.
[15] Bigui W., Cheng Y., Jianlin L., Gang W., Liang D., Xiaosan S., Fuping w., Hua L., and Qing C., Fabrication of Superhydrophilic and Underwater Superoleophobic Quartz Sand Filter for Oil/Water Separation, Journal of Separation and Purification Technology, Vol. 229, Issue March, 2019, pp. 115808.
[16] Men X., Ge B., Li P., Zhu X., Shi X., and Zhang Z., Facile Fabrication of Superhydrophobic Sand: Potential Advantages for Practical Application in Oil-Water Separation, Journal of the Taiwan Institute of Chemical Engineers, Vol. 60, 2016, pp. 651–655.
[17] Yong J., Chen F., Yang Q., Bian H., Du G., Shan C., Hua J., Fang Y., and Hou X., Oil-Water Separation: A Gift from the Desert, Journal of Advanced Materials Interfaces, Vol. 3, Issue 7, 2016, pp. 1–7.
[18] Li J., Xu C., Guo C., Tian H., Zha F., and Guo L., Underoil Superhydrophilic Desert Sand Layer for Efficient Gravity-Directed Water-in-Oil Emulsions Separation with High Flux, Journal of Materials Chemistry A, Vol. 6, Issue 1, 2017, pp. 223–230.
[19] Chen L., Wu Y., and Guo Z., Superhydrophobic Sand Grains Structured with Aligned Cu(OH)2 Nano-Needles for Efficient Oily Water Treatment, Journal of Materials and Design, Vol. 135, 2017, pp. 377–384.
[20] Bigui W., Jianlin L., Gang W., and Qing C., Filtration of Oil from Oily Wastewater via Hydrophobic Modified Quartz Sand Filter Medium, Journal of Water Reuse and Desalination, Vol. 8, Issue 4, 2018, pp. 544–552.
[21] Liu P., Niu L., Tao X., Li X., Zhang Z., and Yu L., Preparation of Superhydrophobic-Oleophilic Quartz Sand Filter and its Application in Oil-Water Separation, Journal of Applied Surface Science, Vol. 447, 2018, pp. 656–663.
[22] Li Z., Wu J., Yue X., Qiu F., Yang D., and Zhang T., Study on the Application of Waste Bricks in Emulsified Oil-Water Separation, Journal of Cleaner Production, Vol. 251, 2020, pp. 119609.
[23] Wang Z., Elimelech M., and Lin S., Environmental Applications of Interfacial Materials with Special Wettability, Journal of Environmental Science and Technology, Vol. 50, Issue 5, 2016, pp. 2132–2150
[24] Wijewardana N. S., Kawamoto, K., Moldrup, P., Komatsu, T., Kurukulasuriya, L. C., and Priyankara, N. H., Characterization of Water Repellency for Hydrophobized Grains with Different Geometries and Sizes, Environmental Earth Sciences, Vol. 74, Issue 7, 2015, pp. 5525–5539
[25] Shi G., Shen Y., Mu P., Wang Q., Yang Y., Ma S., and Li J., Effective Separation of Surfactant-Stabilized Crude Oil-in-Water Emulsions by using Waste Brick Powder-Coated Membranes under Corrosive Conditions, Journal of Green Chemistry, Vol. 22, Issue 4, 2020, pp. 1345–1352. [26] Junaid Z.M., Matsuno A., Saito T., Dang H.T.T., Huyen P.T., and Kawamoto K., Conference proceeding, Characterization of hydrophobicity for Artificially Hydrophobized Autoclave Aerated Concrete Grains, 3rd International Symposium on Coupled Phenomena in Environmental Geotechnics (CPEG), CPEG2020-

124, 2021 "In press".

6th Int. Conf. on Structure, Engineering & Environment (SEE), Kyoto, Japan, Nov.18-20, 2020, ISBN: 978-4-909106056 C3051

HEAVY METAL CHARACTERISTICS OF WASTEWATER FROM BATIK INDUSTRY IN YOGYAKARTA AREA, INDONESIA

Any Juliani1, Suphia Rahmawati2 and Minoru Yoneda1
1Department of Environmental Engineering, Kyoto University, Japan;
2 Faculty of Civil Engineering and Planning, Universitas Islam Indonesia, Indonesia

ABSTRACT

Batik is a traditional Indonesian textile product with a unique production method. It involves the application of wax in its multiple coloring stages. The application of synthetic dyes in batik production raises concern on heavy metal content in its wastewater. As wastewater from most factories is released to the environment without proper treatment, the pollutants including heavy metal content would pose health risks to humans and the environment. However, data on heavy metal characteristics of wastewater from batik industry in Indonesia is very limited. This paper presents the heavy metal characteristic of 17 (seventeen) samples of wastewater from batik factories in Yogyakarta Area, Indonesia. The total concentration of Cr, Co, Ni, Cu, As, Cd, and Pb were measured by using inductively-coupled plasma mass spectrophotometry (ICP-MS). The concentration of Cr, Co, Ni, Cu, As, Cd, and Pb ranged from 9.87 to 101 ppb, 0.03 to 3.89 ppb, 5.37 to 82.8 ppb, 19.7 to 472 ppb, 1.46 to 21.2 ppb, 0.03 to 20.3 ppb and 0.78 to 40.1 ppb respectively. Hierarchical Cluster Analysis (HCA) was then performed to observe group of samples or parameter with similar characteristics that represent similar production method which affects their wastewater characteristics. This would be the basis for risk assessment which can further be used to develop appropriate measures to control negative impact of batik industry to human and environment. However, the result indicates that other factors may affect the heavy metal concentration in batik wastewater which demands further study.

Keywords: Batik Wastewater, Heavy Metal, Cluster Analysis, Risk Assessment

INTRODUCTION

Batik is a traditional Indonesian textile product, although it is also developed in Malaysia [1]. Batik industry is an important economic sector in Indonesia. In 2019, export of batik products from Indonesia reached US$ 52.4 million. It is a significant number as compared to US$ 442 billion of textile product global market value of the same year [2].

Batik production method differs from common method used in textile industries. It involves the application of wax in its multiple coloring stages. A two colored batik sheet will require two times coloring stages. A three colored would require three times coloring stages, and so on. Part of the motive which is not intended to have the first color would be covered by wax to undergo the dyeing process of the first color. Afterward, the wax is removed and the process continues to the second coloring process by using the same method.

The application of wax, dye and also fixing agents in batik production results in wastewater characteristic of high pH, organic content (COD, BOD), total suspended solids (TSS) and color intensity [3]–[6]. Similar to the general textile wastewater, there is also concern on possible heavy metal content in batik wastewater[1],[7],[8]. Heavy metals are part of organic-based coloring dyes to enhance its absorption to fabrics or at least present as impurities of dyes [7] [9]. Various heavy metal including Cd, Pb, Fe, Cu, Zn, Al, Mn, Mg, Ca, Cr and Si were detected in batik wastewater sample from Batik factory in Malaysia with similar production method as that is used in Indonesia [1] [7]. The concentration for each element of heavy metal varies according to production stage[1].

In Indonesia, batik is produced mostly by middle to small scale industries which are categorized as home industry. One characteristic of home industries is their limited capacity in various aspects including occupational and environment health management. Factory workers are being exposed to chemicals involved in the production process with minimum personal protection equipment. On the other hand, batik wastewater from most factories are released to environment without proper treatment. While many batik factories are located in vicinity to housing areas, this improperly handling of wastewater may release pollutants to soil and groundwater. A study conducted by Syuhadah, et.al showed a strong positive correlation between concentration of heavy metals measured in soil and plants surrounding a batik factory and heavy metal concentration in effluents from that particular batik factory [7]. This would pose health risk to human from direct use and

exposure to contaminated soil, water bodies and groundwater. To develop appropriate measure to control this negative impact, risk based approach through risk assessment can be applied. Risk assessment consists of four generic steps, namely, (i) hazard identification, (ii) hazard assessment, (iii) exposure assessment, and (iv) risk characterization [10]. In the case of batik industry, hazard identification as the first step of risk assessment can be conducted through characterization of the source of hazard. In this case, it is wastewater. However, data on heavy metal characteristic of wastewater from batik industry in Indonesia is limited mostly to concentration of total Chromium (Cr), as it is the only heavy metal parameter regulated by Indonesia national standard[11]. On the other hand, study on batik wastewater are mostly focused on the development of treatment technology [12]–[14]. No study had been conducted to assess the risk can be posed by present wastewater handling to the environment and human health. This paper presents the heavy metal characteristic of 17 samples of wastewater from batik factories in Yogyakarta Area as one of the center of batik industries in Indonesia as the initial phase of the risk assessment of batik industry in study area.

MATERIALS AND METHODS

Study Sites and Sampling

Special Region of Yogyakarta is one of provincial administrative area of Indonesia. It is located in Java Island, bordered by the Indian Ocean in the south and sharing land border with Central Java Province. It consists of four regencies, namely: Bantul, Sleman, Kulonprogo and Gunungkidul, and one city, Yogyakarta City as the capital [15]–[17].

Wastewater samples for this study were taken from batik factories located in Yogyakarta City and Bantul Regency (Fig.1). Samples were collected in polypropylene (PP) bottles. Parameter pH was measured on site by using Multiparameter Water Quality Checker Horiba U-50. Samples for heavy metal analysis were acidified with concentrated HNO_3 (grade for heavy metal measurement, 65%, Merck) until pH<2 for preservation. All samples were kept in 4° C until analysis.

Samples were wastewater after dyeing (step 4) and wax removal process (step 5) of batik production as referred to Fig. 2. Table 1 presents from which production process by referring to Fig.2 and type of dye used in the factories where the samples were taken from.

Table 1 Source of samples

Sample Code	Source of Process	Type of dyes used by factory
X1	After step 4	Naphtol
X2	After step 5	Naphtol
X3	After step 4	Naphtol
X4	After step 5	Naphtol
X5	After step 4	Naphtol, Indigosol
X6	After step 4	Naphtol, Indigosol
X7	After step 4	Naphtol, Indigosol
X8	After step 4	Naphtol, Indigosol
X9	After step 4	Naphtol, Indigosol
X10	After step 5	Naphtol, Indigosol
X11	After step 5	Naphtol, Indigosol
X12	After step 4	Remasol
X13	After step 4	Naphtol, Indigosol
X14	After step 4	Naphtol, Indigosol
X15	After step 5	Naphtol, Indigosol
X16	After step 5	Naphtol, Indigosol
X17	After step 4	Naphtol, Indigosol

Fig. 1 Indonesia region (top), Special Region of Yogyakarta (middle), study area (bottom)

Inductively Coupled Plasma Mass Spectrometry (ICP-MS) was used to analyze heavy metal content in the samples. Prior to analysis, samples were pretreated following a modification of EPA method 3015A for microwave assisted acid digestion. Acid mixture of HNO_3 (grade for heavy metal measurement, 61 %, Wako Chemical) and HCl (35-37%, Wako Chemical) were added to samples with the ratio of 9:1 and digested in laboratory microwave oven (CEM type MARS 6 using Easy Prep Plus vessel type). Digestion was set to 800 psi pressure and 200°C temperature held for 15 minutes with ramping time of 15 minutes. Digested samples were then filtered by using 0.45 µm cellulose acetate membrane filter. Prior to measurement, filtered samples were diluted with 1 N HNO_3 solution. Standard solutions were prepared by dilution of standard stock (Wako Chemical) of each elements with 1 N HNO_3 solution. Isotopes used for measurement were ^{52}Cr, ^{59}Co, ^{60}Ni, ^{63}Cu, ^{75}As, ^{111}Cd and ^{208}Pb. Internal standard ^{89}Y and ^{115}In were used to ensure stability during measurement. Limit of detection (LoD) for Cr, Co, Ni, Cu, As, Cd, and Pb were 0.18, 0.05, 0.31, 0.82, 0.07, 0.05, and 0.06 ppb respectively.

Heavy metal in textile related wastewater is associated with dyes which generally are organic compound [7]. Therefore, in addition to heavy metal, organic content in samples was also measured through analysis of Total Organic Carbon (TOC). It was conducted by using TOC analyzer type TOC-V CSN by Shimadzu. Samples were diluted and filtered to remove particulate prior to measurement. Standard solution for TOC measurement was prepared by using KHP ($C_8H_5KO_4$, 99.8-100.2%, Wako Chemical) which was dried and then diluted with milli-Q water to prepare necessary concentration of standard solutions.

Statistical Analysis

Statistical analysis was conducted by using R software version 4.0.0 [18]. By using Mardia Test in "MVN" Package [19], it was checked that the data was multivariate normal after logarithmic transformation. Then, Hierarchical Cluster Analysis (HCA) was performed to group the samples by using Ward's linkage method [18]. To ensure comparability among datasets, standardization was performed before clustering. Dendrogram visualization of HCA was performed by using "factoextra" Package [20].

RESULTS AND DISCUSSIONS

Batik Production Process

In general, there are 2 types of batik which are differentiated by the device used to apply wax on the cloth. The first type is hand painted batik in which a pen like device is used during wax application. Another type is called stamping batik in which a big stamp like device is used for wax application. The stamp is made of copper with usually a 20 x 20 cm^2 size. Basically, both types are produced through the process described in Fig.2.

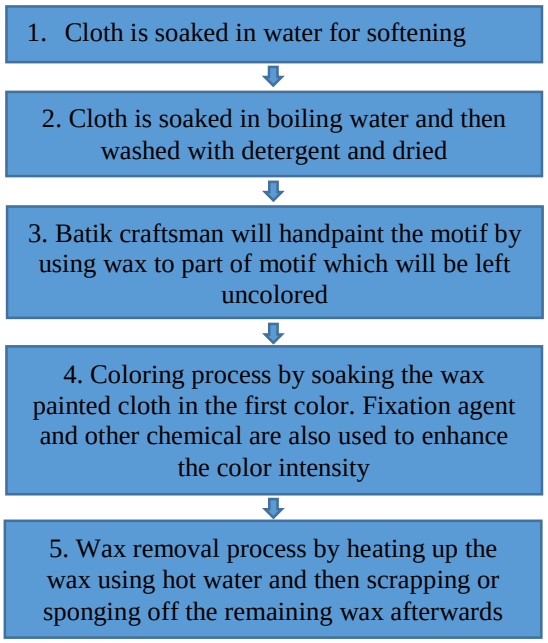

Fig. 2 Batik production process

Step 3-5 will be repeated according to the number of colour would be applied on each production. A "*canting*" is used in step 3 for hand painted type, while a "*cap*" is used in stamp batik making process. Chemical used during process consists of wax, colouring agent both natural or synthetic and fixation agent. Some most commonly used chemical are as presented in Table 3.

Table 2 Most common chemical used in batik industry [21]

Dye	Nat./Syn.*)	Fixation agent
Naphtol	Syn.	Diazonium-salt
Remasol	Syn.	Water glass ($Na_2(SiO_2)_nO$)
Indigosol	Syn.	H_2SO_4, HCl
Indigofera	Nat.	Air
Teger, Jambal, Tingi, Mahogany skin	Nat.	($K_2(SO_4)_2$), ($FeSO_4$), ($CaOH_2$)

*) Nat. = natural ; Syn. = synthetic

Laboratory Analysis Result

Total concentration of some heavy metal elements including Cr, Co, Ni, Cu, As, Cd, Pb as well as pH and Total Organic Carbon (TOC) are presented in Table 4.

Table 3 Descriptive statistics of laboratory analysis result

Parameter	Min.	Max.	Mean	SD
Cr (ppb)	9.87	101	36.9	25.0
Co (ppb)	0.03	3.89	2.05	1.14
Ni (ppb)	5.37	82.8	27.2	22.6
Cu (ppb)	19.7	472	120	110
As (ppb)	1.46	21.2	6.49	5.93
Cd (ppb)	0.03	20.3	3.79	5.34
Pb (ppb)	0.78	40.1	14.5	11.7
pH	6.21	11.1	8.83	1.62
TOC (g/L)	1.25	13.6	3.47	3.11

Heavy metal parameter which is being regulated in Minister of Environment Regulation No.5/2014 on textile wastewater effluent standard and Local Regulation of Yogyakarta Special Region No.7/2016 on Effluent standard for batik industry in Yogyakarta Special Region is only Total Chromium (Cr). The maximum Cr concentration in batik effluent according to both regulations is 1 ppm. Compared to both standards, no sample exceed Cr maximum concentration. Compared to effluent standard in other countries such as Japan and Malaysia, concentration of heavy metal in all samples are also still below standard. Table 4 presents comparison of wastewater data to these standards.

As only Cr which is regulated for batik effluent standard in Indonesia, data on heavy metal content in batik wastewater in Indonesia was mostly limited to this parameter as reported by [11] and [22]. These studies reported the Cr concentration in batik wastewater samples taken from factories in Banyumas, Central Java Region and Sidoarjo, East Java Region respectively. Syahputra, et.al. [12] reported concentration of Cr^{6+} and Pb in batik wastewater taken from one factory in Yogyakarta, the same area with this study. Data on other heavy metal elements in batik wastewater was from batik factories in Malaysia as reported by [1] and [7]. These studies reported heavy metal concentration in, samples taken from batik factories in Kelantan, Malaysia. Other heavy metal elements of Fe, Zn, Al, Mn, Mg, Ca, and Si with concentration of 3.0, 0.29, 12, 0.02, 0.97, 4.23, and 8965 ppm respectively were also reported in [1]. Compared to other studies, heavy metal concentration in samples in this study is relatively lower.

Table 4 Comparison of maximum concentration in samples (ppm) to effluent standards of Indonesia, Japan and Malaysia and to other studies

	Cr	Cr^{6+}	Cr^{3+}	Cu	Ni	As	Cd	Co	Pb
Effluent Standard									
A. Indonesia									
Local [1)]	1.0	-	-	-	-	-	-	-	-
National [2)]	1.0	-	-	-	-	-	-	-	-
B. Japan									
B [1)]	-	0.5	-	-	-	0.1	0.03	-	0.1
B [2)]	2	-	-	3	-	-	-	-	-
C. Malaysia									
C [1)]	-	0.05	0.20	0.20	0.20	0.05	0.01	-	0.10
C [2)]	-	0.05	1.0	1.0	1.0	0.10	0.02	-	0.5
Max. conc. in sample	0.01	-	-	0.47	0.08	0.02	0.02	0.00	0.04
Dewi, et.al [11]	1.1	-	-	-	-	-	-	-	-
Syahputra, et.al [12]	-	0.16	-	-	-	-	-	-	0.47
Suprihatin, et.al [22]	0.06	-	-	-	-	-	-	-	-
Moradi, et.al. [1]	0.08	-	-	0.29	-	-	-	-	0.04
Syuhadah, et.al. [7]									
Site A	0.00	-	-	0.19	-	-	0.01	-	0.16
Site B	0.00	-	-	0.57	-	-	0.01	-	0.34
Site C	0.00	-	-	0.02	-	-	0.00	-	0.47

A 1) Indonesian Minister of Environment Regulation No.5/2014
A 2) Local Regulation of Yogyakarta Special Region No.7/2016
B 1) Japan Standard for the protection of human health
B 2) Japan Standard for the protection of living environment
C 1) Malaysia Standard A: if discharged to inland waters within catchment areas
C 2) Malaysia Standard B: if discharged into other inlands waters or Malaysian waters

Concentration were varied as showed in Table 3 Based on their standard deviation (SD), Cu had the highest variation among all measured metal elements followed by Cr, Ni, Pb, As, Cd and Co respectively. The same order was also applied to the distribution of heavy metal among samples which is Cu>Cr>Ni>Pb>As>Cd>Co. Cu had given the highest concentration compared to other elements. Studies conducted by [1] and [7] presents data on heavy metal concentration in batik wastewater following distribution order of Cu>Cr>Pb and Cu>Pb>Cd>Cr respectively. Compared with these 2 other studies, data in this study is consistent as Cu gives the highest concentration. Cu along with Cr, Ni and Co are predominant element for metal complex azo dyes [23] [24]. Included in azo dyes is naphtol which is commonly used in batik industry.

Hierarchical Cluster Analysis

Hierarchical Cluster Analysis (HCA) was performed to classify samples and parameters into different clusters. Two dendrograms were produced showing clusters of samples and parameters as presented in Fig. 3.

Parameter cluster dendrogram shows that Ni and Cr belongs to the same cluster with the lowest dissimilarity. These parameters also in the same cluster with Cu with higher dissimilarity. This may indicate the Ni, Cr and Cu content in effluent were from the same source. Cr, Cu, Ni along with Co are said to be predominant element for metal complex azo dyes [23] [24] which are the type of dyes mostly used in batik production. Similar to textile wastewater, other source of heavy metals in batik wastewater can be from impurities of chemical used in different stages of production processes [25]. This is represented in dendrogram that other heavy metal elements belong to different cluster than Cu, Ni and Cr. On the other hand, the sample cluster dendrogram shows that sample X17 and X4 are the most similar. However, sample X17 and X4 came from different production stage and X17 also used indigosol dye instead of only napthol like that of X4. This indicates factors other than the type of dye and production stage that affect wastewater characteristic. Also similar to textile wastewater, composition of batik wastewater may vary among factories due to variation of type of fabric, chemicals other than dyes, quality of water and equipment used for production [25].

CONCLUSIONS

Analysis on 17 (seventeen) wastewater samples from batik factories in Yogyakarta Region showed variation among elements and samples. The concentration of Cr, Co, Ni, Cu, As, Cd, and Pb ranged from 9.87 to 101 ppb, 0.03 to 3.89 ppb, 5.37 to 82.8 ppb, 19.7 to 472 ppb, 1.46 to 21.2 ppb, 0.03 to 20.3 ppb and 0.78 to 40.1 ppb respectively.

Hierarchical Cluster Analysis (HCA) produced dendrograms showing cluster of strong similarity among parameters Ni, Cr and Cu which indicates that the source of these metals is from dyes. HCA also indicates that other factors may affect the heavy metal content in batik wastewater which should be clarified through further study.

ACKNOWLEDGMENTS

This research was supported by Indonesia Endowment Fund for Education and Department of Environmental Engineering, Kyoto University.

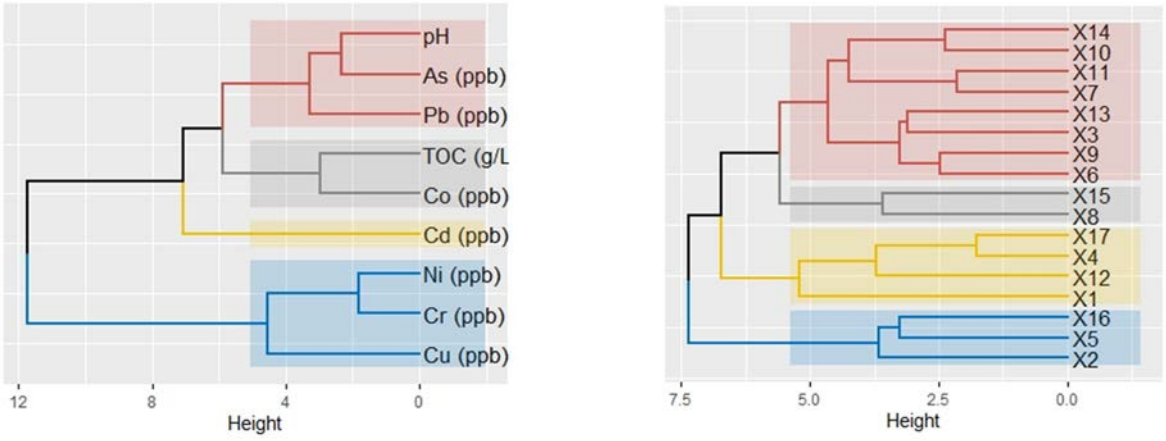

Fig. 3 Dendrogram of Hierarchical Cluster Analysis (HCA) among parameters (left) and samples (right)

REFERENCES

[1] Moradi P, Ranjbar N, Che R, Tiek K, Lee G, Ibrahim S, Park C, Yoon Y., Jang M. An Efficient and Economical Treatment for Batik Textile Wastewater Containing High Levels of Silicate and Organic Pollutants Using A Sequential Process of Acidification, Magnesium Oxide, and Palm Shell-Based Activated Carbon Application. J. of Env. Man., Vol. 184, 2016, 229-239

[2] Ekarina. Ekspor Batik Indonesia Semester I 2019 Tembus Rp 253 Miliar. Katadata Indonesia. 2019. Available from: https://katadata.co.id/berita/2019/09/24/ekspor-batik-indonesia-semester-i-2019-tembus-rp-253-miliar [cited 2020 Jun 30]

[3] Mukimin A, Vistanty H, Zen N, Purwanto A, Wicaksono KA. Performance of Bioequalization-Electrocatalytic Integrated Method for Pollutants Removal of Hand-drawn Batik Wastewater. J. of Water Process Eng. Vol 21, 2018, 77–83.

[4] Khalik W.F., Ho L.N., Ong S., Wong Y., Yusoff N., Ridwan F. Decolorization and Mineralization of Batik Wastewater Through Solar Photocatalytic Process. Sains Malaysiana. Vol. 44 (4), 2015, 607–612.

[5] Syuhadah N., Rohasliney H. A Preliminary Study on Batik Effluent in Kelantan State : A Water Quality Perspective. Int. Conf. on Chem., Bio. and Env. Sci. 2011. 2011. p. 274–276.

[6] Nuzul Z., Talib S.N., Lutfi W., Johari W. Water Quality of Effluent Treatment Systems from Local Batik Industries. 2nd Int. Conf. on Civil & Env. Eng. IOP Conf Series: Earth and Env. Sci, 476, 2020, 012097

[7] Syuhadah N, Muslim NZ, Rohasliney H. Determination of Heavy Metal Contamination from Batik Factory Effluents to the Surrounding Area. Int. J. of Chem., Env. & Biol. Sci., Vol.3 (1), 2015,7–9.

[8] Natalina, Firdaus H. Penurunan Kadar Kromium Heksavalen (Cr^{6+}) dalam Limbah Batik Menggunakan Limbah Udang (Kitosan). Teknik, Vol.38 (2), 2017, 99-102.

[9] Sungur F, Gülmez F. Determination of Metal Contents of Various Fibers Used in Textile Industry by MP-AES. J. of Spec. 2015, 1-5.

[10] Yoneda M., Mokhtar M. Environmental Risk Analysis for Asian-Oriented, Risk-Based Watershed Management. Springer Nature Singapore, 2018, 1-195.

[11] Dewi R.S., Kasiamdari R.S., Martani E., Purwestri Y.A. Efficiency of *Aspergillus* sp. 3 to Reduce Chromium, Sulfide, Ammonia, Phenol, and Fat from Batik Wastewater. IOP Conf. Earth and Env. Sci. 308, 2019, 012003.

[12] Putra R.S., Annisa A.D., Budiarjo S. Batik Wastewater Treatment Using Simultaneous Process of Electrocoagulation and Electro-Assisted Phytoremediation (EAPR). Ind. J. of Chem. Vo. 1680, 2019, 1–11.

[13] Harsini M., Suyanto, Gita Y.Y.Y., Rhodifasari L., Darmokoesomo H. Electrochemical Degradation of Naphthol AS-BO Batik Dyes. J. of Chem. Tech. and Metall. Vol. 52 (6), 2017, 1116–1122.

[14] Sutisna, Wibowo E., Rokhmat M., Rahman D.Y., Murniati R., Khairurrijal, and Abdullah M. Batik Wastewater Treatment Using TiO_2 Nanoparticles Coated on the Surface of Plastic Sheet. Procedia Eng, 170, 2017, 78–83.

[15] Portal Informasi Indonesia. Peta Negara Kesatuan Republik Indonesia. Available at: https://indonesia.go.id/archipelago [cited 2020 Jul 15].

[16] Badan Nasional Penanggulangan Bencana. Peta Sungai Utama di Wilayah G. Merapi | Geospasial – BNPB. Available at: http://geospasial.bnpb.go.id/2010/12/04/peta-sungai-utama-di-wilayah-g-merapi/ [cited 2020 Jul 15]

[17] Kementerian PUPR. Peta Rencana Tata Ruang. Available from: http://bpiw.pu.go.id/uploads/itmp/Arahan_Pengembangan_Kawasan_Pariwisata_DIY.pdf [cited 2020 Jul 15]

[18] R Core Team. R: A Language and Environment for Statistical Computing. R Foundation for Statistical Computing, Vienna, Austria. 2020. Available from: https://www.r-project.org/ [cited 2020 Aug 6]

[19] Korkmaz S., Goksuluk D., Zararsiz G. MVN: An R package for assessing multivariate normality. The R Journal, Vol. 6(2), 151–162.

[20] Kassambara A, Mundt F. Extract and Visualize the Results of Multivariate Data Analyses [R package factoextra version 1.0.7]. Comprehensive R Archive Network (CRAN); 2020. Available from: https://cran.r-project.org/package=factoextra [cited 2020 Aug 6]

[21] Mulyanto. Panduan Pendirian Usaha Kriya Batik. BEKRAF and UNS, 2016, 1–46.

[22] Suprihatin H. Kandungan Organik Limbah Cair Industri Batik Jetis Sidoarjo dan Alternatif Pengolahannya. PPLH Univ. Riau. 2014,130–138.

[23] Maria Z., Ioannis E., Nikolaos N., Eforia T. Synthesis, Characterization and Application of Anionic Metal Complex Azo Dyes As Potential Substitutes for Cr-Complex Dyes. Textile Res. J., Vol. 84(19), 2014, 2036–2044.

[24] Chakraborty JN. Metal Complex Dye. Handbook of Textile and Industrial Dyeing, Clarks M., ed. Woodhead Pub, 2011, 446–465.

[25] Yaseen DA, Scholz M. Textile Dye Wastewater Characteristics and Constituents of Synthetic Effluents: A Critical Review. Int. J. of Env. Sci. and Tech. Vol. 16, 2019, 1193–1226.

6th Int. Conf. on Structure, Engineering & Environment (SEE), Kyoto, Japan, Nov.18-20, 2020, ISBN: 978-4-909106056 C3051

CONSUMER REVIEW WEBSITE-BASED APPLICATION TO DETERMINE POPULARITY INDEX AND SPATIAL DISTRIBUTION OF RESTAURANTS IN BANDUNG

Dewi Susiloningtyas, Syarifah Salma A'idah, Febiana Nur Azizah, and Iqbal Putut Ash Shidiq
Department of Geography, Faculty of Mathematics and Natural Sciences, Universitas Indonesia, Indonesia

ABSTRACT

Consumer review website (CRW) is a web-based type of platform that provides information on one's perspective. In this case, the information provided is a review of a particular object. This information can be used as a spatial database because the object being assessed has spatial attributes in the form of geotagging. One form of CRW is the Zomato application, which provides information on ratings of various types of dining objects (cafes, fine dining, quick bites, stalls). This study utilizes attribute data available in the Zomato application to map the spatial distribution of the restaurant's popularity index in the city of Semarang. The popularity index is built based on the rating of consumers of a restaurant. This study utilizes the application program interface (API) owned by Zomato to get restaurant location data and rating attributes. The popularity index value is divided into three group classifications: high, medium, and low popularity. Using the Geographic Information System (GIS), each classification can be analyzed to see what factors are the differentiators of each restaurant classification. By using Nearest Neighbor Analysis (NNA) and Kernel Density Analysis (KDA), it is known that each classification has a different distribution pattern.

Keywords: CRW, Popularity index, Restaurant, Spatial distribution, NNA

INTRODUCTION

In this digital age, communication and information technology are increasingly advanced. With the growing popularity of the internet among the public, a review has become an essential source in determining the quality of a product that will end in the consumer's decision before purchasing certain goods [1]. The reviews obtained are no longer discussed by word of mouth (WoM) but through a very diverse social media (e-WoM). Consumers can regularly obtain product reviews from online sellers, product websites, blogs, and third-party review platforms where consumers can participate and engage in discussions about their consumption experiences [2]. This consumer review platform or consumer review website (CRW) is now widely used by consumers as their reference in choosing products are following the quality they desired. Nevertheless, for choosing the place to eat, many consumers rely on CRW to choose the restaurant or restaurant that they want to visit.

Bandung is a city with many exciting tourist attractions, including food and beverage tourism, or what is commonly referred to as culinary tourism [3]. With the number of places to eat (restaurants) in Bandung, many tourists are following the reviews from the CRW platforms to choose their place to eat. One of the websites or applications providing consumer reviews for a restaurant is Zomato. Zomato provides information about consumer's reviews on restaurants in the form of ratings and written reviews. Ranking (popularity index) is subjective and could be made based on the food, service, price, location, and environment of a particular restaurant [4]. This popularity index can be displayed or illustrated based on the ranking and distribution of restaurants in a region.

Human perspectives, such as reviews or thoughts, could have been influenced by the so-called 'spatial cognition' of a particular individual. It is a cognitive process of gathering and manipulating information about the nature of the spatial environment and utilizing them in the adaptive process of decision making [5],[6]. Therefore this study aims to determine and map the spatial distribution patterns of restaurants in Bandung based on their popularity index and to find out what factors that are influencing the distribution patterns.

METHODS

Most of the secondary data are gathered from Zomato (www.zomato.com). The information collected from the secondary data is the attributes of a particular restaurant, such as location (latitude and longitude), popularity index, type of restaurant, and types of food served by the restaurant. The geographic information system (GIS) analysis are being utilized to map and to describe the spatial distribution of restaurant based on their popularity index. A cross-tabulation and statistical analysis are

employed to explain which factor is affecting the most.

Study Area

The study is located in the city of Bandung. Bandung City is the capital of West Java Province, Indonesia, which has an area of 167.31 km^2 and divided into 30 sub-districts, covering 151 sub-districts (Figure 1). The city of Bandung has a population of 2,507,888 inhabitants in 2019. Bandung has many attractions that attract tourists to come to visits, such as nature and culinary tourism.

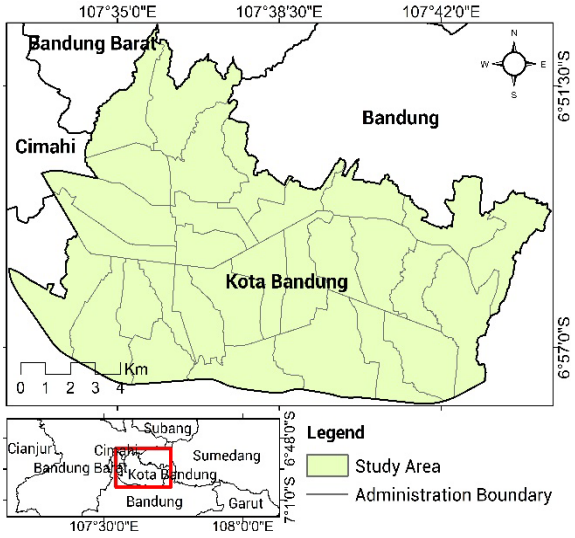

Fig. 1 Study area located in the city of Bandung.

Materials

Some materials used in this study were gathered from the secondary source. Those materials were essential to answer the research questions and to build the hypothesis prior to the conclusions. Those materials are related to the popularity index, accessibility, and urban functional units.

Popularity index

The popularity index was obtained from the Zomato website (www.zomato.com). Zomato uses index values ranging from one to five based on consumer reviews. The thing that also takes into account is the credibility of these consumers. Furtherly, the popularity index is being categorized into three classes (Table 1).

Accessibility

Accessibility is one of the factors that is suspected will affect the distribution of restaurants. Accessibility is representing the distance between the restaurant and the road networks. Furtherly, the road network data are being classified as arterial and collector roads (Figure 2). This data was obtained from Open Street Map (www.openstreetmap.org).

Table 1 Categories of restaurant's popularity index

Popularity index	Category
< 2.9	Low
3 – 3.9	Average
> 4	High

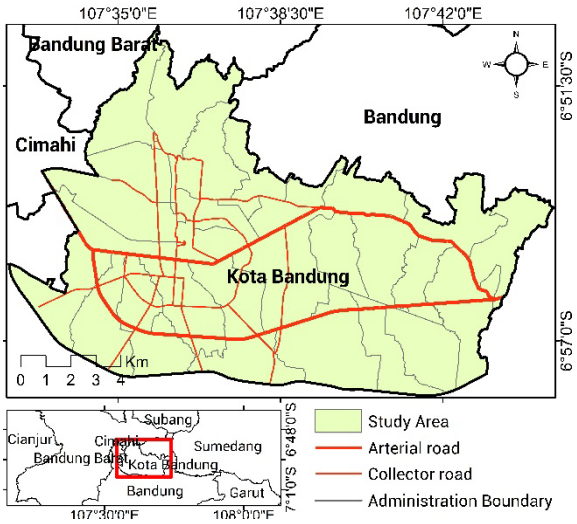

Fig. 2 The artery and collector road networks in the city of Bandung.

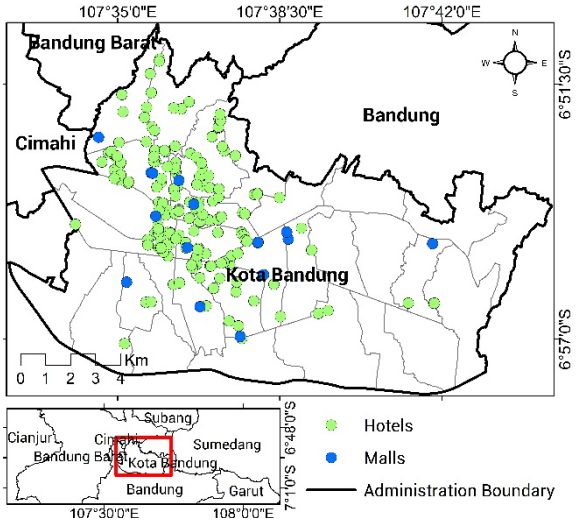

Fig. 3 Distribution of hotels and malls in the city of Bandung.

Urban functional unit

Urban functional units are the geographical units consisting of various interrelated elements in a city that are intended to provide space for people's lives,

production, recreation, and business activities, and provide a pleasant living environment and form an exchange platform [7]. Examples of this functional unit are malls, hotels, offices, hospitals, and banks. This study only limits the urban functionals unit to malls and hotels (Figure 3). Mall and hotel data are obtained from the Open Street Map. In addition, the central business district (CBD) can also influence the distribution of this restaurant. CBD data were obtained from Colliers International Indonesia - Research.

Land-use

Land use can affect the distribution of restaurant popularity related to the type of land use that is at the location of the restaurant. The type of land use used in this study is the type that has functions for settlement, business, social and culture, and tourism.

Data Processing and Data Analysis

Spatial distribution analysis

The analysis was performed using the Nearest Neighbor Analysis (NNA) and Kernel Density Analysis (KDA) methods. NNA is used to determine what distribution patterns are formed, for example, by grouping, spreading, or random. KDA is used to determine the density of existing restaurants per unit of a particular region. These NNA and KDA analyses are being performed using GIS software.

Distance analysis

The distance analysis that will be carried out in this study includes the employment of NEAR tools using GIS software. This analysis is to observe variations in the distance between restaurants and urban functional units (hotels, malls, and CBD). The distance between the restaurant and urban functional unit suspected to have an influence on the restaurant's popularity index. The NEAR tool from GIS software is being utilized to measure the distance. The cross-tabular analysis is used to measure the relationship between restaurant locations, accessibility, and urban functional units.

RESULTS AND DISCUSSIONS

Distribution of Restaurants in Bandung City

In total, there are 4078 restaurants across Bandung City. This study has collected 980 locations of restaurants, with all of them are having the popularity index in their attribute (Figure 4). Most of the restaurants are located in the center of Bandung City, from which large groups of average-popularity restaurants have occurred.

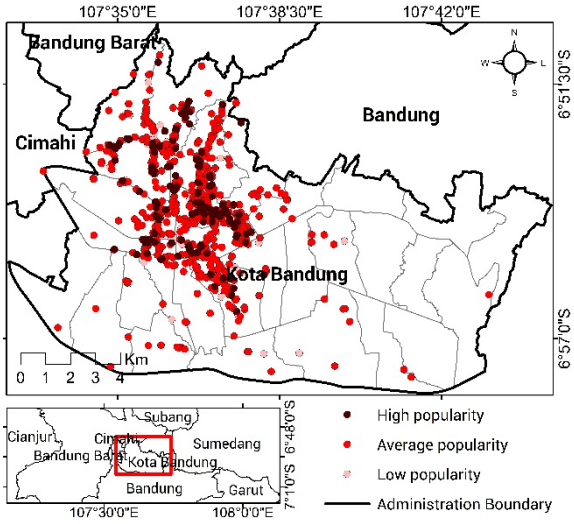

Fig. 4 Location of restaurants based on the popularity index.

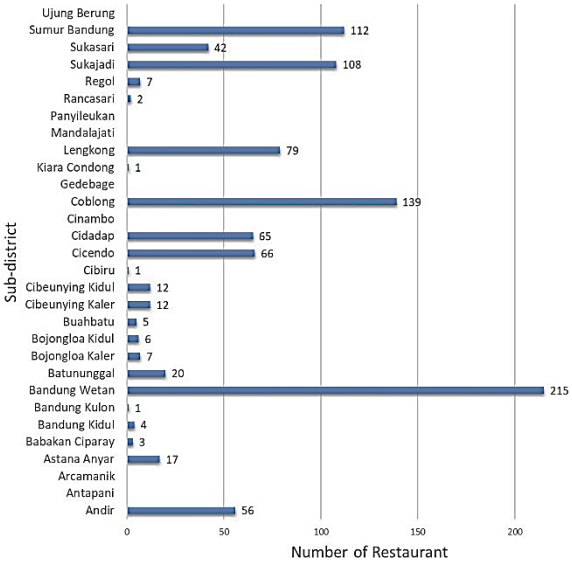

Fig. 5 Number of restaurants on each sub-district.

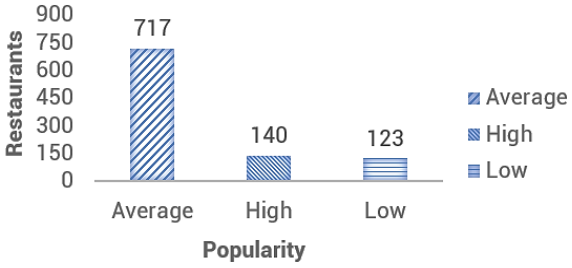

Fig. 6 Number of restaurants based on popularity level.

Figure 4 shows a clustered type of restaurant distribution, especially in the city center. Based on the data, Bandung Wetan is the sub-district with a significant number of indexed restaurants in Bandung City (Figure 5). According to several studies,

Bandung Wetan sub-district is one of the iconic places in Bandung with many clothing and crafting stores filled with creative workers and designers. The need to find a comfortable place for working and channeling their creative minds are becoming the factor behind the rapid growth of cafés and restaurants [8],[9]. Based on the popularity level, it is known that most of the restaurants are in average-popularity, in which the rating score ranges from 3 to 3.9 (Figure 6).

Restaurant's Popularity Distribution

High popularity restaurants

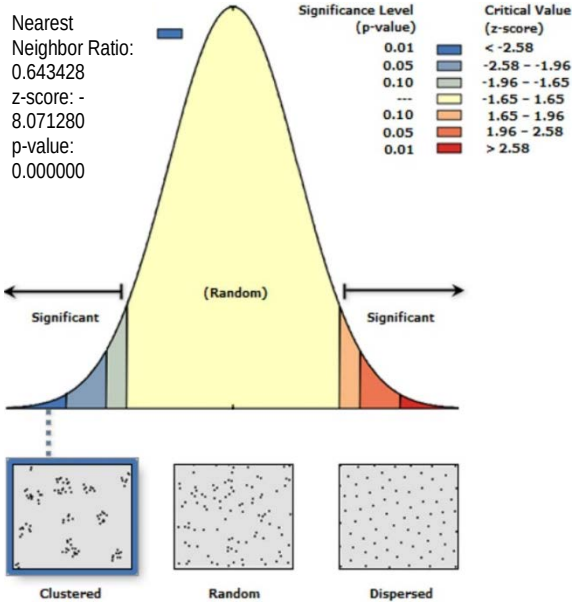

Given the z-score of -8.07128012599, there is a less than 1% likelihood that this clustered pattern could be the result of random chance

Fig. 7 NNA result for high-popularity restaurants in Bandung.

Restaurants with a high-popularity index have a clustering pattern around the center of Bandung. The NNA analysis proves it, which shows the z-score value of -8.0713. Based on the z-score, the distribution type of the high-popularity restaurants is clustered (Figure 7). The KDA analysis shows a similar result where the highest density of the high-popularity restaurants found in Bandung Wetan. Based on the KDA, the highest density shows that there are probably more than 78 high-popularity restaurants per km^2 (Figure 8).

Average popularity restaurants

Restaurants with an average-popularity index are also having a clustering pattern located in Bandung City Center. Restaurants with this category are most dominant among restaurants with low- and high-popularity. The NNA analysis proves it, which shows the z-score value of -27.9306. Based on the z-score, the type of distribution of the average-popularity restaurants is clustered (Figure 9). The KDA for average-popularity restaurant shows a slightly different result, where the highest density occurred in Sukajadi. The highest density class shows that there are probably more than 144 average-popularity restaurants per km^2 (Figure 10).

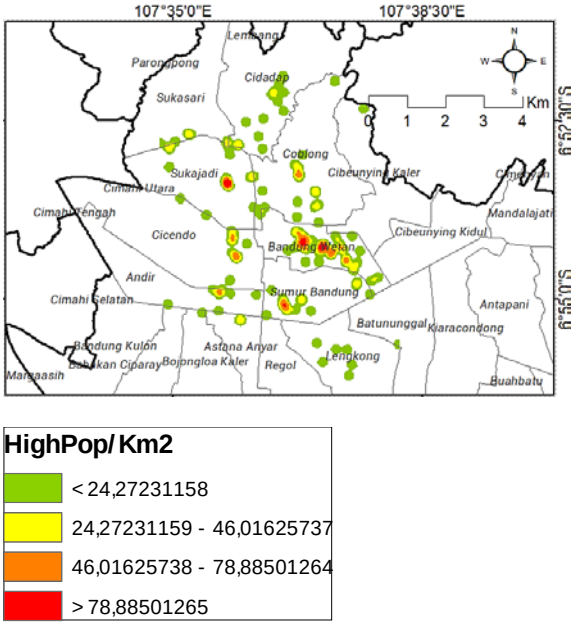

Fig. 8 KDA result for high-popularity restaurants in Bandung.

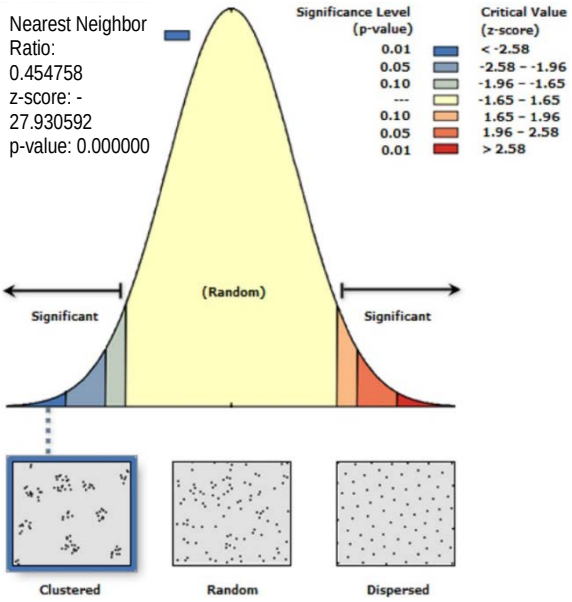

Given the z-score of -27.9305921725, there is a less than 1% likelihood that this clustered pattern could be the result of random chance

Fig. 9 NNA result for average-popularity restaurants in Bandung.

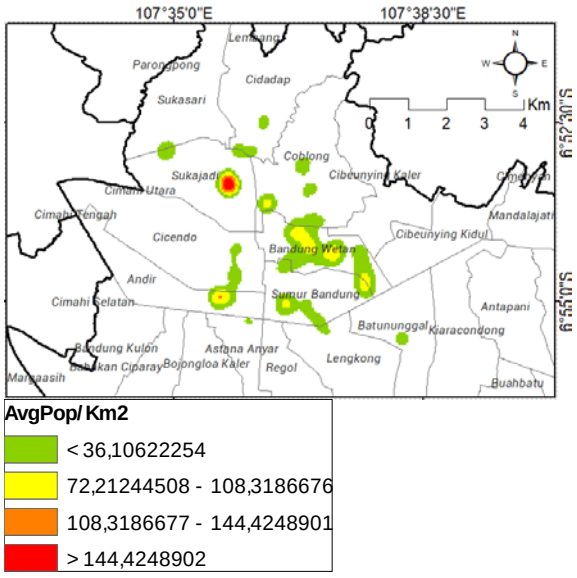

Fig. 10 KDA result for average-popularity restaurants in Bandung.

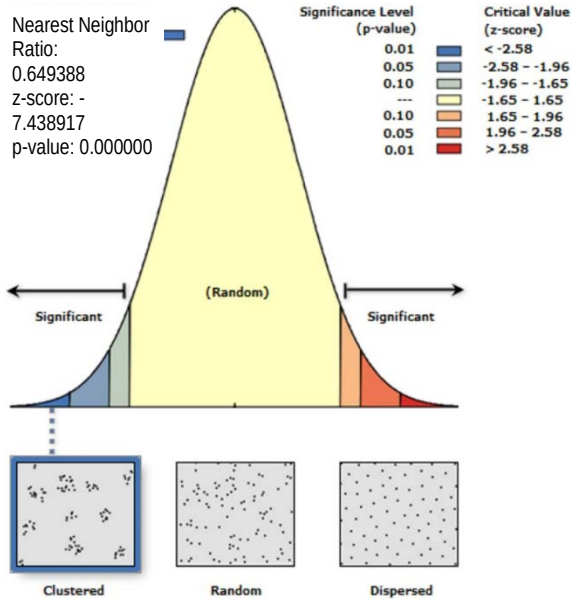

Given the z-score of -7.43891651252, there is a less than 1% likelihood that this clustered pattern could be the result of random chance

Fig. 11 NNA result for low-popularity restaurants in Bandung.

Low popularity restaurants

Restaurants with a low-popularity index also have a clustered pattern in the city of Bandung. This low index is dominant around the Bandung City Center. The z-score from NNA shows a value of -7.438917. Based on the z-score, the distribution type of low-popularity restaurants is clustered (Figure 11). The KDA for low-popularity restaurants shows a slightly different result, where the number of highest density clusters found in Sukajadi, Coblong, and Batununggal (Figure 12). Those areas are slightly far from the city center. The highest density class shows that there are probably more than 36 low-popularity restaurants per km^2 (Figure 12).

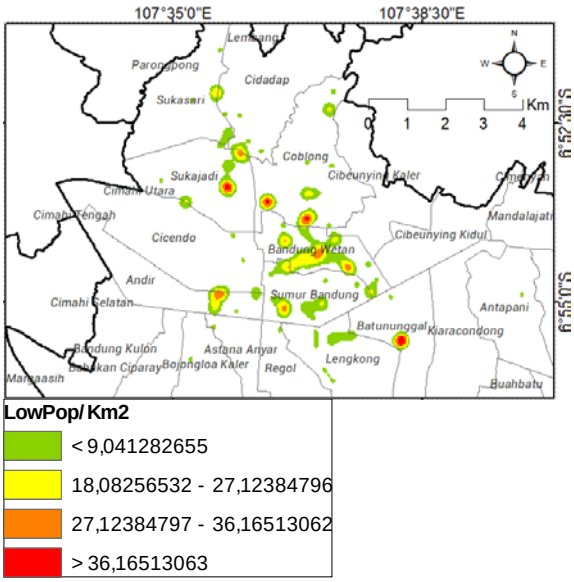

Fig. 12 KDA result for low-popularity restaurants in Bandung.

Distance Analysis

Distance could play a significant role when it comes to someone's preferences. The relative locations or the distance between the restaurant to other specific entities might influence people's perspectives on how they will rate the restaurant. Zhai et al. [10] suggested that the restaurants with high popularity were closed to urban functional units, whereas those with low popularity were at a faraway distance. It was supported by the study from Habib et al. [11], who suggested that a well-reputed restaurant will have less interest if far away. This study tries to examine whether the distance is related to the restaurant's popularity. A cross-tabulation is being employed to measure that condition. Table 2 shows the number of restaurants based on their distance to the road networks (arterial and collector roads).

Based on the table, the majority of low-popularity restaurants are closer to the collector road, which is around 109 restaurants with an average distance of 331 meters. In comparison, there 14 low-popularity restaurants closed to arterial roads, with an average distance of about 1979 meters. Restaurants with average-popularity are also closer to the collector roads (615 restaurants), with an average distance of 418 meters. The number of restaurants with average-popularity near arterial roads is 102, with an average distance of 2033 meters. Similarly, the majority of high-popularity restaurants are near the collector road (133 restaurants), with an average distance of 343

meters. The number of high-popularity restaurants near arterial roads is seven, with an average distance of 2201 meters. Conclusively, 87.4 percent of the total restaurants are closer to the collector roads.

Table 2 Number of restaurants based on the distance to the road networks

Popularity	Num. of nearest rest. to arterial road	Num. of nearest rest. to collector road	Mean distance rest. to arterial road	Mean distance rest. to collector road
Low	14	109	1979,15	331,19
Avg.	102	615	2033,22	418,25
High	7	133	2201,81	343,70

Table 3 shows the number of restaurants based on their distance to the urban functional units (malls and hotels). About 86 percent of the total restaurants are closer to the hotels than to the malls. The high-popularity restaurants are closer to the hotels, with a mean distance of 229 meters. In comparison, only 16 high-popularity restaurants near to the malls, with a mean distance of 953 meters. Restaurants with average-popularity are also closer to the hotels (619 restaurants), with an average distance of 278 meters. The number of restaurants with average-popularity near malls is 98, with an average distance of 1032 meters. Similarly, the majority of low-popularity restaurants are near the hotels (101 restaurants), with an average distance of 270 meters. The number of low-popularity restaurants near malls is 22, with an average distance of 946 meters.

Table 3 Number of restaurants based on the distance to the urban functional units

Popularity	Num. of nearest rest. to hotel	Num. of nearest rest. to mall	Mean distance rest. to hotel	Mean distance rest. to mall
Low	101	22	270,02	946,94
Avg.	619	98	278,91	1032,38
High	124	16	229,12	953,59

CONCLUSIONS

This study concludes that high, average, low popularity restaurants are clustering in Bandung. The densest cluster in high-, average-, and low- popularity groups has up to 78 restaurants/km^2, 144 restaurants/km^2, and 36 restaurants/km^2, respectively. The majority of the restaurants are closer to collector roads rather than arterial roads. The hotels are closer to most of the restaurants, especially the high-popularity restaurants, while only a few restaurants near the malls.

ACKNOWLEDGMENTS

This study is supported and funded by the Directorate Research and Community Services (DPRM), University of Indonesia under the Publikasi Terindeks International (PUTI) 2020 research grant. The authors also express their greatest gratitude and the highest appreciation to Department of Geography, Faculty of Mathematics and Natural Science, University of Indonesia which has facilitated the research activities.

REFERENCES

[1] Zhu, F., and Zhang, X., Impact of online consumer reviews on sales: The moderating role of product and consumer characteristics. Journal of Marketing, Vol. 74, Issue 2, 2010, pp. 133-148.

[2] Kim, S. J., Maslowska, E., and Malthouse, E. C., Understanding the effects of different review features on purchase probability. Int. J. Advert., Vol. 37, Issue 1, 2018, pp. 29-53.

[3] Komaladewi, R., Mulyana, A., and Jatnika, D., The Representation of Culinary Experience as the Future of Indonesian Tourism Cases in Bandung City, West Java. International Journal of Business and Economic Affairs, Vol. 2, Issue 5, 2017, pp. 268-275.

[4] Zhang, Z., Zhang, Z., and Law, R., Positive and negative word of mouth about restaurants: Exploring the asymmetric impact of the performance of attributes. Asia Pacific Journal of Tourism Research, Vol. 19, Issue 2, 2014, pp. 162-180.

[5] Lloyd, R., Cognitive maps: Encoding and decoding information. Annals of the Association of American Geographers, Vol. 79, Issue 1, 1989, pp. 101-124.

[6] Lloyd, R., Spatial cognition: Geographic environments (Vol. 39), Springer Science & Business Media, 1997, pp. 1-264.

[7] Hu, Y., and Han, Y., Identification of Urban Functional Areas Based on POI Data: A Case Study of the Guangzhou Economic and Technological Development Zone, Sustainability, Vol. 11, Issue 5, 2019, pp. 1-15.

[8] Anugrah, I. W., and Suhaeni, T., Pengaruh Kepemimpinan Stratejik Terhadap Strategi Bersaing UKM Café dan Restoran. Jurnal Riset Bisnis dan Investasi, Vol. 3, Issue 3, 2017, pp. 78-88.

[9] Siswanto, M. R., and Choandi, M., Ruang Pertukaran Ide di Bandung Wetan. Jurnal Sains, Teknologi, Urban, Perancangan, Arsitektur

(Stupa), Vol. 2, Issue 1, 2020, pp. 707-718.
[10] Zhai, S., Xu, X., Yang, L., Zhou, M., Zhang, L., and Qiu, B., Mapping the Popularity of Urban Restaurants Using Social Media Data. Applied Geography, Vol. 63, 2015, pp. 113-120.
[11] Habib, M. A., Rakib, M. A., and Hasan, M. A., Location, Time, and Preference Aware Restaurant Recommendation Method. In 2016 19th International Conference on Computer and Information Technology (ICCIT), 2016, pp. 315-320.

Last page, both columns must be same height from top or bottom. Please do not change format of this template

6th Int. Conf. on Structure, Engineering & Environment (SEE), Kyoto, Japan, Nov.18-20, 2020, ISBN: 978-4-909106056 C3051

COMPARATIVE STUDY ON KOREA AND JAPAN URBAN PARKS CONCERNING THE DEVELOPMENT POLITICS AND THE TRANSITION OF SYSTEM

Shinya Tsukada[1], Sangbok Yoon[2], Yeongha Kim[3], Tetsuo Morita[4] and Hiroshi Sugita[5]
[1]Maebashi City Office, [2]Dong-eui University, [3] Dong-A University, [4]Mebashi Institute of Technology, [5]The Institute of Behavioral Sciences

ABSTRACT

Urban parks are open space with trees that provides a place of relaxation and peace for residence. Urban parks have been rapidly constructed in Korea since the Seoul Olympics (1988). On the other hand, In Japan the supply of urban parks is sufficient, and the maintenance and utilization of park that have been stocked during the period of high growth has become a problem. We thought it necessary to compare the parks of Korea and Japan during the period when the environment changed significantly after the Seoul Olympics. This purpose of study is to clarify the characteristics of Korea and Japan parks by comparing them. As a result of this study, the following features were clarified. In the transition of urban park politics, we found that there are similarities in responding to issues such as "diversifying needs", "park master plan", and "private entry". In both Korea and Japan, the important direction of future park policy is considered to be “use and maintenance”.

Keywords: Urban Park, Comparison, Development Politics, Korea and Japan

INTRODUCTION

Both Korea and Japan, which are adjacent to each other, have developed while experiencing the period of high growth after World War II. However, in the future, both countries will continue to experience a declining birthrate and aging population, and due to this effect, the population will decline not only in rural areas but also in urban areas, making economic growth again difficult.

National policies in the future will require international efforts to address environmental issues such as biodiversity and disaster prevention efforts such as large-scale earthquakes. As a solution to these policy issues, it is also meaningful to focus on the park policy, which is a green base, and proceed with the study.

In this paper, based on the future changes in the social situation in Korea and Japan, such as the declining birthrate and aging population, we surveyed the park system in Korea and Japan and the actual usage situation.

By conducting a survey, we examined the direction of the park system and the points to keep in mind when formulating a plan in anticipation of future national trends.

OVERVIEW OF THE STUDY

In this section we summarize the overview of existing research and describes the focus our study.

Lee [1] 's study compared the awareness of green in Korea and Japan. They conducted a questionnaire survey on the awareness of greenery to the residents of Daegu City. According the survey, as a ward associated with green, Daegu citizens associate it with "green(color) and blue(color)" and Sapporo citizens associate it with "park". As a ward associated with park, Daegu citizens associate it with " a place of rest" and Sapporo citizens it with "Child".

Song [2] summarized the history of the development of the park system in Korea and Japan by examining matters related to urban parks in Korea and Japan from 1870 to 1980.

Kang [3] conducted a survey focusing on the relationship between the development of shrines and urban parks under the Japanese rule.

Song et al. [4] compared the flow of major policies concerning urban parks in Korea and Japan since the 1970s.

Kim et al. [5] grasped the actual conditions of the urban park in Ilsan New City and investigated how park users evaluated this urban park. In addition, as a result of a questionnaire survey on future maintenance intentions, it was understood that urban parks utilizing natural forests were desired for future development. By the survey of Kim et al. [6] about the future intentions for urban park development, residents said that they wanted the urban parks with natural forest.

Kin et al. [6] conducted a spatial evaluation of park users in Ilsan New City. As a result of the evaluation, it was clarified that the neighboring parks established by the urban development are used for light sports and nature walks, and the green area ratio of the city is high.

Table 1 Review of urban park politics

A.C.	Korea	Japan
1986	Han-gang Waterfront Site Park Project	Fourth Five-Year Plan for Urban Park
1991		Fifth Five-Year Plan for Urban Park
1993	Revision of Urban Park Law Addition of Physical Education Park	Revision of Urban Park Law Increase in Park Area Level and Change the Type Name
1994	Busan Amenity Plan	Green Master Plan (Formulation: City)
1995		Civic Green Space System
1998		Sixth Five-Year Plan for Urban Parks Green Plan 2000
1999		Expansion of Green Areas
2000	Revision of Urban Park Law (Park MP, Purchase Request System)	Social Capital Development Priority Plan
2003	Established Seoul Green Trust Third Sector Introduction System for Urban Park Maintenance and Creation Projects	Abolition of Attraction Distance Standard for Parks and Establishment of Designated Manager System
2004	Five-Year Plan for National Balanced Development (2004-2008)	Landscape Law Creation of Multi-Dimensional Urban Park System
2005	Urban parks and Open space Law (Park and Open Space Basic Plan System)	
2007	Landscape law	
2009	Private park exception system Imagination Children Park Project (2008-2011)	
2012	Urban Renewal Law	Plan to Extend Life of Park Facilities
2014	Revision of the Landscape Act (Mandatory Landscape Planning) Five-Year Plan for Regional Balanced Development Abolition Guidelines of Long-Term Unexecuted City Planning Facility	
2015	Arboretum ▪ Garden Creation and Promotion Methods Founding of National Garden ▪ Regional Transfer ▪ Private Garden ▪ Community Garden	
2016	Revision of Urban parks and Open space Law Development Exception Business of Private Park Guideline	Development of Open Space for New age
2017		Revision of Urban Park Law Park-PFI Established Legalization of Maintenance and Repair Standards
2018		Planning Guidelines to Extend Life of Park Facility

Sugawara and colleagues [7] clarified the development and characteristics of the civil movements in Korea.

Kim et al. [8] analyzed the causal relationship by conducting a questionnaire survey on residents in order to clarify the influence of the green areas on the slopes of the urban edge on the choice of residential area in Busan City.

Nakanishi et al. [9] investigated the relationship between land use systems in Korea, Japan, and Taiwan.

Nakanishi et al. [10] analyzed the relationship between the city planning master plans of Japan and Korea.

SUTUDY AREA AND STUDY METHODS

As mentioned above, there are many studies that compared Korea and Japan regarding urban parks and greenery. However, few studies have compared Korea and Japan on urban parks and greenery since the Seoul Olympics (1988).

This study clarified the similarities and differences by clarifying the changes in the politics of urban parks in Korea and Japan from the time of Seoul Olympics to the present day. Moreover, the characteristics of urban park were clarified by grasping the amount of improvement for each type of urban park.

The research method was mainly based on the existing literature survey. In addition, based on the results of the survey, basic consideration was given to future issues regarding urban parks.

COMPARATIVE STUDY ON KOREA AND JAPANESE URBAN PARK SYSTEM

Review of Urban Park Politics

Table 1 summarizes the changes in policies regarding urban parks since the Seoul Olympics (1988).

In Korea, a part of the Urban Park Law was revised in 1993, when the Seoul Olympic Games were held, and "Physical Education Park" was added as one of the parks. In 2000, Urban Park Law was completely revised. In 1986, "The plan of Han-gang Waterfront Site Park Project" was formulated.

This plan is also linked to the Han River Renaissance in 2003 based on the "Enactment of the National Land Planning Act of 2000 with the basic principle of nature restoration" in order to improve the natural environment of the Han River waterfront. Based on this plan, the development of the World Cup Park and Urban Park by converting land use of Seoul Forest was promoted.

In 2012, Urban Park Law was revised against the backdrop of decentralization, and Park Master Plan has been created by the city government. In 2015, the Law for the Creation and Promotion of Arboretum and Gardens was enacted to promote the conservation and utilization of valuable gardens.

On the other hand, in Korea, a non-service Urban Park Plan was an issue. To solve this, in 2014 Guideline of a long-term Unexecuted Urban Planning Facility Cancellation was created. In 2016, the “Private Park Development Guidelines” were established to promote the participation of the vitality of the private sector in urban parks.

In 1986, the 4th Five-Year Plan for Urban Park was formulated in 1986. In addition, in 1991, the 5th Five-Year Plan for Urban Park was formulated in Japan.

Table 2 The present situation of urban parks in Korea (2020)

Type	Subdivision	Location	Area [ha]
Urban park	Children's Park	10,627	2,591
	Neighborhood park	5,168	6,181
	Cemetery park	57	2,950
	Urban natural park	65	13,524
	Subtotal	15,917	25,246
Green Space		22,070	22,176
Amusement Park		244	15,509
Physical Education Park		319	2,719
Total (12.7m^2 per person)		38,550	65,650

Table 3 The present situation of urban parks in Japan (2019)

Type	Subdivision	Location	Area [ha]
Urban park in housing area	Block Park	88,052	14,198
	Neighborhood Park	5,792	10,430
	District park	1,619	8,589
	Country Park	(180)	(1,400)
	Subtotal	95,643	34,617
Urban park in city area	General park	1,375	26,099
	Sports park	834	12,978
	Subtotal	2,209	39,077
Urban park in wide area	Wide area Park	215	14,906
	Urban Recreation	6	564
	Subtotal	221	15,470
Urban park in Nationally		17	4,251
Urban park of Green space	Unique Urban Park	1,360	13,713
	Buffer Green Space	240	1,814
	Urban Green Space	8,939	16,259
	Urban Forest	156	932
	Open Space Urban Park	348	163
	Green Road	968	923
	Subtotal	12,011	33,804
Contracted Citizen's Green Space		7	3
Contracted Citizen's Green Space		169	100
Total (10.6m^2 per person)		110,277	127,321

Fig. 1 Green Space in Korea

Fig. 2 Physical Education Park in Korea

Fig. 3 Brock Park in Japan (1)

Fig. 4 Brock Park in Japan (2)

An added issue that was not included in the conventional plan was "meeting diverse needs." In 1993, "Children's Park" was renamed "Block Park".

This reason is that, based on the progress of an aging society, the idea has changed from a uniform park for child to a park with diverse needs. In 1994, against the backdrop of decentralization, by the establishment of Green Master Plan, open spaces and parks were integrated. Also, in 2000, the conventional Five-Year Plan for Urban Parks, etc. was integrated into the Social Capital Development Priority Plan.

Designated Manager System was established in 2003 by amending the Local Autonomy Law against the backdrop of increasing stock and deregulation.

Designated Manager System was also introduced in urban parks, and in 2017, Park-PFI system was created to promote the participation of the vitality of the private sector. On the other hand, the deterioration and renewal of urban park became serious, Park Facility Extension of Life Plan Development Guideline was created in 2018.

The similarities and differences between the urban park policies in Japan and Korea are as follows.

First, regarding the similarities, the type of urban park was changed.

Korea has added the type of Physical Education Park in 1993 after the Seoul Olympics, Japan has changed the children's park to a block park in 1993, and These changes addressed "diversified needs".

The next similarity is the creation of the "Green Master Plan and Landscape Initiatives" created by the city due to the progress of decentralization. Korea enacted Park Master Plan in 2011 and the Landscape Law in 2007, Japan enacted Establishment of Green Master Plan in 1994 and the Landscape Law in 2004.

Third is the entry of private vitality into urban park. Japan introduced Designated Manager System in 2003 and Park-PFI in 2017, and Korea amended the Law Concerning Urban Parks and Green Spaces and prepared the “Private Creation Guidelines” in 2016.

Next is the difference between Korea and Japan. In Korea, with the enactment of the "National Planning Law" in 2003, the tendency to return to nature increased. "World Cup parks that turn garbage collection into parks" and "Seoul forests that turn racetracks and golf courses into parks" are being actively converted into land alongside rivers.

In Japan, the increase in stock and the deterioration of existing facilities are becoming more

serious. Proper maintenance and management of stock has become an important issue, such as notification for the safety of playground equipment in 2002 and showing the basic concept of extending Plan to Extend Life of Park Facilities in 2012.

The Present Situation of Urban Park

Table 2 shows the current status of urban park development in Korea in 2020 (Statistics Agency). The total number of urban parks in Korea is 33,260 locations, 42,995 ha (park area per person is 12.7 m2 / person, 1.29 ha / location). Focusing on the type of park, Green Space have the largest number and area (22,070 locations, 22,176 ha (1.00 ha / location)).

Table 3 shows the current status of urban park development in Japan in 2019 (surveyed by the Ministry of Land). The total number of urban parks in Japan is 110,277 locations and 127,321 ha. Park area per person is 10.6 m2 / person, 1.15 ha / location.

Focusing on the type of park, Block parks have the largest number (88,052 (0.16 ha / location)) and general parks have the largest area (26,099ha (18.9ha / location)).

In Japan, green spaces are included in urban parks, whereas in Korea, green spaces are excluded from urban parks, but in this study, green spaces are included in urban parks [11].

Comparing Korea and Japan, Korea has a total park area of 65,650 ha, urban park area in Japan was 1.9 times larger than that in Korea. On the other hand, the area of parks per person in Korea is 12.7m2 / person, whereas the area of parks per person in Japan is 10.6m2, urban park area of one person in Korea was 1.2 times that of one in Japan.

In addition, the park area per location is 1.29 ha in Korea and 1.15 hectares in Japan, and the park area per location in Korea is 1.1 times that of Japan.

In Korea, construction of skyscrapers for housing has been promoted as a city regeneration project since the Seoul Olympics [12]. As a result, green spaces are increasing at the same time as housing supply [12].

Green Space (Fig.1) is a park like a Green Road in Japan. Green Space and Physical Education Park (Fig.2) have functions that can be used on foot like a block park (Fig.3 and Fig.4) in Japan. As a result of comparing the Korean Physical Education Parks with the Japanese Block Parks, we found that the Japanese Block Parks were used by children, otherwise the Korean Physical Education Parks were used by the elderly.

CONCLUSIONS

In this study, the following was clarified by grasping the changes in urban park policies and the amount of urban park development since the Seoul Olympics in Korea and Japan.

In the transition of urban park policies since the Seoul Olympics, we grasped the similarities corresponding to the issues of " diversifying needs ", "Park Master Plan", and " Private Entry ".

In addition, it has become clear that in Japan, a plan for maintenance and renewal of parks has been formulated in consideration of the increase in stock and renewal of facilities, on the other hand, that in Korea, park maintenance is being promoted by land use conversion.

Furthermore, Japan has approximately 1.9 times the total area of urban parks, etc. as compared with Korea, while Korea has 1.2 times the park area per person and 1.1 per location as compared to Japan.

We were able to understand the actual conditions of development in Korea and Japan and the background of park policy. Both Korea and Japan are facing a population decline and an aging population.

Therefore, how to maintain and update the current stock satisfactorily becomes an issue.

For this reason, Korea is promoting the natural return to parks, but considering that Japan is having difficulty in the maintenance plan for renewal, we think that the maintenance renewal plan should be formulated at this point.

REFERENCES

[1] Lee Y. D., Asakawa S. and Park C. Y., A Comparative Study on Consciousness of Greenery between Inhabitants of Daegu and Sapporo, Japanese Institute Landscape Architecture, Vol. 52, No. 4, 1989, pp. 255-262.

[2] Song T. and Shirai H., A Comparative Study on Japanese and Korean Urban Parks Concerning of Policies since 70's, Japanese Institute Landscape Architecture Vol.55., No. 5, 1992, pp. 13-18.

[3] Kang S., Urban Parks and Prosperity of Japanese Zinza Shrines in Korea, Japanese Institute Landscape Architecture, Vol. 56, No. 5, 1993, pp. 61-66.

[4] Song T. and Hikoe S., A Comparative Study on Japanese and Korean Urban Parks Concerning of Policies since 70's, Japanese Institute Landscape Architecture, Vol. 56, No. 5, 1993, pp. 85-90.

[5] Kim Y. and Sawaki M., The Greenery Park Evaluation Study from View of Inhabitant in case of IIsan New town in Korea, Japanese Institute Landscape Architecture, Vol. 63, No. 5, 2000, pp. 657-662.

[6] Kim Y. and Sawaki M., Spatial Evaluation by Users of Park in Case of Ilsan New Town in Korea, Japanese Institute Landscape Architecture, Vol. 64, No. 5, 2001, pp. 641-646.

[7] Sugawara A., Yoshimura T. and Watanabe S., A

Study on Characteristics and Tasks of Korean Machi-Zukuri, "Maulmandulgi": A Case of Pusan, Korea, Journal of City Planning Institute of Japan, Vol. 38, No. 3, pp. 883-888.

[8] Kim Y., Kaneko T. and Kumagai Y., A Study on the Relation between Slope Green and the Residence Choice in Busan City, Japanese Institute Landscape Architecture Vol.72, No.5, 2009, pp. 859-862.

[9] Fujioka M., Nakanishi M. and Suzuki N., A Comparative Study on Local Implementation of Historic Urban Conservation System in Japan, South Korea and Taiwan, Journal of City Planning Institute of Japan, Vol. 54, No. 3, 2019, pp. 998-1005.

[10] Nakanishi M. and Fujioka M., A Comparative Study on Urban Planning Master Plan in Japan, South Korea and Taiwan, Journal of City Planning Institute of Japan, Vol. 54, No. 3, 2019, pp. 1438-1445.

[11] Park. K. W. and Sakai M., A comparative study was carried out on the development policies of urban parks in japan and Korea, Kyushu University Institutional Repository, Vol. 75, 1996, pp. 27-47.

[12] Li Huien, Changes in urban landscape in Seoul, Korea, Historical Geography, 50-1(237), 2008, pp. 19-33.

6th Int. Conf. on Structure, Engineering & Environment (SEE), Kyoto, Japan, Nov.18-20, 2020, ISBN: 978-4-909106056 C3051

THERMAL ENERGY EVALUATION OF THE INCINERATOR WASTE

Kantayut Trebooniti
Faculty of Industrial Education Rajamangala University of Technology Suvarnabhumi, Thailand

ABSTRACT

This paper evaluates the thermal energy from the incinerator waste. The incinerator system composed of 6 sections: the first section is a waste hopper and feeder, the second section is the rotary kiln primary, the third section is a secondary chamber, the fourth section is the ash cooling conveyer, the fifth section is cyclone and the sixth section is stack. The stack section was interested to consider. The waste and diesel oils were 200 kilograms and 200 liters, respectively. The experimental results presented the temperature ranges on the stack surface by about 180 - 300 C corresponds to thermal energy from the stack, and it appropriated for engineering processes.

Keywords: Incinerator, stack, thermal energy, waste

INTRODUCTION

The rising cost of energy is serious widely in the world and also global warming is one problem from fossil fuels. The alternative energy is interested in developing the energy system to increase efficiency and to reduce emissions. There is alternative energy for different systems such as solar energy, wind energy, etc. Guo et al., 2010 presented the energy and exergy analysis of the power generation system which consists of an economizer, an evaporator, a superheater, a steam turbine, a condenser, and a pump.

San, 2010 performed a second law analysis to determine the efficiency of heat exchanger for waste heat recovery.

Butcher and Reddy, 2007 presented the temperature profiles across the heat recovery steam generator, network output, second law efficiency, and entropy generation that are simulated for various operating conditions.

The waste heat from the combustion is urgent to recover for any system. Shaaban, 2007 presented the management of medical waste at hospitals in Egypt. The medical waste estimated about 75 tons/day from the governmental hospitals in Cairo. The data showed the most appropriate incinerator capacity is 150 kg/h. Bujak, 2009 reported the energy efficiency of the incinerator for medical waste. The experimental result showed the 100 kg of medical waste could be converted to the usable energy by about

600-800 kW, and the energy efficiency is in the range of

47-62%. Ulu et al., 2006 studied the energy and exergy analyses of a raw mill in the cement production. The first and second laws efficiencies are 84.3% and 25.2%, respectively. The heat losses are composed of conduction, convection, and radiation from the surface by about 14300 MJ/h. The potential of energy saving is estimated by about 14300 MJ/h, which is the energy recovery of 15.7% of energy input in the raw mill. The waste heat recovery from the exhaust gas at the top of the chimney had studied by S. Erel, 2009, the thermoelectric converter was installed on the top of the chimney.

The results were showed that electrical energy can be obtained by means thermoelectric converter unit thrown from chimneys in the form of heat energy. The graphical showed the electrical power increasing with temperature difference (hot and cold sides).

This paper presents the thermal energy from incinerator waste focused on the heat loss from the stack surface.

THERMODYNAMICS ANALYSIS

The incinerator waste consists of main equipment as follows: the first section is a waste hopper and feeder, the second section is the rotary kiln primary, the third section is a secondary chamber, the fourth section is the ash cooling conveyer, the fifth section is cyclone and the sixth section is stack. First and second laws of Thermodynamics are considered the system. For the case of steady-state steady flow, the balance equations are applied to evaluate the energy of the equipment. The mass balance equation (Utlu et al., 2006) expressed in the form of the rate as

$$\sum \dot{m}_{in} = \sum \dot{m}_{out} \quad (1)$$

Wherever = mass flow rate at the inlet and is mass flow rate at the outlet.

The general energy balance (Utlu et al., 2006) can be expressed as

$$\sum \dot{E}_{in} = \sum \dot{E}_{out} \quad (2)$$

Or

$$\dot{Q} + \sum \dot{m}_{in} h_{in} = \dot{W} + \sum \dot{m}_{out} h_{out} \quad (3)$$

Where is the rate of net energy transfer in, is the rate of energy transfer out by heat and h is the specific enthalpy.

The first law efficiency (Utlu et al., 2006) expressed as

$$\eta = \frac{\dot{E}_{output}}{\dot{E}_{input}} \quad (4)$$

Where η is an energy efficiency, $\dot{E}_{useful}$ is an energy useful and $\dot{E}_{input}$ is an energy input

Fig. 1 Incinerator waste

INCINERATOR AND WASTE

The incinerator waste was installed at Suphan Buri Province (Fig. 1). The capacity of the incinerator is 300 kg. The incinerator system composed of 6 sections: the first section is a waste hopper and feeder, the second section is the rotary kiln primary, the third section is a secondary chamber, the fourth section is the ash cooling conveyer, the fifth section is cyclone and the sixth section is stack. The waste is medical waste; it composed of cotton and gauze 45%, paper 8%, syringe 15%, glove 25% and other 7%. The high heating value (HHV) and the average density of the medical waste are 12,327 kJ/kg and 280 kg/m3, respectively.

Table 1 Mass of the system

Item	Input material	T_i (K)	m (Kg/h)	Output material	T_o (K)	m (Kg/h)
1	Waste	303	70	Ash	370	10
2	Air	309	750	Dust	390	60
3	Fuel	310	55	Flue	550	805
	Total		875	Total		875

EXPERIMENTAL MEASUREMENT

This experiment was carried out in the summer season in the Suphan Buri province. Thermocouples type K (range: 0-1250 ℃, accuracy ± 0.5 ℃) were installed for measuring the temperature at different positions as shown in Fig. 2. The thermocouples were connected to a data logger (Hioki, Model: 8422-52, accuracy ± 0.8%).

The infrared thermometer (UT 301A) was measured the surface temperature of the stack, combustion chambers and the kiln. The inlet air temperatures intake the combustion chambers were measured using the velocity probe (TSI Model 8380, range 0-50 m/s, error ± 0.5%).

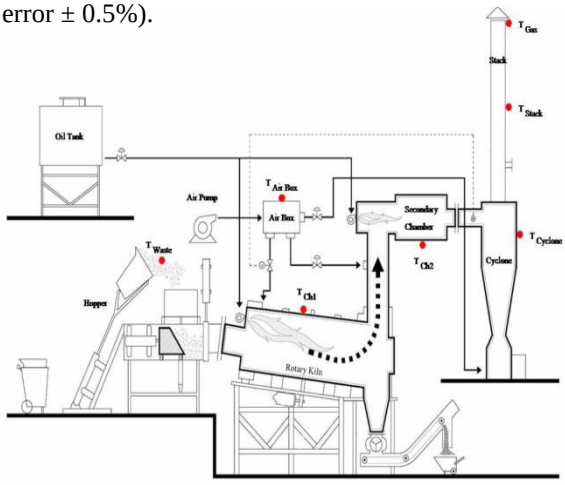

Fig. 2 Schematic of incinerator and measuring positions

RESULT AND DISCUSSION

The mass balance of the system is presented on the law of mass conservation as follows:

$$\sum \dot{m}_{in} = \dot{m}_{waste} + \dot{m}_{f,1} + \dot{m}_{a,1} + \dot{m}_{f,2} + \dot{m}_{a,2} \quad (5)$$

$$\sum \dot{m}_{out} = \dot{m}_{ash} + \dot{m}_{fl} + \dot{m}_{dust} \quad (6)$$

The input and output materials are presented in table 1.

The energy balance of the system, which is arranged according to the energy components given in Table 2. The energy balance in the system is presented on the law of energy conservation as follows:

$$[\dot{m}_{waste}(HHV) + \dot{m}_{f}(HHV) + \dot{m}_{a} c_{p,a} T_{a}] = \dot{Q}_{loss} +$$

$$[\dot{m}_{ash} c_{p,ash} T_{ash} + \dot{m}_{g} c_{p,g} T_{g} + \dot{m}_{dust} c_{p,dust} T_{dust}] (7)$$

Heat losses in the system are composed of three modes of heat transfer. Heat losses with the convection are between outside air temperatures and surface temperatures. The heat losses with the conduction are due to the temperature differences of the outer and inner surfaces. Heat losses with the radiation occurred from the outer surface and ambient air. The total heat losses could be calculated (Utlu et al., 2006) as follows:

$$\dot{Q}_{total} = \dot{Q}_{conv} + \dot{Q}_{cond} + \dot{Q}_{rad} \quad (8)$$

The convection around the surface of the rotary kiln primary, secondary chamber and stack was calculated from

$$\dot{Q}_{conv} = \pi D_{o} hl(T_{sf,out} - T_{a}) \quad (9)$$

The conduction through the cylinder calculated from

$$\dot{Q}_{cond} = \frac{(T_{sf,in} - T_{sf,out})}{\frac{\ln(r_{o} / r_{i})}{2\pi kl}} \quad (10)$$

The radiation from the surface to the ambient air calculated from

$$\dot{Q}_{rad} = \pi D_{o} \varepsilon\sigma(T_{sf,out}^{4} - T_{a}^{4}) \quad (11)$$

The energy efficiency of the system is calculated from Eq. 4, using energy analysis values from table 2, as follows: (or 79.6%)

Due to this experiment, the energy output is heat losses from the surface system and energy input is total materials (waste, oil, and air).

Table 2 Energy balance of the system (Input)

Item	Input material	Cp(kJ/kh)/ HHV(kJ/kg)	T (K)	m (kg/h)	Q (K)
1	Waste	12,327	303	70	862,890
2	Air	1.005	309	750	232,908.75
3	Fuel	43,767.7	310	55	2,407,223.5
	Total			875	3,503,032.25

Table 3 Energy balance of the system (Output)

Item	Output material	Cp(kJ/kh)/ HHV(MJ/kg)	T (K)	m (kg/h)	Q (K)
1	Ash	0.75	370	10	2,775
2	Dust gas	1.05	390	60	24,570
3	Flue gas	1.55	550	805	686,262.5
	Heat losses from surface				2,789,424.75
	Total			875	3,503,032.25

CONCLUSION

This study aims to evaluate the thermal energy utilization for the engineering process. Mass and energy balances were analyzed using the incinerator process. The thermal efficiency was defined by energy losses from the surface to divide energy input. The medical waste was used to combustion and analyzed the thermal energy.

The result showed high thermal efficiency and suitable for use in the waste heat process and application engineering process.

ACKNOWLEDGMENT

The results of this experiment can be accomplished with great help from the consultation of the Faculty of Mechanical Engineering. Thank you to Research and Development Institute. Rajamangala University of Technology Suvarnabhumi, the budget for the research and the Faculty of Mechanical Engineering, Faculty of Industrial Education Suphan Buri Center Providing facilities, tools, and support. The researcher highly appreciates.

REFERENCES

[1] J. Guo, M. Xu and L. Cheng, Thermodynamic analysis of waste heat power generation system. Energy 2010, 35; 2824-2835

[2] J.Y. San, Second law performance of heat exchangers for waste heat recovery. Energy 2010, 35; 1936-1945.

[3] C.J. Butcher and B.V. Reddy. Second law analysis of a waste heat recovery based power generation system. Int. J. Heat and Mass Transfer 2007; 50:2355-2363.

[4] A.F. Shaaban, Process engineering design of pathological waste incinerator with an integrated combustion gases treatment unit. J. Hazardous Materials 2007; 145: 192-202.

[5] J. Burak, Experimental study of the energy efficiency of an incinerator for medical waste. Applied Energy 2009; 86: 2386-2393

6th Int. Conf. on Structure, Engineering & Environment (SEE), Kyoto, Japan, Nov.18-20, 2020, ISBN: 978-4-909106056 C3051

RESEARCH ON THE DURABILITY OF RECYCLED AGGREGATE CONCRETE INCORPORATING HIGH VOLUMES OF BLAST FURNACE SLAG

Chung-Hao Wu[1] and Shu-Ken Lin[2]
[1]Department of Civil Engineering, Chung Yuan Christian University, Taiwan
[2]Department of Civil Engineering, National Chung Hsing University, Taiwan

ABSTRACT

This study experimentally investigated the durability of concrete containing high replacement levels of blast furnace slag. Two kinds of concrete with natural aggregate and recycled aggregate were adopted. Concrete mixtures made with 0%, 15%, 30%, 45%, 60% and 75% replacement of cement with blast furnace slag were prepared for testing. Water-cementitious material ratios are 0.30, 0.34, 0.38 0.42, 0.36 and 0.50. The compressive strength (at 7 days, 28 days, 56 days and 91 days), the resistance to chloride-ion penetration, and the water permeability of concrete (at 28 days, 56 days and 91 days) were measured and presented. Test results indicate that the recycled aggregate concrete showed a similar durability as the natural aggregate concrete. The compressive strength, the durability-related chloride-ion penetration, and the water permeability of concrete containing high replacement level (75%) cement replacement of blast furnace slag was obviously superior to the concrete without blast furnace slag or with lower replacement levels.

Keywords: Blast furnace slag, Recycled aggregated concrete, Water permeability, Chloride ion penetration, Durability

INTRODUCTION

The reuse of waste concrete has always been an important issue in Taiwan. In general, the reuse method is mainly to crush waste concrete as coarse aggregate for producing concrete. This concrete was named recycled aggregate concrete (RAC). The surface of recycled coarse aggregate (RCA) is generally full of pores, presenting high water absorption, which affects the property of the interfacial transition zone in concrete, leading to negative effects for the durability of concrete. In order to improve the durability of RAC, Pozzolans such as fly ash and blast furnace slag are added to concrete, however, there are restrictions on the dosages of the Pozzolans in many national standard codes. For past decades, more and more research results of concrete with high volumes blast furnace slag (BFS) were published, most of them were discussed for natural aggregate concrete (NAC), but rare for the reports relating to the RAC incorporating high replacement levels of BFS, especially for the durability.

R. K. Majhi et al. [1] investigated the fundamental properties of concrete prepared using high volumes of RCA (0%, 50% and 100%) and BFS (0% and 60%), and adding lime (0%, 5%, 7% and 10%) as an alkaline activator. The experimental results revealed that the lime was effective in activating the BFS and enhance the mechanical properties such as compressive strength, splitting tensile strength, flexural strength and bond strength of high volume BFS based RAC.

M. El-Hawary et al. [2] reported the results of experimental research on the durability and performance of various mixtures of RAC incorporating 25% BFS as a cement replacement. The compressive strength, drying shrinkage, water permeability, water absorption, alkali-aggregate reactivity and sulfate content of the concrete mixtures were tested. The results indicated that the addition of mineral slag improved the mechanical properties and durability characteristics of the RACs. Addition of 25% BFS evaluated to be efficient in reducing water absorption, alkali-silica reactivity and sulfate attack in RAC. However, the test results also showed that the introduction of 25% BFS is not effective enough to prevent the excessive expansion of the alkali-carbonate reaction in RAC after 1 year. Furthermore, it has an adverse impact on resisting the water permeability and drying shrinkage of the RAC mixtures.

Y. Khodair et al. [3] examined the effect of RCA on the properties of self-compacting concrete (SCC). Twenty RAC mixtures with different dosages of RCA, fly ash (FA) and BFS were prepared and tested. The results showed that the replacement percentage of RCA (0 ~ 100%) increased, the compressive strengths of concrete decreased at 3, 14, and 28 days, and the tensile strengths decreased at 28 days. Use 50% BFS as a replacement for cement resulted in the least reduction in the split tensile strength of all RAC mixtures when compared to the replacements of 50% FA and 25% FA and 25% BFS. Moreover, the partial

replacement of cement by Pozzolans presented an adverse effect on the 28-days-RAC compressive strength; however, it increased the resistance to chloride permeability.

F. U. A. Shaikh [4] reported the effect of slag fume on the early-age and long-term mechanical properties of RAC. The test results showed that addition of 50% slag fume significantly reduced the mechanical properties of the RAC at early age, while the long-term (56 and 91 days) compressive and tensile strengths of the RAC containing slag fume and 10% silica fume are higher than that of the control RAC mixture. It was also observed that the slow pozzolanic reaction of slag fume contributed to the long-term compressive and tensile strengths of RAC containing slag and 10% silica fume.

R.K. Majhi et al. [5] researched the effects of RCA and BFS on fresh and hardened concrete properties. 16 concrete mixtures were prepared with 0%, 25%, 50% and 100% replacement of natural aggregate by RCA for each 0%, 20%, 40% and 60% replacement of cement by BFS. The test results showed that the workability increases with the use of RCA or BFS or both of these two. The compressive, split tensile and flexural strength decreased with the increase in the replacement percentages of RCA or BFS or both. Water absorption and volume of voids of the concrete mixtures increased with the increase of RCA content. However, the use of BFS improves the quality of the concrete mixtures by improving the ITZ and bond strength between mortar and RCA. The concrete mixture with 50% RCA and 40% BFS achieves the values of these properties closer to those of the concrete without RCA and BFS.

Based on the results of the above mentioned researches, it is seen that RAC with high replacement levels BFS may present better durability and higher compressive strength at later age. Therefore, this study aims to further investigate the fresh properties, compressive strength and durability of RAC incorporating high replacement level of BFS.

EXPERIMENTAL PROGRAM

Test Materials

(1) Water: ordinary water meets the requirements of ASTM C 1602.
(2) Cement: Type I Portland cement produced by Taiwan Cement Company, with a specific gravity of 3.15. The basic properties of cement are shown in Table 1.
(3) Blast Furnace Slag: Grade 120 of ground granulated blast furnace slag obtained from Advanced-Tek Systems Co.,Ltd. in Taiwan. The basic properties of fly ash are shown in Table 1.
(4) Fine Aggregate: natural river sand with a specific gravity of 2.60 and fineness modulus of 2.40.
(5) Coarse Aggregate: crushed river stone with a specific gravity of 2.61, bulk density of 1470 kg/m^3 and D_{max} of 19 mm.
(6) Recycled Coarse Aggregate: crushed waste concrete with a specific gravity of 2.26, bulk density of 1280 kg/m^3 and a diameters of 5 ~ 20 mm.
(7) Superplasticizer (SP): High performance water-reducing agent of Type G with a specific gravity of 1.2 ± 0.02 and the pH value of 7.0 ± 1.0.

Table 1 Composition and physical properties of cement and blast furnace slag

Components	Cement	Blast Furnace Slag
SiO_2 (wt%)	21.4	38.12
Al_2O_3 (wt%)	4.9	7.48
Fe_2O_3 (wt%)	3.8	0.33
CaO (wt%)	64.2	39.86
MgO (wt%)	1.1	10.58
Na_2O (wt%)	0.2	0.36
SO_3 (wt%)	2.1	0.17
K_2O (wt%)	0.44	0.36
Loss on ignition (wt%)	2.1	1.4
Specific surface area (m^2/kg)	336	538
Specific gravity	3.15	2.90

Mixture Proportion and Specimen Preparation

The mixture proportions of concrete were designed according to the ACI 211 for providing the compressive strength of 35 MPa at 28 days. The water to cementitious material ratio (w/cm) ranged from 0.30 to 0.50, and the blast furnace slag content ranged from 0% to 75% by weight of the total cementitious materials as cement replacement. The mixture proportions are shown in Table 2.

The fresh properties of concrete, including slump, air content, unit weight and setting time, were simultaneously measured for each batch. Various specimens for tests were then cast from each mixture, they were: cylinder specimen of φ100 x 200 mm for compressive strength test, cylinder specimen of φ150 x 50 mm for water permeability test, and cylinder specimen of φ100 x 50 mm for chloride-ion permeability test. After removal from the molds, all specimens were moved to a standard moist-curing room until date for testing.

Table 2 Mixture proportions of concrete

Specimen no.	w/cm	W	C	BFS	FA	CA	SP
		kg/m^3					
NC35B00	0.50	210	420	0	800	860	1.1
NC35B15	0.46	193	357	63	839	860	1.0
NC35B30	0.42	176	294	126	878	860	1.8
NC35B45	0.38	160	231	189	918	860	2.6
NC35B60	0.34	143	168	252	956	860	3.6
NC35B75	0.30	126	105	315	995	860	6.3
RC35B00	0.50	210	420	0	793	750	1.1
RC35B15	0.46	193	357	63	832	750	1.5
RC35B30	0.42	176	294	126	871	750	2.3
RC35B45	0.38	160	231	189	910	750	3.6
RC35B60	0.34	143	168	252	950	750	5.9
RC35B75	0.30	126	105	315	989	750	8.7

1 Specimen number: N is normal aggregate concrete, R is recycled aggregate concrete, C35 is the compressive strength of 35MPa, B45 is 45% cement replacement ratio of blast furnace slag.
2 The containing water of Superplasticizer (SP) is not calculated in the mixture design.
3 W: water, C: cement, BFS: blast furnace slag, FA: fine aggregate, CA: coarse aggregate, RCA: recycled coarse aggregate

Testing of Specimens

The compressive strength test that meets the requirement of ASTM C 39 was performed at the ages of 7, 28, 56, and 91 days. According to ASTM C 1202, the resistance of concrete to the penetration of chloride ion was measured in terms of the charge passed through the concrete in coulombs. The water permeability of concrete was tested using a water permeability apparatus subjected to a water pressure of 0.29 MPa for 3 hours to determine the flow through the concrete specimen. The chloride ion penetration and water permeability tests were performed at 28, 56, and 91 days.

RESULTS AND DISCUSSION

Properties of Fresh Concrete

Figure 1 and 2 present the measured results of the slump and air content of concrete. It can be found that the natural aggregate concrete (NAC) and recycled aggregate concrete (RAC) mixtures were mixed by using superplasticizer to produce slumps of 210 mm to 250 mm and 200 mm to 250 mm, respectively. The air contents of NAC and RAC ranged from 1.2% to 2.3% and 1.4% to 3.0%, respectively. These results indicate that the blast furnace slag (BFS) RAC mixtures prepared for the test can exhibit adequate workability.

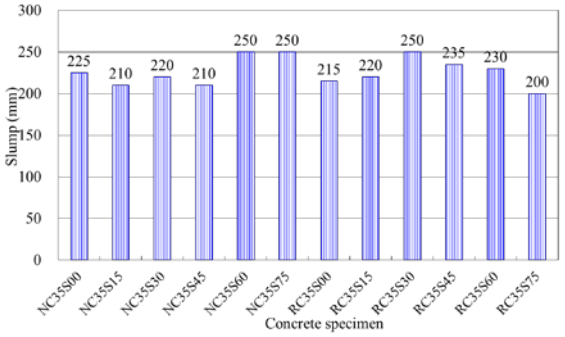

Fig. 1 Slump of concrete.

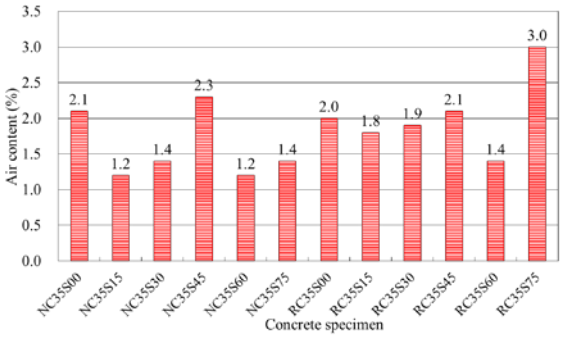

Fig. 2 Air content of concrete.

Compressive Strength of Concrete

Figure 3 shows the compressive strength of the concrete mixtures measured at the ages of 7 days, 28 days, 56 days and 91 days. The strength development of the NAC and RAC series presented a similar trend. At 7 days, the compressive strength for both kinds of the BFS concrete were higher than that of the control concretes without BSF. At 28 days, 56 days and 91 days, the strength of the BSF concretes exceeded obviously that of the control concrete. These results indicate that the BFS mixtures had larger strength gain than that of the control mixtures.

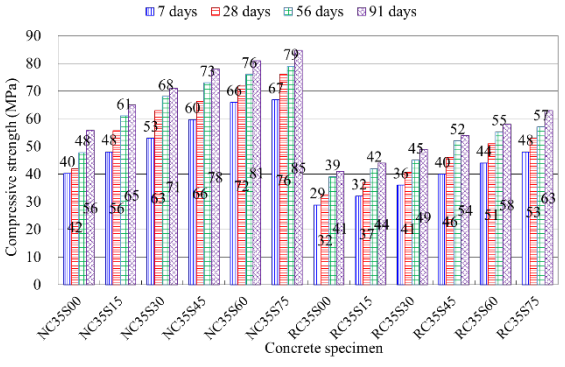

Fig. 3 Compressive strength of concrete.

Resistance to Chloride Ion Penetration

Table 3 summarized the measured results for the resistance of concrete to the chloride-ion penetration, the results are also illustrated in Figure 4. Overall, the characteristic of the resistance to chloride-ion penetration of the RAC was almost similar to the NAC, in which the resistance to the chloride-ion penetration of concrete incorporating BFS was higher than that of control concrete without BFS. At 91 days the total charge passed, in coulombs (C), were 1076 C and 581 C (classified as low and very low permeability) for NC35S75 and RC35S75, and were 6482 C and 8114 C (high permeability) for NC35S00 and RC35S00, respectively. This indicates that incorporating high replacement level (75%) of BFS in concrete may reduce the chloride-ion penetration, resulting in the improvement of the durability of concrete. This is believed to be due to contribution of the pozzolanic effect of the BFS mixtures.

Table 3 The resistance to the chloride-ion penetration of concrete

Specimen no.	Total charge passed (coulombs)			Classification of the chloride-ion permeability*
	28 days	56 days	91 days	
NC35S00	9605	6267	6482	high/high/high
NC35S15	6941	6189	5068	high/high/high
NC35S30	5617	4004	3919	high/high/ moderate
NC35S45	3562	3042	2928	moderate/ moderate/ moderate
NC35S60	2266	1478	1416	moderate/low/ low
NC35S75	1446	1109	1076	low/low/low
RC35S00	10506	8029	8114	high/high/high
RC35S15	6214	4813	4139	high/high/high
RC35S30	5889	4459	3598	high/high/ moderate
RC35S45	2973	2299	2136	moderate/mod erate/moderate
RC35S60	1507	1385	922	low/low/very low
RC35S75	938	861	581	very low/very low/very low

*Charge passed, chloride permeability, coulombs:
> 4000C = high 2000 - 4000C = moderate
1000 - 2000C = low 100 - 1000C = very low
< 100C = negligible

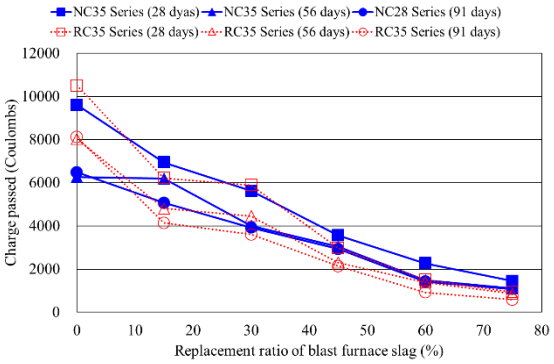

Fig. 4 Relationship of total charge passed and blast furnace slag content.

Water Permeability

The water permeability of concrete was tested using a uniaxial flow apparatus performing on cylinder specimen (φ150 x 50 mm) subjected to a 0.29 MPa pressure for 3 hours. The water permeability was calculated with following formula:

$$\text{Water permeability} = \frac{m_2 - m_1}{m_2} \times 100\% \quad (1)$$

where m_1 = initial weight of specimen,
m_2 = specimen weight after test.

Figure 5 illustrated the measured water permeability of the concrete mixtures. It is seen that the water permeability decreased with the age of concrete for both kinds (NAC and RAC) of BFS concretes. The water permeability of NAC is superior to that of RAC. In addition, incorporating BFS in concrete may inherently reduce the water permeability of concrete. This can be particularly found in NC35S75 and RC35S75 (containing 75% BFS) at later age of 91 days, which have water permeability of 1.22% and 1.88%, compared less than those of NC35S00 and RC35S00 of 4.57% and 7.89%, respectively. These results signify the facts that the concrete containing high replacement level BFS of 75% at later age may exhibit lower water permeability, namely superior durability to the concrete without BFS.

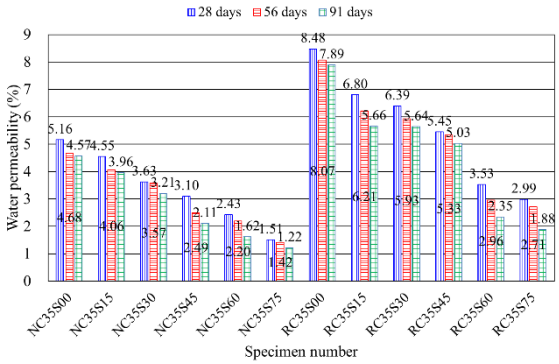

Fig. 5 Water permeability of concrete.

CONCLUSIONS

Based on the results of the experimental work, following conclusions can be drawn:

(1) Both of natural aggregate concrete (NAC) and recycled aggregate concrete (RAC) with the same mix proportion and adequate superplasticizer could present appropriate workability.

(2) The blast furnace slag (BFS) mixtures of both RAC and NAC had larger early compressive strength gain than that of the control mixtures, the strength of BFS concrete could exceed that of the control concrete without BFS at 7 days.

(3) RAC had similar characteristic of the resistance to the chloride ion penetration to NAC. The resistance to the chloride-ion penetration of concrete incorporating BFS was higher than that of control concrete. Especially, incorporating high replacement level (75%) of BFS in concrete may reduce the chloride-ion penetration, resulting in the improvement of the durability of concrete.

(4) The water permeability of NAC was superior to that of RAC. Incorporating BFS in concrete may reduce the water permeability of concrete. The concrete containing BFS of high replacement level (75%) at all ages may exhibit lower water permeability, namely more durable than the concrete without BFS.

(5) The resistance to the chloride ion penetration and water permeability increased with the increment of compressive strength of NAC and RAC. It is considered generally that the durability can be enhanced by increasing the compressive strength of concrete. Hence, it can be proved that adding BFS can be strengthened the durability of RAC.

ACKNOWLEDGEMENTS

The authors appreciate the Architecture and Building Research Institute (ABRI), Taiwan, for the financial support to this research.

REFERENCES

[1] Majhi R. K., Nayak A. N., and Mukharjee B. B., Development of Sustainable Concrete Using Recycled Coarse Aggregate and Ground Granulated Blast Furnace Slag, Construction and Building Materials, Vol. 159, 2018, pp.417-430.

[2] El-Hawary M., Nouh K., and Al-Yaqout A., Durability of Recycled Aggregate Concrete Incorporating Slag, Waste and Resource Management, Vol. 172, Issue 4, 2019, pp. 107-117.

[3] Khodair Y. and Bommareddy B., Self-consolidating Concrete Using Recycled Concrete Aggregate and High Volume of Fly Ash, and Slag, Construction and Building Materials, Vol. 153, 2017, pp. 307-316.

[4] Shaikh F. U. A., Mechanical Properties of Recycled Aggregate Concrete Containing Ternary Blended Cementitious Materials, International Journal of Sustainable Built Environment, Vol. 6, 2017, pp. 536-543.

[5] Majhi R. K., and Nayak A. N., Production of Sustainable Concrete Utilizing High-volume Blast Furnace Slag and Recycled Aggregate with Lime Activator, Journal of Cleaner Production, Vol. 255, 2020.

6th Int. Conf. on Structure, Engineering & Environment (SEE), Kyoto, Japan, Nov.18-20, 2020, ISBN: 978-4-909106056 C3051

NITROGEN FLOW ANALYSIS FROM DIFFERENT LAND-USE OF THE CHI RIVER BASIN (MAHA SARAKHAM REGION, THAILAND)

Nida Chaimoon[1]
[1]
Circular Resource and Environmental Protection Technology Research Unit (CREPT),
Faculty of Engineering, Mahasarakham University, Thailand

ABSTRACT

This paper aims at assessing the effect of land use on nitrogen flows from a significant land-use area in the Chi River basin (Maha Sarakham region) in Thailand. The Chi River is one of the main rivers, and many land use categories affect the quality of the river. Statistical data and referred data was collected as the secondary data from credible sources to identify the flows. The data show a strong effect of land use on nitrogen with the highest load dominated by paddy field (1,589,812 tonne/year), and the lowest value in the community (1,006 tonne/year). Nitrogen flow increased with the fertilizer application in paddy field and farm plants (44,897 tonne/year). Paddy field discharged nitrogen to the Chi River 1,113 T/year. Also, the community without wastewater collection system takes part in a non-point source (NPS) of nitrogen to the Chi River at 299 tonne/year. The management's suggestion is to control fertilizer application, burning of agricultural residue such as rice straw, and wastewater treatment before disposal.
Keywords: Nitrogen; Chi River; Substance Flow Analysis (SFA); Land-Use

INTRODUCTION

Pollution from natural phenomena or human activities and living things actions affects water quality in any water resource. Water quality disturbs the environment, natural resources, human activities, and human health [1, 2]. Pollution can be categorized into point source (PS) and non-point source (NPS) pollution. PS pollution mainly comprises of industrial and domestic wastewater loads, which can be identified through the discharging point or pipe [3]. NPS pollution usually comes from unidentified sources, such as agriculture land, street runoff, and the deposition of atmospheric pollutants [4]. The pattern of NPS pollution leads to the effect of land use on water quality.

Nutrient load is one of significant problems for water resource management, the interaction of nutrient, water and pathways has been traced and tracked by much research in the past. Nutrient load in water is a result of several interacting processes in the basin, including an exchange between cycles in the terrestrial, aquatic, geological, and atmospheric environment. These processes can be characterized into: (1) nutrient release (e.g., through mineralization, weathering, fertilization, atmospheric deposition, sewage effluents); (2) water transport (conducting, e.g., transit time and flow paths); and (3) transformation and immobilization (e.g., denitrification, sedimentation, and adsorption).

Nutrient problems can be magnified by the improper land-use that discharges nutrients to water bodies [5, 6]. Concentrated agricultural activities and rapid urbanization created immense pressure on water quality. The percentage of agricultural land is significantly positive correlated with water pollution due to fertilizer application entering surface water through runoff [7].

Urbanization is associated with changes in land-uses through infrastructure development, population density, and community. The increase in impervious areas (i.e., roads, rooftops, impermeable pavement, and parking lots) results in NPS pollution increase in runoff and transportation of NPS pollutants to receiving waters [8]. The Forest area was considered as net sinks of nitrate [9]. Land-use category is relevant to water quality within a watershed, and landscape alignments may be more sensitive predictors of water quality.

The Chi River is the longest river in Thailand. It is 765 km long. In wet seasons there are often flash floods in the floodplain of the Chi River basin. The river originates in the Phetchabun mountains and then flows to the east part through the central Isan provinces of Chaiyaphum, Khon Kaen, and Maha Sarakham, then turns south in Roi Et and runs through Yasothon and joins the Mun River in the Kanthararom district of Sisaket Province. The Chi River carries approximately 9.3 km^3 of water per annum [10]. Maha Sarakham is the fast-growing city located along the Chi River. It has undergone rapid urbanization. Chi River is used as a water resource of tap water supply, agriculture and fishery.

Substance Flow Analysis (SFA) is an environmental accounting tool used to trace and track environmental problems. SFA is an appropriate method to answer the questions of substance flows from input transformation processes until discharging in system boundary [11]. Therefore, this study aimed to analyze nitrogen flows by SFA

quantitatively, and propose implemented solutions. The results can be one approach to control other nutrients or organic substances in the environment and applied for better NPS and land-use area management.

METHODOLOGY

Substance Flow Analysis (SFA)

Substance Flow Analysis (SFA) is an environmental accounting tool based on the concept of mass balance in a specific area and time. SFA for nitrogen provides a systematic assessment of flows and stocks within a defined system in space and time. It was undertaken to quantify nitrogen flows from different land-use area (as a process) in the Chi river basin (Maha Sarakham region).

System Boundary

The Chi river basin covers the middle part of the northeastern region (Fig.1). The area of the basin in Maha Sarakham province was selected to be the specific system boundary.

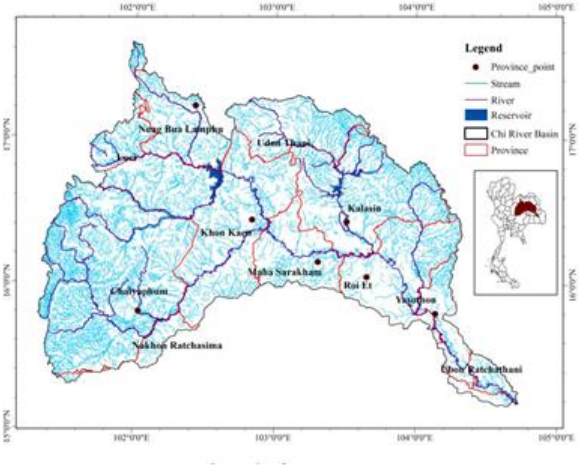

Fig. 1 Chi River Basin [12].

The Chi River basin area is 53.18% of Maha Sarakham province (Fig. 2) which was 2,998 km^2. The land-use area in the system boundary was categorized into community along the Chi River 6.83% (205 km^2), agriculture 82.88% (2,484 km^2), forestry 3.94% (118 km^2) and miscellaneous 2.63% (79 km^2). The activities that have an impact on the Chi River were only community and agriculture along the Chi River. The major agriculture included paddy field 62.17% (1,864 km^2), corn 0.01% (0.3 km^2) and cassava 11.28% (338 km^2). The period of data collection was in the year of 2018 (one year period).

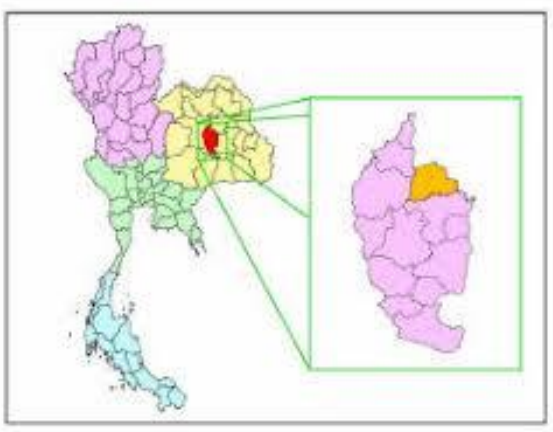

Fig. 2 Maha Sarakham province Location [13]

Data Collection

Nitrogen flows in the system boundary were traced to define quantity and pathway through relevant processes until discharge to the environment. The nitrogen flow diagram of the system boundary is shown in Fig 3.

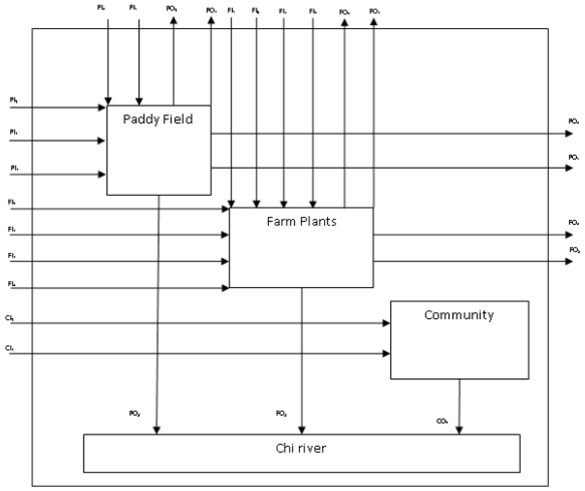

Fig.3 Nitrogen flows

In order to know the nitrogen flows through the various land use categories, secondary data was obtained from official reports by related organizations and relevant literature review [14-29]. Details of data acquisition were described as follows:

Statistical data

Official reports from governmental organizations such as Department of Land Development, National Statistical Office, Department of Irrigation, and Office of Regional Environment.

Reference data

Due to unavailable data in the system boundary, secondary data (nitrogen concentrations) was obtained from a nearby area, which has similar management based on literature review was applied to the nitrogen flows.

Assumption and scope

Main processes in the system boundary were categorized by major agricultural activities affecting the water quality of the Chi River, such as paddy field, cassava and corn farming, community, and the Chi River as the receiving water. Input flows associated with the basic requirement of each process. Stocks were quantified by the accumulated nitrogen from input within the process and may be removed from the process without interruption with the Chi River. Output flows were traced by nitrogen flow in products of the processes or N discharged to other processes.

Calculation

The calculations basically multiplied the flows (which is recognized as activity) of input, output, and stock of each land-use area in the system boundary with their nitrogen concentration ([N], mg N/L). Finally, the results of nitrogen flows were shown in the unit of ton N/year. Nitrogen flows were calculated based on mass balance over the processes. Determination methods for nitrogen flows were summarized in Tables 1-3.

Table 1 Data acquisition and calculation for paddy field

Flows	Material	Calculation
Input	Fertiliser (PI_1)	N in fertilizer × area × loops
	Irrigation (PI_2)	N in irrigated water × area × water consumption × days
	Rain water (PI_3)	N in rainwater × area × loops
	Seed (PI_4)	N in seed × area × loops
	Atmospheric fixation (PI_5)	N in atm × area × loops
Output	Burning (PO_1)	N in input × % burning
	Evaporation (PO_2)	N in input × % evaporation
	Surface runoff (PO_3)	N in input × % burning
	Rice production (PO_4)	N in rice × area
	Rice straw (PO_5)	N in rice straw × area × rice straw
Stock	Infiltration (PS_1)	N in input × % infiltration

Table 2 Data acquisition and calculation for farm plants

Flows	Material	Calculation
Input	Fertiliser corn (FI_1)	% N in fertilizer × area × fertilizer consumption × loops
	Fertiliser cassava (FI_2)	% N in fertilizer × area × fertilizer consumption × loops
	Irrigation corn (FI_3)	N in irrigated water × area × water consumption × loops
	Irrigation cassava (FI_4)	N in irrigated water × area × water consumption × loops
	Rain water corn (FI_5)	N in rainwater × area
	Rain water corn (FI_6)	N in rainwater × area
	Atmospheric fixation corn (FI_7)	N in atm × area × loops
	Atmospheric fixation cassava (FI_8)	N in atm × area × loops
Output	Burning (FO_1)	N in input × % burning
	Evaporation (FO_2)	N in input × % evaporation
	Surface runoff (FO_3)	N in input × factor of runoff
	Corn production (FO_4)	N in corn x area × loops
	Cassava production (FO_5)	N in cassava × area × loops
Stock	Infiltration (FS_1)	N in input × % infiltration

Table 3 Data acquisition and calculation for community

Flows	Material	Calculation
Input	Water supply (CI_1)	N in water supply × water consumption × population
	Rice consumption (CI_2)	N in rice × consumption × population
	Beef consumption	N in beef × consumption ×

	(CI_3)	population
	Pork consumption (CI_4)	N in pork × consumption × population
	Chicken consumption (CI_5)	N in chicken × consumption × population
	Milk consumption (CI_6)	N in milk × consumption × population
	Egg consumption (CI_7)	N in egg × consumption × population
	Fresh water animals consumption (CI_8)	N in fresh water animals × consumption × population
Output	Wastewater (CO_1)	N in wastewater × wastewater generation rate × population
Stock	Infiltration (CS_1)	N in input × % stock

RESULTS AND DISCUSSIONS

SFA calculation of the current situation (2018)

Three processes included in the system boundary were traced to the nitrogen flow and calculated the flows as detailed in the previous section. The results from each process are shown in Tables 4-6 as follows.

Table 4 Nitrogen flows in paddy field process

Flows	Material	Flows (Ton/year)
Input	Fertilizer	42,674
	Irrigation	110,581
	Rainwater	1,402,572
	Seed	18,588
	Atmospheric fixation	15,397
Output	Burning	124,800
	Evaporation	19,078
	Surface runoff	1,113
	Rice production	21,524
	Rice straw	14,628
Stock	Infiltration	1,890

Table 5 Nitrogen flows in farm plant process

Flows	Material	Flows (Ton/year)
Input	Fertilizer corn	4.21
	Fertiliser cassava	2218.86
	Irrigation corn	0.25
	Irrigation cassava	291.62
	Rain water corn	0.17
	Rain water corn	196.53
	Atmospheric fixation corn	0.24
	Atmospheric fixation cassava	84.52
Output	Burning	214.20
	Evaporation	68.23
	Surface runoff	1.96
	Corn production	10.92
	Cassava production	3,943.23
Stock	Infiltration	279.64

Table 6 Nitrogen flows in community process

Flows	Material	Flows (Ton/year)
Input	Water supply	10.10
	Rice consumption	510.84
	Beef consumption	22.69
	Pork consumption	32.68
	Chicken consumption	142.70
	Milk consumption	7.74
	Egg consumption	41.18
	Fresh water animals consumption	237.78
Output	Wastewater	299.09
Stock	Infiltration	100.57

The mass balance of the flows was done to compare to the calculation above. It was found that the paddy field had over the inflow of 1,411,039 tonne/year. This amount of nitrogen could be adsorbed to the soil, whereas the farm had lower input flow than output flow and stock. This could have resulted from mechanisms of cassava planting. The modeled consumption of the community roughly showed that the input was more than stock and output.

The major flow of nitrogen into the Chi River is from the paddy field, which is similar to research done in China [4,7]. People living the Chi river basin are mostly farmers and reach irrigation during drought season and plentiful rainwater in the rainy season. Therefore, farmers in the system boundary can plant rice all year round and leads to high nitrogen flow. However, people who live far from the Chi River but still in the range of the catchment plants corn and cassava, which are the primary farm plants in the northeastern region. Therefore the main land-use area, which affects the nitrogen input in agriculture. The nitrogen flow from the community affects the Chi River due to a non-point source of wastewater discharge. Therefore the suggestion is to control the fertilizer application in the paddy field and burning of agricultural residue. Community should reduce the flow of wastewater discharging into the river by installing wastewater treatment unit.

CONCLUSIONS

Land-use area and activities influence the flow of nitrogen into the Chi River according to the application of fertilizer and other post-harvesting activities. The communities along the Chi River also take responsibility for NPS of nitrogen in terms of wastewater discharge. The strategy could apply to agriculture management and wastewater collection and treatment.

ACKNOWLEDGMENTS

The author wishes to acknowledge the National Research Council of Thailand (NRCT) for research funding.

REFERENCES

[1] Akasaka M., Takamura N., Mitsuhashi H., and Kadono Y. (2010). Effects of land use on aquatic macrophyte diversity and water quality of ponds, *Freshw. Biol*. vol. 55 (4), pp. 909–922.

[2] Lu Y., Song S., Wang R., Liu Z. ,Meng J., Sweetman A.J., Jenkins A., Ferrier R.C., Li, H., Luo W., and Wang, T. (2015). Impacts of soil and water pollution on food safety and health risks in China. *Environ. Int*. vol. 77, pp. 5–15.

[3] Wang W., Liu X., Wang Y., Guo X., and Lu S. (2016). Analysis of point source pollution and water environmental quality variation trends in the Nansi Lake basin from 2002 to 2012. *Environ. Sci. Pollut. Res*. vol. 23 (5), pp. 4886–4897.

[4] Ongley E.D., Xiaolan Z., and Tao Y., (2010). Current status of agricultural and rural non-point source pollution assessment in China. *Environ. Pollut*. vol. 158 (5), pp. 1159–1168.

[5]Valle Junior R.F., Varandas S.G.P., Fernandes L.S., and Pacheco F.A.L., (2014). Groundwater quality in rural watersheds with environmental land use conflicts. *Sci. Total Environ*. vol. 493, pp. 812–827.

[6] Pacheco F.A.L. and Fernandes L.S., (2016). Environmental land use conflicts in catchments: a major cause of amplified nitrate in river water. *Sci. Total Environ*. vol. 548, pp. 173–188.

[7] Tu J. (2011). Spatially varying relationships between land use and water quality across an urbanization gradient explored by geographically weighted regression. *Appl. Geogr*. vol. 31 (1), pp. 376–392.

[8] Wilson, C. and Weng, Q. (2010). Assessing surface water quality and its relation with urban land cover changes in the Lake Calumet Area. *Greater Chicago, Environ. Manag*. vol. 45 (5), pp. 1096–1111.

[9] Pacheco F.A.L., Santos R.M.B., Fernandes L.S., Pereira M.G. and Cortes, R.M.V. (2015). Controls and forecasts of nitrate yields in forested watersheds: a view over mainland Portugal. *Sci. Total Environ*. vol. 537, pp. 421–440.

[10] Wikipedia, (2019). *Maha Sarakham*. URL: http://www.wikipedia.com, access on 04/02/2019

[11] Brunner, P.H. and Rechberger, H. (2004). Practical Handbook of Material Flow Analysis, Lewis Publishes, New York

[12] Arunyanart N. and Limsiri C., Uchaipichat A., (2017). Flood hazards in the Chi River Basin, Thailand: Impact management of climate change. *Applied Ecology and Environmental Research*, vol. 15(4), pp. 841-861.

[13] Ratanopad S. and Kainz W., (2006). Using GIS and map data the analysis of the expansion of salinized soils. paper presented in *the ISPRS Commission IV symposium on Geospatial databases for sustainable development*

[14] Department of Land Development. Thailand (2017). *Land use area in Maha Sarakham*, URL: http://www.ldd.go.th, access on 04/02/2019

[15]Viera-Vargas, M.S. et.al. (2004). Quantification of the Contribution of the N_2 fixation to tropical forage legumes and transfer to associated grass. *Soil Biology and Chemistry*. vol. 27(9), pp. 1193-1200.

[16] Department of Irrigation. (2012). *Water consumption of plants*, URL: http://www.irr.go.th, access on 04/02/2019

[17] Paramee S., Chidtaisong A., Towprayoon S., Asanachinda P., Bashkin V.N. and Tangtham N. (1998). Three-years monitoring results of nitrate and ammonia wet deposition in Thailand. *Environmental Monitoring and Assessment*, vol. 102, pp.27-40.

[18] Rinaudo G., Dreyfus B. and Dommergues Y., (1983). *Sesbania rostrata* green manure and the nitrogen content of rice crop and soil. *Soil Biology and Chemistry*, vol. 15(1), pp. 111-113.

[19] Smil V. (1999), Nitrogen in crop production: An account of global flows, *Global Biogeochemical Cycles*, vol. 13(2), pp. 647-662.

[20] Shan Lin K., Dittert Hongbin Tao, C. Kreye, Yangchu Xu,Qirong Shen, Xiaolin Fan, B. Sattelmacher, and Odum H. T. (1996). The ground-cover rice production system (GCRPS): a successful new approach to

save water and increase nitrogen fertilizer efficiency? Water-wise rice production. paper presented on *the International Workshop on Water-wise Rice Production*.

[21] Liang X.Q., et.al. (2007). Modeling transport and fate of nitrogen fronm urea applied to a near-trench to paddy field. *Environmental Pollution*, vol. 150(3), pp. 313-320.

[22] Kavila, (2013). Utilisation of rice straw in soil conditioning.

[23] Department of Land Development, Thailand (2013). *Farm planting*. URL: http://www.ldd.go.th, access on 04/02/2019

[24] Huwe B., and van der Ploeg R. R. (1991). WHNSIM — a soil nitrogen simulation model for Southern Germany. *Fertilizer Research*, vol. 27, pp. 331-339.

[25] Boddey R.M. (2002). Nitrogen fixation in tropical cropping systems. *Soil Biology and Biochemistry*, vol. 34(12), pp. 1969-1970.

[26] Department of Agriculture Promotion, Thailand (2013). *Application of Biological Fertiliser in soil conditioning*. URL: http://www.doae.go.th, access on 04/02/2019

[27] Provincial Water Work Authority of Thailand, (2012). *Water consumption*. URL: http://www.pwa.co.th, access on 04/02/2019

[28] Heinemann C., et.al. (2005). Influence of amylose-flavor complexation on build-up and breakdown of starch structures in aqueous food model systems. *LWT-Food Science and Technology*. vol. 38(8), pp. 885-894.

[29] Udomsinroj K. (1996). Wastewater treatment, 1st edition Bangkok, Mitnara

6th Int. Conf. on Structure, Engineering & Environment (SEE), Kyoto, Japan, Nov.18-20, 2020, ISBN: 978-4-909106056 C3051

EVALUATION OF ENVIRONMENTAL ENGINEERING EDUCATION PROGRAM FOR STUDENTS FROM SOUTHEAST ASIA TO HIGH SCHOOL IN JAPAN

Kenji Arai[1], Tetsuo Morita[2] and Toshikazu Nishio[3]
[1] Maebashi Institute of Technology Graduate School, [2] Maebashi Institute of Technology, [3] Takasaki Technical High School

ABSTRACT

A high school in Gunma Prefecture, Japan, conducted an environmental engineering education program for international students from Southeast Asia for 13 years from 1998 to 2010. The purpose of this study is to understand the effect of the program on former international students and the Japanese high schools that participated in the environmental education program 10 years after its completion.

International students stayed in a Japanese home for a year and learned environmental engineering technology while interacting with Japanese high school students. In order to sort out the exchange activities between former international students and Japanese high schools, and to conduct a post evaluation of the program, a survey was conducted with former foreign students and the Japanese high school students, the Southeast Asian and Japanese high school staffs, and the host families.

Using the survey data, a logic model for the environmental engineering education program was created. As a result, it was found that three elements of cross-cultural understanding, training agricultural engineers, and acquiring language skills are important for global human resource development. And it was found that the three elements involved four resources/inputs: homestay families, support for language learning, acquisition of agricultural technology, and learning and living experiences in foreign countries. I was able to confirm that the four resources exist in many places throughout the country, and there is a high possibility that the programs can be applied nationwide, and there is a possibility to establish a mechanism to disseminate the programs for global human resource development.

Keywords: engineering education, high school, Southeast Asia, evaluation, logic model

INTRODUCTION

For the development of the agricultural field in Asia and the development of human resources that can play an active role as an international setting, an agricultural high school in Gunma prefecture in Japan, accepted foreign students from Southeast Asia (Philippines, Thailand, Malaysia, Indonesia, Mongolia) for 13 years from 1998 to 2010 as part of the Environmental Engineering Education Program (Asia Agricultural High School International Student Acceptance Project) Even after the program ended, exchanges between former international students and Japanese high schools continued, and now exchange programs between Japanese agricultural high schools and the Philippines and Thailand are continuing.

PURPOSE OF THIS STUDY AND RESEARCH METHOD

Previous Studies

The International Affairs Division of the General Affairs Department of Gunma Prefecture stated that in the promotion of the exchange program for international students of Asian agricultural high schools, as a result of the project there had been a positive effect not only on the international students, but also on the students and staff involved [1].

A study by Goji at Hiroshima University on the influence of the experience of studying in Japan on the intercultural adaptation of ex-students in the workplace of foreign employees suggests that the experience of studying abroad is positive for intercultural adaptation in the workplace. This effect was confirmed by Omae et al. in their study [2].

The positive influence an experience of studying abroad had on voluntary activities and career development was also shown, and that time spent studying abroad may promote voluntary activities and contribute to career development. Iketani's influence and significance of exchange programs with international students on Japanese people. Experience of multicultural coexistence in the usual environment on campus leads to increased contact with foreigners in daily life. And that going out is not necessarily

internationalization. In this way, many previous studies have shown the effects of studying abroad or accepting international students [3].

In Okuda's research trend on the effects of career education and vocational education in high school, most of the studies that examined the effect of career education in high school were biased toward focusing on the effect of "before high school graduation." It reveals that very few studies have analyzed the effects on “employment” [4].

Purpose of This Study

The environmental engineering education program implemented in Gunma Prefecture was implemented as an advanced example of local government in career education and international understanding education. Utilization of resources such as farms and agricultural high schools in local governments, ex-students who have completed the project still have exchanges with Japan, short-term exchange programs between Japan and Asia started, agricultural technology in Asian countries the feature of this research is that it is highly likely to lead to the development of human resources with the ability. The Asian Agricultural High School International Student Acceptance Program has completed 178 students in 13 years, and most of them have advanced to agriculture and related industries. Many former international students return to their home countries and play an active role as leaders in agriculture and related industries, and some former international students are playing an active role as a bridge between Asia and Japan by taking advantage of the Japanese language skills they have learned. However, there are no cases that summarize the business and specifically present the effect.

Therefore, in this research, the structure of the program is organized by the logic model. In order to understand the content of the project and the effect, I got the information about the program from the materials and teachers in charge. 10 years have passed since the end of the project, and some former international students and teachers in charge interviewed about the merit and demerit of the project and its difficulties. After that, the implemented projects were analyzed and evaluated item by item. Although there are very few cases of ex-post evaluation, it is important in this research that the evaluation was made after the project was completed.

In this study, based on the fact that Okuda's post-project impact analysis is scarce, we investigated the career paths of former international students after the project and the impact of the project. Takada showed that in the current situation and challenges [5] of university management plans, medium-term plans that clarify the logical structure according to the logic model are desirable for the formulation of medium-term plans for national universities. In this research, we considered the research method with reference to the structural analysis using the logic model presented by Takada.

The aim of this study is to reveal the effects that have been given to former international students and the Japanese high schools 10 years after the end of the environmental education program.

Research Method and Target

The research method was as follows. The logic model was applied to structurally deconstruct the contents of the program, and to understand the resources utilized in each component, the activity contents, and the produced results. The logic model is a systematic diagram of the path toward the realization of the ultimate vision of a business or organization, and is likened to a business blueprint.

The research target is a project to accept international students from Asia to Japan. There are 178 former international students. Since 10 years have passed since the end of the project, it was difficult to obtain quantitative information from all former foreign students, such as conducting a questionnaire with all of them. Therefore, we conducted a hearing from 33 former international students who we could contact and visit, and conducted a questionnaire and a hearing from the faculty members who were in charge of the international students at that time, constructed a logic model, analyzed and evaluated it. We also conducted a supplementary survey on mutual exchange between Asian countries and Japanese high school students, which began in 2012. The specific method is as follows.

1) Implementation of environmental engineering education program and hearing survey
2) Construction of logic model for environmental engineering education program
3) Analyze and evaluate the logic model to understand the effect of the program.

EDUCATION PROGRAM AND SURVEY

Engineering Education Program

International students from Southeast Asia will stay home in the home of a Japanese family for a year and learn environmental engineering and agricultural techniques while interacting with Japanese high school students. Students came to Japan in May and for the first semester until August, they mainly studied Japanese at Gunma Prefectural Seta Agriculture and Forestry High School. During the second semester starting from September, students will be divided into eight agricultural high schools in Gunma prefecture, depending on the learning content of their international students, and they will stay in a family centered on farmers. In August, they experienced about a month of farm stay and practiced practically to learn agricultural technology.

Fig. 1 Experience of various agricultural training (taken by the international exchange teacher)

Fig. 2 Language learning and life in Japan (taken by the international exchange teacher)

Fig. 1 shows various agricultural training experiences such as rice planting, crops, biotechnology, livestock, and landscaping. Fig. 2 shows Japanese training and life in Japan.

Hearing Survey

In order to understand the structure of the program, the staff in charge of international students at the time provided information such as the annual schedule of the program, the timetable of the international students, the event plan, and the career paths of the current international students. Interviews were conducted with former international students and the staff in charge of international students in September and December 2019 for former international students, and in February and March 2020 for former staff in charge of international students. The contents of the interview were the merits and demerits of the program, and the difficulties in implementing the program.

The items identified as merits in the results of the interview survey were learning languages, understanding different cultures, establishing connections with Japan, having a valuable experience in adolescence, and being exposed to agricultural and advanced technologies. Disadvantages include high prices, differences in lifestyle and religion, and food deference.

Among N=33, the career paths of ex-international students obtained from the interview survey were show that they were more likely to work in agriculture and agriculture-related industries. And they active as a leader in various fields.

LOGIC MODEL ANALYSIS

Logic Model for Program

In this study, an environmental engineering program was analyzed and a logic model was created. Table 1 shows the flow of the manifestation of planning effects along the framework of resources, activities, outputs, and outcomes.

The purpose, inputs, activities, initial outcomes, intermediate outcomes, and final outcomes of the logic model of the environmental engineering education program are shown below. The background

Table 1 Concept of logic model and each component (Created by the author)

Elements	Difinition	Main cases
Purpose	What the plan aimes for	Human resource development capable of international success
Resources	Management resources used to excute the plan	・Homestay families ・Support for language learning ・Agricultural technology acquisition ・Learning and life experience in Japan
Activity	Means for implementing the plan	・Home stay ・Lessons and life abroad ・Learning and practical training at agricultural high school ・Practice at farms and research facilities ・Support by assigning Japanese teachers ・Daily language activities
Initial outcome	Elements needed to achieve the intermediate outcome	・Home stay ・Experience living abroad ・Agricultural knowledge acquisition ・Agricultural practical skills acquisition ・Language learning support
Intermediate outcome	Elements needed for final outcome	・Intercultural understanding ・Agricultural engineer training ・Language acquisition
Final outcome	Goals of what they are trying to change	・Development of global human resources

to the successful business was that agriculture, which was a key industry, was in danger of declining as the economic growth of Asian countries proceeded, and the aim was to rebuild agriculture in Asia. The purpose of the program was to achieve the aim of developing human resources who can be active internationally.

Table 1 shows the definition of the constituent elements in the logic model and the cases handled in the research. The purpose of what the plan aims at is set, and the necessary elements to achieve it are resources. Table 1 shows the relationship between resources and final outcomes.

A short-term exchange program between Japan and Asian countries started in 2012, triggered by an environmental engineering education program. Compared to the one-year program, there are advantages such as the lower cost and shorter duration that makes it easier to participate in, and it can be expected to play a role as an opportunity to develop human resources who can play an active role internationally.

Analysis by Logic Model

Purpose

The environmental engineering education program was started with the aim of agricultural reconstruction and economic development in Asian countries. Against this background, in Asian countries, agriculture has been a key industry of the country until recently, but due to recent changes in the industrial structure due to economic growth and the decline of agriculture, the reconstruction of agriculture has become an issue. Based on this, this program aims to develop human resources who can play an active role internationally.

Resources (inputs)

Resources (inputs) are all management resources used for executing the plan. The number of families accepting international students was 149. In language learning, 5 Japanese teachers, 1 counselor, classmates, HR teachers, exchanges among international students, etc. were supported. All the elements and conditions that agriculture can tackle, such as nature, farmland, prefecture agricultural high school and agricultural college, agricultural testing grounds, farmers, and agricultural engineers, were taken as agricultural technology acquisition. In addition to the above, the participation of international students in school events and daily life were taken as learning and life experiences at Japanese high schools.

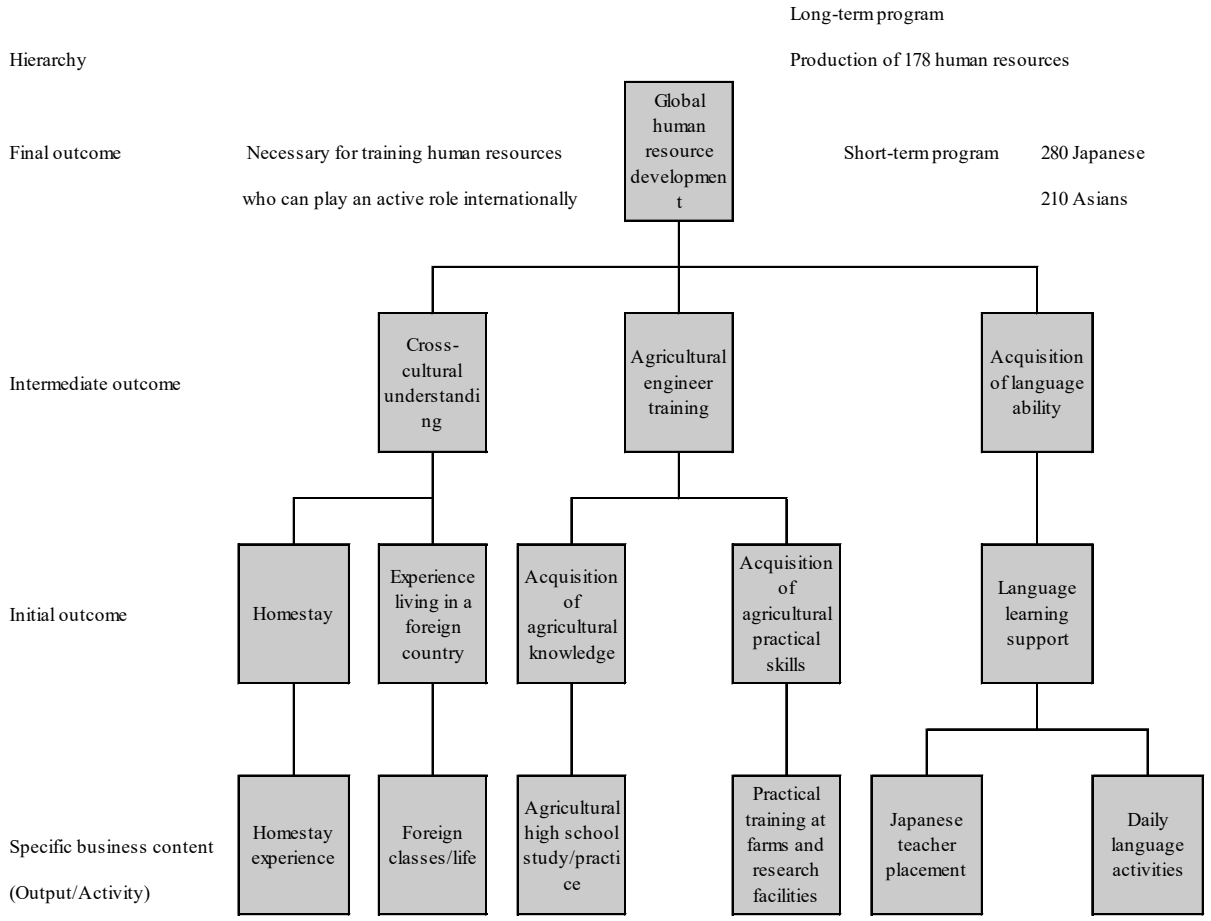

Fig. 3 Structure of the Program (Created by the author)

Status of activities

This study dealt with two programs. It is a one-year environmental engineering education program from Southeast Asia to a Japanese high school, and a short-term mutual exchange between high school students between Japan and the Philippines and Japan and Thailand since 2012.

Activities in the program include homestay for cross-cultural understanding and lessons/living in foreign countries, learning/practice at agricultural high schools to train agricultural engineers and practical training at farms and research facilities, and language acquisition. Support by a Japanese teacher for daily activities and daily language activities.

Status of initial outcome

As an intermediate outcome, homestay to realize cross-cultural understanding, life experience in foreign countries, acquisition of agricultural knowledge to realize cultivation of agricultural engineers, acquisition of agricultural practical ability, and language learning support for acquisition of language ability are initial outcomes.

Status of interim outcomes

Intermediate outcomes are cross-cultural understanding for global human resource development, agricultural engineer training, and language acquisition, and these are the conditions for achieving the final outcome.

Status of final outcome

The goal of the program is to develop human resources who can be active internationally. Therefore, the final outcome was global human resource development. In the long-term program, 178 international students from Southeast Asia completed one year study abroad in Japan, and in the short-term program of mutual exchange between Japan and Asia, a total of 280 Japanese high school students and 210 Philippine and Thai high school students have finished the exchange.

Effects of Program

The structure was created from the results of hearing the program, the logic model of the environmental engineering program, and the concept of each component (Table 1). Fig. 3 is a model of the situation in which international students from Southeast Asia got their current course after studying for one year in Japan. It was found that the flow of inputs, outputs, and outcomes has the structure shown in the figure, which leads to the achievement of the project purpose.

From Fig. 3 and Table 1, four resources (inputs), homestay, support for language learning, acquisition of agricultural technology, learning and living experience overseas are important elements of the program and are linked to outputs and outcomes.

It was found that activities that utilize the four resources have the effect of leading to an understanding of different cultures and an improvement in motivation for learning, leading to the path to agriculture and related industries, and leading to the development of human resources who can play an active role internationally.

The resources used in this program are available to many local governments throughout Japan, and we believe that if the program spreads nationwide in the future, it will lead to further global human resource development.

CONCLUTION

Results of This Study

The results obtained in the present study can be summarized as follows:

1) Cross-cultural understanding is important for global human resource development.
2) It is important to train agricultural engineers to develop global human resources.
3) Acquisition of language skills is important for global human resource development.
4) 1) to 3) are linked to global human resource development.

This study evaluated an environmental engineering education program for international students from Southeast Asia to Japanese high schools.

By implementing the program, we also found that there is a tendency to get a profession that makes use of specialized skills, that international exchange continues even after the project ends, which can lead to language learning opportunities and an improvement in learners' motivation.

Through an environmental engineering program that lasted 10 years, 178 global human resources have been trained and are active. It also led to a short-term mutual exchange program, with 280 Japanese high school students and 210 Asian high school students completing the program, improving cross-cultural understanding and language skills, learning agricultural technology in Asian countries, and improving motivation to learn.

From the above, it was found that there is an effect of improving the motivation of high school students, and by recognizing this effect, the cooperation of high schools and local residents can be obtained, and the effectiveness of this program could be demonstrated empirically.

Subject for Next Study

We created a logic model to show the structure and effects of the long-term study abroad program (Figure 3). In addition, the structure of the short-term interaction program was outlined. The short-term exchange is realistic considering the ease of participation because of reduced financial costs and the effect on many students, and as a result, it continues even now. In many cases, short-term exchanges have led to long-term study abroad and international work. The long-term study abroad program has immeasurable effects such as cross-cultural understanding and language learning effect, but the financial burden is large. From this, we think that it is important to focus on short-term exchanges and build a system that will lead to long-term exchanges and future work. Economic support such as scholarships and crowdfunding is also required in the mechanism, and it is possible to quantitatively show the effects of the benefits of long-term exchange and to create a transition from short-term exchange programs to long-term programs and global human resource development. This is a future issue. It is also an issue to evaluate programs in local governments that practice environmental engineering education programs outside Gunma prefecture.

REFERENCES

[1] General Affairs Department of Gunma Prefecture, Promotion of exchange programs for Asian agricultural high school students, Municipal Internationalization Forum, No. 175, 2004. pp. 8-11.

[2] Omae Y., Kasuya R., Yoshino K., Mitsui T. and and Takahashi H., Effects on Self-activity and Career of Experience of Studying Abroad, Journal of Japan Educational Technology, Vol. 40, No. Suppl., 2016, pp. 21-24.
[3] Iketani T., The Value of the Joint Instruction with International Students at Kobe Shoin Women's University, Journal of the Faculty of Letters, Kobe Shoin Women's University, No. 5, 2016, pp55-70.
[4] Okuda J., A Review of Studies on Effect of Career Education and Vocational, Bulletin of Hokuriku University, No.47, 2019, pp.37-56.
[5] Takada E., Current Status and Issues of University Management Plans: Focusing on Analysis of National University Mid-term Plans from Logic Model Perspective, Kobe University, University Education Research, No. 28, 2020, pp.29-39.

6th Int. Conf. on Structure, Engineering & Environment (SEE), Kyoto, Japan, Nov.18-20, 2020, ISBN: 978-4-909106056 C3051

CAUSAL RELATIONSHIP MODEL OF PROBLEMS IN PUBLIC SECTOR PROCUREMENT

Tanayut Chaitongrat[1], Surapong Liwthaisong[2], *Preenithi Aksorn[3], Wuttipong Kusonkhum[4], Narong Leungbootnak[5], and Korb Srinavin[6]
[1,2] Faculty of Architecture, Urban Design and Creative Arts, Mahasarakham University, Thailand;
[3-6] Faculty of Engineering, Khon kaen University, Thailand

ABSTRACT

Although e-Government Procurement System has been adopted and used in the public sectors, small amount of studies has concerned about the procurement relating to a construction sector. This research, therefore, was intended to investigate concordance between a hypothetical causal model and empirical information. Questionnaires were used with 353 samples from the government officers. Statistical analysis was conducted by utilizing SPSS 25 and AMOS 25 to determine percentage, mean, standard deviation, factor analysis and structural equation modeling (SEM). Results revealed that the analysis model was in accordance with empirical information which resulted in Chi square ($\chi 2$) = 43.376, $\chi 2$/df = 1.276, df = 34, p = 0.130, NFI = 0.989, GFI = 0.979, CFI = 0.998, RAR = 0.008, RMSE = 0.028 and R2 value = 0.819. This indicated that the causal relationship model from this study was appropriately corresponding to the empirical information at a substantial level.

Keywords: Causal relationship model, Government Procurement, Project Management

INTRODUCTION

Public procurements are highly significant for a national budget allocation in many departments such as educational management, state security, infrastructures, basic structures, health cares, and public safety [1]-[3]. Such the government procurements and supplies management are significant in many departments. Therefore, public procurements are considered the heart of delivering civil services and demonstrating results of the state's operational achievements.

The average values of the public procurements for each country ranged between 10-15% of the total Gross Domestic Product (GDP) [4]. The procurements are particularly more evidenced in construction industry which resulted in 2 billion US dollars per year [5].

In order to reciprocate the world's economic growth, procurement processes in many countries have rapidly developed in different aspects. Amid the changing environment, the rapid developments were designed to facilitate and enhance tasks execution that are performed by public and private sectors as well as the civil society [6]. As a result, the state has been enabled to perform its tasks in strengthening the private sector which mutually contributes to the development of the country's sustainable growths [7]. Technology advancement that play a significant role is all public and private organizations mostly rely on information technology to receive higher volume, rapidly transferred, and constantly updated information. Hence, the technology consequently helps to enhance work productivities. [8].

Although e-Government Procurement System has been adopted and used in the public sector, many problems related to the process remain unresolved and the actual needs of stakeholders remain unfulfilled [9]. Several research and media reports have reflected upon the problems which include non-transparent procurement in public sector's construction projects, purchase prices which are higher than the actual price, and nepotism [10]. Ware et al. (2007) [11]. divided the corruptions from the government procurement into four types: 1) bribery, 2) bid rigging, 3) a false company, and 4) others. These issues allow people who are responsible for the procurement could have financial gains from indirect profits by reducing quality of supplies. The compromised quality consequently contributes to massive losses of the annual government's expenditure which were around 10-20% of a project spending [12]. Moreover, construction materials that are acquired through the procurement process may not commensurate with whether prices or quality [13]. These issues have raised the many authors' interests to discover the best solutions for developing the public sector's procurements. [2]-[4],[8]. However, small amount studies have concerned about the procurement relating to a construction sector.

Therefore, this research aimed to synthesize problems that are related to the Government procurement regarding the construction projects and to develop the causal relationship model of such problems. The research hypothesis is the Causal Relationship Model of Problems in the Public Sector

Procurements fits with the empirical information. The results of the research will benefit many state agencies' operations as well as other organizations in Thailand and abroad in adopting to their respective works.

LITERATURE REVIEW

The previous studies by Chaitongrat et al. (2017) and Leungbootnak et al. (2018) [5]-[6] mentioned the problems in public sector procurement focusing on the Government construction projects in 3 key factors (Fig. 1) which are;

Factors 1: The Planning Process (PP) factors referred to lack of staff's understanding in rules and regulations. [6] stated that the lack of understanding could cause the problems in 3 different ways: which are; 1) Preparation problems (PPA), 2) Announcement and clarification problems (PPB), and 3) Procurement process problems (PPC). As a result, many suppliers were unable to prepare document on time. Hence, there were less competitors in the process.

Factors 2: the project managements and technicality (PMP) indicated to the complication in working procedure, budgeting, and assessments which could contribute to low-quality of partners of contract. This factor consisted of 2 observed variables, which are; 1) Project management problems (PPE) and 2) Technical problems (PPD).

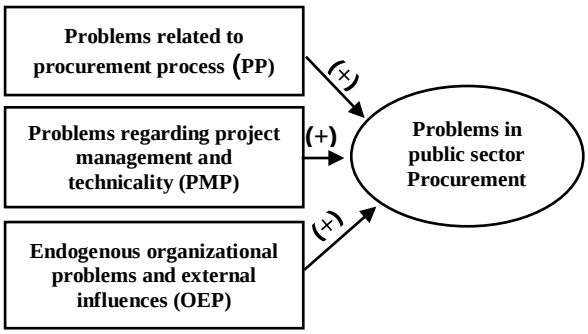

Fig. 1 Hypothesis Measurement Model.

Factors 3: Endogenous organizational problems and external influences (OEP) imply to the inter- and intra- organization conflict which could deliver the delaying of a projects. This factor consisted of 2 observed variables, which are; 1) Internal problems (PPF) and 2) External problems (PPG).

RESEARCH METHODOLOGY

This research was intended to develop a causal relationship model of problems in public sector procurements for research methodology as following;

A. Units of analysis of this quantitative research were based on state's construction project procurements.

B. Population and samples

In this research, population and samples consisted of 5,024,885 procurements of state's construction projects (data acquired between October 2018 – September 2019) The number of samples were determined at approximately 20 times of observed variables in accordance with the concept that was developed by Hairs et al. (2010) [14]. This concept suggested that the lowest criteria in determining samples to analyze Structural Equation Modelling (SEM) should be 5-10 respondents per 1 evaluative parameter. This research model comprised of 36 parameters which indicated that 180-360 construction projects that involved state's procurement were required.

C. Instrument and its quality

This research employed questionnaires [15]. The construction of the research tool and its quality evaluation were made in the following steps.

1) Studying of documents, concepts, theories, and research that are relevant to components which constitute the procurement problems.

2) Formation of 40 questions which were divided into two parts; personal factors, and problems related to procurement of construction projects. The questions were constructed as standard measurements in reference to Rating Scale designed by Likert's 5 assessment levels of the highest, high, moderate, low, and the lowest.

3) The questionnaires were assessed by a panel of 5 experts, in order to determine language appropriateness, concordance between questions and research objectives, and content validity.

4) Assessment scores as determined by the experts were furthered tested for Index of Item-Objective Congruence (IOC). Only questions that received IOC index value of 0.60 or higher were selected.

5) Amendments of questions as per recommendations by the panel of 5 experts were executed which finally yielded the last 36 questions.

6) Trying out of questionnaires with a population of 30 who were not participating in the actual research. Then, each question were evaluated for discrimination values, in order to itemize the question that received discrimination values at 0.20 or higher. All of these 36 questions scored discrimination values between 0.22 and 0.73 whilst the overall confidence of this questionnaires was 0.986 which illustrated that the questionnaire is highly trustworthy.

D. *Data collection*

The government officers were systematically contacted for assistance and cooperation. The data collection process, initiated in January 2020 and completed in February 2020, received 360 of completed questionnaires which were accounted for 100% of the response rate.

E. *Data analysis*

Computer packages, SPSS25 and AMOS25, were used to assess concordance between the model and empirical information by considering statistical Chi – square, Adjusted Goodness of Fit Index (AGFI), and Root Mean Square Residual (RMR).

Data analysis was divided into 3 phases which were; 1) the results of information analysis regarding samples' backgrounds, 2) the results of basic statistical analysis of variables that were used in the research by considering mean, standard deviation, elaboration regarding each studied variable and percentage analysis of Nominal Variable and Ordinal Variable, 3) the results of Causal Relationship Model of Problems in Public Sector Procurements which was determined against Goodness of Fit of the model as per 9 assessment criteria which were; p-value or X2, X2/df, Normal Fit Index (NFI), Goodness of Fit Index (GFI), Fit Index (CFI), Standardized RMR, and Root Mean Square Error of Approximate (RMSEA) [16].

RESULTS

1) Respondent profiles

54.4% of the sample groups were male. The majority of samples were between 41 and 50 years of age which formed 33.7%. As for educational background, bachelor degree holders represented a majority of the respondents which accounted for 63.74 %. Most of these individuals have worked in a material department (46.7%), and Building Inspectors Committee (22.9%), respectively. The average experience in procurement of construction projects was 9.5 years (SD=7.6). The procurements mostly belong to local administration organizations (36.5%), and followed by other governmental agencies (34.6%). Lastly, the construction projects mostly involved with building constructions (35.1%) and road constructions (34.0%). (Table 1).

2) According to the development of Causal Relationship Model of Problems in Public Sector Procurements by using Structural Equation Modelling (SEM) to determine concordance of the model and empirical information, 3 exogenous variables were revealed 3 main factors which are; Planning Process (PP), Other Exogenous Problems (OEP), and Project Management Problem (PMP).

There were also 4 mediating variables involved which were, Procurement Project Management (PPM), Conduct Procurement (ConP), Administer Procurement (AP) and Closing Procurement (CP). According to the concordance assessment of Causal Relationship Model of Problems in Public Sector Procurements, results were; Chi square ($\chi 2$) = 43.376, $\chi 2/df$ = 1.276, df = 34, p = 0.130, NFI = 0.989, GFI = 979, CFI = 0.998, RAR = 0.008, RMSE = 0.028 and the value of R^2 = 0.819. Thus, the model is in accordance with the empirical information from this research. The model is capable of explaining and predicting problems that are related to public sector procurements at 81.9 % as further elaborated in Figure 2 and Table 1.

Table 1 Demographic profiles (n=353)

Factors	Frequency	Percentage	Mean	SD
Gender			-	-
Female	161	45.6	-	-
Male	192	54.4		
Age (years)			-	-
< 20	0	0	-	-
21-30	26	7.4	-	-
31-40	102	28.9	-	-
41-50	119	33.7	-	-
51-60	106	30.0		
Level of education			-	-
Diploma degree	32	9.1	-	-
Bachelor degree	225	63.74	-	-
Master degree	91	25.8	-	-
Doctoral degree	5	1.4		
Positions			-	-
Director of a division	28	7.9	-	-
Purchasing committee	75	21.2	-	-
Committee of Building Inspector	84	22.9	-	-
A material department's officer	165	46.7	-	-
A user	14	4.0		
Average experiences in construction projects (years)	-	-	9.5	7.6
Type of organizations			-	-
General government	122	34.6	-	-
State Enterprises	40	11.3	-	-
Educational Institution	43	12.2	-	-
Government hospital	9	2.5	-	-
Local Administration Organizations	129	36.5	-	-
Other governmental agencies	10	2.8		
Types of construction projects			-	-
Building constructions	124	35.1	-	-
Road constructions	6	1.7	-	-
System utilities	28	7.9		

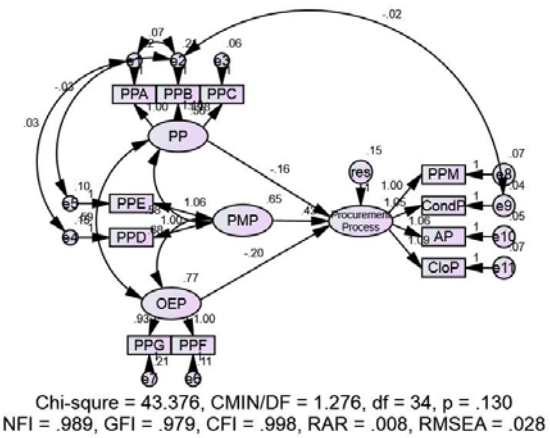

Fig. 2 Results of accuracy analysis of the Causal Relationship Model of Problems in Public Sector Procurements.

3) According to an analysis of the Direct Effect and Indirect effect of variables that influence problems related to public sector's procurements of construction project, there are 7 variables that generally influence such procurements at statistical significance level of 0.05. These variables namely; preparation and planning, announcement and explanation, evaluate contractor, management, technicality, exogenous problems, and indigenous problems. Three variables that one-directionally influenced problems of public sector's procurements of construction projects were procurement procedures, endogenous organizational problems and external influences, and project management and technicality (Table 2).

Table 2 Statistical concordance of the accuracy analysis of the Causal Relationship Model of Problems in Public Sector Procurements (PPSC)

Index	Criteria	Prior to Model Adjustment		After Model Adjustment	
		Statistical Value	Assessment Results	Statistical Value	Assessment Results
X^2/df	< 3.00	2.693	Pass	1.28	Pass
p-value of X^2	> 0.05	<0.001	Fail	0.13	Pass
NFI	> 0.90	0.974	Pass	0.99	Pass
GFI	> 0.90	0.950	Pass	0.98	Pass
CFI	> 0.95	0.984	Pass	0.99	Pass
RMR	< 0.08	0.012	Pass	0.01	Pass
RMSEA	< 0.08	0.069	Pass	0.03	Pass
R^2	0.5-1	-	-	0.82	Pass

Table 3 Concordance value of the measuring model for each latent variables related to PPSC Model.

Latent Variable	Observed Variables	Regression Weights				Regression Standardized Weight	R^2
		Estimate	SE	CR	p		
PP	PPA	1	-	-	-	0.85	0.71
	PPB	1.10	0.04	26.70	*	0.87	0.76
	PPC	1.19	0.05	25.61	*	0.97	0.93
	Path coefficient =0.51						
PMP	PPE	1	-	-	-	0.90	0.81
	PPD	1.06	0.04	29.45	*	0.94	0.88
	Path coefficient =0.33						
OEP	PPF	1	-	-	-	0.94	0.88
	PPG	0.93	0.04	26.02	*	0.87	0.76
	Path coefficient =0.40						
							0.82

Note: * Statistical significant level ($p<0.05$)

Table 3 illustrates concordance of each variable in the measuring model which, when construct the model by using these variables, revealed that the model of problems in public sector's procurement was statistically significant. In addition, the standardized regression weights that ranged between 0.85 to 0.97. Each of these variables related to latent variables and square multiple correlation value (R^2) at statistical significance level. The coefficient of determination of the observable variables of the problem in procurements was calculated to be between 71 to 93 %. The highest standardized regression weights were that of evaluate contractor (β = 0.97), endogenous organizational problem (β = 0.94) and technicality (β = 0.94), and preparation and planning (β = 0.85) respectively.

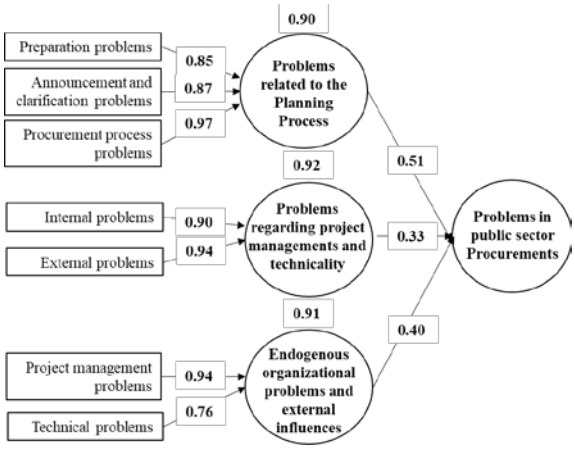

Fig. 3 PPSC model for Thai public construction project procurements

The model in Figure 2 showed a set of guidelines on PPSC for Thai public construction project procurements with the weight in each latent factor:

1) Problems related to the Planning Proces: the government should focus on the procurement planning since the beginning of the process; the TOR writing and specification, then making an anouncement, and providing enough time to writing a

proposal correctly. Last but not least, the government should monitor the middle price for the government partnerships

2) Problems regarding project managements and technicality: the government should be strict on the procurement timeline, conflict between stakholders, and the quality of the construction projects.

3) Endogenous organizational problems and external influences: the government should emphasis on a budget allocation for a construction project in order to reduce some problems about the low-quality of interested vendors sending their proposal lower than the middle price. Moreover, the related organizations suppose to focus on risks from the interorgnaisation that can effect the governent procurement.

DISCUSSUION

According to the results, state's construction project procurements are highly problematic due to many causes for which 3 compositions are capable of explaining the said problems at 82 %. These compositions are;

1) Problems related to procurement process: As per the research, path coefficient value was at 0.51 and the problems mainly stemmed from evaluate contractors, announcement and explanation, and work preparation and planning. This finding is in line with; the 2012 reports from the Office of the Auditor General of Thailand (OAG) which sated that problems and inaccuracy in the procurements were due to the absence of the procurement planning, and Chonpitakwong B. et al., 2009 [17]. which studied obstacles in implementing the e-Procurement system.

2) Endogenous organizational problems and exogenous organizational problems: These problems resulted in the path coefficient of 0.33 which due mainly to endogenous problems of state offices and exogenous problems of state offices. The finding was supported by [10] . who explained that operators must thoroughly and carefully study each step of the procurement process.

3) Project management problems and technicality: The research resulted in the path coefficient value of 0.40 which due mainly to problems related to project management and technicality.

The Concordance assessment of the Structural Problem Equation Model of Public Sector Procurements revealed that the Causal Relationship Model of the Problems that influences Public Sector Procurements that has been developed well related to the empirical information. As per the research, statistical chi square value was not significant (P-value =0.130), relative chi square value was 1.276, NFI index was 0.989, GFI index was 0.979, CFI index was 0.998, whereas Standardized RMR value was 0.008 and RMSEA value was 0.028. All of these value were compatible with the pre-determined criteria which could be illustrated as per the following reasons;

1) Due to the Structural Problem Equation Model of the Public Sector Procurements that has been developed by utilizing theories and other previous research are relevant to this research, and by adhering to the content validity. Each step requires contextual analysis of the problem's components by prioritizing prior to being used to construct the questionnaire that subsequently checked by qualified experts and subjected to further adjustments prior to being used with trial samples. The questionnaire was proven to have high reliability, and in accordance with empirical information as its construct validity was verified by existing IOC of latent variable measurement model that has been developed by using relevant theories and research. Furthermore, the questionnaire's confidence level which was determined by assessment of the collected information was also high as well. Therefore, the above mentioned reason may enhance the efficiency of the structural equation model that is related to public sector's construction project procurement. Although further adjustment of the model maybe required, but this helps to shape the model to be more statistically appropriate.

2) According to the sample group of this research, expressions and practices were in accordance with the theories and other research that were used to develop the structural equation model of problems in public sector's procurements of construction project. The phenomenon could have been a reflection of the actuality in the public sector's procurements that has been practiced. All of the findings indicated that the developed model is in accordance with empirical information and vice versa. Also, there are 3 variables of direct influence coefficient which were; problems that are related to procurement process, endogenous and exogenous organizational problems, and project management problems and technicality.

CONCLUSION

The research reveals problems in public sector's construction project procurement are highly problematic. There were 36 problems that were found which could be categorised, as per the main components, into 3 groups; the problems that are related to procurement process, the endogenous and exogenous organizational problems, and the project management problems and technicality. As a result, the obtained information could be used to explain the variance value of all variables at 82 %. Each component's details can be concluded hereafter;

1) The problems that are related to procurement process, the research revealed that state offices were generally highly problematic which, upon considering factor loading of each observed variables, stipulated that such problems were; problem with evaluate contractor $\beta = 0.935$, problems with

announcement and work explanation $\beta = 0.874$, and problems with preparation and planning $\beta = 0.850$.

2) The eendogenous and exogenous organizational problems, the research revealed that state offices were generally highly problematic which, upon considering factor loading of each observed variables, stipulated that such problems were; problem with project management $\beta = 0.935$ and problems with technicality $\beta = 0.898$.

3) Problems that are related to project management and technicality, the research revealed that state offices were generally highly problematic which, upon considering factor loading of each observed variables, stipulated that such problems were; endogenous organizational problems $\beta = 0.938$ and exogenous organizational problems $\beta = 0.873$.

The concordance assessment of the structural relationship model that affects the public sector's construction procurements, developed by using empirical information, revealed a good level of concordance which was determined by referring to; statistical chi square value that was not significant (P-value =0.130), relationship chi square (1.276), NFI index (0.989), GFI index (0.979), CFI index (0.998), Standardized RMR (0.008) and RMSEA (0.028).

Upon considering direct influences, indirect influences and overall influences of the problems in public sector's construction project procurement, this can be concluded that; direct influences has direct influence coefficient values of 3 variables which in descending order of values, were; the problems of procurement process, the endogenous organizational problem and exogenous influences, and the problems in project management and technicality which had path coefficient values at the values of 0.507, 0.395 and 0.334 respectively.

ACKNOWLEDFEMENT

The study is supported by Mahasarakham University which are gratefully acknowledged.

REFERENCES

[1] Dzuke A., & Naude M.J.A., Procurement challenges in the Zimbabwean public sector: A preliminary study, Journal of Transport and Supply Chain Management, Vol. 9 Issue 1, 2015, pp. 1–9, DOI: https://doi.org/10.4102/jtscm.v9i1.166.

[2] Hazra J., A procurement model in an electronic market with coordination costs, International Conference on Industrial Engineering and Engineering Management, Accession Number: 12490097, 2011, DOI: 10.1109/IEEM.2011.6118139.

[3] Kevitt M., & Davis, Supplier development and public procurement: Allies, coaches and bedfellows, International Journal of Public Sector Management, Vol 27 Issue 7, 2013, pp. 550-563, DOI: 10.1108/IJPSM-03-2014-0041.

[4] Khoman, S., Wanrak M., Vatchareeya T., Chayun T., Chatchai C., Sutthi S., Sittikorn N., & Napon S., The World Trade Organisation's government procurement agreement: A study of thailand's preparation for accession, 2009, Research report submitted to the Comptroller-General's Department, Monistry of Finance. Bangkok; Thailand. (in Thai).

[5] Leungbootnak N., Chaithongrat T., & Aksorn P., An Exploratory Factor Analysis of Government Construction Procurement Problems, MATEC Web of Conferences 192, 02053, 2018, pp.1-4, DOI: https://doi.org/10.1051/matecconf/201819202057.

[6] Chaithongrat T., Leungbootnak N., Aksorn P., & Manu P., Application of Confirmatory Factor Analysis in Government Construction Procurement Problems in Thailand, International Transaction Journal of Engineering, Management, & Applied Sciences & Technologies., Vol 8, Issue 3, 2017, pp. 221-231.

[7] Brammer S., & Walker H., Sustainable procurement in the public sector: An international comparative study, International Journal of Operations & Production Management, Vol 31, Issue 4, 2011, pp. 452-476, DOI: 10.1108/01443571111119551.

[8] Du, J., Jiao,Y.Y., Jiao, R.J., Kumar, A. & Ma, M., A case study of obsolete part procurement process reengineering. Paper presented at the 2007 IEEE International Conference on Industrial Engineering and Engineering Management, 2 - 5 Dec 2007, Furama Riverfront Hotel, Singapore, DOI: 10.1109/IEEM.2007.4419410.

[9] Chaithongrat T., Leungbootnak N., & Aksorn P., Exploratory Factors Analysis of the Corruption in Public Procurement, Engineering Journal of Research and Development, Vol 29, Issue 3, 2018, pp. 5-14.

[10] Chaitongrat T., Leungbootnak N., Kusonkhum W., Deewong W., Srinavin K., Measurement model of good governance in government procurement, IOP Conference Series Materials Science and Engineering, 639:012024, Volume 639, Issue 1, 2019, DOI: 10.1088/1757-899X/639/1/012024.

[11] Ware N., Hopper K., Tugenberg T., Dickey B., Fisher D., Connectedness and citizenship: Redefining social integration. Psychiatric Services. 2007 April; in press. 2007.

[12] Chaithongrat T., Leungbootnak N., & Aksorn P., A Confirmatory Factors Analysis of the Success factors on Government Construction Procurement Project, SWU Engineering Journal, Vol 13, Issue 2, (2018), pp. 131-140.

[13] ADB, Quality Guidance Note on Procurement, 2018, DOI: http://dx.doi.org/10.22617/TIM189229-2.

[14] Hair J.F., Black W.C., Babin B.J., & Anderson R.E., Multivariate Data Analysis, Seventh Edition, 2010, Prentice Hall, Upper Saddle River, New Jersey.

[15] Neuman W.L., Social research methods: qualitative and quantitative approaches, 2011, Boston, MA: Pearson.

[16] Andy F., Discovering statistics using IBM SPSS statistics. 4th edition, 2013, Sage Publications Ltd. London, United Kingdom.

[17] Chonpitakwong B., Kusonkhum W., Chaitongrat T., Srinavin K., & Charnwasununth P.,

Readiness of Applying Big Data Technology for Construction Management in Thai Government. Hindrance of Applying Big Data Technology for Construction Management in Thai Government, The 4th International Conference on Civil and Building Materiais , January 17-20, 2020, Okonawa, Japan.

6th Int. Conf. on Structure, Engineering & Environment (SEE), Kyoto, Japan, Nov.18-20, 2020, ISBN: 978-4-909106056 C3051

MOLECULAR IDENTIFICATION OF A CARBONIC ANHYDRASE-PRODUCING BACTERIUM ISOLATED FROM A NATTO IN INDONESIA TO BE USED IN BIOCONCRETE DEVELOPMENT

Tomone Ikai[1,a], Masahide Uomi[1,2,a], Diana Waturangi[3], Hiroshi Yonemitsu[1], Masa-aki Yoshida[4], Januarti J. Ekaputri[2], *Davin H. E. Setiamarga[1]

[1] National Institute of Technology (KOSEN), Wakayama College, Gobo, Wakayama, Japan
[2] Institut Teknologi Sepuluh Nopember (ITS), Sukolilo, Surabaya, East Java, Indonesia
[3] Atma Jaya Catholic University of Indonesia, Jakarta, Indonesia
[4] Oki Marine Biological Station, Shimane University, Oki, Shimane, Japan
[a] *Equal contributors*
* *Corresponding Author / Senior Author*

ABSTRACT

Recently, research about the inclusion of bacterial agents with biomineralizing capability in building materials with extra features, such as concrete with added strength and self-healing capability, has been popular in the field of civil engineering. Previously, we reported the isolation of a $CaCO_3$-producing bacterium from an Indonesian *natto*, and have tested its usefulness as a biomineralizing agent in fly-ash and OPC pastes. Here, we report the initial result of molecular and biochemical characterizations of the bacterium, in order to confidently identify its species, and the presence of *ß-carbonic anhydrase* gene in its genome, which was confirmed by genomic exploration by PCR and crude enzyme activity measurement. First, BLASTn analysis of the *16S-rRNA* gene suggested that the organism belonged to the genus *Bacillus*, and that it was either *B. safensis* or *B. pumilus* (sequence identity = 99.86; E-value = 0). Subsequent phylogenetic analysis of the gene revealed that it was *B. safensis*. Genomic exploration by PCR using specific primers also indicated the presence of *ß-carbonic anhydrase* gene in its genome. Sequence analyses of *ß-carbonic anhydrase* also confirmed that our bacterium is *B. safensis* (sequence identity = 99.34; e-value = 2E-153). Our present results provided a set of additional evidence, that our previous report about increased strength and presence of aragonite crystals in OPC paste and fly-ash-based geopolymer paste specimens with bacterial addition, were caused by the presence of *B. safensis* inside the specimens. In the future, other molecular and biochemical characterizations of the bacteria are still needed. However, we are confident that our results presented here is an important piece of information for future studies on this bacterium, and on its utilization as a biomineralizing agent in alternative building materials.

***Keywords**:* Bacillus, *biomineralization, bio-concrete, ß-carbonic anhydrase, natto*

INTRODUCTION

Recently, many studies on the utilization of microorganisms with biomineralization capability in the field of general constructions have been conducted. These studies have different aims, for example, (1) letting the microbes produce micropore filler (usually calcium carbonate ($CaCO_3$)) in building materials such as cement-based or geopolymer-based concretes, in order to strengthen the materials [1]; (2) allowing the microbes to produce calcium carbonate crystal deposits to fill in cracks in concrete structures (the "self-healing" concrete) [2]; (3) stabilizing soil particles by letting the microbes to produce $CaCO_3$ precipitates to bind the soil particles to one another and thus preventing soil liquefaction [3]. The process of precipitating $CaCO_3$ assisted by chemical reactions catalyzed by enzymes produced by microorganisms is called the "Microbial-Induced Calcite Precipitation (MICP) [1][4].

In most of these studies, the biomineralizing microbial agent used is ureolytic bacteria such as *Sporosarcina pasteuri* [5]. Such bacteria produce the enzyme urease, which catalyzes urea hydrolysis. The reaction happens in two steps: First, the enzyme urease hydrolyzes urea and produce carbonate ions. The produce carbonate ions then bind with available calcium ions in the surroundings, forming the calcium carbonate [6]. The reaction can be shown as follows:

Step 1: $CO(NH_2)_2 + 2H_2O \rightarrow 2NH_4^+ + CO_3^{2-}$

Step 2: $Ca^{2+} + CO_3^{2-} \rightarrow CaCO_3$ (1)

The calcium carbonate is then precipitated into the micropores of the concrete specimens. Meanwhile, calcium sources, such as calcium chloride, are often added to the biomineralizing system.

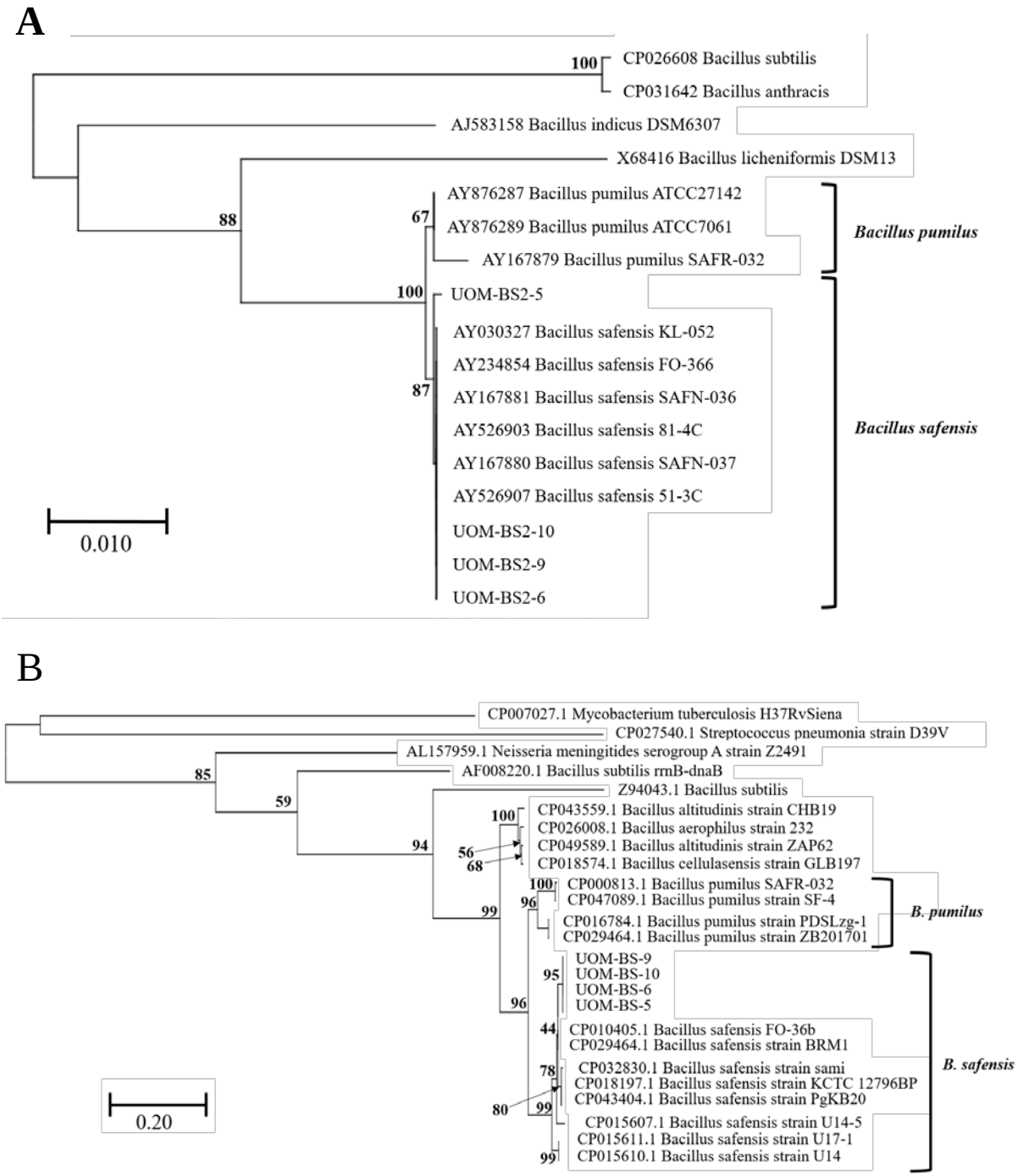

Figure 1. Maximum Likelihood phylogenies of the A: *16S-rRNA*, and B: *carbonic anhydrase* genes. Nodal bootstrap values lower than 40% are not shown. The UOM_BS numbers refer to the same strain of *Bacillus safensis*, which we named the IDN-1 strain.

Urease-based MICP has been very popular in civil engineering, and its prospect has been studied extensively [6]. However, urease-based MICP requires external addition of urea to the object of biomineralization to either the target concrete or the target soil. Urea and calcium chloride additions might bring unwanted side effect to target systems. For example, urea might compromise the durability of the concrete and might cause corrosion of the reinforcing metal, because it produces the strongly acidic nitrates and nitrites [7]. When used for geoengineering purposes, adding a massive amount of urea and calcium chloride might cause environmental pollution. Besides that, the production of ammonia as a byproduct might cause health concerns since ammonia is harmful to the human body if inhaled [8].

Another popular MICP method is by using microorganisms with the ability to produce the enzyme ß-Carbonic Anhydrase (CA) [1][9]. CA catalyzes the interaction of CO_2 and HCO_3^-.

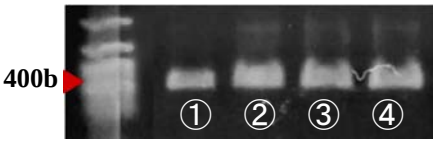

Figure 2. The result of PCR genomic survey for *carbonic anhydrase* gene in the bacterial isolate. (①UOM_BS_5, ②UOM_BS_6, ③UOM_BS_9, ④UOM_BS_10).

Afterward, HCO_3^- produces the carbonate ions, which then bind with available calcium ions to produce calcium carbonate.

Step 1: $CO_2 + H_2O \rightarrow HCO_3^- + H^+$

$(HCO_3^- \rightarrow CO_3^{2-} + H^+)$

Step 2: $Ca^{2+} + CO_3^{2-} \rightarrow CaCO_3$ (2)

Bacteria of the genus *Bacillus* are known to have this enzyme, and also known for the ability to survive in harsh environments, including in highly alkaline environments inside concretes [10]. Previously, we collected a bacterial strain from a natto sold in a market in Indonesia. Commonly, the bacterium used for natto fermentation is of the genus *Bacillus*. In that study, we evaluated the biominerali-zing performance of the bacterial strain in cement and geopolymer pastes [11]. We found that calcium carbonate ($CaCO_3$) was deposited in the micropores of specimens made from geopolymer paste and concrete paste, if the bacteria was added into the mixture. Specimens with bacterial addition showed an increase in compressional strength. The presence of $CaCO_3$ precipitate in the specimens with bacteria was confirmed by XRD, while the presence of natto bacteria was confirmed by SEM. In addition, the crystal aggregates of $CaCO_3$ formed in the presence of organisms, including CA enzyme-producing bacteria, were aragonite and calcite [11][12]. Although we were able to show that our bacteria were most likely the cause of the increased strength in both the geopolymer and cement pastes, in that study, we did not report any detailed characterization of the bacteria themselves. A quick BLASTn analysis of the *16S-rRNA* gene of the bacteria indicated that it was of the genus *Bacillus*. However, no decisive species identification of the bacterium was presented.

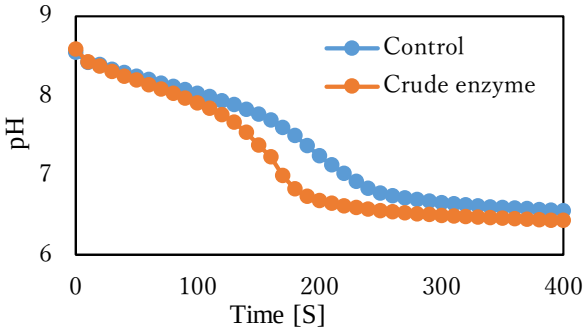

Figure 3. A diagram showing extracted total crude enzyme activity to catalyze the reaction to lower the pH of Tris-HCl (pH: 8.5) in the presence of CO_2. The control was the mixture of Tris-HCl and CO_2 but without the crude enzyme. The reaction proceeded faster with the addition of crude enzyme when compared to the control.

Here, we report our molecular genetics and biochemical characterizations of the isolated bacterium. From our *16S-rRNA* molecular phylogenetics analysis, the bacteria were identified as *Bacillus safensis*. Our genomic survey using specific primers for the *ß-carbonic anhydrase* gene also showed the presence of the gene, and sequence analyses supported the *16S-rRNA* phylogeny. Enzymatic activity of the crude enzyme was also assesed, by investigating the crude enzyme's ability to decrease pH. We also investigated the amount of CO_2 produced by bacterial expiration, which is not present in most target systems such as cement paste or geopolymer paste.

MATERIAL AND METHODS

(1) Bacterial Isolation

The bacterial strain used in this study was isolated from a *natto* pack purchased from a market in Surabaya, East Java, Indonesia. We named the strain as "IDN-1" strain. Glycerol stocks from isolated single colonies were prepared and stored at -80°C. Subsequent analyses used the four colonies obtained from these glycerol stocks of IDN-1, which we named UOM_BS_5, UOM_BS_6, UOM_BS_9, UOM_BS_10 (Fig. 2).

(2) Sequence Analyses

2-1 Sequence data acquisitions

16S-rRNA gene amplification was conducted following standard PCR protocol for bacteria, using the bacterial universal primer 27F/1492R [13], with annealing temperature of 50°C. Sequencing using both Forward and Reverse primers were outsourced to FASMAC, Inc., Japan. Obtained sequences were used as queries for BLASTn searches of the Genbank nr database for species identification.

ß-carbonic anhydrase (*ca*) gene was amplified using specific primers designed in this study. First, the nucleotide sequences of the six strains of *Bacillus safensis* and one strain of *Bacillus subtilis* were downloaded from GenBank. The sequences were aligned using MAFFT (online ver.) [14] under the G-INS-i algorithm to allow for an alignment over the entire sequence length. A set of specific primers for *ca* (saf_F1, saf_R1; Table 1) were designed based on these sequences. Sequences were visualized in MEGA 7 [15]. PCR using these primers was performed at the annealing temperature of 55°C. PCR products sequencing was outsourced to FASMAC, Inc, and obtained sequences were used in subsequent analyses such as homology searches using BLASTn,

and phylogenetic analysis.

2-2 Phylogenetic analyses

We obtained *16S-rRNA* gene sequence data for four colonies (designated as UOM_BS_5, UOM_BS_6, UOM_BS_9, UOM_BS_10). Sequences of six strains of *B. safensis* and three strains of *B. pumilus* were collected from Genbank. The *16S-rRNA* sequences of *B. licheniformis*, *B. indicus*, *B. anthracis*, and *B. subtilis*, also from Genbank, were used as outgroups. Sequences were aligned using MAFFT ver. 7 using the Q-INS-i algorithm to allow for the consideration of secondary structures. Aligned sequences were edited to remove ambiguously aligned regions using the online version of GBlocks ver. 0.91b [16] under the least stringent setting. MEGA X [17] and Mesquite ver. 3.61 [18] were used to visualize the sequences. Model selections performed using MEGA X under the AIC parameter suggested GTR+G as the best fit model. Maximum Likelihood (ML) phylogenetic analyses with 1000 bootstrap replications were conducted in MEGA X.

Table 1. Specific primers for *carbonic anhydrase* designed in this study

Primer	Base sequence
Forward	
saf_F1	CGTGCATGGATACYCGTCTKKTGG
Reverse	
saf_R1	CACRCTCKCTTCMACTGAATCAAAGC

Phylogenetic analysis for the *carbonic anhydrase* gene were also conducted on the sequences obtained from the same four colonies used for the *16S-rRNA* analysis. Sequences of eight strains of *B. safensis*, four strains of *B. pumilus*, two strains each of *B. subtilis* and *B. altitudini*, and 1 strain each of *B. aerophilu*, *B. cellulasensis*, *Mycobacterium tuberculosis*, *Neisseria meningitides*, and *Streptococcus pneumoniae* were downloaded from Genbank and used in the analysis. Sequences were aligned using MAFFT ver. 7 using the G-INS-i algorithm. Model selection in Mega X under both the BIC and AICc parameters suggested K2+G+I as the best fitting model. Afterward, Maximum Likelihood (ML) phylogenetic analyses with 1000 bootstrap replications were conducted in MEGA X.

(3) Crude Enzyme Activity Assay

A total of 3µL of cultured bacteria in LB broth (shaken at 37°C for 24 hours) was centrifuged (10,000 rpm, RT, 10 min). After washing, the pellet was suspended in distilled water to achieve a cell density of of OD_{600} 1. Bacteria cells were lysed by ultrasonication (TOMY, UD-201). Afterward, the suspension was centrifuged (12,000 rpm, RT, 5 min), and the supernatant was collected as the crude enzyme.

Enzyme activity was assessed by measuring the drop of pH of the substrate + enzyme solution (the "enzyme solution"). 0.2mL of crude enzyme was added to a solution of 9mL of 20mM Tris-HCl (pH 8.5; on ice). Afterward, 6mL of CO_2 saturated water (ice cold) was added to the solution, and the time for the pH to drop 8.5 to pH 6.4 was measured. The control solution contains only the Tris-HCl and CO_2-saturated water.

(4) Characterizations Of The Isolated Bacterium

4-1 Growth curve

Bacterial cells were cultured in 5mL of LB liquid medium was prepared in test tubes with and without shaking at 37ºC. Turbidity was measured using a spectrophotometer (TAITEC, miniphoto518R) for 2 hours each up to 24 hours, then 4 hours each up to 32 hours, and finally 12 hours later, at 44 hours, for the final measurement.

4-2 Measuring bacterial CO_2 emissions

We measured the amount of CO_2 produced through respiration by living bacterial cells. In a completely sealed desiccator, test tubes containing 5mL LB broth bacterial solution were incubated at 37ºC in an incubator. The amount of expirated CO_2 concentration in the desiccator was measured during stationary incubation by using a gas detector tube (GASTEC). The first measurement was taken for every 2 hours for the first 6 hours. The fourth measurement was taken 4 hours later, and the fifth at the 17^{th} hour. Afterward, from the 17^{th} to 81^{st} hours, measurements were taken for every 8 hours.

RESULTS

(1) Molecular Identification Of The Bacterial Species Using The *16S-rRNA* Gene

1420 bp-long sequences were obtained for the *16S-rRNA* gene after assembling forward and reverse sequences. BLASTn searches suggested that this bacterium belongs to the genus *Bacillus*, either *B. safensis* or *B. pumilus* (sequence identity = 99.86, E-value = 0). The resulting phylogeny showed that our bacterial samples are indeed *B. safensis* because they formed a monophyletic clade with other *B. safensis* sequences (bootstrap support = 87%) (Fig. 1A).

(2) *ß-carbonic anhydrase* Sequence Analyses

We confirmed the presence of *ß-carbonic anhydrase* (*ca*) in the genome of our *B. safensis* by PCR survey (Fig. 2). 307 bp-long sequences were

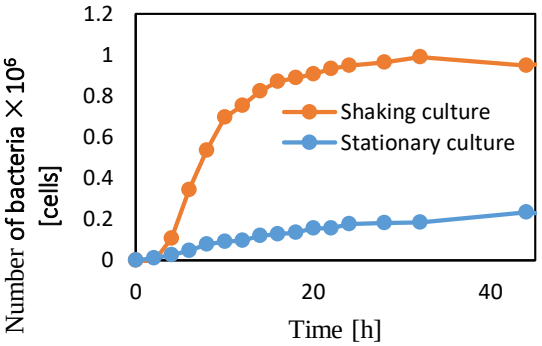

Figure 4. Bacterial growth curves of our isolate, cultured with shaking culture and stationary. The growth of stationary culture was slower when compared to shaking culture.

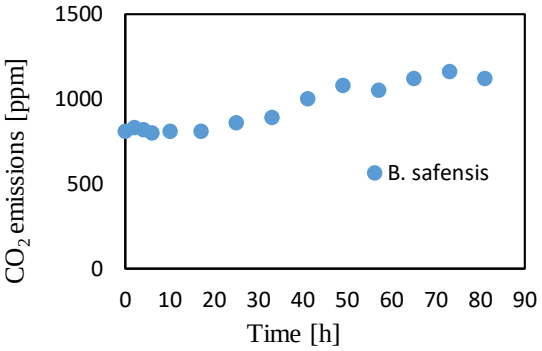

Figure 5. CO_2 expiration by *Bacillus safensis*. The amount of expirated CO_2 increased in proportion to the incubation time of the stationary culture (shown in Fig. 4).

obtained after assembling forward and reverse sequences. BLASTn searches confirmed that the sequences were homologs of *ca* of *B. safensis* (sequence identity = 99.34; e-value = 2E-153). In the *ca* phylogeny, our sequences formed a monophyletic clade with other *B. safensis* sequences (bootstrap support = 99%), and thus further confirmed the identity of our isolate (Fig. 2B).

(3) Crude Enzyme Activity

The initial pH of both the enzyme solution (20mM Tris-HCl + CO_2-saturated water + crude enzyme extract)) and those of the control solution (only 20mM Tris-HCl + CO_2-saturated water) were 8.58. Up to about 100 seconds, the pH of both the enzyme and control solutions slowly decreased to ca. 7.91. However after that, pH of the enzyme solution decreased at a significantly faster rate than that of the control (from 7.91 at 100th second to 6.68 at 200th second, a decrease of pH value of 1.23 in the span of 100 seconds). The control solution's pH decreased by only 0.79, from 8.03 to 7.24 over the same time period. The result (Fig. 3) indicated that the Carbonic Anhydrase (CA) enzyme from our *B. safensis* isolate is active.

(4) Growth Curve

The bacteria were cultured with shaking and without (stationary culture). Bacterial growth of the shaking culture was found to be in the exponential growth phase until the 10th hour, and then entered the stationary phase at around the 15th hour (Fig. 4). Meanwhile with the stationary culture, the bacterial growth was slower when compared to the shaking culture. This is indicated by the tendency of the number of bacteria to increase in proportion to time, and still increasing even after 44 hours of cultivation.

(5) CO_2 Expiration

The CO_2 concentration in the gas phase was 810 ppm at 0 hours. The values did not change much until about 20 hours, but after 20 hours, they began to increase, and the CO_2 concentration was 1160 ppm at 73 hours. This result suggests that the CO2 emission of *B. safensis* during stationary culture (Fig. 4) was about 300 ppm in 73 hours (Fig. 5).

DISCUSSION

(1) Our *Bacillus safensis* Isolate Has An Active ß-Carbonic Anhydrase Enzyme

Genomic exploration by PCR using primers specific for *ß-carbonic anhydrase* revealed the presence of the gene in the genome of *B. safensis* (Fig. 2). Meanwhile, the activity of the enzyme was confirmed by crude enzyme analysis (Fig. 3).

This results provide additional evidences that our previous reports about the higher strength of the fly ash-based geopolymer paste with bacterial addition (when compared to those without), and the presence of aragonite crystals in the specimens could probably be attributed to *B. safensis* presence in the specimens. Without doubt, however, further studies, which include molecular, microbiological, and biochemical assessments of fly-ash geopolymer paste and concrete specimens, to confirm the actual presence of the bacteria in them, are still needed to confirm this observation.

(2) Phylogenetic Analyses of two genes increased the Confidence of the Bacterial Identification

BLASTn searches of the *16S-rRNA* gene alone could not determine whether our isolate was *B. pumilus* or *B. safensis*, despite the relatively long sequence length. However, phylogenetic analysis of the sequences helped to identify that our isolate is *B. safensis*. However, previous studies have indicated that the two species are actually not decisively identifiable only by *16S-rRNA* sequence analyses [19]. Those studies suggested that the housekeeping gene *gyrB* is useful for this purpose. In this study,

however, we also conducted BLASTn searches and phylogenetic analysis of the gene *ß-carbonic anhydrase* (*ca*), which results also confirmed that our isolate is *B. safensis*. Therefore, our study here showed that this gene is probably also useful, for differentiating the two closely related species of *B. safensis* and *B. pumilus*. While we are very confident that our molecular identification result reported here is correct, in the future, we intend to do further confirmation, by conducting sequence analyses of *gyrB*.

(3) Our Present Results Corroborate Our Previous Bio-Geopolymer Paste Study

We succeeded in confirming the presence and activity of the enzyme ß-Carbonic Anhydrase (CA) in the isolate. We also revealed that the isolate respirations caused CO_2 concentration to increase proportionaly with the growth in stationary culture of bacterial. Since the actual reaction in the concrete takes place under conditions such as stationary incubation rather than shaking culture, it is likely that CO2 will also follow the increase in this result. These results allowed us to hypothesize an explanation for our previous study using fly-ash-based geopolymer paste [11][20].

Fly-ash usually does not contain any calcium. However, fly-ash obtained from power plants in Indonesia has high calcium contents because of incomplete combustions caused by low temperature burning [21]. Our previous study used fly-ash from an Indonesian power plant to make the geopolymer paste. When *B. safensis* grew inside the paste, it also expirate CO_2, which was dissolved in the surrounding moisture content. It was then catalyzed by CA and became CO_3^{2-} ions, which then bound to the calcium ions that are abundant in the fly-ash, and formed calcium carbonate, which then fill the pores of the paste specimens.

Although many further studies to validate our hypothesis above are still needed, we are confident that the progress report published here contains valuable information on both the understanding of *Bacillus safensis*, and the development of alternative geopolymer-based building materials.

ACKNOWLEDGEMENTS

DHES work was partially supported by the National Institute of Technology, Wakayama College Competitive Internal Research Grant for Education and Research 2016, 2018, and The Asahi Glass Foundation Research Grant 2016. DHES, TI, and MU thanked Masataka Kusube (National Institute of Technology, Wakayama College) for invaluable discussions.

REFERENCES

[1] Alshalif A.F., Irwan J.M., Othman N, Al-Gheethi A, Hassan A., Nasser I.M. Potential of carbonic anhydrase and urease bacteria for sequestration of CO_2 into aerated concrete. MATEC Web of Conferences Vol. 138, 01019, 2017.

[2] Wiktor V., Jonkers H.M. Quantification of crack-healing in novel bacteria-based self-healing concrete, Cement and Concrete Composites. Volume 33, Issue 7, pp. 763-770, 2011.

[3] Ivanov V., Chu J. Applications of microorganisms to geotechnical engineering for bioclogging and biocementation of soil in situ. Reviews in Environmental Science and Bio/Technology, 2008.

[4] Chaparro-Acuña S.P., Becerra-Jiménez M.L., Martínez-Zambrano J.J., Rojas-Sarmiento H.A. Soil bacteria that precipitate calcium carbonate: mechanism and applications of the process. Acta Agronomica. Vol. 67, No. 2, pp. 277-288, 2018

[5] Whiffin V.S. Microbial CaCO3 precipitation for the production of biocement. PhD thesis of Murdoch University, 2004.

[6] Bang S.S., Galinat J.K., Ramakrishnan V. Calcite Precipitation Induced by Polyurethane-Immobilized *Bacillus Pasteurii*, Enzyme and Microbial Technology. Volume 28, Issues 4–5, pp. 404-409, 2001.

[7] Sadegzadeh M., Page C.L., Vassiet P.R.W. Effects of urea on durability of reinforced concrete, Magazine of Concrete Research. Vol. 45, No. 164, pp. 179-186, 1998.

[8] Li M., Fu Q.L., Zhang Q., Achal V., Kawasaki S., Bio-grout based on microbially induced sand solidification by means of asparaginase activity, Scientific Reports Vol. 5, 16128, 2015.

[9] Sundaram S. Thakur I.S. Induction of calcite precipitation through heightened production of extracellular carbonic anhydrase by CO2 sequestering bacteria. *Bioresource Technology*, Vol. 253, pp. 368-371, 2018.

[10] Zhang Z., Lian B., Hou W., Chen M., Li X., Li Y. *Bacillus mucilaginosus* can capture atmospheric CO2 by carbonic anhydrase. African Journal of Microbiology Research Vol. 5 pp. 106-112, 2011.

[11] Setiamarga D.H.E., Uomi M., Waturangi D., Suhartono M.T., Shovitri M., Kusube M., Yonemitsu H., Hirano H., Ekaputri J.J. Exploration Of The Potentials Of Carbonic Anhydrase producing Bacteria Utilization In Geopolymer-Based Bioconcrete Development, 9th Int. Conf. on Geotechnique, Construction Materials and Environment, 1231–1236, 2019.

[12] Alshalif A.F., Irwan J.M., Othman N., Zamer M.M., Anneza L.H. Carbon Dioxide (CO2)

Sequestration In Bio-Concrete, An Overview. MATEC Web of Conferences, Vol. 103, 05016, 2017.

[13] Weisburg W.G., Barns S.M., Pelletier D.A., Lane D.J. 16S ribosomal DNA amplification for phylogenetic study, Journal of Bacteriology. Vol. 173, No.2, 697-703, 1991.

[14] Katoh K., Rozewicki J., Yamada K.D. MAFFT online service: multiple sequence alignment, interactive sequence choice and visualization. Briefings in Bioinformatics, 20(4), 1160–1166 2019.

[15] Kumar S., Stecher G., Tamura K. MEGA7: Molecular Evolutionary Genetics Analysis version 7.0. Molecular Biology and Evolution. Vol. 33, 1870-1874, 2016.

[16] Castresana J. Selection of Conserved Blocks from Multiple Alignments for Their Use in Phylogenetic Analysis. Molecular Biology and Evolution, Volume 17, Issue 4, pp. 540–552, 2000.

[17] Kumar S., Stecher G., Li M., Knyaz C., Tamura K. MEGA X: Molecular Evolutionary Genetics Analysis across Computing Platforms. Molecular Biology and Evolution. Volume 35, Issue 6, pp. 1547–1549, 2018.

[18] Maddison W.P., Maddison D.R. Mesquite: a modular system for evolutionary analysis, Version 3.61, 2019. (http://www.mesquiteproject .org)

[19] Satomi M., Duc M.T.L., Venkateswaran K. *Bacillus safensis* sp. nov., isolated from spacecraft and assembly-facility surfaces, International Journal of Systematic and Evolutionary Microbiology, 56, 1735–1740, 2006.

[20] Wulandari K.D., Ekaputri J.J., Triwulan, Fujiyama C., Setiamarga D.H.E. Effects of microbial agents to the properties of fly ash-based paste. MATEC Web of Conferences 195, 01012, 2018.

[21] Ekaputri J.J., Ulum M.B., Ridho B., Susanto T.E., Abdullah M.M.A.B. A Comprehensive Characterization and Determination of Fly Ashes In Indonesia using Different Methods. Vol. 754-755, pp. 320-325, 2015.

6th Int. Conf. on Structure, Engineering & Environment (SEE), Kyoto, Japan, Nov.18-20, 2020, ISBN: 978-4-909106056 C3051

INFLUENCE OF RICE HUSK ASH WASTE ON COMPACTABILITY OF SOIL

Sayful Kabir Khan[1, 2], Najmun Nahar[1, 3], Zakaria Hossain[1 3], Noma Tamaki[4]
[1]Graduate School of Bioresources, Mie University, Japan, [2]Directorate General of Food, Ministry of Food, Bangladesh, [3]Life and Earth Science, Jagannath University, Bangladesh,
[4]Make Integrated Technology Company, Osaka, Japan

ABSTRACT

Usually, measurement of optimum moisture content and maximum dry density is essential for assessing the quality control of the compacted fill or earthwork constructions as the parameters of compaction characteristics. Rice husk ash, which is plentifully available in many rice-producing countries, can be used as a construction material. The present study mainly tries to investigate the effect of rice husk ash on compaction characteristics of sandy soil classified as A-2-4 or SW-SM for soil stabilization. Six different percentages of rice husk ash amount with soil considered for the standard Proctor compaction test. The result revealed that with increasing the amount of rice husk ash, the optimum moisture content increased but decreased the maximum dry density of soil. It can conclude that the utilization of soil-rice husk ash combination is beneficial for ground improvement.

Keywords: Soil texture; Optimum moisture content; Maximum dry density; Soil stabilization

INTRODUCTION

Rice is one of the most consumed food items throughout the world, and the annual global paddy production estimates for the year 2010 are 678 million tons, which implies 149.16 million tons of rice husk production that year [1]. Rice husk is an agricultural by-product of rice and produced from paddy during the milling process [2], which is plentifully available in many rice-producing countries [3]. Rice Husk Ash (RHA) forms when rice husk burns under controlled temperature [4]. Every year more than 20 million tons of RHA are produced over the globe [5-6]. Due to lack of its utilization, the large amount of RHA is discarded at open places, riversides, and abandoned areas, which causes environmental pollution [7] and also poses a health hazard due to local air pollution. However, RHA is a pozzolanic material, and it contains around 85–90% amorphous silica, which is reactive as a pozzolan to replace part of Portland cement [8-9] that can potentially use as a construction material for the various geotechnical application. On the other side, the production of cement, a key binding component of concrete, is costly, consumes high energy, depletes natural resources, and emits vast amounts of greenhouse gases [10] that also causes environmental degradation, severe pollution [11-13], and even health hazards. So, if most of the RHA use in ground improvement, it would not only get rid of dumping RHA but would also have decreased the CO_2 emissions to the atmosphere by bringing down the cement production. As a pozzolanic material, usage of rice husk ash in cement/concrete that brings about some advantages, like improving strength, enhancing durability, or decreasing carbon dioxide emissions, etc. [14].

RHA is not a new material for soil improvement. The application of RHA in soil has shown dramatic success in many types of soils around the world. Soil compaction is an essential part of the construction of building foundations, roadways, walkways, and earth retaining structures, highway embankments, earth dams, foundations, and many other engineering structures [15]. Soil compactibility illustrates the mechanical behavior of soil, which is influenced by the soil texture, water content, inherent bulk density, structural stability, organic matter, soluble salts, and compactive energy [16]. Regarding the compactability, mixing of rice husk ash (RHA) with soil increases the optimum moisture content (OMC) and decreases the maximum dry density (MDD) [6, 17-20]. There are many pieces of research on compaction characteristics of soil [21- 25]. Still, very few studies have been conducted on compaction on the ground with RHA [17, 25-28], where a small amount of RHA was used. Therefore, the present study attempts to present the effects of lower to a higher amount of RHA on the compaction characteristic of soil.

MATERIALS AND LABORATORY TEST

Materials Used

In this study, testing specimen made of soil and RHA. The soil sample has collected from the Handa area, Tsu City, Mie Prefecture, Japan. The physical

properties of soil were determined through a series of laboratory tests and presented in Table 1. From the graph of particle size distribution by sieve and hydrometer analysis of soil, the coefficient of gradation (C_u) and the coefficient of curvature (C_c) values are correspondingly 9.275 and 0.906, and from the Atterberg limit test, the plasticity index (PI) is 8.55%. According to the Unified Classification of Sandy soils by ASTM D-2487, the particular soil is well-graded sand with silt, and the symbol is SW-SM as the coefficient of gradation (C_u) of soil particles are greater than or equal to 6, and the coefficient of curvature (Cc) value is between 1 and 3 ($C_u \geq 6$ and $1 \leq C_c \leq 3$) besides with plasticity index is greater than 7 (PI >7). According to the American Association of State Highway and Transportation Officials (AASHTO) soil classification system, the particular soil is Silty gravel and sand (A-2-4), where percent passing no. 200 sieve ≤ 35%, LL ≤ 40 and PI ≤ 10 (Fig.1 and Table 1).

Table 1 Physical properties of soil

Parameters	Values
Specific gravity (ρs)	2.74 g/cm^3
Maximum dry density ($\gamma_{dry\ max}$)	1.696 g/cm^3
Optimum Water Content ($W_{opt.}$)	17.50%
Sand (75 µm - 2 mm)	89%
Silt (5 - 75 µm)	9%
Clay < 5 µm	2%
Liquid limit, LL	37.52%
Plastic limit, PL	28.97%
Plasticity Index, PI	8.55%
AASHTO classification	A-2-4
ASTM D-2487 classification	SW-SM

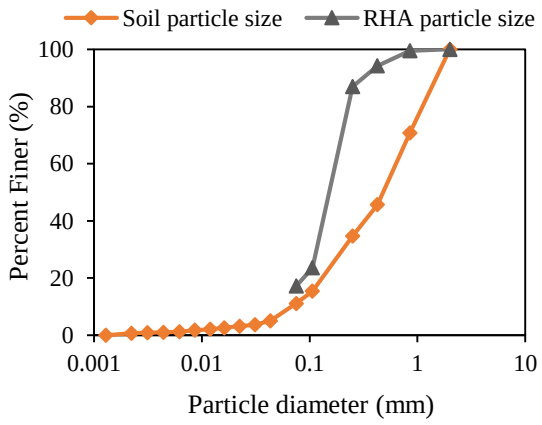

Fig. 1 Particle size distribution curve of soil and RHA

Readymade RHA collected from Make Integrated Technology (MIT) Company, Osaka, Japan. Table 2 represents the basic properties of RHA, and Fig.1 also shows the particle size distribution of RHA with soil particle size. Available ordinary tap water in the laboratory was used in all of the specimens.

Table 2 Physical and chemical properties of RHA

Properties	Parameters	Values
Physical properties	Average Particle Size	0.1 to 0.3 µm
	Loss of Ignition	85%
	Specific Gravity	0.12 g/cm3
	Burning Temperature	600°C
	Burning Time	24 hours
Chemical properties	Silica (SiO_2)	91.10%
	Carbon dioxide (CO_2)	4.35%
	Potassium Oxide (K_2O)	2.40%
	Calcium Oxide (CaO)	0.57%
	Phosphorous Penta Oxide (P_2O_5)	0.52%
	Sulphur Tri Oxide (SO_3)	0.38%
	Chlorine (Cl)	0.18%
	Magnesium Oxide (MgO)	0.16%
	Manganese Oxide (MnO)	0.14%
	Iron Oxide (Fe_2O_3)	0.05%
	Alumina (Al_2O_3)	0.03%
	Others	0.12%

Mix Designs of Specimen

In this study, the mixing design of the specimen, from nominal to a maximal percentage of RHA amount of soil weight considered to understand the effects of RHA on the samples. Initially, Soil addition with RHA of 0.5%, 1.0%, 1.5% used, and later the percentage of RHA amount was mixed ten times higher than that of the previous amount, and the amount was 5%, 10%, and 15% RHA which presented with index in Table 3.

Table 3 Investigated mixtures with indices

Mix design	Index
Soil (Control)	Control
Soil + 0.5% RHA	S+0.5R
Soil + 1.0% RHA	S+1.0R
Soil + 1.5% RHA	S+1.5R
Soil + 5% RHA	S+5R
Soil + 10% RHA	S+10R
Soil + 15% RHA	S+15R

Laboratory Test

Compaction test

According to Japanese Industrial Standards (JIS-A-1210), the Standard Proctor compaction test was conducted to determine the optimum moisture content (OMC) and maximum dry density (MDD) of soil control and other mix types. The applied apparatus for performing the test was a 10 cm diameter cylindrical compaction mold equipped with a base and a collar, rammer mass of 2.5 kg, and a falling height of 30 cm (Fig. 2).

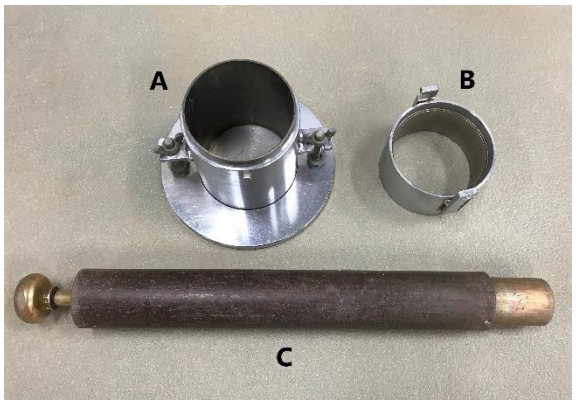

Fig.2 Standard Proctor compaction apparatus- A) Base with mold; B) Collar; and C) Rammer

In the compaction mold, the RHA mixed soil compacted in three layers with 25 blows for each layer. For each mix type, Soil-RHA was manually mixed homogenously in dry condition. Subsequently, different moisture contents were added homogeneously by manual mixing like the previous step for getting the expected moisture content (Fig. 3).

Fig. 3 Water mixing manually with air-dried soil for reaching expected water content

For measuring the water content, samples were collected from the top, middle, and bottom layers by equally separating the three layers after extruding the compacted specimen from the mold. Then each layer of a sample was divided into nine parts from where the central part was taken as a sample for the oven-dry weight (Fig. 4). Similar way, water was added repeatedly to get the optimum water content and maximum dry density.

Fig. 4 Sample collection from the central part of a layer in a specimen for oven-dry weight after compaction

RESULT AND DISCUSSIONS

Compaction Characteristics

The variations of MDD and OMC with RHA addition with soil are presented in Figs. 5 and 6. The figures illustrate that with increasing the amount of RHA, OMC increases, but MDD decreases significantly.

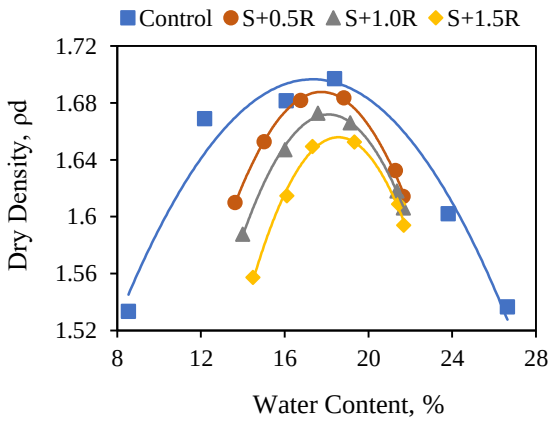

Fig. 5 Compaction curves of control and soil-RHA combination types

The OMC of control was 17.5%, and MDD was 1.696 g/cm^3. Soil with RHA of 0.5%. 1% and 1.5% mixing displayed the little increasing tendency (0.4%) of OMC and slightly decreasing tendency (0.016 g/cm^3) of MDD. Furthermore, soil addition with RHA of 5%, 10%, and 15% exhibited a comparatively more increasing tendency of OMC and

decreasing trend of MDD than that of 0.5%. 1% and 1.5% RHA mixed soil (Table 4 and Fig. 7), which indicates a higher percentage of RHA amount with soil gives a higher OMC and a lower MDD value of a specimen. Because after mixing the RHA with soil, the quantity of fines increases in the soil that needs more water for hydration [26]. This trend was also found in some researches [6, 17-19, 27]. The declining tendency of dry density of soil specifies that the low compaction energy requires achieving the MDD of a particular specimen that reduces the compaction cost [29-30].

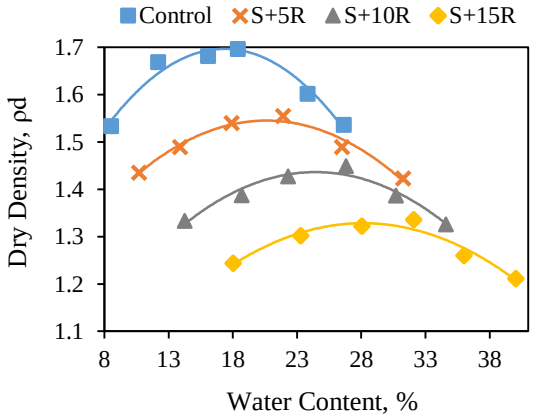

Fig. 6 Compaction curves of control and soil-RHA combination types

Table 4 Compaction characteristics of specimens

Index	OMC (%)	MDD, ρd
Control	17.5	1.696
S+0.5R	17.8	1.688
S+1.0R	18.2	1.672
S+1.5R	18.6	1.656
S+5R	21.0	1.545
S+10R	25.0	1.436
S+15R	29.0	1.330

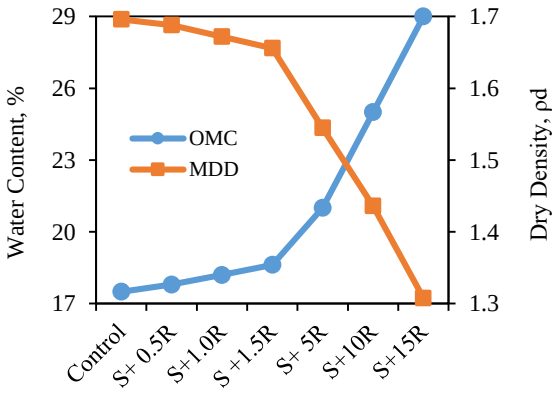

Fig. 7 Variation of OMC and MDD of control and soil-RHA combination types

CONCLUSIONS

The following conclusions can be drawn based on the results obtained from the compaction test on soil-RHA in the paper:

- The OMC increases with increasing the amount of RHA in the soil, but MDD decreases.
- The specimen mixing types S+5R, S+10R, and S+15R, exhibited a comparatively more increasing tendency of OMC and decreasing trend of MDD than that of S+0.5R, S+1.0R, and S+1.5R specimen types.
- Utilization of RHA waste with soil can apply in road projects or other ground improvement purposes where a massive amount of earth materials need. The successful application of the waste material can reduce construction costs significantly, which will also be environment-friendly.

REFERENCES

[1] Food and Agriculture Organization of the United Nations, World paddy production, 2008.
[2] Singh, B., Rice husk ash. In Waste and Supplementary Cementitious Materials in Concrete, 2018, pp. 417-460.
[3] Chandrasekhar, S. A. T. H. Y., Satyanarayana, K. G., Pramada, P. N., Raghavan, P., and Gupta, T. N., Review processing, properties and applications of reactive silica from rice husk—an overview, Journal of materials science, Vol. 38, Issue 15, 2003, pp. 3159-3168.
[4] Babaso, P. N., and Sharanagouda, H., Rice husk and its applications: review, International journal of current microbiology and applied sciences, Vol. 6, Issue 10, 2017, pp. 1144-1156.
[5] Soltani, N., Bahrami, A., Pech-Canul, M. I., and González, L. A., Review on the physicochemical treatments of rice husk for production of advanced materials, Chemical engineering journal, Vol. 264, 2015, pp. 899-935.
[6] Alhassan, M., Permeability of lateritic soil treated with lime and rice husk ash, Assumption University Journal of Thailand, Vol. 12, Issue 2, 2008, 115-120.
[7] Pode, R., Potential applications of rice husk ash waste from rice husk biomass power plant, Renewable and Sustainable Energy Reviews, Vol. 53, 2016, pp. 1468-1485.
[8] Chopra, D., and Siddique, R., Strength, permeability and microstructure of self-compacting concrete containing rice husk ash, Biosystems engineering, Vol. 130, 2015, pp. 72-80.

[9] Ramakrishnan, S., Velrajkumar, G., and Ranjith, S., Behavior of cement-rice husk ash concrete for pavement, International Journal of Emerging Trends in Engineering and Development, Vol.1, 2014, Issue 4.

[10] Khan, R., Jabbar, A., Ahmad, I., Khan, W., Khan, A. N., and Mirza, J., Reduction in environmental problems using rice-husk ash in concrete, Construction and Building Materials, Vol. 30, 2012, pp. 360-365.

[11] Malhotra, V. M., Role of supplementary cementing materials in reducing greenhouse gas emissions, In Infrastructure regeneration and rehabilitation improving the quality of life through better construction: a vision for the next millennium, 1999, pp. 27-42.

[12] Sabir, B. B., Wild, S., and Bai, J., Metakaolin and calcined clays as pozzolans for concrete: a review, Cement and concrete composites, Vol. 23, Issue 6, 2001, pp. 441-454.

[13] Worrell, E., Price, L., Martin, N., Hendriks, C., and Meida, L. O., Carbon dioxide emissions from the global cement industry, Annual review of energy and the environment, Vol. 26, Issue 1, 2001, pp. 303-329.

[14] Siddique, R., and Khan, M. I., Supplementary cementing materials, 2011, Springer Science & Business Media.

[15] Ibrahim, M.I.A., PREDICTION OF COMPACTION PARAMETERS FROM FINE SOIL INDEX PROPERTIES (Doctoral dissertation, Sudan University of Science and Technology), 2018.

[16] Thacker, D.J., Campbell, J.A., Johnson, R.L., The Effect of Soil Compaction on Root Penetration, Mechanical Impedance and Moisture-Density Relationships of Selected Soils of Alberta. Alberta Conservation and Land Reclamation Management Group Report #RRTAC OF-9, 1994, pp. 37

[17] Basha, E. A., Hashim, R., Mahmud, H. B., and Muntohar, A. S., Stabilization of residual soil with rice husk ash and cement, construction and building materials, Vol. 19, Issue 6, 2005, pp. 448-453.

[18] Kaur, I. and Jha, J. N., Effects of Rice Husk Ash - Cement Mixtures on Stabilization of Clayey Soils, IJCA Proceedings on International Conference on Advancements in Engineering and Technology Vol. 8, 2016, pp.30-33.

[19] Ahmad, J., Rosli, M. I. F., and Rahman, A. S. A., The Effect of Rice Husk Ash (RHA) Mixtures on Geotechnical Properties of Soil, In Regional Conference on Science, Technology and Social Sciences, 2018, pp. 345-352.

[20] Qasim, M., Bashir, A., Tanvir, M. and Anees, MM, Effect of rice husk ash on soil stabilization, Bulletin of Energy Economics (BEE), Vol. 3, Issue 1, 2015, pp. 10-17.

[21] Jumikis, A. R., Geology and soils of the Newark (NJ) metropolitan area. J. Soil Mech. Found. Eng., Vol. 93, SM2, 1946, pp. 71–95.

[22] Boltz, L. R., Bension, C. H. and Boutwell, G. P. 1998. Estimating optimum water content and maximum dry unit weight for compacted clays. J. Geotech. Geoenviron. Eng., Vol. 124, Issue 9, 1998, pp. 907–912.

[23] Sridharan, A., and Nagaraj, H. B., Soil compaction and permeability prediction models. Ground Improve, Vol. 9, Issue 1, 2005, pp. 17–22.

[24] Matteo, L. D., Bigotti, F. and Ricco, R., Best – fit models to estimate modified proctor properties of compacted soil. J. Geotech. Geoenviron. Eng., Vol.135, Issue 7, 2009, pp. 992–996.

[25] Bera, A. K. and Ghosh, A., Regression model for prediction of optimum moisture content and maximum dry unit weight of fine grained soil, Int. J. Geotech. Eng., Vol. 5, Issue 3, 2011, pp. 297–305

[26] Eberemu, A. O., and Sada, H., Compressibility characteristics of compacted black cotton soil treated with rice husk ash, Nigerian Journal of Technology, Vol. 32, Issue 3, 2013, pp. 507-521.

[27] Qu, J., Li, B., Wei, T., Li, C. and Liu, B., Effects of rice-husk ash on soil consistency and compactibility, Catena, Vol. 122, 2014, pp.54-60.

[28] Behak, L., Soil Stabilization with Rice Husk Ash. Rice-Technology and production, 2017, pp. 29.

[29] Muntohar, A. S., and Hantoro, G., Influence of rice husk ash and lime on engineering properties of a clayey subgrade, Electronic Journal of Geotechnical Engineering, Vol. 5, 2000, pp. 1-9.

[30] Eisazadeh, A., Bhurtel, A. and Phai, H., May. Compaction characteristics of Bangkok clay stabilized using rice husk ash, bottom ash, and lime. In IOP Conference Series: Materials Science and Engineering, Vol. 527, 2019, Issue 1, pp. 012039,

SEE-Pattaya 2021

The Seventh International Conference on

Structure, Engineering & Environment

10-12 November 2021

Pattaya, Thailand

- The "International Journal of GEOMATE" is a Scientific Journal of the GEOMATE International Society that encompasses a broad area in Geotechnique, Construction Materials and Environment.
- The key objective of this journal is to promote interdisciplinary research from various regions of the globe.
- The editorial board of the journal is comprised of extensively qualified researchers, academicians, scientists from Japan and other countries of the world.
- It is peer-reviewed Journal that is published quarterly till 2015 and now monthly. All articles published in this journal are available on line.
- Contributors may download the manuscript preparation template for submitting paper or contact to the Editors-in-Chief

[editor@geomatejournal.com]